Étude de population des noyaux actifs de galaxie au TeV avec les télescopes H.E.S.S. et étude de variabilité du blazar PKS 2155-304 avec modélisation SSC

Jill Chevalier

Communauté
UNIVERSITÉ Grenoble Alpes

THÈSE

Pour obtenir le grade de

DOCTEUR DE LA COMMUNAUTE UNIVERSITE GRENOBLE ALPES

Spécialité : Physique Subatomique et Astroparticules

Arrêté ministériel : 25 mai 2016

Présentée par

Jill CHEVALIER

Thèse dirigée par **Giovanni LAMANNA (LAPP/IN2P3)** et codirigée par **David SANCHEZ (LAPP/IN2P3)**

préparée au sein du **Laboratoire d'Annecy de Physique des Particules**
dans **l'École Doctorale de Physique**

Étude de population des noyaux actifs de galaxie au TeV avec les télescopes H.E.S.S. et étude de variabilité du blazar PKS 2155-304 avec modélisation SSC

Active Galactic Nuclei population study at TeV with the H.E.S.S. telescopes and variability studies of the blazar PKS 2155-304 with SSC modelling

Thèse soutenue publiquement le **28 juin 2017**,
devant le jury composé de :

Monsieur Benoît REVENU
Directeur de recherche, SUBATECH, Rapporteur
Monsieur Mosé MARIOTTI
Professeur, Université de Padoue, Rapporteur
Monsieur Jean-Philippe LENAIN
Chargé de recherhe, LPNHE, Examinateur
Monsieur Pierre SALATI
Professeur, LAPTh, Président

"There is a theory which states that if ever anyone discovers exactly what the Universe is for and why it is here, it will instantanely disappear and be replaced by something even more bizarre and inexplicable.
There is another theory which states that this has already happened."

The Hitchhiker's Guide to the Galaxy, Douglas Adams

Avant-propos (version française)

Ce travail de thèse a été produit pendant mes 3 ans au LAPP (Laboratoire d'Annecy de Physique des Particules) après être arrivée en Octobre 2014 dans l'équipe d'astronomie γ. Il concerne, comme le titre l'indique, l'étude des noyaux actifs de galaxie pour essayer de mieux comprendre ces bêtes cosmiques.

Ce manuscrit est écrit en anglais pour une meilleure diffusion mais contient tout de même des résumés en français à la fin de chaque partie et est organisé de la manière suivante :

- Partie 1 : c'est la partie d'introduction qui explique comment l'astronomie γ s'est développée pour étudier les sources du rayonnement cosmique (Chapitre 1) et qui présente en détails les noyaux actifs de galaxie (Chapitre 2). Le but de ce deuxième chapitre est de faire comprendre ce qu'est un noyau actif galaxie pour ensuite se concentrer plus spécifiquement sur les blazars (leurs différents types et les questions encore sans réponse sur leur fonctionnement) qui seront les objets au centre de toutes les analyses des autres chapitres.

- Partie 2 : "Observations au TeV avec les télescopes H.E.S.S.". J'ai eu la chance de faire partie de la collaboration H.E.S.S. pendant ma thèse, ce qui m'a permis de prendre part à plusieurs projets. Tout d'abord le Chapitre 3 introduit le principe de détection Cherenkov utilisé pour détecter les photons γ qui arrivent dans notre atmosphère. Les télescopes H.E.S.S. et la chaîne d'analyse sont ensuite présentés, de manière à ce que les résultats d'analyses des chapitres suivants soient facilement compréhensibles. Les chapitres 4, 5 et 6 décrivent chacun des projets différents auxquels j'ai participé :

  - Chapitre 4 : "Simulations Run-Wise", un projet très technique consistant à changer de schéma de simulation afin de mieux comprendre notre instrument.
  - Chapitre 5 : "HEGS", un projet d'étude du ciel extragalactique avec les télescopes H.E.S.S. afin de faire des études de populations de noyaux actifs de galaxie.
  - Chapitre 6 : "Exploration de la séquence blazar avec H.E.S.S.". La séquence blazar reste encore à vérifier notamment au TeV où ce sont majoritairement des HBLs qui sont détectés. Ce chapitre présente comment j'ai sélectionné des blazars (de type LBL et X-HBL) afin de les observer avec H.E.S.S., ainsi que les analyses après observations.

- Partie 3 : cette partie présente le projet qui a été au coeur de ma thèse depuis le début et concerne l'étude de la variabilité du blazar PKS 2155-304. On dispose d'une grande quantité de données sur ce blazar, je les ais donc analysées afin d'étudier sa signature en variabilité. Ensuite, dans le Chapitre 8, je compare les résultats des données à ceux d'un modèle leptonique particulier pour voir si ce modèle est valide ou non. Il serait très intéressant de voir ces études de variabilité appliquées à d'autres blazars, c'est le but du dernier chapitre.

Foreword

This thesis work has been done during the 3 years I spent working at the LAPP (Laboratoire d'Annecy de Physique des Particules), after my arrival in October 2014 in the γ-ray astronomy team. As the title says, it is on the study of active galactic nuclei to try to understand better these cosmic beasts.

This manuscript is written in English for a better diffusion but will have summaries written in French and is organized as follow:

- Part 1: it is the introduction part, explaining how γ-ray astronomy started and developed to study the sources of cosmic rays (Chapter 1) and presenting in details what are active galactic nuclei to focus more on blazars afterwards (their different types and the questions still waiting for answers) as they will be in the center of all the analyses presented in other chapters.

- Part 2: "TeV observations with H.E.S.S.". I had the chance to be part of the H.E.S.S. Collaboration and to be involved in different projects. Before describing them, Chapter 3 describes the Cherenkov detection principle used to detect γ rays arriving in our atmosphere. The H.E.S.S. telescopes and the corresponding analysis chain are presented in order to make the next analysis results easy to grab. Chapters 4, 5 and 6 describe each a different project in which I took part:

  - Chapter 4 : "Run-Wise Simulations", a very technical project to change the simulation framework in order to understand better our instrument.
  - Chapter 5 : "HEGS", a survey of the TeV extragalactic sky with the H.E.S.S. telescopes to do population studies of active galactic nuclei.
  - Chapter 6 : "Exploring the blazar sequence with H.E.S.S.". The blazar sequence still has to be verified at TeV energies where HBLs are the main type of blazars detected. This chapter presents how I selected blazars (of LBL and X-HBL types) to observe them to try to understand better the blazar sequence.

- Part 3: this part presents the project which has been at the heart of my work since the beginning of the thesis and is about the study of the variability of the blazar PKS 2155-304. Chapter 7 presents the data and time series analyses I made on the huge dataset we have on this object. Then, Chapter 8 is dedicated to the development of a time-dependent model to compare the theoretical expectations to the experimental results, in order to validate or not this type of model. It would be of great interest to see these kind of variability studies applied to other blazars, this is the topic of the last chapter.

Acknowledgements

It is customary to thank first people from the jury and the director of the thesis. But since in the small discours I gave after my PhD defense, I shamefully forgot to thank my parents[1], I will start with them. So thank you a thousand times Mom and Dad, for a lot of things, to have supported me to go in science to do what I wanted to and also to have always been here for me during this three not always easy years.

Now, back to custom. I want to thank the jury to have read these 200 pages and to have given me some nice feedback and most of all to have appreciate my work!

Many thanks also to the whole AstroGamma team at LAPP: David, Armand, Gilles, Giovanni, Cyril, Thomas, Florian & Quentin. It was cool working with you in the nice environment of the lab. Special thanks to David, you followed me the entire way, even after you realised I was not drinking nor preparing coffee.

In 3 years, you (fortunately!) make some friends, some of them were in the same lab or in the H.E.S.S. Collaboration, doing a PhD or a post-doc or even permanent. I spent really good time with Cécile, Yoann, Marine, Sami, Cyril, Vivian, Laura, Mathieu, Mathieu, Mathieu, Mathieu and Matthieu (yes all different persons), Sabrina, Markus, Floriana, Daniel, Olga and all the lab climbing team and many more... I enjoyed a lot our time together at the lab, during collaboration meetings or conferences, or just chilling around the lake or in the mountains.

Special big thanks (the ones where I am doing a heart shape with my hands, cheesy time coming) to Éva, Benoît, Cécile and Sabrina. Éva, I know you since university in Bordeaux and we always stayed in touch, I was always happy to go back to Bordeaux to see you and you are convinced I will have a Nobel prize one day (I can try). Benoît, aka Benuts, we became friends thanks to beer and gnocchis at Grenoble during the last year of Master, but since then, we talked almost everyday to share our PhD joys and sadnesses or just news about our lifes (and we both know a lot of stuff happened!). Cécile, I met you the first day I arrived in Annecy to find a flat, and now we go running, hiking, chilling, climbing together and I loved (and still love) it! Sabrina you are the best reason I am glad I was in the H.E.S.S. Collaboration I think. I met a lot of cool people with whom I had a lot of good times/beers but you were the best one I could visit to go running and laughing in the mountains with!

And last but not least, thank you Simon. It is a euphemism/understatement to say I am happy I met you. There are a lot of stuffs I could say but I don't want to sound too cheesy (but I'm already sounding cheesy I think right?[2]). Thank you for supporting me during the hard writing period (unfortunately for you, you arrived right in the middle of it), for the snowboarding, wakeboarding, skating, hiking and whatever-ing nice times I am having with you!

I will stop here as I never meant to write something so long and I'm reaching the bottom of the page but if I had a peotic side, I would thank also the mountains, lakes, rivers, forests and winters of the Alps for giving me such a good time during this three years!

[1] I blame the stress and the fatigue, I did not do it on purpose I swear! Will you ever forgive me?

[2] Also I can't write something like "Duuuuuude, it was nice to do all the booooooom chakalaka things with you to remove some stress, high five, your GF"

Contents

List of Abbreviations

AGN	Active Galactic Nuclei
BLR / BLRG	Broad Nine Region / Broad Line Radio Galaxy
CGRO	Compton Gamma Ray Observatory
CTA	Cherenov Telescopes Array
EBL	Extragalactic Background Light
Fermi-LAT	*Fermi* Large Area Telescope
FR	Faranoff-Riley
FSRQ	Flat Spectrum Radio Quasars
GUI	Graphical User Interface
HE	High Energy
H.E.S.S.	High Energy Stereoscopic System
HBL	High frequency peaked BLLac
HSP	High Synchrotron Peaked
HEGS	H.E.S.S. ExtraGalatic sky Survey
IACT	Imaging Atmospheric Cherenkov Telescopes
IBL	Intermediate frequency peaked BLLac
ISP	Intermediate Synchrotron Peaked
LBL	Low frequency peaked BLLac
LSP	Low Synchrotron Peaked
LSP	Lomb-Scargle Periodogram
MAGIC	MajorAtmospheric Gamma-ray Imaging Cherenkov Telescopes
MWL	Multi-wavelength
NLR / NLRG	Narrow Line Region / Narrow Line Radio Galaxy
NSB	Night Sky Background
PSD	Power Spectral Density
PSF	Point Spread Function
RLQ	Radio Loud Quasar
RQQ	Radio Quiet Quasar
RWS	Run Wise Simulations
RXTE	*Rossi X-ray Timing Explorer*
SED	Spectral Energy Distribution
SMARTS	Small and Moderate Aperture Research Telescope System
SSC	Synchrotron Self-Compton
Sy	Seyfert galaxy
***Swift*-XRT**	*Swift* X-Ray Telescope
ToO	Target of Opportunity
TS	Test Statistic
UHECR	Ultra High Energy Cosmic Rays
UL	Upper Limit
VERITAS	Very Energetic Radiation Imaging Telescope Array System
VHE	Very High Energy
XMM-Newton	X-ray Multi Mirror Mission

Part I

Introduction

Chapter 1

A brief history of the γ-ray astronomy

Contents

The γ-ray astronomy started ~ 50 years ago and is now expanding to reach the golden age. Everything started with finding the cosmic rays origin. More than 100 years have passed since the discovery of the cosmic ray radiation. Nevertheless, the question of its origin is still one of the biggest issue in the field of astrophysics. To answer it, astrophysicists started to study the objects where the particles could be accelerated up to PeV energies, to explain the origin of the cosmic rays of the highest energy, leading to the growth of the field of γ-ray astronomy. Nowadays we observe γ rays to have a better understanding on the processes at plays in supernova remnants, pulsars and active galactic nuclei and to study the Universe and its properties (dark matter, extragalactic background light...)

1.1 Cosmic rays

Cosmic rays were discovered by Victor Hess in 1912. They are charged particles (mainly protons, then electrons, their anti-particles and nuclei) travelling through the Universe until they get detected on Earth. When arriving on Earth, they interact with the atmosphere creating showers of secondary particles propagating towards the ground. The study of the cosmic ray atmospheric showers led to several particle physics discoveries:

the positron by Carl David Anderson in 1932, who was awarded 4 years later the Nobel Prize for his discovery, and other particles like muons and mesons some years later.

Several experiments like CREAM, PAMELA and more recently AMS-02 and the Pierre Auger Observatory studied the cosmic rays to understand better their nature and their origin. What are they? Where do they come from? How are they produced?

Figure 1.1 shows the cosmic ray spectrum. It can be described by a power law[1] ($\propto E^{-\Gamma}$) over more than 10 decades in energy and more than 30 in flux. But looking closer, there are two breaks in the spectrum, generally called the knee, at 1 PeV, and the ankle at 4×10^3 PeV.

Before the knee, the power law index is $\Gamma = 2.7$ and the particles are believed to originate from our galaxy. The trajectory of charged particles through the Galaxy is curved due to the Galactic magnetic field. This curvature is caracterised by the Larmor radius $R \sim E/ZB$, where E is the energy of the particle, Z is the charge and B the magnetic field strength. If the particle if energetic enough its Larmor radius is greater than the characteristic size of the Galaxy $\sim 10^4$ pc, and the particle escapes. After the knee, the power law index softens at $\Gamma = 3$ and the origin of the particles of higher energy is still subject to debate: are the particles accelerated in galactic Pevatrons or are particles coming from extragalactic accelerators? The ankle is caracterised by a hardening of the spectrum with $\Gamma = 2.5$ and such highly energetic particles are thought to be from extragalactic origin.

Victor Hess discovered the cosmic rays during a balloon measurement to assess the origin of a radiation which was discharging electroscopes.

In the beginning of the 20th century, it has been discovered that electroscopes where spontaneously discharging. Scientists first guessed that it was due to the natural radioactivity of Earth.

Between 1911 and 1912, Victor Hess did several ballon flies (left panel below) to measure the discharge speed of electroscopes at different altitudes, up to 5300 m.

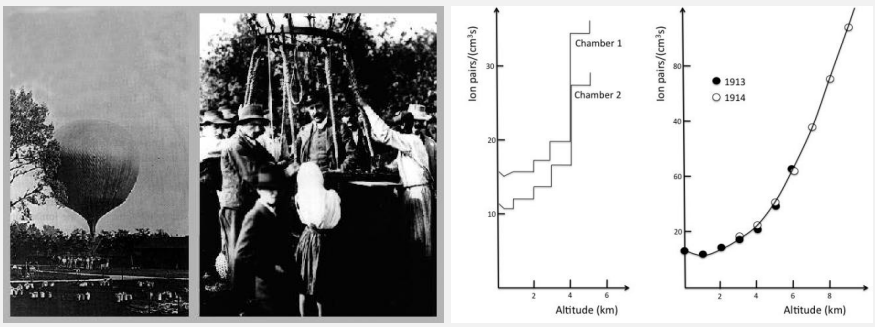

His results (empty circles on the right panel above) showed that the ionisation decreases around 1000 m then increases strongly with altitude, proving the extra-terrestrial origin of the radiation, called after cosmic rays.

The dependency of the ionisation levels with East-West direction (done in 1933 by Pierre Auger and Louis Leprince-Ringet) shows that cosmic rays are positively charged particles.

[1] Except the really low energy part where cosmic rays undergo solar modulation

Since cosmic rays are deflected by the Galactic magnetic fields, we need a neutral messenger, like photons, propagating in straight line to trace back their origin. The presence of very high energy photons (in the TeV range) indicates the presence of ultra high energy cosmic rays (UHECR, $E \sim 1$ PeV) in order to produce them. Cosmic accelerators able to accelerate particles up to PeV energies are generally called Pevatrons (HESS Collaboration et al., 2016). This is how the quest for cosmic accelerators like supernovae, pulsars, active galactic nuclei and more began in the γ-ray astronomy.

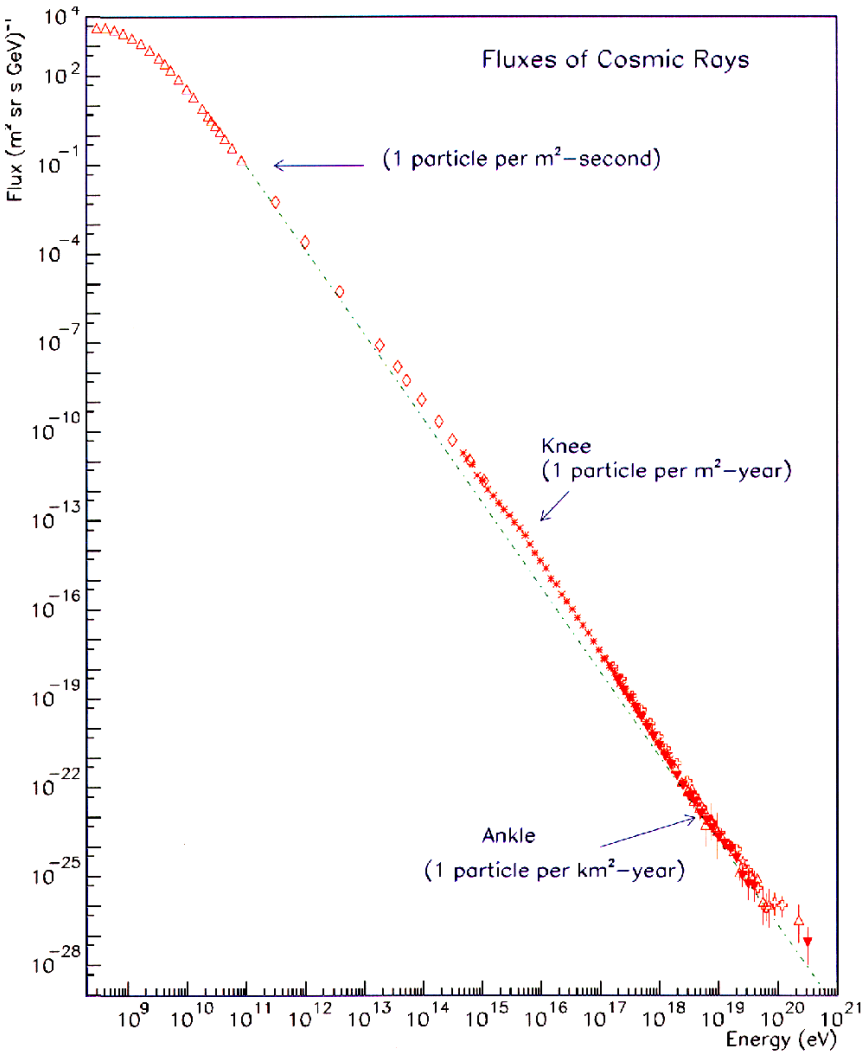

FIGURE 1.1: Cosmic ray spectrum (see text for more details) with data accumulated from different experiments (©Cronin, Gaisser, Swordy).

1.2 Photon radiation processes

γ rays can be produced by cosmic rays during their acceleration in the sources or during their propagation. As they travel in straight lines, γ-rays are used to probe the cosmic ray origin. It is important to know the different ways to produce γ rays and how they interact with the medium in order to understand the flux we observe on Earth.

Several different processes can create γ rays and the most dominant ones are presented in the following and will be in competition, as we will see in the next chapter, to explain the emission of blazars.

Photons can be produced by leptonic or hadronic processes/channels. Leptons (generally electrons and positrons) can produce synchrotron, Inverse Compton or Bremsstrahlung radiation. Hadrons (generally protons) will produce γ-rays mainly by photo-pion production.

1.2.1 Synchrotron process

According to the Maxwell's equations, every charged particle accelerated (by whatever means) emits radiation. Synchrotron radiation is produced when a relativistic charged particle flies in a magnetic field (the non relativistic case being called cyclotron radiation).

In the following, the term electron will refer to electron and positron since they behave the same in this case. Heavier particles such as protons can also emit Synchrotron radiation but this process can be considered negligible compared to the Synchrotron emission of electrons[2].

Let's consider a relativistic electron of energy $h\nu = \gamma mc^2$ (mass m, charge e, speed $\beta = v/c$, relativistic Lorentz factor $\gamma = 1/\sqrt{1-\beta^2}$) moving at an angle θ with respect to the magnetic field B. The Synchrotron losses per frequency and solid angle units are defined by:

$$\frac{\mathrm{d}P}{\mathrm{d}\Omega}(\nu,\gamma,\theta) = 2\,\sigma_T c\gamma^2\beta^2 U_B f(\nu)\frac{\sin^2\theta}{2\pi} \tag{1.1}$$

where $\sigma_T = 8\pi/3 \times (e^2/mc^2)^2$ is the Thomson cross section and $U_\mathrm{B} = B^2/8\pi$ the density of magnetic energy. The function $f(\nu)$ is defined as:

$$f(\nu) = \frac{9\sqrt{3}}{8\pi}\frac{1}{\nu_c}\left(\frac{\nu}{\nu_c}\right) \text{ with } F(x) = x\int_x^\infty K_{5/3}(t)\mathrm{d}t \tag{1.2}$$

where $K_{5/3}$ is the modified Bessel function of 5/3 order. ν_c is the critical frequency defined by:

$$2\pi\nu_c = \frac{3}{2}\frac{\gamma^2 eB\sin\theta}{mc} \tag{1.3}$$

$f(\nu)$ is defined normalized, meaning that $\int_0^\infty f(\nu)\mathrm{d}\nu = 1$. By integrating over the solid angle and assuming an isotropic emission:

$$P_\mathrm{sync}(\nu,\gamma) = \frac{4}{3}\sigma_T c\gamma^2\beta^2 U_B f(\nu) \tag{1.4}$$

$$\Leftrightarrow P_\mathrm{sync}(\gamma) = \frac{4}{3}\sigma_T c\gamma^2\beta^2 U_B \tag{1.5}$$

The emitted Synchrotron power is proportional to the square of the electron energy γ and to the square of the magnetic field B: $P_\mathrm{sync} \propto \gamma^2 B^2$. The more the electron is energetic and the more the magnetic field is strong, the more it will emit Synchrotron photons and looses energy.

The characteristic time of cooling for the Synchrotron process is

$$t_\mathrm{cool} = \frac{\gamma}{\dot{\gamma}_\mathrm{s}} = \frac{3mc}{4\sigma_\mathrm{T}\gamma\beta^2 U_\mathrm{B}} \tag{1.6}$$

[2] since $m_p \gg m_e$ the Synchrotron cooling time (Equation 1.6) will be longer for protons than for electrons

where $\dot{\gamma}_{\rm s}$ is defined as the Synchrotron cooling rate. High energy electrons will lose energy faster, especially in a strong magnetic field. For an electron going at $0.99\ c$ in a magnetic field of 0.1 G, the cooling time is of 350 years.

The Synchroton emission is polarised (Rybicki and Lightman, 1979). The polarisation rate depends on the frequency and can be written as (Bjornsson and Blumenthal, 1982):

$$\Pi(\nu) = \frac{1+\alpha(\nu)}{5/3+\alpha(\nu)} \tag{1.7}$$

where α is the frequency-dependent photon index. This formula is valid only if the magnetic field lines are aligned.

1.2.2 Inverse Compton process

A charged particle can give away part of its energy to a photon of low energy by the process of Inverse Compton diffusion. There are two regimes in this process:

- the Thomson regime: when the energy of the photon is negligible compared to the mass energy of the electron: $E_{\rm ph} \ll 2mc^2$;
- the Klein-Nishina regime: when the energy of the photon is much larger than the mass energy of the electron: $E_{\rm ph} \gg 2mc^2$. All of the electron energy is transfered to the photon.

Let's consider an isotropic photon field of energy $h\nu_0 = \epsilon_0 mc^2$. Averaging over the direction of arrival of the electrons, one has the Inverse Compton power:

$$P_{\rm IC}(\nu,\gamma,\nu_0) = \frac{4}{3}\sigma_T c\gamma^2\beta^2 U_{\rm ph}(\nu_0) g(\nu,\gamma,\nu_0) \tag{1.8}$$

where $U_{\rm ph}$ is the energy density of the soft photons (the low energy photons before the Inverse Compton interaction):

$$U_{\rm ph}(\nu_0) = mc^2 \int \epsilon_0 n(\epsilon_0) {\rm d}\epsilon_0 \tag{1.9}$$

The function $g(\nu,\gamma,\nu_0)$ is normalized such as its integration over ν is 1, and has two definitions depending on the Thomson or Klein-Nishina regime:

$$g(\nu,\gamma,\nu_0) = 6x^2\frac{(1-x)}{\nu} \text{ (Thomson regime)} \tag{1.10}$$

$$g(\nu,\gamma,\nu_0) = \frac{9x^2}{\nu}[2\kappa\ln\kappa + (1-\kappa)(1+2\kappa+\gamma\epsilon_0 x)] \text{ (Klein-Nishina regime)} \tag{1.11}$$

with $x = \nu/4\nu_0\gamma^2$ and $\kappa^{-1} = x^{-1} - 1$.

The emitted power by Inverse Compton scattering (integrating over ν) is:

$$P_{\rm IC}(\gamma,\nu_0) = \frac{4}{3}\sigma_T c\gamma^2\beta^2 U_{\rm ph}(\nu_0) \tag{1.12}$$

Like the Synchrotron losses, the Inverse Compton ones are proportional to γ^2.

Equations 1.5 and 1.12 are similar. The ratio of the Synchrotron losses over the Inverse Compton losses is the ratio of the density of magnetic energy $U_{\rm B}$ and the energy density of soft photons $U_{\rm ph}$:

$$\frac{P_{\rm sync}}{P_{\rm IC}} = \frac{U_{\rm B}}{U_{\rm ph}} \tag{1.13}$$

Like Equation 1.6, the Inverse Compton cooling time can be defined as: $t_{\rm cool} = \gamma/\dot{\gamma}_{\rm IC}$ with the Inverse Compton cooling rate $\dot{\gamma}_{\rm IC} = P_{\rm IC}(\gamma)/mc^2$. Combining Equations 1.12 with the previous one, one gets:

$$t_{\rm cool} = \frac{3}{4}\frac{mc}{\sigma_T c\gamma\beta^2 U_{\rm ph}} \tag{1.14}$$

The more energetic the electron is, the faster it will loose its energy by Inverse Compton scattering. Also, the more seeds photons for the scattering, the more energy the electron will loose.

1.2.3 Bremsstrahlung

Bremsstrahlung is a radiation produced by a charged particles when it crosses the electromagnetic field of an ion or nucleus. This process is particularly effective on electrons and the energy of the emitted photon can be of the same order of magnitude as the initial energy of the electron. The electrons around the nucleus hide its charge, so the more electrons the ion will have, the less the interaction will be effective.

The total power emitted by an electron of energy E evolving in the interstellar medium (partially ionized) can be written (Rybicki and Lightman, 1979):

$$P_{\rm brem} = \frac{e^6}{16\pi^3\varepsilon_0^3 m^2 c^4 \hbar}\sum_i^N n_i Z_i(Z_i+1)E\left[\ln(183/Z_i^{1/3}) - \frac{1}{8}\right] \tag{1.15}$$

where N is the total species of ion, each of them of density n_i and charge Z_i.

For example, the characteristic time of the Bremsstrahlung in a neutral medium of density n is:

$$t_{\rm brem} = 4\times10^7\left(\frac{n}{1\ {\rm cm}^{-3}}\right)\ {\rm years} \tag{1.16}$$

In the interstellar medium, assuming $n \sim 10^{-3}$ ions per cm^3, $t_{\rm brem} \sim 40,000$ years, quite negligible compared to the other characteristic times of the other processes. For an electron population with a density described by a power law of index p, the spectrum of the Bremsstrahlung is also a power law of index p (Longair, 2011).

1.2.4 Photo-pion production

As seen at the beginning of this chapter, cosmic rays are mostly composed of protons which can interact with the interstellar medium. They can interact with a cold nucleus (mainly hydrogen) and create secondary particles by inelastic collision:

$$\begin{aligned} p + p \rightarrow\ & \pi^0 + \pi^+ + \pi^- \\ & \pi^0 \rightarrow \gamma + \gamma \text{ with a life time of } t_{\pi^0} \sim 8\times10^{-17}\ {\rm s} \end{aligned} \tag{1.17}$$

The π^+ and π^- will decay into leptons (electrons, muons and neutrinos). The electrons will be able to produce photons from the leptonic processes described above while the neutrinos might be detected on Earth.

The π^0 has 99% of chances to decay into a γ pair. Each γ will have an energy of $E_\gamma = m_{\pi^0}c^2/2 \sim 70$ MeV. The π^0 will have, on average, 17% of the energy of the initial cosmic ray. Considering that the energy of the initial cosmic ray is much larger than the energy of the hydrogen nucleus, a γ produced in these conditions will have on average 8.5% of the cosmic ray initial energy (if the cosmic ray particle has an energy of $E = 1$ TeV, then $E_\gamma = 85$ GeV).

Acceleration processes give a spectrum which can be approximated by a power law $J_p(Ep) \propto E_p^{-\Gamma}$. The γ-ray spectrum Φ_γ produced by a proton distribution in a medium mainly composed of hydrogen of density n_H is (Kelner, Aharonian, and Bugayov, 2006):

$$\Phi_\gamma(E_\gamma) = cn_H \int_0^1 \sigma_{\mathrm{p-p}}(E_p) J_p(E_p) F_\gamma(x, E_p) \frac{\mathrm{d}x}{x} \text{ where } x = \frac{E_\gamma}{E_p} \tag{1.18}$$

with $\sigma_{\mathrm{p-p}}$ is the cross section for the inelastic proton-proton interaction and $F(x, E_p)$ is the analytical function parametrized by the equation 58 of Kelner, Aharonian, and Bugayov, 2006.

Since $\sigma_{\mathrm{p-p}}$ is almost constant above 1 GeV, the γ-ray spectrum follows the one of the proton population at high energy.

However the (inter)galactic medium and the cosmic rays are not only composed of protons but also from a small fraction of heavier nuclei. Because of this, the normalisation of the γ-ray spectrum is underestimated and a correction factor of 1.45 should be applied ($n = 1.45 n_H$) to take this effect into account (Dermer, 1986).

The characteristic time for this hadronic process is:

$$t_{pp\to\pi^0} = 5.3 \times 10^7 \left(\frac{n}{1\ \mathrm{cm}^{-3}}\right)^{-1} \text{ years} \tag{1.19}$$

In the galactic medium, this process is totally ineffective with a cooling time of $t_{pp\to\pi^0} \sim 5.2 \times 10^{10}$ years.

1.3 A glimpse at the non thermal universe

1.3.1 Supernova remnants, pulsars and active galaxies

Supernova remnants

A supernova is the spectacular death of a star of mass $M > 8\,M_\odot$. Such an event is so extreme that its luminosity can reach the one of its host galaxy. So bright that it can be seen by the naked eye, supernovae events have been recorded since Antiquity.

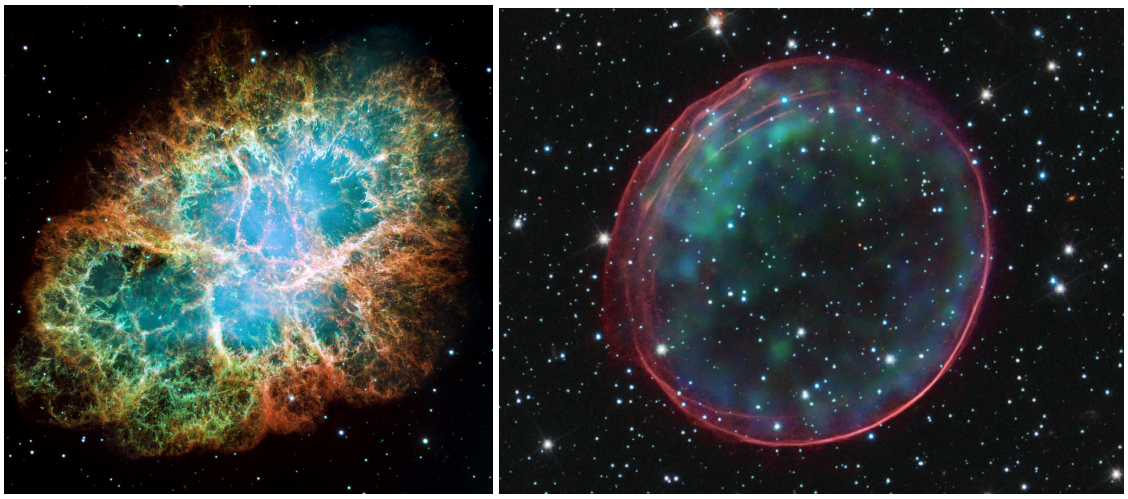

FIGURE 1.2: Optical and X-ray composite pictures of the Crab Nebula (©NASA, ESA, J. Hester and A. Loll) on the left and of SNR 0509-67.5 in the Large Magellanic Cloud (©X-ray: NASA/CXC/SAO/J.Hughes et al, Optical: NASA/ESA/Hubble Heritage Team (STScI/AURA)) on the right.

There are several types of supernovae (SN Ia, SN Ib, SN II...) depending on spectral characteristics and physical properties. The SN Ia type corresponds to the explosion of a white dwarf reaching the limit of the Chandrasekhar mass, because it was accreting matter from a companion star. The others types (II, Ib and Ic) correspond to massive stars which have exhausted their fusion fuel. The difference between the II, Ib and Ic types resides in their spectrum depending if it shows line of helium, silicium or other. The gravitational force wins over the radial pressure since the fusion is no longer going on. The core of the star collapses on itself while the external layers explode. The core transform into a compact object: neutron star or black hole depending on the star's mass. Figure 1.2 shows the ejected matter form the supernova remnant (SNR) for the Crab Nebula and SNR 0509-67.5. After the supernova, the ejecta expands in the Galactic medium like a shell.

The non-thermal emission coming from SNR shows that electrons and/or protons are accelerated in the shocks of the ejecta. However the mechanisms and the particle population is still not clear since new observations sometimes challenge the main models. Moreover there is still an uncertainty on the fact that SNR could accelerate particles up to high energies. A great review on supernova at γ-ray energies can be found in Hewitt and Lemoine-Goumard, 2015.

Pulsars

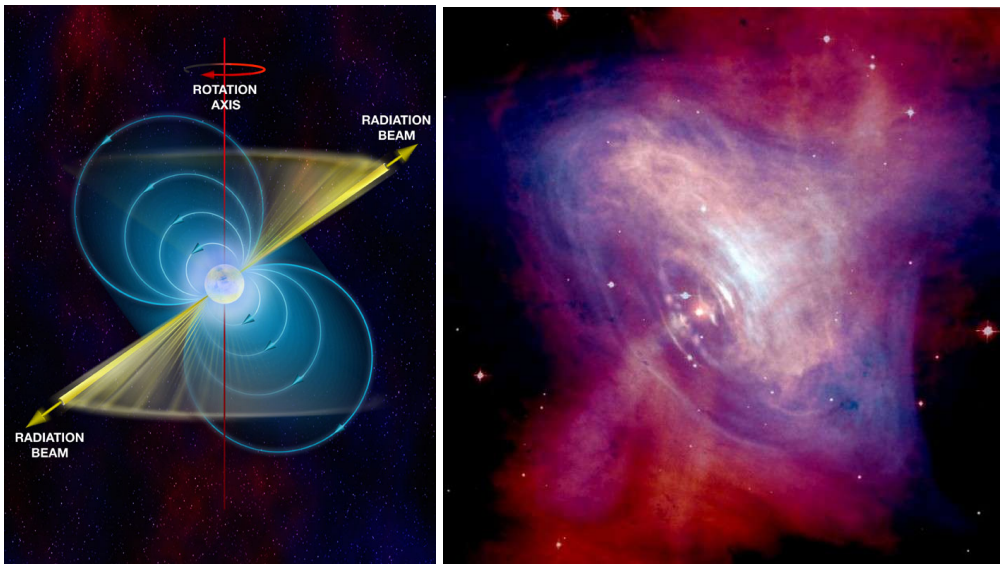

FIGURE 1.3: Left: illustration of pulsars as spinning neutron stars (©Bill Saxton, NRAO/AUI/NSF). Right: composite image of the Crab pulsar inside the Crab Nebula (©NASA).

Supernovae can give birth to neutron stars when the mass of the dying star is more or less below $28\,M_\odot$ (otherwise it will be a stellar mass black hole). Neutron stars can be in binary systems or alone and rotation-powered. They have a strong magnetic field, supposedly $B \sim 10^{11} - 10^{13}$ G, and when the magnetic axis is inclined with respect to the spins axis, the neutron star can be seen pulsing from Earth (if the beam is aligned with the observer's line of sight). These objects are called pulsars (see left panel of Figure 1.3). They were first discovered by accident by Hewish & Bell in 1967 because of their characteristic pulsation in radio.

The pulse is generally easily seen in radio and optical. When the pulsar is young enough it can also be detected in X-ray and GeV. This is the case for the famous pulsars of the Crab nebula, shown in the right panel of Figure 1.3, and of Vela.

Pulsars are though to be efficient particles accelerators thanks to their rotational power and their huge magnetic fields. The detection and study of highly energetic γ rays coming from pulsars can help to determine which process produce them in order to know if pulsars could be Pevatrons or not.

Pulsars display extreme properties allowing to study ultra dense matter, extreme magneto-hydrodynamics and general relativity. A recent and exhaustive review on pulsars can be found in Grenier and Harding, 2015.

Active galactic nuclei

Active galactic nuclei (AGN) are giant luminous beasts lying in the center of some galaxies. They are so bright that their luminosity can outshine the rest of the galaxy. They draw their energy/power from a central supermassive black hole which attracts the surrounding matter and stars, creating an accretion disk arount it. Some AGN ($\sim 10\%$ of them) eject matter at speeds close to the speed of light, creating relativistic jets.

AGN were discovered approximately 50 years ago (see Seyfert, 1943 and Hazard, Mackey, and Shimmins, 1963 for example) but a lot of mystery remains. They are the main candidate to explain the origin of cosmic rays after the knee. Chapter 2 will present as exhaustively as possible every details and challenges related on AGN.

FIGURE 1.4: Composite image of the AGN IC 3639 (©ESO / NASA / JPL-Caltech / STScI).

Gamma-Ray Burst (GRB)

During the cold war time, between the 60s and 70s, the US army launched satellites called Vela to monitor the nuclear activity of the USSR. These satellites were built to detect radiations emitted from possible nuclear bomb trials. When signal was detected in 1972,

the WW III almost started... Fortunately the satellites were capable of triangulation and it showed that the direction of the γ signal was not somewhere on Earth, but from a random position in the sky. This was the first detection of a gamma-ray burst (GRB).

GRBs are extreme explosions, known to be the brighest electromagnetic events in the Universe. Especially because they occur in a short time window, from seconds to few hours. The nature of the progenitor of GRB is still subject to debate: hypernova, merger event or tidal disruption events?

GRBs are classified into short and long GRBs depending on their duration (less or more than 2 seconds). Long events constitute $\sim 70\%$ of the GRB population and their origin is thought to be different than the one for short GRBs.

1.3.2 The dark matter mystery

It is believed by most of the scientific community that $\sim 84\%$ of the matter content of the Universe is dark matter: particles interacting mostly via the gravitational force. We do not have any direct proof of its existence but many astronomical observations could be explained thanks to the existence of dark matter: rotation curves of galaxies, formation of the cosmological structures, gravitational lensing, the missing mass of galaxies clusters, ...

FIGURE 1.5: Composite image of the galaxy cluster Abell 520. It shows the distribution of light and matter during a merger of two galaxy clusters. The starlight from galaxies is represented in orange (seen in optical), the green regions show the distribution of hot gas (seen in X-ray) and the blue areas show where most of the mass is, meaning the dark matter. ©NASA.

Figure 1.5 shows the distributions of dark matter (blue, derived from gravitational lensing observations with the Hubble Wide Field Planetary Camera 2), galaxies (orange, derived from the starlight observations of the Canada-France-Hawaii Telescope) and hot gas (green, detected by the NASA's Chandra X-ray Observatory) in the galaxy cluster Abell 520. This galaxy cluster is the merger of two other massive galaxy clusters. The gas is evidence that the collision took place because it is collisional. The image shows that the center of the cluster is filled with an unseen mass and hot gas whereas the galaxies and stars (collisionless in this kind of event) are located at the edge of the cluster. Dark matter has also a non collisionless behavior and most of the mass of the cluster (dark matter + gas) stays in the center.

A lot of efforts are done in order to detect dark matter, directly or indirectly, or by producing it at the Large Hadron Collider at CERN. In the main theory, dark matter is thought to be made of WIMPs (Weakly Interacting Massive Particles) which could produce γ-ray photons as a result of their annihilation. This would produce a line in the γ-ray spectrum around the WIMP mass. High energy experiments are looking for such a signature while cosmic ray experiments are trying to measure as precisely as possible the cosmic ray spectrum (especially for anti particles) in order to assess or not if a part of it could be explained by annihilation of dark matter.

1.3.3 The Extragalactic Background Light (EBL)

The EBL is a background photon field created by the accumulation of radiation of star formation processes. Figure 1.6 shows that it radiates in infrared and optical, from 0.1 to 1000 μm.

Looking at its spectral energy distribution, the EBL can be separated in 2 components: the first in optical is the light coming from stellar and galatic emissions and the second in infrared is coming from the dust re-emission.

During their propagation in the Universe γ rays have a certain probability to interact with the EBL photons field to create a e^+e^- pair. This absorption makes the Universe opaque to γ rays at high redshift. For example the emission of high redshift AGN will be absorbed making them difficult to detect. The maximum redshift is generally set around $z \sim 1$ but it also depends on the spectral properties of the emitting source.

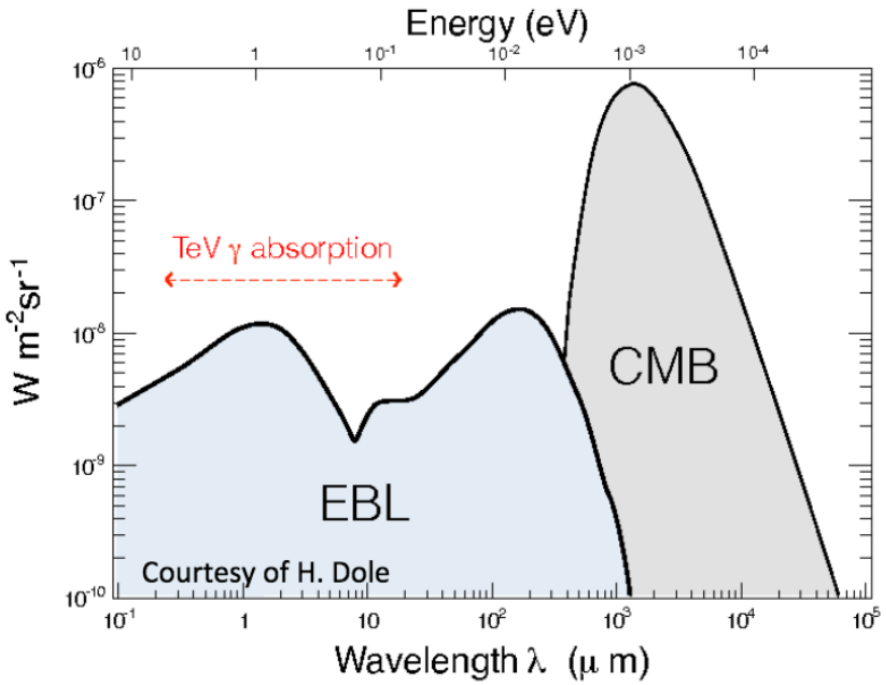

FIGURE 1.6: Spectral energy distrubition of the EBL along with the cosmic microwave background at longer wavelength.

1.4 The growth of the γ-ray astronomy

The Earth's atmosphere being opaque to γ rays, one has to try to get rid of it. The balloon experiments were unsuccessful because of the domination of the secondary γ created by the cosmic rays' atmospheric showers at high altitude. Space-based telescopes were needed.

1.4.1 The first γ-ray space-based telescopes

The first γ-ray satellites were launched at the end of the 60s and beginning of the 70s. OSO 3 (Orbiting Solar Observatory 3), operating between 1967 and 1968 to look at solar flares, showed the Milky Way as a bright γ-ray source above 50 MeV (Kraushaar et al., 1972).

Satellites like SAS-2 (Small Astronomy Satellite 2, 1972-1973, Fichtel et al., 1975) above 35 MeV and COS-B (1975-1982, Swanenburg, 1981) above 100 MeV, confirmed the diffuse emission of the Galaxy but also detected the Crab and Vela nebulae, along with their pulsed emission. Thanks to its longer livetime, COS-B produced a catalog containing 25 sources (left panel of Figure 1.7, Swanenburg et al., 1981), including an extralagatic one: the AGN 3C 273.

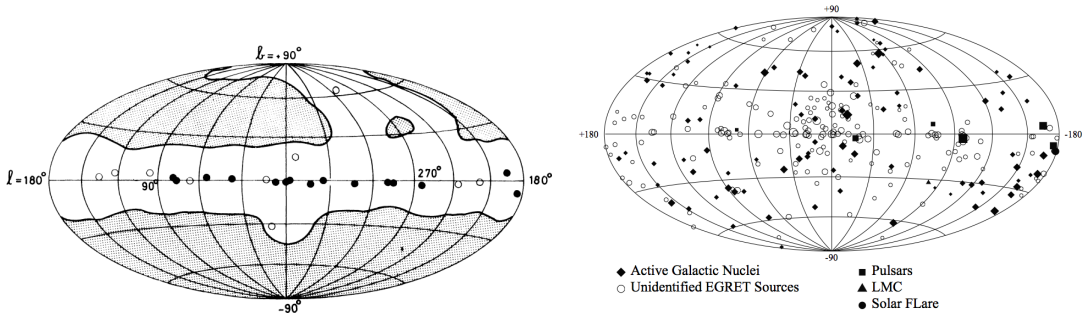

FIGURE 1.7: Left: COS-B sky map from Swanenburg et al., 1981. Right: Third EGRET Catalogue sky map from Hartman et al., 1999.

1.4.2 The CGRO era

In the 80s, the NASA developed a new satellite, the Compton Gamma Ray Observatory (CGRO, left panel of Figure 1.8) featuring 4 different instruments covering a large energy range from X-ray to γ rays (20 keV - 30 GeV). The CGRO was running from 1991 to 2000. It was composed of BATSE (Burst and Transient Source Experiment), OSSE (Oriented Scintillation Spectrometer Experiment), COMPTEL (Imaging Compton Telescope) and of EGRET (Energetic Gamma-ray Experiment Telescope). EGRET had an energy range from 20 MeV to 10 GeV with a better angular precision ($0.1°$) compared to its predecessor COS-B.

The CGRO mission was a success. The BATSE instrument detected approximately 2700 GRBs (on average one per day) uniformely distributed in the sky, disproving their Galactic origin as it was assumed for many years. The Third EGRET Catalogue (right panel of Figure 1.7, Hartman et al., 1999) showed 271 γ-ray sources including many AGN, signing the beginnings of the extragalactic γ-ray astronomy. Even if half of the sources of the catalogue were unassociated, it was one of the first γ-ray sky map and it showed the diversity of phenomena detectable in high energy.

FIGURE 1.8: Left: Deployment of the CGRO where EGRET can be seen (the dark bump at the bottom) along with OSSE and COMPTEL. Right: Illustration of the *Fermi* satellite with the LAT mounted on top.

1.4.3 The *Fermi* era

The Large Area Telescope (LAT, 20 MeV < E < 300 GeV, Atwood et al., 2009) is a pair conversion detector onboard the *Fermi* Gamma-ray Space Telescope (right panel of Figure 1.8) and operates since July 2008.

The LAT took advantage of the success of EGRET along with the new technological improvements coming from the particle physics. Its energy resolution is better than 15 % and the angular resolution of the instrument improved significantly (3° at 100 MeV and 0.04° at 100 GeV) compared to EGRET.

After the 25 sources detected by COS-B and 271 by EGRET, the *Fermi* Large Area Telescope Third Source Catalogue (3FGL, Acero et al., 2015) was released by the *Fermi* Collaboration using the first 4 years of data containing 3034 sources (more than 1000 being extragalactic) between 100 MeV and 300 GeV (Figure 1.9).

Almost 10 years have passed since the launch of *Fermi*, and it could last some more years since the non-stop monitoring of the LAT is very useful to study the behaviour of γ-ray sources with time.[3] *Fermi*-LAT data, along with the analysis tools, are public.

1.4.4 Ground based telescopes to reach higher energies

New technics have to be developed in order to detect γ rays from the ground. The idea of detecting cosmic and γ rays using the Cherenkov flash produced by the particles shower was stated by Blackett, 1948. The energy threshold of ground based telescopes is higher than space-based telescopes because if the incident γ is not energetic enough, the Cherenkov light will be too faint to be detected. More details about atmospheric showers and Cherenkov detection are provided in Chapter 4.

The first atmospheric Cherenkov telescopes (ACT) were operational in the 60s but the sensitivity was too low to see a γ signal popping out of the cosmic rays background.

The Whipple observatory (Figure 1.10), was operational in 1968 with a 10 meters mirror, huge for the time. At first, Whipple was not able to do better than its predecessors. After several technical improvements, the use of simulations to better understand the instrument response function and the application of the Hillas reconstruction (Hillas, 1985), the Whipple collaboration improved the background rejection and announced the first very high energy γ-ray source discovery in 1989: the Crab nebula (Weekes et al., 1989).

[3] The *Fermi* satellite orbits the Earth once every 96 minutes and can scan the full sky in two orbits thanks to the north-south rocking of the satellite with respect to its orbital plane.

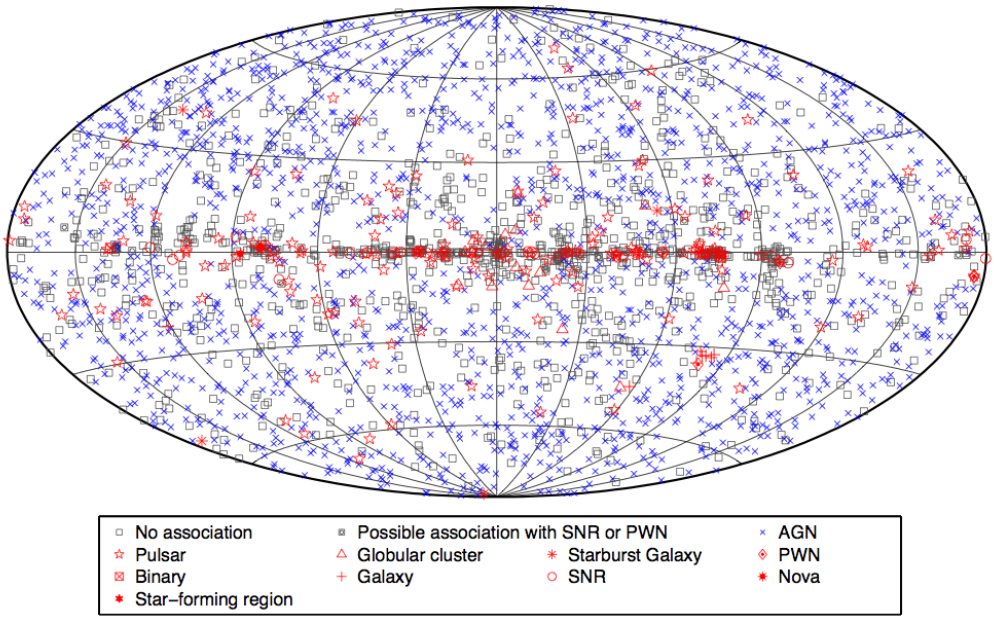

FIGURE 1.9: Sky map of the 3FGL catalog (Acero et al., 2015).

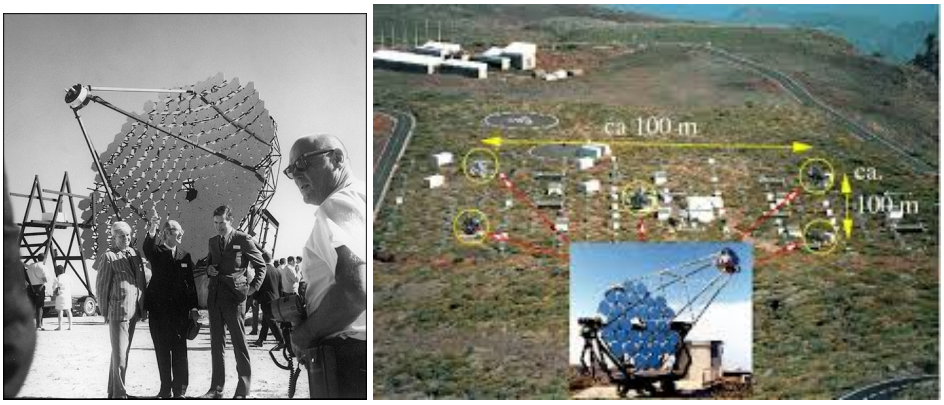

FIGURE 1.10: Pictures of the Whipple telescope (left) and the HEGRA telescopes (right).

Several other experiments using different technics confirmed the Crab signal: ASGAT (Goret et al., 1993) and THEMISTOCLE (Baillon et al., 1993).

This first discovery allowed the instruments to go through a serie of improvements. After increasing the number of pixels of their camera (from 37 to 109 pixels), Whipple announced in 1992 their second discovery: the AGN Markarian 421 (Mkn 421, Punch et al., 1992).

After this, several new instruments were developed, each of them trying new technics and improvements: CANGAROO I (1992-1998, Hara et al., 1993), MARK VI (1995-2000, Armstrong et al., 1999), HEGRA (1996-2002, Daum, Hermann, and HEGRA Collaboration, 1997), CAT (1996-2002, Barrau et al., 1998; Le Bohec et al., 1998). With its 5 telescopes (right panel of Figure 1.10), HEGRA showed the importance of the stereoscopy to image the Cherenkov cone and improve the background rejection. CAT showed that a fine-pixelised and fast camera could decrease the energy threshold.

The knowlegde gained from the first and second generations of ACT allowed to develop a third, more sensitive, generation of imaging atmospheric cherenkov telescopes in

the 2000s: H.E.S.S., MAGIC and VERITAS, which will be discussed in more details in the beginning of Chapter 4.

Before the advent of the third generation, only a handful of VHE sources were known, 2 Galactic (the Crab nebula and the SNR RX J1713.7-3946) and 6 AGN: Mkn 421, Mkn 501, 1ES 1959+650, PKS 2155-304. Since then more than 200 sources have been discovered at VHE, as shown in Figure 1.11, and this number will continue growing in the future with HAWC (González, 2011) and soon CTA.

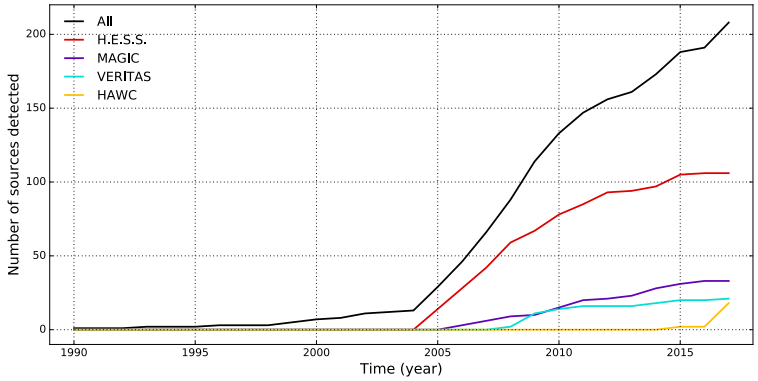

FIGURE 1.11: *Kifune* plot (T. Kifune was the first to show such a plot at the ICRC in Rome in 1995, since then, this kind of plot is named after him) showing the evolution of the number of VHE sources discovered with time.

The High-Altitude Water Cherenkov Gamma-Ray Observatory (Figure 1.12) is running since 2014 and already detected $\sim$ 20 sources between 100 GeV and 100 TeV. This observatory is located on the flanks of the Sierra Negra volcano near Puebla, Mexico at an altitude of 4100 meters. HAWC is a powerful VHE energy experiment to monitor the γ-ray sky with a duty cycle of almost 100 %. Two-third of the sky is observed in 24 hours, allowing to build long-term light curves for variability studies of active galactic nuclei.

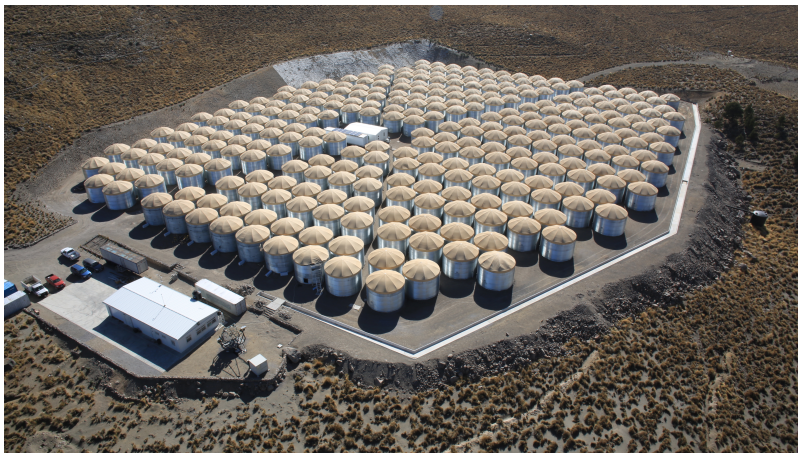

FIGURE 1.12: The HAWC Observatory (INAOE).

Chapter 2

The world of active galactic nuclei

Contents

Active galactic nuclei (AGN) are known to be one of the most energetic classes of objects in our Universe. A galaxy is defined as active when its nucleus is brighter than the rest of the galaxy. About 10% of the galaxy population is active.

Their discovery is relatively recent, 50 to 60 years ago. The beginnings of the field of AGN were a bit chaotic, with a lot of discoveries showing different features, different views of the same class of objects. Although our understanding of AGN have improved since then, the more we look, the more mystery arises.

This chapter aims to show the current status of our knowlege on AGN, starting with a historical journey to understand how they were discovered and how the standard AGN paradigm emerged.

I will focus after on the blazar sequence and on the emission models to introduce all of the concepts which will be used from Chapter 6 to 10.

2.1 The discovery of active galactic nuclei

2.1.1 Seyfert galaxies, radio galaxies and quasars

In 1943, Carl Keenan Seyfert discovered several galaxies with the same features, a bright nucleus and wider than usual emission lines (Seyfert, 1943). Spectograms showed permitted and also forbidden emission lines which were enlarged. Figure 2.1 (left panel) from Seyfert, 1943 shows the $\lambda 4860$, $\lambda 4959$ and $\lambda 5007$ lines for the nebulae NGC 1068, NGC 3516 and NGC 4151. In each objects, the lines have a different width, showing different Doppler shifts from 3,000 to 8,500 km.s^{-1}. Nowadays, AGN with these features are called Seyfert galaxies, but the field of AGN did not start here. First, the advent of radio-astronomy (thanks to technological improvements due to WW II) was needed.

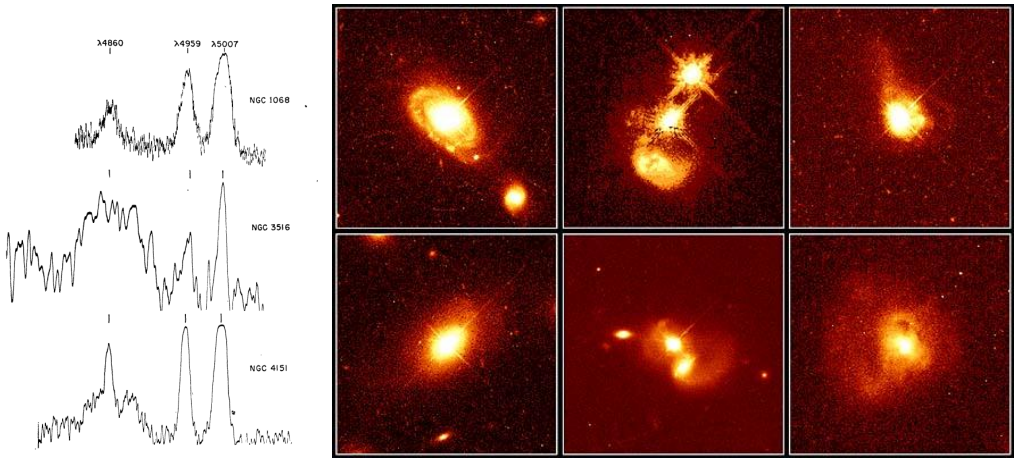

FIGURE 2.1: Left: Emission lines for the nebulae NGC 1068, NGC 3516 and NGC 4151 (Seyfert, 1943). Right: gallery of different quasars seen in optical ©J. Bahcall (IAS, Princeton), M. Disney (Univ. Wales), NASA

A radio survey of the Milky Way at 60 MHz led to the accidental discovery of a fluctuating source in the Cygnus constellation (Hey, Parsons, and Phillips, 1946). Two years later, this discovery is confirmed by Bolton and Stanley, 1948. They deduced a temperature of 4×10^6 K at 100 MHz and for the first time the thermal origin of the emission of bright objects like this one was said to be doubtful. This source was baptized Cygnus A and opened a new class: radio galaxies. In the early 50s, Baade and Minkowski, 1954 analyzed the emission lines of Cygnus A and found a Doppler shift of 16,840 km.s^{-1} implying a distance of 31 Mpc[1] and an enormous optical luminosity of 8×10^{42} erg.s^{-1}. During the same period, Hanbury Brown, Jennison, and Gupta, 1952 and Jennison and Das Gupta, 1953 reported two equal components of 2×0.3 arcmin around Cygnus A, separated by 1.5 arcmin. This morphology was puzzling and thought to be peculiar until more extragalactic radio sources displayed the same feature.

In 1949, Virgo A and Centaurus A were detected in radio and respectively associated with M 87 and NGC 5128 in optical. The complementarity between optical and radio observations was starting. In the following years, the detection of known Seyfert galaxies in radio suggested a link between Seyfert and radio galaxies.

The year of 1961 saw a new discovery in radio: 3C 48. The source was associated with an object in optical looking like a star even if the spectrum showed broad lines and variability (Matthews et al., 1961). At the time, people thought of a new type of star (no

[1]For the assumed Hubble constant at that time $H_0 = 540$ km.s^{-1}.Mpc^{-1}. Nowadays, $H_0 = 70$ km.s^{-1}.Mpc^{-1} and the current distance of Cygnus A is 230 Mpc. The parsec is defined as $648000/\pi$ astronomic units $\sim 3.1 \times 10^{16}$ meters.

links with radio galaxies or Seyfert galaxies then) until the discovery of a similar object in 1963: 3C 273, which was displaying the same features as 3C 48. Spectroscopy analysis showed a redshift of $z = 0.16$, implying the impossibility for the object to be a star. Soon after, the redshift of 3C 48 was derived giving $z = 0.37$ (for more technical details see Hazard, Mackey, and Shimmins, 1963, Schmidt, 1963, Oke, 1963 and Greenstein and Matthews, 1963). Objects like them were named quasi-stellar radio sources (QSRS) or quasi-stellar sources (QSS), which was shorten to quasars.

Figure 2.1 (right panel) is the Astronomy Picture of the Day (APOD) of November 25, 1996, showing pictures of quasars captured by the Hubble Space Telescope. The quasars are extremely bright (with diffraction spikes, like stars) and the host galaxy can be seen, sometimes spiral, elliptical or even during merging phases.

The end of the 60s marks the advent of the extragalactic X-ray astronomy, with M 87 and 3C 273 detected in 1967 and Centaurus A in 1970. More and more sources were discovered in radio, optical and X-ray with or without association in other waveband.

2.1.2 The game of the 60s: guessing what causes the high luminosity of AGN

What does power AGN? They are extremely bright despite their extragalactic distances. In the 60s, several ideas, which could seem weird now that we have a clearer picture, were explored.

Because of the puzzling morphology of radio galaxies (such as the double source structure around Centaurus A), the first idea was that they were the results of two galaxies in collision.

In 1961, Burbidge, 1961 suggested that the high luminosity could be explained by the chain reaction of supernovae ocurring in a dense cluster in the nuclei. Additional ideas exploring the dense cluster or supernova possibilities were explored by Cameron, 1962, Spitzer and Saslaw, 1966, Arons, Kulsrud, and Ostriker, 1975 and Terlevich and Melnick, 1985.

In 1963, the idea of a supermassive star ($\sim 10^8 M_\odot$) was proposed (Hoyle and Fowler, 1963a; Hoyle and Fowler, 1963b). The star would produce large amount of gravitational and thermonuclear energy. The model could also take into account the acceleration of relativistic particles and the ejection of gas clouds to explain the broad line emissions of Seyfert galaxies.

One year later, Salpeter, 1964 came with the idea that quasars could be powered by a supermassive black hole ($M_{\rm BH} \sim 10^9 M_\odot$) located in the center of the nuclei surrounded by an accretion disk. This idea is now part of the current AGN paradigm (see Section A.2 and Figure 2.3 later) but it did not receive much attention until 1969 and the 70s.

Lynden-Bell, 1969 proposed a similar idea as Salpeter and explored the emission expected from the accretion disk surrounding the black hole. He noted that *"with different values of the [black hole mass and accretion rate] these disks are capable of providing an explanation for a large fraction of the incredible phenomena of high energy astrophysics, including galactic nuclei, Seyfert galaxies, quasars and cosmic rays"*. Still, one had to wait until the discovery of stellar mass black holes in X-ray pulsars (pioneed by the detection of Cyg X-1, Oda et al., 1971) to see the idea of a black hole fed by an accretion disk accepted.

The terminology of AGN to regroup the Seyfert galaxies, radio galaxies and quasars appeared in the end of the 60s, being widely used after 1974[2] when the black hole idea was proposed. There were evidence of black hole feeding quasars but also evidence of black holes at the center of all galactic nuclei. To differenciate, the term "active" was added.

[2]Looking at a simple bibliographical search on http://adsabs.harvard.edu/

2.1.3 The riddle of the superluminal motion

The end of the 60s saw the advent of very long baselined interferometry (VLBI) in radio astronomy. This new technic improved drastically the angular resolution in radio observations and several AGN showed components of $\sim 10^{-3}$ arcsec.

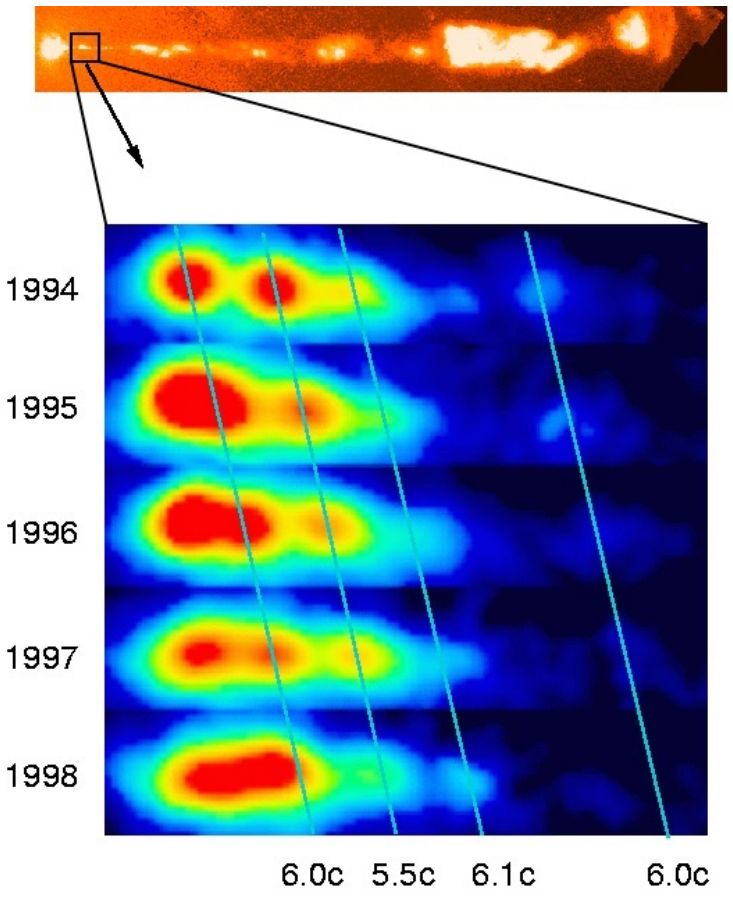

FIGURE 2.2: Hubble Space Telescope images showing the apparent supraluminal motion of matter in the inner region of the relativistic jet of M 87 (Biretta, Sparks, and Macchetto, 1999).

Observations in October 1970 from Knight et al., 1971 and in February 1971 from Whitney et al., 1971 showed a double source structure in 3C 279. In October, the structure was separated by 1.55×10^{-3} arcsec. The measurement the next February showed a separation of 1.69×10^{-3} arcsec. Given the redshift of 0.538 of the source, a change of 0.14×10^{-3} arcsec in 4 months was implying that the structure was moving at supraluminic speeds (~ 10 times the speed of light here).

Another AGN, 3C 273 was showing the same feature. Matter moving faster than light was known to be impossible and several models tried to interprate this observation. One of them was called the Christmas Tree[3] model (Whitney et al., 1971; Cohen et al., 1971). The apparently moving faster than light radio blobs would be blinking, like a Christmas tinsel, and the blob seen in February would be a different one that the one seen in October.

Figure 2.2 illustrates the apparent supraluminic motion of matter (reaching 6 times the speed of light) inside the jet of M 87 with images taken every year by the Hubble Space Telescope (Biretta, Sparks, and Macchetto, 1999).

[3] I personally love how scientists can be inventive to find nice names for models.

The explanation for such supraluminic observations came with the jet model of Rees, 1966 (see also the review of Blandford and Königl, 1979b; Blandford and Königl, 1979a): matter expelled from the nuclei at relativistic speed forming a jet.

Supraluminal motion: explanation

Let's consider a blob of matter ejecting photons at t_1 from the point A and at $t_2 = t_1 + dt$ at the point B after travelling the distance D. The observer, at point O, sees the photons from A at t'_1 and the photons from B at $t'_2 = t'_1 + \mathrm{d}t'$:

$$\begin{aligned} t'_1 &= t_1 + \frac{D_L + v\mathrm{d}t\cos\theta}{c} \text{ and } t'2 = t_2 + \frac{D_L}{c} \\ \mathrm{d}t' &= \mathrm{d}t \times (1 - \beta\cos\theta) \\ \Leftrightarrow \mathrm{d}t &= \frac{\mathrm{d}t'}{1 - \beta\cos\theta} \text{ where } \beta = v/c. \end{aligned}$$

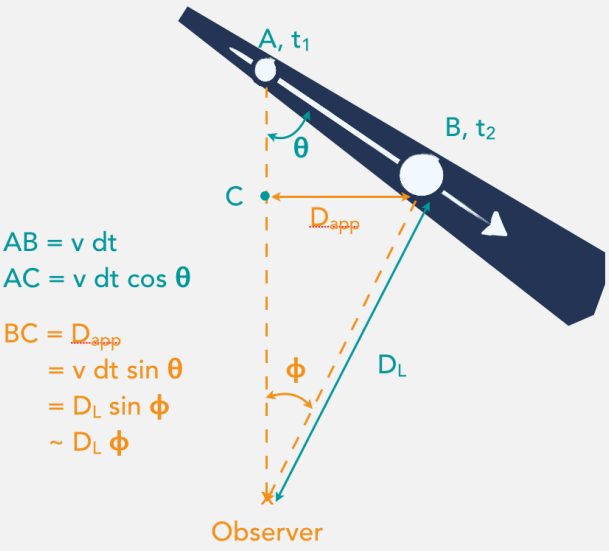

So the apparent transverse velocity seen by the observer is:

$$\begin{aligned} \beta_{\mathrm{app}} &= \frac{D_{\mathrm{app}}}{c\mathrm{d}t'} \\ &= \frac{\beta\sin\theta}{1 - \beta\cos\theta} \end{aligned}$$

The observer sees a supraluminal motion when:

$$\beta_{\mathrm{app}} > 1 \Leftrightarrow \beta(\sin\theta + \cos\theta) > 1$$

Fixing $\theta = 45°$ (as an example), it means that $\beta > 1/\sqrt{2} \Leftrightarrow v > c/\sqrt{2}$ to see an apparent speed faster than light. Also if θ gets smaller (the cosine value will grow above $\sqrt{2}/2$ towards 1 while the sinus value will decrease towards 0), the apparent velocity will appear even larger.

2.2 Fifty years after their discovery what do we know?

Shields, 1999, from whom most of the historic facts of the previous section are taken, wrote that *"much remains to be done to understand the physical processes at work in AGN. In spite of much good work, the origin and fueling of the hole, the physics of the disk, and the jet production mechanism still are not well understood."*. Almost 20 years later, this statement is still true and can be read in almost all introductions or abstracts in AGN papers[4].

2.2.1 The standard AGN paradigm

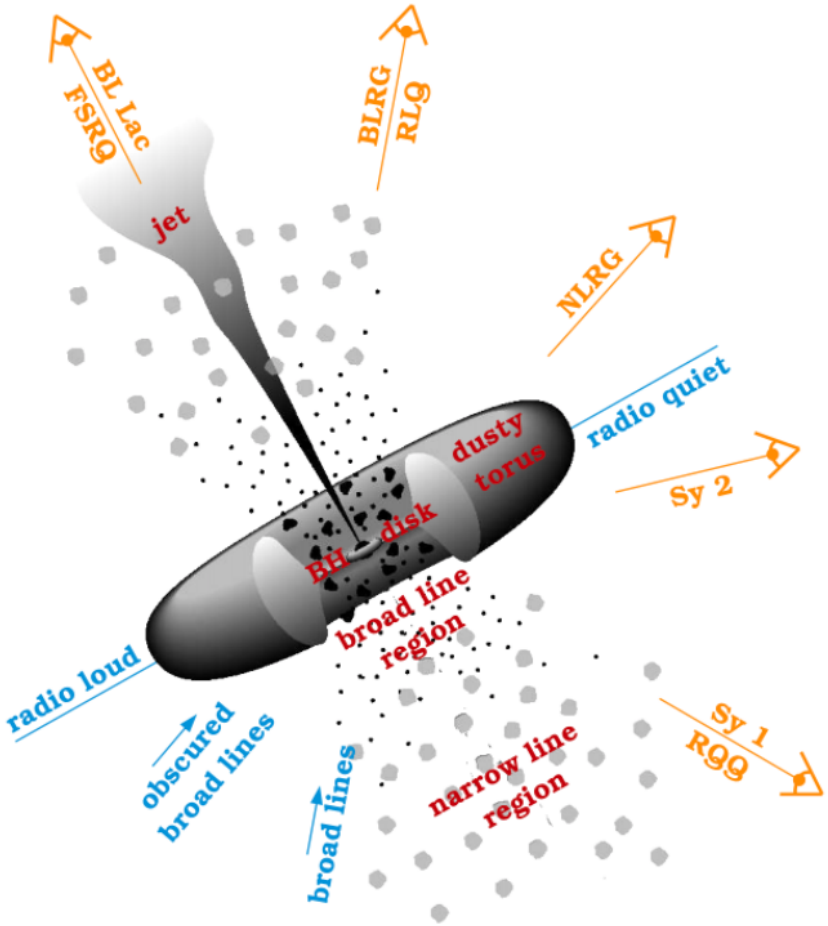

FIGURE 2.3: Schematic view of AGN with black hole, disk, dusty torus, BLR and NLR. The picture also shows how AGN are seen depending on the angle of view ©Biteau, 2013.

The standard AGN paradigm is derived from all the discoveries made in the last years. This unification model started to came out in the late 70s with the work of Rowan-Robinson, 1977 followed by Lawrence and Elvis, 1982, Begelman, Blandford, and Rees, 1984 and Urry and Padovani, 1995.

The picture is now clear on the fact that AGN are composed of a supermassive black hole (generally $M_{\rm BH} \sim 10^6 - 10^9 M_\odot$) surrounded by an accretion disk and a dust torus.

[4]This does not mean no improvement has been done in the last 20 years, a lot of different paths have been explored but nothing new, clear and solid really emerged.

Figure 2.3 shows an illustration of this. Gas clouds, trapped into the gravitational well of the black hole are rotating around it and are responsible of spectral lines visible in the optical spectra of AGN. The broad line region (BLR) is responsible of large lines while the narrow line region (NLR), further, is responsible of narrower lines. In 10 % of the cases, the AGN features a relativistc jet, expelling matter almost at the speed of light into the inter-galactic medium. Jetted AGN will be classified as radio loud galaxies whereas AGN with no jet will be classified as radio quiet (respectively top and bottom part of Figure 2.3). The separation between radio-quiet and radio-loud can also be defined by the ratio $R = L_{5\mathrm{GHz}}/L_{\mathrm{B}}$ of the luminosities at 5 GHz ($L_{5\mathrm{GHz}}$) and in the B optical band (L_{B}). If $R > 10$ the AGN is defined as radio loud.

The link between the black hole, the jet and the disk

There are a lot of unknowns here: How does the jet of plasma forms? What is the exact composition of the plasma? How much energy goes into the particles and into the Poynting flux?

It seems clear that particles from the disk are accelerated and transported into the jet. But how? Jets are also observed in young stellar objects (YSOs) and microquasars. They all share common physical components with AGN: a central graviting source, an accretion disk and a strong magnetic field. There could be a scale (in mass and radius) independent universal mechanism to explain the formation of jet.

The magnetic field seems to play an important role in launching and collimating the jet (Pudritz, Hardcastle, and Gabuzda, 2012). There are two main known mechanisms to explain a structured outflow: the Blandford-Payne process (BP, Blandford and Payne, 1982) and the Blandford-Znajek process (BZ, Blandford and Znajek, 1977). But still, magnetohydrodynamics simulations do not manage to link accretion and ejection along with the collimation of relativistic jets (Bogovalov and Tsinganos, 2001; Bogovalov, 2001; Pelletier, 2004).

The composition of the jet itself is subject to debate. Purely leptonic jet does not seem physical but a lepto-hadronic jet would require much more power than the accretion power to be accelerated. Ghisellini et al., 2014 showed that even the accretion power might not be enough to power AGN jets, and in this case a possible additional source of energy would be the black hole spin.

Moreover the difference between the radio loud and radio quiet AGN could come from the nature of the black hole. Schwarzchild and Kerr black holes differ by their spin/angular momentum J. While Schwarzchild black holes have $J = 0$, Kerr black holes are characterized by $J > 0$. Pure Schwarzchild black holes are not expected to exist. But Kerr black holes with low spin and high spin could exist and the additional energy of the high spin could launch a jet.

The broad and narrow line regions

The broad and narrow line regions (BLR and NLR) are regions of ionized matter gravitationnally bounded to the black hole moving at ~ 10 km.s^{-1}. The NLR is thought to be more extended than the BLR, this is represented also on Figure 2.3. The BLR being closer to the central emitting region, it is still not sure if clouds are in infall, outflow or orbital motion.

The echo mapping (also called reverberation mapping, Blandford and McKee, 1982) is a technic developed to probe the BLR region in 1982. The photons coming from the BLR are expected to vary the same way as the continuum but with some time delay, days to weeks generally. This continuum is supposed to originate from the accretion

disk. The time delay between the variations in the continuum and the echo seen in the emission lines is the average light travel time from the accretion disk to the BLR. Since the accretion disk is supposed to be very compact, the distance the light travels can be interpreted as the BLR radius.

One of the first result from this technique came from a series of observations carried at the end of the 80s (Clavel et al., 1991; Peterson et al., 1991; Dietrich et al., 1993; Maoz et al., 1993). Observations lasted 8 months and achieved a time resolution of a few days. The results showed that the continuum and BLR variations appeared to be in phase with time lags of a few days. However, the highest ionization lines seemed to respond faster (in 2 to 10 days) to the continuum variations than the lower ionization lines (20-30 days) showing a radial ionization stratification of the BLR. This stratification behavior has been seen several times in other studies (Peterson and Wandel, 2000; Kollatschny et al., 2001).

Bentz et al., 2013 showed a relationship between the BLR radius (using the time delay of the $H\beta$ line) and the luminosity of the AGN (Figure 2.4). The BLR typical radius is between 1 and 100 light days ($0.8 - 80$ mpc) and scales with the AGN luminosity.

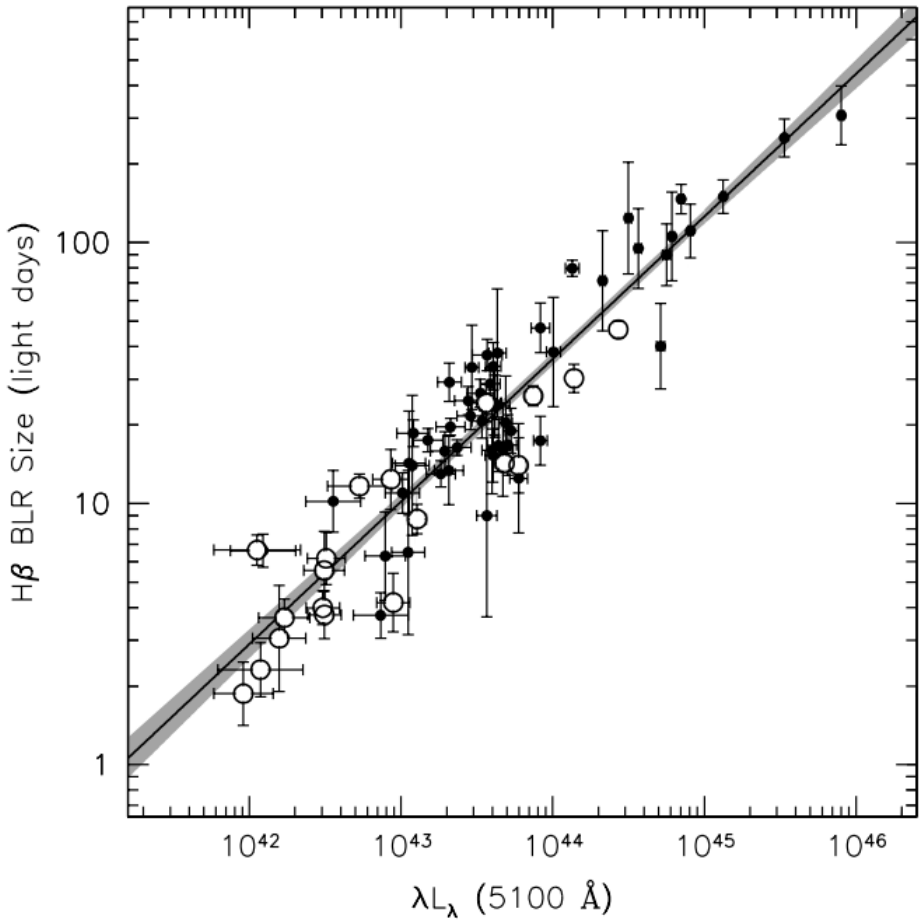

FIGURE 2.4: Scatter plot of the BLR size versus the AGN luminosity in the wavelenght $\lambda = 510$ nm showing a scaling relationship (Bentz et al., 2013).

2.2.2 The AGN zoo

Fanaroff and Riley, 1974 showed the radio loud AGN could be separated in 2 categories noted FR I and FR II for Fanaroff-Riley galaxies of type I or II. FR I are characterised by

bright and wide jets. The left panel Figure 2.5 shows a radio image of the radio loud AGN 3C 296. Its jets are wide with the maximum of the emission located near the central emitting region. On the other hand, in FR II, the jets are strongly collimated and less luminous. On the right panel of Figure 2.5, the jets of 3C 47 are almost invisible near the central emitting region. Hotspots are visible in the radio lobes, where the jets interact with the extragalactic medium. Generally, the radio power of FR II radio galaxies is larger than for FR I, with the limit between the two populations at $\sim 4 \times 10^{40}$ erg.s^{-1}.

This morphological difference has been completed by Ledlow and Owen, 1996. They showed that the two classes could be separated looking at their radio and optical luminosity. The radio luminosity goes roughly as the square of the optical luminosity of the host, indicating an apparent link between the two subclasses.

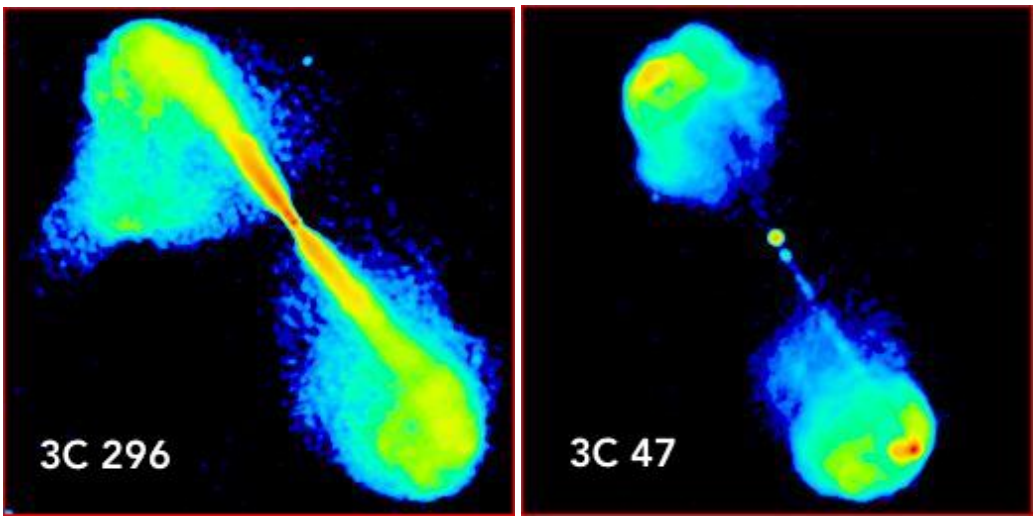

FIGURE 2.5: The AGN 3C 296 on the left features the characteristics of a FR I while 3C 47 on the right corresponds to a FR II.

Figure 2.3 shows also how the different types of AGN are defined depending on the orientation of the AGN with respect to the observer.

Radio quiet AGN regroup the radio quiet quasars and the Seyfert 1 and 2 galaxies (Sy 1 and Sy 2). The particularity of the Seyfert galaxies is that their emission is dominated by the BLR or the NLR. Sy 2 are dominated by the NLR because the dusty torus obscurs the BLR. On the other hand, Sy 1 are dominated by the BLR, even if the NLR is in the line of sight, because the BRL is closer to the central source, and so, brighter.

Radio loud AGN are composed of broad line radio galaxies (BLRG, also called RLQ for radio loud quasars) and narrow line radio galaxies (NLRG) which are are the radio loud equivalent of the Sy 2 and Sy 1 galaxies. Last but not least, radio loud AGN are called blazars when the jet is closely aligned with the line of sight of the observer. This last class is more remarquable as its emission is dominated by the jet.

2.2.3 The blazar class

Blazars display a non-thermal emission dominated by the jet, with the luminosity and energy boosted by the Doppler effect, spanning from the radio up to TeV energies.

Blazars can be divided in two classes: flat spectrum radio quasars (FSRQ) and BL Lac[5] objects. The separation from the two comes from their optical spectrum: if the equivalent

[5]The name comes from the first object of the class, BL Lacertae, which at first was associated to a variable star.

width of the lines are larger than $5\mathring{A}$ the blazar is defined as a FSRQ, otherwise it is BL Lac (Urry and Padovani, 1995). Figure 2.6 shows that the optical spectrum of FSRQ is mainly flat with clear emission lines while the one of BL Lac displays no feature. Since they do not exhibit strong emission lines, the determination of the redshift of BL Lac is sometimes complicated (almost half of the BL Lacs have no redshift in the 3LAC catalog).

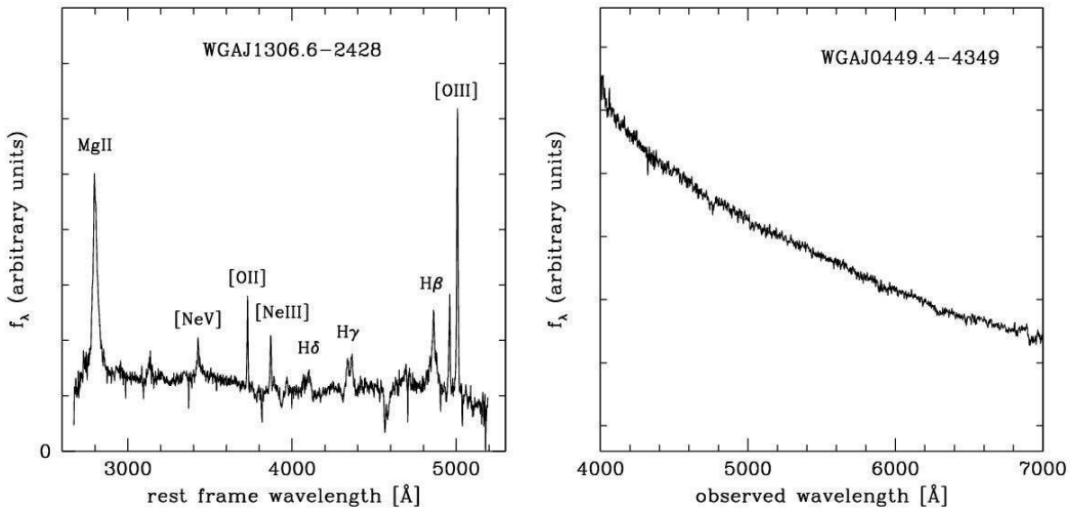

FIGURE 2.6: Optical spectra of a FSRQ (left) mostly flat with a lot of emission lines, and a BL Lac (right) showing no line.

When resolved, the jets of FSRQ mostly exhibit FR-II like structures while those of BL Lacs can belong to either class (Ledlow and Owen, 1996; Antonucci, 2011). Because of the lack of emission lines, the environment of the jet of BL Lac is tought to be less crowded with BLR and NLR than for FSRQ. For the latest, the jet would interact with the clouds and produce the hot emission at the start of the jet.

FSRQ are more powerful than BL Lac with a bolometric luminosity of $10^{46} - 10^{48}$ erg.s^{-1} for FSRQ and $10^{45} - 10^{46}$ erg.s^{-1} for BL Lacs.

The emission of blazars and AGN is usually represented using a diagram called spectral energy distribution (SED). It shows the flux density in function of the frequency or the energy. The flux density can be defined either by the frequency or the energy:

$$\nu F(\nu) = E^2 \frac{dN}{dE} \tag{2.1}$$

where ν is the frequency, $F(\nu)$ the flux density, E the energy and $\mathrm{d}N/\mathrm{d}E$ the differential flux.

The SED of blazars is characterized by two bumps, with the peaks luminosity and position varying from blazars to blazars. Figure 2.7 shows the SED of 4 blazars (the FSRQs PKS 1510-089 and 3C 273 and the BL Lacs BL Lacertae and Mkn 421) using multi-wavelength data from ASI Science Data Center[6]. They all display two bumps although the luminosity and detailed shapes are different.

In the current blazar paradigm the first bump is explained by Synchrotron emission, with electron spinning in the magnetic field of the jet. The origin of the second bump is still unclear and will be discussed in more details in Section 2.4.

BL Lacs are further classified as Low and High Frequency Peaked BL Lacs (LBL and HBL) depending on whether $\alpha_{\mathrm{rx}} = \log(F_{5\mathrm{GHz}}/F_{1\mathrm{keV}})/7.68$ is greater than or less than

[6]ASDC: http://tools.asdc.asi.it/index.jsp

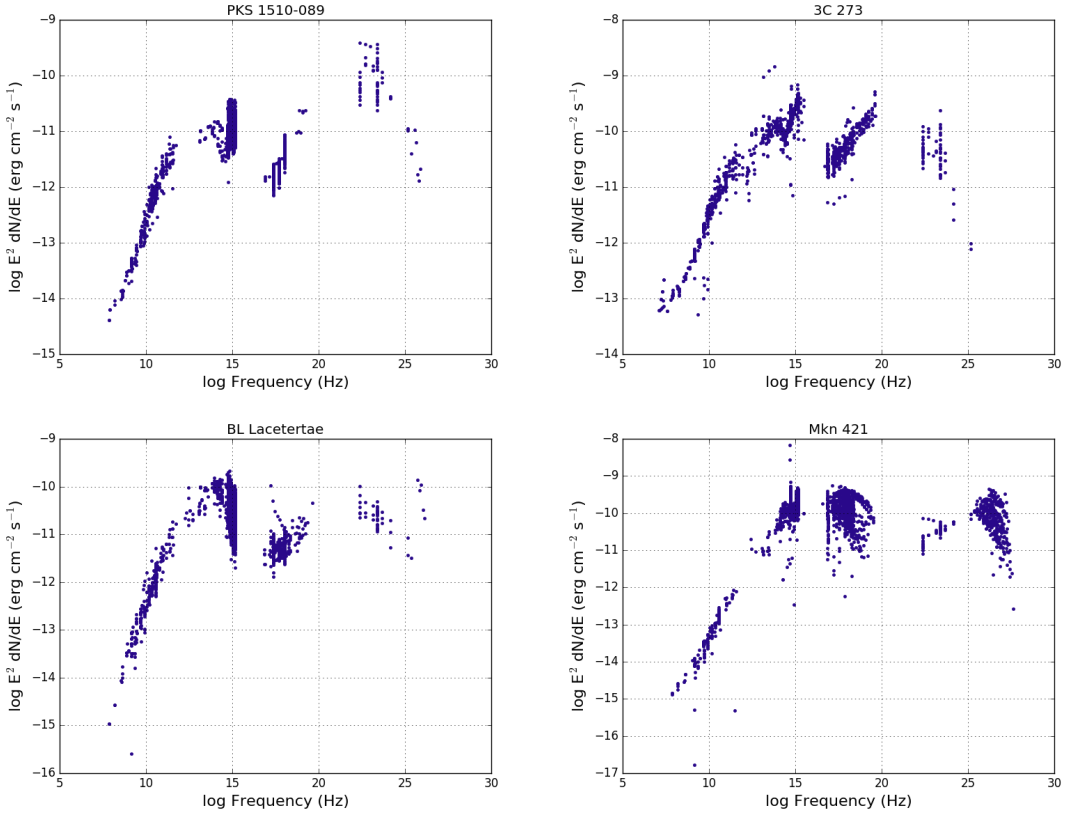

FIGURE 2.7: SEDs of the FSRQ objects PKS 1510-089 & 3C 273 and the BL Lac objects BL Lacertae & Mkn 421 using publicly available data from ASDC. The two broad bumps are clearly visible in each of them. The spread on the vertical axis is due to the intrinsic variability of the objects.

0.75 respectively ($F_{5\mathrm{GHz}}$ and $F_{1\mathrm{keV}}$ are the fluxes of the object at 5 GHz and 1 keV). This definition is phenomenological as most of the LBL were detected in radio but not in X-ray and most of the HBL were detected in X-ray but not in radio.

The difference between blazars can be linked at the position of the Synchrotron peak. FSRQs and LBLs show a peak at smaller frequencies than HBL. A new definition of the blazar sub-classes arises, using the position of the Synchrotron peak:

- Low Synchrotron peaked blazar (LSP): $\nu_{\mathrm{peak}} < 10^{14}$ Hz
- Intermediate Synchrotron peaked blazar (ISP): $10^{14} < \nu_{\mathrm{peak}} < 10^{15}$ Hz
- High Synchrotron peaked blazar (HSP): $\nu_{\mathrm{peak}} > 10^{15}$ Hz

Generally, the LSP and HSP correspond respectively to FSRQ+LBL and HBL, with the ISP being an intermediate class between the two. In the following of this work, because of a short cut[7] made in the field by many astrophysicists, I will refer to HSP, ISP and LSP using the historical classification names: HBL, IBL and LBL.

Last but not least, blazars are known to be highly variable, either on long time scales or short time scales with flares. This is why the SEDs of Figure 2.7 are wide: data in a specific energy band were taken at different times when the blazar was either in high or low state (or in between). This variability will be of great importance in this thesis (especially for Chapter 9 and Chapter 10), hence the subject deserves its own section and will be developped in Section 2.5 at the end of this chapter.

[7] bad habit

Relativistic beaming: explanation

Matter in the jet is moving at velocities close to the speed of light. When an emitting plasma has a relativistic motion with respect to a fixed observer, its emission is beamed in the direction of motion. The strength of the beaming is measured with the Doppler factor:

$$\delta = \frac{1}{\Gamma(1 - \beta \cos\theta)}$$

where β is the speed of the plasma in c units, θ is the angle between the direction of motion and the line of sight and Γ is the Lorentz factor defined as:

$$\Gamma = \frac{1}{\sqrt{1 - \beta^2}}$$

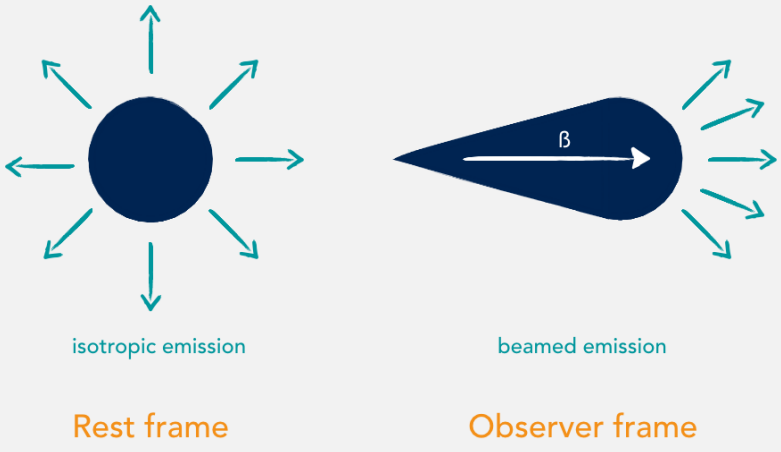

Because of space contraction and time dilation, the observer sees a much more intense emission. The emission for the observer $F_{\rm obs}$ is boosted compared to the emission F in the rest frame:

$$F_{\rm obs} = \frac{F}{[\Gamma(1 - \beta \cos\theta)]^3}$$

If the speed of the blob of plasma is $\beta = 0.9$ and the angle $\theta = 5°$, the boosting factor will be ~ 75.

AGN type	Description
Radio-loud galaxy	AGN with a jet $R = L_{5\mathrm{GHz}}/L_{\mathrm{B}} > 10$
NLRG	Narrow Line Radio Galaxy It is a radio loud galaxy seen on the side such as the emission in optical shows lines from the NLR
BLRG	Broad Line Radio Galaxy It is a radio loud galaxy seen on the side such as the emission in optical shows lines from the BLR (dominating over the NLR)
Blazar	Radio loud galaxy seen with the jet pointing at the observer, the emission is boosted by the Doppler effect
FSRQ	Flat Spectrum Radio Quasar Blazar with the optical spectrum having emission lines because of the presence of clouds (NLR & BLR)
BL Lac	Blazar with no clear feature in its optical spectrum, if lines are present they are few and narrow
FR-I	Radio-loud galaxy with most of the radio power in the jet next to the central region. Equivalent to an FSRQ seen on the side
FR-II	Radio-loud galaxy with most of the radio power in the radio lobes. Equivalent to a BL Lac seen on the side
Radio-quiet galaxy	AGN with no jet $R = L_{5\mathrm{GHz}}/L_{\mathrm{B}} < 10$
Seyfert 2	Radio-quiet galaxy seen from the side such as the emission in optical is dominated by the NLR. Equivalent of NLRG with no jet
Seyfert 1	Radio-quiet galaxy seen from the side such as the emission in optical is dominated by the BLR. Equivalent of BLRG with no jet
Quasar	AGN seen from above. Term generally used for radio-quiet galaxy but can be applied for blazars as well

TABLE 2.1: Summary table of the AGN types discussed in Section A.2.

2.3 Focus on the blazar sequence

2.3.1 Introduction of the blazar sequence in 1998

Fossati et al., 1998 showed the possible existence of a continuum between FSRQ and BL Lac objects. Using a sample of 126 sources (with 33 having γ-ray data), they binned their sample into 5 bins of radio energy to derive the average SEDs presented on the right panel of Figure 2.8. This illustrates the idea of a sequence from FSRQs to BL Lacs, going through LBLs, IBLs and HBLs.

Their results showed several trends, controlled only with the bolometric luminosity (or the radio luminosity since they are correlated):

1. There is an anti-correlation between the position of the Synchrotron peak and the radio luminosity with $\nu_{\rm peak}^{\rm sync}$ decreasing with increasing luminosity (left panel of Figure 2.8).

2. The Compton dominance, defined as the ratio of the second peak luminosity over the Synchrotron peak luminosity $L_{\rm Comp}/L_{\rm Sync}$, increases with the luminosity.

3. The γ-ray spectrum become steeper while the X-ray spectrum becomes harder with increasing luminosity. This is an effet of the "reddening": FSRQ are redder than HBL (which are bluer) meaning than they are less energetic.

For Fossati et al., 1998, there is *"evidence for well defined sequence in the properties of HBL, LBL and FSRQ with increasing importance of an external radiation field [ed the BLR and NLR]"*. The interpretation of Ghisellini et al., 1998 goes to the same conclusion, saying that these properties were due to a different amount of radiative cooling (assuming the same acceleration/emission mechanisms for all blazars).

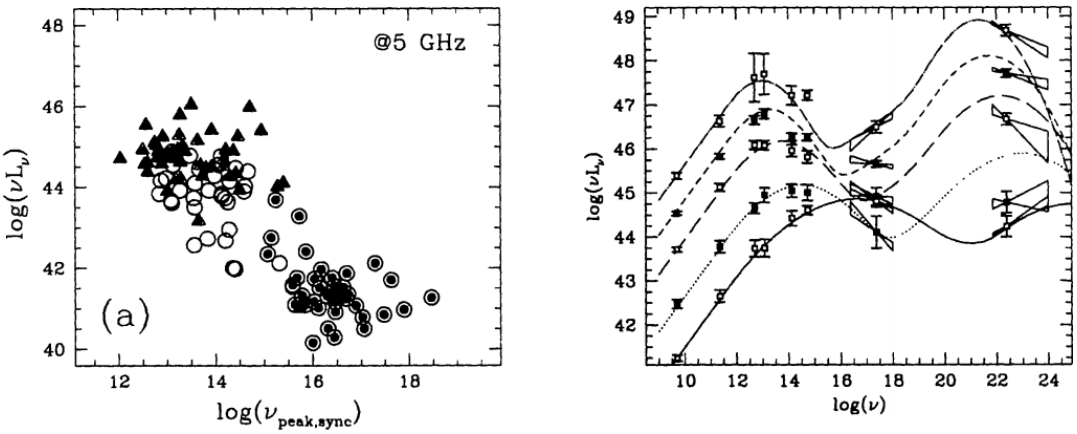

FIGURE 2.8: Left: Scatter plot of the radio luminosity versus the peak frequency of the Synchrotron component for FSRQ (triangles) and BL Lacs (empty and filled circles). Right: Average SEDs showing the sequence of blazars (Fossati et al., 1998).

However, these results are phenomenological, based on few sources which were the brightest sources detected at that time. Updates and revisitations of the blazar sequence have been done since (Ghisellini and Tavecchio, 2008; Ghisellini, 2016; Ghisellini et al., 2017).

2.3.2 Is the blazar sequence really valid?

However, some observations do not match the blazar sequence. For instance, the HBL PKS 2155-304 underwent a huge flare in July 2006 (Aharonian et al., 2007a; Aharonian et al., 2009a). The corresponding SED is shown on Figure 2.9. The quiescent state (black point) is compatible with a HBL from the blazar sequence. But during the flare the luminosity of the Synchrotron peak does not seem to change a lot while the Compton dominance increases drastically. The blazar RGB J1629+4008 does not fit the blazar sequence neither. The presence of emission lines puts it in the FSRQ class but the Synchrotron peak frequency around 10^{16} Hz should classify it as an HBL (Padovani et al., 2002).

Padovani, 2007 investigated the validity of the blazar sequence and found that some of the blazar sequence observations were not confirmed. He found no correlation between $\nu_{\rm peak}^{\rm Sync}$ and the radio power and that FSRQs could exist with high $\nu_{\rm peak}^{\rm Sync}$.

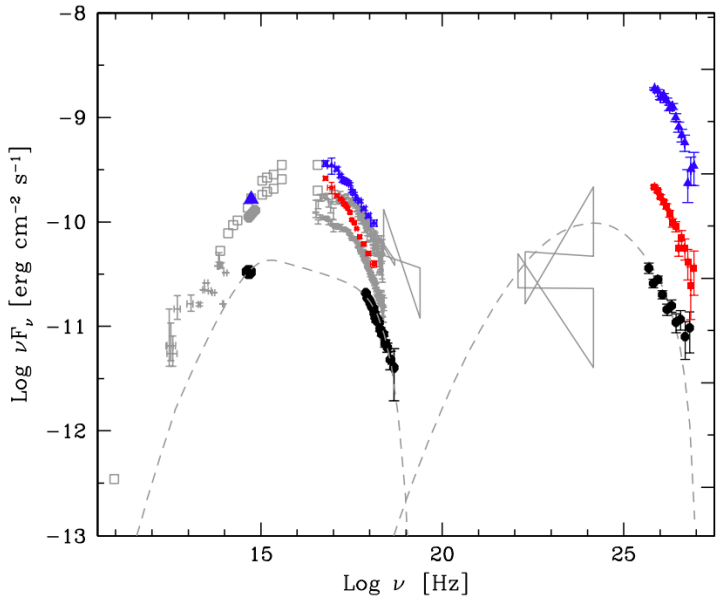

FIGURE 2.9: SED of PKS 2155-304 showing the lowest (red) and highest (blue) states of the flare. The black data are 2003 data of the quiescent state (Aharonian et al., 2009a).

The blazar sequence of Fossati et al., 1998 predict than the VHE γ-ray flux is fainter for FSQR/LBL than for HBL objects, meaning that HBLs will be more easily detectable by VHE experiments than FSRQs/LBLs. Ghisellini et al., 2017 predict a different behavior in the TeV range (keep in mind that 10^{26} Hz $\simeq$ 400 GeV, the order of energy of the threshold of VHE experiments), where the luminosity of FSRQs is higher than HBL in the VHE range.

2.3.3 Revisitation and updates confirming the blazar sequence

A blazar sequence ruled by only one observed parameter seems strange. Efforts have been done to have a better understanding of the blazar sequence (if a blazar sequence exists). Is it ruled by the presence of the BLR? Is it ruled by different regimes of accretion rates?

Ghisellini et al., 2017 revisited the blazar sequence using *Fermi*-LAT data of the 3LAC (Ackermann et al., 2015b). Instead of binning the sample into radio bins, they binned it into γ-ray bins and separated FSRQs from BL Lacs, showing both classes were following a sequence. Figure 2.10 shows the sequences from FSRQs, BL Lacs and all blazars.

FSRQs alone do form a sequence. The shape of their SED does not change much with luminosity, the position of the Synchrotron and Compton peak are steady but the Compton dominance increases with the γ-ray luminosity, resulting also in a hardening of the X-ray slope.

BL Lacs form also a sequence with more changes in the shape. The Synchrotron and Compton peak positions decrease with the γ-ray luminosity, indicating a reddening of the BL Lacs with luminosity. Alike the FSRQs, the Compton dominance increases with the luminosity, resulting in a hardening of the X-ray slope.

When looking at the whole sample of blazars, FSRQs and BL Lacs together, the sequence looks like the original sequence of Fossati with small differences explained by the fact that the smaller sample of Fossati was "the tip of the iceberg" of what we see now. At high luminosity, the properties of FSRQs dominate the sample while at low luminosity,

the properties of BL Lacs dominate the sample (since there are few low luminosity FSRQ and high luminosity BL Lacs).

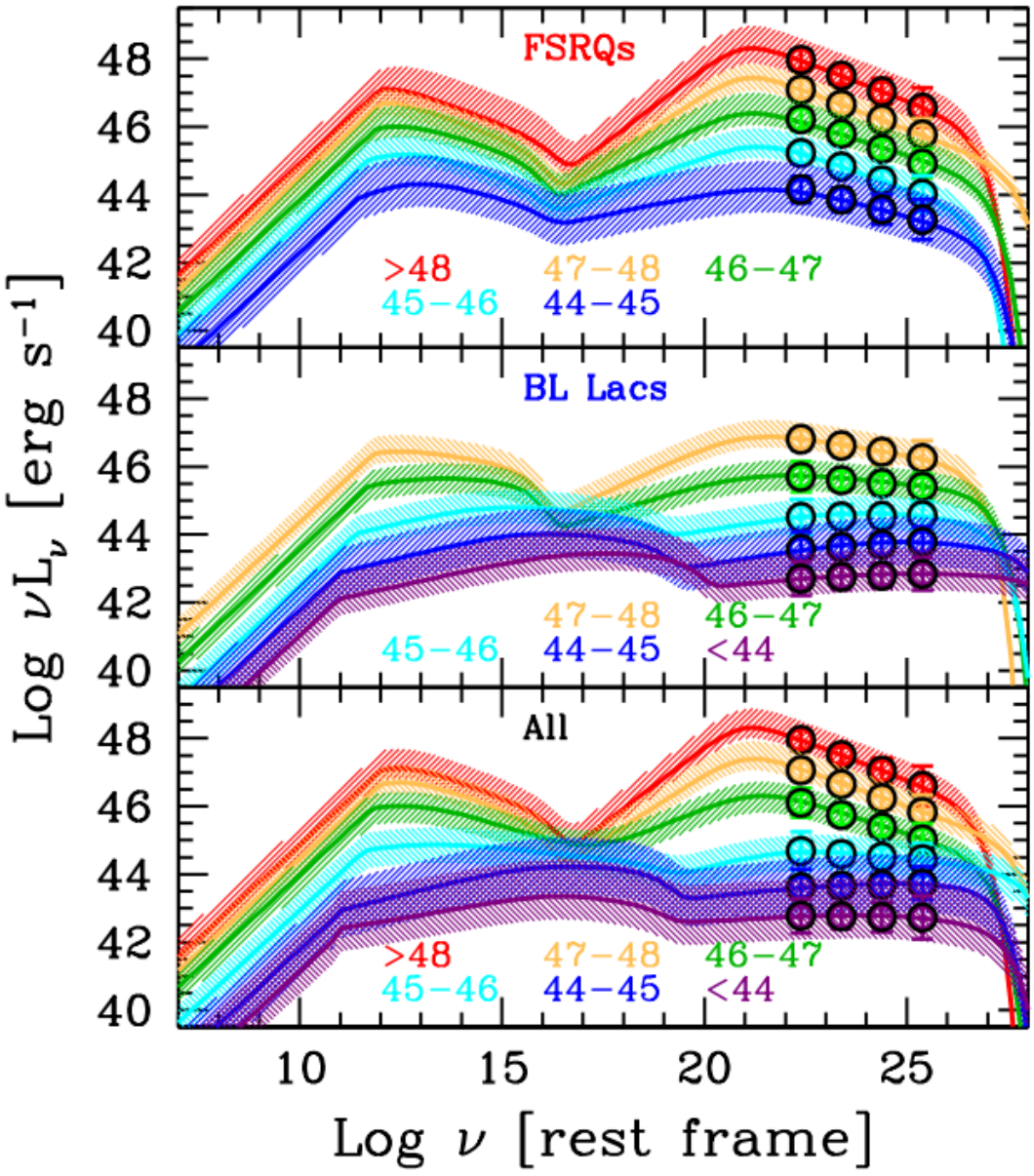

FIGURE 2.10: New blazar sequence from Ghisellini et al., 2017 with separation between FSRQs and BL Lacs (top and middle) and the whole sample (bottom).

Up to now[8], there are 6 FSRQs, 2 LBLs, 8 IBLs and 48 HBLs detected in the VHE range. More FSRQ and LBL objects are needed to be able to validate or not the blazar sequence at VHE. Chapter 7 is dedicated to a recent proposal in the H.E.S.S. Collaboration to detect more objects in order to probe the blazar sequence and increase the current understanding.

[8]checking TeVCat (http://tevcat.uchicago.edu/) on 12th April 2017

2.4 Models of blazar emission

It is not yet known what is the mechanism at play producing the non-thermal emission seen, several possibilities exist. The low energy emission (generally said to go from radio to X-ray) is known to be produced by Synchrotron emission from relativistic electrons in the magnetic field of the jet. Observations show a polarisation of the emission at low energy, typical of Synchrotron emission.

Two classes of model exist to provide an explanation to the emission of the high energy part: hadronic and leptonic.

In the leptonic framework, the high energy emission is explained by Inverse Compton scattering by the same electron population producing the Synchrotron emission. The target photons for the Inverse Compton scattering can be:

- the Synchrotron photons produced before by the electron population → Synchrotron Self-Compton model (SSC, this model will be described in more details in Chapter 10);
- the photons from the disk, the BLR or the torus → external Compton model.

In the hadronic framework[9], the high energy emission could be explained by:

- Synchrotron emission from the protons spinning into the magnetic field of the jet;
- photo-pion production: the protons of the jet interact with each other producing π^0, π^+ and π^- among other particles. The π^0 decays into a $\gamma\gamma$ pair while the $\pi^\pm$ decay into leptons and neutrinos.

2.4.1 Leptonic and hadronic models: two classes of models to describe the blazar emission

Hadronic and leptonic models are in competition to explain the origin of the high energy part of the emission. The problem is that the SED of blazars can sometimes be explained by both models. Sometimes a leptonic model will succeed where a hadronic model does not, sometimes the other way around (sometimes both will fail). But no model manages to describe all blazars at once. Figure 2.11 shows leptonic and hadronic fits to the SEDs of BL Lacertae and W Comae (more examples are available in Böttcher et al., 2013). In both cases, models do not manage to account properly for the VHE emission. For BL Lacertae the SED of the leptonic model does not go to high enough energy while the hadronic modelisation outstrips (also the X-ray component is not powerful enough in the hadronic case). For W Comae, the leptonic model does not go to energies high enough and the hadronic model looks better even if a component seems to be missing.

Both leptonic and hadronic models are not working well. Figure 2.12 shows the leptonic and hadronic modelling of the multi-wavelength SED of the HBL PKS 2155-304 (with contemporaneous data coming from Aharonian et al., 2009b).

2.4.2 Hadronic models: pros and cons

One of the motivation for hadronic models is to explain the presence of UHECR and very high energy neutrinos seen for example by IceCube which could be coincident with the position of some TeV blazars (Mücke and Protheroe, 2001).

[9] hadronic models are often called lepto-hadronic as electron are needed to explain the Synchrotron emission at low energy.

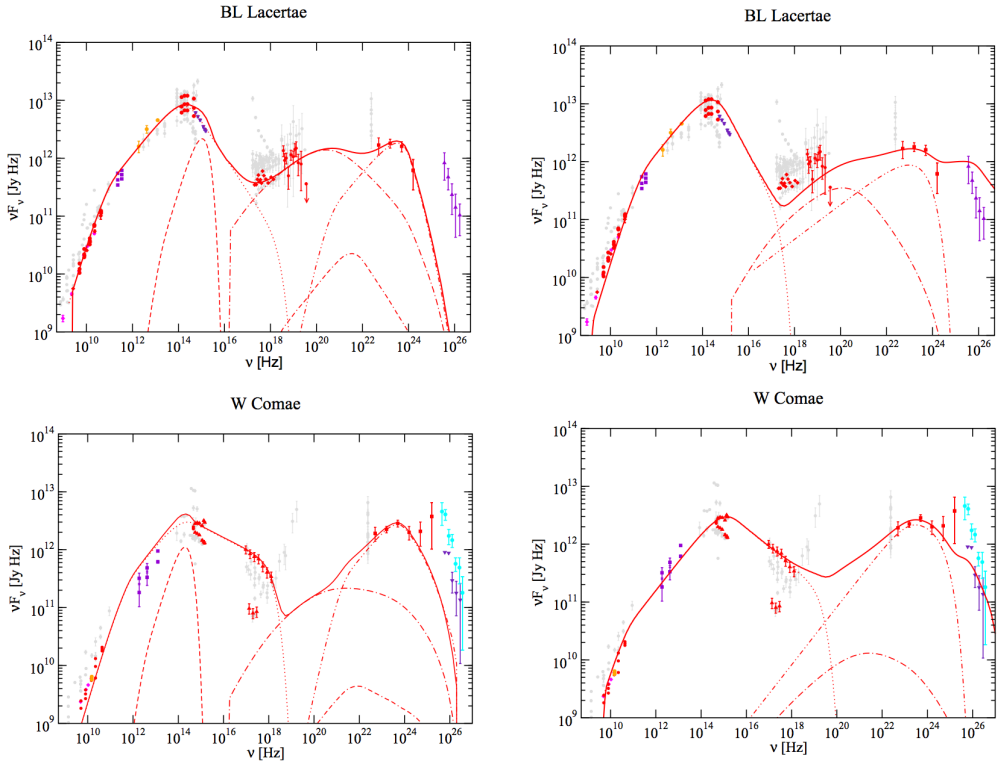

FIGURE 2.11: Example of SED with leptonic (left) and hadronic (right) modelisation for BL Lacertae (top) and W Comae (bottom) (Böttcher et al., 2013). The points of all colors are the data while the red line is the modelisation of the SED taking into account several processes (dashed and dotted lines).

However, hadronic processes are known to be quite inefficient and a tremendous amount of power in the jet would be required in order to accelerate protons above 10^6 TeV. The model of powerful jets from Böttcher et al., 2013 has been tested by Zdziarski and Böttcher, 2015. They concluded that hadronic model can not work for the majority of the blazars population because they require huge jet power. Those jets should be slow and wide, which is not what is observed. Also the accretion regime would be different. One could postulate the existence of special blazars but it would not be compatible with the uniformity predicted by the blazar sequence (see Section 2.3).

However, the jet composition is not expected to be purely leptonic nor purely hadronic. In a lepto-hadronic jet with a leptonic domination, hadrons could still be accelerated in order to explain the UHECR and the neutrinos even if the hadronic processes are not dominating the observed emission.

2.4.3 Leptonic models: pros and cons

The SED of HBL objects is generally well described by leptonic models like the Synchrotron Self Compton (to be described more precisely in Chapter 10) where the second bump of the SED is explained by Inverse Compton scattering. The top panel of Figure 2.12 shows the SED of the known HBL PKS 2155-304 succesfully modelled with the SSC model.

The weakness of such a simple model is that it fails when applied to other types of blazars like FSRQ & LBL and extreme HBLs despite working well on HBL. The emission of objects like PKS 1510-089 (FSRQ) and Ap Librae (LBL) can not be explained

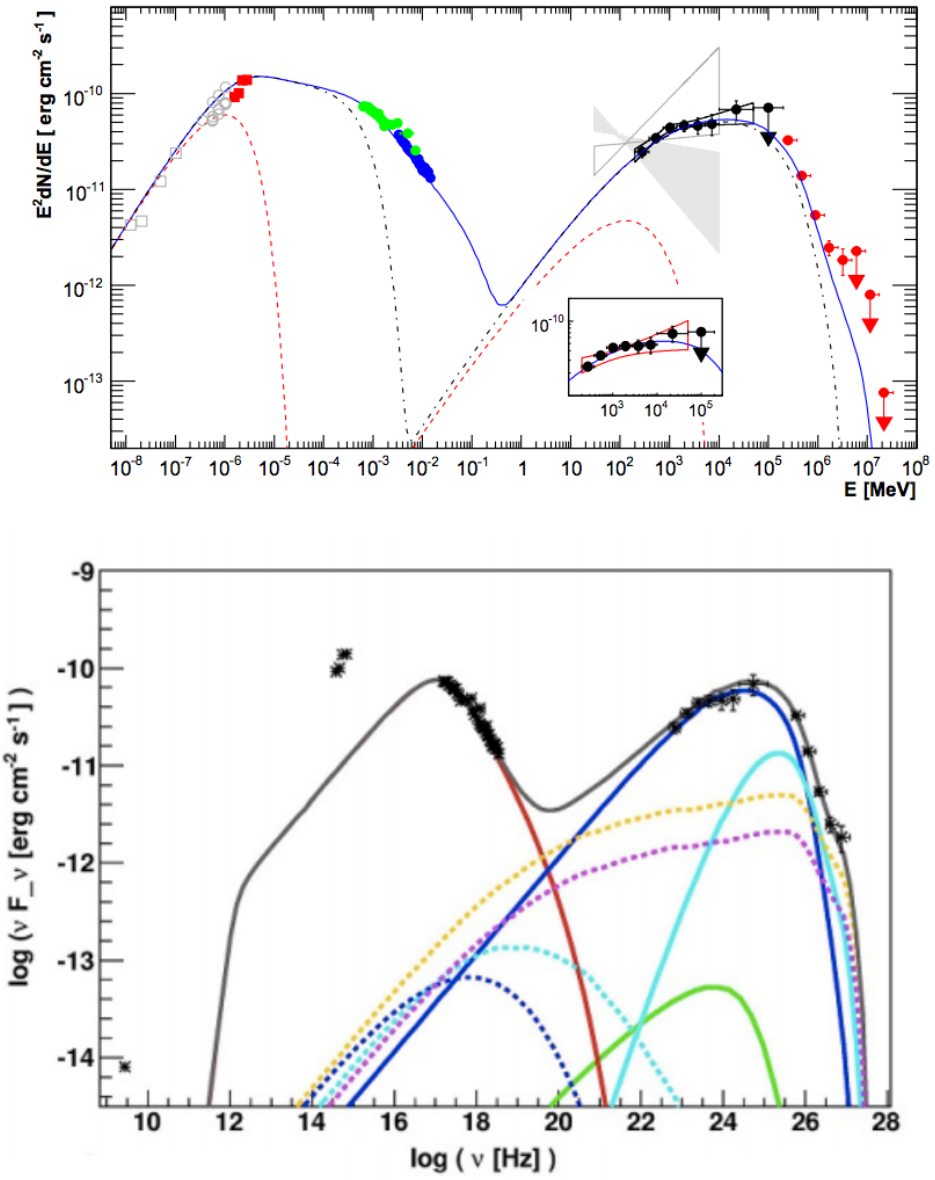

FIGURE 2.12: SED of the HBL PKS 2155-304 with SSC modelling at the top (Aharonian et al., 2009b) and hadronic modelling at the bottom (Cerruti et al., 2012).

with the SSC model and external Compton is required. Concerning extreme HBLs, like 1ES 0229+200, parameters of the SSC have to reach non physical values to fit their SEDs (the introduction of Chapter 7 will go into more details).

Again, looking at the AGN paradigm and at the blazar sequence, this does not go with the idea that all blazars should be described by the same model.

2.5 Variability: a key to the understanding of blazars?

All blazars are supposed to be more or less the same according to the blazar paradigm, so they are supposed to be described by a global and common model for all of them, with some part dominating others depending of the parameters for each blazar.

As already mentionned earlier, one of the striking properties of blazars is their variability. The brightness of blazar can vary at all time scales, from minutes to days to months to years, with this behaviour being seen at all wavelengths, from radio to X-rays and gamma rays.

The SED, which is not enough to disentangle between classes of models, is a time-averaged flux, which smoothens and hides the variability in the different energy bands. So we have to look at the flux with more dimensions: light curves. Light curves show the evolution of the flux with time and the variability can be directly seen if present. Figure 2.13 shows the *Fermi*-LAT (between 100 MeV and 300 GeV) public[10] light curves of three blazars: PKS 1502+106, PKS 0805-077 and BL Lacertae. These light curves span over 8 years of monitoring and some flares can be seen along with low states. In both cases, there is still a stochastic visible variability.

Leptonic and hadronic models use different particles to explain the emission (this is the humble electron vs. the massive proton), hence their different characteristic times provide the possibility to differentiate variability signatures.

In the framework of leptonic models, correlations between energy bands are expected since the emission is produced by a single particles population. Whereas hadronic models will have more difficulties to explain correlated variability. Several observations were made in that way where the optical fluxes were correlated to the GeV or TeV ones, sometimes the X-ray flux were correlated to the TeV flux. However, some blazars like Mkn 421, Mkn 501 and 1ES 1959+650, have displayed orphan flares (Fraija et al., 2015; Sahu, Oliveros, and Sanabria, 2013). The particularity of these flares is that they are seen in only one particular wavelength, while observations in other wavelengths showed no flare or change of activity. Leptonic models can not explain orphan flares while hadronic models can. They assume that the flare may originate from relativistic protons, interacting with an external photon field supplied by electron-synchrotron radiation (Böttcher, 2005).

Chapter 9 will present variability studies, including correlations, made on the long term multi-wavelength data set of the HBL PKS 2155-304 followed by a SSC modelling of the long term light curve in Chapter 10.

[10] https://fermi.gsfc.nasa.gov/ssc/data/access/lat/msl_lc/

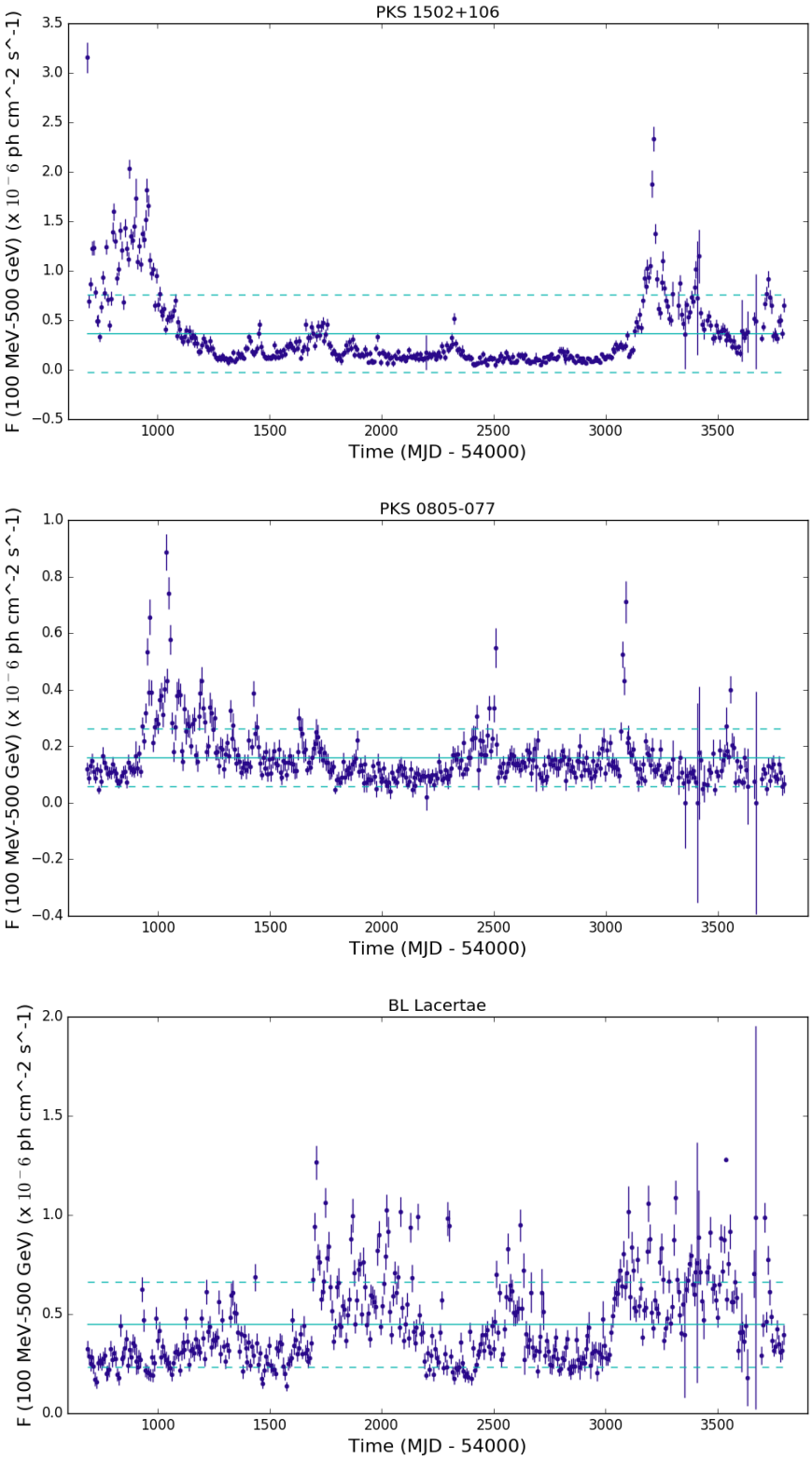

FIGURE 2.13: Example of light curves from the *Fermi*-LAT publicly available data. From top to bottom: PKS 1502+106, PKS 0805-077 and BL Lacertae. The blue lines represent the average and standard deviation (dashed) of the flux.

Chapter 3

Résumé de la Partie 1 (French)

Une brève histoire de l'astronomie γ

En 1912, Victor Hess découvre le rayonnement cosmique : des particules chargées qui bombardent notre atmosphère. Leur énergie va de quelques GeV à plusieurs centaines de EeV et leur flux s'étale sur 30 ordres de grandeur (Figure 3.1). Comment ces particules sont accélérées jusqu'à de telles énergies et où ?

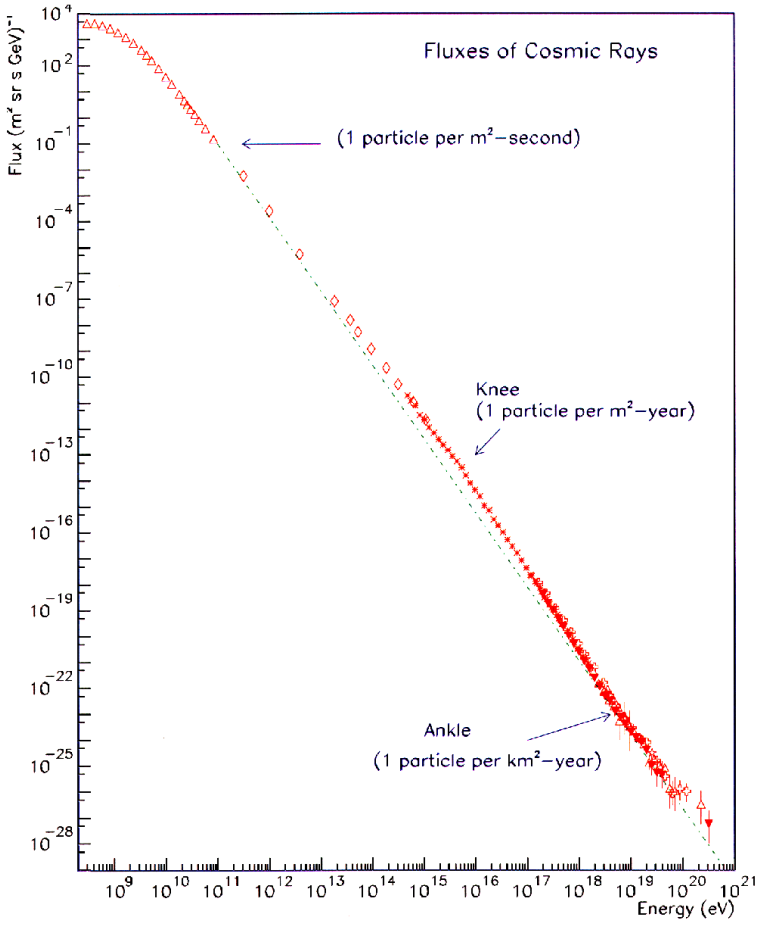

FIGURE 3.1: Spectre du rayonnement cosmique venant de données accumulées par différentes expériences (©Cronin, Gaisser, Swordy).

En détectant directement le rayonnement cosmique, l'information sur sa direction d'arrivée est perdue car la trajectoire des particules chargées est courbée à cause des champs magnétiques galactique et extragalactique. Mais lorsque ces particules sont accélérées ou lors de certaines interactions elles produisent un rayonnement lumineux (par

Synchrotron, Inverse Compton, Bremsstrahlung ou production de photo-pion) et ces photons se propageront en ligne droite. Ainsi l'étude du rayonnement lumineux, de la radio jusqu'au plus hautes énergies, permet de connaître les sources du rayonnement cosmiques. Dans notre galaxie, les restes de supernova et les pulsars sont connus pour accélérer la partie basse énergie du spectre des rayons cosmiques. Concernant l'origine des rayons cosmiques d'ultra haute énergie (au dessus de 10^{18} eV), les noyaux actifs de galaxies sont à ce jour les meilleurs candidats pour accélérer des particules jusqu'à de telles énergies.

Afin d'étudier la partie haute énergie de ce rayonnement pour comprendre son origine, l'astronomie γ s'est développée, tout d'abord avec des satellites tels que SAS-2, COS-B, CGRO-EGRET et *Fermi*-LAT. Grâce à eux, et notamment à *Fermi*-LAT qui est encore en fonctionnement, nous avons des cartes du ciel du rayonnement γ au GeV et des catalogues de sources comme représenté sur la Figure 3.2.

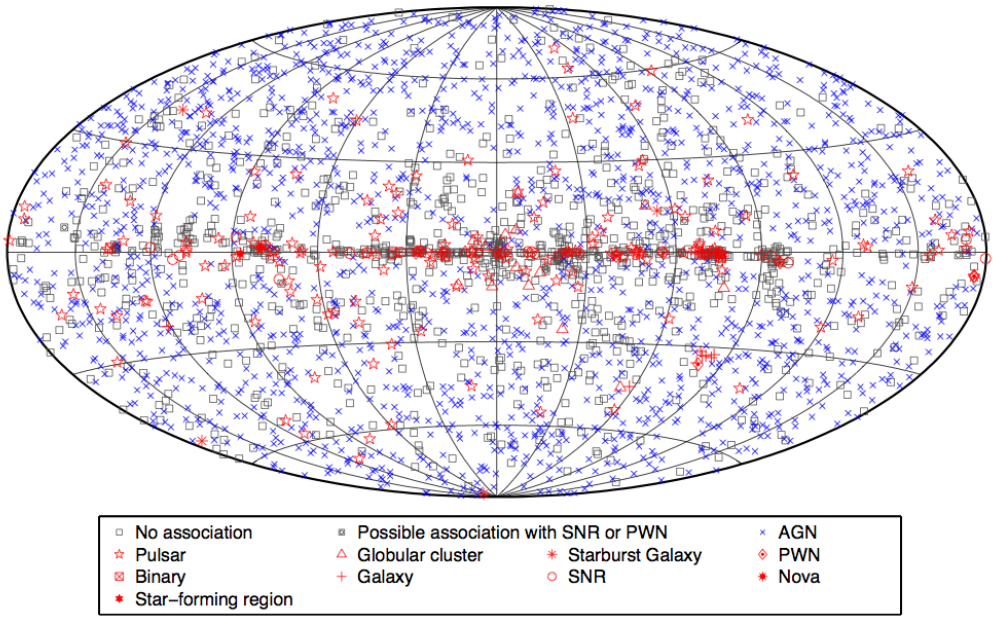

FIGURE 3.2: Carte du ciel du catalogue 3FGL (Acero et al., 2015) utilisant les 4 premières années de prise de données du *Fermi*-LAT.

Pour aller à plus haute énergie (jusqu'au TeV), il a fallu développer des télescopes au sol qui utilisent le rayonnement Cherenkov de la gerbe de particules secondaires pour détecter les γ qui arrivent dans l'atmosphère. Whipple fut le premier télescope Cherenkov à être développé dans les années 60. La première source γ de très haute énergie, la nébuleuse du Crabe, fut découverte en 1989. Depuis de nombreuses expériences se sont succédées, chacune amenant son lot de découvertes et ses améliorations techniques. Aujourd'hui, trois expériences Cherenkov existent : H.E.S.S., MAGIC et VERITAS et plus de 200 sources γ sont connues.

Le monde des noyaux actifs de galaxie

Les noyaux actifs de galaxie (communément appelés AGN pour *active galactic nuclei* en anglais) sont parmis les phénomènes les plus violents de l'Univers. La découverte de ce type d'objet date des années 40, avec tout d'abord les galaxies de Seyfert puis les galaxies radio et les quasars dans les années 60. Mais à cette époque les scientifiques ne savaient

pas vraiment que ce qu'ils avaient découvert était des facettes différentes du même type d'objet, et il a fallu attendre le modèle d'unification d'Urry and Padovani, 1995 pour clarifier le domaine.

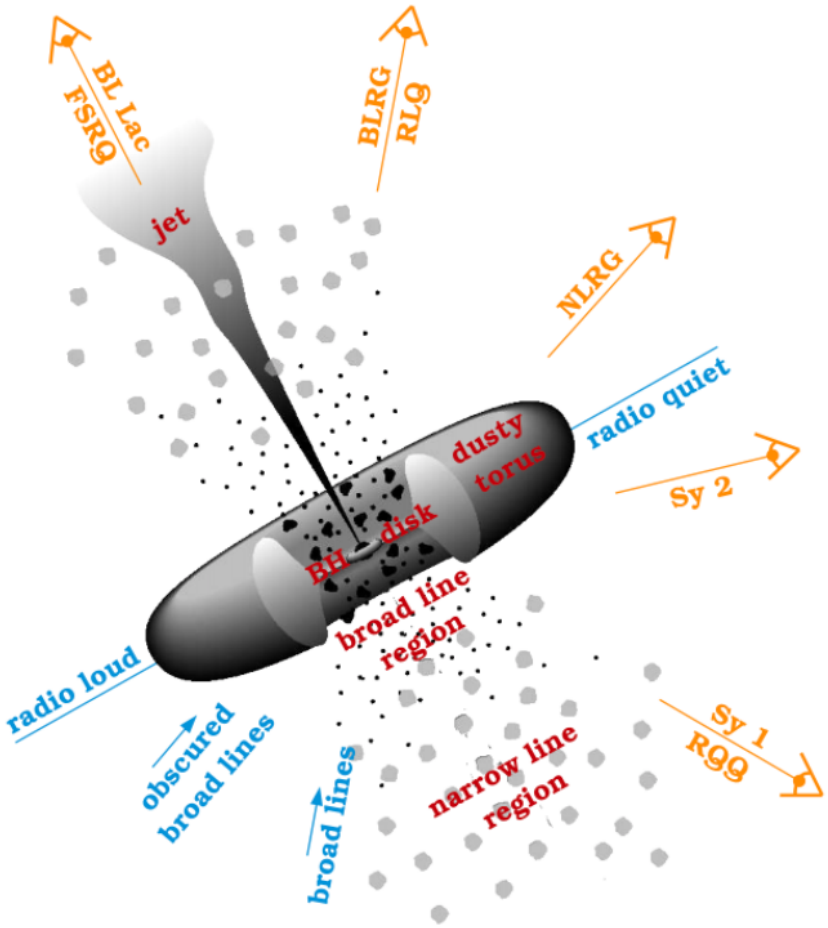

FIGURE 3.3: Schéma d'un AGN avec son trou noir supermassif, disque d'accretion, tore de matière et les nuages de matière environnants. L'image montre aussi les différents types d'AGN en fonction de l'orientation de l'objet par rapport à l'observateur ©Biteau, 2013.

La Figure 3.3 montre un AGN schématisé. Les AGN possèdent en leur centre un trou noir supermassif qui accrète la matière environnante, ce qui forme un disque d'accrétion. Dans certains cas, l'AGN expulsera de la matière à des vitesses proches de celle de la lummière dans le milieu intergalactique. Les AGN possédant ce jet de matière relativiste sont appelés AGN *radio-loud* et ceux qui n'en ont pas AGN *radio-quiet*. Car ce jet, en interagissant avec le milieu intergalactique, produit de fortes radiations en radio. Des nuages de matière, plus ou moins denses et gros (les BLR et NLR pour *Broad* et *Narrow line regions*), gravitent dans l'environnement proche du trou noir et produisent des lignes d'émission dans le spectre optique.

On voit bien qu'à cause de leur topologie, les AGN vont nous apparaître différents suivant leur orientation. En considérant seulement les AGN *radio-loud*, car il sera majoritairement question d'eux dans la suite de cette thèse, il y a trois possibilités :

- en regardant proche de la tranche, on verra le jet par le côté et l'émission est dominée par la *Narrow line region* car la *Broad line region* est cachée par le tore de matière. On dit que l'AGN est de type NLRG pour *Narrow Line Radio Galaxy*;
- si l'AGN est vu de biais, on dit qu'il est de type BLRG pour *Broad Line Radio Galaxy* car l'émission est dominée par la *Broad line region* (plus lumineuse que la NLR car plus proche du trou noir et du disque);
- si le jet est aligné avec la ligne de visée, on a affaire à un blazar : l'émission est dominée par le jet, ce qui booste le flux en terme de luminosité et d'énergie.

Les blazars sont très intéressant à étudier car ils permettent de s'affranchir des effets d'angle de vue, parfois d'absorption et de ré-émission par les BLR et NLR, et aussi car grâce au boost Doppler du jet, ils sont plus faciles à détecter.

Historiquement, les blazars ont été séparés en deux classes : les *Flat Spectrum Radio Quasars* (FSRQ) et les BL Lac, en fonction de la largeur des lignes d'émission présentes dans le spectre en optique. Les FSRQ possèdent de larges lignes d'émission alors que les BL Lac n'en possèdent presque pas, comme représenté sur la Figure 3.4. On pense que cette différence vient de l'environnement du coeur de l'AGN : les FSRQ possèderait plus de nuages (BLR et NLR) que les BL Lac qui en auraient peu ou quasiment pas.

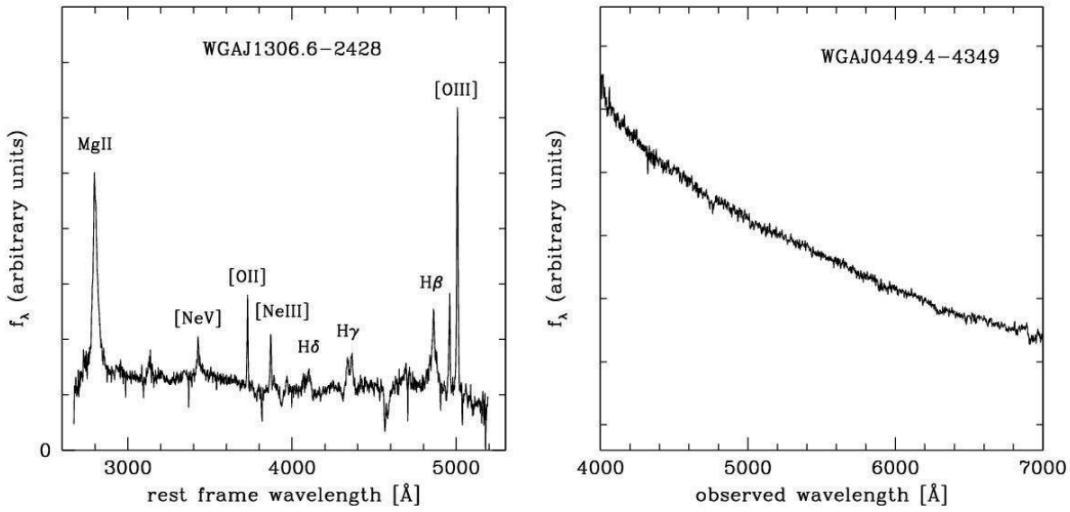

FIGURE 3.4: Spectre optique d'un FSRQ (gauche), plat avec beaucoup de lignes d'émission, et d'un BL Lac (droite) ne montrant aucune caractéristique particulière.

Les blazars sont caractérisés par une émission non thermique dont la distribution spectrale en énergie (ou SED pour *spectral energy distribution* en anglais) peut être schématisée par deux bosses : l'une à basse énergie (radio, optique, rayons X) et l'autre à haute énergie (GeV-TeV). Dans le paradigme actuel des blazar, le premier pic s'explique grâce à l'émission Synchrotron d'électrons dans le champ magnétique du jet. Plus de mystère entoure l'origine du deuxième pic.

La Figure 3.5 montre en exemple la SED du blazar Mkn 421 où les deux bosses sont clairement visibles. Les blazars sont aussi connus pour leur variabilité, que ce soit sur des courtes (minutes ou heures) ou longues échelles de temps (jours ou plus). C'est pourquoi on peut observer un étalement vertical des points de la SED pour une même gamme en

énergie : ce sont des données prises à des moments différents où l'objet était dans un état bas, haut ou intermédiaire.

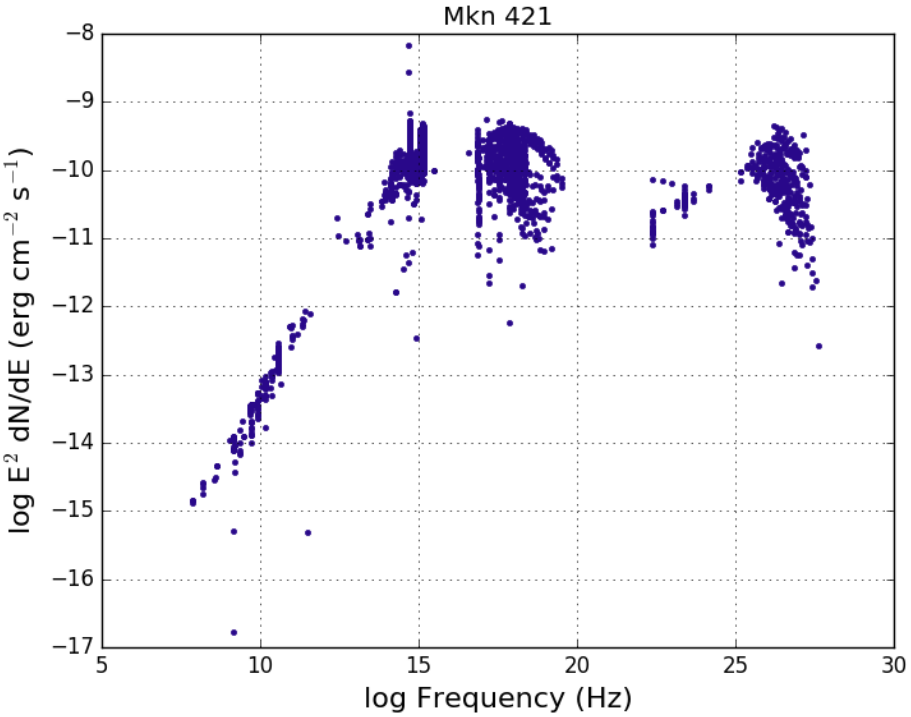

FIGURE 3.5: SED du BL Lac Mkn 421 (données public venant d'ASDC).

La SED des blazars peut montrer des différences suivant la luminosité de l'objet et la position des pics. Les BL Lac sont séparés entre LBL et HBL pour *Low* et *High Frequency Peaked BL Lac* en fonction du ratio de leur luminosité en radio et en rayons X, mais cette différence peut aussi se voir dans la SED où les LBL piquent à plus basse énergie que les HBL.

Ainsi une définition plus récente classe les blazars en fonction de leur SED, notamment de la position du pic Synchrotron :

- *Low Synchrotron peaked blazar* (LSP) : $\nu_{\rm peak} < 10^{14}$ Hz;
- *Intermediate Synchrotron peaked blazar* (ISP) : $10^{14} < \nu_{\rm peak} < 10^{15}$ Hz;
- *High Synchrotron peaked blazar* (HSP) : $\nu_{\rm peak} > 10^{54}$ Hz;

Généralement les LSP sont des FSRQ et LBL et les HSP des HBL, les ISP étant une classe entre les deux.

Fossati et al., 1998 proposèrent la séquence blazar (Figure 3.6) : il y aurait un continuum entre les FSRQ et les BL Lac. Ils montrèrent notamment qu'il y avait une corrélation entre la position du pic Synchrotron et la luminosité radio (ou bolométrique). Les FSRQ et LBL qui piquent à basse énergie sont en général plus lumineux que les HBL qui vont par contre à plus haute énergie. Cette corrélation s'expliquerait notamment à cause de la présence de radiation externe venant des BLR qui absorberait l'émission pour la réémettre à plus basse énergie. Les FSRQ et LBL seraient plus difficile à observer au TeV à cause de leur spectre beaucoup plus mou que les HBL.

Cette sequence blazar a été revisitée récemment par Ghisellini et al., 2017 qui montrèrent qu'il y avait une séquence pour les FSRQ et les BL Lac séparément, ainsi qu'une séquence commune. Au TeV, cette séquence reste à vérifier. En effet, la stratégie d'observation des télescopes Cherenkov a biaisé les observations vers les HBL et il y a très peu de FSRQ et LBL dans l'échantillon des blazars connus au TeV. Le Chapitre 6 est dédié à l'exploration de la séquence blazar au TeV en pointant vers de nouveaux objets prometteurs.

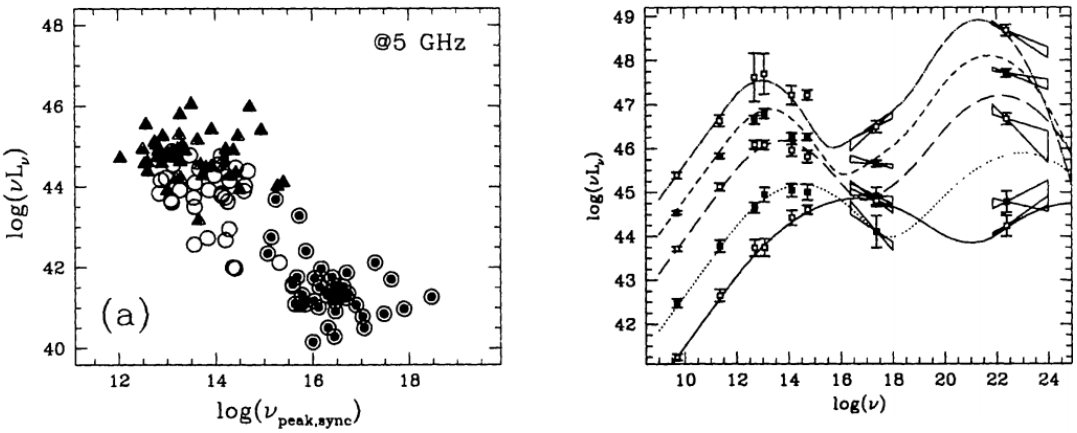

FIGURE 3.6: Gauche: luminosité radio versus fréquence du pic Synchrotron pour les FSRQ (triangles) et les BL Lac (cercles remplis et vides). Droite : SED moyennes montrant la séquence entre les blazars (Fossati et al., 1998).

Le (ou les) mécanisme produisant l'émission non thermique à haute énergie, dans la gamme du GeV et du TeV, n'est pas encore connu. Plusieurs possibilités existent et peuvent se ranger dans deux catégories : les modèles leptoniques et les modèles hadroniques. Dans les modèles leptoniques, les particules émettrices sont des électrons et peuvent rayonner en γ grâce notamment au processus Inverse Compton, soit sur la population de photons Synchrotron créés précédemment (on parle dans ce cas de modèle *Synchrotron Self Compton* en anglais, raccourci en SSC), soit sur un champ de photons externes venant par exemple du disque ou des BLR (on parle alors de Compton externe). Dans le cas des modèles hadroniques, les particules en jeu sont des protons, qui peuvent produirent du rayonnement Synchrotron dans la gamme des hautes énergies ou alors produire des photons γ par production de photo-pions.

Ces deux classes de modèles, bien que très différentes de part les particules et les processus en jeu, arrivent à décrire l'émission des blazars de manière égale, ce qui nous laisse avec une dégénérescence. Mais, comme le montre la courbe de lumière en Figure 3.7, les blazars sont très variables et la SED montre l'émission moyennée dans le temps. Hors un modèle d'émission, s'il arrive à expliquer l'émission moyennée dans le temps, doit aussi pouvoir expliquer cette variabilité stochastique. Un modèle leptonique est sensé avoir une signature en variabilité différente d'un modèle hadronique, les masses de l'électron et du proton étant très différentes de même que les temps caractéristiques des processus d'émission. En comparant les signatures en variabilité attendues pour chaque modèle aux données, cette dégénérescence pourrait être levée. C'est le but des deux chapitres de la Partie 3 où le Chapitre 7 présente l'analyse des données du blazar PKS 2155-304 et la caractérisation de sa variabilité long terme et où le Chapitre 8 présente l'étude du modèle SSC dans sa version dynamique pour essayer de reproduire les résultats du chapitre précédent.

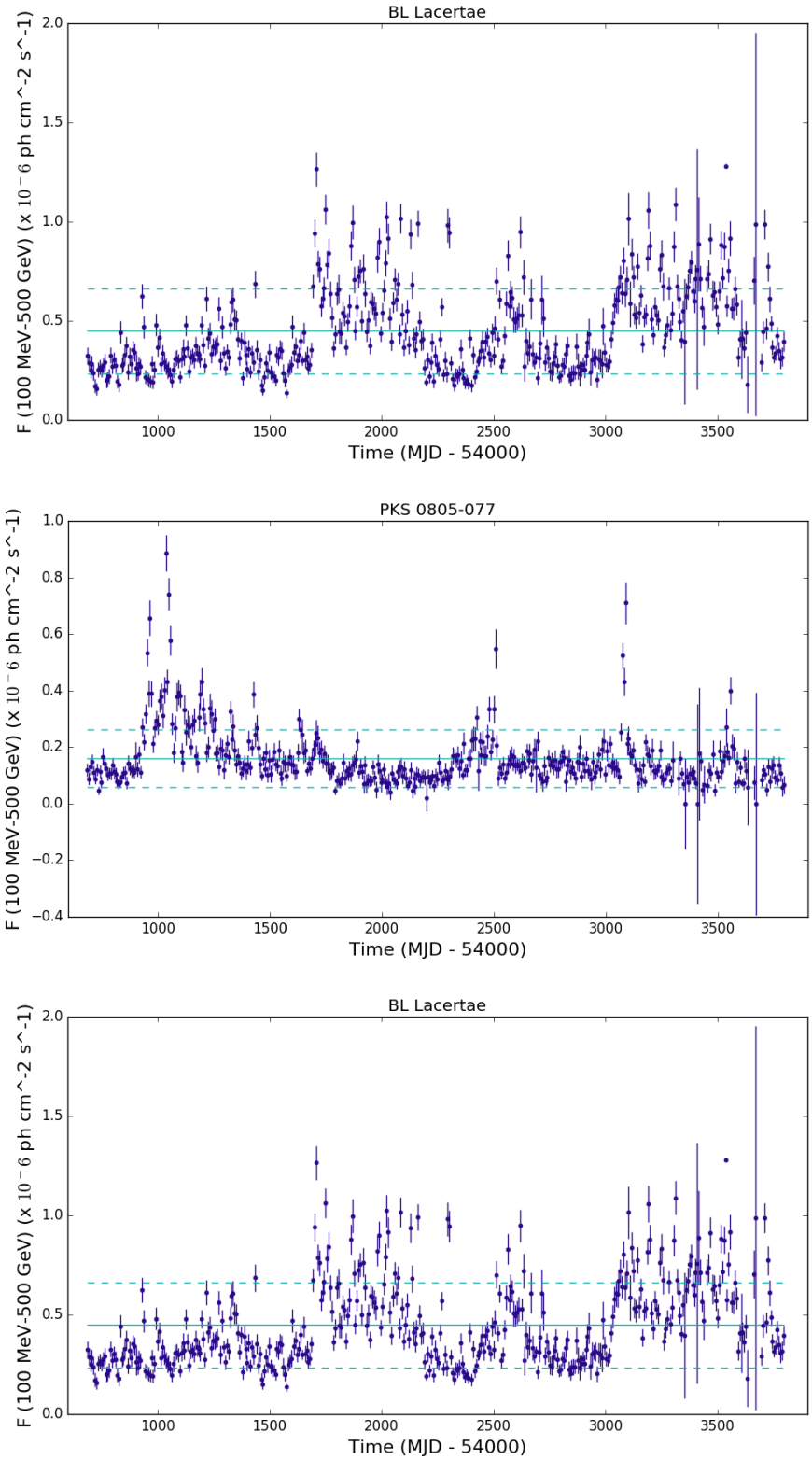

FIGURE 3.7: Exemple de courbe de lumière (évolution du flux en fonction du temps) pour les blazars BL Lacertae, PKS 0805-077 et PKS 1502+106 avec les données publiques *Fermi*-LAT.

Part II

TeV observations with H.E.S.S.

Chapter 4

Detection of very high energy γ rays and the H.E.S.S. telescopes

Contents

As seen on Chapter 1, the field of VHE γ-ray astronomy started to expand in the 90s using the Cherenkov light emitted by the secondary particles of the shower. The Cherenkov detection technique of VHE γ rays will be presented in more details in Section 4.1 along with the third generation Imaging Atmospheric Cherenkov Telescopes (IACTs), H.E.S.S., MAGIC and VERITAS.

The rest of the chapter focuses more on the High Energy Stereoscopic System (aka H.E.S.S. in honor of Victor Hess, discoverer of the cosmic rays), an array of 5 IACTs located in the Khomas Highland, Namibia.

Section 4.3 details the analysis used in H.E.S.S. (and for all the H.E.S.S. results presented in this thesis), from the calibration of the data to the runs and events selection uand reconstruction sed to construct spectra and light curves.

4.1 The detection of VHE γ-rays

4.1.1 Atmospheric particles showers

When particles (cosmic rays and gammas) arrive in the atmosphere, they produce a particles shower propagating towards the ground. Leptons and hadrons will create showers

with a different morphology (Figure 4.1). Electrons, positrons and photons will create similar electromagnetic cascades which are thin and collimated, whereas protons and heavier nuclei will create hadronic ones, broader and messier.

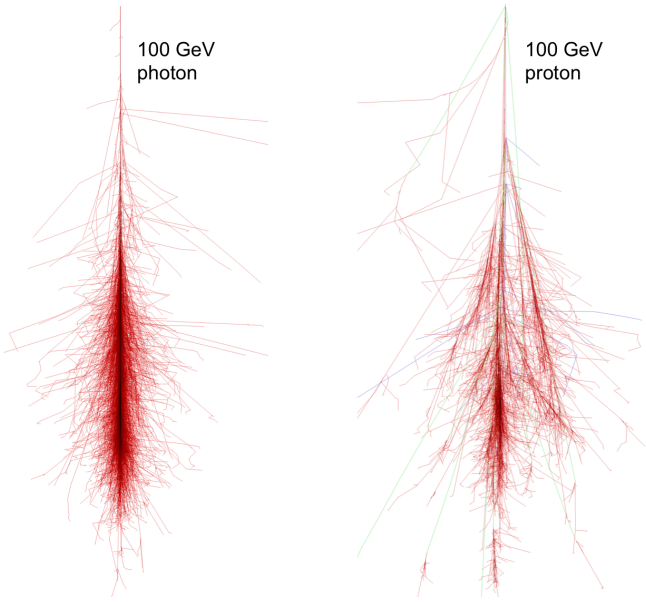

FIGURE 4.1: Showers from a photon (left) and a proton (right). Each line represents the path a particle during the shower development. ©CORSIKA.

The secondary particles are relativistic and propagates faster than the speed of light in the air. Hence they produce Cherenkov radiation which can be detected by ground-based IACTs.

Another technique consists in detecting the particles of the showers when they reach the ground. The resulting energy threshold is higher than IACTs ($\sim$ TeV) because it requires highly energetic primary particles. HAWC (High-Altitude Water Cherenkov Gamma-Ray Observatory) is composed of 300 water tanks designed to detect these cascades (González, 2011).

4.1.2 Detection of Cherenkov light

A charged particle propagating into a dielectric medium will polarize it. But when the particle is relativistic the polarization is late compared to the travel of the initial particle since it propagates slower, and it produces a coherent wave-front. The light created by this phenomenom is called Cherenkov light.

The Cherenkov light is emitted in the UV and blue regions of the electromagnetic spectrum and is very faint, composed on very few photons. It forms a cone with an opening angle of $\cos\theta_c = \frac{1}{\beta\eta}$ where β is the speed of the relativistic particle and η the refraction index of the medium. The number of Cherenkov photon emitted per wavelength unit λ and per trace unit x is:

$$\frac{d^2N}{d\lambda dx} = 2\pi\alpha\frac{\sin^2\theta}{\lambda^2} \tag{4.1}$$

where α is the fine-structure constant. Since the number of Cherenkov photons emitted is proportional to the length of the particles traces x which is roughly proportional to the energy of the primary particle, measuring the number of Cherenkov photons allows to mesure the energy of the primary γ photon.

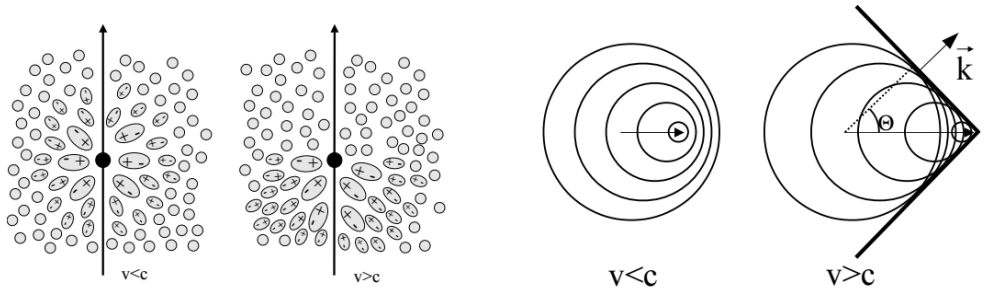

FIGURE 4.2: Left: Illustration of the polarization of the medium induced by the crossing of a relativistic electron. Right: Construction of the Cherenkov wave-front.

The Cherenkov light is a flash and only lasts a few nanoseconds. Hence it requires top notch technology to detect it in good conditions. In IACTs, Cherenkov light is collected by mirrors to be reflected on cameras. These cameras take a picture of the particle showers thanks to the Cherenkov flash.

Cameras used are precise with several hundreds of pixels. It allows IACTs to have very powerful discrimination capabilities between the Cherenkov light produced by photons or by protons.

4.1.3 H.E.S.S., MAGIC, VERITAS & CTA

Today, there are 3 major IACTs experiments (Figure 4.3): the High Energy Stereoscopic System (H.E.S.S.) in Namibia, the Major Atmospheric Gamma-Ray Imaging Cherenkov (MAGIC) in the Canary Islands and the Very Energetic Radiation Imaging Telescope Array System (VERITAS) in the U.S. They all follow the important concepts of IACTs which have been tested years before with the previous generation of Cherenkov telescopes:

1. Large mirror to collect as much Cherenkov light as possible. With larger mirror, IACTs can decrease their energy threshold.

2. Stereoscopic observations (Figure 4.12) in order to have a better energy and angular resolution as well as a better separation power between γ and hadrons.

3. Fine pixelized camera to have a detailed image of the shower, in order again to have a better energy and angular resolution as well as a better separation between gammas and hadrons.

4. Fast electronics to capture the Cherenkov light without integrating too much background to keep the energy threshold low.

Before the advent of the third generation of IACTs, only 7 VHE sources were known (see Chapter 1 for more details). Since then, the field of very high energy gamma ray astronomy never stopped to develop. With the advent of H.E.S.S., MAGIC and VERITAS, almost 200 of VHE sources, including $\sim$ 70 AGN, have been discovered. Despite their huge scientific success, these telescopes are at least 10 years old. A new generation of IACTs, taking advantage of the new advancements in technology and more telescopes to achieve a better sensitivity needs to be planned.

Cherenkov Telescope Array (CTA, Figure 4.4) is the new project of IACTs. Scientists from H.E.S.S., MAGIC and VERITAS came together in order to create the largest VHE observatory in the world. The array of different sized telescopes (small, medium and large) will be split in two sites:

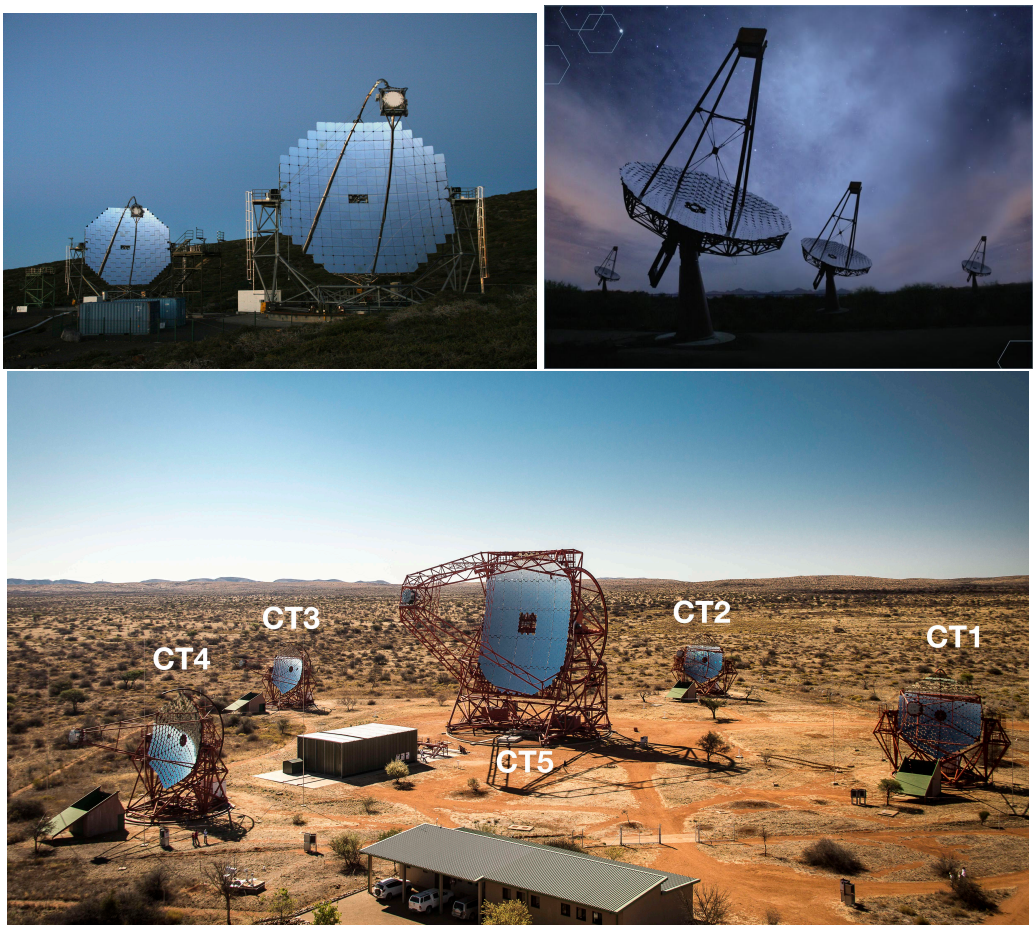

FIGURE 4.3: Pictures of the current IACT arrays in the world: MAGIC (top left), VERITAS (bottom left) and H.E.S.S. (bottom).

- Northern hemisphere (La Palma, Spain): this site will be devoted to the extragalactic observations and will have $\sim$ 20 telescopes;
- Southern hemisphere (ESO Observatory): this site will be specialized in Galactic studies, with a good coverage of all the Galactic plane and will have $\sim$ 100 telescopes.

The rest of the chapter will focus on the H.E.S.S. telescopes. Since the beginning of the experiment, they discovered 106 VHE sources, and more are expected to be discovered until the end of the experiment.

4.2 The H.E.S.S. array

4.2.1 Geographical location

H.E.S.S. is the only IACTs array located in the Southern hemisphere which is an advantage to observe the Galaxy plane and center in good zenith conditions.

The H.E.S.S. telescopes are in Namibia, a coutry not known for its high population density but rather for the very good quality of the sky at night. Due to the low number of inhabitants and the lack of big infrastructures there is no pollution (light or air pollution) in the majority of the country. Moreover, the Khomas Highland are at 1800 m in altitude, facilitating the detection of the Cherenkov showers.

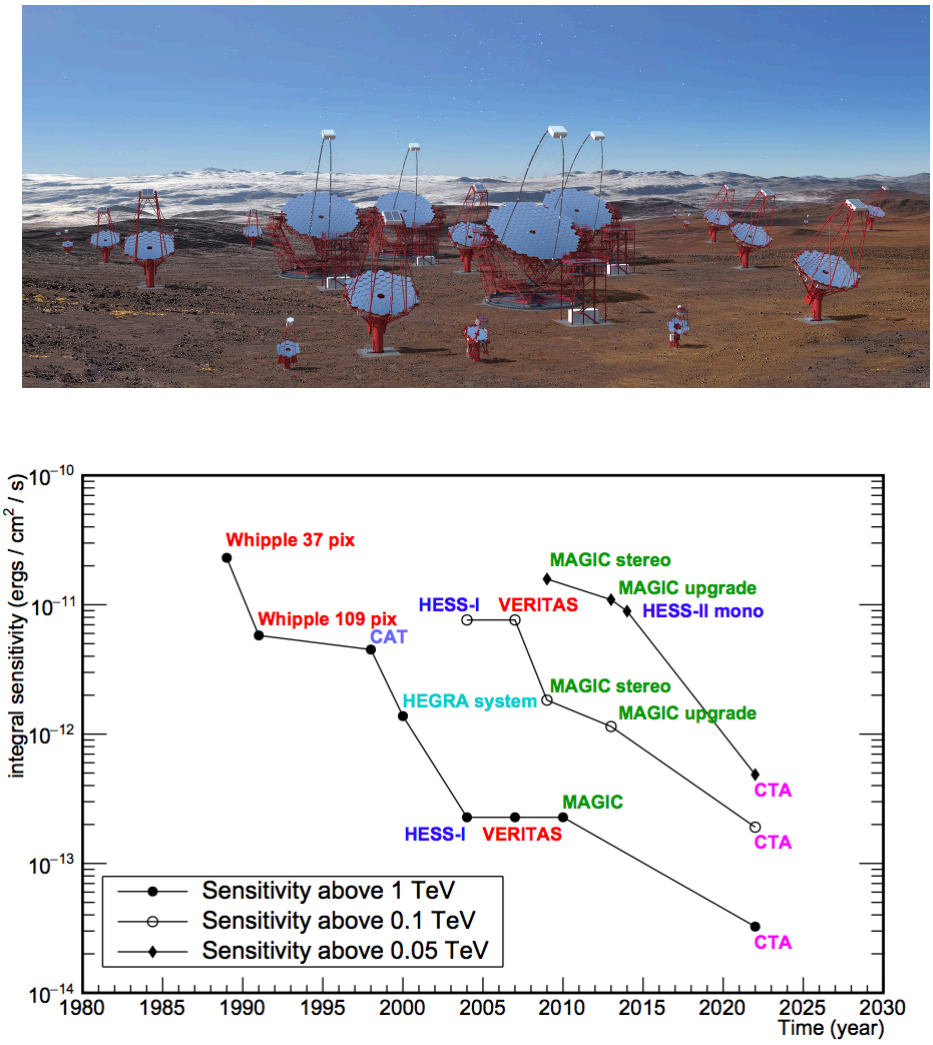

FIGURE 4.4: Top: Sketch of the Southern CTA array ©CTA. Bottom: Evolution of the integral sensitiviy of the IACTs over time above 50 GeV (filled diamonds), 100 GeV (open circles) and 1 TeV (filled circles).

4.2.2 More details about the telescopes

H.E.S.S. Phase-I and II

H.E.S.S. Phase-I, or H.E.S.S.-I, spans from 2004 to 2012. At this time, the array was composed of four 12 meters telescopes, distributed at the corners of a square of 120 meters. This distance has been chosen as a good compromise between seeing a lot of showers and enabling at least two telescopes to see the same shower to apply the stereoscopic reconstruction method. Telescopes are named by number: Cherenkov Telescope 1, 2, 3 and 4, or CT1, CT2, CT3 and CT4. During this period, the energy range of the instrument was from $\sim$ 200 GeV up to $\sim$ 10 TeV. The field of view was of 5° with an angular resolution better than 0.1°.

H.E.S.S. Phase-II, or H.E.S.S.-II, started in 2012 with a new telescope (CT5) placed in the center of the square formed by CT1-2-3-4. The dish of 28×32 meters allows to detect fainter showers and to decrease the energy threshold of the array down to $\sim$ 30 GeV. Decreasing the energy threshold of the array is useful to detect more sources and to fill

the gap with the *Fermi*-LAT range which goes up to 300 GeV for most of the sources[1]. The field of view of CT5 is smaller than the other telescopes with $3.2°$. CT5 camera is mounted on rails and can move, to change the focus distance with a 0.05 mm precision. The distance between the telescopes and the atmospheric showers depends on the zenith angle, tuning the focus distance could help seeing the showers better. Effects of the autofocus won't be discussed in the following but the thesis of Cyril Trichard is latest work done on it in the H.E.S.S. Collaboration discusses this topic (Trichard, 2015).

Cameras

The camera of each CT1-4 telescope is the same and composed of 960 photo-multipliers (PMs), also called pixels, organized in 60 drawers (right panel of Figure 4.5). Each drawer contains 16 pixels, forming a square-like shape. For CT5, the camera is working the same way but with 2048 pixels organized in 128 drawers. Each pixel features a Winston cone on top in order to limit its field of view to the mirror only and to fill the gap between the PMs[2] (right panel of Figure 4.5).

The data acquisition in each pixel is fast (with a readout window of about 10-20 ns), to limit the noise coming from the night sky background (NSB) and because of the small duration of the Cherenknov light. The trigger rate of the camera is ~ 1.4 kHz for CT1-4 and ~ 4 kHz for CT5.

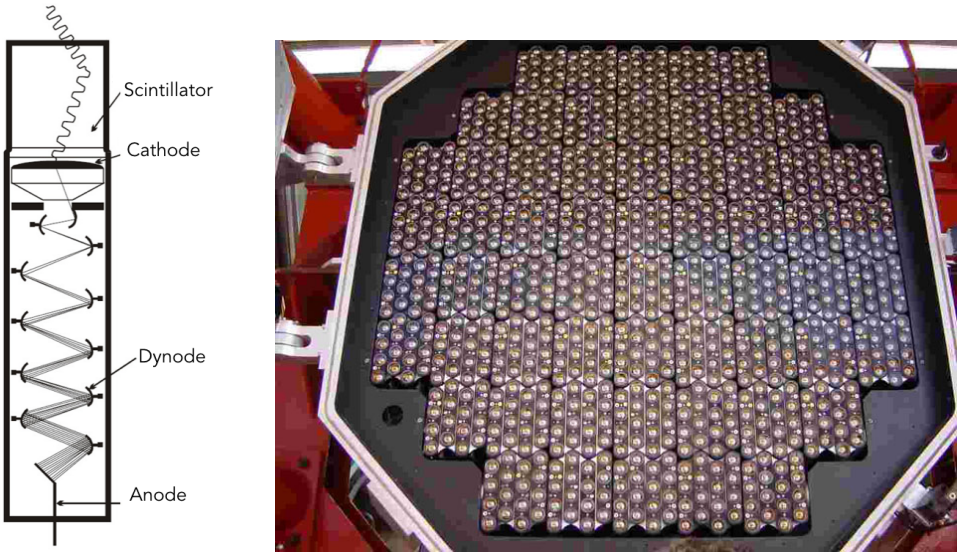

FIGURE 4.5: Left: Illustration of a photomultiplier tube. Right: Picture of one of the cameras, 960 PM with their Winston cones.

PMs are composed of a photocathode, dynodes and an anode (left panel Figure 4.5). The photocathode converts light into electrons, called in this case photo-electrons. The electric field in the PM tube accelerates the photo-electrons towards the anode. At each dynode, the number of photo-electrons rises a lot. At the end of the PM, the electrons flux is high enough to create and detect an electric current. One can define the gain of the PM with $G = Ne_f/Ne_i$ where Ne_i is the initial number of photo-electrons after the photocathode and Ne_f the number of electrons at the end. The gain depends on the

[1] Still, the spectrum is dominated by the low energy part and the astrophysical mecanisms are badly constrained at these energies.

[2] The PM surface is round whereas a pixel in the camera is represented as an hexagon because of the shape of the Winston cone.

electric field applied to the PM and can be modified by tuning the high voltage. For the PMs of the H.E.S.S. cameras, the gain is of this order of 10^5.

4.2.3 Observations with the H.E.S.S. telescopes

Data taking

H.E.S.S. only observes during the dark time, when the Sun and the Moon are 18° below the horizon. The cameras, to detect the Cherenkov light, have to be very sensitive and the light of the Moon could spoil the detector or contaminate the data.

In order to keep a good atmosphere during observations, the data are taken only when the weather is clear. During the night, the atmosphere is monitored by several secondary detectors. It helps knowing the evolution of the temperature and the humidity, also to detect the presence of clouds in the sky.

An observation lasts 28 minutes (we call it a run) in order not to move too much in zenith angle and to cut the data volume which would be too heavy to handle. During these 28 minutes, the telescopes are slowly moving to keep the pointing position on the wished target.

Observation and trigger configurations

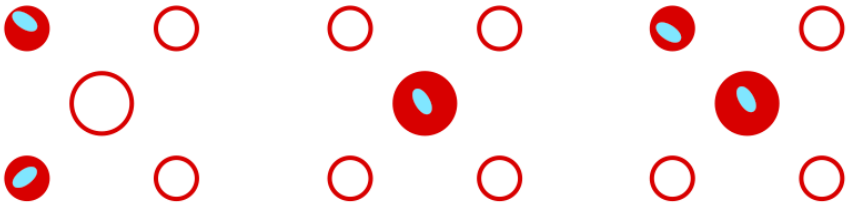

FIGURE 4.6: Different trigger configurations for the H.E.S.S. array. Each red circle represents a telescope (with CT5 in the middle), filled circled represented the telescopes which trigerred on a Cherenkov flash. Left: H.E.S.S.-I Stereo, at least 2 H.E.S.S.-I telescopes. Middle: CT5 Mono. Right: H.E.S.S.-II Stereo, at least 2 telescopes, no difference made between CT1-4 and CT5.

Having 5 telescopes of 2 different types gives several possibilities to observe the sky as represented on Figure 4.6:

1. Stereo H.E.S.S.-I trigger (left): only the CT1-2-3-4 telescopes observe together, to trigger an event at least 2 telescopes must see and trigger on the Cherenkov shower. No information from CT5 is taken.

2. Mono (middle): CT5 is triggering on its own without looking at whether or not CT1-4 triggered.

3. Hybrid (right): all the telescopes observe together but each subarray follow its own trigger (CT5 can trigger in Mono or in coincidence with the other telescopes) to be able to use the stereoscopic and monoscopic reconstructions when analysing the data.

A camera triggers when the Cherenkov signal has been observed by enough pixel. But what is enough? Cameras are divided into 38 sectors of 64 pixels each to maximize

the chances to trigger on a shower and not on background light. The trigger decision occurs when the Cherenkov light in a single sector exceeds 4 photo-electrons (this is the pixel threshold) in at least 3 neighbouring pixels (this is the sector threshold) within a time window of ~ 1.3 ns (to reject NSB events).

In case the event triggered, the trigger decision of the camera is send to the central trigger. If at least 2 telescopes (in the stereoscopic case) triggered on the same event, it is readout and kept.

During the trigger decision, the telescope can not take data. We call dead time fraction the time between the trigger decision in one camera and the reception of the central trigger confirmation signal in that telescope.

4.3 Data analysis principle

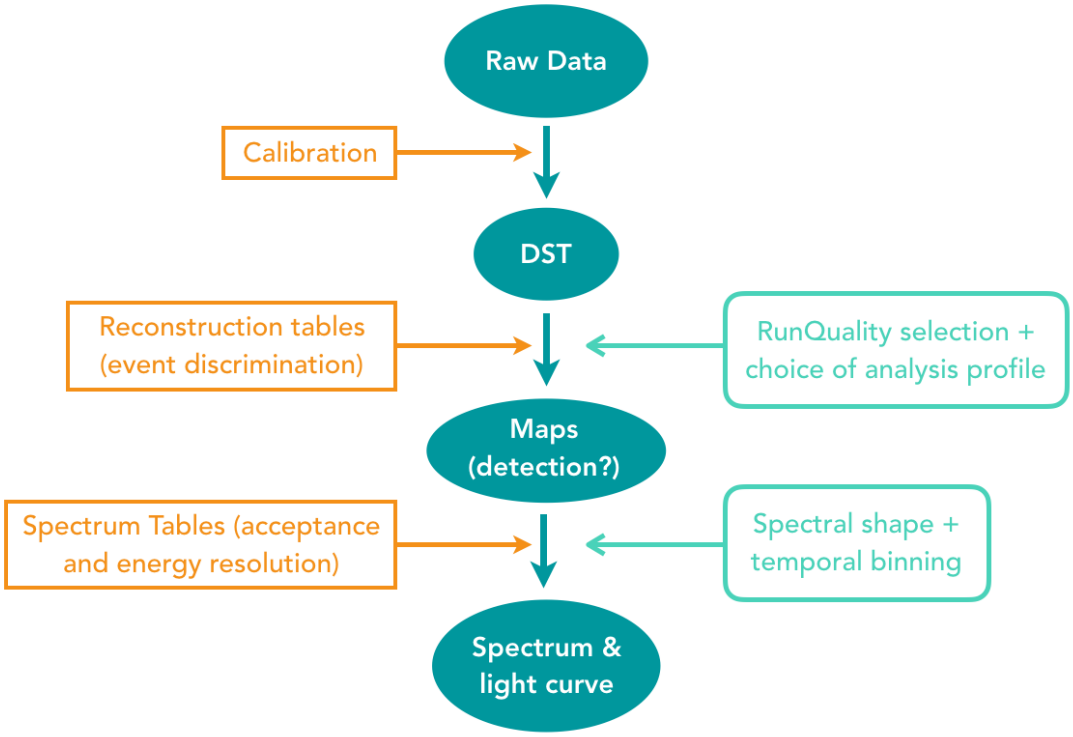

FIGURE 4.7: Principle schema describing the analysis framework of the `ParisAnalysis` chain of H.E.S.S.

The analysis of the data follows different steps represented on the scheme of Figure 4.7 and described in details in the following sections.

First, one needs to know how many Cherenkov photons have been detected in each pixel: this is the calibration step. After their calibration, each run has to pass the quality cuts, in order to be sure the observation conditions and the telescope status were correct. Then, the analysis, following the chosen profile, will determine if an event should be identified as γ-ray photon or a hadron and reconstructs their energy and direction of arrival. The majority of the events are triggered by cosmic rays (protons and heavier

hadrons, generally a thousand time more numerous than γ rays), meaning that the discrimination process is critical. Finally, assuming a certain spectral shape, one can derive the spectral informations and the light curve of the source.

4.3.1 Calibration

Calibration is critical to be able to know the number of Cherenkov photons per pixel and trace it back to the flux and energy of the γ source. To estimate these numbers, one has to convert the charge, the number of ADC (Analog to Digital Converter) counts, in number of photo-electrons. A converter is used to digitalize the current measured at the end of the PM. Gain is measured in two channels, high and low, in order to prevent saturation when a bright event appears (low channel, LG) while still being sensitive to faint signal (high channel, HG). The relation between the amplitude in photo-electron with the charge in ADC counts ($ADC^{HG,LG}$) in each channel is:

$$A^{HG} = \frac{ADC^{HG} - P^{HG}}{\gamma_e^{ADC,HG}} \times C_{FF} \tag{4.2}$$

$$A^{LG} = \frac{ADC^{LG} - P^{LG}}{\gamma_e^{ADC,HG}} \times \frac{HG}{LG} \times C_{FF} \tag{4.3}$$

- P^{HG} and P^{LG} are the pedestals in ADC counts in the high and low gain channels. The pedestals are the electronic signal at the end of the PMs when no photon is detected;
- $\gamma_e^{ADC,HG}$ is the gain for a single photo-electron (single PE) in ADC counts;
- C_{FF} is the flatfield coefficient. It is the deviation of the pixel response regarding the average response of the other pixels;
- HG/LG is the ratio of amplification between the two channels (High-Low ratio).

Each of these values must be determined for each pixel in order to be able to know the characteristics of the initial γ photon. They can be computed during the observations run or require dedicated runs.

Gain

Single PE runs have to be done in order to know the gain value. The telescope is parked in its shelter during dark time in order to prevent any light from the NSB. A pulsed LED illuminates the camera to produce on average one photo-electron per pixel. The charge distribution (in the HG channel) is fitted with the formula:

$$\begin{aligned} G(x) &= N\frac{e^{-\mu}}{\sqrt{2\pi}\sigma_p}\exp\left(-\frac{(x-P_{HG})^2}{2\sigma_p^2}\right) \\ &+ N \times N_s \sum_{n=1}^{m\gg 1} \frac{e^{-\mu}}{\sqrt{2\pi n}\sigma_p}\frac{\mu^n}{n!}\exp\left(-\frac{(x-(P_{HG}+n\gamma_{HG}))^2}{2n\sigma_{\gamma_e}^2}\right) \end{aligned} \tag{4.4}$$

- N is the number of trigger;
- μ is the average luminosity corresponding to the average number of photo-electrons per trigger;

- P_{HG} is the pedestal position in the HG channel;
- σ_p is the width of the pedestal;
- σ_{γ_e} is the width of the photo-electron peak;
- γ_{HG} is the gain of the PM;
- N_s is the normalisation factor (~ 1 because of the Poissonian distribution).

The signal is the sum of the pedestal (described by a Gaussian) and the sum of the n photo-electrons, each of them described by a Gaussian of width $\sqrt{n}\sigma_{\gamma_e}$. The left panel of Figure 4.8 shows the charge distribution of charge for one PM, the first gaussian is the pedestal and the second one is the single photo-electron signal. The gain is the distance between the two gaussians.

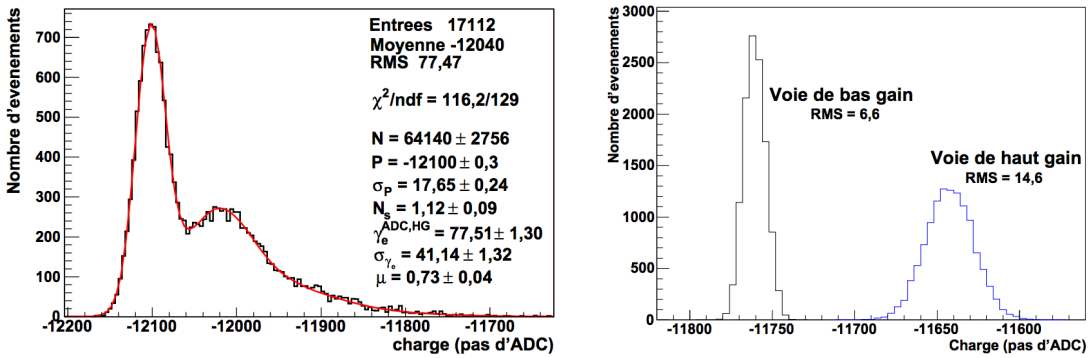

FIGURE 4.8: Left: Charge distribution in ADC counts during a single PE run. Right: pedestals for the low and high gain channels (Rolland, 2005).

Pedestal

Pedestals are the noise of all the acquisition system. It depends on the electronic components of the system and of the temperature inside the camera (or even inside the drawer). Pedestals could be measured during single PE runs or during runs when the camera is running with the lid closed.

However, the camera temperature can change during the night and the NSB widens the pedestal width. Pedestals have to be measured during the data taking every 2 minutes to see the evolution with the temperature. On average, $\sim$ 20 pixels per camera trigger on a Cherenkov signal, the others only see NSB. They are used to determine the pedestals.

High-low ratio

Since the gain for a single photo-electron is too low to be measured in the low gain channel, it has to be computed using the high gain and the high-low ratio HG/LG.

$$HG/LG = \frac{ADC^{HG} - P^{HG}}{ADC^{LG} - P^{LG}} \tag{4.5}$$

The pedestals $P^{LG,HG}$ are already known in both channels. The ADC counts in the LG and HG channels $ADC^{LG,HG}$ are measured. The high-low ratio is ~ 13 giving an average gain of ~ 6 ADC counts for the low gain channel (see right panel of Figure 4.8).

Flatfield

The efficiency of the light collection is different pixel to pixel, depending on the reflectivity of the Wintson cones, the efficiency of the cathode/dynodes and so on. These inhomogeneities between pixels have to be corrected, using the flatfield coefficient C_{FF}, to prevent bias in the reconstruction.

Flatfield runs are done during the dark time with the telescope at $\sim 90^{\circ}$ of zenith angle (parallel to the ground). A LED and an isotropic diffuser in the center of the dish illuminate the camera. The uniformity of the light probes the homogeneity of the pixels response. The flatfield coefficient measures the relative efficiency of light collection for each pixel:

$$C_{FF} = \frac{< I >_{\text{camera}}}{< I >_{\text{pixel}}} \tag{4.6}$$

where $< I >_{\text{camera}}$ and $< I >_{\text{pixel}}$ are the average luminosity measured for the camera and for a pixel during the run.

Optical efficiency

The optical efficiency is the percentage of Cherenkov photons which are detected over all the emitted photons. The optical efficiency of the array is tricky to compute as it depends on the reflectivity of the mirrors and of the Winston cones, the wavelength of the photon, the quantum efficiency of the PMs... These parameters are not easy to quantify as they evolve with time. For a H.E.S.S. telescope at its maximum efficiency, the optical efficiency is of the order of $\sim 10\%$. But with the dust on the optics and telescopes getting older, this value decreases in time.

Using muons we are able to measure the total optical efficiency and its evolution with time. Relativistic muons create a Cherenkov ring in the camera, the radius of the ring being equal to the Cherenkov cone angle. If not all the light of the Cherenkov light from the muon is seen, there is an arc in the camera instead of a ring. Figure 4.9 shows an illustration of both cases. Since muons are relativistic the cone angle of the Cherenkov shower depends only on its energy and the quantity of light depends only on the length of the muon course in the atmosphere.

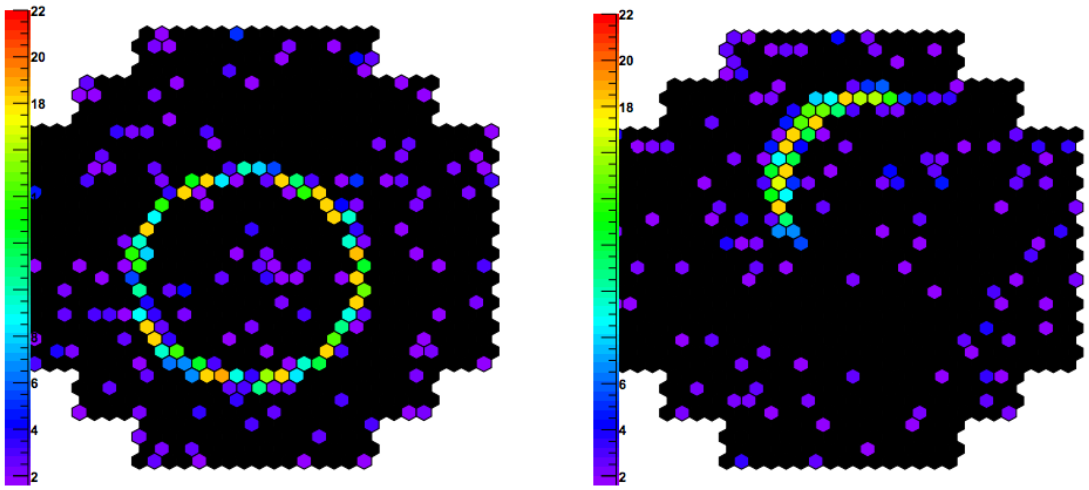

FIGURE 4.9: Examples of muons images in the cameras during observations (Rolland, 2005).

Muons images are modelled using Monte Carlo simulations. Then models and data are compared in order to determine the muon characteristics. For more details, the thesis of Chalme-Calvet, 2015 is the latest work done on it in the H.E.S.S. Collaboration .

Broken pixels

Sometimes, some pixels in the cameras don't work. They are commonly referred as broken pixels and needs to be identified and removed during the calibration not to corrupt the event reconstruction.

Problems leading to a broken pixel are diverse. It can be an alimentation problem giving bad charges values in the PM or because one of the calibration parameter presented above couldn't be computed properly.

Also, a pixel is defined as broken when it is turned off. Stars and shooting stars entering the cameras field of view cause to turn off some pixels during the acquisition. They are too bright for the sensitive H.E.S.S. cameras.

For more details about the calibration of the cameras of the H.E.S.S. telescopes, the thesis of Rolland, 2005 is a good reference.

4.3.2 The run quality selection

Quality cuts have to be applied in order to make sure the run is acceptable and ensure detection or precise spectral studies. Standard cuts were defined in the collaboration in order to ensure the data are of good quality and the results won't be biased or corrupted. There are called the RunQuality cuts. Several profiles exist depending on the analysis wanted (Stereo with or without CT5, Mono), the cuts being different for CT5 and the other telescopes.

The general standard parameters cuts can be described as follow:

- Run properties:
  - Number of telescopes: a minimum of 3 telescopes per run is required to ensure a good stereoscopic reconstruction[3]. If CT5 is observing alone, this cut does not apply.
  - Duration of the run: if the run is too short (because of techniqueal issues which stop the run), it is discarded because of the lack of statistics.
- Central trigger (trigger of the observing array): this is the trigger used when observing in stereoscopic configuration. A central trigger decision is generally made when at least 2 telescopes send a triggering order within a coincidence window of 80 ns.
  - Zenith corrected rate (in Hz): the trigger rate evolves with the zenith angle (the deeper the atmosphere, the smaller the trigger rate because only energetic showers are detected). An abnormal value for the trigger rate can be the sign of a hardware problem.
  - Stability (in % of the rate): it is the RMS of the trigger rate divided by the average rate. An unstable trigger rate is the sign of clouds passing in the field of view.

[3] It doesn't mean that an event with only two telescopes won't be reconstructed.

  - Dead time fraction (in %): generally 5 to 15 % of the duration of the run is dead time, in case this number is too high it could mean that something was not working properly with the telescopes.

- Telescope trigger: it is the same as the central trigger but telescope per telescope.
  - Stability (in % of the rate).
  - Dead time fraction (in %).
  - Pixel/Sector thresholds: the signal in a single sector should exceed 4 photo-electrons in at least 3 neighbouring pixels.

- Autofocus position (in mm) and error (in %) of the CT5 camera.

- Meteo: since the atmosphere is our calorimeter, its status (humidity, clouds, wind) is of importance for the development of the Cherenkov shower.
  - Radiometer temperature (in degrees): radiometer on each telescopes are scanning the sky. The temperature measured is related to the humidity level and the cloud coverage.
  - Radiometer stability (in %): when the radiometer temperature is rapidly changing it means that clouds are passing in the field of view, changing the trigger during the observations.
  - Relative humidity: in case the atmosphere is too humid, it changes its properties compared to our simulations. Plus, a high humidity value (80-90 %) is a sign of coming rain.

- Broken pixels fraction (per telescope): when too much pixels are broken, the reconstruction of the event can't be trusted.

Because of the hybrid array which is H.E.S.S. there are several cuts profiles: HESS 1 Standard/Loose, HESS 2 Mono Standard, HESS 2 Stereo Standard requiring CT5 in the array, HESS 2 Stereo Standard (CT5 is accepted but not madatory), HESS 2 Hybrid Standard (a mix of Mono and Stereo). Each profile has quality cuts optimised for the telescopes and the corresponding analysis (see next Section 4.3.7).

For more details about the run quality parameters of H.E.S.S., the thesis of Mathieu Kiefer is a good reference (Kieffer, 2015).

In order to have an idea about how much runs are lost because of each cuts, I did a quick study, taking a raw runlist for the 3 main profiles HESS 1 Standard, HESS 2 Stereo Standard (CT1-5, CT5 not mandatory) and HESS 2 Mono Standard, and applying the standard cuts one by one.

1. The HESS 1 Standard profile is the standard profile for CT1-4 stereo analyses. The raw runlist contains 196483 runs between run 18132 and 79894 (the whole H.E.S.S. Phase-I between 2004 and 2012).

2. The HESS 2 Stereo Standard profile is the standard Stereo profile since the beginning of the H.E.S.S. Phase-II. The raw runlist contains 11115 runs from run 76335 to 123748 (from the beginning of H.E.S.S. Phase-II until August 2016).

3. The HESS 2 Mono Standard is only looking at runs containing CT5, if CT1-4 are in the array, they will just be ignored later in the analysis. The raw runlist has the same boudaries as the HESS 2 Stereo Standard but contains 7612 runs (Mono runs already selected).

Then on each raw runlist, cuts of the specific profile are applied one by one to know how many runs are lost each time. Of course, with this method, some runs are discarded by several cuts. So the total percentage of runs not passing the quality cuts is not the sum of the percentage of runs cut per cut criteria. The numbers are presented in Table 4.1 on page 78.

The HESS 1 Std cuts throw away 20.1 % of the runs mainly because of the central trigger cuts and the CT1-4 trigger rate cuts, which are sometimes related. In both of them, the stability of the trigger is the reason why so many runs are bad. Either it is because of clouds were passing above the telescopes' field of view or because of some hardware issues in the camera.

The H.E.S.S. Phase-II is less efficient in term of data taking when looking at the number for the HESS 2 Stereo Std and HESS 2 Mono Std profiles. The HESS 2 Stereo Std profile cuts 37.1 %, almost twice as much as the HESS 1 Std (which is also just a Stereo profile, but only with CT1-4). Again, the CT1-4 trigger rate cuts are the main ones, cutting 24.0 % of the runs, but the pixel/sector threshold is dominating over the stability of the trigger because a lot of runs don't have this information in the runs database (for an unknown reason), hence these runs are discarded. Then, the run properties are cutting 18.6 %. This is a huge fraction of runs compared to the 3.9 % of the HESS 1 Std profile knowing that the cut is the same and that there is sometimes one more telescope in the array. Also, the number of broken pixels in the CT1-4 and CT5 cameras is discarding a non negligeable part of the runs.

The HESS 2 Mono profile cuts 26.4 % of the runs. This is easier to analyse because there is only one telescope involved. The broken pixels of the camera are the main issue cutting almost 14 % of the runs (also the cut is harder than for CT1-4, 5 % of broken pixels allowed instead of 15 %, but it is because the Mono reconstruction requires more precision). Almost 10 % of the runs are cut because of their too short duration, because the camera experiences a problem in the first minutes of the run.

4.3.3 Event discrimination and reconstruction

As seen in Section 4.1, showers produced by gammas/electrons or by hadrons are different. Electromagnetic showers tend to be more collimated, while hadronic showers are wider and contain sub-electromagnetic cascades. This difference can be seen in the resulting image of the Cherenkov shower on Figure 4.10. The Cherenkov image of a photon looks like an ellipse whereas the image of a hadron will be messier and wider.

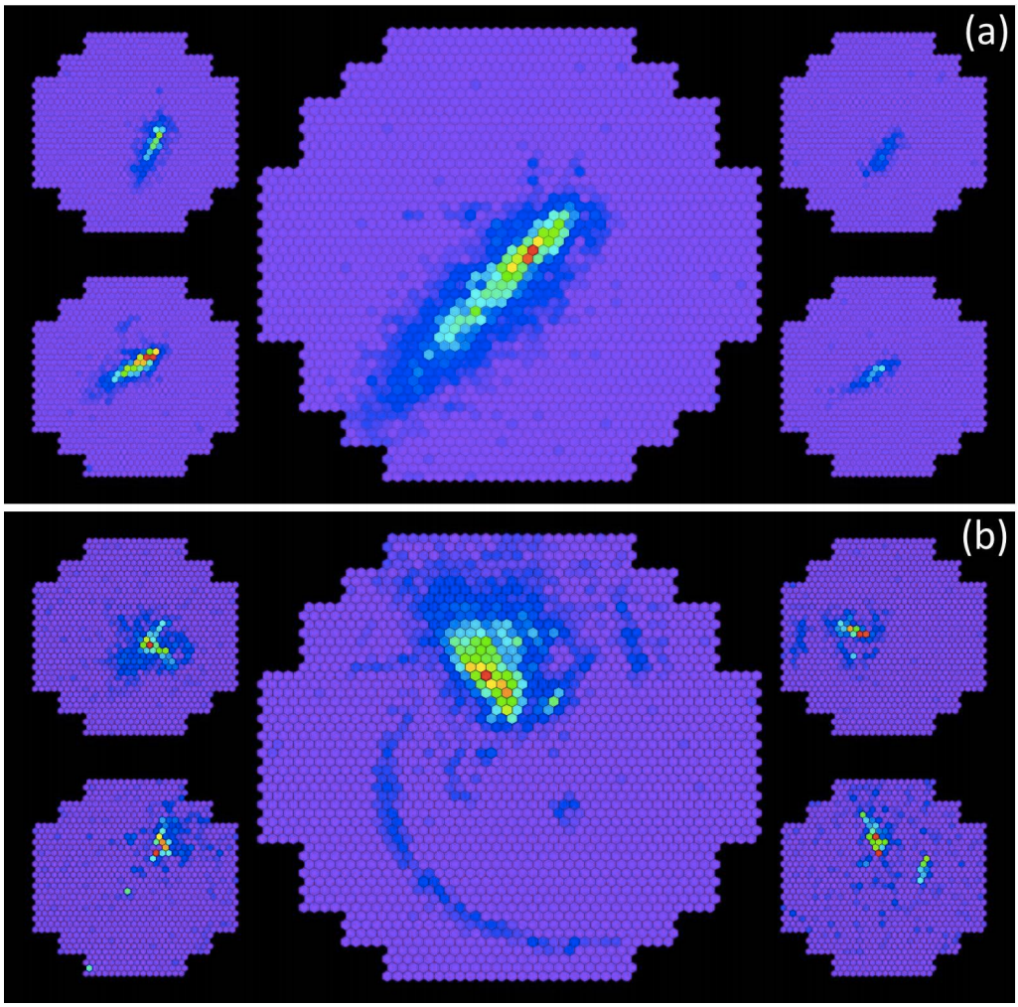

FIGURE 4.10: Examples of image of atmospheric showers produced by a photon (top) and a cosmic ray hadron (bottom) in the H.E.S.S. cameras.

The Hillas reconstruction

The first effective method used in IACTs to discriminate and reconstruct events is the Hillas reconstruction (Hillas, 1985). It uses the elliptical shape of the gamma-ray shower and parametrise it by an ellipse. There are 6 parameters represented on Figure 4.11:

- the width w of the ellipse;
- the lenght L of the ellipse;
- the angular distance d between the camera center and the ellipse center of gravity (also called *Nomimal Distance*);

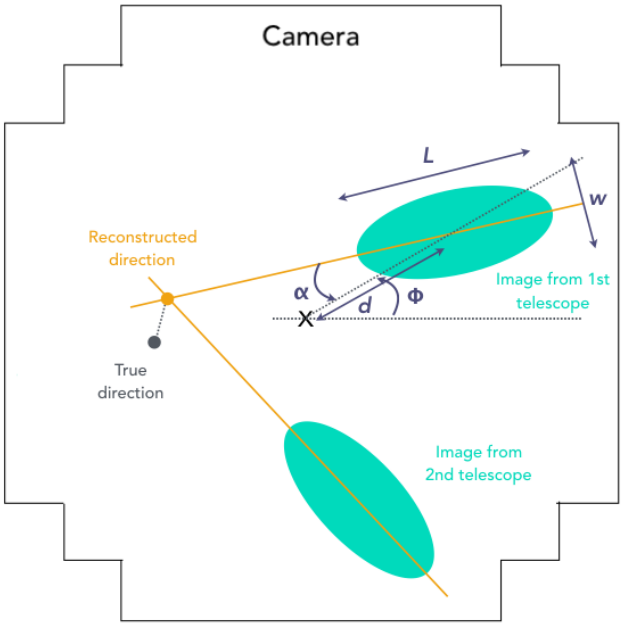

FIGURE 4.11: Hillas parametrisation.

- the azimuthal angle ϕ;
- the orientation angle α;
- the amplitude of the image.

But before being able to reconstruct the ellipse parameter, each image has to be cleaned to reduce the contamination from the night sky background. The intensity is supposed to be Gaussian on the longitudinal and transverse axis. The energy of the primary γ will be reconstructed using simulations using the amplitude and impact parameter (projection of the cascade direction on the ground) of the ellipse.

Stereoscopic observations (Figure 4.12) help to combine informations to reconstruct the direction of the γ and the impact parameter, defined as the projection of the shower direction on the ground.

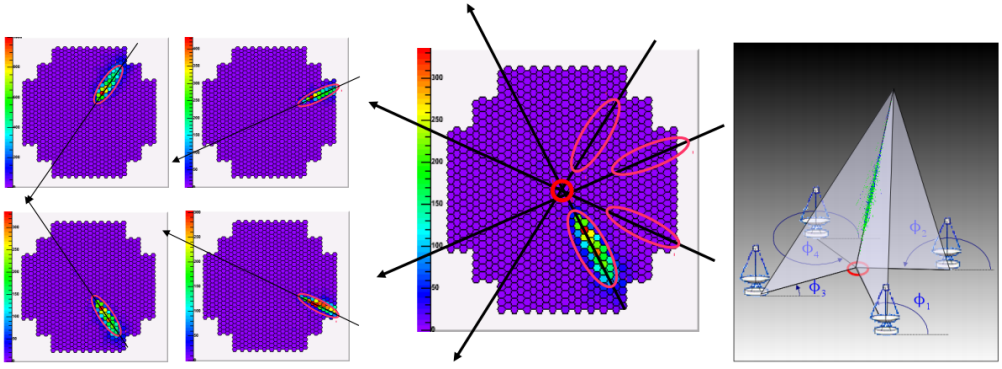

FIGURE 4.12: Geometric reconstruction of the shower direction and impact in stereoscopic mode.

However, the Hillas reconstruction is highly sensitive to the amount and position of the broken pixels in the cameras. Images with broken pixels or located close to the edge

or the camera will have badly reconstructed parameters. This is why there is a cut applied on the *Nominal Distance* d to reject such events.

The Model reconstruction

Nowadays, a more powerful reconstruction called Model is used. This framework has been invented for the data analysis of the CAT experiment (Le Bohec et al., 1998) and adapted to H.E.S.S. by de Naurois and Rolland, 2009. This reconstruction is the one used in every analysis presented hereafter and is described in the following.

The Model analysis is semi-analytical. It compares template images with real shower images in order to reconstruct the parameters from the initial particle. The templates depends on several parameters:

- the direction of the shower (zenith and azimuth angles);
- the impact parameter;
- the energy of the initial particle;
- the depth of first interaction.

Templates are generated for the different configurations[4] and give the expected quantity of Cherenkov light in the focal plane of the camera. A convolution of the template image with the camera pixels gives a model image we can compare to the real event or to simulations. Figure 4.13 shows 2 examples of images obtain by the model, with the Cherenkov light density per pixel (3D) and the corresponding image in the camera's focal plane (2D). They differ only by the value of the impact parameter.

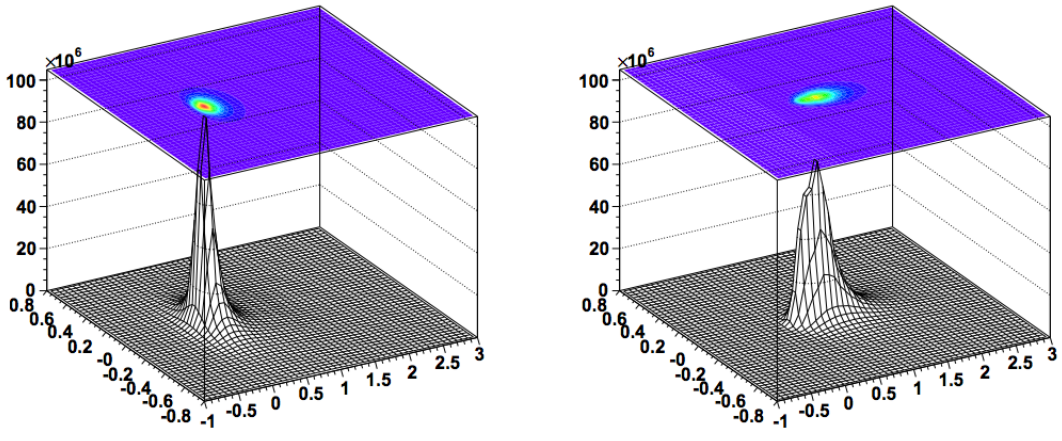

FIGURE 4.13: Model from a 1 TeV shower started at one radiation length and falling 20 m (left) and 100 m away from the telescope (de Naurois and Rolland, 2009). The impact parameter has an impact on the shape of the Cherenkov shower seen.

The comparison is done pixel per pixel, comparing the observed amplitude s_i to the expected amplitude μ_i.The likelihood minimisation gives the best parameter set of the event (direction, energy, impact parameter and first interaction depth).

[4] They are stored in a database and form a library of Cherenkov images.

The log likelihood is used to build the *Goodness* variable (also called goodness-of-fit) allowing to discriminate between showers initiated by photons and hadrons. It is defined as the normalised sum over all pixels of the difference between the log-likelihood of the pixel $\ln \mathcal{L}(s_i|\mu_i)$ and its expected value $< \ln \mathcal{L} > |\mu_i$:

$$G = \frac{1}{\sqrt{2N_{\rm dof}}} \sum_i (\ln \mathcal{L}(s_i|\mu_i) - < \ln \mathcal{L} > |\mu_i) \tag{4.7}$$

where $N_{\rm dof}$ is the number of degrees of freedom (the number of pixel minus the number of parameters).

G is distributed as a Gaussian centered on 0 with variance of 1 and can be used to estimate the probability of an event to be a γ.

After the goodness-of-fit estimation, pixels are separated in two classes to define the *ShowerGoodness* (1) and the *BackgroundGoodness* (2) variables:

1. The shower heart, with pixels with more than 0.01 photo-electrons predicted by the model and a row of three neighbourgh pixels, is used to define the *ShowerGoodness*.
2. The other pixels of the camera, identified as background, are used to define the *BackgroundGoodness*.

The *ShowerGoodness* is more sensitive to the morphological differences between hadronic showers and model templates, increasing the discrimination power. As for the *BackgroundGoodness*, it is more sensitive to diffuse emission and the secondary showers from hadronic showers.

These variables are scaled over the telescopes and become the *MeanScaledShowerGoodness* and *MeanScaledBackgroundGoodness*. The main cut to discriminate γ from hadrons is done using the *MeanScaledShowerGoodness*. Figure 4.14 shows the *ShowerGoodness* distributions along with the cut. It removes more than 95 % of the background and keeps $\sim$ 70 % of the signal.

The Model analysis has an energy resolution of 8 to 12 % with a bias $<$ 5 % over the whole energy range and an angular resolution $< 0.1^\circ$ (going down to 0.06° at energies greater than 500 GeV).

The standard cuts used in the Model analysis to select events are:

- *Nominal distance*: $< 2^\circ$ (the distance between the center of the ellispe and the center of the field of view)
- Minimum charge (the minimum charge in the camera): 60 photo-electrons
- *MeanScaledShowerGoodness*: [-3:0.6]
- *PrimaryDepth*: [-1:4] (the depth of the interaction of the primary particle)
- *MeanScaledBackgroundGoodness*: < -2
- *NSBLikelihood*: < -1 (it represents the probability of an event to be NSB)

with images from at least two telescopes satisfying these cuts. An event passing the cuts is defined as a γ-like event[5].

The *MeanScaledShowerGoodness* and *MeanScaldeBackgroundGoodness* are the same variable as the *ShowerGoodness* and *BackgroundGoodness* but scaled and averaged on all the telescopes which triggered on the events:

$$\text{Scaled } x = \frac{x - \overline{x}}{\sigma_x} \text{ and Mean Scaled } x = \frac{1}{\sqrt{n}} \sum_n \text{Scaled } x \tag{4.8}$$

[5]The event is reconstructed as a γ photon, but the chances of being a hadrons are not zero.

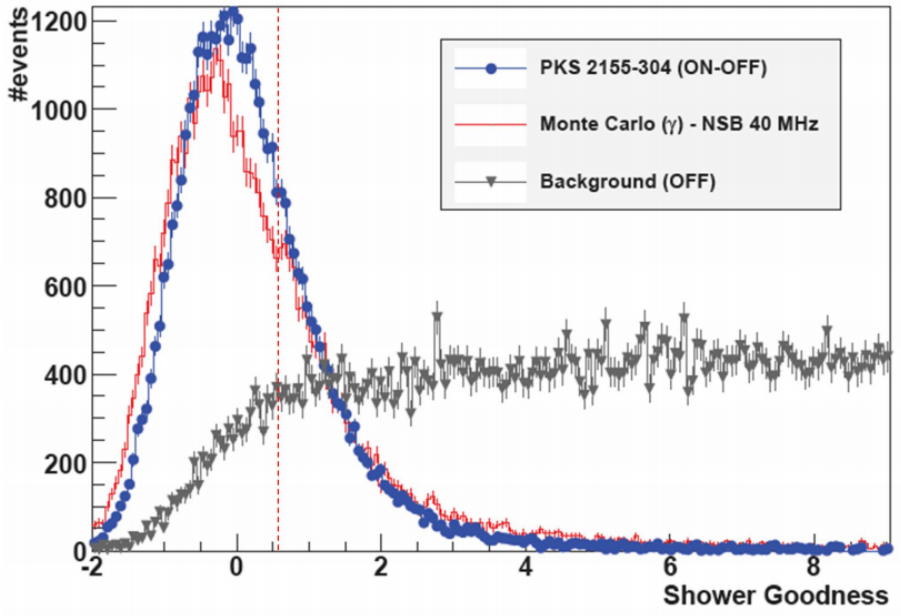

FIGURE 4.14: Distribution of the *ShowerGoodness* variable. Red: distribution for simulated γ. Blue: distribution for the ON-OFF γ observed in the direction of PKS 2155-304. Grey: distribution for the real background events. The red dashed line indicates the position of the cut. (de Naurois and Rolland, 2009)

4.3.4 Acceptance

The acceptance is defined as the probability to detect an event, to accept it from the trigger of the array to through the reconstruction step. Acceptance allows to determine the background of cosmic rays and substract it to the field of view and corresponds to the sensitivity of the array. Acceptance is computed for each run because changes in the observation conditions (zenith angle, meteo, broken pixels...) have an impact on its value. This is why the acceptance for γ-like events has to be computed on data. However to characterise properly the telescopes response to γ-like events, the background has to be computed without the exclusion regions. Exclusion regions are defined on regions of the field of view were there is the potential source or a known source of γ rays. If a γ-ray source in the field of view is not in the exclusion regions, the background will be overestimated, leading to bias in the analysis.

The main methods to compute the acceptance in the H.E.S.S. analysis framework are the radial acceptance and the 2D acceptance.

Radial acceptance

This method can estimate the acceptance for each run, allowing to take into account different observation conditions from one run to another. The radial acceptance assumes a radial symmetry of the camera. Each event (outside of the exclusion regions) is weighted according to its distance r from the camera center with a weight:

$$w = \frac{\pi}{\pi - \theta} \quad \text{with } \cos\theta = \frac{r_0^2 + r^2 - d^2}{2 r_0 r} \tag{4.9}$$

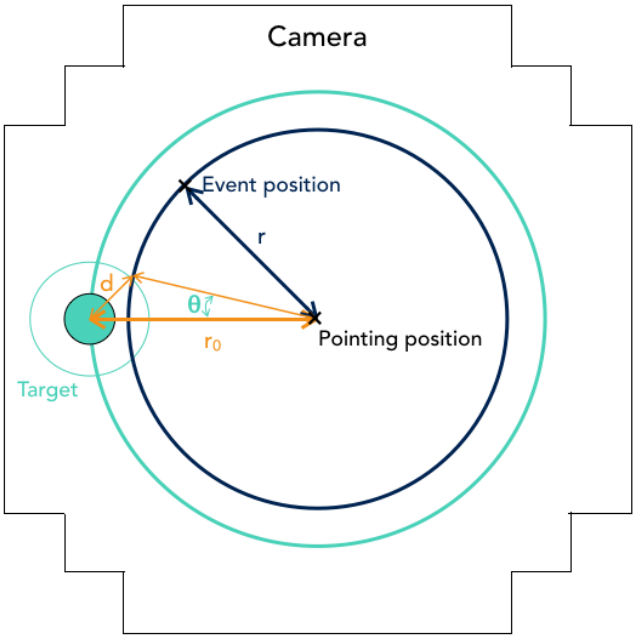

FIGURE 4.15: Computation of the radial acceptance. If an event is at the distance r of the pointing position (= camera center) with $r_0 - d < r < r_0 + d$ the weight w is attributed to it.

where r_0 and d are the position and radius of the target. Figure 4.15 shows an illustration of the computation of the radial acceptance. With this method, the target can't be at the center of the field of view and needs to be offset of few degrees.

Even if the radial symmetry is an assumption of the reality (the camera is not spherical and not uniform because of the different response from different pixels), this method is the only way to compute the acceptance run by run.

2D acceptance

Here, the radial symmetry assumption is no longer needed. The acceptance is computed on a set of runs with the pointed source at different positions in the field of view (positive and negative offsets in Right Ascension and declination). This will smooth the background fluctuations and allow to compute the acceptance in all the field of view since the exclusion regions will be at a different position for every run.

The exposure map of the field of view is computed by summing the exposure maps of each runs without taking into account the exclusions regions. The events map is created the same way. Then the event map is divided by the exposure map to give the acceptance map. The process is illustrated on Figure 4.16.

The 2D acceptance is computed on γ-like events and on the events that were rejected by selection criteria described in Section 4.3.3. The background events being more numerous than the γ-like events, we can compare the two maps which needs to be similar (see Figure 4.17). The limit of these methods lies in the number of runs in the field of view. Figure 4.17 shows an example of this effect. At the top, only one run is used to compute the 2D acceptance: there are a lot of fluctuations and we can see the exclusion region. At the bottom, a larger runlist is used and the acceptance is smoother.

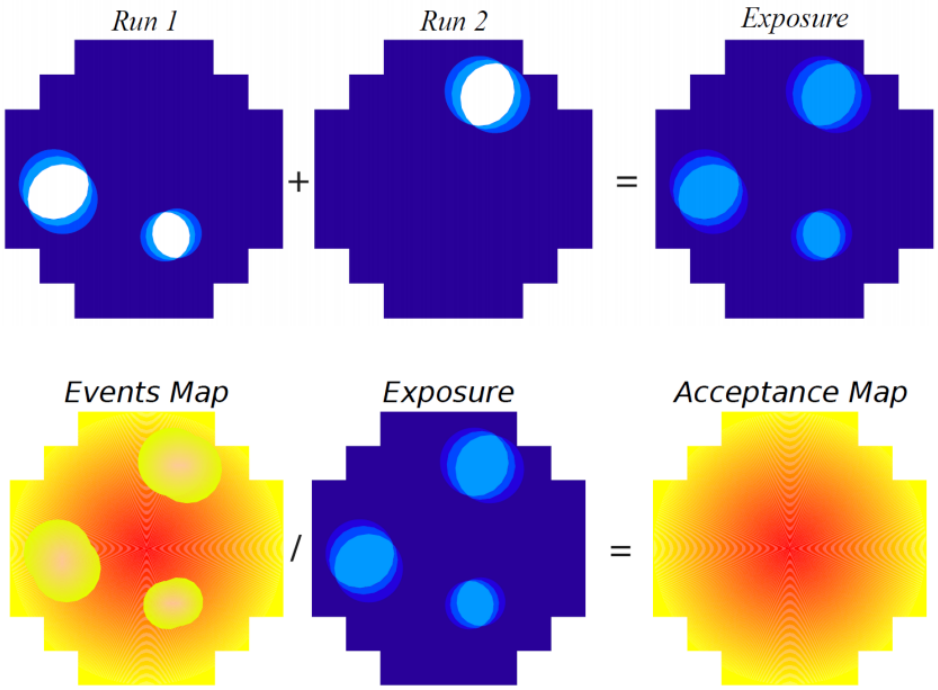

FIGURE 4.16: Computation of the 2D acceptance. Top: computation of the exposure map, exclusions regions are shown in white. Bottom: the events map divided by the exposure map gives the acceptance map (Naurois, 2012).

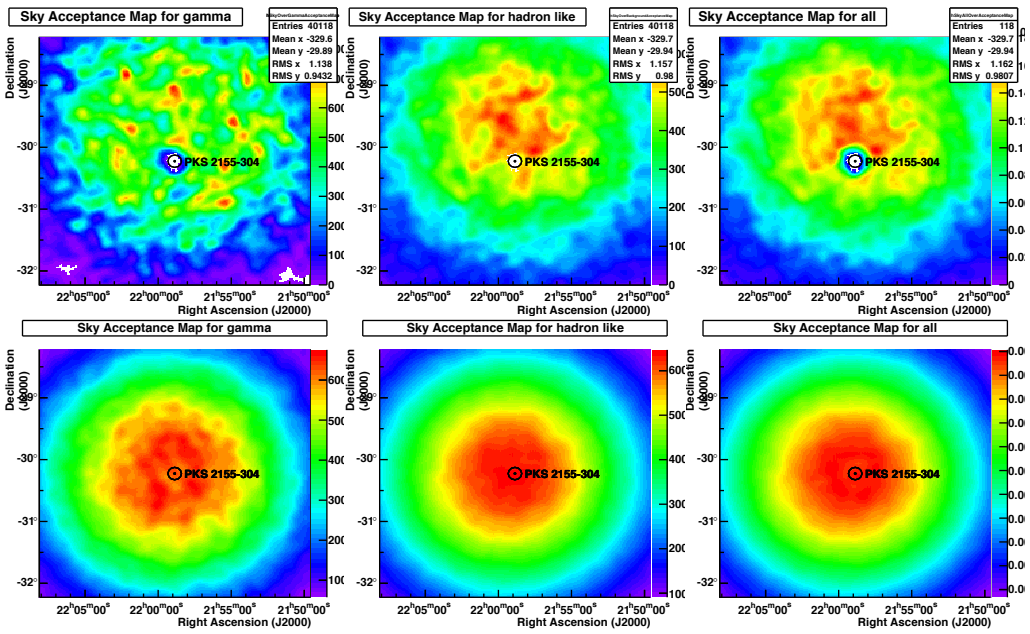

FIGURE 4.17: Example of the acceptance maps for γ-like, hadrons-like and all events computed with 1 (top) and 221 runs (bottom) on PKS 2155-304.

4.3.5 Significance and maps computation with the ON-OFF method

Despite the Model cuts (Section 4.3.3), there are still a lot of background events considered as γ-like events that prevent us to detect the source. This is where the ON-OFF method plays a role.

ON-OFF method

The ON region is defined on the region of interest while the OFF regions are defined in the field of view around the ON region. The number of background events (normalised by the OFF surface with respect to the ON surface) are then substracted to the number of ON events and the remaining number of events is the signal excess.

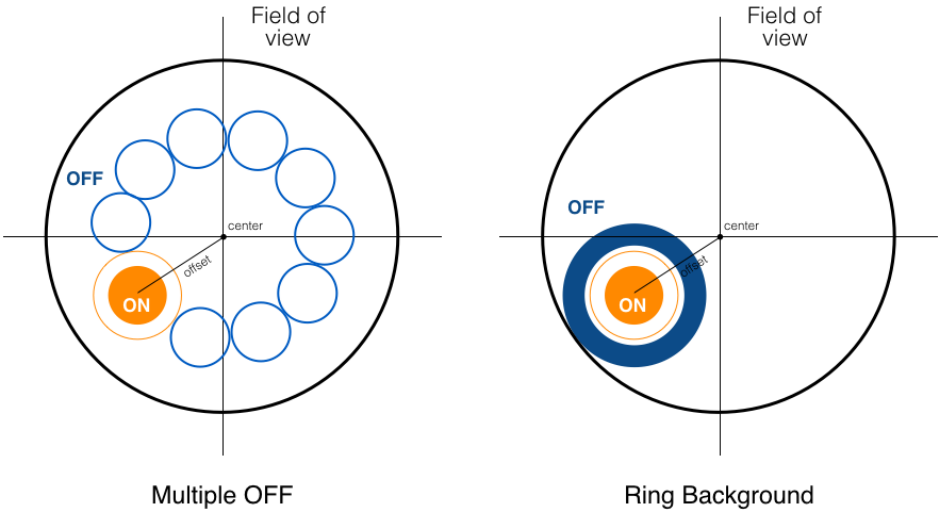

FIGURE 4.18: Illustration of the Multiple OFF (left) and Ring Background methods (right). A safety ring is defined around the ON region to prevent any contamination in the OFF regions.

There are two main ON-OFF methods: Multiple OFF and Ring Background, showed on Figure 4.18.

With the Multiple OFF, each OFF region has the same size as the ON region and is distributed in the field of view with the same offset as the ON region (if there is an exclusion region, the OFF region is not defined on it). The source has to be offset (generally $0.5°$ to $0.7°$) in order to be able to define the OFF regions. The Ring Background uses a ring to define the OFF region around the ON region.

The number of excess events is given by:

$$N_{\text{excess}} = N_{ON} - N_{OFF}/\alpha \tag{4.10}$$

where α is the normalisation factor:

$$\alpha = \frac{\int_{OFF} Acc^{\gamma}_{OFF}(\Phi_x, \Phi_y, \Phi_z, E, t) d\Phi_x d\Phi_y d\Phi_z dE dt}{\int_{ON} Acc^{\gamma}_{ON}(\Phi_x, \Phi_y, \Phi_z, E, t) d\Phi_x d\Phi_y d\Phi_z dE dt} \tag{4.11}$$

defined by the acceptance Acc^{γ} in the ON and OFF regions, depending on the angular coordinates $\Phi_{x,y,z}$ of the event, the energy E and the time of exposure t. Since t is the same for the ON and OFF regions, α can be simplified and represented by the ratio of the

OFF and ON surfaces:

$$\alpha = \frac{\text{Area}_{OFF}}{\text{Area}_{ON}} \tag{4.12}$$

For the Multiple OFF method, α is just the number of OFF regions. This method is used to derive spectra because we are less dependent on the acceptance while the maps are derived with the Ring Background method (which is impossible with the Multiple OFF because the ON region can't be at the center).

Significance

From this we can derive the significance of the ON-OFF excess with the standard method of Li and Ma, 1983. The general formula is:

$$N_\sigma = \sqrt{-2 \ln \lambda} \tag{4.13}$$

with

$$\lambda = \left[\frac{\alpha}{1+\alpha}\left(\frac{N_{ON}+N_{OFF}}{N_{ON}}\right)\right]^{N_{ON}} \times \left[\frac{1}{1+\alpha}\left(\frac{N_{ON}+N_{OFF}}{N_{OFF}}\right)\right]^{N_{OFF}} \tag{4.14}$$

When α is close to 1, like in the Multiple OFF and Ring Background methods, the significance can be approximated by:

$$N_\sigma = \frac{N_{ON} - \alpha N_{OFF}}{\sqrt{\alpha(N_{ON}+N_{OFF})}} \tag{4.15}$$

The significance N_σ is used to assess the detection (or not) of a source. If $N_\sigma \geq 5$, this is a detection (discovery if it is the first time the source is detected), it means that there is a probability $p < 5.94 \times 10^{-7}$ that the signal seen is due to fluctuations. If $N_\sigma \geq 3$, it is considered that there is a hint of signal ($p < 2.70 \times 10^{-3}$).

Maps computation

Observations are graphically represented as excess or significance maps in order to test the presence of a γ source in the whole field of view. The ON-OFF method used to compute such maps is the Ring Background.

The significance distribution of the background regions should follow a Gaussian centered on 0 with a width of 1. If the exclusion are not well defined (γ-ray source not in the exclusion region list, size of the exclusion region too small...) it can create holes or hotspots in the maps because the background is overestimated.

Maps are an easy way to see if the analysis went well. In case of systematics in the analysis or bad calibration, it can be seen directly on the map.

For their computation, the maps are oversampled, the size of the pixels being smaller than the instrument resolution. Each pixel is given its own value and the value of its neighbours in a radius equivalent to the angular resolution of the instrument. This is the top-hat method. Another method, the smoothing one, consists of convoluting the events map with the point spread function (PSF) of the instrument.

Figure 4.19 shows an example of excess and significance maps along with the significance distribution. The excess and significance maps show clearly the presence of the source at the center, with fluctuations in the background. The total significance distribution shows the presence of the source up to $\sim 60\sigma$ (in black) while the significance distribution out of the exclusion regions is shown in red and corresponds, as expected, to a Gaussian(0,1). Maps are 2D representations. The 1D equivalent is called Theta2 plot. It

is the event distribution versus the square of the angular distance from the pointing position. An example is shown in Figure 4.20. In case of the presence of the source, it shows a clear peak around $\Theta^2 = 0$ deg^2. The distribution at large angles shows the remaining hadronic and electronq γ-like background.

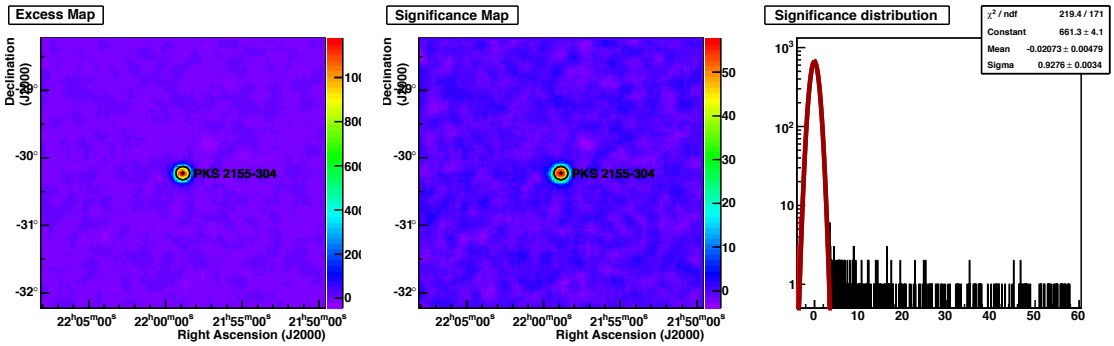

FIGURE 4.19: Excess (left) and significance (middle) maps along with the significance distribution and the fit for the background (right) for observations towards PKS 2155-304.

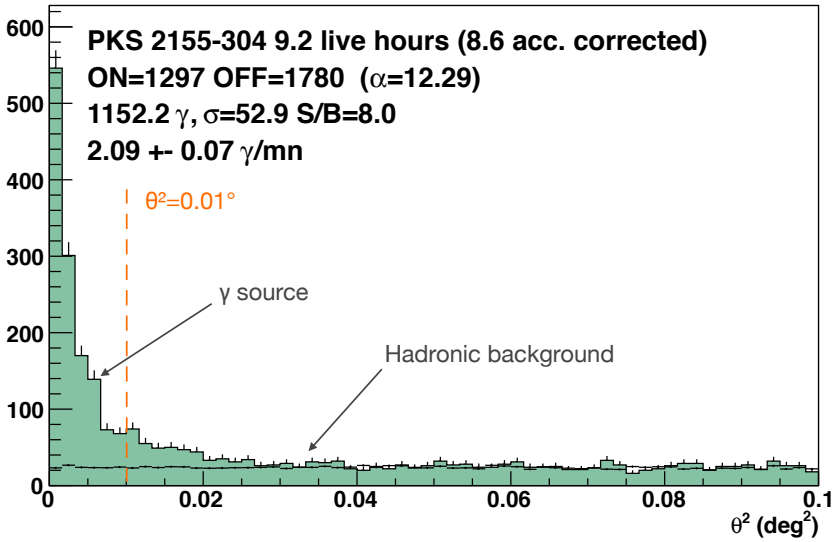

FIGURE 4.20: Events distribution versus the square of the angular distance from the pointing position (also called Theta2 plot) for observations towards PKS 2155-304. The point source cut used for extragalactic observations is set at 0.01 deg^2.

4.3.6 Spectrum and light curve computation

The spectral reconstruction method used in the analysis has been initially developped for the CAT experiment (Piron et al., 2001). It compares the number of events per energy bins to predictions, the later being simulated with the assumption of a spectral shape. The spectral characteristics of the source are derived by a maximum likelihood estimation.

It requires a good knowlegde of the energy resolution and of the acceptance of the detector and their dependency with the observation conditions (zenith angle, offset, optical efficiency).

Acceptance and energy resolution

Acceptance for γ is computed using simulations. Several sets of acceptance are computed and stored in what we call acceptance tables depending on the true energy, the zenith and azimutal angles, the offset and the optical efficiency. The energy resolution is the probability that an event at a true energy $E_{\rm true}$ is reconstructed at the energy $E_{\rm rec}$ and is stored in what we call resolution tables. Figure 4.21 shows an example of energy resolution for a fixed set of parameters. The energy resolution of the H.E.S.S. telescopes is better than 15 % between $\sim$ 200 GeV and $\sim$ 20 TeV, with a bias lower than 5 % (in log space).

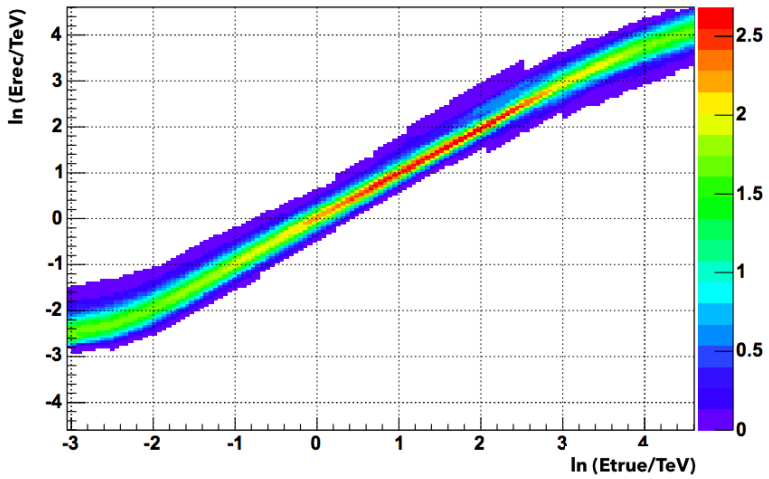

FIGURE 4.21: Example of probability density to reconstruct a γ event of energy $E_{\rm true}$ (x-axis) at an energy of $E_{\rm rec}$ (y-axis) (Rolland, 2005). The color scale represents the probability density function normalized at 1 for a fixed $E_{\rm true}$.

A sampling of the parameter space is done to produce enough tables to describe precisely the instrument.

The spectrum will be derived above a certain energy threshold in order not to be dominated by systematics at too low energy. This energy threshold depends on the observation conditions: a high zenith angle will increase the energy threshold as the particles have more atmosphere to go through. The energy threshold $E_{\rm th}$ is generally defined as the energy where the acceptance is equal to 10-15 % of its maximum value. It prevents the introduction of bias in the reconstruction.

Maximum likelihood method

In this method, a spectral shape is assumed and convolved with the instrument response function to be compared with observations and the likeliness of the spectral hypothesis is tested. The number of expected photons is:

$$n_\gamma^{ie,iz,ir,id} = T_{ON} \int_{E_{min}^{ie}}^{E_{max}^{ie}} dE_{rec} \int_0^\infty dE \frac{dN}{dE} A(E,\theta_{iz},\delta_{id},\mu_{ir}) P(\theta_{iz},\delta_{id},\mu_{ir},E,E_{rec}) \quad (4.16)$$

where $n_\gamma^{ie,iz,ir,id}$ is the number of γ expected in the phase space interval $\Delta_{ie,iz,ir,id}$ described hereafter. T_{ON} is the observation time, dN/dE is the assumed spectral shape, $A(E,\theta_{iz},\delta_{id},\mu_{ir})$ is the acceptance at the energy E and $P(\theta_{iz},\delta_{id},\mu_{ir},E,E_{rec})$ is the probability to reconstruct an event of energy E at the energy E_{rec}. The parameters are binned into intervals:

- zenith angle θ_{iz} with $\Delta \cos\theta = 0.02$,
- optical efficiency μ_{ir} with $\Delta\mu = 0.1$,
- off axis angle δ_{id} with $\Delta\delta = 0.5°$,
- reconstructed energy $E_{rec} \in [E^{ie}_{min}, E^{ie}_{max}]$ with $\Delta \ln E_{rec} = 0.25$.

In every interval, the events of the ON and OFF regions ($N^{ie,iz,ir,id}_{ON}$ and $N^{ie,iz,ir,id}_{OFF}$) are computed and the γ ray excess follows the relation:

$$S^{obs}_{ie,iz,ir,id} = N^{ie,iz,ir,id}_{ON} - N^{ie,iz,ir,id}_{OFF}/\alpha \tag{4.17}$$

A likelihood function, taking into account the poissonian fluctuations of the number of ON and OFF events, can be used and maximized to deduce the parameters of the spectral shape. The details of the method are fully described in Rolland, 2005.

The most common spectral shapes are:

- the power law:
$$\frac{dN}{dE} = \Phi_0 \left(\frac{E}{E_0}\right)^{-\Gamma} \tag{4.18}$$
where Γ is the photon index and Φ_0 the normalisation (generally in cm^{-2}.s^{-1}.TeV^{-1}) at the energy E_0 in TeV.
- the power law with exponential cut off:
$$\frac{dN}{dE} = \Phi_0 \left(\frac{E}{E_0}\right)^{-\Gamma} \exp\left(-\frac{E}{E_{cut}}\right) \tag{4.19}$$
where E_{cut} is the cut off energy in TeV.
- the broken power law: the same as Equation 4.18 with $\Gamma = \Gamma_1$ is $E < E_0$ or $\Gamma = \Gamma_2$ is $E > E_0$.
- the log parabola:
$$\frac{dN}{dE} = \Phi_0 \left(\frac{E}{E_0}\right)^{-(\alpha+\beta\log(E/E_0))} \tag{4.20}$$
where α is the power law index and β represents the curvature.

Fits can be compared to determine the most probable spectral shape between two spectral hypotheses H_1 and H_2. To do so, we compute the two likelihoods and their ratio:

$$\lambda = -2 \ln \frac{\mathcal{L}_{H_1}}{\mathcal{L}_{H_2}} \tag{4.21}$$

If $\lambda > 0$, H_1 is the most probable hypothesis and if $\Delta N_{DOF} = 1$ the significance of the preference is simply $\sqrt{\lambda}$.

Light curves

Light curves are the evolution of the integrated flux (between $E_{\rm min}$ and $E_{\rm max}$) with time. The temporal binning of the H.E.S.S. light curves is generally run-wise or night-wise, unless the source is really faint and several nights have to be integrated together. In the case of a very bright source, the binning can be intra-run.

The light curve determination relies on a spectral shape hypothesis for which the likelihood maximisation is done in each time bin, leaving the normalisation Φ_0 free and the other parameters (photon index for example) fixed at their mean value. So basically, a point in a light curve is an integrated spectrum with the normalisation free to vary.

Light curves are of great interest to see if a source is variable or not, either on the long time or for flares.

4.3.7 The different analysis profiles

Stereo, Mono & Combined

Several analysis profiles have been defined, depending on the telescopes available during observations and depending also on the science targeted.

The Mono analysis uses only events triggered by CT5, no matter if CT5 was observing the source with the other telescopes. It is best to study sources at a lower energy threshold (H. E. S. S. Collaboration et al., 2016b).

The Stereo analysis uses events triggered by 2 or more telescopes. There are two Stereo chains depending if CT5 is in the array or not. The Stereo H.E.S.S.-I profile is optimised for CT1-4 while the Stereo H.E.S.S.-II profile is optimised taking into account CT5 in the array.

The Combined analysis uses all events. If the event has been triggered only by CT1-4, the reconstruction chosen is Stereo. If the event has been triggered by CT5 only, the reconstruction is Mono. If the event has been triggered by CT1-5, the reconstruction chosen between Mono and Stereo is the one with the smallest uncertainty. The Combined analysis is similar to the Stereo since the Stereo reconstruction is generally more precise than the Mono.

Standard, Loose and Faint cuts

Not all the sources have the same brightness and same environment. Some of them might be bright and easy to detect in a low NSB environment, while other are fainter and in a region of the sky where the NSB is stronger. This is why several sub-profiles have been defined for the Stereo, Mono and Combined analyses.

The main difference between the Standard, Loose and Faint profiles is based on the *NSBGoodness* cut. The *NSBGoodness* is an analysis variable giving the probability of an event to be a background event due to visible photons in the field of view.

The harder the cut on *NSBGoodness*, the more we reject noise eventually but also signal. This is useful for fields of view with a lot of noise to be sure the signal is not too contaminated. On the contrary, the looser the cut, the more we have noise but also more signal. The game here is to find the best compromise to have a good signal over noise ratio. Generally in the extragalactic fields of view, we are not really annoyed by night sky background, so for weak sources, it is interesting, and still safe, to use Loose cuts. Most of the H.E.S.S. analyses use the Standard cuts to stay on the safe side.

		HESS 1 Std		HESS 2 Stereo		HESS 2 Mono	
Selection cuts	**Cut value**	**Runs lost**		**Runs lost**		**Runs lost**	
		Number	**Percentage**	**Number**	**Percentage**	**Number**	**Percentage**
Run properties		**762**	**3.9 %**	**2065**	**18.6 %**	**734**	**9.6 %**
Number of telescopes	≥ 3	473	2.4 %	1445	13.0 %		
Run duration	≥ 5 min	305	1.6 %	787	7.1 %	734	9.6 %
Central trigger		**2971**	**15.1** %				
Zenith corrected rate	$\in$ [100,600] Hz	1214	6.2 %				
Stability	≤ 4 %	1930	9.8 %				
Dead time fraction	≥ 80 %	359	1.8 %				
CT1-4 trigger rate		**1893**	**9.6** %	**2670**	**24.0 %**		
Stability	≤ 10 %	1416	7.2 %	1099	9.9 %		
Dead time fraction	≤ 15 %	263	1.3 %	390	3.5 %		
Pixel/sector thresholds	≥ 4 / 2.5	370	1.9 %	1462	13.2 %		
CT5 trigger rate				**853**	**7.7 %**	**853**	**11.2 %**
Stability	≤ 10 %			174	1.6 %	174	2.3 %
Dead time fraction	≤ 15 %			806	7.3 %	806	10.6 %
Pixel/sector thresholds	4 / 2.5			1	$\sim$0 %	1	$\sim$0 %
Autofocus				**54**	**0.5** %	**54**	**0.5** %
Position	$\in$ [60,80] mm			12	0.1 %	12	0.1 %
Error	$\in$ [-5,5] %			54	0.5 %	54	0.5 %
Meteo		**980**	**5.0 %**	**460**	**4.1 %**	**17**	**0.2 %**
Radiometer temperature	$\leq$ -20	1893	1.8 %	140	1.3 %		
Radiometer stability	≤ 3	357	3.5 %	340	3.1 %		
Relative humidity	≤ 90 %	85	0.4 %	17	0.2 %	17	0.2 %
Calibration		**216**	**1.2 %**	**1502**	**13.5 %**	**1040**	**13.7 %**
Broken pixels CT1-4	≤ 15 %	216	1.2 %	566	5.1 %		
Broken pixels CT5	≤ 5 %			1040	9.4 %	1040	13.7 %
Total		**3950**	**20.1 %**	**4122**	**37.1 %**	**2008**	**26.4 %**

TABLE 4.1: RunQuality effect on a runlist for the HESS 1 Standard, HESS 2 Stereo Standard and HESS 2 Mono Standard profiles.

Chapter 5

Run-Wise simulations (RWS): a new way to describe the instrument

Contents

IACTs use the Earth's atmosphere as a calorimeter and there is no test beam of VHE γ-ray to test the instrument response function and the reconstruction methods. Analyses have to rely on simulations. As seen in Chapter 4, simulations are used in the rejection of background events (Scaled Cuts Tables), in the energy reconstruction (Energy Lookup Tables) and in the calculation of the energy spectrum (Acceptance Tables and Energy Resolution Tables).

Section 5.1 describes the current scheme of the H.E.S.S. simulations framework (called *classical* in the following), with the modules `Kaskade` and `Smash` representing respectively the shower and instrument simulations. Because of the limited parameter space of the current simulations, the instrument and observation conditions are not described in the most perfect way (see Section 5.2).

Section 5.4 presents a new simulation scheme called Run-Wise. Each run will have its own simulation with the parameters of the simulation matching the exact ones of the observation. This new scheme describes the instrument and the observation conditions in a much better way and will reduce the systematics of the current analysis.

This chapter is much more technical than the others in this thesis, digging into the simulation code written in C++. However the motivation is purely physical: we want to better describe the observing conditions and the instrument to reduce the systematics.

5.1 The classical simulations

5.1.1 Shower simulations with `Kaskade`

There are two main atmospheric shower simulation frameworks: `Kaskade` developed by Kertzman and Sembroski, 1994 and used in the French side of the H.E.S.S. Collaboration and `Corsika` developed by Heck et al., 1998 and used in the German side of the H.E.S.S. Collaboration. These codes are based on Monte Carlo algorithms. The following work has been done with `Kaskade`. The class simulating the showers in the atmosphere is called `Kaskade::Engine` and takes into account the following processes: pair production, Bremsstrahlung, multiple diffusion of electrons, Compton scattering, energy losses by ionisation, Bhabha and Möller diffusions, electron-positron annihilation and the magnetic field bending (depending on the azimuth angle).

Each particle of the shower is tracked and, for the charged ones, their Cherenkov emission is computed. The absorption of the Cherenkov light by the atmosphere is also taken into account with an atmosphere model. The one used for H.E.S.S. is computed using MODTRAN, a program which computes the atmosphere transparency. Measures used for this date from 1999 and are supposed to be stay unchanged with time. But with the muons measurements, it is known that the atmosphere transparency evolves with time. This is not taken into account and is thought to be one of the main source of systematics between the data and Monte Carlo comparison.

The illustration of Figure 5.1 sums up how the `Kaskade` simulation works. The main part of the simulation is made by the `Kaskade::Engine` class. However, three other classes are of importance:

- `Kaskade::CherenkovEmission`: the Cherenkov emission is not strictly related to the shower development and is more connected to the instrument itself in this framework.
- `Kaskade::Telescope`: this class contains the description of the layout of the telescopes with their number, position and size.
- `Kaskade::QuantumEfficiency`: this class applies the quantum efficiency (several values are available) of the photo-multipliers after the Cherenkov stage to limit the size of the output file.

Input file

The input file read by `Kaskade::Engine` contains all of the parameters needed to run the simulation:

- The particles type: gamma, electron, muon, hadron... In total 43 different types exist.

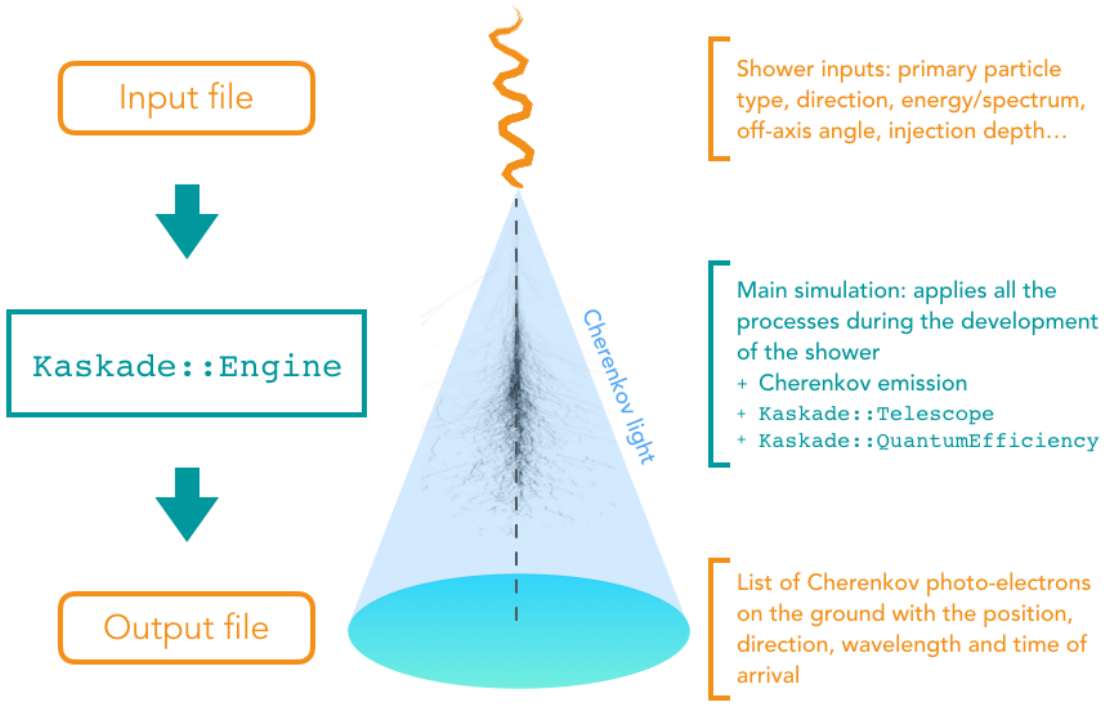

FIGURE 5.1: Illustration on the workflow of `Kaskade` with the informations of the input and output files.

- The direction of the primary particles (azimuth and zenith angles).
- The off-axis angle (the source is not at the center of the camera but offset, see Chapter 4 for more details).
- The energy or spectrum of the particles: particules are simulated either at fixed energy or with a power law spectrum.

These are the main parameters of the simulation, other parameters exist but they are generally fixed: the minimum and maximum energy of the particles, the injection depth (the altitude at which the primary particles will interact with the atmosphere, the number of simulated showers...).

Output file

The output file of `Kaskade::Engine` consists in different informations for the Cherenkov photo-electron (after applying the quantum efficiency of the photo-multipliers) on the ground: position, direction, wavelength and time of arrival. This file will be the input file for the `Smash` detector simulation.

5.1.2 Instrument simulations with `Smash`

`Smash` is a set of classes for the H.E.S.S. detector simulation. The name does not come from tennis but from SiMulation with sASH, `Sash` being a set of classes for the camera geometry, the MC photons data and the pixels data. First, it reads the output from `Kaskade` which contains the primary particle information and the Cherenkov photons.

Photon propagation

A photon bunch from an event of the shower simulation is a `Sash::MCPhotonBunch` object with coordinates in the ground system. It is propagated to the camera with the method `Smash::MCTelescope::ProcessMCPhoton`. Several methods (not described here for the sake of simplicity as they won't be re-used after) inside this process are called to determine which mirrors have been hit or not by the `Sash::MCPhotonBunch`. Here the whole structure of the dish with each mirror is taken into account along with the shadow of the structure of the telescope arms on the mirrors. Figure 5.2 represents the process in a schematic way. Then the `Sash::MCPhotonBunch` is propagated to the camera and the hit pixels. A photo-electron is added in the pixel if it is hit with `Smash::MCTelescope::AddPE`.

Here the timing of each photon is of importance and everything is carefully computed. The arrival time of the photo-electron is saved for the trigger and readout simulation.

The object `Smash::TelescopeMirrorConfig` reads the mirrors reflectivity, Winston cones efficiency and so on from a simulation database which contains a limited amount of configurations to describe the reality.

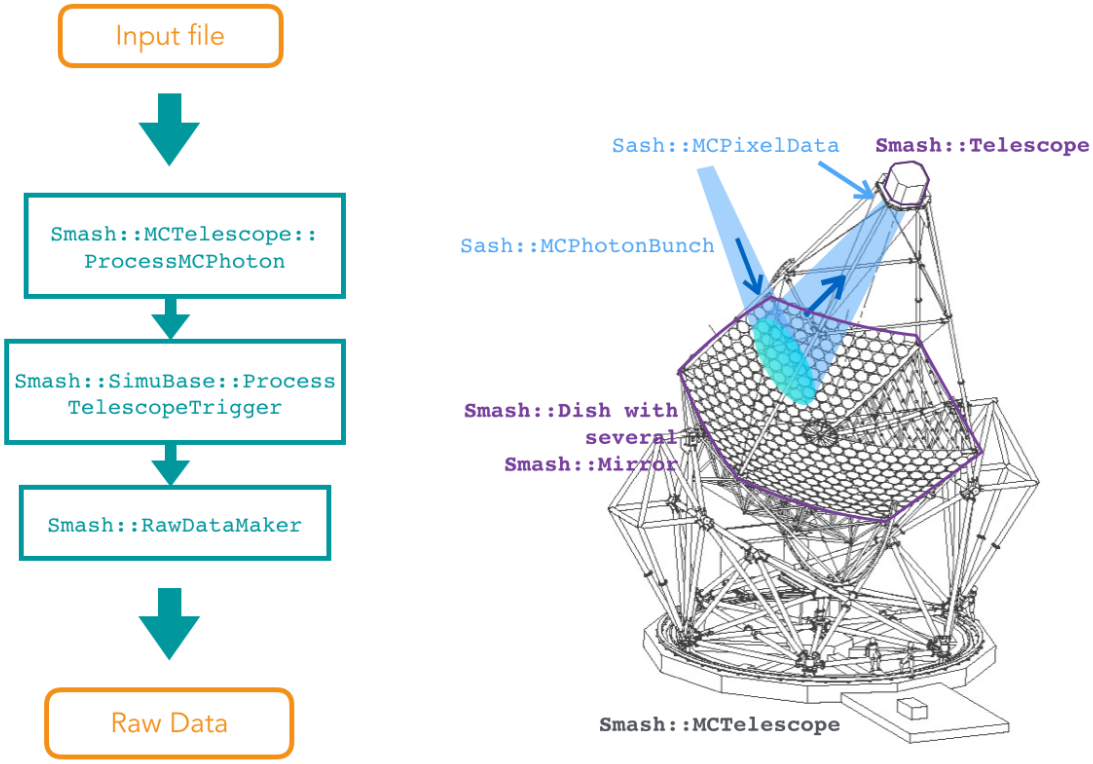

FIGURE 5.2: Illustration of how `Smash` works with the different classes and the input and output files. The dish is described by the object `Smash::Dish` containing several `Smash::Mirror`. The whole telescope is an object `Smash::MCTelescope` while the camera is a `Smash::Telescope` object. The `Sash::MCPhotonBunch` propagates through the mirrors and the information is a `Sash::MCPixelData` object at the end of `Smash::MCTelescope::ProcessMCPhoton`.

Trigger simulation

The class `Smash::SimuBase::ProcessTelescopeTrigger` simulates the trigger with the following steps:

1. building the pixels comparator signal from the arrival times of photons in the pixels. The pixel comparator looks at the number of photo-electrons in each pixel;
2. building the sector comparator signal. The sector comparator searches for 3 pixels in the same sector containing more than 4 photo-electrons (see Section 4.3.2 of Chapter 4 for more details on the trigger thresholds);
3. process the local trigger: if the pixel and sector signal are above the trigger threshold, the event triggers the acquisition;
4. processing the module `Smash::MCTelescope::ProcessIntensities` if the event trigerred in order to compute the intensity in the cameras.

The object `Smash::TelescopeElectronicConfig` stores the electronic configuration of the pixels which had previously been read from the database.

Raw data

Raw data are produced by the maker `Smash::RawDataMaker` using every event which triggered. The amplitudes for each photo-electron saved in `Sash::MCPixelData` and the calibration parameters like the pedestals, the flatfield, the gain and so on are used.

However the values used for these parameters are constant. For example the gain and high-low-ratio are the same for each pixel of each camera (they follow a distribution computed a priori). The presence of broken pixels is not taken into account neither. The camera is supposed to be perfect and homogeneous.

After this, the raw data file is treated like the data and will be calibrated to produce a DST file which will be analyzed by the `ParisAnalysis` chain.

5.1.3 Simulation of the observations

`Kaskade` and `Smash` use various parameters to simulate different showers in different observation conditions. A tremendous set of simulations exist due to the large parameter space and the need for high statistics. The parameters of the shower configuration are the following:

- the particle type: gamma, electron, muon, proton, helium, mixed cosmic rays;
- the azimuth angle (important relative to the magnetic field): 0 (North), 45, 90 (East), 135, 180 (South), 225, 270 (West) and 315 degrees. However only North and South are simulated;
- the zenith angle (important relative to the depth of atmosphere travelled): 0, 18, 26, 32, 37, 41, 46, 50, 53, 57, 60, 63, 67, 70 degrees;
- the offaxis angle: 0, 0.5, 1, 1.5, 2, 2.5, 3, 3.5, 4 and 4.5 degrees;
- the energy (fixed) or spectral index of the particle spectrum:
  - fixed energy: 0.02, 0.03, 0.05, 0.08, 0.125, 0.2, 0.3, 0.5, 0.8, 1.25, 2, 3, 5, 8, 12.5, 20, 30, 50 and 80 TeV

– power law with photon index: 2, 2.2, 2.4, 2.6, 2.8, 3, 3.2, 3.4, 3.6, 3.8

Taking all of the possible configurations into account, this leads to at 34,720 shower configurations for one particle and 208,320 overall. Then one has to add the instrument configuration: several configurations exist to describe the gain, optical efficiency, NSB.... since these parameters evolve with time and depend on the observation conditions. Figure 5.3 illustrates the set of parameters of the simulation framework with the azimuth & zenith angles, the optical efficiency and NSB rates.

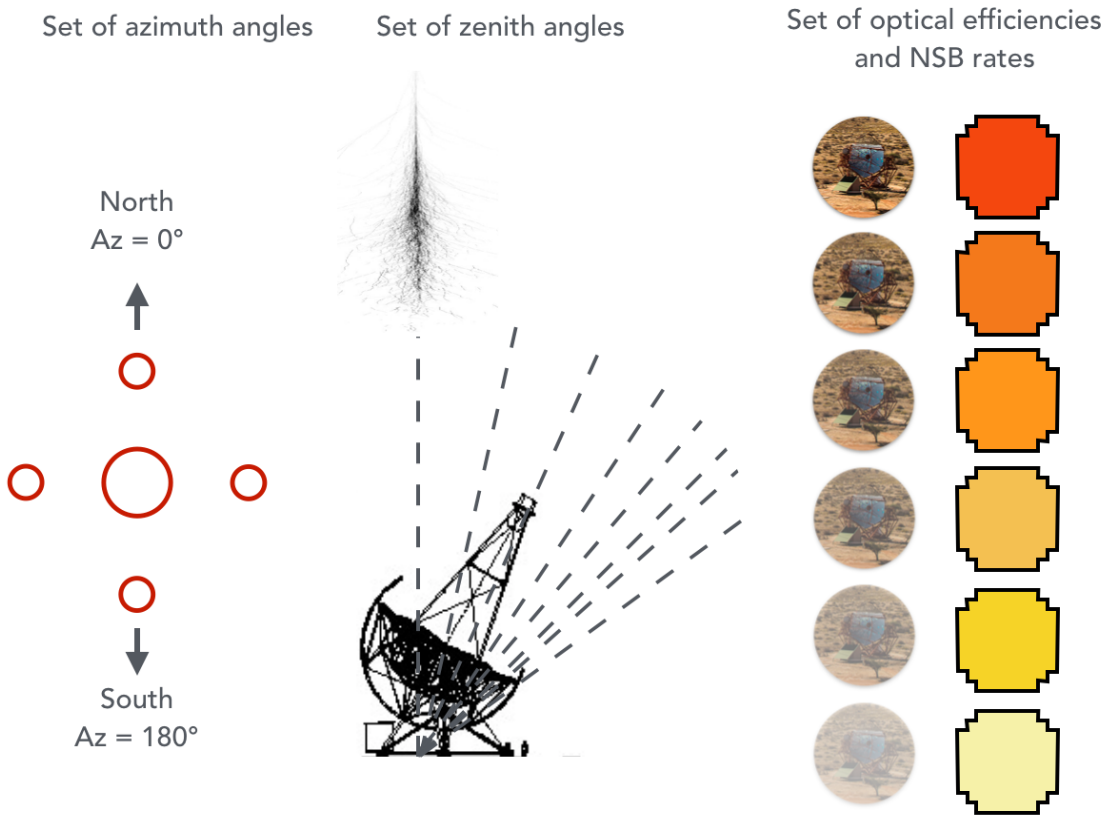

FIGURE 5.3: Illustration of the classical simulation framework: simulations are done with different sets of azimuth & zenith angles, optical efficiency and NSB rate.

5.2 Limitations and symptoms of the *classical* framework

5.2.1 Limitations

The *classical* simulation scheme has its limits (non exhaustive list):

- One has to interpolate between azimuth and zenith angles because of the limited space parameter of the tables. If an observation is done with a zenith angle of $21°$, an azimuth angle of $30°$ and an off-axis angle of $0.5°$, one would need 4 sets of simulations:
  - zen = $18°$, az = $0°$, off-axis angle = $0.5°$
  - zen = $18°$, az = $180°$, off-axis angle = $0.5°$
  - zen = $26°$, az = $0°$, off-axis angle = $0.5°$

  - zen = 26°, az = 180°, off-axis angle = 0.5°

  The results obtained will result of the interpolation between the single results from each simulations. In the current case, interpolation is made also on the offset angle, the optical efficiency and the energy.

- There is only one atmosphere model, while we expect the atmosphere to change according to the seasons (even intra night).
- The calibration (as described in Section 4.3.1 in Chapter 4) used in `Smash` is always the same and does not correspond to the real detector.
- The telescopes track the source during the 28 minutes run, resulting in a change of azimuth and zenith angle with time.

These limitations have effects on our observables. As an illustration, I present in the following two of them: the discrepancy between the energy distributions from data and simulations and the so-called PSF problem.

5.2.2 Shift in the reconstructed energy

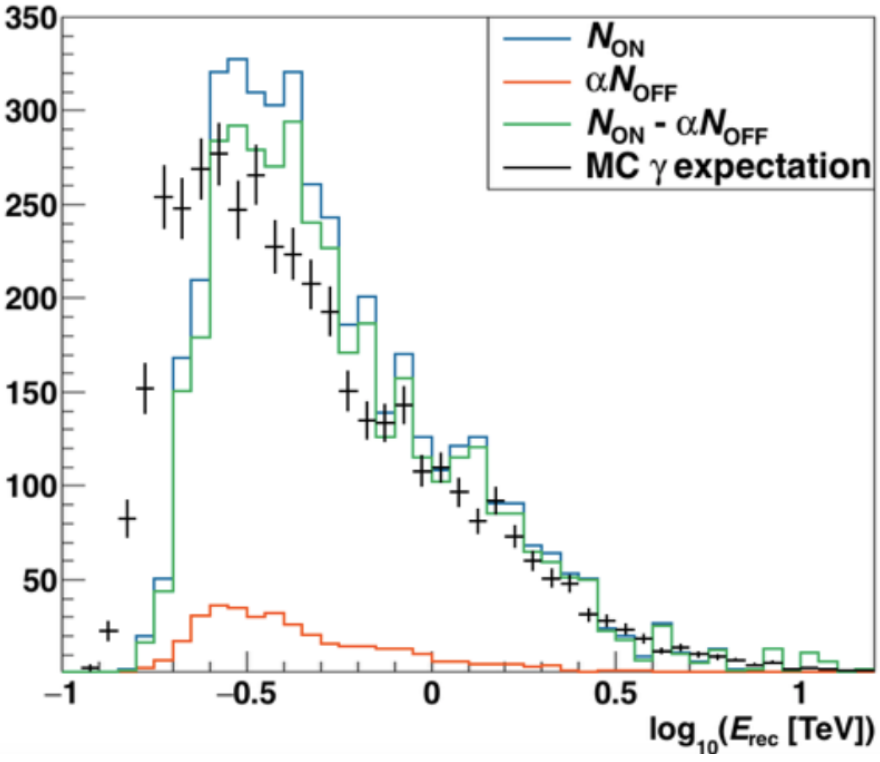

FIGURE 5.4: Histograms of the reconstructed energy for the data (green) and the MC γ expectation (black points).

Figure 5.4 shows the energy distribution of the events from MC simulations (black points) and from a Crab dataset (green line for the excess) for a `Mono` analysis (with CT5 data only). There is a shift of the distribution where the MC goes at lower energy.

This systematic effect is taken into account by cutting the events below $\log E \sim -0.6 \leftrightarrow 0.250$ TeV[1].

The agreement between the MC and the data at higher energy is good but not perfect.

5.2.3 The PSF problem

The point spread function (PSF) of the instrument is the reconstructed size of a point-like source and is assumed to be of the order of $0.01°$. There is a spread of the apparent size of the source due to the error on the reconstructed direction of arrival of the events. On the analysis side, the PSF is defined as the radius containing 68 % of the events R_{68}.

AGN are point-like source for H.E.S.S. However, a study showed that the image of AGN after analysis was not point-like but with a systematic extension of $\sim 0.023°$. The extension of 13 AGN is shown on Figure 5.5. The dataset of these 13 objects has different observation conditions (zenith, azimuth, livetime) and each source has a different spectral behavior and a different redshift. Hence, this effect is not a physical one because it is on average the same for all AGN, with no other dependence. If we were to see a redshift-dependent extension, the extension would increase with the redshift because of the pair halo effect.

Moreover, this issue is problematic for morphology studies, especially on radio galaxies to know if we resolve the jet at TeV or not.

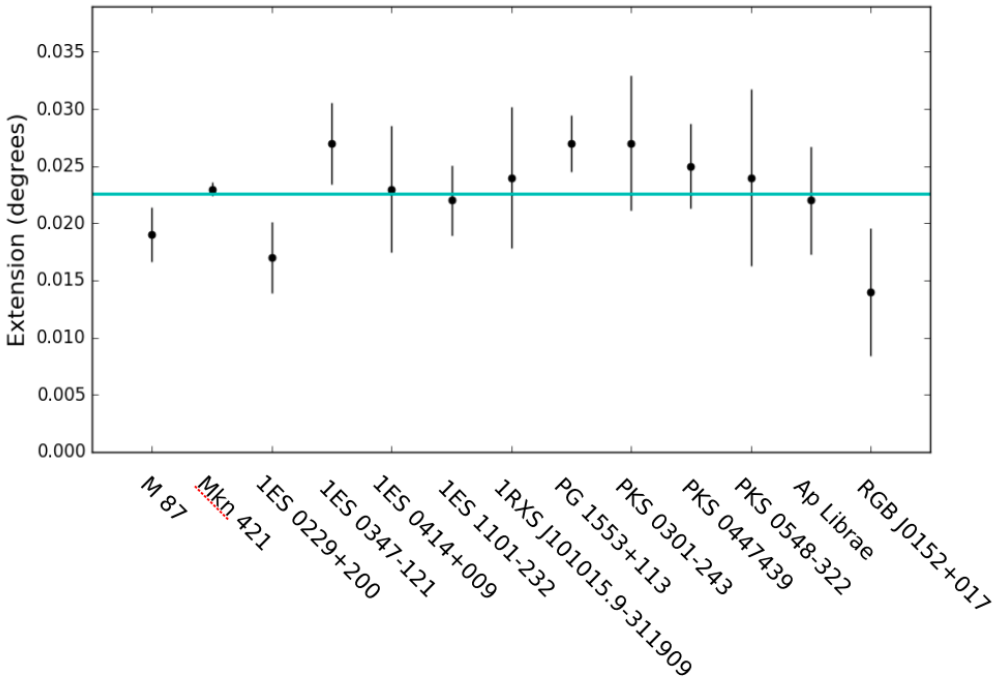

FIGURE 5.5: Extensions of several point-like AGN sources. The blue line represents the average of all at $\sim 0.023°$ (Analysis by F. Brun).

[1]The exact value of the energy threshold will depend also on the observation conditions, like the array observing, the zenith, hence the cut applied in the analysis is specific for each analysis.

5.3 Preliminary study: The effects of the broken pixels

The PSF estimation relies on simulations where the instrument is assumed to be in a perfect hardware state. However we know it is not the case in real life. For example, we know that in each run, there is a certain amount of broken pixels in each camera. Broken pixels have an effect on the event reconstruction, and this is why we reject run with a too high percentage of broken pixels.

In order to test the effect of the broken pixels on the PSF, new simulations were made where the broken pixel pattern on the run was simulated for each run. Each run had his own simulation set, requiring much more computation time, but finding an average pattern was impossible as the causes to have a broken pixel are diverse. Tests have been made on the runs on the blazar PKS 2155-304.

Figure 5.6 shows the PSF from the classical simulations and the simulations including the effect of the broken pixels. The containement radius R_{68} increased by 7.6 % when taking into account the broken pixels.

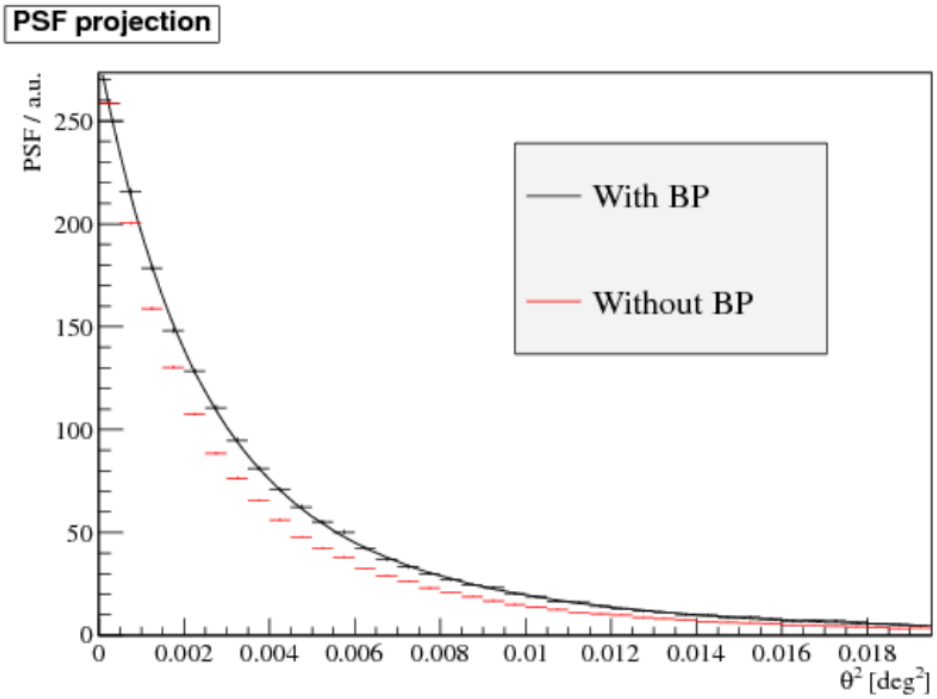

FIGURE 5.6: Profile of the PSF from the "classical" simulation (red points) and the ones inluding the broken pixels (black point). The black line is the fit to the profile. Courtesy of D. Sanchez & V. Marandon.

This could explain the systematic and non-physical extension of AGN. To correctly take into account the effect of the broken pixels, one would need to simulate each run with its broken pixel pattern.

5.4 The new Run-Wise scheme of simulations

5.4.1 Principle

The broken pixels are not the only parameter not properly taken into account. The zenith and azimuth angles are always "in between" since they are fixed in the simulations but an

almost infinite number of possibilities exists. The real optical efficiency is not the same for each telescope (and evolves with time), however, in the current simulation scheme, we use the same for the whole array. Also, the values of the calibration parameters (gain, high-low ratio...) and of the NSB is not the same in each pixel.

A new simulation framework, called Run-Wise, aims to take into account all of the observation conditions (angles, optical efficiencies, NSB, calibration...). Each run will have its own simulation, where each effect is simulated with actual values in each pixel of each camera, instead of using a set of pre-defined simulations.

This is illustrated in Figure 5.7 (in opposition of Figure 5.3), where each telescope has its own optical efficiency, broken pixel pattern and NSB rate.

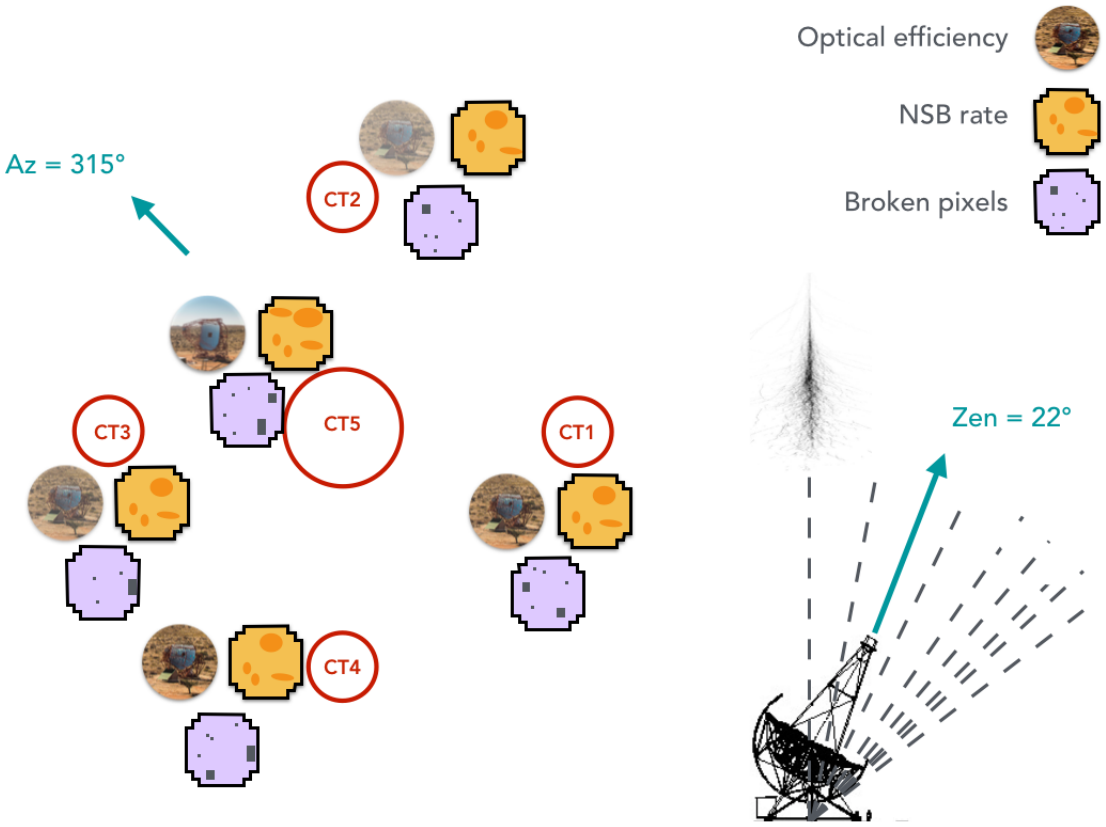

FIGURE 5.7: Illustration of the Run-Wise simulation framework: simulations are made taking into account the actual observation conditions i.e. the zenith & azimuth angles, the optical efficiency and broken pixel of each telescopes and the real non-homogeneous NSB rates.

5.4.2 Changes in the simulation framework

The first part of the work is to adapt or modify the existing framework to add more parameters: readout of the database, loops over the cameras and pixels to add the new pixel-wise information. Several parts of the simulation code had to be changed.

Readout of the real calibration and observation conditions

The class `Kaskade::HESSConfigReader` has been updated to become the Run-Wise version called `Kaskade::HESSRunConfigReader`. Instead of doing the simulation on

pre-set values, this new class will go into the database to find all of the values of interest to simulate the run in the same conditions (zenith, azimuth and off-axis angles for example). Same for the configuration reader class of `Smash`: `Smash::ConfigReader` became `Smash::RunConfigReader` in order to read properly all the run informations like the azimuth and zenith angles and the telescope list.

The way the layout of the array was made had to be changed because it was hard-coded including CT1, CT2, CT3, CT4 and CT5. But what if the run we are simulating has only CT1, CT2, CT4 and CT5 in the array? Then the telescopes list in `Kaskade` and `Smash` will not match. The classes `Kaskade::TelescopeList` and `Smash::RunSummary` were corrected to be more flexible.

The module `ParisCalibration::ParisCalibrationFinder` is used to read the calibration coefficients. It already existed but has been updated to connect to the database to read and store the calibration coefficients for each pixel of each camera for each run.

Application: Implementation of the real NSB input

In the *classical* simulation scheme, the NSB rate were uniform in the camera but we know it is not the case during observations. Moreover the NSB is different depending on whether observations are made looking at a galactic or an extragalactic region. This work demanded modifications in different modules: `Smash`, `Calibration`, `ParisCalibration` and `ParisRunQuality` (taking care of the simulation of the calibration and of the telescopes).

The NSB information is located in the pedestals of the run and has to be extracted to be read by `Smash` and put correctly in each pixel.

A new class `ParisRunQuality::NSBMaker` was created. It computes several NSB properties from the pedestal information for each pixel of each camera per run. The mean of the NSB rate along with its RMS, slope and dispersion will be computed and stored in the *Calibration* database.

From this, the `ParisCalibration::ParisCalibrationFinder` class has been updated to read the new informations contained in the database and fill the two objects `Calibration::TelescopeNSB` and `Calibration::PixelNSB`, which were updated as well to contain more information.

The previous NSB maker from `Smash::RunNSBMaker` was using the *classical* calibration and a value of the NSB of 100 MHz. The number of NSB photons creating a photo-electron in the PM was drawn following a Poisson probability law around the NSB value. In the new maker `Smash::RunNSBMaker`, the calibration used is the real one and we retrieve the mean of the real NSB value, looping over each camera and looping inside each of their pixels to put the NSB value from `Calibration::TelescopeNSB` and `Calibration::PixelNSB` in each pixel. The Poisson law to convert the NSB value in photo-electrons is the same.

Implementing the pointing uncertainties and tracking

The pointing and tracking of the telescopes on a source is not 100 % accurate but the pointing model of the simulations does not take this into account. For normal observations, the uncertainty is though to be of the order of ~ 20 arcsec. Since it is impossible to know exactly the pointing uncertainty for each telescope for each run, assumptions have to be made. We assume that the pointing uncertainties are similar to a slight shift of the overall sky coordinates. This is represented on Figure 5.8. This change is implemented at the analysis level by shifting the analysis position away from the actual source by 20-30 arcsec.

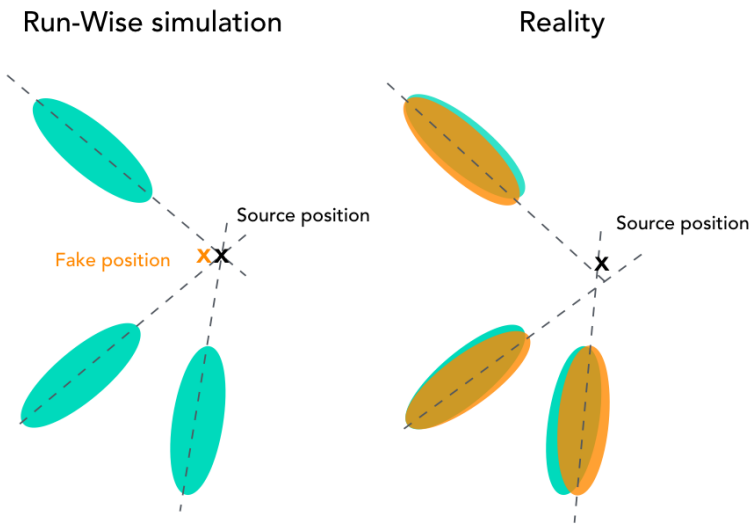

FIGURE 5.8: The pointing uncertainties are handled in the RWS (left) by shifting the position of the source to mimic the effect of the mis-pointing in real life (right).

The tracking of the source during the duration of the run has been added in the simulation. Every changes in azimuth and zenith angles with time is taken into account, the shower and telescope moving together during the simulation.

5.5 Tests of the calibration

The goal of these tests is to see if the detector configuration, taken from the data, is set properly (= do our modifications work?). To do so, we choose a specific run (run number 83100 on the Galactic center Sgr A*) to have a look at the gains, high-low ratio, flatfields, pedestals, broken pixels, optical efficiency and the NSB rates. The run is simulated knowing the input calibration and we check the calibration after the simulation.

5.5.1 Gain

Figure 5.9 shows the results of the gain for each pixel in the CT1 camera for the data (left) and after the simulation (right) along with the gain distribution for all the pixels. The distributions look alike, which is good, showing that the readout of the gains is working. The mean of the projected values agrees very well, however, the RMS of the fitted values is slightly larger than the RMS of the input values. This is because the fit enlarges the distribution: when using a constant input, the distribution of the fitted values still has a width.

5.5.2 High-low ratio

Looking back at the definition of the amplitudes in photo-electron for the high and low gain channels (Equation 4.2 and 4.3 from Chapter 4), the value of the high-low ratio has only an impact on the low gain channel. Hence, by taking two different calibrations as an input, the charge display of the low gain channel should change while the one of the high gain channel should stay unchanged. Figure 5.10 shows the charge display of the CT1 camera of the high gain (top) and low gain (bottom) channels for a default constant

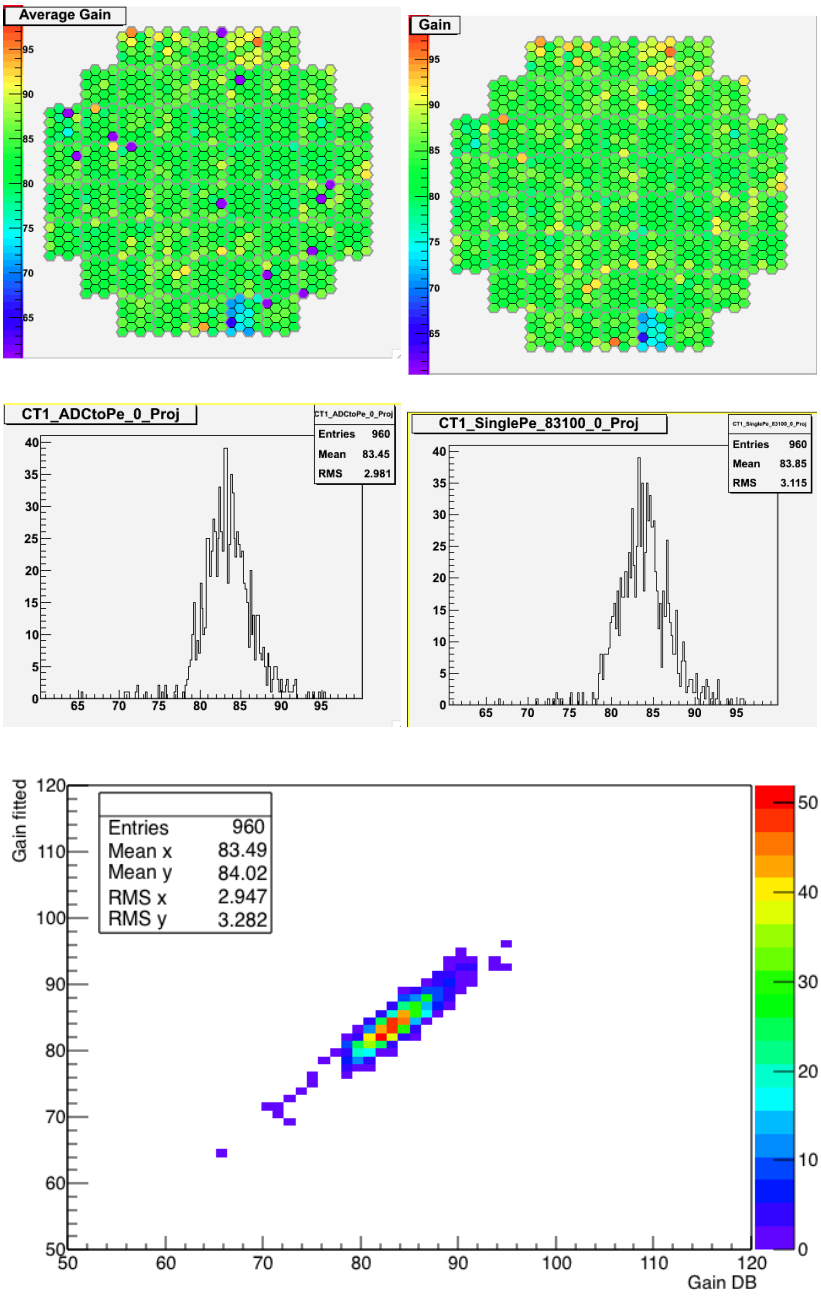

FIGURE 5.9: Top left: Input value of the gain from the database. Top right: Reconstructed/fitted gain after calibration. Bottom: Correlation between the fitted gain and database ones.

value (left) and for the value from the run (right). As expected, only the values of the low gain channel change.

5.5.3 Broken pixels

In the `Calibration` database, the broken pixel information tells if the pixel is considered as broken or not. If so, the flag is set to a number corresponding to the reason the pixel is broken: turned off only for this run (star in the field of view), electronic issue, pixel actually broken... A simple display of the camera shows if the readout of the database works. Figure 5.11 shows on the left the broken pixels of the CT1 camera for run

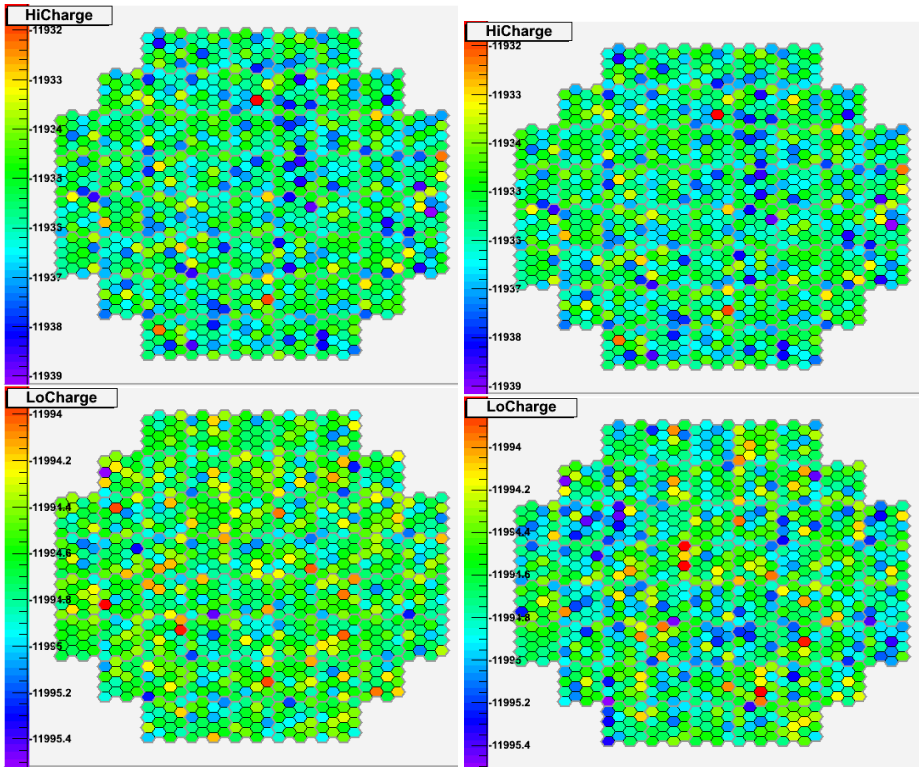

FIGURE 5.10: Charges display for the CT1 camera. Left: Fixed High-low ratio. Right: Real High-low ratio. When taking different input for the high-low ratio, the high gain channel (at the top) is not changing while the low gain one (at the bottom) is.

83100 (purple: the pixel is operational, other color: broken) and on the right the gain for the CT1 camera after simulation (the pixels in purple are the ones considered as broken).

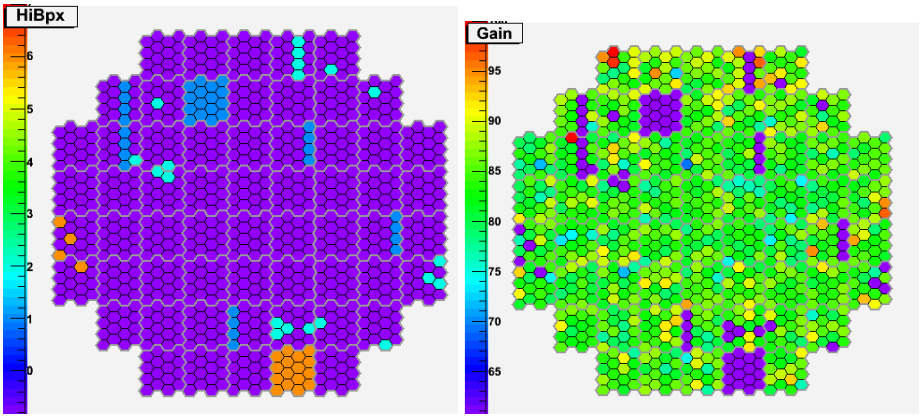

FIGURE 5.11: Left: readout of the broken pixels from the database (dark blue, light blue and orange). Right: The broken pixels are in purple and not used for the SinglePE fit.

5.5.4 Optical efficiency

The optical efficiency can be evaluated by looking at the number of photons in the mirrors and in the camera after the simulation. For a input relative efficiency of 100%[2], taking a random event in the simulation of the run 83100, we have:

- CT4: mirrors 1181 photons - camera 1112 photons
- CT5: mirrors 5845 photons - camera 5505 photons

Giving a ratio of 94% for both, meaning that the relative optical efficiency is of 94% in the simulations. Whereas, for the actual relative efficiency of the run (61.4% for CT4 and 89.5% for CT5), we have:

- CT4: mirrors 1350 photons - camera 757 photons $\Rightarrow$ ratio/0.94 = 60%
- CT5: mirrors 6391 photons - camera 5486 photons $\Rightarrow$ ratio/0.94 = 91%

This shows that the optical efficiency is correctly set in the Run-Wise simulation framework since we retrieve the same value (at the statistical error) in each telescope.

5.5.5 NSB

The run 83100 was not chosen randomly but because it is a pointed observation toward the galactic center Sgr A* which is known to be a high NSB (Night Sky Background) region, perfect to test the calibration and the NSB readout.

Figure 5.12 shows the NSB rates for CT1-5 in units of MHz. Before the implementation of the Run-Wise framework, the NSB levels were supposed constant in all the cameras with a rate generally at 100 MHz. In a region of high NSB like Sgr A*, the part of the camera at $\sim$ 100 MHz are the one showing no NSB (blue of the left side of the cameras) while the NSB is not uniform and around 200 MHz. The scale is a bit different for CT5 with higher NSB level, possibly because of the larger optical efficiency of the telescope ($\sim 90\%$ compared to $\sim 60 - 70\%$ for CT1-4).

These plots prove that the whole framework and implementation are working properly.

[2]The nominal optical efficiency of the instrument is 11%, which we convert to a relative optical efficiency afterwards.

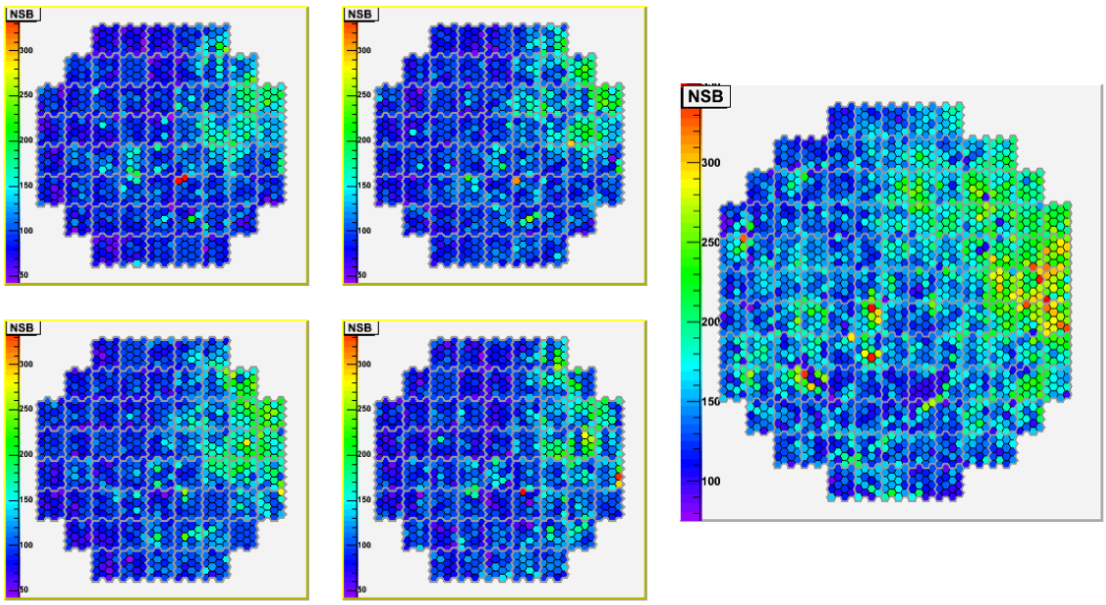

FIGURE 5.12: NSB rates for CT1-4 (small cameras) and CT5 (big camera on the right) in MHz for the simulated data on the run 83100 on Sgr A*.

RWS: Summary

Compared to the classical MC simulation, the Run-Wise simulations take into account the following effects:

- azimuth angle → the Earth magnetic field should have an influence on the PSF
- zenith angle → no more interpolation between the predefined limited values
- tracking of the source position during the run → it will take into account the change of azimuth and zenith angle during the run
- optical efficiency → each telescope has an optical efficiency evolving with time independent from each other
- calibration coefficient → the gain, high-low ratio... and especially the broken pixels, highly differing for each run
- NSB → not uniform nor constant, changing depending on the field of view
- dead time fraction → it has an influence on the multiplicity of each event

The simulation of all of these parameters and effects should lead to a much better description of the instrument and of the observation conditions, hence to a better understanding of the PSF. However, one needs to be aware that Run-Wise simulations share some limitations with the classical framework: the same general atmospheric model is used.

5.6 Results

The results presented in the following are preliminary results. This work was done during the year 2016. After that, the Run-Wise simulation framework has been updated to take into account more technical code-related details.

5.6.1 Energy distribution

The dataset used here is composed of 4 runs from the Crab Nebulae (100491, 100492, 101321, 101451, containing 4 or 5 telescopes including CT5). These runs were analyzed with the lastest version (`v32`) of the `ParisAnalysis` soft using the `Prod8` DSTs.

Figure 5.13 shows the energy distribution of the events for the data and for the corresponding Run-Wise simulations. Unlike Figure 5.4, the MC simulations and the data are almost perfectly compatible, with the same energy threshold. There is still a small mismatch at higher energy which has been investigated. It was related to the pedestal computation which was not properly done and it has been corrected in the next update of the RWS code.

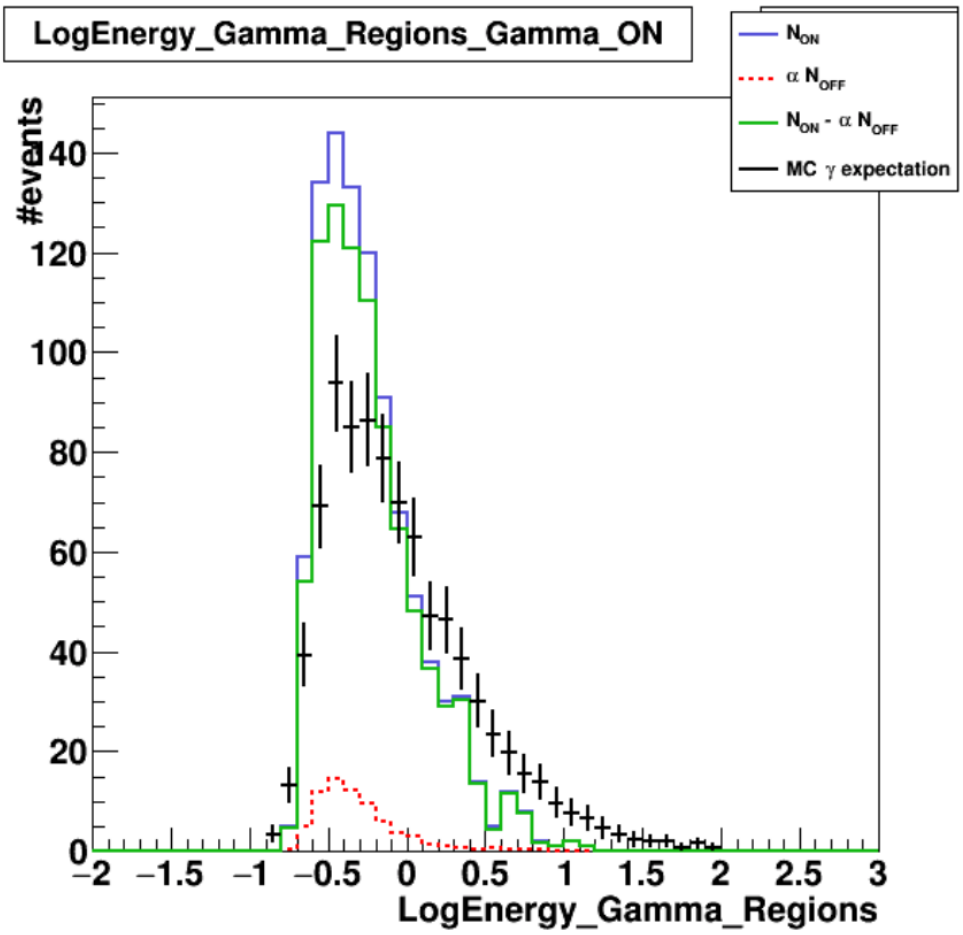

FIGURE 5.13: Histograms of the reconstructed energies for the Run-Wise simulations (in black) and the data (in green).

5.6.2 PSF

PSF tests were done on the 3 brightest runs of the 2006 flare of the blazar PKS 2155-304. This event is a very good test bench because it can be considered as background free thanks to its high statistics and the γ-ray beam is known to be point like because of causality reasons (the variability time scale of the order of a minute implies a size of the emitting region of the order of 0.7×10^{-3} light-day).

The top panel of Figure 5.14 shows the θ^2 plots for the data (in blue) and the Run-Wise MC (in orange). The agreement is great, especially knowing how bad it was before. The containement radius agrees as well with $R_{68} = 0.0694 \pm 0.0008$ deg^2 for the MC and $R_{68} = 0.0696 \pm 0.0014$ deg^2 for the data.

This was done with an offset of 30 arcsec for the pointing uncertainty in the simulations. If we ignore the offset (bottom panel of Figure 5.14), the containement radius for the simulation becomes smaller with $R_{68} = 0.0686 \pm 0.0008$ deg^2. If one looks closer at the first bin of the data histogram, one sees that the data lies below the MC expectation and below the second bin as well. This is likely to be a result of the pointing uncertainties.

5.7 Conclusion

The simulations currently used in H.E.S.S. show critical symptoms:

1. the MC do not fit the energy distribution of the events when compared to the data;
2. the simulated PSF is too small compared to the residual extension ($\sim 0.023°$) seen on AGN.

These simulations are done with limited parameters describing the instrument in a perfect hardware state and with limited observation conditions. Only sets of azimuth & zenith angles, optical efficiencies, NSB rates and so on (the list can be long) exist and some effects, like the broken pixels of the cameras, are not even taken into account.

A new simulation framework, the Run-Wise simulations, aims to take into account all of this to simulate properly every run. Instead of having a set of limited simulations, each run will have its own simulation, with the same azimuth & zenith angles, the same optical efficiency and broken pixel pattern as the run for each telescope/camera.

A lot of changes had to be made in the simulation and analysis code of the collaboration to implement the readout of the real observation conditions and of the real calibration. Once the readout was working, we were able to make some first tests to see how the Run-Wise simulations impacted the distributions of the analysis variables, especially the energy distribution, and the PSF.

The agreement between the data and the Run-Wise MC improved a lot compared to what we had with the classical MC. The PSF from the data and from the Run-Wise MC agrees very well: Run-Wise simulations are able to reproduce properly the Model++ CT1-4 PSF.

This work is of great importance for the next generation of IACTs: CTA. With more telescopes of different sizes and with different cameras, the combinatorial for the multiplicity and the observation conditions is huge and the classical simulation scheme can not be an option. In this view, H.E.S.S. served as a test bench before using the Run-Wise Simulations for CTA.

This work has been done mainly in collaboration with Markus Holler (leader of the task force), David Sanchez, Mathieu de Naurois and Jean-Philippe Lenain. A publication to present the Run-Wise Simulation scheme and its application in the H.E.S.S. framework with the final results, is currently in preparation.

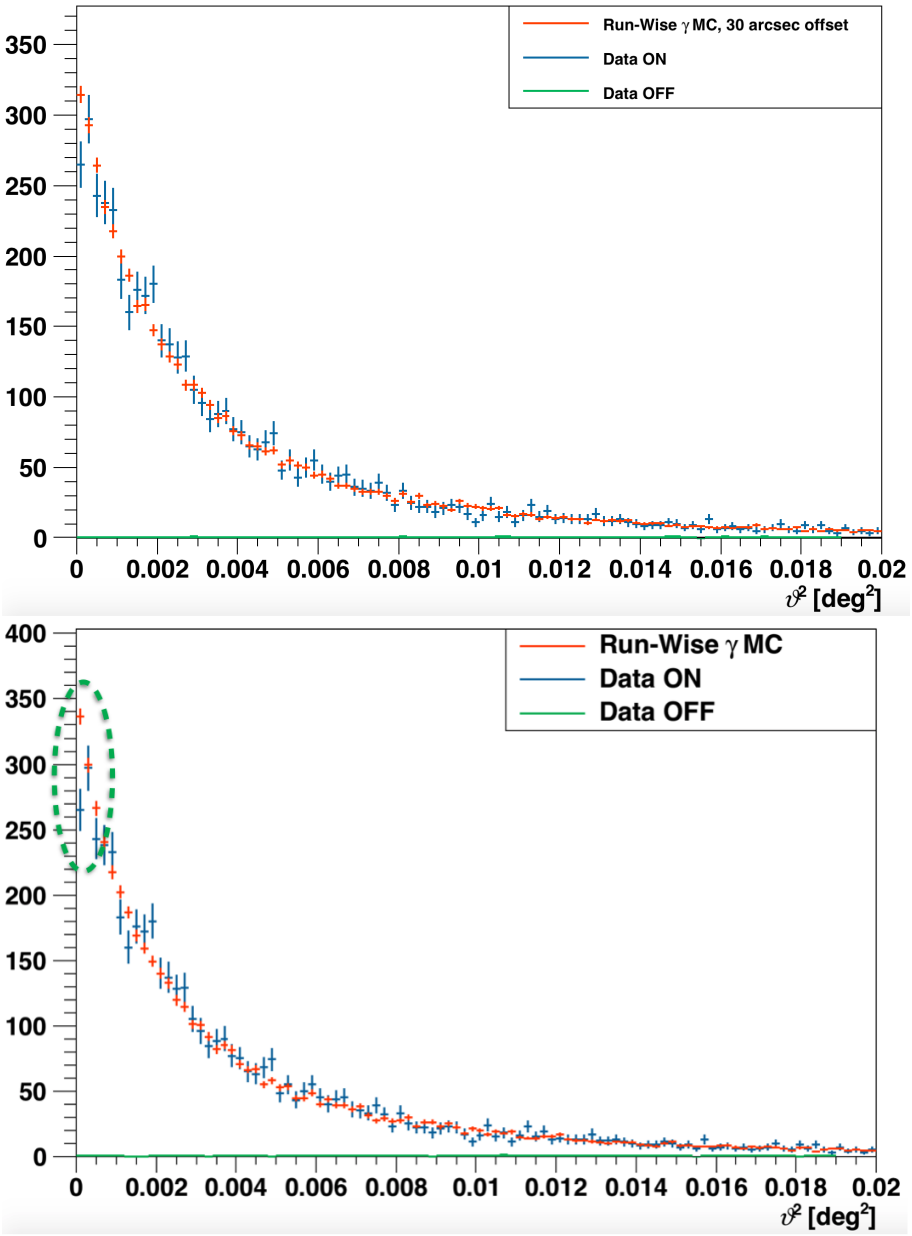

FIGURE 5.14: Theta2 histogram comparing the data (in blue) with the Run-Wise MC (orange). Top: Run-Wise simulation done taking into account an offset of 30 arcsec for the pointing position. Bottom: Run-Wise simulation done without taking into account the pointing uncertainties.

Chapter 6

HEGS: the H.E.S.S. ExtraGalactic sky Survey

Contents

Being in the Southern hemisphere, H.E.S.S. has the advantage to observe in really good conditions the Galactic plane of the Milky Way for Galactic studies. It was a good opportunity to study the whole Galactic plane at high resolution (~ 0.1 deg) in TeV γ-rays, leading to the HGPS project: H.E.S.S. Galactic Plane Survey (Carrigan et al., 2013), a series of observations to scan most of the Galactic plane. The HGPS discovered new sources, studied in more details already known sources to better understand their morphology and the emission processes at play. This study has revealed a diverse population of cosmic accelerators in the Galaxy, from pulsars, pulsar wind nebulae, supernova remnants and binary systems. The goal of the HGPS is to release a catalog of the TeV sources in the Galactic plane to the scientific community.

Due to the size of the sky, it's more difficult to proceed the same way for the extragalactic regions (especially with only 5 telescopes, CTA will be more suited to this). But still, since the beginning of the experiment with the full array in 2004, H.E.S.S. has observed a lot of extragalactic regions, and the H.E.S.S. ExtraGalactic sky Survey (a.k.a. HEGS) aims to take advantage of all of these observations to release a catalog of the H.E.S.S. extragalactic TeV sky.

HEGS follows the HGPS idea of only taking H.E.S.S.-I runs to construct a catalog which will be released to the scientific community. Contrary to the HGPS, HEGS will not be a continuous surface of observations, but rather composed of clusters of runs in the sky. Each of them will be studied, looking at energy thresholds, sensitivities, possible detections of (new) sources in the fields of view, their significance, if they are variable or not... Having close runs clustered together has the advantage to give a better exposure to the edges of the maps.

Section 6.1 presents the features of the run selection and of the clustering I performed in order to construct the dataset. Section 6.2 describes the details of the analysis which are a bit more specific than what has been presented in Chapter 4.

Although the run selection and the analyses for the final release are wished to be done with the latest version of the H.E.S.S. analysis soft (`0-8-32` with `Prod8` DST), a reprocessing of all the DST of the H.E.S.S. data delayed the analysis. Hence, Section 6.3 and Section 6.4 will present preliminary results done with the older `0-8-24` version of the analysis soft and the `Prod24` DST (and a slightly different runslist) while Sections 6.1 and 6.2 are based on the `0-8-32` version. Even if the versions and the runlists are different, the scientific results are not expected to change a lot.

6.1 Run selection and clustering

6.1.1 Run selection

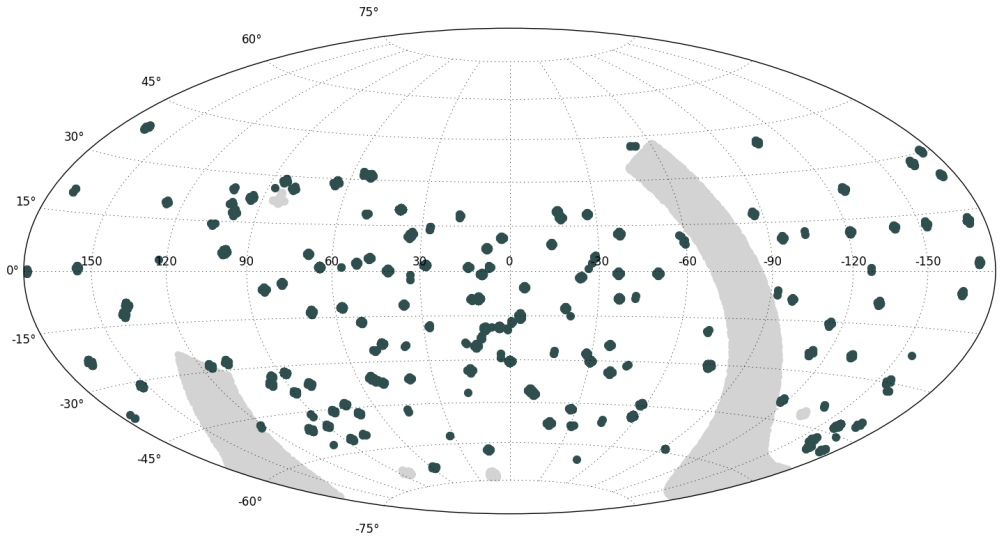

FIGURE 6.1: Skymap in equatorial coordinates of all the selected extragalatic runs taken by H.E.S.S from the beginning of 2004 to the end of 2012. The grey shaded areas are the exclusions regions (HGPS, LMC, SMC, Crab Nebula and SN 1006).

The run selection is done with the version `0-8-32` of the `ParisRunQuality` software following the `H.E.S.S.-I standard` quality cuts selecting all the good runs between the run `18416` (21/01/2004) and the run `79831` (16/12/2012) giving 14682 runs

in total[1] (for more details on the run selection and quality cuts, see Section 4.3.2 of Chapter 4).

Since this runlist contains the HGPS and several others known galactic sources (like the Large and Small Magellanic Clouds, the Crab Nebula and a supernova remnant called SN 1006), they have to be excluded as they are not of interest in an extragalactic survey. For the Crab, LMC, SMC and SN 1006, the exclusion is done based on the runslists (selected with the same analysis version and profile) of each source. For the HGPS, the exclusion is done excluding all the runs into the region of the galactic survey. Hence we remove all the runs with a galactic longitude $-115.5° < l < 77.5°$ and latitude $|b| < 7.5°$. This cut leads to 7477 runs.

In the H.E.S.S. collaboration, each analysis has to be cross-checked before being published. This means each HEGS run has to be cross-checked to know if both analyses are compatible. Hence we need to have only common runs between the `ParisAnalysis` and `HAP` (name of the German analysis chains) runslists. A `HAP` version of the HEGS runslist following the `HAP`'s run quality cuts, has been done excluding also the HGPS, LMC, SMC, Crab nebula and SN 1006. The `HAP` runslist contains 7221 runs. The common runslist of the two analysis chains has 6499 runs displayed in the skymap of Figure 6.1 where the extragalactic runs are the dark blue circles and the grey areas are the excluded "galactic"[2] regions.

6.1.2 Clustering

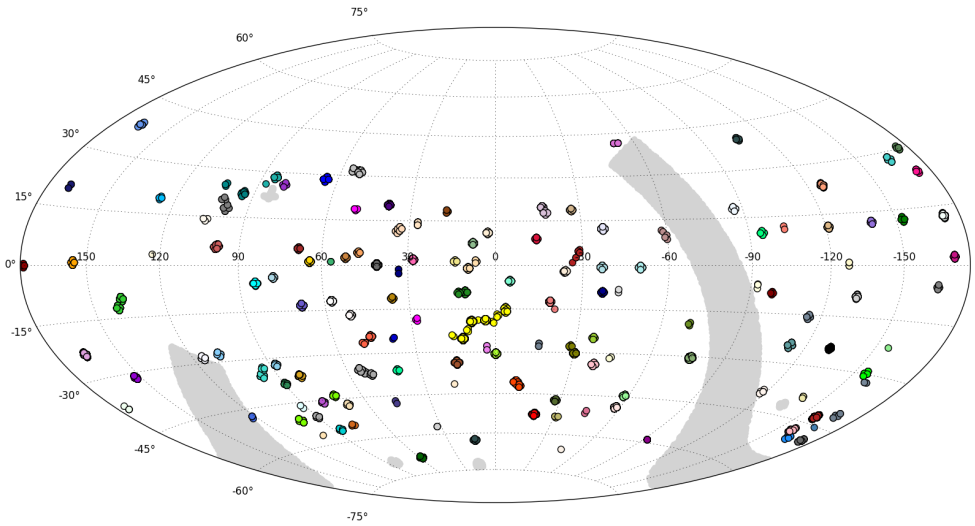

FIGURE 6.2: Skymap in equatorial coordinates of the 123 extragalatic RunsCluster, each circle represents a run, each color represents a RunsCluster. The grey shaded areas are the exclusions regions.

[1] It represents 75% of all (galactic + extragalactic) the observation runs taken between the beginning of 2004 and the end of 2012.

[2] Properly speaking the LMC and SMC are not galactic sources, but they contain galactic emitting TeV objects.

The DBSCAN tool from the library scikit-learn[3] is used to cluster the runs. The algorithm looks at the coordinates and size of each run, and clusterize them together if they overlap. When runs are clusterized together, they will form a RunsCluster. The field of view of a run is 2° around the pointing position. Then, in order for 2 runs to belong to the same RunsCluster, the distance between the two pointing position has to be $\leq 4^\circ$.

Safety checks have been done to be sure every run in each RunsCluster belongs to this RunsCluster (by computing the distance between each run and see if it's not above 4°). We also checked the distance between each run of each RunsCluster and if it's below 4°, the RunsClusters are merged together because a part of their field of view overlaps.

Only two RunsClusters needed to be merged and no RunsCluster needed to be splitted. This leads to 123 RunsClusters, displayed on the sky map of Figure 6.2, one color representing one RunsCluster.

6.2 Analysis procedure and products

The first part of the analysis uses the framework of Paris Analysis described in Chapter 4. Each run is analyzed with the most recent and stable software version, PA 0-8-32, using the Prod8 DST. For each RunsCluster, the merging gives a standard results file containing the classical analysis products like acceptance from data, significance and excess maps, as well as θ^2 plots and all the debugging plots. The only change is that we choose to keep the gamma-like events stored in the results file.

6.2.1 Gamma-like events and radial lookup tables

In the analysis procedure of ParisAnalysis, events are discriminated to know if the Cherenkov shower observed has initially been produced by a photon, an electron, a proton or any other particle. All the gamma-like events are treated as photons even if the sample is contaminated by some mis-reconstructed protons and by electron as they produce the same kind of shower as the photons.

These gamma-like events are used to compute what are called "radial lookup tables". They are used to estimate the shape of the instrument response as a function of the observation conditions and to estimate the background. To make a proper estimation of the background, the computation of the tables makes sure to exclude the known γ-ray sources in each field of view. In the classical scheme of the analysis, the acceptance is computed on the data, leading in some cases to some inconstitancies or errors due to the lack of statistics (see Section 4.3.4 of Chapter 4).

Here all the gamma-like events of the HEGS data set (the 6499 runs) are used to compute the radial lookup tables. A table here refers to the evolution of the acceptance of the instrument in function of the energy E and the distance from the pointing position θ^2 as shown on Figure 6.3.

There is one table per analysis configuration (Loose, Std and Faint), per zenith angle (0° to 70° with steps of 10°) and per observation configuration (3 or 4 telescopes). In order to have a good mapping of the $[\log E, \theta^2]$ parameter space, there are 90 energy bins between $\log E = -1.5$ and $\log E = 3$ (in TeV) and 100 θ^2 bins between 0 and 9 (in deg^2).

[3] http://scikit-learn.org/stable/modules/generated/sklearn.cluster.dbscan.html

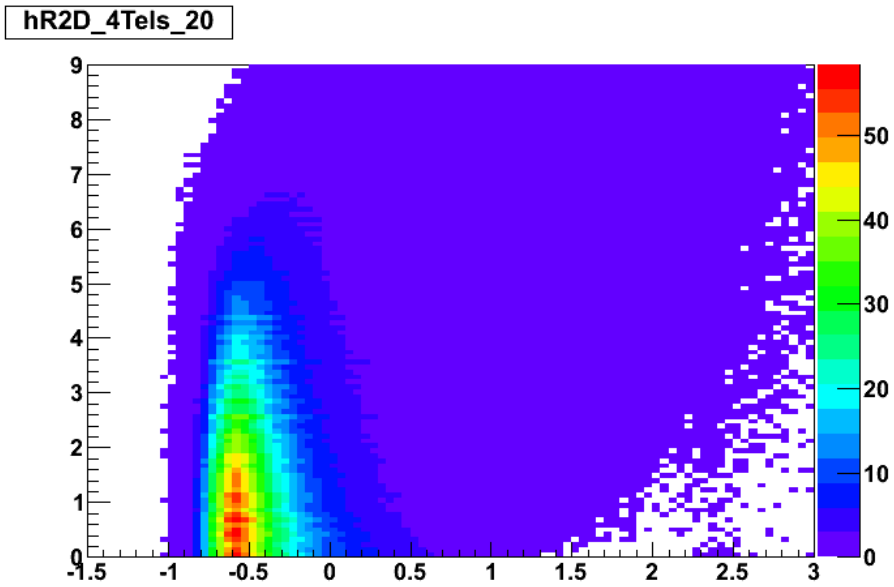

FIGURE 6.3: Example of a radial lookup table for 4 telescopes at a zenith angle of 20° with the Std configuration. The x axis represents the logarithm of the energy (in TeV), the y axis is the θ^2 and the color scale shows the acceptance value.

6.2.2 Maps production

The scripts, called `Survey Suite`[4], used to compute the maps read the acceptance from the radial lookup tables and the events stored in the results file.

There are several maps configurations possible depending on the cuts, bin size and method used. Here is the configuration chosen for the following maps are:

- Standard cuts;
- Acceptance from the radial lookup tables;
- Psi-cut = 2° (the cut to restraine the field of view not to have too much edges);
- The safe threshold is computed with the acceptance method[5]: 15% of the acceptance maximum, computed for each run at an offset of 2°;
- Bin size = 0.02° (the size of a bin on a map to compute the excess and significance);
- Maps are computed using the Ring Background method (see Section 4.3.5 of Chapter 4);
- The spectral index to compute fluxes is fixed at $\Gamma = 3$;
- All tables are generated assuming source are point-like.

The maps computed with the `Survey Suite` range from the basic maps (excess map, significance map, observation condition maps...) along with flux maps and ON-OFF test maps.

[4] coming from the HGPS framework

[5] The alternative is the bias method: the safe energy threshold is defined as the energy above which the bias in energy reconstruction is less than a given value ($\sim 10 - 15\%$).

Flux maps

A set of maps containing flux related informations can be computed: differential flux map, integrated flux map, upper limit map (and the corresponding error maps). The principle is to compare the number of observed γ (excess) to the number of γ expected from Monte-Carlo simulations.

The integrated flux F is computed using the formula:

$$F = \frac{N_\gamma}{N_{\rm exp}} \int_{E_1}^{E_2} \Phi_{\rm ref}(E) \mathrm{d}E \tag{6.1}$$

where N_γ is the number of excess coming from the analysis, $N_{\rm exp}$ is the number of expected excess of γ and $\Phi_{\rm ref}(E)$ is the spectral shape, here assumed to be a power law of index $\Gamma = 3$. Once the spectral shape fixed, all the information is in the $N_\gamma/N_{\rm exp}$ ratio. $N_{\rm exp}$ is given by:

$$N_{\rm exp} = \sum_{R \in \rm runs} T_R \int_{E_{\rm min}}^{\infty} \Phi_{\rm ref}(E_r) A_{\rm eff}(E_r, q_R) \mathrm{d}E_r \tag{6.2}$$

with E_r being the reconstructed energy, $E_{\rm min}$ the threshold energy of the observation, T_R the livetime of the run R, q_R the observations parameters of the run R (azimuth and zenith angles, telescopes participating in the observation, optical efficiency...) used to compute the effective area $A_{\rm eff}$ which is assumed constant during the run. $N_{\rm exp}$ is computed for each position of the sky in the field of view to create the count map of expected γ rays. From the count map, the integrated flux map can be derived using Equation 6.1 with (in this work) $E_1 = 1$ TeV and $E_2 = \infty$.

Then, the differential flux map at 1 TeV can be computed by simply dividing the number of excess events by the area time map (which is also computed at 1 TeV in units of m^2.s.TeV). The error on the flux is computed by dividing the error on the excess by the area time map value. This procedure is done bin per bin for each map.

The integrated flux map (and its error), chosen to be above 1 TeV, is computed by integrating the differential flux at 1 TeV, assuming a power law spectral shape of index 3.

A script called `FindPosition.C` was created to retrieve all of the informations of interest for a given position. If the position [RA,Dec] is in the HEGS fields of view, the script will print: the number of runs, the observation time, number of excess (along with the number of ON and OFF events and the α) and the differential and integrated flux values (with their error), the sensitivity and the upper limits.

This is how the values presented in the Section 6.3 and 6.4 have been extracted.

ON-OFF test maps

The ON-OFF test in the time domain is the same ON-OFF method used to compute the maps described in Section 4.3.3 of Chapter 4 but in the time dimension.

Let's consider N runs on a position of interest defined by its coordinates. The ON region will be firstly defined on the first run and the number of ON events $N^1_{\rm ON}$ will be the number of events in the first run. The number of OFF events $N^1_{\rm OFF}$ will be the number of events in all the $N-1$ other runs. The α_1 factor, to compute the excess $N_{\rm ON} - \alpha N_{\rm OFF}$ is defined as the ratio of the integrated acceptance in each time bins. The significance of the ON-OFF test can be calculated for each time bin with the Li and Ma, 1983 formula.

This procedure is iterative and each time bin will be defined as the ON region following an iterative process illustrated on the top panel of Figure 6.4. In this example the

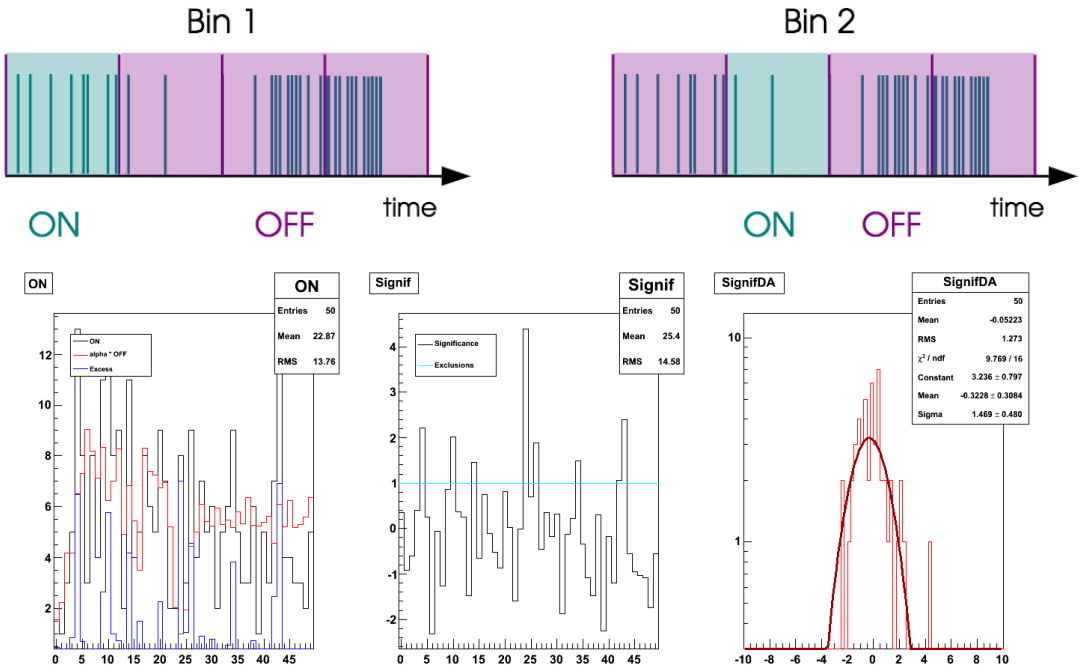

FIGURE 6.4: Top: Illustration of the iterative process of the temporal ON-OFF test. Each blue line represents an event. The ON region is moving in each bin. Bottom: 1D histograms of the ON-OFF test.

size of the time bin is chosen as a run but it could be smaller or larger (depending on the events statistic).

The bottom panel of Figure 6.4 shows the resulting 1D histogram. The first panel shows the N_{ON} (black), $\alpha \times N_{\mathrm{OFF}}$ (red) and excess (blue) as a function of run number. The second panel shows the significance value of the excess in each time bin. The distribution of these significance values is shown on the third panel. In this example, the test has been done on a position where the maximum significance value of the ON-OFF Test is 4.4.

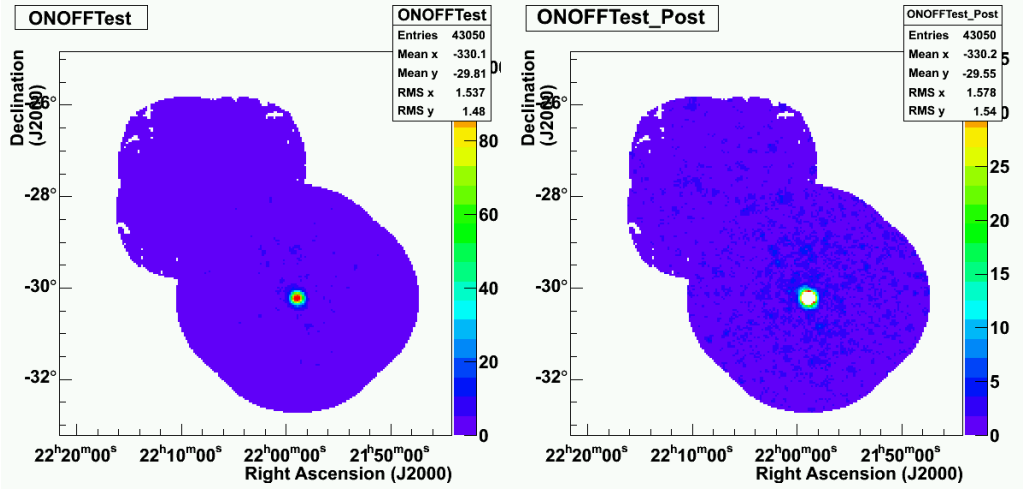

FIGURE 6.5: Example of ON-OFF Test maps from RunsCluster 0 in the field of view of PKS 2155-304. The map on the right is corrected from the trials.

This test is done for each pixel of the field of view, giving a map of the ON-OFF test displayed on the left panel of Figure 6.5. However, this map has to be corrected from the

trials (number of time bins in that pixel) to not over-estimate the significance of the test. The right panel of Figure 6.5 shows the post trial map. The post-trial map will be the one I will refer to when using the ON-OFF Test map values.

6.3 Sanity checks

6.3.1 Checks with the UL paper

In order to check if the upper limit derivation from the HEGS scripts is correct, the values were compared to the latest H.E.S.S. AGN upper limit paper (H. E. S. S. Collaboration et al., 2014), which performed a dedicated analysis on each source.

Figure 6.6 shows a good agreement between the upper limits derived by HEGS and the published ones. The left panel displays a scatter plot of the upper limits from the paper versus the ones from HEGS. A correlation with a scatter can be seen, with a tendancy of being maybe more conservative in the HEGS results as it can be seen on the right panel of Figure 6.6, with a distribution going more to the positive values ($\Leftrightarrow$ UL_Maps > UL_Paper).

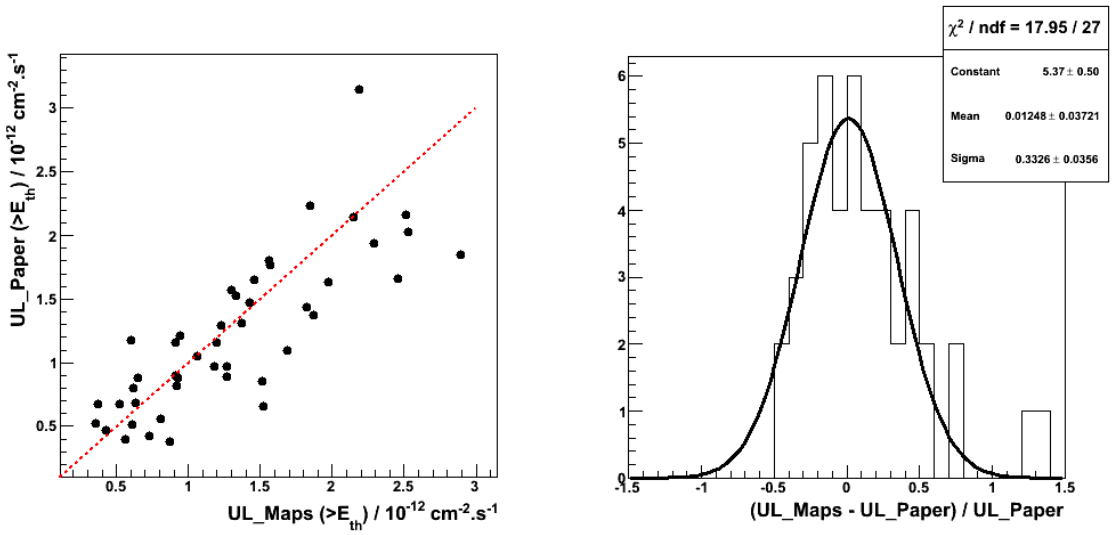

FIGURE 6.6: Left: Scatter plot of the upper limits on the flux from H. E. S. S. Collaboration et al., 2014 versus the HEGS flux. Right: Distribution of the normalized difference of the flux's limits.

It has to be noted that the results from H. E. S. S. Collaboration et al., 2014 come from a different analysis with different DST version, background estimation, acceptance tables and so on. So it is really satisfying to have compatible results.

6.3.2 Cheks with the H.E.S.S. detected sources

Upper limits derivation is working well, what about the detected known sources now? For several known sources[6] the flux obtained from the HEGS maps and from a dedicated ON-OFF analysis, with the same runlist, are compared.

The comparison of the fluxes can be seen on Figure 6.7, representing the scatter plot of the differential flux at 1 TeV from the HEGS maps and from the dedicated analysis. The

[6]16 in total: M 87, Mkn 421, 1ES 0229+200, 1ES 0347-121, 1ES 0414+009, 1ES 1101-232, 1ES 2322-40.9, 1RXS J101015.9-311909, PG 1553+113, PKS 0301-243, PKS 0447-439, PKS 0548-322, PKS 1510-089, PKS 1514-241, RGB J0152+017 and SHBL J001355.9-185406

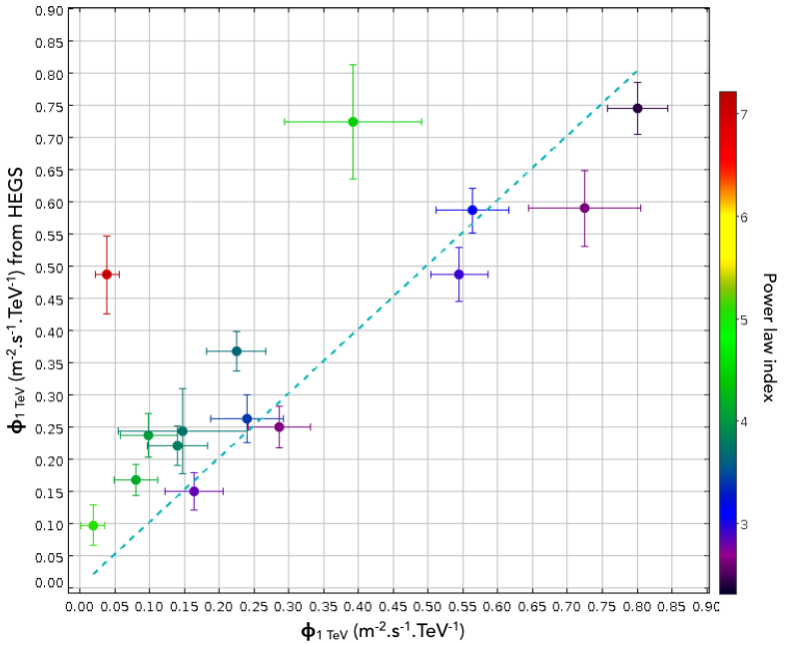

FIGURE 6.7: Comparison of the differential flux at 1 TeV of the HEGS maps (y-axis) with the dedicated ON-OFF analysis (x-axis). The color scale represent the photon index value known for each sources.

correlation is satisfying because the spread can easily be explained looking at the spectral index for each sources. The sources with a fitted spectral index around the one used in HEGS ($\Gamma = 3$), so between 2.5 and 3.5 (between purple and blue-green) show comparable results. But for sources with a fitted spectral index above 4 (green to red) the difference is bigger (as expected). Again, knowning that the analysis version might not always be the same, results show a good compatibility.

6.4 Results

6.4.1 ON-OFF Test maps of known TeV sources

Figure 6.8 and 6.9 show all of the ON-OFF Test maps of all the known TeV blazars observed with H.E.S.S., 28 in total. How many sources are variable for the ON-OFF Test?

Among all the fields of view there are 2 FSRQs, 1 LBL, 22 HBLs and 3 FR I (radio galaxies) known at TeV. The full list is shown on Table 6.1. Only 5 sources, all HBLs (PKS 2155-304, Mkn 421, PKS 2005-489, Mkn 501 & H 2356-309), are seen as variable with an ON-OFF Test value above $5\ \sigma$. Seeing variability or not does not really depends on the observation time since variability is detected on Mkn 501 in 6 hours, the source just has to be variable or flaring.

However, it is known that some sources on this list underwent flares observed by H.E.S.S. Why do we not see them? M 87 has been observed by H.E.S.S. during a flare (Raue et al., 2012) but its ON-OFF Test value of $4.5\ \sigma$, still showing a hint of variability, is below the $5\ \sigma$ threshold.

PKS 1510-089 is showing a hint of variability as well, with an ON-OFF Test value of $4.7\ \sigma$. In the discovery paper of the source (H.E.S.S. Collaboration et al., 2013), the dataset did not show significant variability (with a constant fit of $\chi^2 = 20.4$ for 11 degrees of freedom). Interestingly, the HEGS significance map does not show any signal (above

4.5 σ) on the position of PKS 1510-089 but the source is visible on the ON-OFF Test map proving the efficiency of this technic to detect sources thanks to their variability. The non-detection of PKS 1510-089 in HEGS can be explained by the different runslists used: 74 runs are taken on PKS 1510-089 in HEGS, giving a total observation time of 31.7 hours while H.E.S.S. Collaboration et al., 2013 reported the detection on 15.8 hours. Moreover, the observations leading to the detection of PKS 1510-089 were made during known high flux states. If the source was more quiet afterwards, the new 15 hours of observations integrated only noise, hiding the signal of PKS 1510-089.

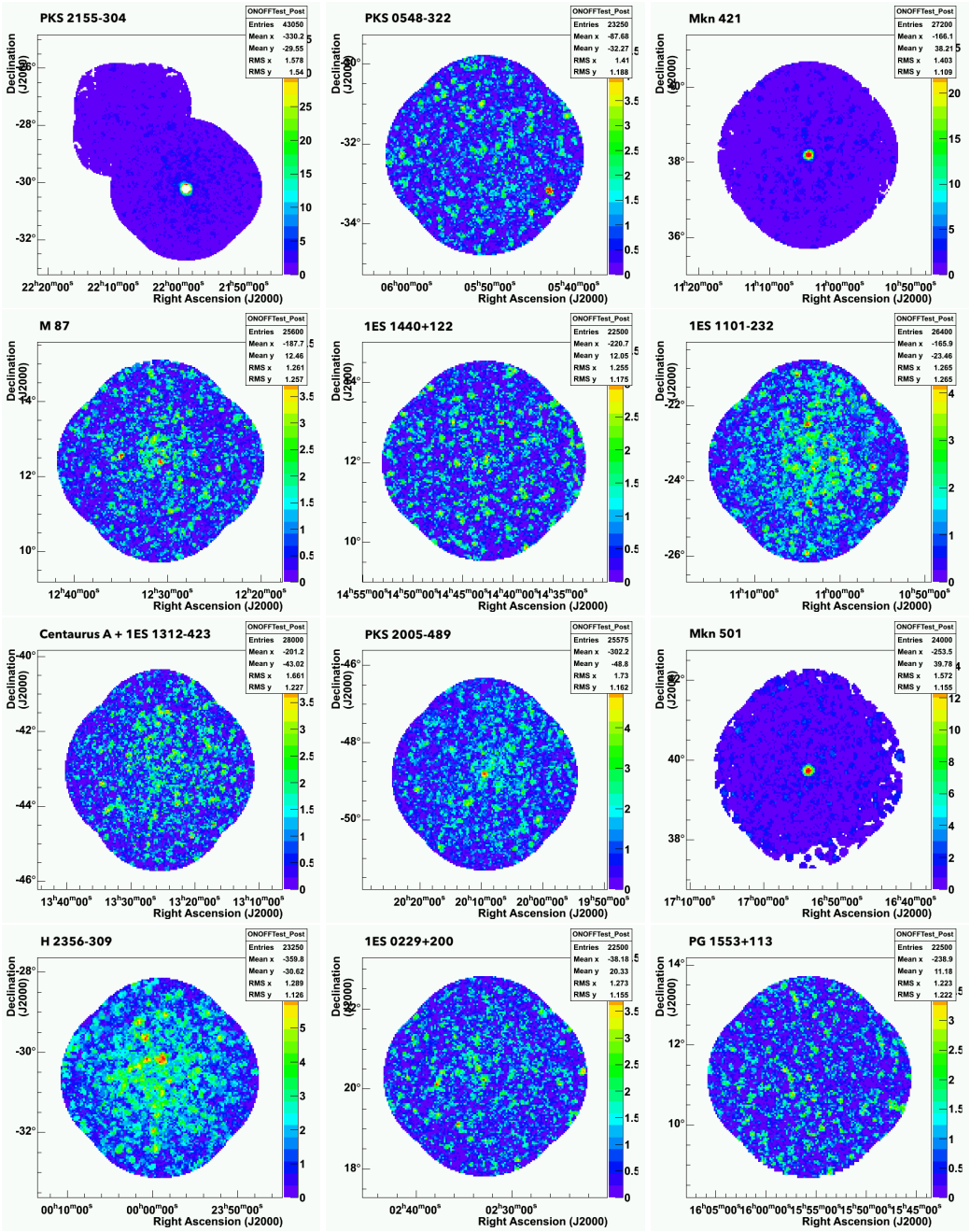

FIGURE 6.8: ON-OFF Test maps for all the known TeV sources observed in HEGS (to follow on Figure 6.9).

RunsCluster	Source name	Type	Livetime	ON-OFF Test > 5 σ
RC67	3C 279	FSRQ	5.5 h	no
RC99	PKS 1510-089	FSRQ	31.7 h	no
RC111	Ap Librae	LBL	20.1 h	no
RC0	**PKS 2155-304**	**HBL**	**348.0 h**	**yes**
RC3	PKS 0548-322	HBL	46.6 h	no
RC4	**Mkn 421**	**HBL**	**22.1 h**	**yes**
RC10	1ES 1440-122	HBL	11.3 h	no
RC11	1ES 1101-232	HBL	68.6 h	no
RC12	1ES 1312-423	HBL	31 h	no
RC14	**PKS 2005-489**	**HBL**	**147.3 h**	**yes**
RC15	**Mkn 501**	**HBL**	**5.9 h**	**yes**
RC16	**H 2356-309**	**HBL**	**168.1 h**	**yes**
RC23	1ES 0229+200	HBL	116.4 h	no
RC32	PG 1553+113	HBL	29.8 h	no
RC44	1ES 0414+009	HBL	83.0 h	no
RC47	1ES 0347-121	HBL	52.4 h	no
RC64	1RXS J101015.9-311909	HBL	55.8 h	no
RC84	RGB J0152+017	HBL	49.4 h	no
RC90	SHBL J001355.9-185406	HBL	40.5	no
RC90	KUV 00311-1938	HBL	58.7 h	no
RC102	PKS 0301-243	HBL	41.8 h	no
RC105	PKS 0447-439	HBL	17.5 h	no
RC106	1ES 0647+250	HBL	1.0 h	no
RC117	RBS 0413	HBL	4.1 h	no
RC138	PKS 1440-389	HBL	2.5 h	no
RC5	M 87	FR I	78.0 h	no
RC12	Centaurus A	FR I	218.1 h	no
RC97	PKS 0625-35	FR I	6.0 h	no

TABLE 6.1: List of known TeV AGN in the HEGS fields of view, with number of the RunsCluster, source name, type of the object, time of observation on the object in hours and the answer to is the ON-OFF Test value greater than 5 σ. AGN with an ON-OFF Test value greater than 5σ are in bold font.

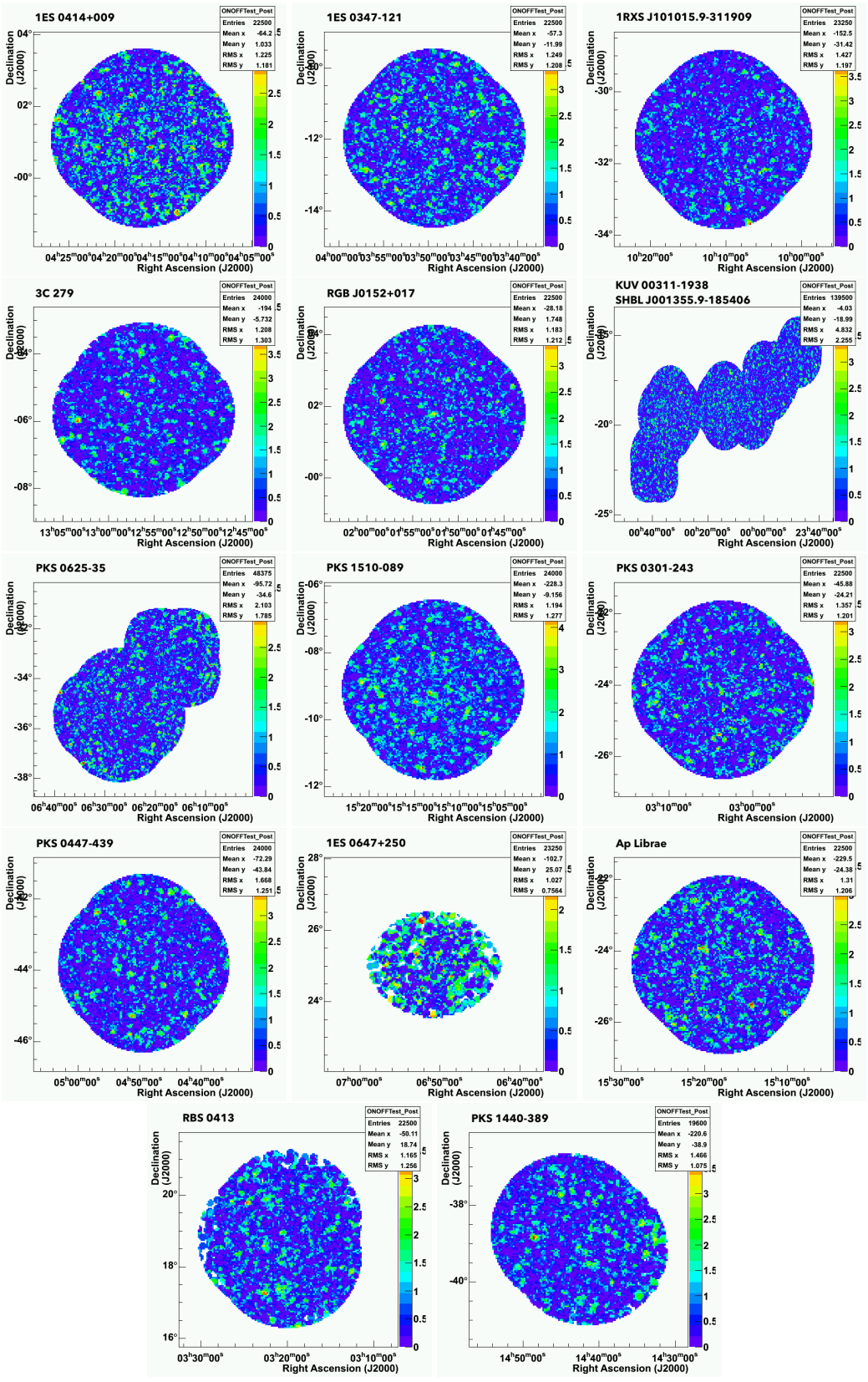

FIGURE 6.9: Following of Figure 6.8.

6.4.2 Un-detected 3FGL sources in the HEGS fields of view

HEGS, in its preliminary version, spans $\sim$ 2700 deg^2 in the sky, so some objects were observed even though they were not the one pointed at. There are 168 AGN (blazars and radio galaxies) in the 3FGL which have been observed by H.E.S.S., among them some are known TeV sources like PKS 2155-304, Mkn 421 and 501 or Centaurus A. Nevertheless, 150 objects unknown at TeV have been observed. What constraints can HEGS put on the 3FGL sources appearing in the HEGS fields of view?

I had a look at the 3FGL catalog for all of them to compare the 3FGL flux and its extrapolation absorbed by the EBL to the HEGS upper limits. The EBL absorption is done using the model of Franceschini, Rodighiero, and Vaccari, 2008 under the assumption that the spectrum does not have any intrinsic curvature.

Upper limits constrains

Upper limits on the flux are derived assuming a power law spectrum:

$$\frac{\mathrm{d}N}{\mathrm{d}E} = \Phi_0 \left(\frac{E}{E_0}\right)^{-\Gamma} \tag{6.3}$$

where $\mathrm{d}N/\mathrm{d}E$ is the differential flux in cm^{-2}.s^{-1}.erg^{-1}, Φ_0 the differential flux at the reference energy E_0 (generally taken at 1 TeV) and Γ is the power law index. To derive an upper limit on the flux, the spectral index is fixed at $\Gamma = 3$ and the fit derives the upper limit on the flux. If the source had been brighter than the upper limit we have, it should have been detectable with the sensitivity and observation time.

For 75 % of the 3FGL sources in our fields of view, the HEGS upper limit is above the expected flux and can not bring any constraint. The SEDs of this category is not shown in the following.

Among the remaining 25 %, I present the SEDs of the 20 brighest sources of the 3FGL catalog in the 1-300 GeV range. Figures 6.10, 6.11 and 6.12 display the SEDs of these 20 AGN with the 3FGL spectrum from 100 MeV to 100 GeV in orange, its extrapolation up to 10 TeV in yellow, the expected EBL absorbed spectrum in blue and the HEGS upper limit in black along with the common name of the object, its type and redshift and the observation time at this position.

For 12 objects (3FGL J1117.0+2014, 3FGL J2324.7-4040, 3FGL J0334.3-3726, 3FGL J1217.8+3007, 3FGL J1221.3+3010, 3FGL J0050.6-0929, 3FGL J0022.1-1855, 3FGL J0325.6-1648, 3FGL J1328.5-4728, 3FGL J0051.2-6241, 3FGL J0543.9-5531 and 3FGL J1917.7-1921), the HEGS upper limit is greatly below the EBL absorbed flux indicating the presence of an intrinsic curvature of the spectrum from GeV to TeV, otherwise we should have detected the source. For the remaining 8 objects, there is a tension between the HEGS upper limit and the EBL absorbed flux where there is a hint of intrinsic curvature.

The observation times are not so high (generally around 10 hours) so it may be that with only a modest time investment, we could detect more objects and expand the current extragalactic TeV catalog.

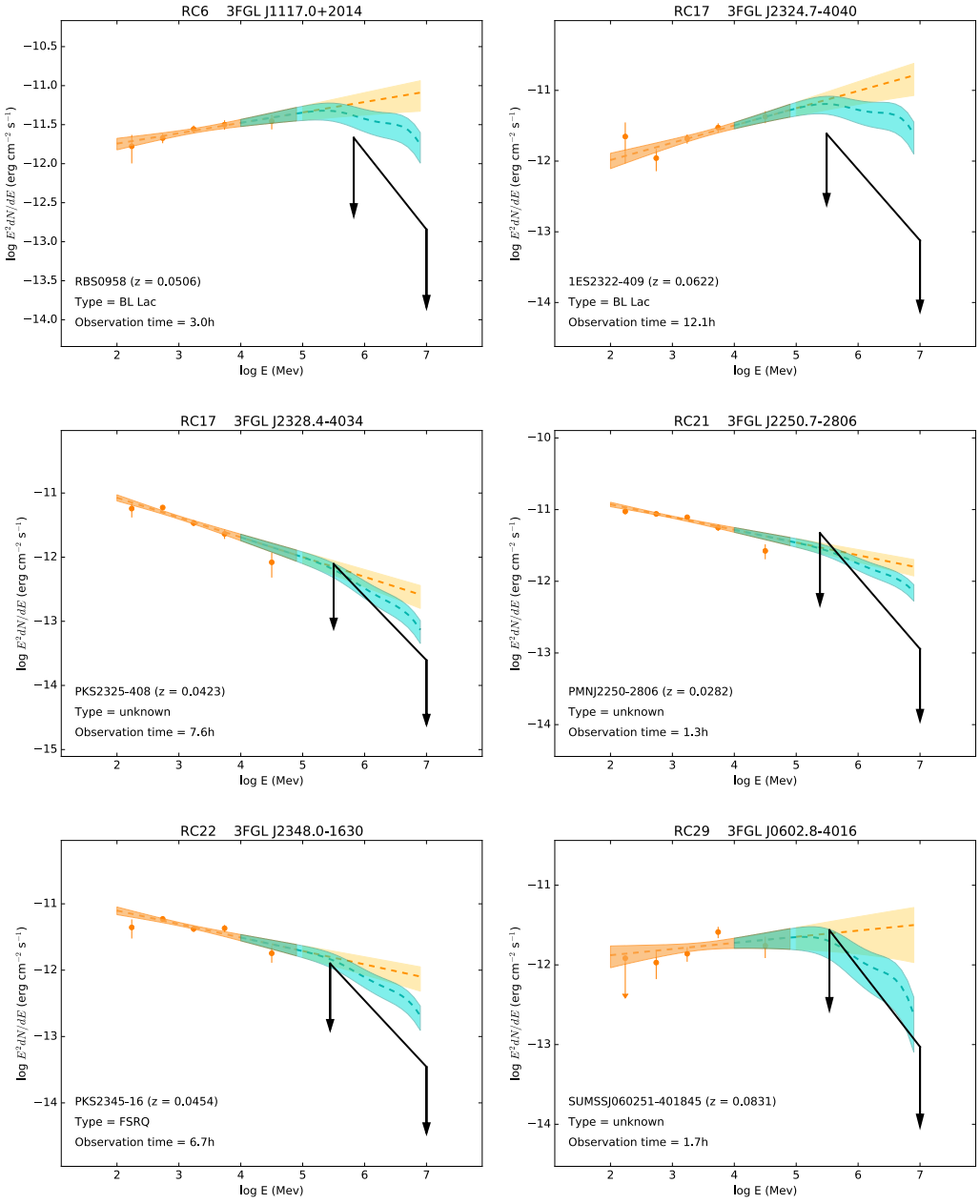

FIGURE 6.10: SEDs of the 20 3FGL sources appearing in the HEGS fields of view where HEGS is constraining compared to the 3FGL. The 3FGL spectrum is shown in orange, with its extrapolation up to 10 TeV in yellow. The corresponding EBL absorbed flux is in blue and the HEGS upper limit in black. Following in Figure 6.11 and 6.12

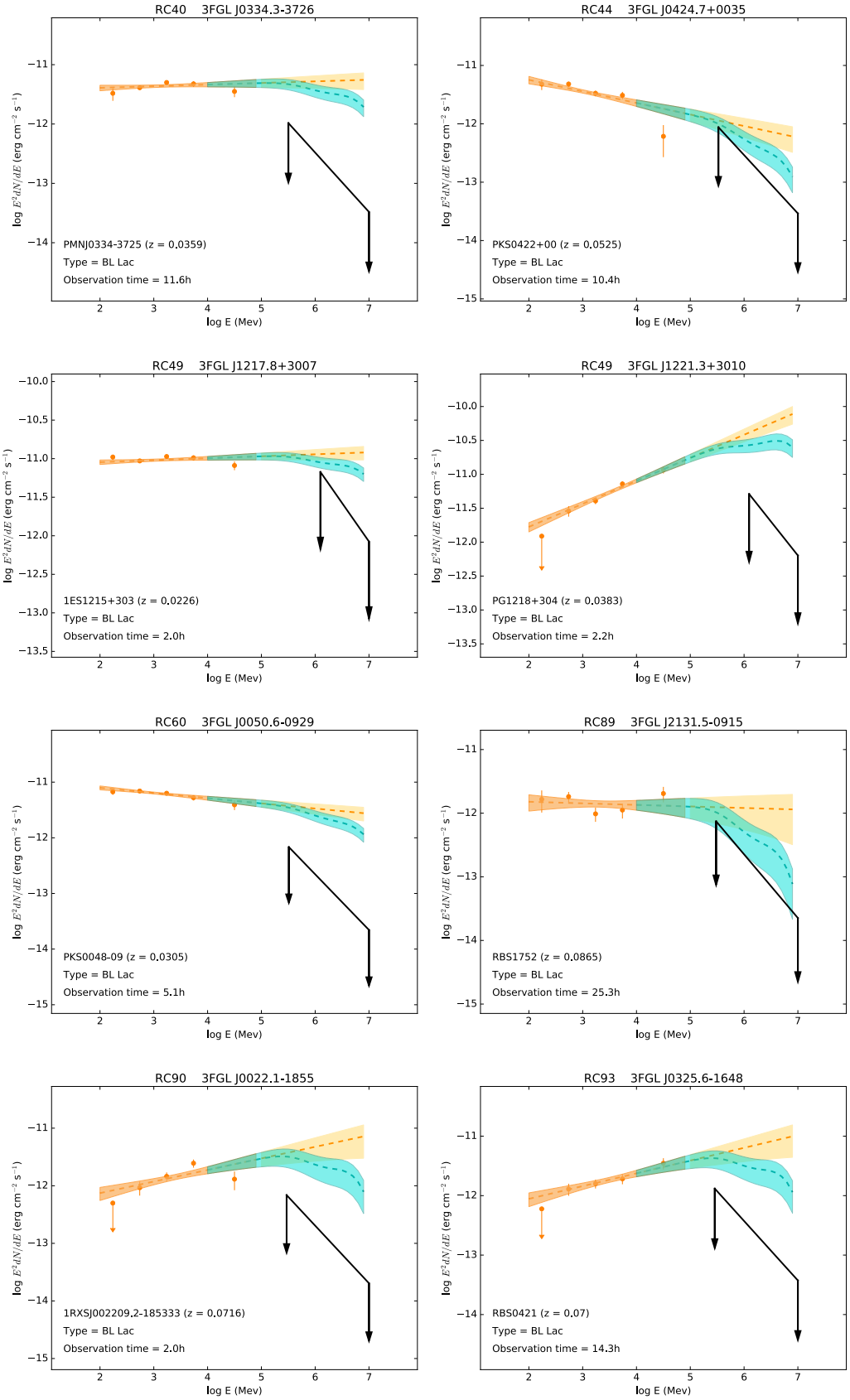

FIGURE 6.11: Same as Figure 6.10 and 6.12.

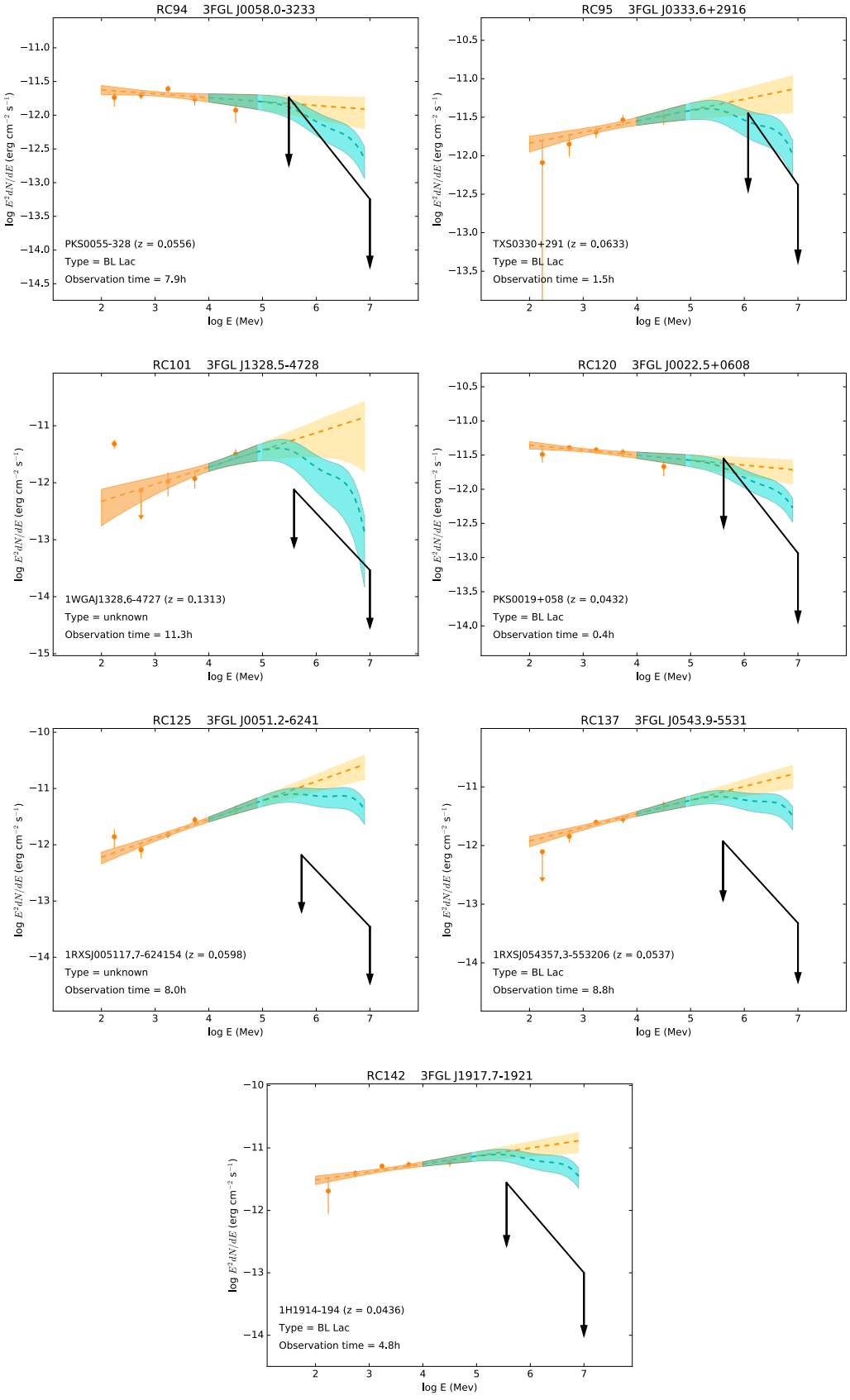

FIGURE 6.12: Same as Figure 6.10 and 6.11.

Comparison with ROMA-BZCAT

Before the launch of *Fermi*-LAT and the release of their different catalogs, the targets for AGN observations were chosen looking at their radio and X-ray fluxes. A source bright in radio contains a lot of soft photons to be scattered by high energy electrons to produce TeV emission. And bright X-ray sources are rich in high energy electrons. The combination of the two should give a source bright in VHE γ-rays as well, as stated in Costamante and Ghisellini, 2002 and illustrated on Figure 6.13.

Figure 6.13 shows the radio flux at 1.4 GHz and the X-ray flux between 0.1 and 2.4 keV of blazars from the Roma-BZCAT (Massaro et al., 2009). The Roma-BZCAT is a multi-frequency catalog of blazars including different surveys in the radio, optical and X-ray bands. The know TeV emitters from TeVCat which are in the Roma-BZCAT as well are represented in red and tend to be in the upper right part of the plot ($\rightarrow$ bright in radio and in X-ray).

I looked at where the 3FGL undetected sources in HEGS were placed in this diagram (for those in BZCAT). They are uniformly distributed in the X-ray-radio plane (blue and green), meaning that some of them fulfill the bright in radio and bright in X-ray criteria and are not detected.

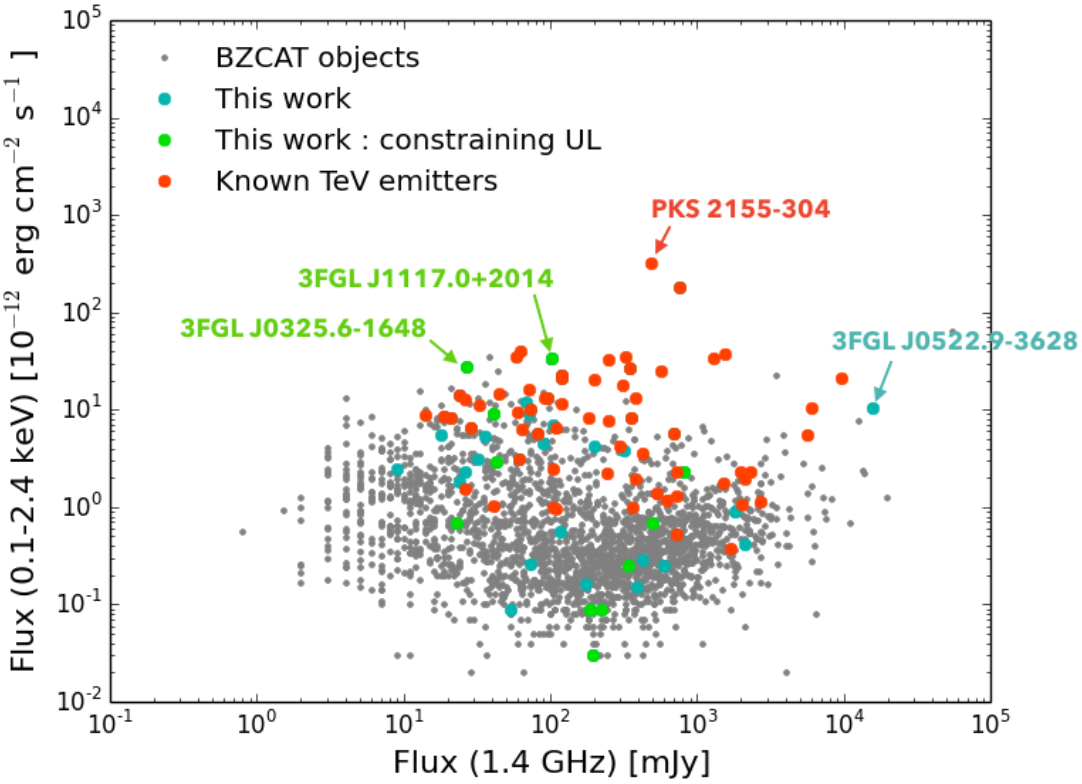

FIGURE 6.13: X-ray flux between 0.1 and 2.4 keV versus the radio flux at 1.4 GHz for the blazars listed in the Roma-BZCAT catalog (grey). The 3FGL sources in our fields of view that are in the BZCAT as well are shown in blue for the ones with no HEGS constraint and in green for the one presented in Section 6.4.2

Focus on 3FGL J0325.6-1648, 3FGL J1117.0+2014 and 3FGL J0522.9-3628

The objects 3FGL J0325.6-1648, 3FGL J1117.0+2014 and 3FGL J0522.9-3628 are the 3 brightest 3FGL sources of this study in X-ray, with 3FGL J0522.9-3628 being among the brighest BZCAT sources in radio.

The multi-wavelenth SED, using data from ASDC[7], of these sources are presented in Figure 6.14.

The 3LAC catalog classifies 3FGL J0325.6-1648 and 3FGL J1117.0+2014 as HSP since their synchrotron peak frequency is above 10^{15} Hz. The HEGS upper limits on these two sources are constraining, below the EBL flux level, indicating the presence of an intrisic curvature. The blazar 3FGL J0522.9-3628 is classified as an LSP ($\nu_{\rm sync} = 10^{13.6}$ Hz), and being a blazar of unknown type, one can not know if it falls in the FSRQ or BL Lac class. The HEGS upper limit on this one is not constraining despite 15 hours of observations because of the rapid falling log-parabola spectrum (the EBL absorption is negligible with a redshift of $z = 0.0321$).

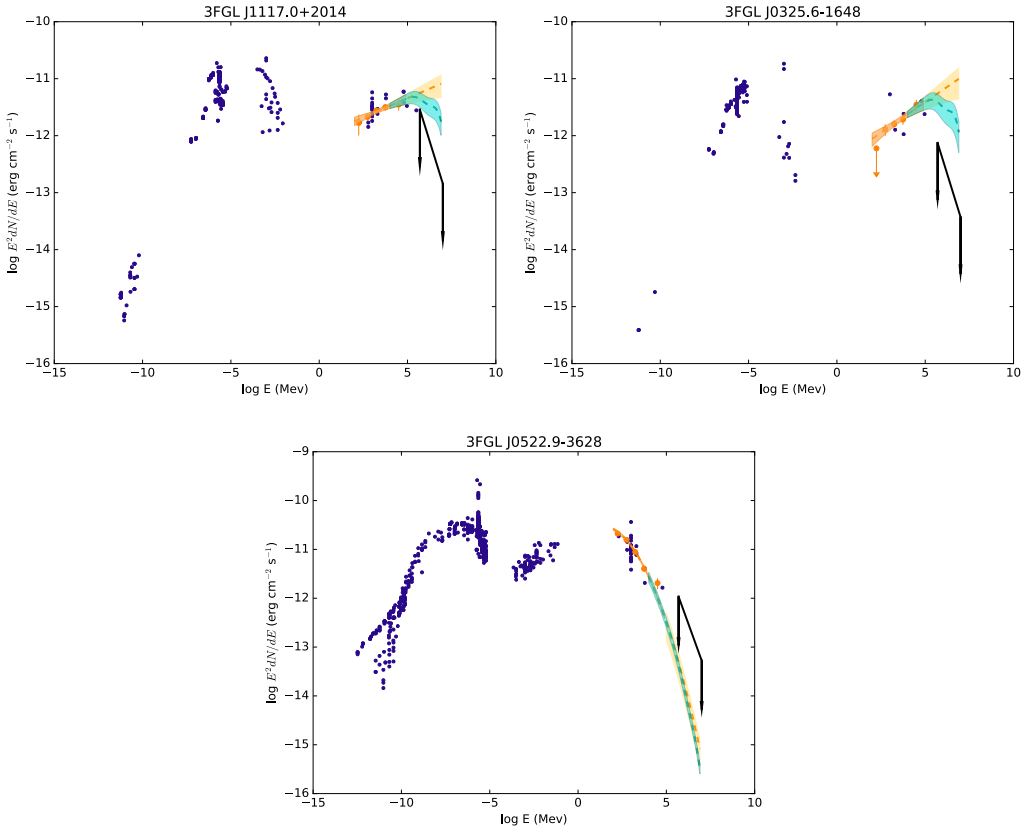

FIGURE 6.14: SEDs of 3FGL J1117.0+2014, 3FGL J0325.6-1648 and 3FGL J0522.9-3628. Data from the ASDC are the dark blue points while the 3FGL and HEGS spectra are represented as on Figure 6.10.

One could think that this past observation strategy was not the right rule to follow, as some bright radio/X-ray sources like these 3 are not detected. How many objects bright in these bands have been observed and not detected in the past years of TeV observations?

[7] http://tools.asdc.asi.it/SED/

6.4.3 Looking for hotspots

In the `0-8-24` version of HEGS, there are 7986 runs passing the quality cuts divided in 146 RunsClusters. Significance and ON-OFF Test maps are looked for hotspots (a hotspot is defined when the significance is greater than 4.5σ). In total:

- 45 hotspots are found in the significance maps:
  - 25 of them are known sources taken into account in the exclusion regions.
  - 20 of unknown origin $\rightarrow$ it could be an artefact or a fluctuation on the map or a hint of a new source.
- 54 variability hotspots are found in the ON-OFF Test maps:
  - 8 of them are known sources.
  - 45 of them are of unknown origin $\rightarrow$ it could be an artefact or a fluctuation on the map or a hint of a new transient source.

An algorithm written in C++ called `maskmap` has been developped to applied a mask and keep only the pixel with a significance above a chosen threshold. The position (center of gravity) of the hotspot is then computed. The position reconstruction accuracy $\Delta\theta$ has been checked looking at known sources like PKS 2155-304, Mkn 421, Mkn 501... and is on average of the order of $0.06°$.

Figure 6.15 shows the significance maps of the RunsCluster 0, containing PKS 2155-304, as an example, with the significance maps including the source (right) and excluding it (middle). The masked map on the left shows in red only the pixels with a significance above the 4.5σ threshold. Three hotspots are visible, one being PKS 2155-304 (with a position reconstructed at $0.01°$ from the known position), and two being artefacts because they are directly on the edge of the map (and no known source from catalogs is close to them). Figure 6.16 is the same, showing only the significance excluding the source and the masked map, but the information is splitted between low and high energy with a separation at 1 TeV.

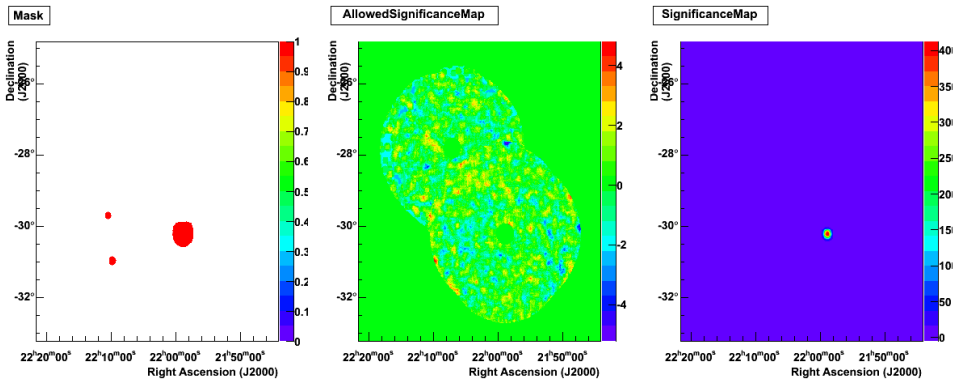

FIGURE 6.15: Example with maps from RunsCluster 0 in the field of view of PKS 2155-304: Significance maps with (from right to left) the total significance map, the significance map without the exclusion region and the masked map showing region with $\sigma > 4.5$ only.

My work here is to have a look at all the hotspots one by one, to see if it corresponds to a hint of signal or to an artefact of the analysis. I looked for possible counterparts in

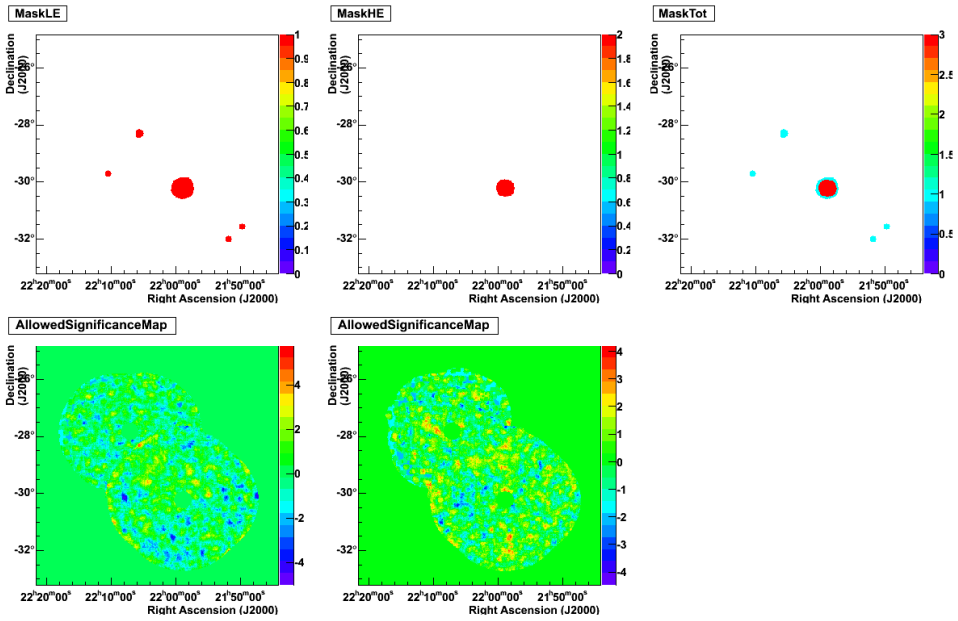

FIGURE 6.16: Example with maps below (left) and above (middle) 1 TeV from RunsCluster 0 in the field of view of PKS 2155-304. Top: masked map showing region with $\sigma > 4.5$ only for the low energy, high energy maps and both. Bottom: Allowed significance maps below and above 1 TeV.

databases like SIMBAD[8] and NED[9] and in the *Fermi* catalogs (3FGL, 2FHL and FAVA[10]). The following sections present some selected highlights of the analysis I performed.

6.4.4 [RunsCluster 3] A double hotspot

RunsCluster 3 contains the blazar PKS 0548-322 at the position RA = 87.669 & Dec = -32.271 and shows several hotspots:

1. On the significance map (top panel of Figure 6.17):
   - at the position RA = 87.68 & Dec = -32.32 ($\sigma_{\max} = 9.0$) corresponding to PKS 0548-322 ($\Delta\theta = 0.05°$)
   - at the position RA = 88.18 & Dec = -32.94 ($\sigma_{\max} = 4.7$)
2. On the ON-OFF Test map (bottom left panel of Figure 6.17):
   - at the position RA = 85.78 & Dec = -33.21 ($\sigma_{\max} = 4.8$)
3. On the significance map above 1 TeV (bottom middle and right panels of Figure 6.17):
   - at the position RA = 87.73 & Dec = -32.34 ($\sigma_{\max} = 5.1$) corresponding to PKS 0548-322
   - at the position RA = 85.67 & Dec = -33.24 ($\sigma_{\max} = 4.8$)

[8] http://simbad.u-strasbg.fr/simbad/
[9] https://ned.ipac.caltech.edu/
[10] *Fermi* All-sky Variability Analysis: https://fermi.gsfc.nasa.gov/ssc/data/access/lat/FAVA/

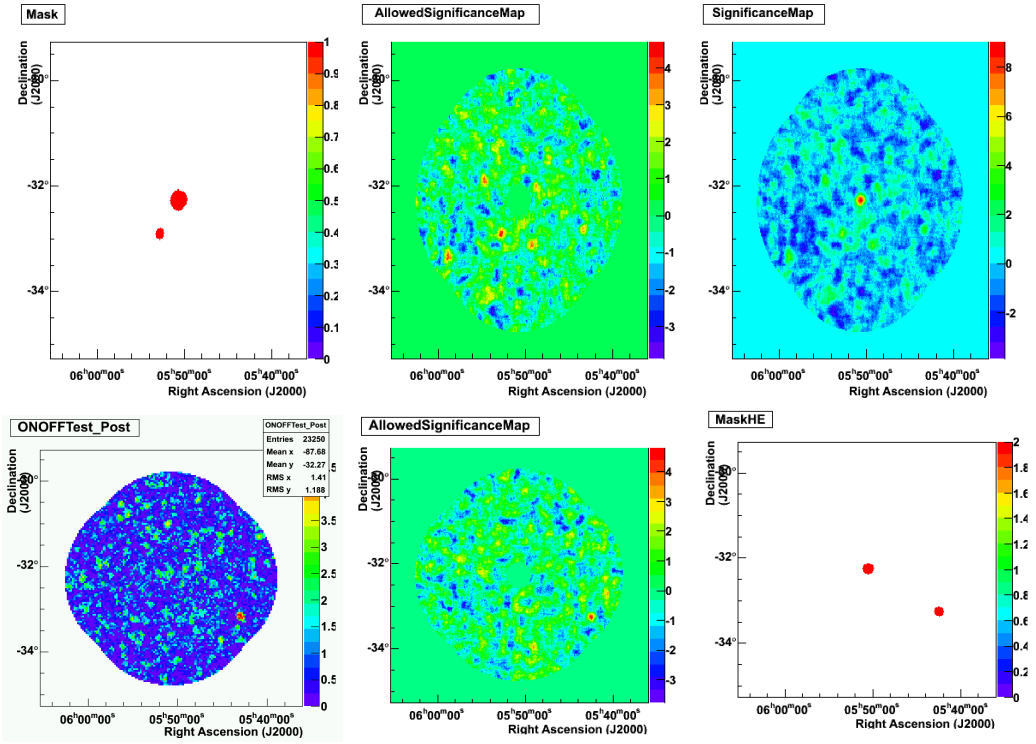

FIGURE 6.17: RunsCluster 3. Top: Significance maps. Bottom left: ON-OFF Test (post-trials) map. Bottom middle and right: Signifiance map above 1 TeV with the corresponding masked map.

There is one galaxy, NVSS J055235-330106, close to the hotspot at the position RA = 88.18 & Dec = -32.94 ($\Delta\theta = 0.08°$). On the NED database, this galaxy is classified as a radio source but is not in the *Fermi* catalogs.

The hotspot seen in the ON-OFF Test map and in the high energy significance map is the one of interest here as it is seen in 2 different maps. The two reconstructed positions are almost at the same position ($\Delta\theta = 0.09°$). There is nothing in the SIMBAD database in a radius of $0.1°$ around the position of the hotspot. However, 41 objects are found in NED, including 2 radio galaxies: NVSS J224104+200053 ($\Delta\theta = 0.02°$) and NVSS J224106+195745 ($\Delta\theta = 0.07°$). These radio galaxies are not in the 3FGL and nothing around this position is in the 2FHL or the 3FGL neither. But a source in FAVA (with one flare alert) catalog at $\Delta\theta = 1.2°$ exist: 1RXS J053629.4-334302 (in the 2FGL catalog under the name 2FGL J0536.2-3348). Still it's a big angular distance to claim an association.

The light curve derived on the hotspot position to see when the variability appears show a strange behavior (see Figure 6.18 with the high flux with large error) typical of a systematic effect. Because of this, no conclusion can be made since the physical origin of this double hotspot is unclear.

6.4.5 [RunsCluster 9] Detection of 3C 273?

H.E.S.S. never detected 3C 273, and the significance map on the left panel of Figure 6.19 shows not even a hint of signal. The ON-OFF Test map displayed on the right panel of the same figure, shows two hotspots:

1. at the position RA = 187.06 & Dec = 2.63 ($\sigma_{\max} = 5.1$)
2. at the position RA = 187.98 & Dec = 3.95 ($\sigma_{\max} = 4.6$)

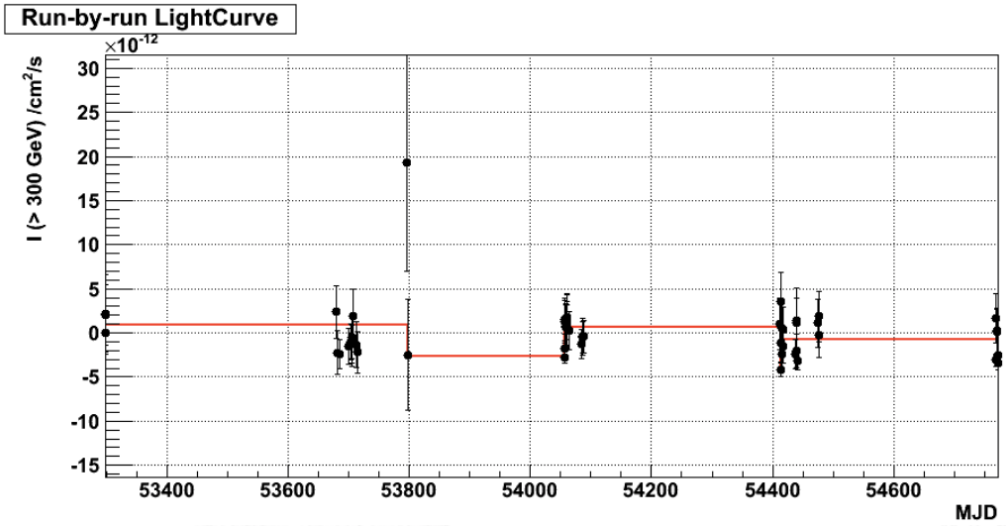

FIGURE 6.18: Light curve of the variability hotspot of RunsCluster 3.

The FAVA catalog showed a source at RA = 187.43 & Dec = 2.16 with 10 flares corresponding to 3C 273. The hotspot number 1 is at an angular distance of $0.6°$ from the position of 3C 273, so after a short moment of excitation, it is quite unlikely that the two are linked.

Moreover, the light curves of the two variability hotspots (Figure 6.20) display a weird behavior. They both have a high flux with a large error on the same run and this high flux could cause the high significativity seen in the ON-OFF Test.

As for RunsCluster 3, this is most likely a systematic effect. After further checks on other RunsCluster, this effect is visible in several of them. This could be due to the bad calibration of some runs or the bad quality of them. This is one of the reaons why it was decided to wait for the new production of DST and the new version of the analysis soft.

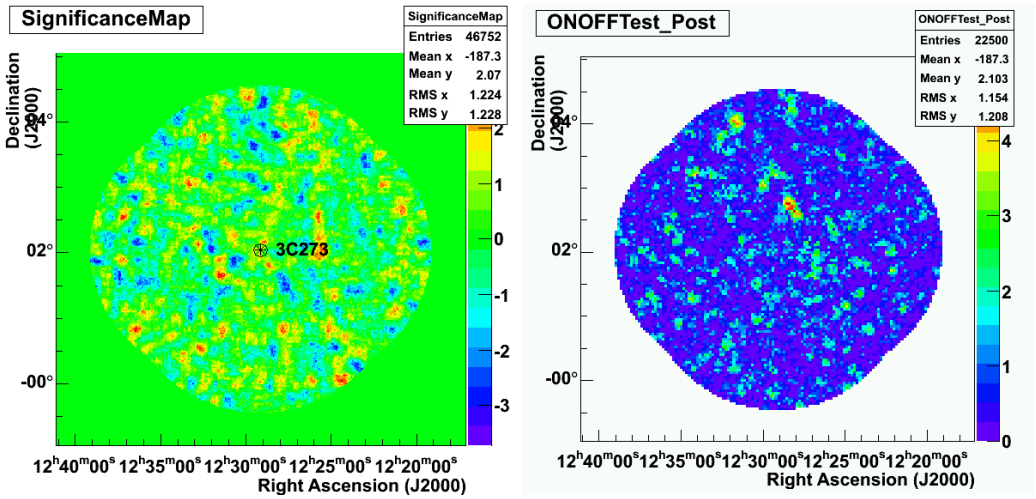

FIGURE 6.19: RunsCluster 9. Left: Total significance map with the position of 3C 273. Right: ON-OFF Test (post-trials) map.

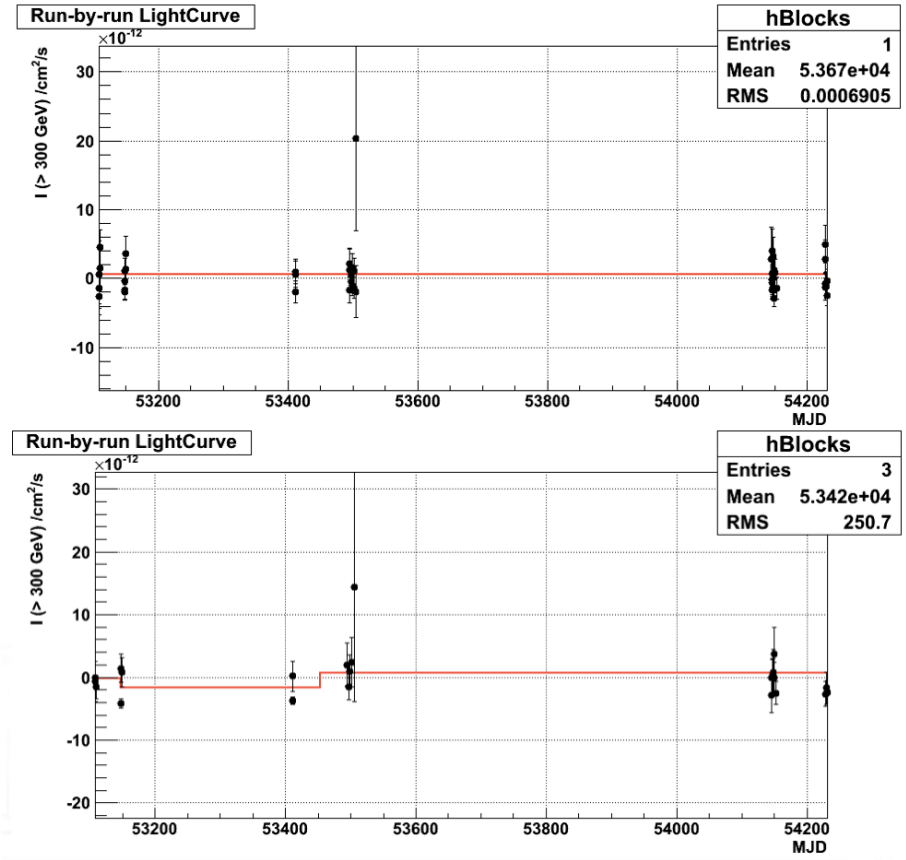

FIGURE 6.20: Light curves of the two hotspots of RunsCluster 9. Top: first hotspot at RA = 187.06 & Dec = 2.63. Bottom: second hotspot at RA = 187.98 & Dec = 3.95.

6.4.6 [RunsCluster 24] Detection of Pictor A?

RunsCluster 24 contains 55 runs taken on the radio galaxy Pictor A. This object has never been detected at TeV and shows here a hint of signal with a hotspot at 4.5σ at RA = 79.81 & Dec = 45.71 ($\Delta\theta = 0.11°$). The significance maps are shown in Figure 6.21.

An upper limit on the flux has been derived to see if it was constraining compared to the 3FGL flux. The SED is shown on Figure 6.22, where the HEGS data, being above the 3FGL extrapolated flux and the EBL absorbed spectrum, bring no constraint. It was then decided to wait for the new Prod8 version of the DSTs and the new analysis version.

Dedicated analysis of Pictor A

Even if at the time of the writing of this manuscript not all the Prod8 DST were produced to re-run the whole HEGS analysis, some runs were already reprocessed. This is the case for Pictor A where 45 runs are available[11].

In 18 hours of livetime, the analysis gives only 2.7σ, less than what was seen with HEGS, not enough to claim anything.

[11]The runslists between the different analysis version are expected to be different because of the new calibration and the new cuts defining the profiles in the `0-8-32` version of the analysis.

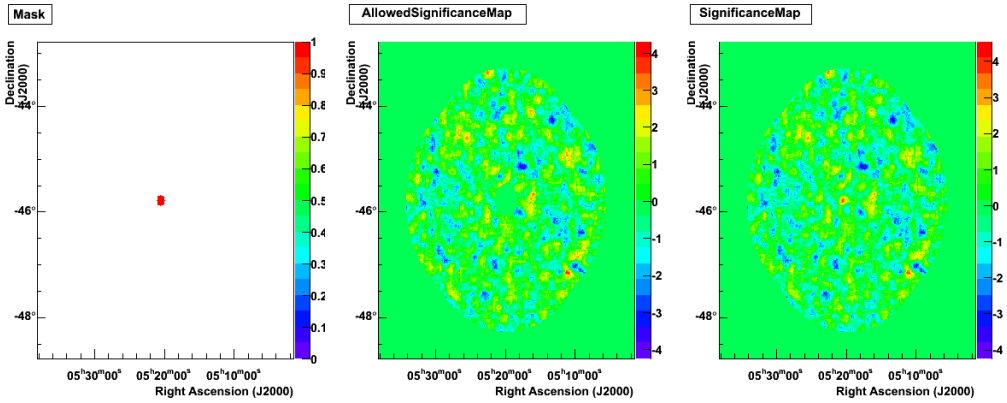

FIGURE 6.21: RunsCluster 24. Significance maps with (from right to left) the total significance map, the significance map without the exclusion region and the masked map showing region with $\sigma > 4.5$ only.

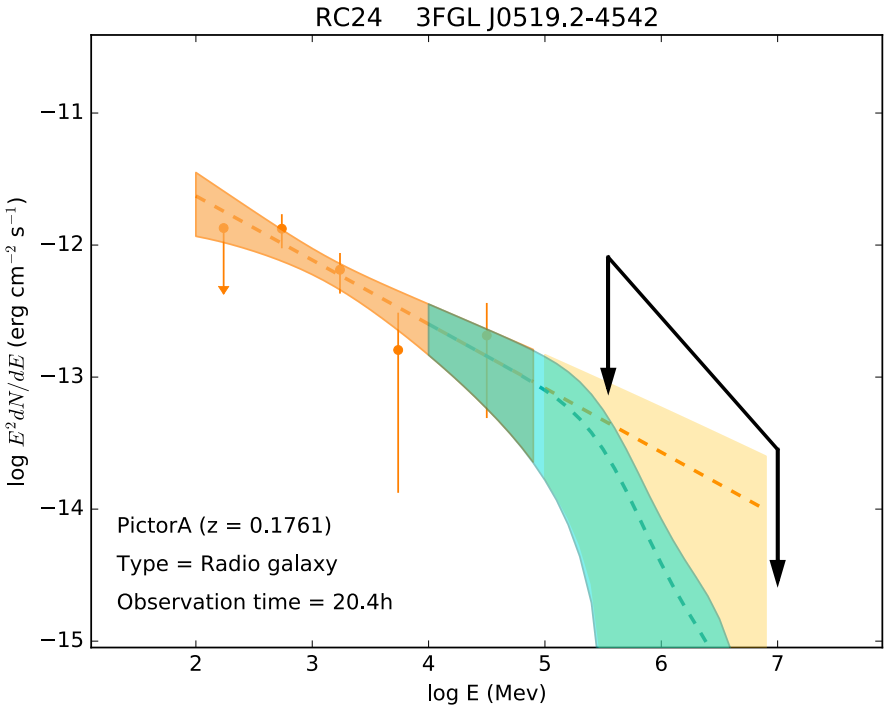

FIGURE 6.22: SED of Pictor A with the 3FGL spectrum from 100 MeV to 100 GeV in orange, its extrapolation to 10 TeV in yellow, the EBL absorbed spectrum in blue and the non constraining HEGS upper limits in black.

6.5 Conclusion

The HEGS project of doing a survey of the extragalactic TeV sky with HESS is still ongoing at the time of the writing. The new analysis using the last version of the analysis and the last production of DST is currently running and the new maps should be avalaible soon to start the search for new sources, and we expect exciting results!

This work has been done in collaboration with Francois Brun (task leader) and David Sanchez. A publication is planned where we will release a catalog to the scientific community. This catalog is likely to contain significance, flux, upper limit and ON-OFF test

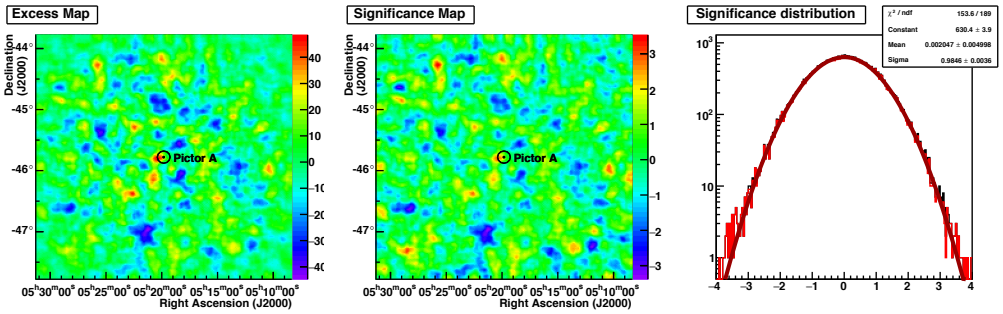

FIGURE 6.23: Significance maps of the dedicated analysis of Pictor A.

maps. Some of the results in this coming paper will focus on interesting fields of view with possible new detections.

This survey is quite timely with the arrival of CTA which will be more suited than H.E.S.S. for an all-sky extragalactic survey with more telescopes and a better sensitivity. HEGS will shed some light on some interesting (or not) fields of view if CTA chooses to do an extragalactic survey, with a focus on hotspots and possible associations. If so, the analysis tools developped for HEGS could be adapted for the CTA analysis. They have already been adapted for the extragalactic round-up performed in the H.E.S.S. Collaboration. This allows to check the data of each period to see if something new popped out. The round up operation along with these tools is presented in Appendix A.

Chapter 7

Exploring the blazar sequence with H.E.S.S.

Contents

7.1 The blazar sequence at VHE

When looking at the TeV sources catalog TeVCat[1] (see the TeV sky map on Figure 7.1), the vast majority of blazars ($\sim 75\%$) detected in the TeV range are HBLs with only 2 LBLs: Ap Librae (H.E.S.S. Collaboration et al., 2015) and the newly discovered OT 081[2]; and 6 FSRQs including: PKS 1510-089, 3C 279 and PKS 0736+017 seen with H.E.S.S. (Wagner and H.E.S.S. Collaboration, 2010; Cerruti et al., 2016). This difference can mainly be explained by two facts : 1) LBLs and FSRQs tend to have a lower peak frequency and then a lower flux in the VHE range making them difficult to detect, 2) The past observation strategy of Cherenkov telescopes has biased the observations toward HBL objects, selecting sources

[1] http://tevcat.uchicago.edu/
[2] http://www.astronomerstelegram.org/?read=9267

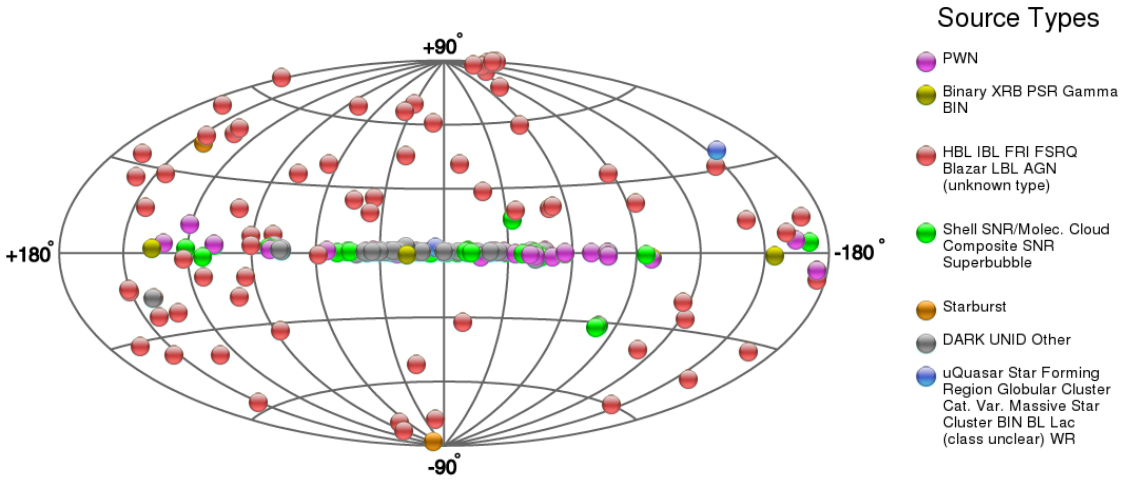

FIGURE 7.1: TeVCat sky map of all the TeV sources ever discovered. The red circles are the AGN.

bright in radio and X-ray (Costamante and Ghisellini, 2002, , and see also Figure 6.13 in the previous chapter).

The blazar sequence, linking FSRQ anb BL Lac objects, has been presented in the Section 2.3 of Chapter 2. The detection of new LBLs and FSRQs at VHE is of interest to probe this sequence and the links between the different types of blazars. Since HBLs (in their quiescent state) are generally well described with a one-zone, time-independent Synchrotron Self-Compton (SSC) model, which is not the case for LBL and FSRQ objects. More data at TeV energies on those objects could help construct a full SED to study these classes more in details and maybe try to find one model to rule all the blazars.

The environment of the jet and the localisation of the emission region can also be probed by TeV observations. Detecting objects at TeV energy with a strong broad line region (BLR), as for FSRQs and LBLs, would mean that the BLR radiation doesn't prevent the escape of the VHE radiation, probably indicating that the γ-ray emission region must be (at least) near the outer edge of the BLR (on parsec scales).

At the other end of the blazar sequence, there could be extreme HBLs (X-HBLs, Bonnoli et al., 2015), with a synchrotron peak frequency higher than the HBLs, so possibly with a second peak also at higher energy with a hard VHE spectrum. They offer a significant potential to probe the density of the extragalatic background light (EBL, Domínguez et al., 2011; Gilmore et al., 2009) and provide experimental means to limit the magnitude of the intergalactic magnetic field (IGMF, Neronov and Semikoz, 2009) when their redshift is known, because their VHE spectrum is supposed to stay hard even after absorption. Their Inverse Compton peak in the multi-TeV regime challenges the one zone SSC model.

7.1.1 A small knowlegde on LBLs at VHE with Ap Librae

At the moment, the only[3] LBL ever studied at TeV, is Ap Librae (H.E.S.S. Collaboration et al., 2015; Sanchez et al., 2015, and references therein).

[3]BL Lacertae and S5 0716+714 are sometimes referred as LBL but they fall into the IBL class in TeVCat.

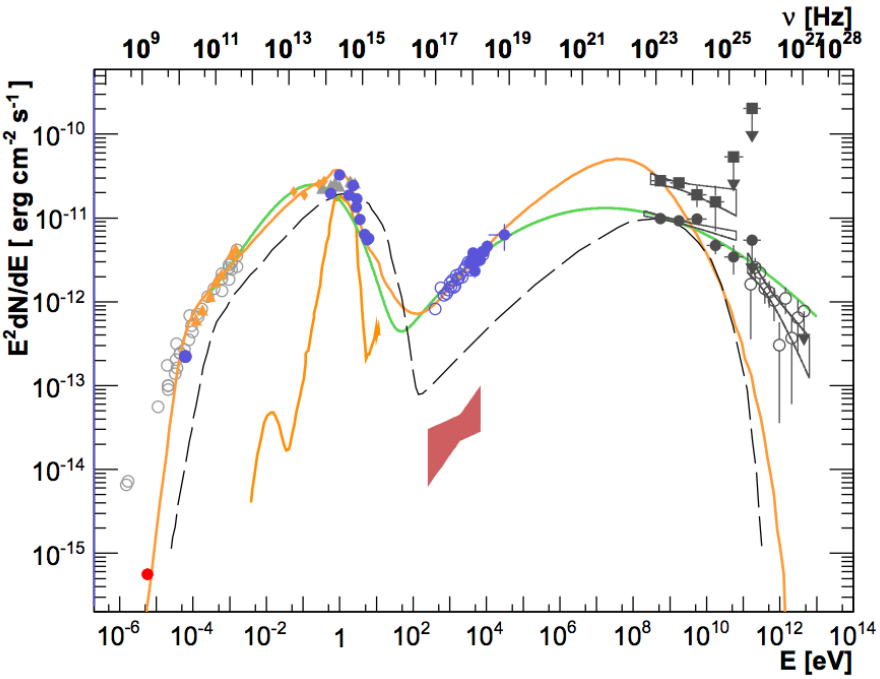

FIGURE 7.2: SED of the LBL Ap Librae from Sanchez et al., 2015. The orange, blue and grey points are the MWL data. The red point and the red butterfly are the radio flux and the spectrum from the extended jet. The orange line is the SSC SED modeling of the source and in green is a polynomial fit.

This object has been discovered in radio in the Parkes catalog (Wright and Otrupcek, 1990) in the 60s under the name PKS 1514-241, and was qualified as variable in optical in the 70s. The TeV emission has been discovered in 2010 by H.E.S.S.[4].

Figure 7.2 displays the multi-wavelength SED of Ap Librae. The low energy bump is narrow, going from radio to optical. Contrariwise, the high energy bump is very broad, going from X-ray to TeV, indicating that the same process is producing the whole range. Due to its shape, this SED is hard to reproduce with a SSC model, especially because of the wide high energy bump. The fit is good for the lower energy part of the SED but the predicted spectrum is too soft in the HE and VHE range. More complicated models are then required to account for this exotic SED shape.

Ap Librae features an extended jet seen in X-ray (Kaufmann, Wagner, and Tibolla, 2013; Sanchez et al., 2015) and is the only blazar with such a feature. A model from Böttcher, Dermer, and Finke, 2008 proposed that photons from the CMB could be up-scattered by the electrons in an extented jet to make VHE γ rays. The result of such a modelling is shown on the top panel of Figure 7.3. The model can also account for the extented jet emission. However this Inverse Compton scattering of CMB photons stays controversial (see Meyer and Georganopoulos, 2014 and references therein for more details).

Hervet, Boisson, and Sol, 2015 modelled the MWL emission of Ap Librae using a blob-in-jet SSC scenario. The result is presented on the bottom panel of Figure 7.3. Several components are taken into account: the classical SSC emission of the blob and the jet, the external Inverse Compton from the blob-jet interaction and the blob-BLR interaction.

[4]ATel # 2743 Very High Energy gamma-ray emission from AP Lib detected by H.E.S.S. http://www.astronomerstelegram.org/?read=2743

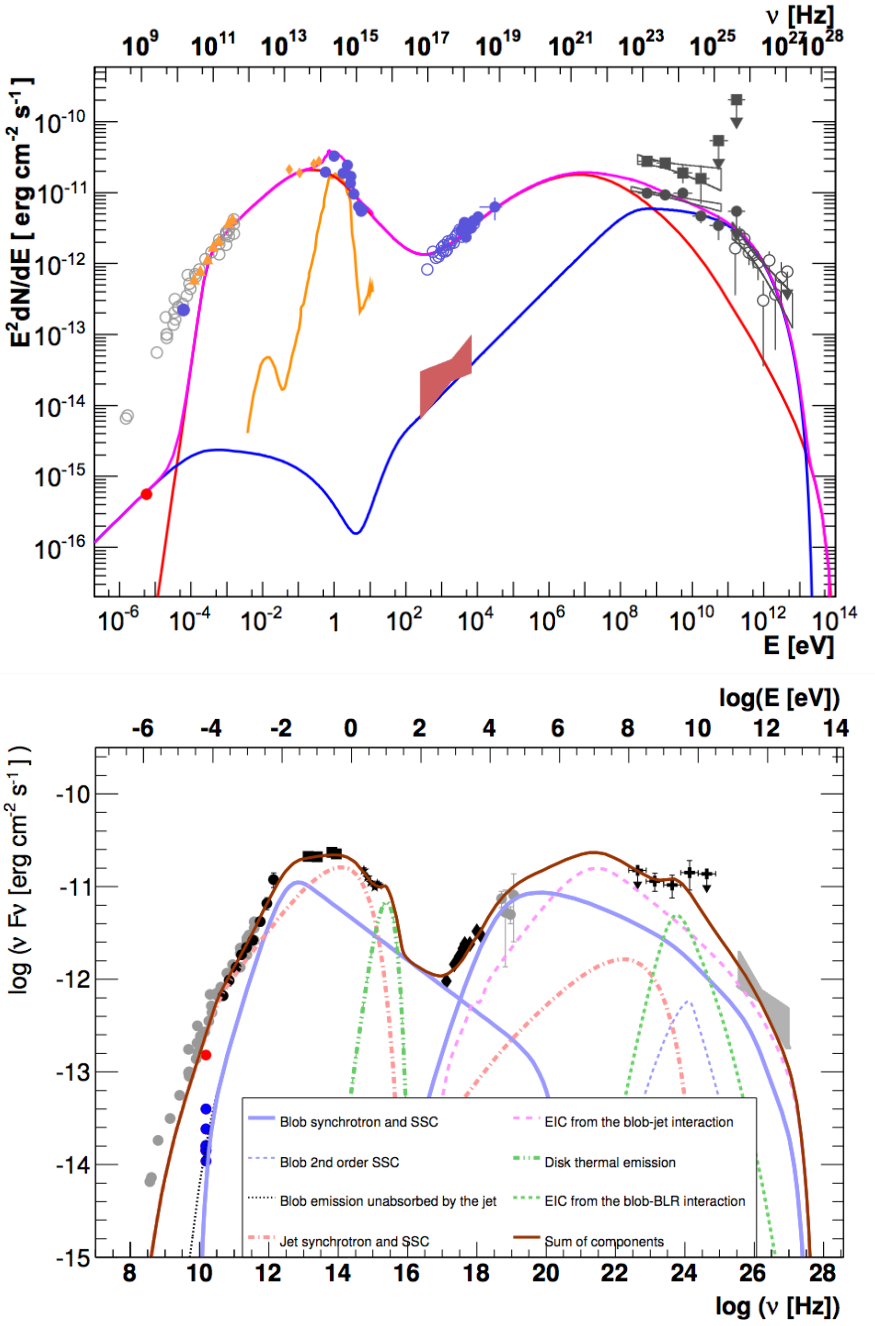

FIGURE 7.3: SEDs of the LBL Ap Librae from Sanchez et al., 2015 using the model of Böttcher, Dermer, and Finke, 2008 (top) and Hervet, Boisson, and Sol, 2015 (bottom). Top: the orange, blue and grey points are the MWL data. The red point and the red butterfly are the radio flux and the spectrum from the extended jet. The red line is the results of the SSC model from the compact component while the blue line represents the flux originating from the extended jet, the pink line is the sum of both. Bottom: Black points are quasi-simultaneous data while grey points are non-simultaneous observations. The different lines represent the different contribution to the multi-component SSC modelling.

However the "blue bump" from the emission of the galaxy is not taken into account. This model reproduces quite well the SED of Ap Librae, except the high energy part of the *Fermi*-LAT spectrum. As LBL seem to have a busier environment than HBL it seems reasonable to add components from the disk and BLR. On the contrary, HBL being cleaner, these components wouldn't affect the SSC modelling. Ap Librae seems to be a blazar between the FSQR and BL Lac classes. The challenge is to know if it is really specific to Ap Librae (is it a peculiar LBL?) or to all the LBL sub-class. How do the other LBLs behave? Similarly to Ap Librae or not? Every LBLs are supposed to behave the same. With more LBLs detections at VHE, we could answer these questions and disentangle the models.

7.1.2 VHE view of FSRQs with PKS 1510-089 & 3C 279

FSRQs are difficult to detect at VHE because their spectra is too soft. 3C 279 was discovered during the radio survey to construct the Third Cambridge Catalogue in 1959 (Edge et al., 1959). The object underwent two strong γ-ray flares in 1991 and 1996 recorded by EGRET showing it was variable at high energy. The detection of VHE emission by MAGIC (Errando et al., 2008) made it the first FSRQ detected at TeV. As Ap Librae, PKS 1510-089 was firstly detected in radio with the Parkes survey in the 60s with optical data coming in the 70s. Its VHE emission was discovered in 2010 by H.E.S.S. (Wagner and H.E.S.S. Collaboration, 2010). These two objects were the first FSRQs detected at TeV and only 4 more followed.

In Aleksić et al., 2014, the MAGIC collaboration tried to model the VHE emission of the PKS 1510-089 with Inverse Compton on different photon seeds. Either the seed photons originate from the infrared torus either from a slow sheath of the jet. As seen on Figure 7.4, both models fit well the SED, with a small preference for the last one. This result shows that the emission of PKS 1510-089 can't be modelled with a simple one-zone SSC model and needs external contribution.

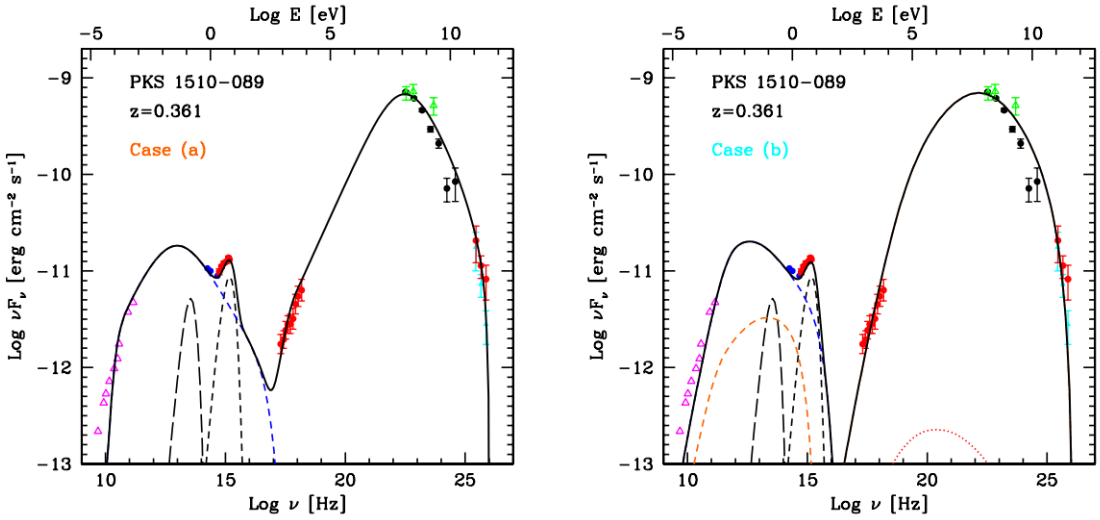

FIGURE 7.4: SED of the FSRQ PKS 1510-089 (Aleksić et al., 2014), the points are the MWL data, and the black curve the fit of the SED. Case a: the low energy is modeled by Synchrotron emission and the high energy by extern Compton. Case b: Same model assuming the emission region is situated in the radio core.

3C 279, has been studied at the same time in the quiescent state (Zheng and Yang, 2016). The results they found are compatible with the ones of PKS 1510-089. Multiple

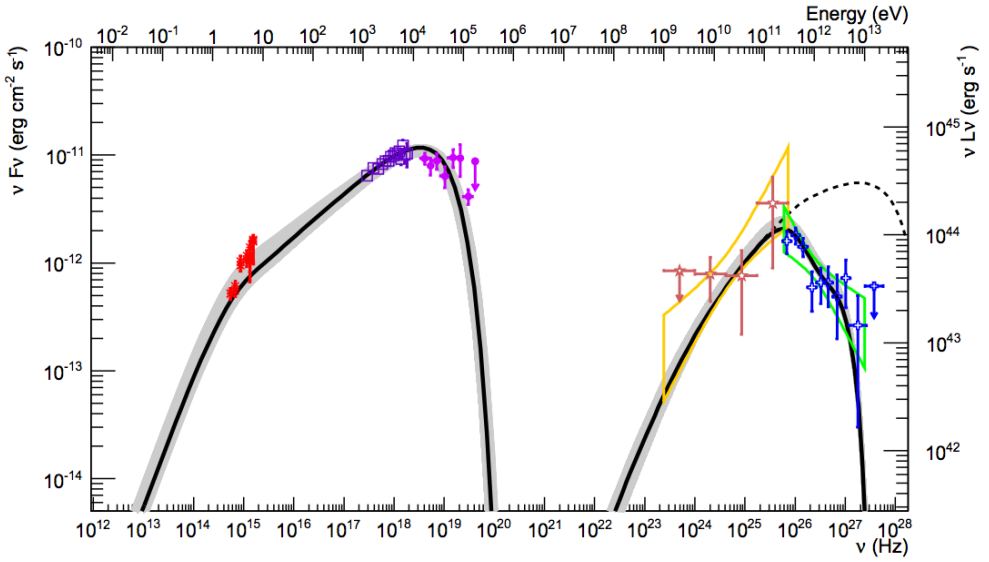

FIGURE 7.5: SED of the X-HBL 1ES 0229+200 (Aliu et al., 2014). Points are observations from *Swift*-UVOT (red), *Swift*-XRT (purple), *Swift*-BAT (pink), *Fermi*-LAT (orange + yellow for the statistical uncertainty on the spectral model) and VERITAS (blue + gren for the statistical uncertainty on the spectral model). The black line represents the best SSC model and the dotted line the emission before absorption by the EBL.

components, corresponding to different seeds photons (accretion disk, dust torus, BLR), have to be added to the simple SSC model explain the multi-wavelength SED.

7.1.3 Is the BL Lac 1ES 0229+200 part of a new X-HBL sub-class?

1ES 0229+200 has been detected for the first time in X-ray in the 90s by the *Einstein* Slew Survey (Elvis et al., 1992). It was classified as a HBL few years later by Giommi, Ansari, and Micol, 1995.

But now, 1ES 0229+200 is thought to be an extreme HBL with a synchrotron peak frequency $> 10^{18}$ Hz. The redshift of $z = 0.1396$ shows it is a relatively distant blazar, however, the VHE spectrum stays quite hard with an index of $\Gamma \sim 2.5$ despite the potentially strong EBL absorption which softened the intrinsic emission. Based on the current EBL models, Aharonian et al., 2007b showed that the intrinsic index of the source should be harder that 1.5 (or the EBL is weaker than what is expected and closer to the lower limits of the galaxy counts). An SSC model has been tested on 1ES 0229+200 by Aliu et al., 2014 (see Figure 7.5). They report the need of a really high minimun value of 53 for the Doppler factor. Generally for HBL, the highest Doppler factors are $\delta \sim 40$. Some other parameters of the SSC required higher values than is generally expected in SSC models (like the magnetic field strength or the minimum energy).

7.1.4 Towards a new observation strategy

At the end of 2015, the H.E.S.S. collaboration shifted its extragalactic observation strategy from single source discoveries to key science projects[5]. It has been decided that the blazar

[5]To prepare the ground for the CTA area and also because there was nothing new to do with a new random HBL discovery.

sequence will be a key science project (along with high γ-ray opacities, high energy neutrinos, Gamma-Ray Bursts...). The blazar sequence being one of my interest in the study of blazars, I led the entire proposal, from the source selection and the proposal writing to the analysis of the final data.

The goal of this proposal is to target FSRQ, LBL and X-HBL objects to extend the small view we have of them at VHE and study emission models in more details.

The first internal H.E.S.S. proposal concerning the blazar sequence was submitted at the beginning of 2016 for the following year of observations. The following sections present the work done on the 2016 version of the proposal along with the results of the observations. At the end of 2016, the blazar sequence proposal was updated to take into account new information the 2016 data provided. New observations will hopefully be taken during the 2017 year.

7.2 Selection of good candidates for H.E.S.S. observations

7.2.1 Selection based on *Fermi* catalogs

All the sources have been selected using the Second *Fermi*-LAT Catalog of High-Energy Sources (2FHL, Ajello et al., 2015), between 50 GeV and 2 TeV, matching informations from the *Fermi*-LAT 4 years catalog (3FGL, Ferrara et al., 2015) and the Third Catalog of AGN (3LAC, Ackermann et al., 2015b).

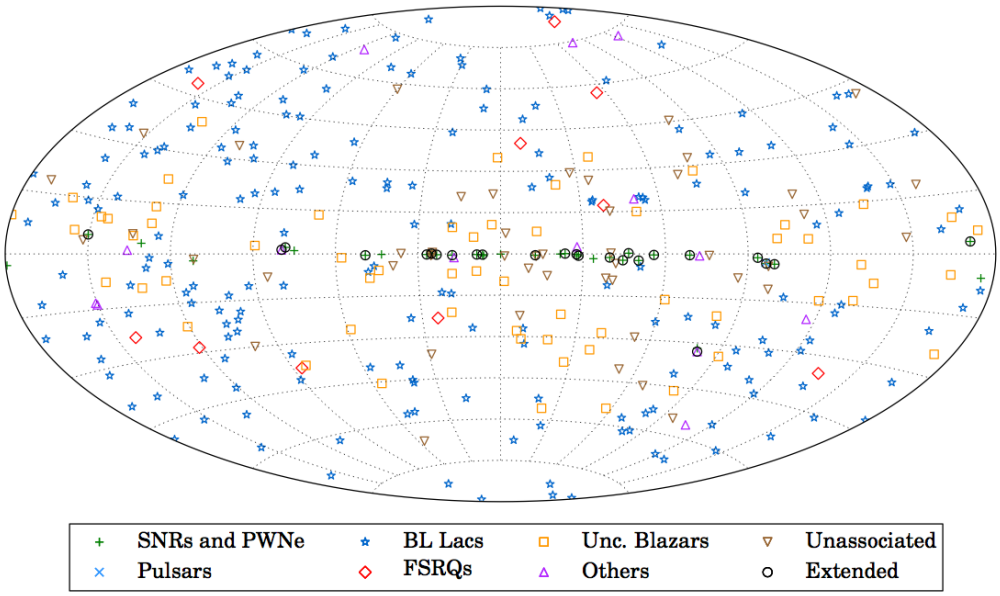

FIGURE 7.6: Sky map (in galactic coordinates) of the 2FHL catalog. Courtesy of the *Fermi* Collaboration.

Fermi-LAT data are useful when working at high energy because its energy range, between 100 MeV up to hundreds of GeV, meets the energy range of H.E.S.S. which begins at $\sim 50 - 200$ GeV. This allows us to have a good coverage of the second peak of the SED of blazars. The 2FHL contains 360 objects, from supernova remnants, pulsar wind nebulae to AGN and starburst galaxies. This sample is dominated by AGN with 271 radio galaxies and blazars (blue crosses, red diamonds and yellow squares on Figure 7.6).

The selection of good candidates is mainly based on the 2FHL which has a higher energy threshold of 50 GeV to select only the hard sources seen by the LAT which have more chances to be detectable at VHE. Moreover, with an energy range starting at 50 GeV

up to 2 TeV, the flux observed is expected to already have been absorbed by the EBL. Hence when extrapolating the 2FHL observed spectrum, it allows to make a hypothesis on the flux H.E.S.S. could see.

A first geographical selection has been made on the coordinates of the sources to ensure visibility by the H.E.S.S. array ($-73.27° < \mathrm{Dec} < 26.73°$) and on the object class to select only blazars (BL Lac, FSRQ and BCU, which are blazars of uncertain type).

7.2.2 LBLs and FSRQs selection based on 2FHL catalog

LBL and FSRQ candidates have been selected using a cut on the Synchrotron peak frequency provided by the 2FHL and 3FGL catalogs: $\nu_{\mathrm{peak}} < 10^{15}$ Hz . This cut gives 46 objects: 28 LBLs/IBLs, 7 FSRQs and 11 BCUs, with 40 of them unknown and 5 known at TeV. Among the known TeV sources are the FSRQs 4C +21.35, PKS 1510-089 and 3C 279, the LBL Ap Librae and the BCU PKS 0548-322[6]. These sources, except the BCU, emerge as some of the brightest of the selection: 3.16% of the Crab flux for 4C+ 21.35, 2.67% for PKS 1510-089, 2.33% for Ap Librae, 1.09% for 3C 279 and 0.66% for PKS 0548-322.

Objects with a lack of multi-wavelength data which have a reduced scientific interest are removed[7], as the X-ray spectrum of the candidates will be useful to compare with Ap Librae for LBLs and PKS 1510-089 for FSRQs. This leads to 19 targets unknown at TeV energies: 3 FSRQs and 16 LBLs.

Among this dataset of preselected targets, objects of interest are selected based on their multi-wavelength SED, especially their X-ray spectrum. LBL candidates are chosen when they exhibits a hard spectra in the X-ray range ($\Gamma < 2$), meaning that X-ray might not be produced by Synchrotron radiation. This leads to 7 LBL and 2 FSRQ candidates. At the very end, sources with a time estimation impossible to reach with H.E.S.S. are removed (their 2FHL spectrum being too soft), removing the two FSRQs and one LBL.

The final 6 LBL candidates are presented in the top part of Table 7.1 and their SEDs are shown in Figure 7.7 and compared with the SED of AP Librae.

3 sources were found to have information concerning the BLR luminosity: PKS 0454-234, PKS 1958-179 and PKS 0426-380 with the respective luminosities in log(erg/s): 44.41, 44.15, 44.04. The ones with the brightest BLR are of interest to probe the γ-ray emission localisation. Unfortunately, their 2FHL spectrum was too soft leading to impossible detection times (thousands of hours).

7.2.3 X-HBLs selection based on 2FHL catalog

X-HBL candidates have been selected based on the intrinsic 2FHL index Γ_{intr} to be smaller than 2 to select source with a high energy bump in the multi-TeV regime. The intrinsic index is corrected from the EBL absorption effect (when the redshift of the source is known) and provided in the *Fermi* catalogs. This cut gives 25 objects, with 18 unknown at TeV energies. The 7 known TeV sources are: 1ES 0647+250, 1RXS J101015.9-311909, HESS J1943+213, 1ES 0414+009, RBS 0413, 1ES 0347-121 and MS 13121-4221. Unlike the LBL/FSRQ selection where the known TeV sources were the brightest, the brightness of the known X-HBL candidates goes from 0.91% to 7.32% of the Crab, with intermediate values around 1% and 2%.

Information about the distance of the source being of importance for future studies, it has been required that the sources have a known redshift, leading to 7 targets presented in the bottom part of Table 7.1. Their SEDs are shown in Figure 7.8.

[6] PKS 0548-322 is classified as an HBL in TeVCat but its Synchrotron peak frequency value in the 2FHL puts it in the LBL/LSP class.

[7] These MWL data are taken on the SED Builder website http://tools.asdc.asi.it/SED/

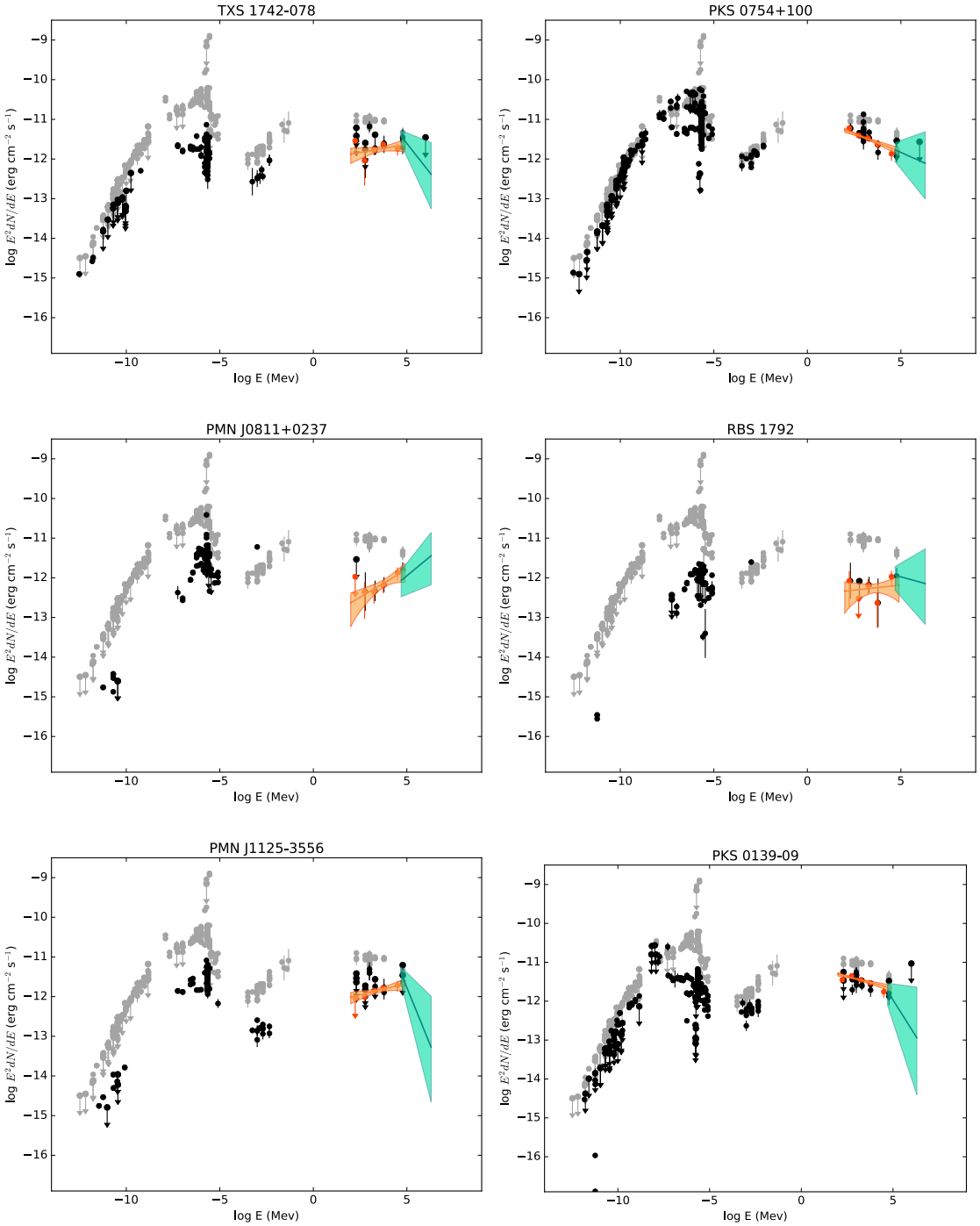

FIGURE 7.7: SED of the LBL candidates selected in the 2FHL. The black points are the MWL data of the source from SED Builder, the grey data points are the MWL data from SED Builder of the LBL Ap Librae for comparison. The 3FGL spectral data are shown with the pink butterfly, and in dark blue for the 2FHL. From left to right and top to bottom: TXS 1742-078, PKS 0754+100, PMN J0811+0237, RBS 1792, PMN J1125-3556 and PKS 0139-09.

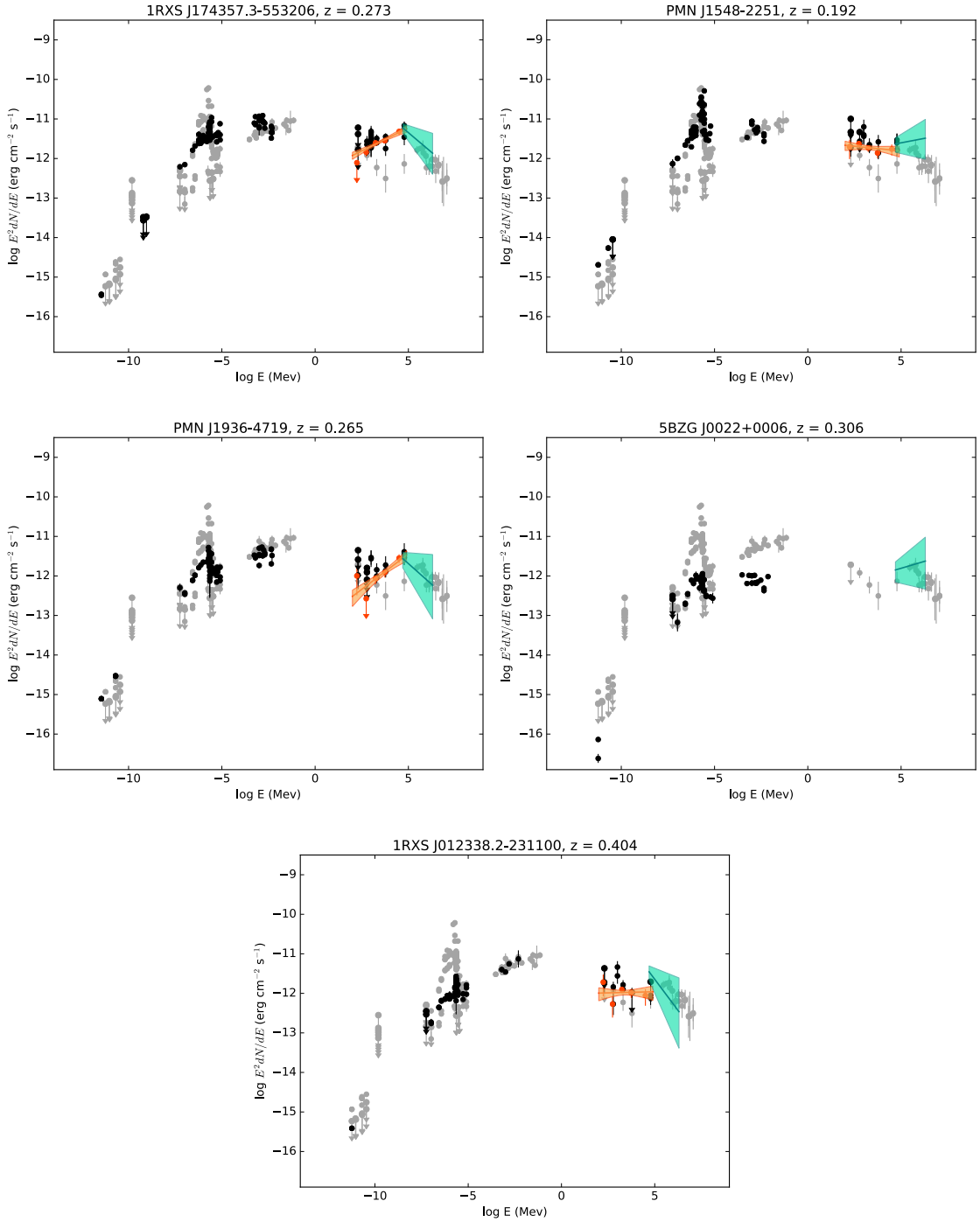

FIGURE 7.8: SED of the X-HBL candidates selected in the 2FHL. The black points are the MWL data of the source from SED Builder, the grey data points are the MWL data from SED Builder of the X-HBL 1ES 0229+200 for comparison. The 3FGL spectral data are shown with the pink butterfly, and in dark blue for the 2FHL. From left to right and top to bottom: 1RXS J054357.2-553206, PMN J1548-2251, PMN J1936-4719, 5BZG J0022+0006 and 1RXS J012338.2-231100.

Association	RA	Dec	Flux (%Crab)	Redshift	$T_{5\sigma}$ (hours)
LBL candidates					
TXS 1742-078	266.372	−7.8764	1.69	ND	27
PKS 0754+100	119.212	9.92	1.01	0.266	16
PMN J0811+0237	122.979	2.643	0.91	ND	3
RBS 1792	328.298	−0.6867	0.73	0.341	29
PMN J1125-3556	171.419	−35.9328	1.27	0.284	317
PKS 0139-09	25.3361	−9.4568	0.75	0.73	227
X-HBL candidates					
1RXS J054357.3-553206	85.9992	−55.5577	3.06	0.273	4
PMN J1548-2251	237.188	−22.8202	1.80	0.192	2
PMN J1936-4719	294.238	−47.3534	1.39	0.265	21
5BZG J0022+0006	5.5001	0.1059	1.14	0.306	5
1RXS J012338.2-231100	20.9299	−23.1482	1.56	0.404	34

TABLE 7.1: Sources proposed for observations in 2016, with position (RA & Dec J2000 in degrees), class, 2FHL flux in percentage of the one of the Crab, redshift when known, time for a 5σ detection in Hybrid, with an energy threshold of 0.1 TeV.

7.2.4 Time estimation

A tool to estimate the time needed to reach 5σ for the unknown TeV sources has been developed within the collaboration. It takes into account the array sensitivity (depending if the observations are supposed to be taken in Stereo or Mono), the zenith angle of the observations, the photon index of the source and the flux above a certain threshold (here 50 GeV). It then computes the energy threshold expected for the observation conditions and the flux above it along with the time needed in this configuration to have a detection.

Four of the sources (PMN J0811+0237, 1RXS J054357.3-553206, PMN J1548-2251 and 5BZG J0022+0006) have a $T_{5\sigma} < 5$ hours, so we requested twice the detection time written on Table 7.1 to be sure to have enough statistics to do a spectral study in case of a discovery.

Two sources have an estimated time greater than 200 hours (PMN J1125-3556 and PKS 0139-09) and are considered as a multi-year program.

7.3 Observations and results

On 11 sources proposed, 6 sources were observed during the year 2016:

- 3 LBL candidates: RBS 1792, PMN J1125-3556, PKS 0139-09
- 3 X-HBL candidates: PMN J1548-2251, 5BZG J0022+0006, 1RXS J012338.2-231100

The following parts present the analysis results on each source. All runs are selected following the run quality cuts of the `H.E.S.S. 2 Stereo Standard` profile (runs with CT1 to CT5, CT5 being non mandatory) since the sources were requested to be observed in this configuration. They are analyzed with the `M++ Stereo Loose` profile using the `v32` of the `ParisAnalysis` software and the `Prod8` DST. The `Loose` analysis profile has, as the name says, looser cut on the NSB Goodness variable than the

`Standard` profile, allowing weak sources to be detected more easily if the field of view is clear.

In case observations were performed in Mono, the same procedure is applied but with a `H.E.S.S. 2 Mono Standard` run quality selection to perform a `M++ Mono Loose` analysis.

All the important figures showing the results are in Figure 7.9 and 7.10 for the maps, Figure 7.11 for the θ^2 distributions and Figure 7.12 for the evolution of the signal with time.

7.3.1 RBS 1792

RBS 1792 has been observed for 122 runs, with 87 of them passing the Stereo run quality cuts. The `M++ Stereo Loose` analysis gave no signal, as shown on the first map on Figure 7.9 and the first θ^2 histogram of Figure 7.11, with very few chances of evolution in time since the significance is quite flat after ~ 30 hours of observations (see first panel of Figure 7.12). The time estimated to have a 5σ detection was of 29 hours. Despite 33.7 hours of observations, no signal is found.

7.3.2 PMN J1125-3556

PMN J1125-3556 has been observed for 38 runs, with 23 of them passing the Stereo run quality cuts. As RBS 1792, the `M++ Stereo Loose` analysis gave no signal (second map on Figure 7.9 and the second θ^2 histogram of Figure 7.11), with again very few chances of evolution in time (see second panel of Figure 7.12). This was expected as the source is a multi-year source.

7.3.3 PKS 0139-09

This LBL candidate has been observed for 55 runs with 38 runs passing the Stereo run quality cuts. This source was considered as a multi-year program since 227 hours of observation were estimated to have a detection. Without surprise, the `M++ Stereo Loose` analysis shows no signal (third panels of Figures 7.9, 7.11 and 7.12). However, the significance on the source is decreasing with time, giving little hopes for future observations.

7.3.4 PMN J1548-2251

The X-HBL candidate PMN 1548-2251 has been observed for 9 runs and 6 of them passed the run quality cuts. The `M++ Stereo Loose` analysis gives a 3.3 σ signal with only 2.2 hours of observations. The first panel of Figure 7.10 shows the maps with the significance distribution. The hotspot corresponding to the source is clearly visible as the background is well normalized. The 3.3 σ appears on the θ^2 distribution which could be better with a bit more of observation time. The evolution of the significance with time cannot say much in such a short time because of statistical fluctuations but obtaining 3σ in only 2 hours of observations is good.

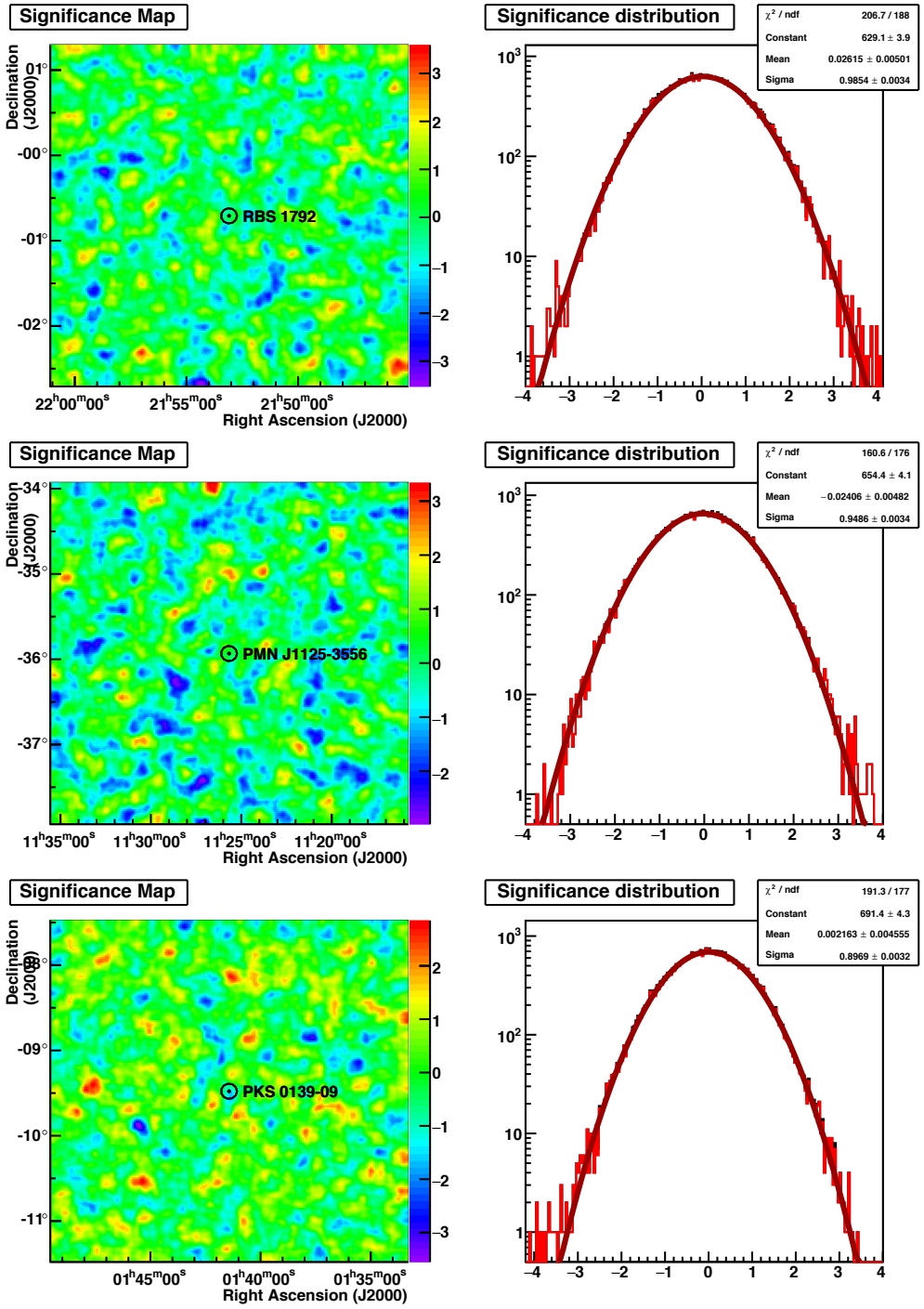

FIGURE 7.9: Significance map and distribution for the observed LBL candidates of the blazar sequence proposal. From top to bottom: RBS 1792, PMN J1125-3556, PKS 0139.

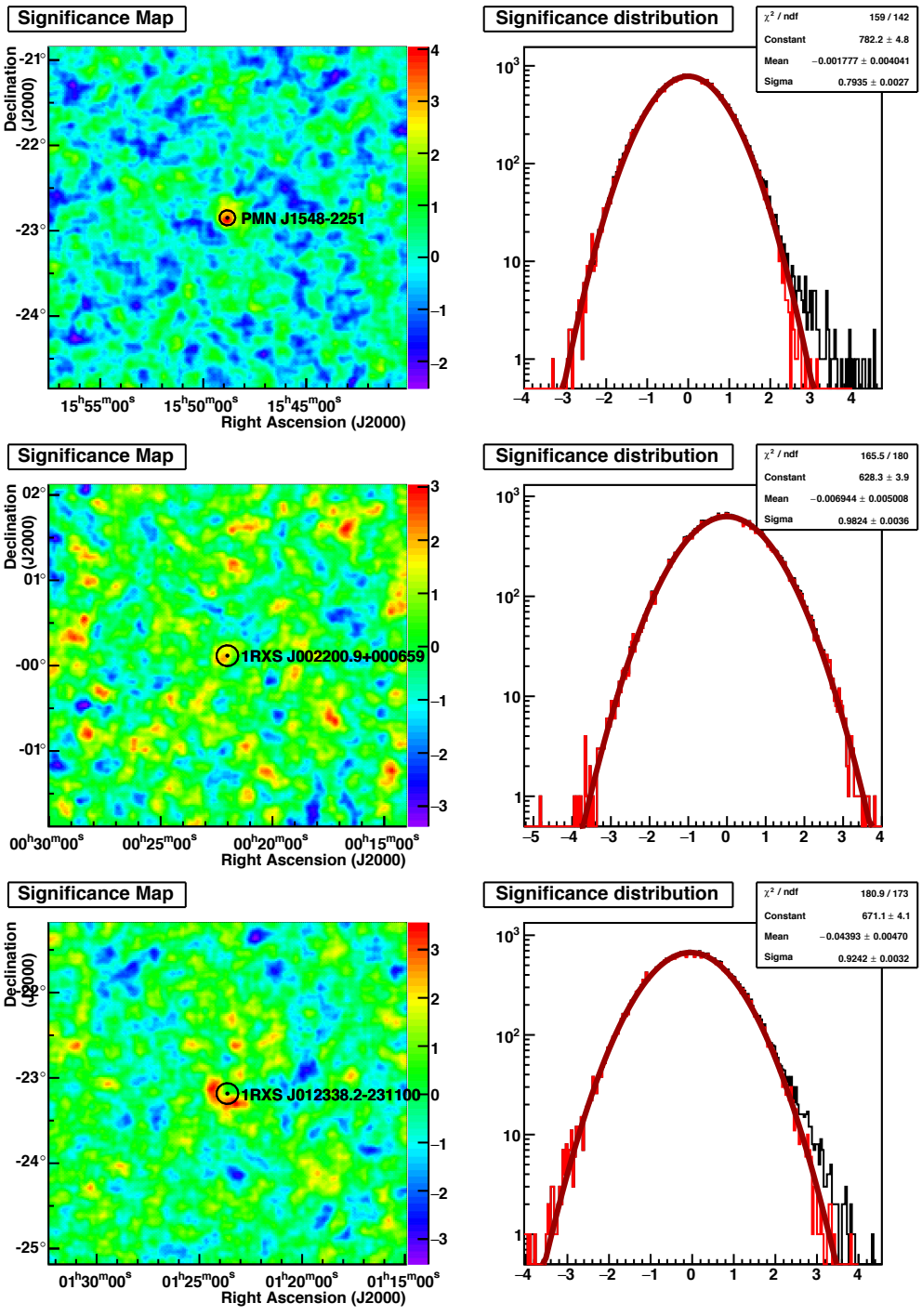

FIGURE 7.10: Excess and significance maps and significance distributions for the observed X-HBL candidates of the blazar sequence proposal. From top to bottom: PMN J1548-2251, 5BZG J0022+0006 and 1RXS J012338.2-321100.

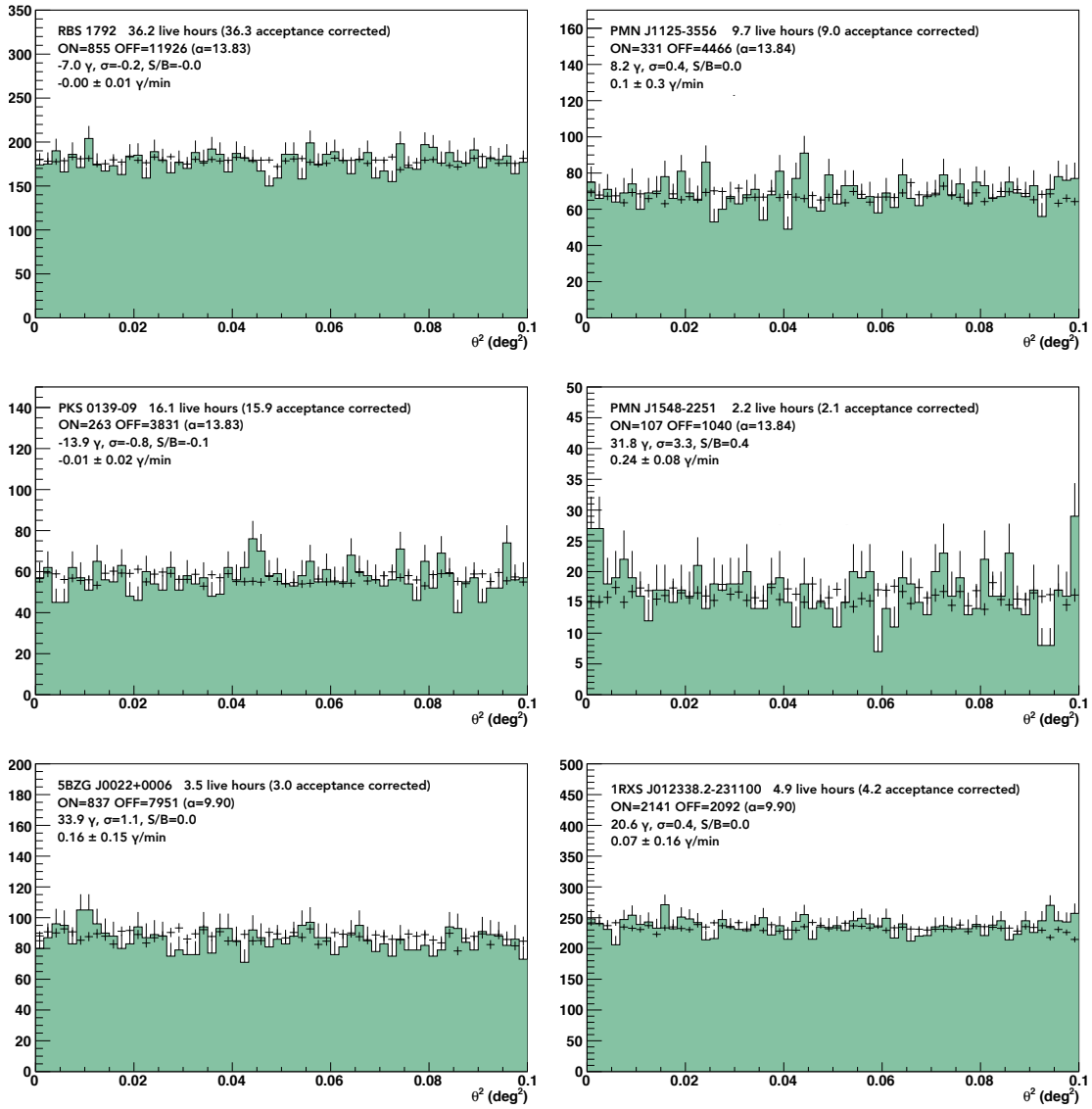

FIGURE 7.11: θ^2 distributions for the observed sources of the blazar sequence proposal. From left to right and top to bottom: RBS 1792, PMN J1125-3556, PKS 0139-09, PMN J1548-2251, 5BZG J0022+0006 and 1RXS J012338.2-321100.

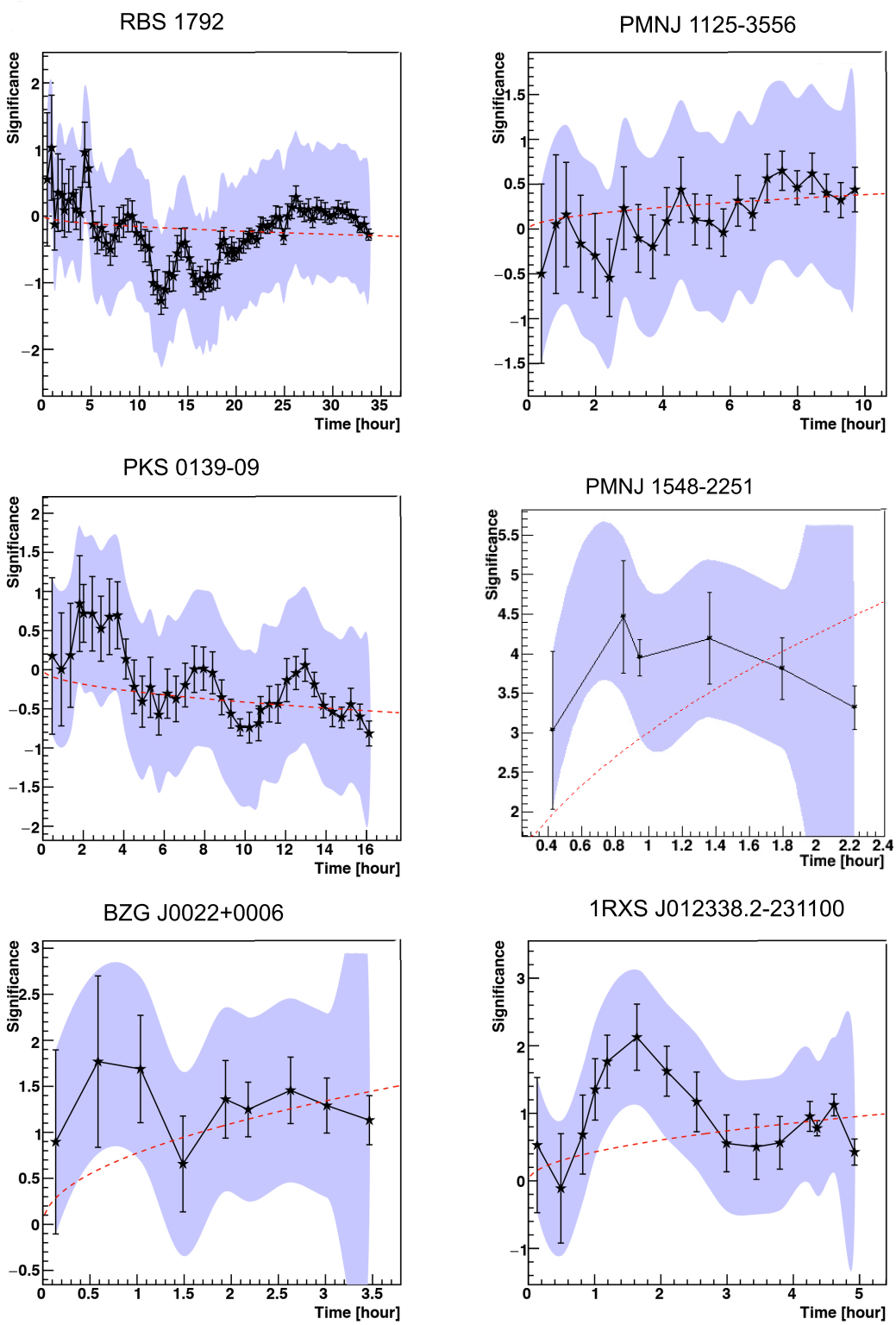

FIGURE 7.12: Evolution of the significance with time for the observed sources of the blazar sequence proposal. From left to right and top to bottom: RBS 1792, PMN J1125-3556, PKS 0139, PMN J1548-2251, 5BZG J0022+0006 and 1RXS J012338.2-321100.

7.3.5 5BZG J0022+0006

The X-HBL candidate 5BZG J0022+0006 has been observed for 11 runs, but mostly in Mono, with 9 runs passing the Mono run quality cuts. The `M++ Mono Loose` shows no signal with 3.5 hours of data (second panel of Figure 7.10 and fourth panels of Figures 7.11 and 7.12). The time estimation to reach a detection was 5 hours in Stereo, quite promising for a detection. But in Mono, this time was estimated to be 71 hours.

7.3.6 1RXS J012338.2-231100

The X-HBL candidate 1RXS J012338.2-231100 has been observed for 21 runs, but mostly in Mono, with 15 runs passing the Mono run quality cuts. The `M++ Mono Loose` shows no signal with $\sim$ 5 hours of data (last panels of Figure 7.10, 7.11 and 7.12). The time estimation to reach a detection was 34 hours in Stereo. In Mono, this time was estimated to be 181 hours.

The $\sim 3\sigma$ region around the source position on the last panels of Figure 7.10 could be either a statistical fluctuations or an artefacts from the Mono reconstruction.

7.3.7 Can we put constrains on the SEDs?

For each of the sources observed by H.E.S.S. upper limits on the flux have been derived following the same method as described in Section 6.4.2, assuming a power law spectrum of fixed index $\Gamma = 3$.

The H.E.S.S. analysis does not give the upper limit on the differential spectrum Φ_0 but only the integrated flux above a certain energy $\Phi_{\rm int}(> E)$ defined as the integral of the differential flux:

$$\Phi_{\rm int}(> E_{\rm min}) = \int_{E_{\rm min}}^{E_{\rm max}} \Phi_0 \left(\frac{E}{E_0}\right)^{-\Gamma} {\rm d}E \tag{7.1}$$

$$\Leftrightarrow \Phi_0 = \frac{\Phi_{\rm int}(> E_{\rm min})}{E_{\rm max}^{-\Gamma+1} - E_{\rm min}^{-\Gamma+1}} \left(-\Gamma + 1\right) E_0^{-\Gamma} \tag{7.2}$$

$$= 2\Phi_{\rm int}(> E_{\rm min}) \frac{E_0^{-\Gamma}}{E_{\rm min}^{-\Gamma+1}} \tag{7.3}$$

with $E_{\rm min}$ being the energy threshold of the observation, chosen at 200 GeV, $E_{\rm max} =$ 10 TeV and $E_0 = 1$ TeV.

The H.E.S.S. upper limits (between 0.2 and 10 TeV) are represented on Figure 7.13 along with the 3FGL and 2FHL data presented before. For the LBL PMN J1125-3556, the upper limit is not constraining compared to the *Fermi*-LAT SEDs, however H.E.S.S. performed only $\sim$ 10 hours of observations on this weak source. For the other 2 LBLs, RBS 1792 and PKS 0139-09, and the X-HBLs 5BZG J0022+0006 and 1RXS J012338.2-231100, the upper limits are constraining and show than the 2FHL spectra are mainly dominated by the low energy part (around 50 GeV). Hence it is not as hard as expected in the TeV, either because of the intrinsic curvature of the source or because of the EBL absorption.

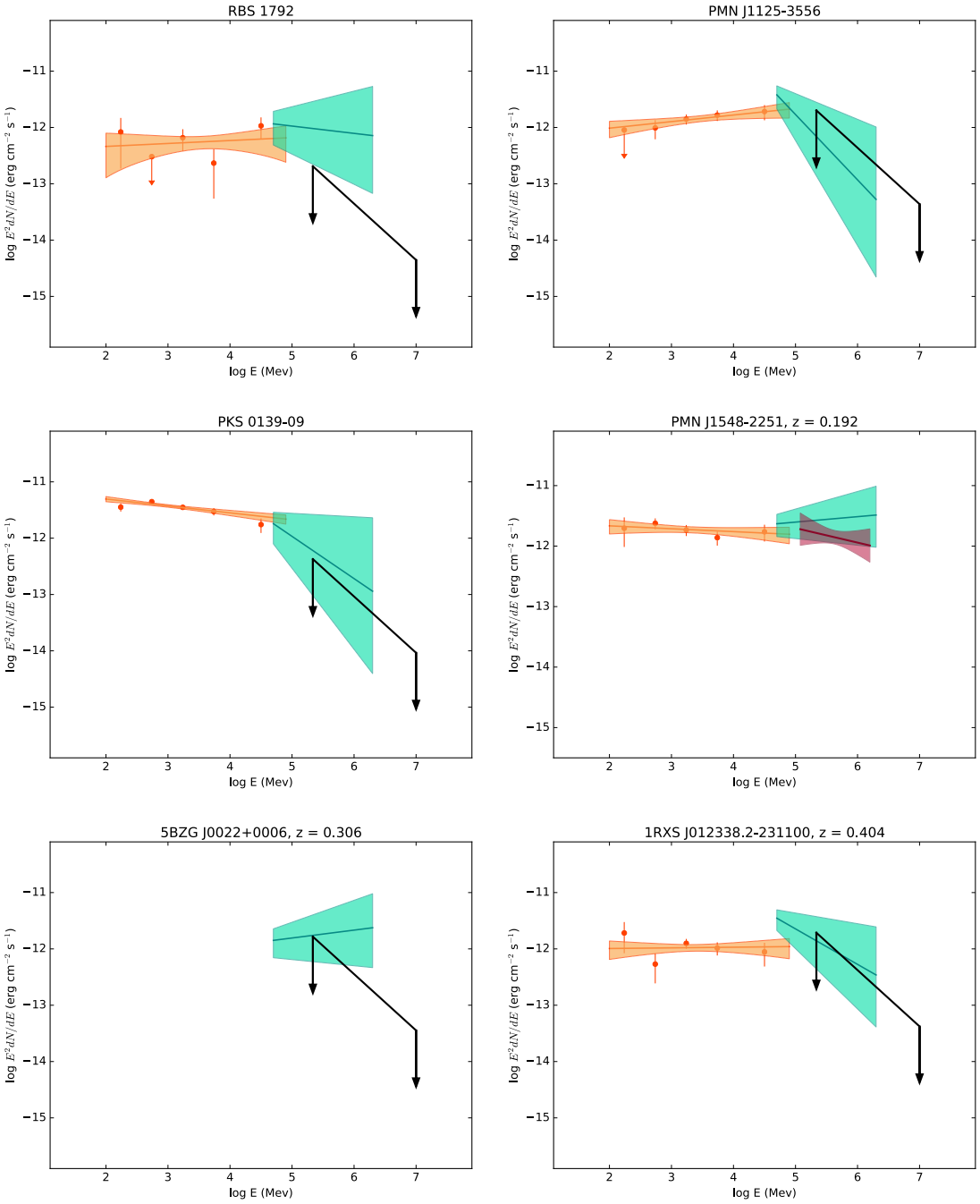

FIGURE 7.13: SED of observed sources during 2016 with a zoom on the GeV-TeV range. The 3FGL spectral data are shown with the orange butterfly, and in blue for the 2FHL. The black line is the H.E.S.S. upper limit on the flux. The orange pink is the H.E.S.S. spectra (only for PMN 1548-2251). From left to right and top to bottom: RBS 1792, PMN J1125-3556, PKS 0139-09, PMN J1548-2251, 5BZG J0022+0006 and 1RXS J012338.2-231100.

7.3.8 Focus on PMN J1548-2251

For PMN J1548-2251, which showed a hint of detection, I made a "tentative" spectrum (red butterfly on the fourth panel of Figure 7.13). Normally, one should wait to obtain 5σ because a spectrum derived with 3σ will have larger statistical errors due to the evident lack of statistics. The spectrum is described by a power law of index $\Gamma = 2.24 \pm 0.44$ between 0.12 and 1.58 TeV. The flux at 1 TeV is of $(0.71 \pm 0.32) \times 10^{-12}$ cm^{-2}.s^{-1}.TeV^{-1}. The agreement between the H.E.S.S. and *Fermi*-LAT spectra is really good.

The photon index of 2.24 ± 0.44 is softer compared to the index of 1.91 ± 43 from the 2FHL, but they stay within the statistical errors. It is also compatible with the index of 2.05 ± 0.08 from the 3FGL.

Figure 7.14 shows the combinaison of Figure 7.8 and Figure 7.13 with the multi-wavelength SED of the source from ASDC and the 3FGL, 2FHL and H.E.S.S. spectra. The position of the high energy peak can not be constrained even with the H.E.S.S. spectrum, although the VHE behavior of the source looks like 1ES 0229+200 (grey points).

One would need X-ray data on a larger energy range to know if the X-ray spectrum if soft, or hard like 1ES 0229+200.

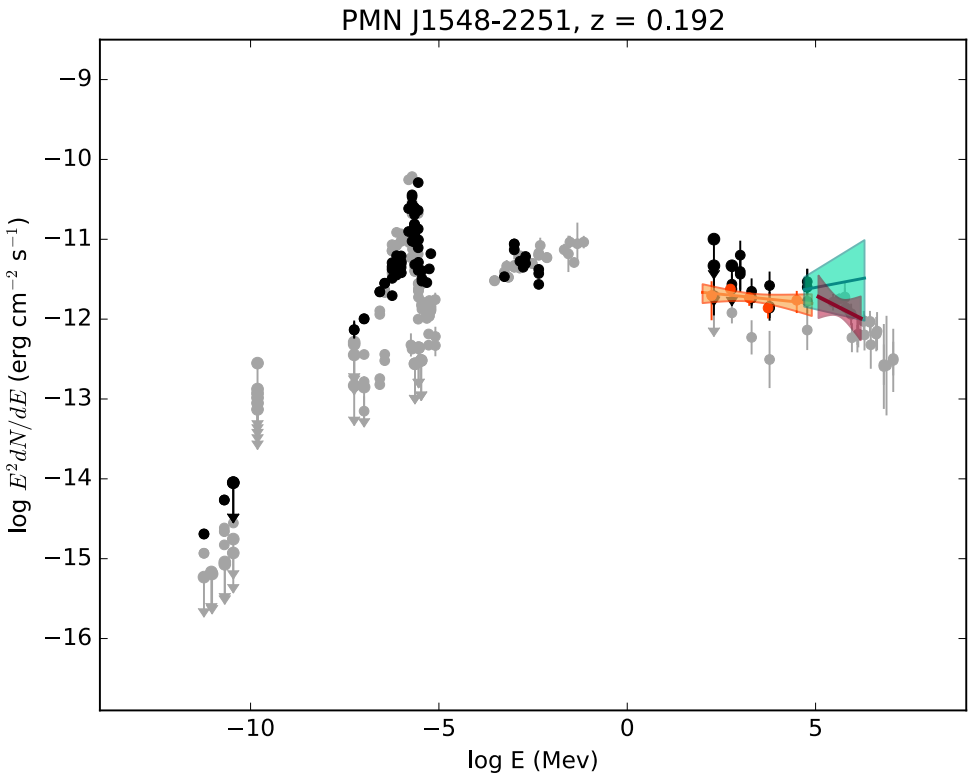

FIGURE 7.14: Multi-walength SED of PMN J1548-2251 (as in Figure 7.8) with the H.E.S.S. spectrum.

7.4 Conclusion

This proposal have been updated at the beginning of 2017 to take into account new information coming from the 2016 observations. Along with this, comes an update of the time estimation tool. It is supposed to describe better the instrument in different configurations and its sensitivity, although the required time for a detection might be optimistic.

Sources of interest which have not been observed have been kept, hoping they will get some time in 2017. More time than the amount given by the time estimation tool have been asked, to correct from a too optimistic time and to have a bit more than 5 σ in case of discovery. Everything is summed up in Table 7.2 which is an update of the 2016 table.

PMN J1548-2251 is the most promising of the sources. It is close to discovery with only 2 hours of observations, so we asked for 10 more hours to be sure to have a source detection with enough statistics have a good quality spectrum at TeV. PMN J1125-3556 stays in the proposal but no further observations has been asked on it, the new time estimation gave 30 hours so in already 10 hours, there should have been more than 0 σ.

Two new sources appear in the 2017 version of the proposal: 1RXS J171405.2-202747 and TXS 0637-128. They are two promising X-HBL candidates. They were not present in the 2016 version of the proposal because their redshift is unknown and at first we requested this information to be known. But their SEDs (see Figure 7.15) look as favorable as the other candidates with a hard 2FHL index and possibly the second bump beginning in the *Fermi*-LAT range $\sim$ 1 GeV. If H.E.S.S. sees something, it might trigger observations in other wavelentghs to determine their redshifts.

Association	RA	Dec	Flux (%Crab)	Redshift	$T_{5\sigma}$ (hours)
LBL candidates					
TXS 1742-078	266.372	−7.8764	1.69	ND	10
PKS 0754+100	119.212	9.92	1.01	0.266	10
PMN J0811+0237	122.979	2.643	0.91	ND	5
RBS 1792	328.298	−0.6867	0.73	0.341	0
PMN J1125-3556	171.419	−35.9328	1.27	0.284	0
PKS 0139-09	25.3361	−9.4568	0.75	0.73	30
X-HBL candidates					
1RXS J054357.3-553206	85.9992	−55.5577	3.06	0.273	5
PMN J1548-2251	237.188	−22.8202	1.80	0.192	10
PMN J1936-4719	294.238	−47.3534	1.39	0.265	10
5BZG J0022+0006	5.5001	0.1059	1.14	0.306	5
1RXS J012338.2-231100	20.9299	−23.1482	1.56	0.404	5
1RXS J171405.2-202747	258.533	−20.496	1.60	ND	10
TXS 0637-128	100.030	−12.8876	1.57	ND	10

TABLE 7.2: Sources proposed for observations in 2017, with position (RA & Dec J2000), class (FSRQ, LBL, BCU and X-HBL), 2FHL flux in Crab percentage, redshift when known, time for a 5σ detection in Hybrid, with an energy threshold of 0.1 TeV.

The study of the blazar sequence at TeV is just at its first steps. Not all the wanted sources have been observed or detected, but some of them might be detectable with only a short time of observation (PMN J1548-2251 for the X-HBLs and possibly PMN J011+0237 for the LBLs). This key science project will continue until the end of H.E.S.S., hopefully with more data and detection of new sources.

With the arrival of CTA in the next years, systematics population studies will be facilitated thanks to the increased number of telescopes.

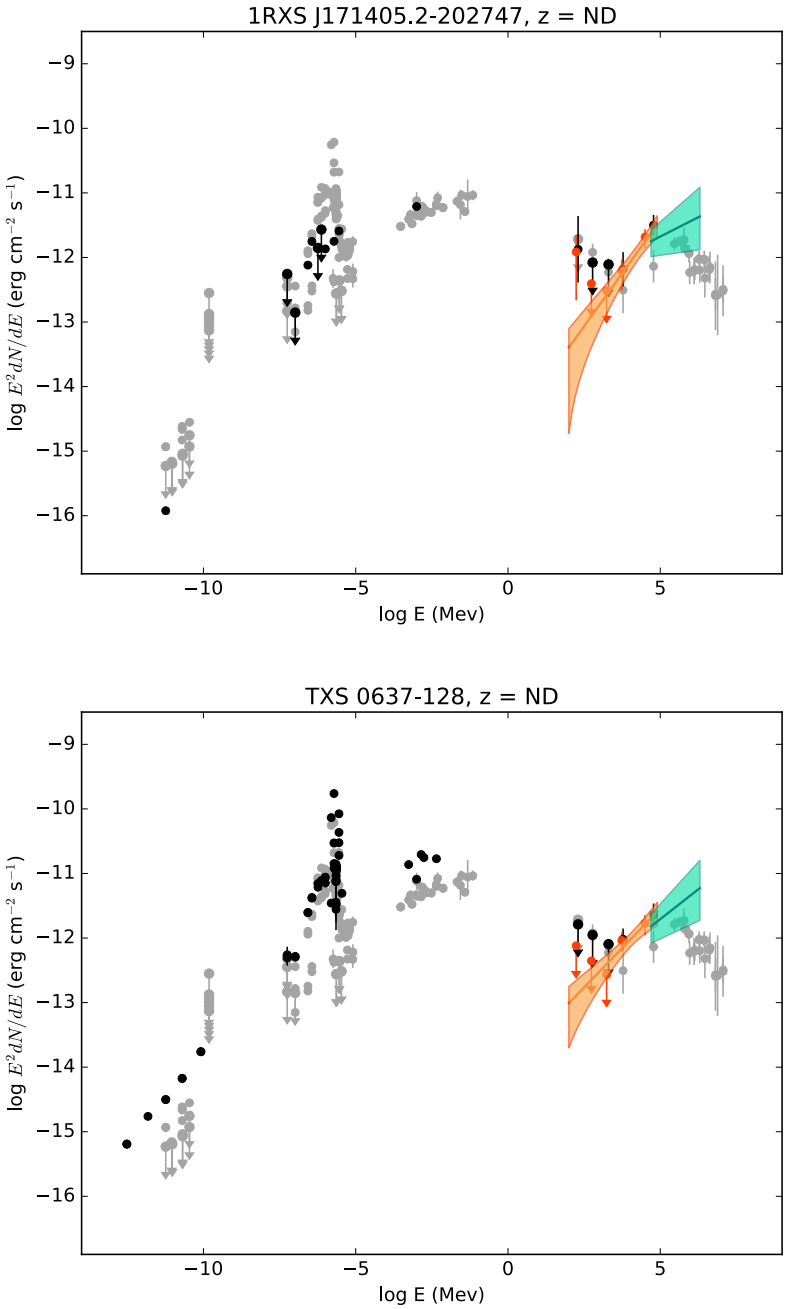

FIGURE 7.15: SED of the new X-HBL candidates for the 2017 update of the proposal: 1RXS J171405.2-202747 (top) and TXS 0637-128 (bottom). The black points are the MWL data of the source from SED Builder and the grey points are the ones of 1ES 0229+200 for comparison. The 3FGL spectral data are shown in pink and in dark blue for the 2FHL.

Chapter 8

Résumé de la Partie 2 (French)

Détection de γ de très haute énergie et les télescopes H.E.S.S.

Le réseau de télescopes H.E.S.S. (pour *High Energy Stereoscopic System*, voir Figure 8.1) est situé sur le plateau de Khomas en Namibie. Inaugurés en 2004, les quatre premiers télescopes, avec un miroir de 12 mètres de diamètre, permettent d'atteindre un seuil en énergie d'environ 200 GeV. En 2012, un cinquième télescope est ajouté au réseau. Ce dernier est plus grand, avec un miroir de presque 30 mètres de diamètre, et permet de descendre le seuil en énergie de tout le réseau autour d'une dizaine de GeV.

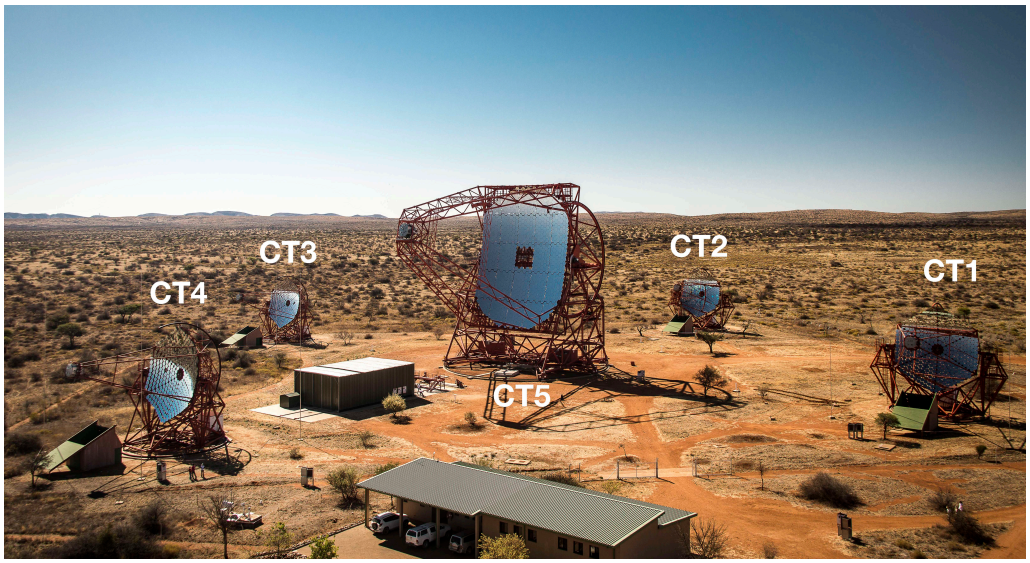

FIGURE 8.1: Photographie du réseau de télescopes H.E.S.S. en Namibie.

Ces télescopes utilisent le principe de la détection Cherenkov : un photon γ, en arrivant dans l'atmosphère, va interagir avec celle-ci et créer une gerbe de particules qui va se propager vers le sol plus vite que la lumière dans le milieu ; ces particules vont ioniser le milieu et créer une lumière, appelée lumière Cherenkov, qui va se propager vers le sol. Cette lumière est collectée par les miroirs des télescopes et focalisée vers des caméras finement pixelisées. C'est à partir des images de ces flashs de lumière Cherenkov que l'analyse va reconstruire les caractéristiques de la particule incidente (direction d'arrivée et énergie) pour dériver des spectres et des courbes de lumière.

Tout d'abord il faut calibrer les données, c'est à dire, à partir du signal électrique en sortie des pixels de chaque caméra, dériver la densité de lumière Cherenkov pour chaque événement dans chaque pixel. Cela permet d'avoir des images de gerbes de lumière Cherenkov dans les caméras (Figure 8.2) pour ensuite reconstruire les événements. Il se trouve que les particules les plus énergétiques du rayonnement cosmique, généralement

des protons et des électrons, vont aussi produire une cascade de particules et un flash de lumière Cherenkov. Cela va constituer un bruit de fond important. Cependant, la forme de la gerbe de particules et donc du flash de lumière Cherenkov est différente pour les leptons et les hadrons. La Figure 8.2 montre deux événements, le premier produit par un photon et le deuxième par un proton. Les photons et électrons produisent un flash de lumière dont l'image peut facilement être paramétrée par une ellipse alors que les hadrons produisent un flash de lumière plus étendu et moins lisse.

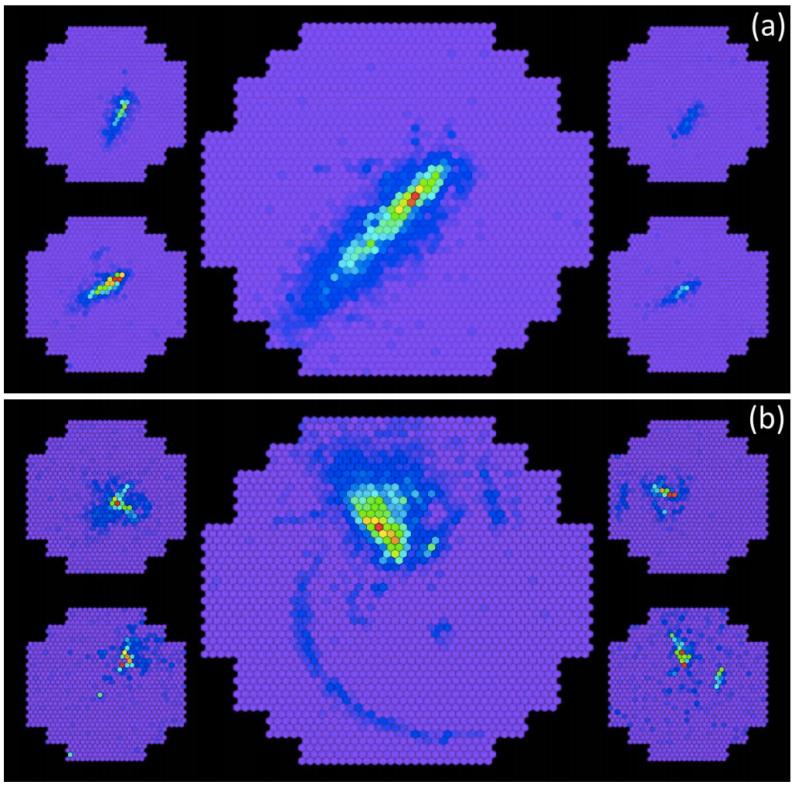

FIGURE 8.2: Exemples d'images de flash Cherenkov sur les caméras des télescopes H.E.S.S. avec un événement produit par un photon (en haut) et par un proton (en bas).

En se servant de ces différences de forme, on peut sélectionner les événement γ pour ensuite contruire des cartes d'excess et de significativité (Figure 8.3). Ces cartes permettent de voir si l'objet observé est détecté et si l'analyse s'est bien passée (le fond doit être bien normalisé). À partir de cet excès, des spectres et courbes de lumière peuvent être dérivés afin de faire de la physique avec les résultats.

Les simulations Run-Wise : une nouvelle façon de décrire l'instrument

Les télescopes Cherenkov utilisent l'atmosphère terrestre comme calorimètre et il n'existe aucun faisceau test de photons γ pour connaître la fonction de réponse de l'instrument (atmosphère + télescopes) et tester les méthodes de reconstruction. Les analyses dépendent donc de simulations, notamment pour reconstruire l'énergie du photon incident.

Actuellement, les simulations sont faites en deux temps avec les classes `Kaskade` et `Smash`. `Kaskade` simule le développement des gerbes dans l'atmosphère et l'émission de lumière Cherenkov et enregistre en sortie la densité de lumière Cherenkov au sol.

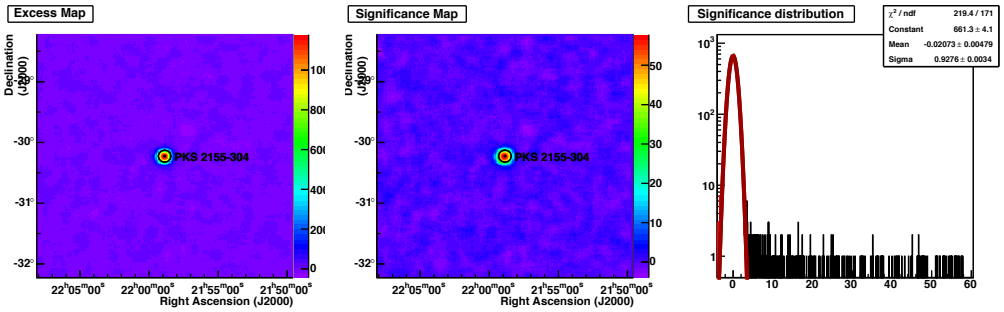

FIGURE 8.3: Cartes d'excès (gauche) et de significance (milieu) avec la distribution de significance à droite qui permet de voir si le fond est bien normalisé.

`Smash` simule les télescopes, de l'arrivée des photons Cherenkov sur les miroirs et les caméras et à toute l'électronique d'acquisition.

Les simulations sont produites pour différentes configurations en fonction de la valeur des angles zénithaux et azimuthaux, de la nature et énergie de la particule incidente et de l'efficacité optique des télescopes par exemple. En prenant en compte tous les paramètres, cela donne 208 320 simulations possibles pour un photon γ. Malgré ce grand nombre de simulation, l'espace des phases est limité et il faut tout de même interpoler entre les simulations pour les comparer aux données. Cette interpolation peut produire des incohérences lors de la comparaison données-simulations. Lorsqu'on regarde par exemple l'histogramme des énergies reconstruites sur la Figure 8.4, on se rend compte que les simulations (points noirs) vont à plus basse énergie que les données (ligne verte). Cela veut dire qu'on ne comprend pas entièrement notre instrument à basse énergie, ce qui pose problème car c'est là où il y a le plus de statistique.

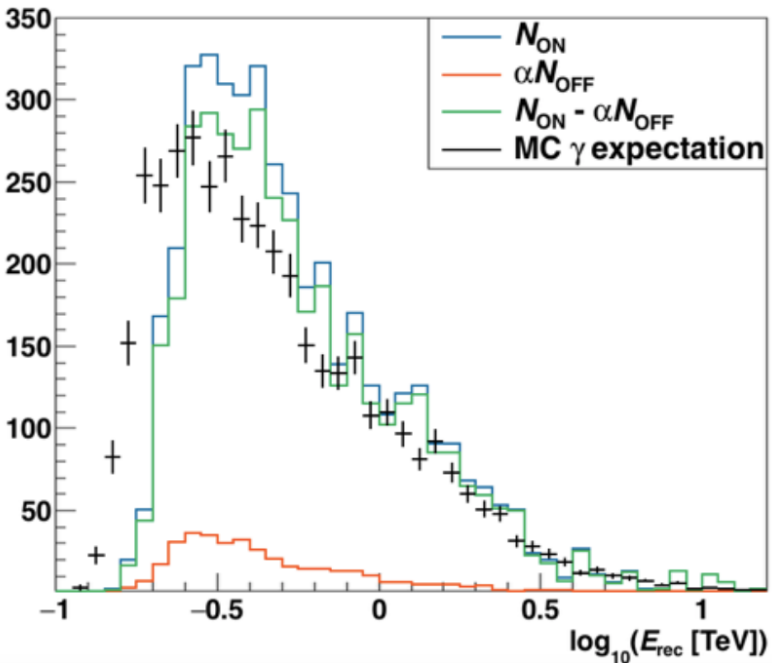

FIGURE 8.4: Histogrammes des énergies reconstruites pour les données (vert) et les simulations (noir).

Il y a aussi le problème de la PSF (*Point Spread Function* en anglais, c'est la fonction d'étalement de l'instrument) : l'image d'un objet ponctuel dans le ciel n'est pas un point, mais est étalée. Seulement cet étalement est évalué à environ $0.01°$ dans les simulations et les données montrent que les AGN (des objets ponctuels) ont une extension résiduelle d'en moyenne $0.023°$.

Il se trouve que les simulations utilisées sont trop parfaites, elles considèrent les télescopes dans un état parfait comme à neuf. Seulement, pendant la prise de données, certains pixels peuvent être éteints, ce qui ajoute une erreur sur la reconstruction de la direction d'arrivée de la particule initiale, et l'efficacité optique de chaque télescope est différente et diminue avec le temps.

Ainsi un nouveau schéma de simulation doit être mis en place pour prendre en compte de manière plus précise des paramètres de simulations. Plutôt que d'augmenter l'espace des phases et donc le nombre de simulations, nous avons choisi de faire une simulation dédiée pour chaque run. Cette simulation prendra directement en compte les conditions d'observations telles que les vrais angles zénithaux et azimuthaux, l'efficacité optique de chaque télescopes individuellement, les pixels éteints de chaque caméras ainsi que tous les autres coefficients de calibration et pour finir le bruit de fond de ciel (aussi appelé NSB pour *Night Sky Background* en anglais).

De nombreux changements ont dû être implémentés dans le code de simulation afin d'aller chercher l'information sur les conditions d'observation dans les bases de données et les introduire dans la simulation. Il a ensuite fallu vérifier si tous ces changements avaient bien été pris en compte avant de passer à l'étape d'analyse suivante pour pouvoir comparer ces simulations aux données et voir l'effet de ces changements.

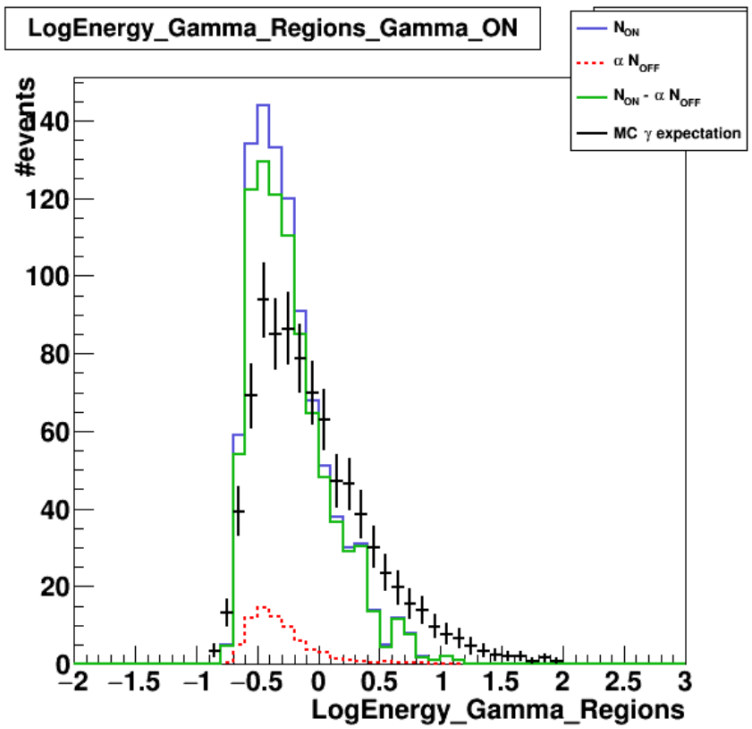

FIGURE 8.5: Histogrammes des énergies reconstruites pour les simulations Run-Wise (en noir) et les données (en vert).

Les résultats préliminaires des tests qui ont suivi ces changements sont positifs et on voit une nette amélioration dans les problèmes de reconstruction en énergie et de PSF. La Figure 8.5 montre les histogrammes des énergies reconstruites pour des données (ligne verte) et les simulations Run-Wise (points noirs). Si on compare à la Figure 8.4, on voit une nette amélioration au niveau du seuil en énergie qui est remonté pour les simulations une fois les conditions d'observations prises en compte. La problème de la PSF se voit lui aussi résolu avec des premiers tests qui montrent un élargissement de la PSF des simulations dont la valeur numérique rejoint celle des données.

En conclusion, les premiers tests du nouveau schéma de simulations Run-Wise sont positifs et montrent une amélioration comparé à ce que les simulations classiques donnent. Ce travail est important pour H.E.S.S mais aussi pour la prochaine génération de télescopes Cherenkov : CTA (Cherenkov Telescope Array) qui disposera de nombreux types de télescopes différents et d'un espace des phases gigantesque par rapport à ce que nous traitons aujourd'hui.

HEGS : l'étude du ciel extragalactique avec H.E.S.S.

Étant situé dans l'hémisphère Sud, H.E.S.S. a l'avantage de pouvoir observer le plan galactique dand de bonnes conditions. C'est pourquoi le projet d'étude du plan galactique a commencé (HGPS pour *H.E.S.S. Galatic Plane Survey* en anglais). Le but du HGPS est de publier un catalogue des sources au TeV dans le plan galactique.

À cause de la taille du ciel, il est difficile de faire de même pour les régions extragalatiques. Cependant, depuis ses débuts en 2004, H.E.S.S. a observé beaucoup de régions extragalactiques. Le projet HEGS (*H.E.S.S. ExtraGalactic sky Survey* en anglais) a pour but d'utiliser toutes ces observations pour publier un catalogue des sources extragalactiques au TeV.

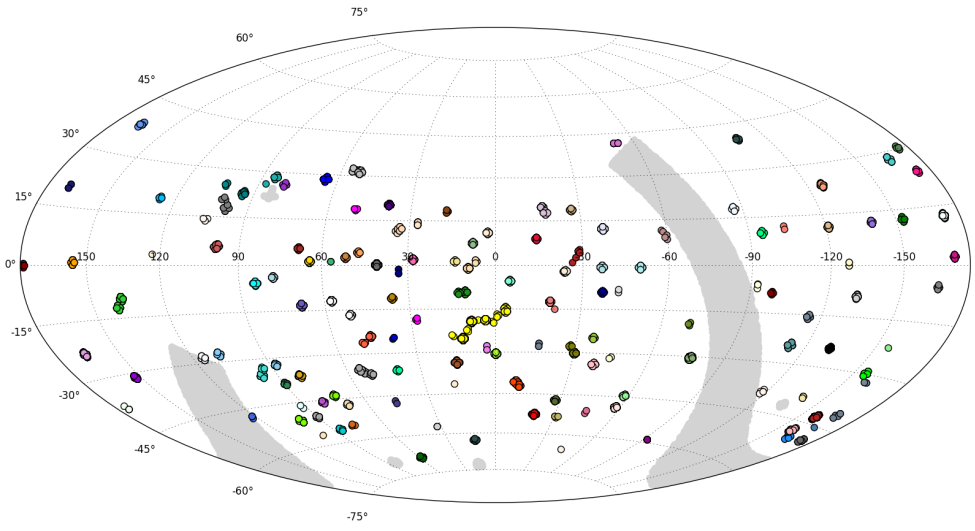

FIGURE 8.6: Carte du ciel, en coordonnées équatoriales, des 123 clusters extragalactiques. Chaque cercle représente un run, chaque couleur un cluster de runs (les zones grises étant les régions exclues de cette analyse : le plan galactique, le LMC, SMC, la nébuleuse du Crabe et SN 1006).

Les runs sélectionnés sont les runs H.E.S.S.-I pris entre 2004 et 2012 ce qui donne en tout 6499 runs après application des coupures de qualité et qui couvrent environ $2700\ \mathrm{deg}^2$. Ces runs sont affichés sur la Figure 8.6 où chaque couleur représente un cluster de runs : chaque run ayant une partie de son champ de vue en commun d'autres runs est clusterisé avec ceux-ci. Cela donne au final 123 clusters extragalactiques de runs. Ces clusters seront analysés un à un pour étudier la présence de sources γ et d'objets transients. La recherche d'objet transient se fait avec une méthode ON-OFF dans le temps. Les analyses présentées ici sont préliminaires car faites avec la version `0-8-24` de l'analyse et les DST `Prod6`. Au moment de l'écriture, l'analyse est encore cours avec la version la plus récente et la plus stable de l'analyse : `0-8-32` avec les DST `Prod8`.

Après avoir analysés tous les champs de vue, des vérifications sont faites sur les sources déjà connues dont les flux et caractéristiques spectrales ont été publiées pour voir si l'analyse HEGS a bien fonctionnée. Une fois l'analyse validée, nous pouvons étudier tous les champs de vue pour rechercher des points chauds (des endroits où la significance dépasse $4.5\ \sigma$) qui pourrait s'avérer être des sources γ encore inconnues, des transients et dériver des limites supérieures sur les sources des catalogues *Fermi* non-détectées par H.E.S.S.

Les sources 3FGL présentes dans les champs de vue HEGS

HEGS couvre environ $2700\ \mathrm{deg}^2$ dans le ciel, donc certains objets ont été observés alors que ce n'était pas les cibles des pointés, ils étaient simplement présents dans le champ de vue. Il y a en tout 168 AGN du catalogue *Fermi* 3FGL qui ont été observés par H.E.S.S. Certains sont déjà connus au TeV, mais ce n'est pas le cas pour environ 150 de ces objets, quelles contraintes peut-on apporter sur leur spectre au TeV ?

J'ai donc regardé le spectre du 3FGL pour chacune de ces sources, son absorption par l'EBL (*Extragalactic Background Light*, c'est un fond diffus de photon de basse énergie avec lesquels les γ peuvent interagir lors de leur propagation) et la limite supérieure de HEGS sur le spectre au TeV. La Figure 8.7 montre en exemple la SED de deux sources pour lesquelles nous avons des limites supérieures contraignantes : avec le temps d'observation et la sensibilité des télescopes, connaissant (hypothétiquement) le flux prédit par *Fermi*, la source aurait du être détectée.

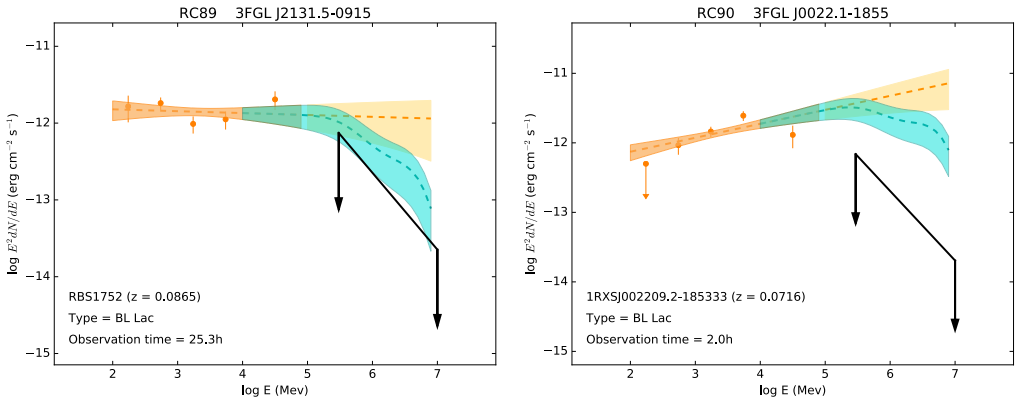

FIGURE 8.7: SEDs de 2 sources du 3FGL qui étaient dans les champs de vue des observations H.E.S.S. Le spectre du 3FGL est montré en orange, son extrapolation jusqu'à 10 TeV en jaune. Le flux attendu avec absorption de l'EBL est montré en bleu et la limite supérieur dérivée par HEGS en noir.

Il y a plusieurs possibilités pour expliquer l'absence de détection d'une source malgré une limite supérieure contraignante. Tout d'abord, les blazars étant variables, la source pouvait très bien se trouver dans un état de flux beaucoup plus bas que le flux donné par le 3FGL (qui est un flux moyen sur 4 ans). Ensuite, l'hypothèse d'extrapolation peut être fragilisée du fait qu'il pourrait y avoir une cassure ou courbure intrinsèque dans le spectre qui dépend du comportement de la population de particules émettrice.

Il se trouve qu'avant l'ère *Fermi*, les choix d'observations se faisaient en fonction du flux radio et du flux en X : un fort flux radio montrait qu'il y avait beaucoup de photons de basse énergie et un fort flux en X montrait qu'il y avait beaucoup d'électrons de haute énergie. Dans le cadre d'un processus Inverse Compton, cela laissait présager un fort flux en γ (Costamante and Ghisellini, 2002).

Si l'on regarde les sources connues au TeV qui sont dans catalogue Roma-BZCAT (catalogue contenant les flux radio et X de plusieurs blazars), on voit qu'elles répondent toutes au critère précédent (points rouges sur la Figure 8.8). Seulement, si on regarde la position des sources 3FGL non détectées par H.E.S.S., on voit qu'elles sont distribuées uniformément dans cet espace : il y a même des objets non détectés dans la partie haut flux radio-X, montrant que cette stratégie d'observation biaisée n'était peut-être pas si optimale que ça. En effet, il n'y a jamais d'information ou de publication sur les observations qui n'ont rien donné.

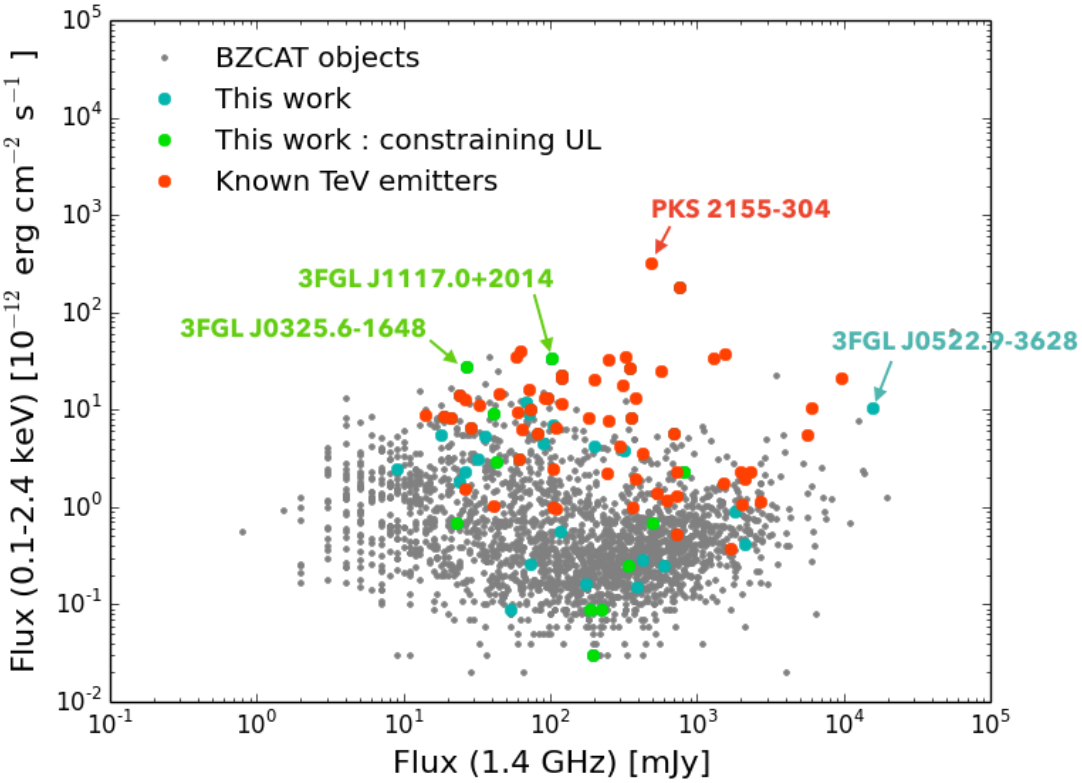

FIGURE 8.8: Flux en X entre 0.1 et 2.4 TeV versus le flux radio à 1.4 GHz pour les blazars du catalogue Roma-BZCAT (en gris). Les sources du 3FGL des champs de vue HEGS sont en blue pour celles qui n'ont pas de limites contraignantes et en vert pour celles qui ont des limites contraignantes.

Recherche à l'aveugle de sources et de transients

Parmi tous les champs de vue HEGS, il se peut qu'il y ait du signal jamais vu auparavant. Ainsi tous les champs de vue sont testés à l'aveugle : un masque est appliqué sur toutes les cartes de significativité pour ne laisser passer le signal que s'il est au-dessus de $4.5\,\sigma$, on dit dans ce cas là que l'on a un point chaud ou *hotspot*. En tout plusieurs hotspots sont trouvés dans les cartes de significance sur toute la gamme en énergie, en-dessous et au-dessus de 1 TeV et dans les cartes de ON-OFF Test.

Pour chacun d'entre eux j'ai regardé si des contreparties existent dans d'autres catalogues (les catalogues *Fermi* mais aussi les bases de données SIMBAD et NED).

Après vérification, aucune nouvelle source fut découverte lors de cette recherche à l'aveugle. Cependant, cette analyse a été faite avec une ancienne version du soft d'analyse (`0-8-24`) qui contient encore quelques failles, certains hotspots devait leur existence seulement à une systématique dans l'analyse et non à cause d'une raison physique. C'est pourquoi cette recherche à l'aveugle sera refaite une fois l'analyse fini avec la dernière version du soft de H.E.S.S. (`0-8-32`).

En conclusion, ce projet d'étude du ciel extragalactique avec H.E.S.S. est toujours en cours et permettra à la collaboration de publier un catalogue des champs de vue extragalactiques à la communauté scientifique. Ce projet prépare aussi le terrain pour CTA, qui avec ses nombreux télescopes sera plus à même de faire un scan du ciel extragalactique.

Exploration de la séquence blazar avec H.E.S.S.

Quand on regarde le catalogue TeVCat[1] qui répertorie toutes les sources connues au TeV, on voit que la majorité des blazars (environ 75 %) détectés au TeV sont des HBL. Il y a seulement 2 LBL : Ap Librae (H.E.S.S. Collaboration et al., 2015) et OT 081 récemment découvert[2], et 6 FSRQ. Cette différence peut s'expliquer par deux raisons :

1. Si on croit la séquence blazar (présentées dans la Section 2.3 du Chapitre 2), les LBL et FSRQ ont généralement un pic Synchrotron à plus basse fréquence et donc un flux plus bas (avec un spectre plus mou) dans la gamme du TeV ce qui les rend difficiles à détecter;

2. La stratégie d'observation des télescopes Cherenkov a biaisé les observations vers les HBL en sélectionnant des sources brillantes en radio et en X qui dans le modèle d'émission Inverse Compton donnerait beaucoup de photons à haute énergie (Costamante and Ghisellini, 2002).

La détection de nouveaux blazars de type FSRQ et LBL à très haute énergie serait très intéressante pour sonder la séquence blazar à ces énergies. La SED des HBL est généralement bien décrite par un modèle SSC, et ce n'est pas le cas pour les LBL et FSRQ. Leur SED plus complexe demande des modèles d'émission plus complexes. Par exemple, la modélisation de la SED du FSRQ PKS 1510-089 (Figure 8.9) et du LBL Ap Librae (Figure 8.10) fait intervenir soit une seconde population de photons pour faire de l'Inverse Compton, soit d'autres zones qui interagissent les unes avec les autres. En admettant que tous les blazars se ressemblent et qu'il y a une séquence continue pour passer des FSRQ aux HBL, alors un modèle unique devrait pouvoir reproduire la SED des FRSQ, LBL et HBL.

[1] http://tevcat.uchicago.edu/

[2] http://www.astronomerstelegram.org/?read=9267

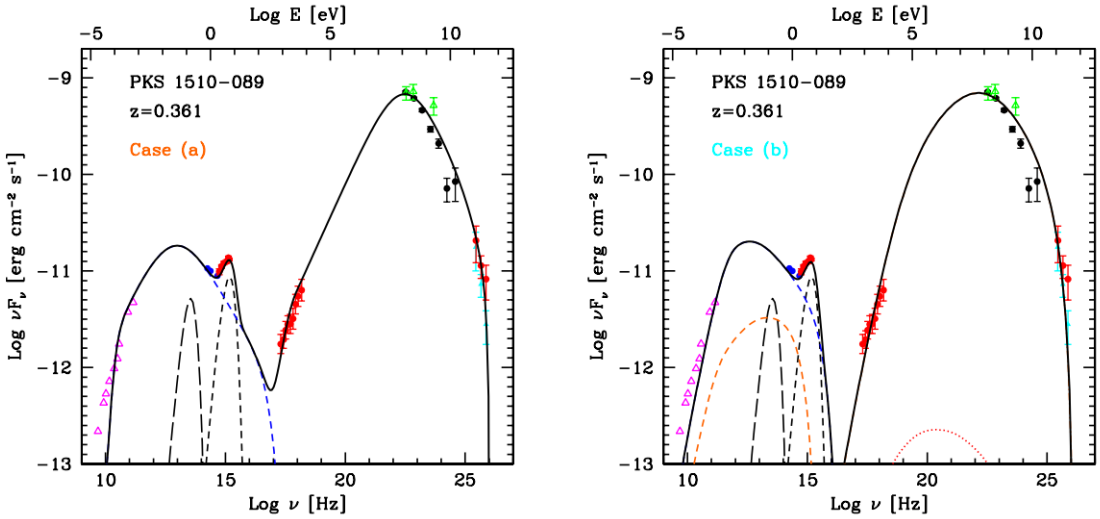

FIGURE 8.9: SED du FSRQ PKS 1510-089 (Aleksić et al., 2014), les points sont les données multi-longueur d'onde et la courbe noire l'ajustement du modèle (à gauche l'émission au GeV-TeV est faite par du Compton externe tandis qu'à droite l'hypothèse de localisation de l'émission change).

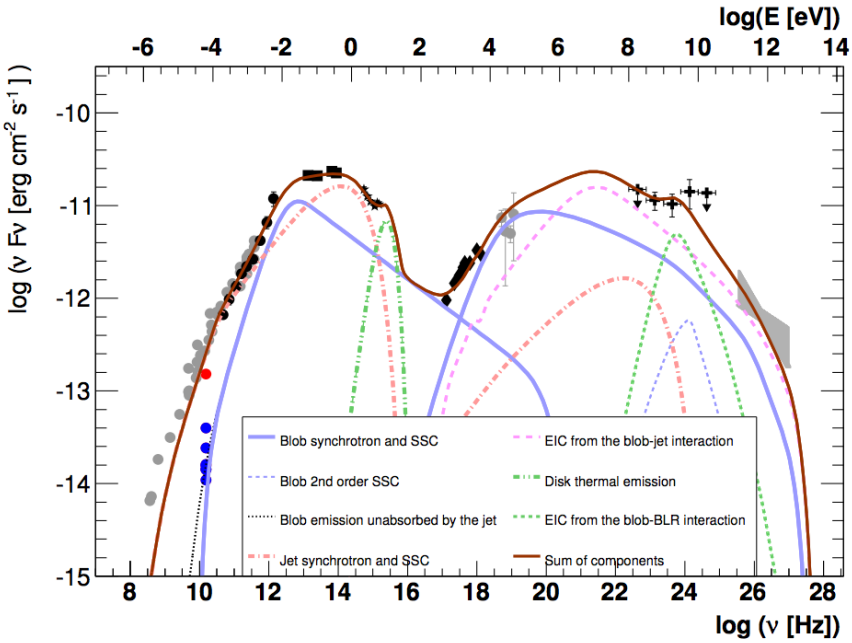

FIGURE 8.10: SED du LBL Ap Librae (Hervet, Boisson, and Sol, 2015). Les points sont les données multi-longueur d'onde et les différentes lignes représentent les différentes contribution à la modélisation multi-composantes.

À l'autre extémité de la séquence blazar, il pourrait y avoir des HBL extrêmes (notés X-HBL), avec un pic Synchrotron à plus haute fréquence que les HBL, donc possiblement un second pic dans la gamme du TeV. Le BL Lac 1ES 0229+200 pourrait bien être le premier blazar détectés au TeV à faire parti de cette nouvelle classe. Sa SED challenge le modèle SSC car les valeurs numériques des paramètres physiques tels que la norme du champ magnétique, le facteur Doppler ou l'énergie minimale des particles, doivent être trop hautes.

La proposition d'observation de la séquence blazar au TeV avec les télescopes H.E.S.S. a vu le jour à la fin de l'année 2015. Le but est de pointer vers des FSRQ, LBL et X-HBL prometteurs pour voir si le comportement que l'on voit actuellement au TeV est particulier ou commun dans ces classes d'objets.

La sélection s'est basée sur le catalogue *Fermi* du 2FHL qui contient les sources dures détectées par le *Fermi*-LAT entre 50 GeV et 2 TeV, une gamme en énergie qui correspond à H.E.S.S. Des coupures ont été appliquées pour ne sélectionner seulement les blazars correspondants aux classes FSRQ, LBL et X-HBL, avec une autre coupure pour avoir seulement les objets détectables en un temps raisonnable. Au final, 11 sources, listées dans le Tableau 8.1 sont sélectionnées pour faire partie de la proposition d'observations.

Nom	RA	Dec	Flux (%Crabe)	Redshift	$T_{5\sigma}$ (heures)
Candidats LBL					
TXS 1742-078	266.372	−7.8764	1.69	ND	27
PKS 0754+100	119.212	9.92	1.01	0.266	16
PMN J0811+0237	122.979	2.643	0.91	ND	3
RBS 1792	328.298	−0.6867	0.73	0.341	29
PMN J1125-3556	171.419	−35.9328	1.27	0.284	317
PKS 0139-09	25.3361	−9.4568	0.75	0.73	227
Candidats X-HBL					
1RXS J054357.3-553206	85.9992	−55.5577	3.06	0.273	4
PMN J1548-2251	237.188	−22.8202	1.80	0.192	2
PMN J1936-4719	294.238	−47.3534	1.39	0.265	21
5BZG J0022+0006	5.5001	0.1059	1.14	0.306	5
1RXS J012338.2-231100	20.9299	−23.1482	1.56	0.404	34

TABLE 8.1: Sources pour les demandes d'observations de 2016, avec position (RA & Dec J2000 en degrés), classe, flux dans le 2FHL en pourcentage du flux du Crabe, redshift quand il est connu et le temps nécessaire pour avoir une détection à 5 σ avec un seuil en énergie de 0.1 TeV.

Sur ces 11 sources, 6 d'entre elles ont été observées pendant l'année 2016 : RBS 1792, PMN J1125-3556, PKS 0139-09, PMN J1548-2251, 5BZG J0022+0006 et 1RXS J012338.2-231100. L'analyse ne montre aucune détection pour ces sources, mais PMN J1548-2251 montre un début de signal à 3.3 σ en seulement 2 heures d'observations, ce qui est très prometteur. L'analyse sur cette source a été poussée plus loin de manière à dériver un spectre représenté en rouge sur la Figure 8.11.

L'indice du spectre dérivé des données H.E.S.S. est en accord avec les données *Fermi* mais ne permet pas de contraindre la position du pic à très haute énergie, plus de données sont nécessaires afin d'augmenter la statistique.

Cette proposition d'observation a été mise à jour au début de l'année 2017 pour tenir compte des informations contenues dans les données de 2016. La liste des sources correspondantes (avec le nouveau temps d'observation demandé) est montrée dans le Tableau 8.2. PMN J1548-2251 est l'un des objets les plus prometteurs actuellement et de nouvelles observations ont été prise entre Février et Mai 2017 et seront analysées dès qu'elles auront été calibrées. Du côté des LBL, PMN J0811-3556 pourrait possiblement être détecté aussi en très peu de temps.

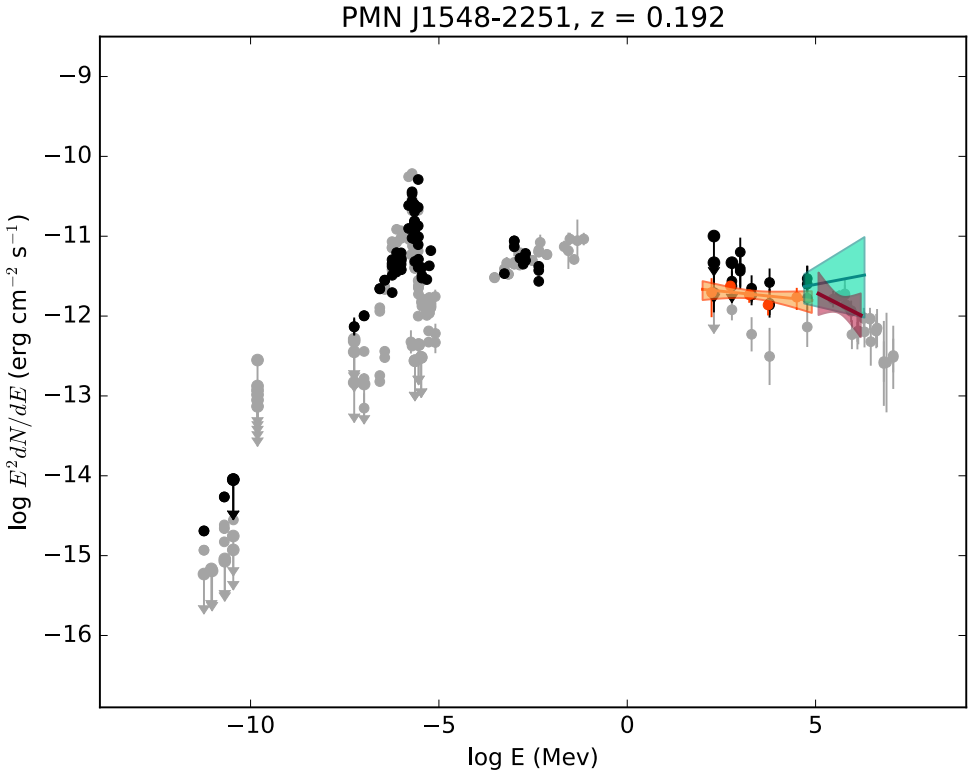

FIGURE 8.11: SED de PMN J1548-2251 : les points noirs sont les données multi-longueur d'onde venant de l'ASDC tandis que les courbes orange, bleu et rouge sont respectivement les spectres du 3FGL, 2FHL et H.E.S.S. Les points gris sont la SED de 1ES 0229+200 pour comparer.

Nom	RA	Dec	Flux (%Crabe)	Redshift	$T_{5\sigma}$ (heures)
Candidats LBL					
TXS 1742-078	266.372	−7.8764	1.69	ND	10
PKS 0754+100	119.212	9.92	1.01	0.266	10
PMN J0811+0237	122.979	2.643	0.91	ND	5
RBS 1792	328.298	−0.6867	0.73	0.341	0
PMN J1125-3556	171.419	−35.9328	1.27	0.284	0
PKS 0139-09	25.3361	−9.4568	0.75	0.73	30
Candidats X-HBL					
1RXS J054357.3-553206	85.9992	−55.5577	3.06	0.273	5
PMN J1548-2251	237.188	−22.8202	1.80	0.192	10
PMN J1936-4719	294.238	−47.3534	1.39	0.265	10
5BZG J0022+0006	5.5001	0.1059	1.14	0.306	5
1RXS J012338.2-231100	20.9299	−23.1482	1.56	0.404	5
1RXS J171405.2-202747	258.533	−20.496	1.60	ND	10
TXS 0637-128	100.030	−12.8876	1.57	ND	10

TABLE 8.2: Sources pour les demandes d'observations de 2017, avec position (RA & Dec J2000 en degrés), classe, flux dans le 2FHL en pourcentage du flux du Crabe, redshift quand il est connu et le temps nécessaire pour avoir une détection à 5 σ avec un seuil en énergie de 0.1 TeV.

Part III

Advanced variability study of the blazar PKS 2155-304

Chapter 9

Characterization of the long term variability of PKS 2155-304

Contents

PKS 2155-304 (redshift $z = 0.116$; Falomo, Pesce, and Treves, 1993) is a very well known blazar detected at TeV for the first time in 1999 (Chadwick et al., 1999). This object was first discovered during the Parkes radio survey (Wright and Otrupcek, 1990) and has been classified as an HBL thanks to X-ray observations from the HEAO-1 satellite (Schwartz et al., 1979). The HE γ-ray emission of PKS 2155-304 has been detected by EGRET with a hard photon index of $\Gamma = 1.7$ (Vestrand, Stacy, and Sreekumar, 1995).

Being one of the brightest blazar of the Southern Hemisphere, it is regularly observed by H.E.S.S. since the beginning of the experiment, either for physics or to be used as a calibration source. PKS 2155-304 is detected on short time scales, generally in one run, by H.E.S.S. In July 2006, the source underwent a flare with a flux more than a hundred times larger than what measured before (Aharonian et al., 2007a).

9.1 Introduction

9.1.1 The importance of variability studies

As presented in the Section 2.5 of Chapter 2, variability is now one of the key to understand blazars emission along with the link between the supermassive black hole, accretion disk, relativistic jet and clouds region. When looking at HBL, it appears that leptonic and hadronic models can both explain the multi-wavelength SED of blazars (see Figure 2.12 of Chapter 2).

In the previous chapter, we presented how having informations on TeV spectra could help improve our understanding of FSRQ, LBL and X-HBL objects. For HBL, it is the contrary, almost 50 HBLs are listed on TeVCat. The TeV spectra of most HBLs are already well known and we still do not know for sure which model is best suited to explain their emission. Moreover, emission models do not have to explain only the time-averaged emission represented by the SED but they should also account for the variability we observe.

Variability is a signature of the emission processes. Leptonic and hadronic models do not use the same particles (it is the light electron versus the heavy proton), so we do not expect the same variability pattern from them because they will not have the same characteristic times (see Section 2.5 from Chapter 2).

9.1.2 Short term temporal studies at TeV

At first, temporal studies where made on flares. Such bright and violent events were puzzling. So when they occured, several instruments were trying to catch them in order to have simultaneous light curves covering the events in different energy ranges. Flares are also useful to probe the central engine as the shortest variability time scale is thought to be related to the size of the event horizon of the black hole.

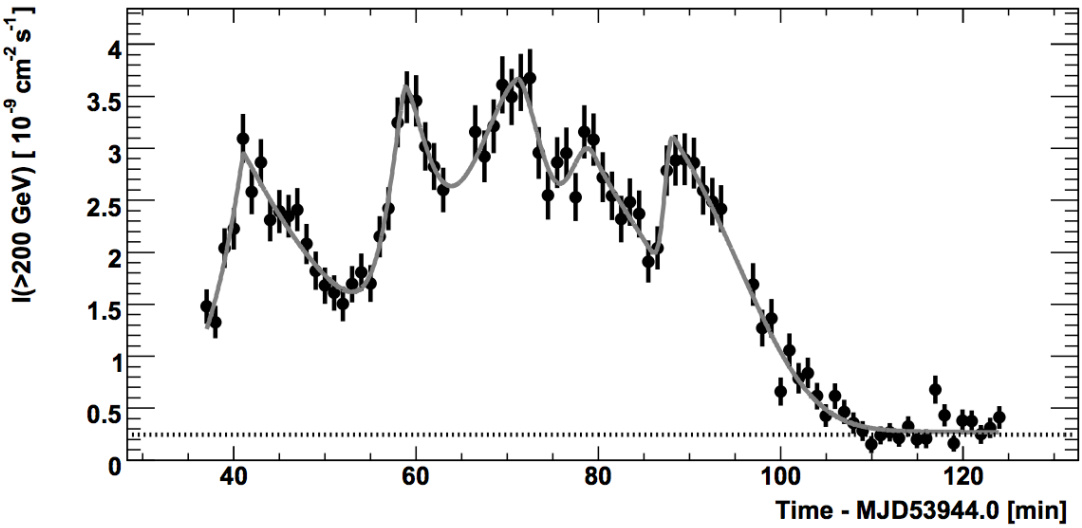

FIGURE 9.1: Light curve of the 2006 flare of PKS 2155-304 catched by H.E.S.S. (Aharonian et al., 2007a). Flux points are computed in 1 min bins. The dotted line represents, for comparison the flux of the Crab and the curve is the fit (five bursts and a constant flux).

One of the most famous flare at very high energy is the July 2006 flare of PKS 2155-304 (see Figure 9.1, Aharonian et al., 2007a). It has been characterized by pure red noise

(the power spectral density follows a power law $f(\omega) \propto \omega^{-\beta}$, ω being the frequency and β the power law index) with $\beta = 2$ above 200 GeV on time scales down to one minute. Abramowski et al., 2010 also showed that the flux during this outburst had a lognormal behavior, a variability increasing with the energy and that the X-ray and VHE ranges were correlated. However it is interesting to note that in a longer term (11 days) multi-wavelength study of the low state of PKS 2155-304, no clear correlation between the X-ray and VHE bands was found while a clear optical/VHE correlation is found (Aharonian et al., 2009b).

There have been several flares in different wavelengths for other blazars (Mkn 501, Mkn 421, PKS 1510, M 87, PG 1553+113...), this section does not claim to be exhaustive on each time series analysis of each flare. They are generally a great opportunity to study correlations between energy bands, either to study violation of the Lorentz Invariance or to study the emission/acceleration models which could results in correlation (or not) between energy bands and time lags (or not).

9.1.3 The early days of the long term multi-wavelength studies

Since few years, most of the electromagnetic spectrum is covered by radio, optical, X-ray and γ-ray experiments.

Experiments like *Fermi* with the Large Area Telescope (LAT) in GeV is perfectly suited to monitor the sky and construct long term light curves. The *Fermi*-LAT is monitoring the GeV sky since its launch in 2008, giving light curves of several years. After the launch of the *Fermi*-LAT, the consortium running the optical telescopes SMARTS (Small and Moderate Aperture Research Telescope System Bonning et al., 2012) decided to follow the monitoring of the blazars the LAT was observing.

But already 20 years ago, a monitoring project called WEBT (Whole Earth Blazar Telescope[1]) starting using radio, infrared and optical telescopes to obtain continuous, high-temporal-density light curves.

Also in radio, MOJAVE (Monitoring Of Jets in Active galactic nuclei with VLBA Experiments[2]) is a long term monitoring program of AGN, imaging their jet in radio with VLBA (Very Long Baseline Array).

X-ray experiments like *RXTE* (*Rossi X-ray Timing Explorer*[3]), *Swift*-XRT (*Swift* X-ray telescope[4]) and XMM-Newton (X-Ray Multi Mirror Mission[5]) have observed some sources regularly as well, sometimes following dedicated multi-wavelength campains.

Long term multi-wavelength studies of blazars are still rare, especially with high energy data. There are few blazars with long term multi-wavelength data set, because at the beginning, the VHE experiments splitted their observations between too many different targets and also because few sources are bright enough for the sensitivity of IACTs to be detected in one run or night.

The BL Lac Markarian 421 (Mkn 421) was the first extragalactic TeV emitter ever detected (Punch et al., 1992). It is regularly observed by the MAGIC experiment which recently released a long term multi-wavelength study of the blazar in Ahnen et al., 2016a with light curves of 2.3 years in VHE, from March 2007 to June 2009 (see Figure 9.2).

Mkn 501 is similar to Mkn 421 and has been detected at TeV for the fist time by Whipple in 1996 (Quinn et al., 1996). This HBL was the target of several multi-wavelength campains (Aleksić et al., 2015; Ahnen et al., 2016b) including MAGIC, VERITAS and

[1] http://www.oato.inaf.it/blazars/webt/
[2] http://www.physics.purdue.edu/astro/MOJAVE/index.html
[3] https://heasarc.gsfc.nasa.gov/docs/xte/XTE.html
[4] https://www.swift.psu.edu/xrt/
[5] https://www.cosmos.esa.int/web/xmm-newton

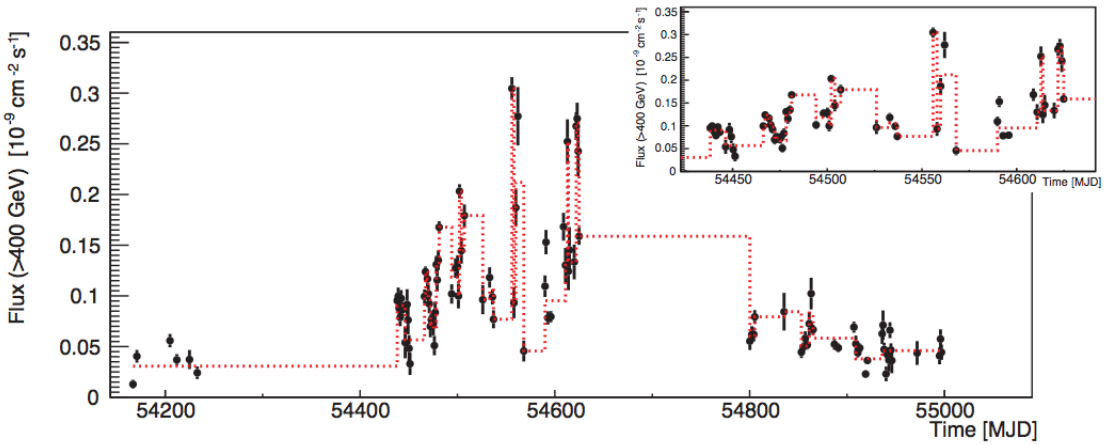

FIGURE 9.2: MAGIC light curve from Ahnen et al., 2016a above 400 GeV of Mkn 421 between March 2007 and June 2009. The red dotted line represents the Bayesian Blocks. The more the blocks, the more the variability.

Whipple data, along with radio, optical and X-ray observations. These campaigns were spanning 3 to 5 months in 2008 and 2009.

At other wavelength, the BL Lac object PKS 0735+178 had a rather impressive optical data set with 23 years, along with shorter term optical, radio and *Fermi*-LAT light curves, gathered and analyzed by Goyal et al., 2017 to study its power spectral density (PSD).

Evolution of the variability with the energy

Ahnen et al., 2016a and Ahnen et al., 2016b looked at the variability of Mkn 421 and Mkn 501 in each energy range using the fractional variability $F_{\rm var}$. It is defined as the normalized excess variance (Vaughan et al., 2003):

$$F_{\rm var} = \frac{\sqrt{S^2 - \overline{\sigma_{\rm err}^2}}}{\overline{\Phi}} \tag{9.1}$$

where $\overline{\Phi}$ is the mean flux, S^2 its variance and $\overline{\sigma_{\rm err}^2}$ the mean square error.

As shown on Figure 9.3, the variability seems to rise from radio to TeV, with low values for the radio and optical light curves. For Mkn 421, the variability levels are similar between the X-ray and VHE ranges while the variability in X-ray for Mkn 501 is around $0.2 - 0.3$ and above 0.4 for the VHE datasets.

The variability levels of Mkn 421 were found to be non stationary, they are different depending at which period we look at, although this could be a temporal windowing effect. Similarly, the 2008 multi-wavelength campain on Mkn 501 (Aleksić et al., 2015) showed lower level of variability compared to the 2009 campain (Ahnen et al., 2016b), with a similar trend of $F_{\rm var}$ increasing with increasing energy.

Correlations between different energy ranges

The Bayesian Block algorithm (Scargle, 2002) is suited to identify different levels of flux in the VHE light curve of Mkn 421, with quiescient and flaring periods (see the light curve on Figure 9.2). It appears that the X-ray light curve is directly correlated with the MAGIC light curve, showing a similar behavior of quiet and active periods in the X-ray. This correlation suggests that the X-ray and γ-ray photons are produced by the same particle

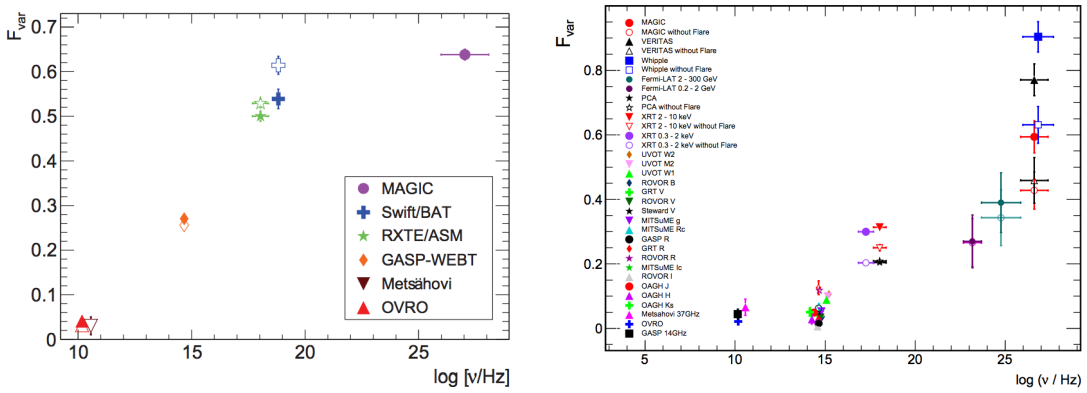

FIGURE 9.3: Evolution $F_{\rm var}$ with the frequency for the multi-wavelength light curves of Mkn 421 (left, Ahnen et al., 2016a) and Mkn 501 (right, Ahnen et al., 2016b).

population, like electron in the SSC process. Moreover, the different variability behavior at lower energy could be explained by cooler electrons or different emission regions, as proposed by the authors. However, no correlation is found with the optical and radio band.

During its two multi-wavelength campains, Mkn 501 showed no significant correlation between each bands.

Concerning PKS 0735+178, the radio-optical light curves do not seem to be correlated with the *Fermi*-LAT on month-like time scale.

Power spectral density of blazars' light curves

The power spectral density (PSD) shows how the power is divided in the different frequencies (or equivalently time scales). PSDs of blazars are often characterized by power law noise: $f(\omega) \propto \omega^{-\beta}$, where ω is the frequency and β the power law index.

The 23-years long light curve of PKS 0735+178 allowed to study the PSD in optical from decades of years down to minutes. The optical light curve is characterized by red noise ($\beta = 2$) throughout the entire time domain with no flattening or break from years to days (see Figure 9.4). However, the HE γ-ray light curve from the *Fermi*-LAT displays a power law behavior as well but with an index $\beta \sim 1$ (flicker/pink noise, for more details about the type of power law noise, see Appendix **??**).

A similar behavior as PKS 0735+170 was found for PKS 2155-304. The optical PSD is characterized by a red noise with $\beta = 1.8^{+0.1}_{-0.2}$ (Kastendieck, Ashley, and Horns, 2011). However, the HE and VHE PSD are characterized by flicker noise, their PSD is flatter, with power law indexes of $\beta_{\rm HE} = 1.20^{+0.21}_{-0.23}$ and $\beta_{\rm VHE} = 1.10^{+0.13}_{-0.13}$ (H. E. S. S. Collaboration et al., 2016a).

The values of the power law index in the different energy ranges are ranging from 1 to 2. In the framework of leptonic models like the SSC, the PSD of the Synchrotron component should be the same, or even flatter, than the PSD of the Inverse Compton component (Finke and Becker, 2014). Looking at the values of β listed in the paragraph for PKS 2155-304, the expectations from leptonic models and the data are non consistent.

Looking for a lognormal behavior

PSD, correlations and $F_{\rm var}$ are not the only ways to look at variability. They provide information mainly on emission processes. Looking at the lognormal (or not lognormal)

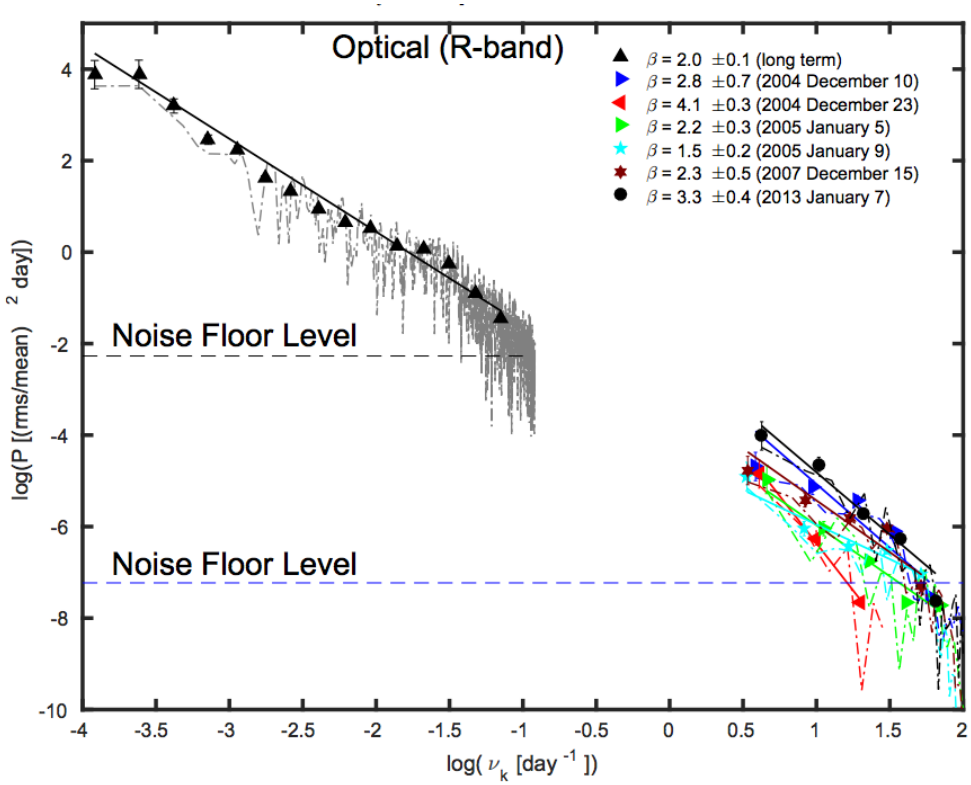

FIGURE 9.4: PSD of the composite optical (R-band) light curve of PKS 0735+178 from Goyal et al., 2017. The lines show the raw periodogram while the filled symbols denote the binned logarithmic periodogram estimates.

behavior of the source is a way to look at the origin of the variability. It is believed that lognormality is linked to the accretion disk and the underlying accretion process (Uttley and McHardy, 2001). The BL Lac object BL Lacertae showed evidence of lognormality in its X-ray long term light curve (Giebels and Degrange, 2009). The 2006 flare of PKS 2155-304 was also characterized by a log-normal behavior in TeV (Abramowski et al., 2010).

9.2 The huge multi-wavelength data of PKS 2155-304

As some of the blazars discussed above, PKS 2155-304 is one of the blazars which has been monitored by several experiments, not only H.E.S.S. Other experiments as well have observed it in different wavelengths, from radio to GeV since several years. This object is known to be variable at all wavelengths and is then perfectly suited to do multi-wavelength variability studies. For this purpose a multi-wavelength dataset on PKS 2155-304 has been selected to study in detail the long term variability of the blazar.

In this work, data of the following experiments are used to characterize the long term multi-wavelength behavior or PKS 2155-304:

- H.E.S.S. data cover 9 years (2004 - 2012) in the very high energy band (E > 200 GeV)
- *Fermi*-LAT data coves 5.5 years (2008 - 2013) of full monitoring in the high energy band (100 MeV < E < 300 GeV)
- The X-ray dataset (0.3 < E < 10 keV) is composed of *RXTE*, *Swift*-XRT and XMM-Newtom data and cover 9 years (2005 - 2013)

- The optical dataset from SMARTS follows the *Fermi* LAT monitoring with 5.5 years of monitoring in 4 optical bands (J, R, V and B).

The analysis of each dataset is presented in the following sections.

The variability and time series analysis such as the variability energy profile $F_{\rm var}(E)$, discrete correlation function, power spectral density and the search of lognormal behavior is presented in Section 9.3.

A first version of this work has been presented at the International Cosmic Ray Conference in 2015 (ICRC; Chevalier et al., 2015). Moreover, the H.E.S.S. and *Fermi*-LAT light curves along with some time series analysis have been published in a H.E.S.S. Collaboration paper called "Characterizing the γ-ray long-term variability of PKS 2155-304 with H.E.S.S. and *Fermi*-LAT" (H. E. S. S. Collaboration et al., 2017). I was responsible of this paper in the collaboration and took care of all the intra-collaboration review process as well. This paper will be referred in the following as Paper H.E.S.S. PKS 2155-304. The physical results associated with this paper have been the Source of the Month of H.E.S.S. in October 2016[6].

9.2.1 VHE dataset with H.E.S.S.

The present analysis is based on VHE data taken with the completed H.E.S.S. Phase-I between MJD 53200 (July 14, 2004) and 56246 (November 15, 2012), using three or four telescopes. The source underwent an extreme VHE flux outburst in July/August 2006 with peak fluxes exceeding the average flux level of the long-term emission by a factor of ~ 100, during which it showed rapid variability on timescales as short as 2 min (Aharonian et al., 2007a). This high flux state ($\overline{\Phi} = (75.2 \pm 0.8) \times 10^{-11}$ cm^{-2} s^{-1} above 200 GeV) is excluded from the data set because it corresponds to a different flux population not related to the low state (see Figure 3 of Abramowski et al., 2010). The remaining data constitute the basis for the time-series analysis, and will be referred to as the *quiescent* data set in the following.

In total, about 328 hours of data passed standard quality cuts as defined in Aharonian et al., 2006, with a mean zenith angle of 21° resulting in an average energy threshold of 178 GeV. The data set has been analyzed with the Model analysis chain using standard cuts (de Naurois and Rolland, 2009) above 200 GeV.

The total detection significance in the quiescent data set of PKS 2155-304 corresponds to 341σ. In order to take into account indications of a spectral variability in the VHE domain during the quiescent state (Abramowski et al., 2010), the nightly fluxes are derived with a separate spectral fit of the spectrum for each year.

Tests have been done to choose either to derive the light curve using a power law (PL) or log-parabolic (LP) spectrum depending on which one fits the data the best. The log-parabola is defined as

$$\frac{\mathrm{d}N}{\mathrm{d}E} \propto E^{-a-b\log E} \tag{9.2}$$

with a and b corresponding to the power law index and curvature index, respectively. The power law and log-parabola are nested models: a log-parabola with zero curvature ($b = 0$) is a power law.

The log likelihood values $\log \mathcal{L}$ are presented in Table 9.1 for each year and all years taken into account. A statistical test (TS) defined as

$$TS = 2(\log \mathcal{L}_{\rm LP} - \log \mathcal{L}_{\rm PL})$$

[6] https://www.mpi-hd.mpg.de/hfm/HESS/pages/home/som/2016/10/ The Source of the Month is a way to share H.E.S.S. physics with the public with accessible texts.

Year	$-\log\mathcal{L}$ (PL)	$-\log\mathcal{L}$ (LP)	TS	Significance
2004	-199.3	-64.4	269.8	16.4
2005	-14	-11.4	5.2	2.3
2006	-104.8	-81.8	46.0	6.8
2007	-19.7	-19.6	0.2	0.4
2008	-41.7	-33.4	16.6	4.1
2009	-28.8	-25.0	7.6	2.8
2010	-17.9	-16.9	2.0	1.4
2011	-23.0	-21.3	3.4	1.8
2012	-51.1	-49.8	2.6	1.6
All	-523.9	-343.2	361.4	19.0

TABLE 9.1: Values of the log likelihood for the power law and log-parabola spectra, with TS and significance.

Year	$a \pm \sigma_a$	$b \pm \sigma_b$
2004	2.95 ± 0.03	0.37 ± 0.03
2005	3.27 ± 0.12	0.25 ± 0.12
2006	3.27 ± 0.04	0.24 ± 0.04
2007	3.38 ± 0.08	-0.03 ± 0.07
2008	3.28 ± 0.04	0.12 ± 0.03
2009	3.14 ± 0.08	0.18 ± 0.07
2010	3.24 ± 0.08	0.10 ± 0.07
2011	3.08 ± 0.10	0.13 ± 0.08
2012	3.27 ± 0.01	0.12 ± 0.09
All	3.08 ± 0.02	0.26 ± 0.02

TABLE 9.2: Values of the log parabola parameters of the log parabola spectra (Eq. 9.2). Spectra are shown on Figure 9.5.

tells which shape is the best. Since the power law is nested in the log-parabola, there is only one degree of freedom of difference between the two and the TS can be approximated as the square of the significance: $\sigma \simeq \sqrt{TS}$ (Willis theorem).

Table 9.1 shows the likelihood, TS and significance values for each year. The log parabola shape has been chosen over the power law one because for each year the fit was better, even though for some year the significance of the log-parabola fit over the power law one is low.

The values for a and b are summarized in Table 9.2; the average values are $\overline{a} = 3.209$ and $\overline{b} = 0.164$. The variance for the first parameter $s_a^2 = 0.017$ is larger than the expected variance $\overline{\sigma_a^2} = 0.005$ due to the uncertainties σ_a on the individual best fit values. The same is true for the second parameter with $s_b^2 = 0.114$ and $\overline{\sigma_b^2} = 0.005$. This could be indicative of a variable spectrum.

Variations within a season, however, are unlikely to affect the analysis presented here as the inferred small changes in the spectral parameters only result in small changes in the integral flux.

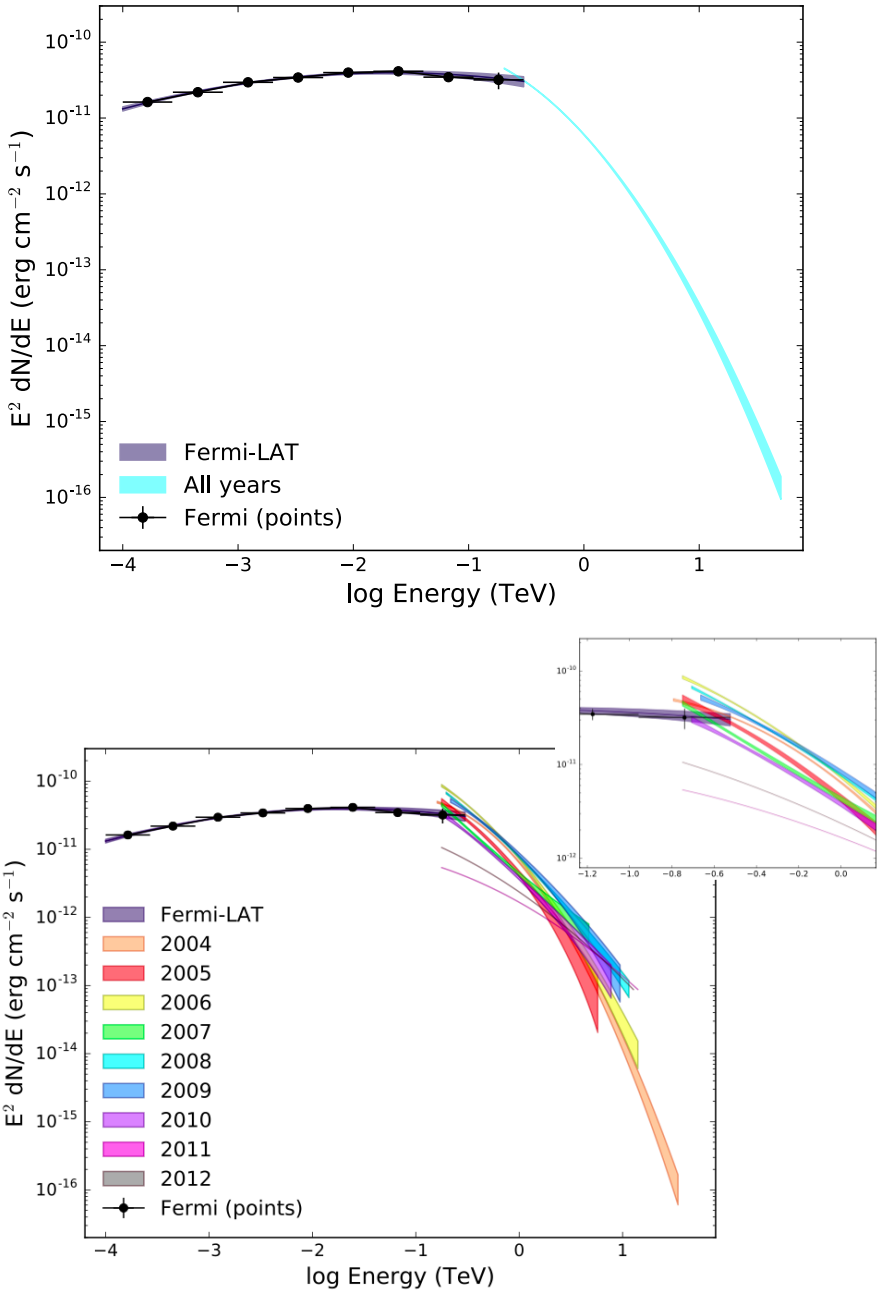

FIGURE 9.5: Fermi and H.E.S.S. SEDs (yearly for H.E.S.S) of PKS 2155-304. Each color represents a different year while the overall spectrum of PKS 2155-304 on the whole data set is in black. The panel at the top right is a zoom to see better the common energy range of H.E.S.S. and Fermi spectra.

Energy range	Mean flux ($cm^{-2}.s^{-1}$)	F_{var}
0.2 - 10 TeV	5.10×10^{-11}	0.66 ± 0.01
0.2 - 0.63 TeV	6.99×10^{-11}	0.65 ± 0.01
0.63 - 10 TeV	0.11×10^{-11}	1.18 ± 0.01

TABLE 9.3: Mean flux and F_{var} values for each energy ranges of the H.E.S.S. analysis.

The resulting quiescent light curve has an average flux of $(5.10 \pm 0.41) \times 10^{-11}\,\mathrm{cm}^{-2}\,\mathrm{s}^{-1}$ above 200 GeV and is shown in Figure 9.7.

The analysis results were cross-checked using different analysis methods and calibration chains (e.g., Aharonian et al., 2006), yielding compatible results.

This analysis procedure has been applied to the same data set using the following energy cuts: 0.2-0.63 and 0.63-125 TeV, the cut at 0.63 TeV being chosen to have approximately the same statistics in each energy band. The light curves of these two bins are shown on Figure 9.6. Table 9.3 presents the mean flux values for each energy range along with the corresponding F_{var}.

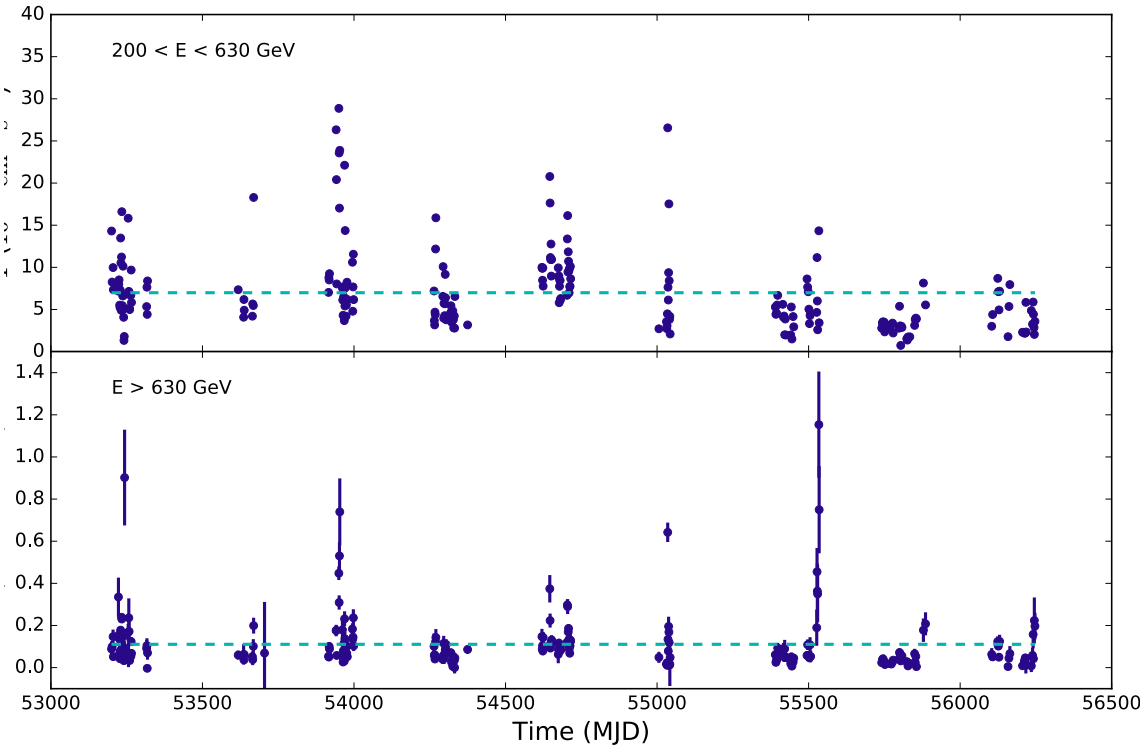

FIGURE 9.6: H.E.S.S. light curve below and above 630 GeV. The dashed line indicates the average flux.

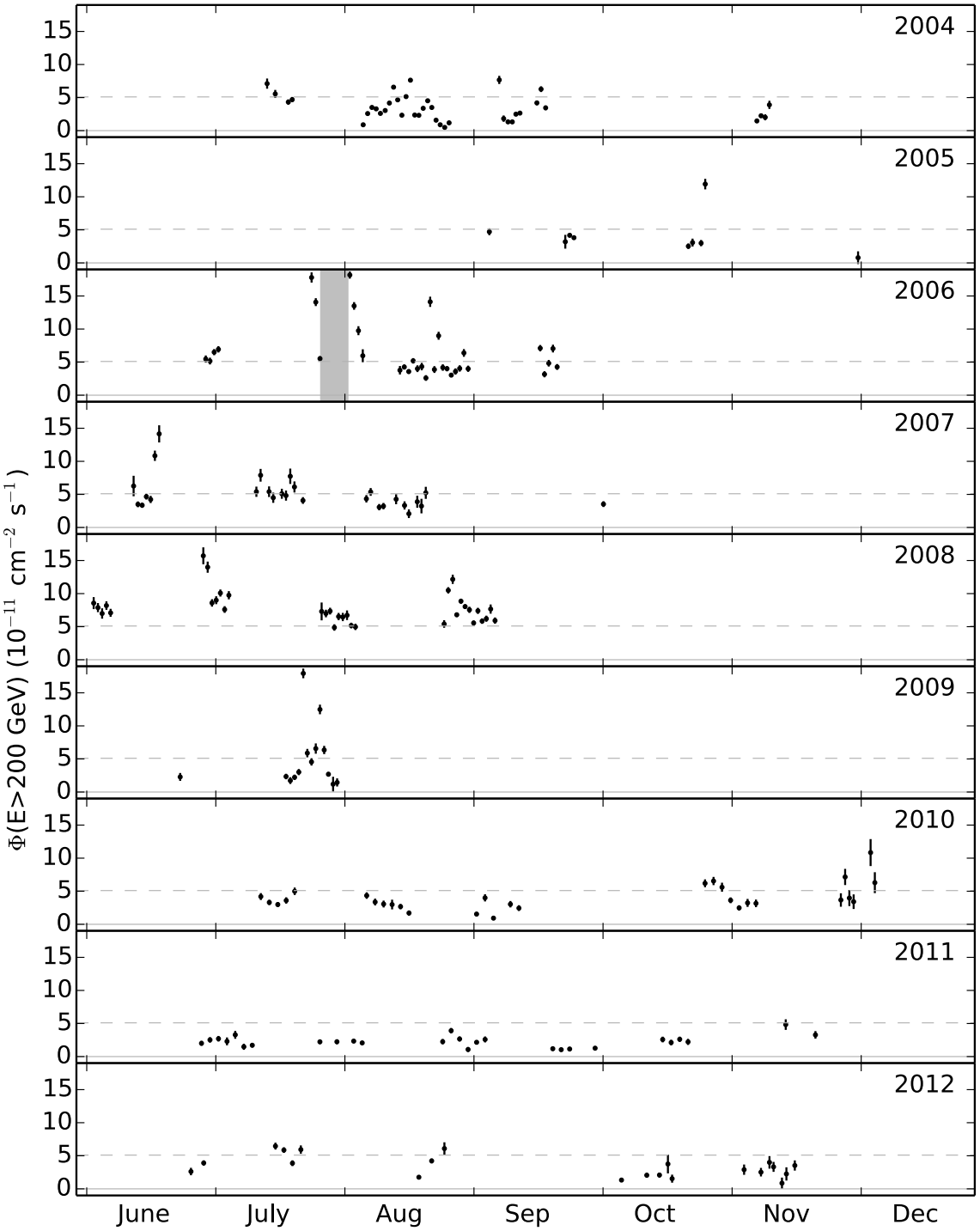

FIGURE 9.7: H.E.S.S. light curve of nightly fluxes above 200 GeV excluding the high state in July/August 2006 (gray-shaded area). The gray-dashed horizontal line marks the average flux of the quiescent state.

9.2.2 HE dataset with *Fermi*-LAT

The set of observational data for PKS 2155-304 used here covers about 5.5 years, from MJD 54688 (August 10, 2008) to 56688 (January 31, 2014). Events are selected between 100 MeV and 300 GeV in a region of interest (ROI) of 15° around PKS 2155-304. The detector is described by the P7REP_SOURCE_V15 instrument response function[7]. The HE light curve is obtained with the tool Enrico (Sanchez and Deil, 2013) using the *Fermi* Science Tools v9r32p5[8], with a 10 days binning to ensure enough statistics in each bin. The prefactor of the diffuse galactic background (gll_iem_v05) and the normalization of the isotropic diffuse emission (iso_source_v05) are left free to vary in the likelihood fit.

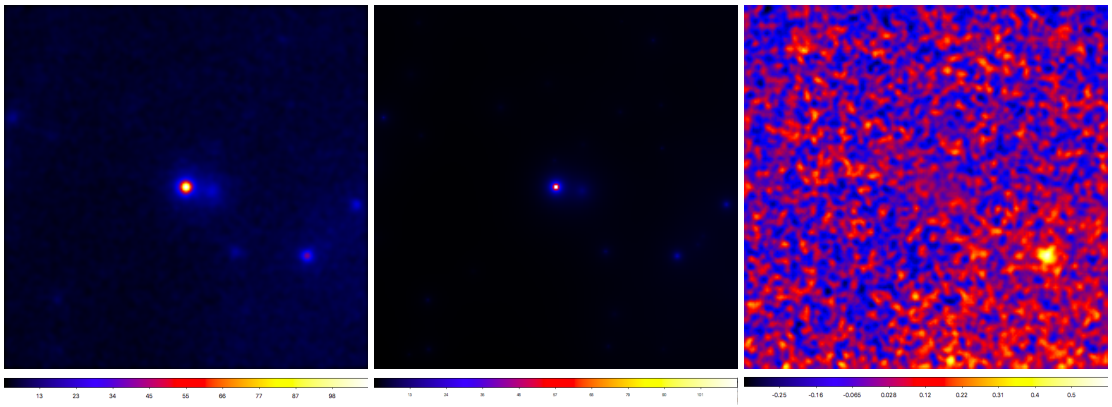

FIGURE 9.8: From left to right: Count map, model map and residual map of the *Fermi*-LAT analysis.

All sources from the third LAT source catalog (3FGL; Acero et al., 2015) within 15° of PKS 2155-304 are included in the sky model to ensure a good background modelling. The HE spectra of PKS 2155-304 and all sources within 3° are fitted following the spectral shape of the 3FGL catalog. The spectra of PKS 2155-304, 3FGL J2151.6-2744 and 3FGL J2159.2-2841 are modelled with a simple power law, while for 3FGL J2151.8-3025 a log-parabolic shape is assumed. The indices and pre-factors are left free. All other components are fixed to the values in the 3FGL catalog.

Figure 9.8 displays 3 maps produced during the analysis: count map, model map and residual map. The model map comes from the sky model described above. The residual map, which is the count map minus the model one, allows to check if every source in the field of view of the analysis has been modelled properly. The residual map should be smooth. There seems to be a hot area at the bottom right but it is negligible as the spot is far from the source.

PKS 2155-304 is detected with a significance of 156 σ with a photon index of 1.83 ± 0.01. The photon counts of PKS 2155-304 are integrated into 201 bins of 10 days.

The resulting light curve has an average flux of $1.20 \pm 0.03 \times 10^{-7}\,\mathrm{cm}^{-2}\,\mathrm{s}^{-1}$ between 100 MeV and 300 GeV and is shown in Fig. 9.9. The same analysis has been applied below and above 1 GeV. The resulting light curves are show on Figure 9.10. Table 9.4 shows the mean flux values and the F_{var} for each energy range analyzed.

[7] http://fermi.gsfc.nasa.gov/ssc/data/analysis/documentation/Pass7REP_usage.html

[8] cf. the *Fermi* Science Support Center web site http://fermi.gsfc.nasa.gov/ssc/

Energy range	Mean flux ($cm^{-2}.s^{-1}$)	F_{var}
0.1 - 300 GeV	1.20×10^{-7}	0.42 ± 0.04
0.1 - 1 GeV	0.91×10^{-7}	0.36 ± 0.04
1 - 300 GeV	0.19×10^{-7}	0.43 ± 0.02

TABLE 9.4: Mean flux and F_{var} values for each energy ranges of the *Fermi*-LAT analysis.

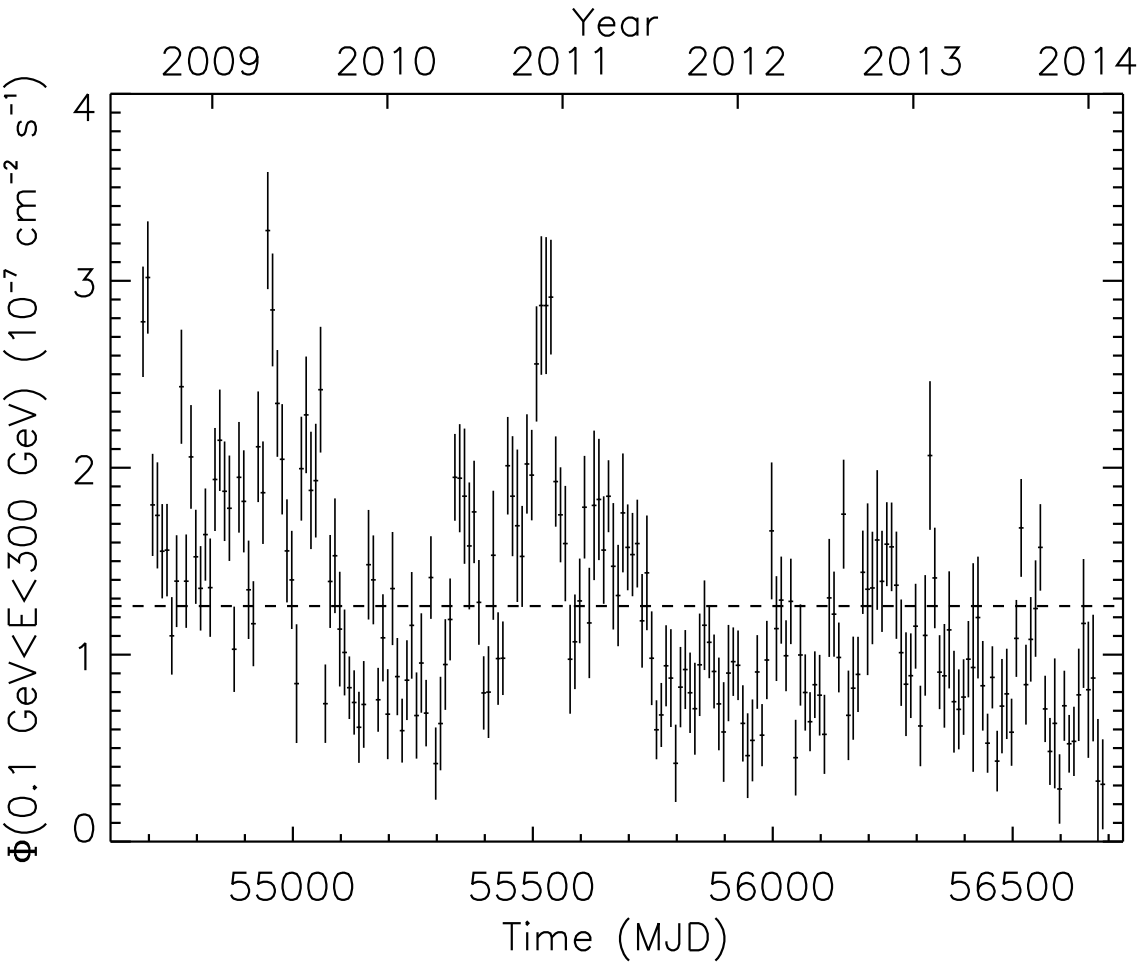

FIGURE 9.9: Light curve of the integral fluxes between 0.1 and 300 GeV in bins of ten days measured with *Fermi*-LAT from Paper H.E.S.S. PKS 2155-304. The dashed line indicates the average flux.

9.2.3 X-ray dataset with *RXTE*, *Swift*-XRT and XMM-Newton

X-ray experiments are older than GeV or TeV experiments since the technology was developed earlier. Hence they have monitored the sky since a longer time. Because of its regular outbursts, PKS 2155-304 triggered quite a lot of Target of Opportonity (ToO) observations. In 2008, *RXTE* and *Swift* started an interesting monitoring program. Monitoring data from XMM-Newton complete the data set.

Because of the activity of PKS 2155-304 in X-ray, the resulting light curve contains a lot of ToO. They have been removed, by hand looking at the history of the data-taking, in order to not bias the data set and only have the light curve of the quiescent state of PKS 2155-304.

The light curve, shown on Figure 9.11, goes from MJD 53501 to 55474 in five different

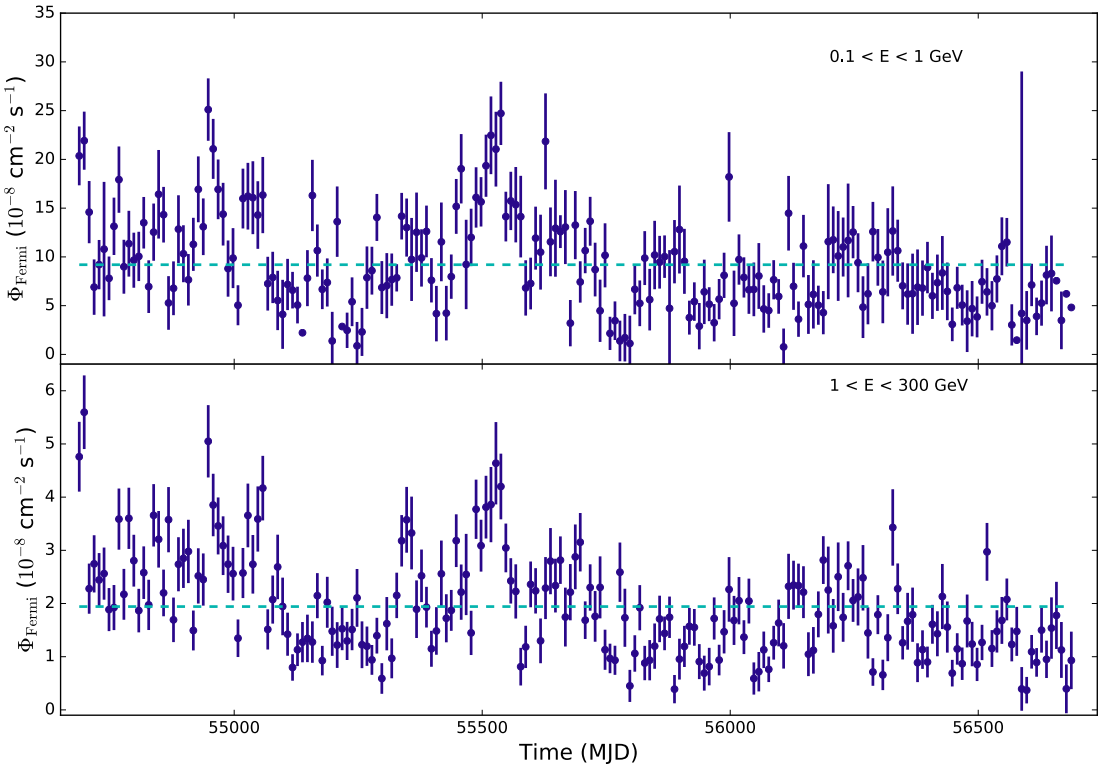

FIGURE 9.10: Light curve of the integral fluxes below and above 1 GeV in bins of ten days measured with *Fermi*-LAT. The dashed line indicates the average flux.

energy ranges. The main energy range, 2 to 10 keV, is the common of all three instruments. The sub energy ranges are: 0.3-2 keV (only *Swift* and XMM), 2-4 keV, 4-7 keV, 7-10 keV with their light curves shown on Figure 9.12.

RXTE data consists in already analyzed light curved publicly available[9] in four energy ranges: the full range from 2 to 10 keV and three subranges 2-4, 4-7 and 7-10 keV.

Swift data were analyzed using the package `HEASOFT 6.16` in the following energy bands: 0.3-2, 2-4, 4-7, 7-10 and 2-10 keV. The data were recalibrated using the last update of `CALDB` and reduced using the standard procedures `xrtpipeline` and `xrtproducts`. Caution has been taken to properly account for pile-up effects for corresponding affected exposures, and spectral fits were performed using `Xspec 12.8.2` assuming a power-law spectrum. Data have been corrected from the Galactic absorption with $n_{\rm H} = 1.48 \times 10^{20}$ cm^{-2}.

XMM public EPIC (European Photon Imaging Camera) data were reduced using the SAS software package (version 14.0) and analyzed following Tatischeff, Decourchelle, and Maurin, 2012 in the following energy ranges: 0.3-2, 2-4, 4-7, 7-10 and 2-10 keV. As for *Swift*-XRT, data have been corrected from the Galactic absorption with $n_{\rm H} = 1.48 \times 10^{20}$ cm^{-2} (Kalberla et al., 2005).

In all common energy bins, light curves of the three instruments are combined to construct an overall X-ray light curve. The final light curve presented in Figure 9.11 goes

[9] http://cass.ucsd.edu/rxteagn/

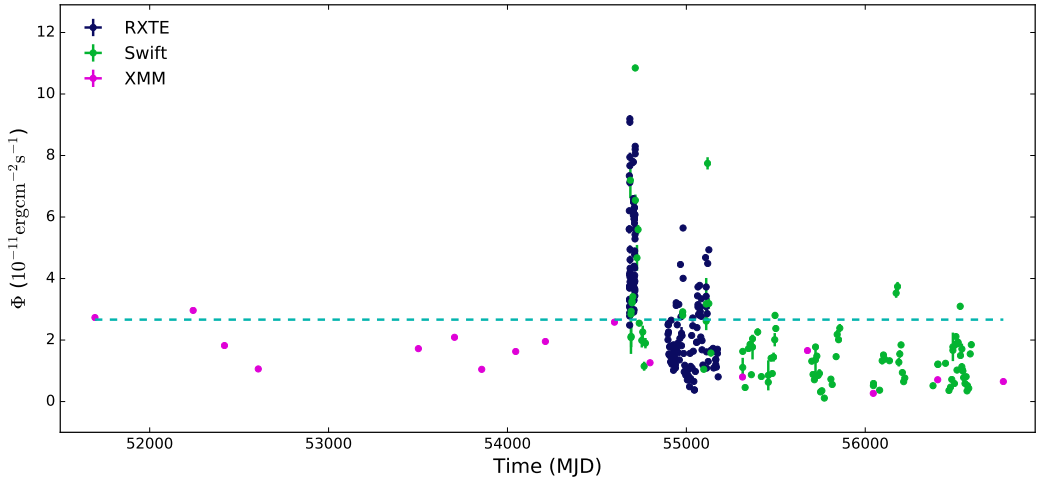

FIGURE 9.11: Light curve of the integral X-ray fluxes in the main range 2-10 keV. *Swift*-XRT data are the black dots, *RXTE* data are represented with a blue square and XMM-Newton data with a pink triangle.

from MJD 53501 to 55474 with an average flux of 2.67×10^{-11} erg.cm^{-2}.s^{-1}. Table 9.5 shows the mean flux and $F_{\rm var}$ values for the 5 energy bins.

Energy range	Mean flux (erg.cm^{-2}.s^{-1})	$F_{\rm var}$
2 - 10 keV	2.67×10^{-11}	0.74
0.3 - 2 keV	5.89×10^{-11}	0.59
2 - 4 keV	1.71×10^{-11}	0.72
4 - 7 keV	0.76×10^{-11}	0.80
7 - 10 keV	0.36×10^{-11}	0.89

TABLE 9.5: Mean flux and $F_{\rm var}$ values for each energy ranges of the X-ray analysis.

9.2.4 Optical dataset with SMARTS

SMARTS (Bonning et al., 2012) consists of four 1-meter class telescopes on Cerro Tololo, Chile. Their data are of particular interest since the consortium launched a program to observe the blazars monitored by the *Fermi*-LAT (those visible from Chile at least) using 700 hours per year with two of the four telescopes. This program is called SMARTS Optical/IR Obsevations of Fermi Blazars.

Their data are publicly available[10]. Magnitudes are corrected for the absorption of the Galactic foreground using Schlafly and Finkbeiner, 2011 and converted to a spectral flux density using zero flux values of Cohen, Walker, and Witteborn, 1992. The light curves (Fig.9.13) are taken in four bands (J, R, V and B) from MJD 54603 to 56622, following the monitoring of *Fermi*. The mean flux and variability value for each band can be found on Table 9.6.

In this energy band, the units are quite different from the ones usually used elsewhere: the flux is expressed in Jansky (Jy) instead of $\rm cm.^{-2}s^{-1}$ or $\rm erg.cm^{-2}.s^{-1}$ and the energies are expressed in optical band names instead of electron-Volts.

[10] http://www.astro.yale.edu/smarts/glast/home.php#

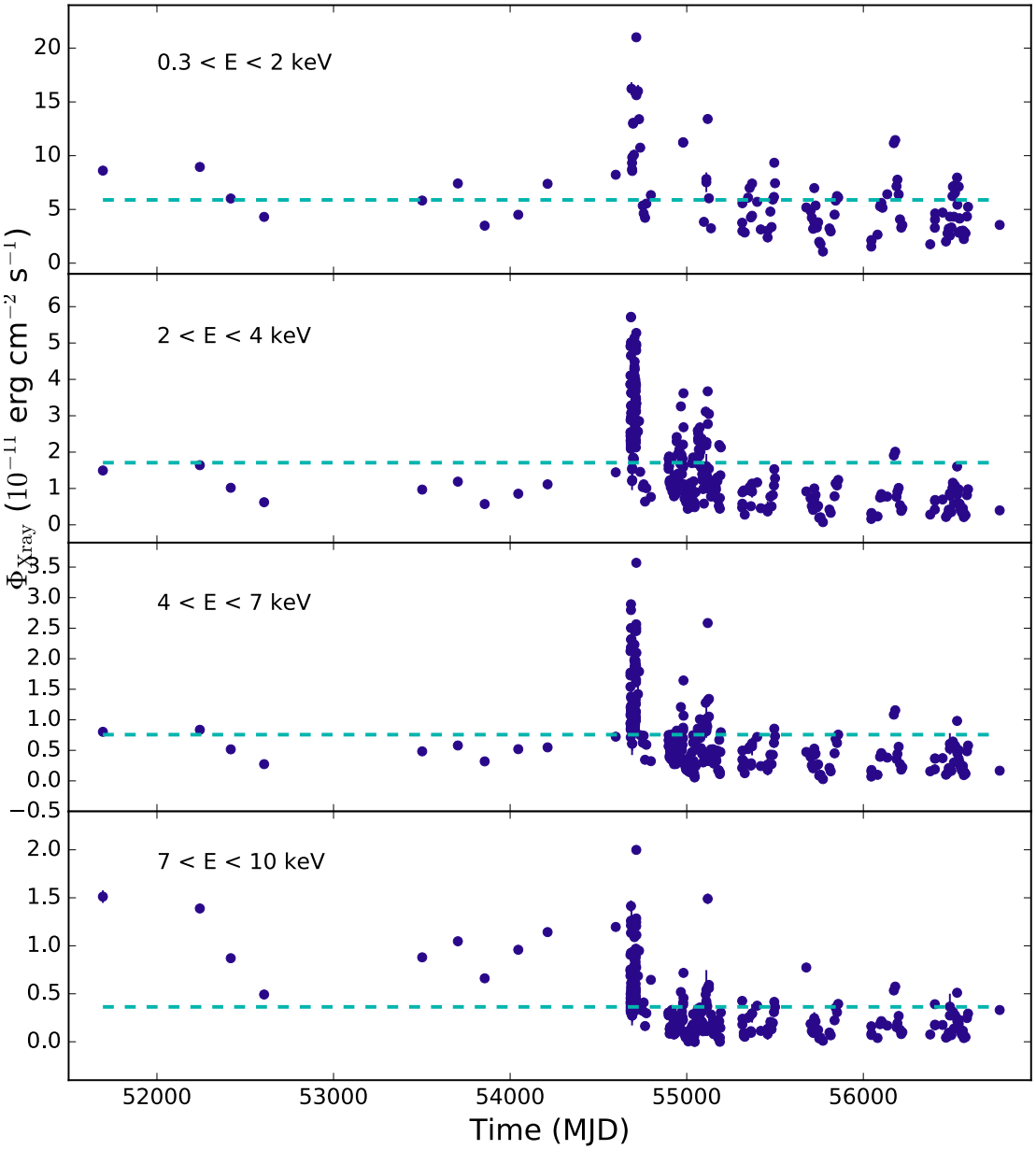

FIGURE 9.12: Light curves of the integral X-ray fluxes in the subranges (from top to bottom) 0.3-2 keV, 2-4 keV, 4-7 keV and 7-10 keV. Unlike Figure 9.11 data from *Swift*-XRT, *RXTE* and XMM-Newton are all in the same color.

The Jansky can be expressed by :

$$1\mathrm{Jy} = 10^{-23}\mathrm{erg.cm}^{-2}.\mathrm{s}^{-1}.\mathrm{Hz}^{-1}$$

where the Hz^{-1} represents the energy band width associated with every optical band.

The photometric system is represented by a letter and each letter designates a particular section of the electromagnetic spectrum. The values used in this work are:

- B: $\lambda = 445 \pm 94$ nm $\leftrightarrow E = 2.79^{+0.75}_{-0.49}$ eV
- V: $\lambda = 551 \pm 88$ nm $\leftrightarrow E = 2.25^{+0.43}_{-0.31}$ eV
- R: $\lambda = 658 \pm 138$ nm $\leftrightarrow E = 1.88^{+0.50}_{-0.33}$ eV
- J: $\lambda = 1220 \pm 213$ nm $\leftrightarrow E = 1.02^{+0.21}_{-0.15}$ eV

Energy range	Mean flux (Jy)	F_{var}
J	3.18×10^{-2}	0.38
R	1.81×10^{-2}	0.37
V	1.79×10^{-2}	0.37
B	1.46×10^{-2}	0.38

TABLE 9.6: Mean flux and F_{var} values for each energy ranges of the SMARTS light curves.

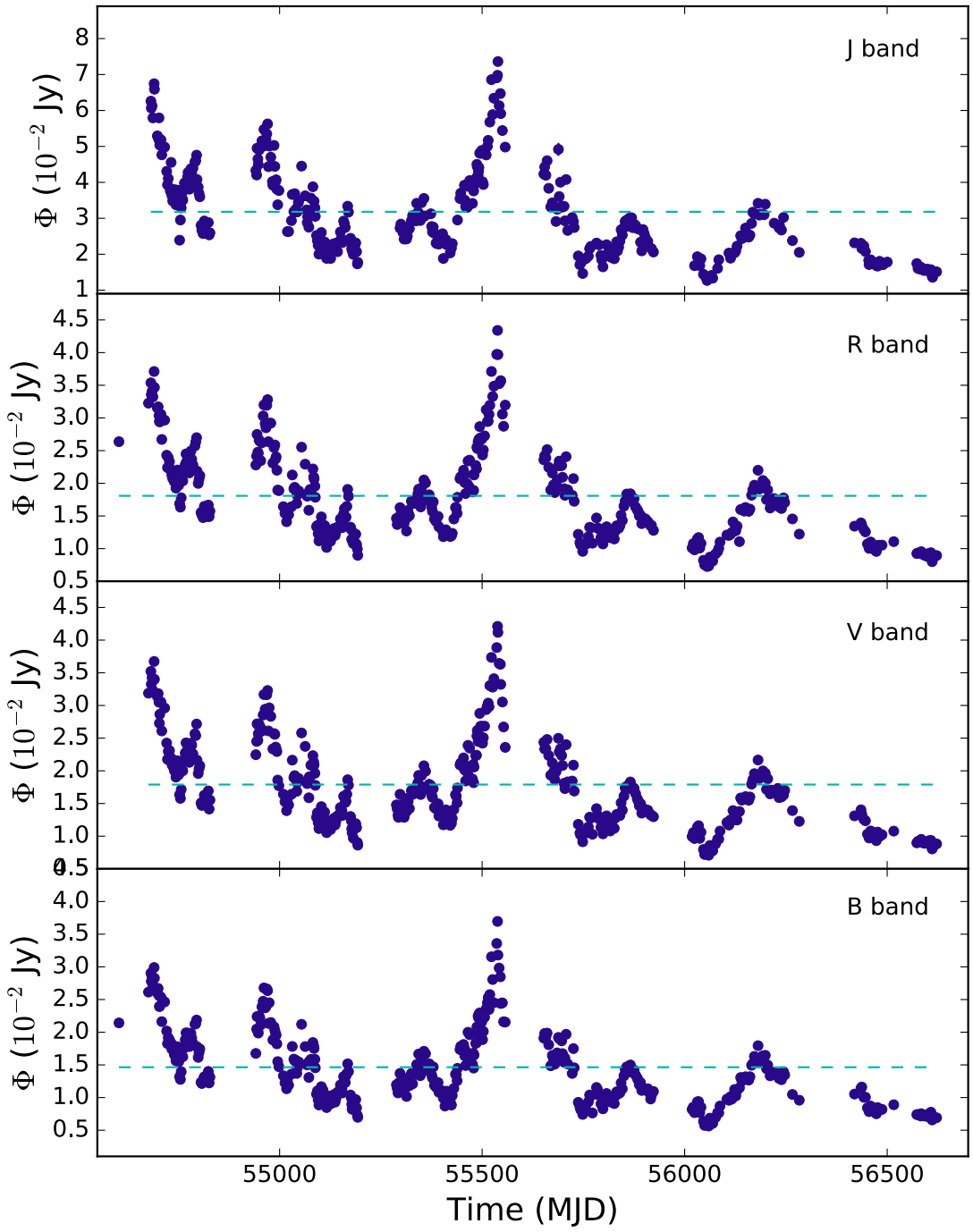

FIGURE 9.13: Light curve of the SMARTS optical fluxes in the J, R, V and B bands (from top to bottom) measured with SMARTS. The dashed line indicates the average flux.

9.3 Time series analyses

In the following I will present time series analysis on all the different light curves presented in Section 9.2, allowing to study the variability of the blazar at different time scales and from optical to TeV.

9.3.1 PSD in γ rays

In Paper H.E.S.S. PKS 2155-304, the H.E.S.S. and *Fermi*-LAT light curves have been studied looking at their lognormal behavior (see Section 9.3.5) and their PSD. Figure 9.14 shows the H.E.S.S. and *Fermi*-LAT PSD from Paper H.E.S.S. PKS 2155-304. This analysis showed that light curves in the GeV and TeV ranges are well described by a flicker noise with $\beta_{\text{H.E.S.S.}} = 1.10^{+0.10}_{-0.13}$ and $\beta_{Fermi} = 1.20^{+0.21}_{-0.23}$. To derive these numbers, light curves with power law noise were simulated with different power law index values and rebinned following the temporal binning of the data. Their PSDs were then fitted to the data to find the best fit. The power law index value given above corresponds to the initial value of the power law noise of the un-binned light curves. Because of the temporal binning, the time series loose power at different time scales especially in H.E.S.S. were the power law index of the PSD of the data is closer to 0.

In both ranges, no break is found.

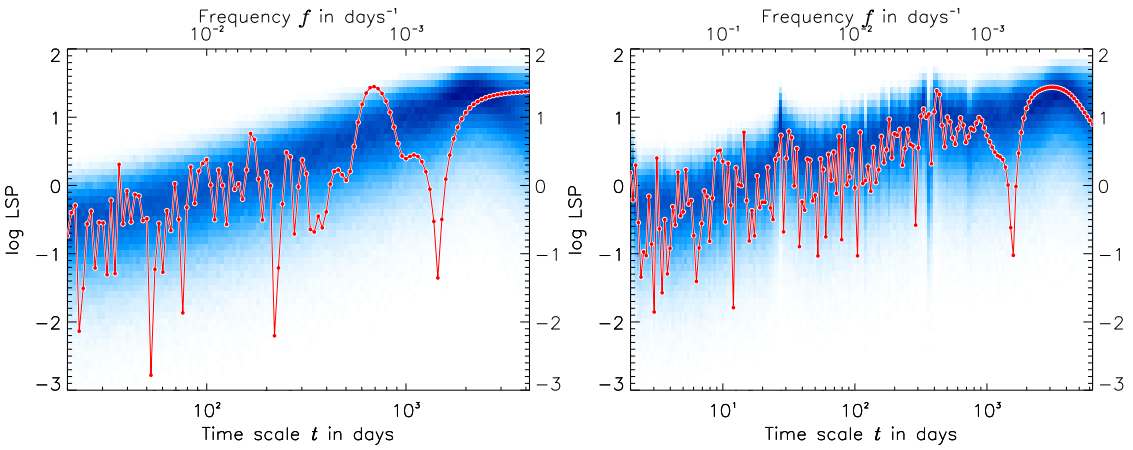

FIGURE 9.14: PSD of the quiescent light curve of PKS 2155-304. The red solid line represents the data and blue histograms are the best fit PSD of the simulated light curves. Left: *Fermi*-LAT. Right: H.E.S.S.

9.3.2 Variability energy distribution $F_{\text{var}}(E)$

The fractional root mean square variability (see Equation 9.1) is a very handful tool to quantify the amount of variability in light curves and compare different energy bands.

Figure 9.15 shows the evolution of the variability with energy, where F_{var} is computed for each energy of the dataset presented in Section 9.2.

The optical and GeV variability are around the same value of $\sim 40\%$ showing that these two energy bands behave the same in terms of variability. The variability in the X-ray and TeV ranges are higher, with a strong increase reaching $\sim 120\%$ in TeV. Interestingly, this variability energy profile shows the same behavior in the Synchrotron high energy parts of the SED.

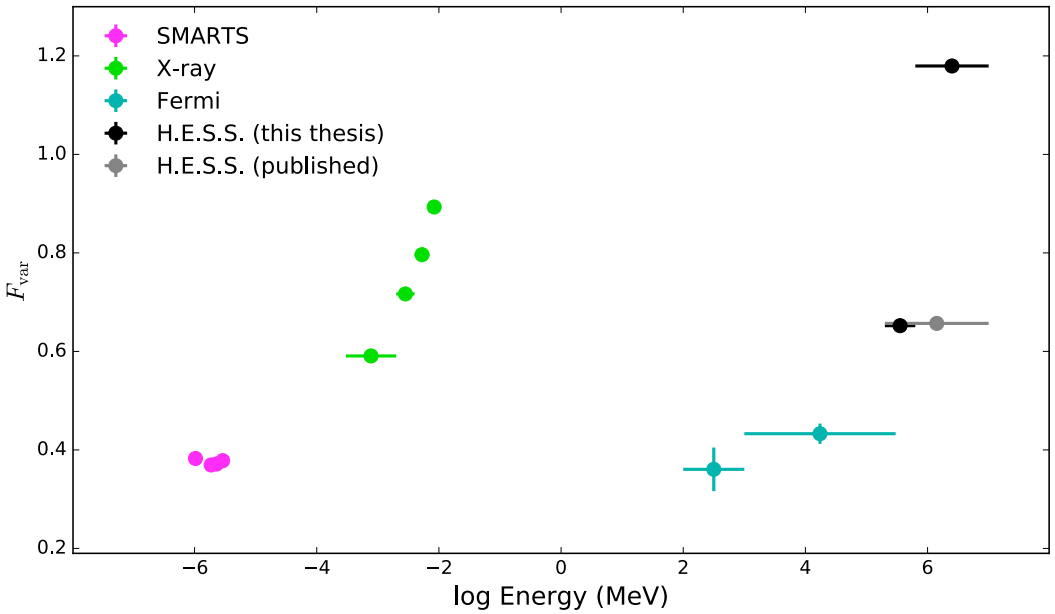

FIGURE 9.15: Variability profile $F_{\rm var}(E)$ for the whole dataset: the 4 energy bins of SMARTS (pink), the 4 X-ray energy bins composed of *RXTE*, *Swift*-XRT and XMM-Newtom data (green), the 2 energy bins of *Fermi* LAT (blue) and the H.E.S.S. points (black). The grey H.E.S.S. point corresponds to the one published in Paper H.E.S.S. PKS 2155-304.

The grey point on Figure 9.15 corresponds to the $F_{\rm var}$ value for the published H.E.S.S. light curve of Paper H.E.S.S. PKS 2155-304 over the full H.E.S.S. energy range. By splitting the energy range in two parts, we gain more information with a really significative increase of the variability betwen 200 GeV and $\sim$ 10 TeV.

9.3.3 Cross-correlations

Correlation studies can probe the link between processes, particles population, and emitting regions. In the framework of the SSC model, where the same electron population emits both the Synchrotron and Inverse Compton radiation, correlations between energy bands are expected especially between eV-GeV and keV-TeV ranges. *Fermi*-LAT and SMARTS light curves, being quasi contemporaneous and quasi continuous, are the best data set to test it. The X-ray and H.E.S.S. data are too sparse to study in details the correlations with these energy bands and come up with a conclusion.

To test the correlation between two light curves, a discrete correlation function (DCF) is used. The GeV and optical light curves have different binning, hence the SMARTS flux are re-binned on the 10-day binning of the *Fermi*-LAT light curve to compute the Pearson correlation factor for each time lag. This method gives the same results using the method of Edelson and Krolik, 1988 except that the DCF is perfectly normalized between -1 and 1. To evaluate confidence intervals, 1000 light curves for each band have been simulated following the power law noise of the data with the method of Timmer and Koenig, 1995 (explained in more details in Section 10.3 of Chapter 10). The *Fermi*-LAT light curve has already been characterized in Paper H.E.S.S. PKS 2155-304 by a power-law index $\beta \simeq 1.2$. The PSD of SMARTS light curves have been fitted by a power-law, showing also $\beta \simeq 1.2$ (see next subsection). Then the temporal binning and windowing

of the real data is applied along with the re-binning of the SMARTS data to compute the DCF. Each DCF is presented along with the one sigma limit of the results of the simulated light curves.

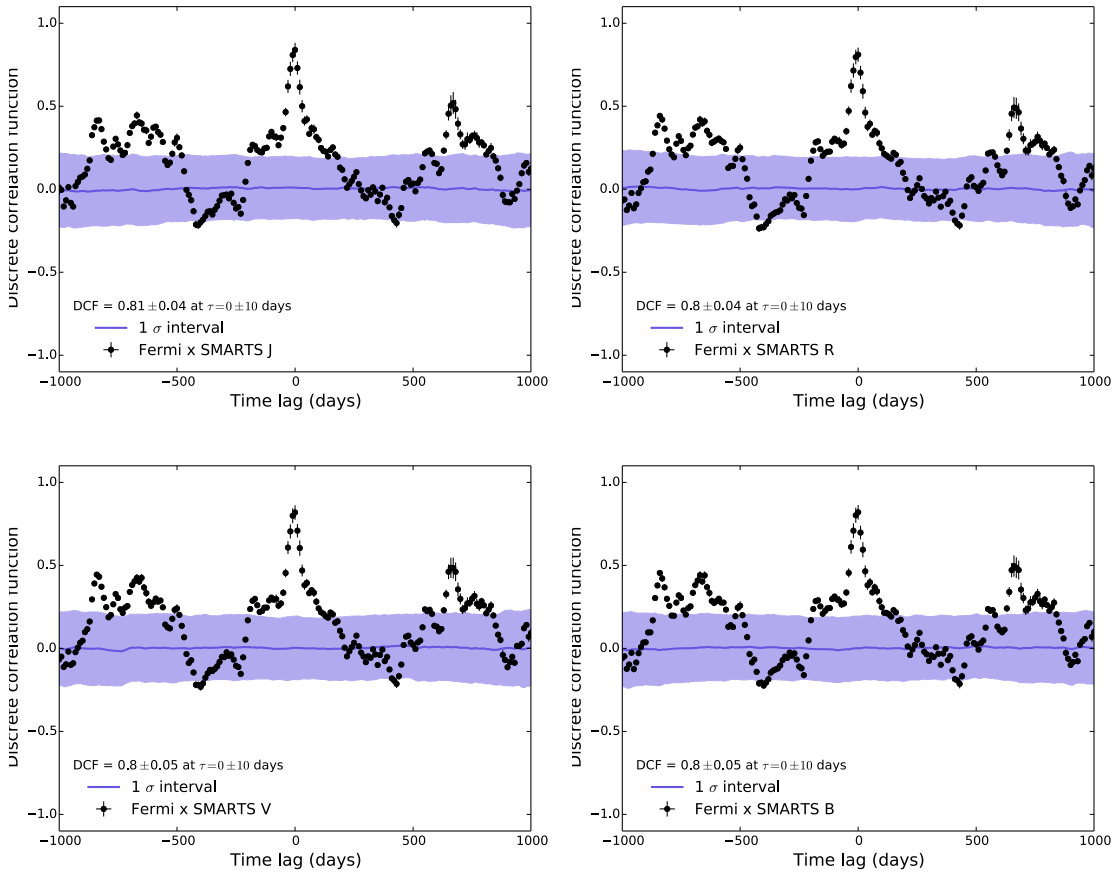

FIGURE 9.16: Discrete Correlation Function (DCF) between the *Fermi*-LAT and SMARTS light curve (black points), the value of the correlation at $\tau = 0$ is always around 0.8. The blue curves show the one sigma confidence level using the Monte Carlo. Top left: *Fermi*-LAT x J-band. Top righ: *Fermi*-LAT x R-band. Bottom left: *Fermi*-LAT x V-band. Bottom right: *Fermi*-LAT x B-band.

For the SMARTS x *Fermi* light curves, the DCF shows a maximum of $\sim 0.82 \pm 0.04$ for all four DCFs at a time lag $\tau = 0 \pm 10$ days showing that the GeV and optical ranges of PKS 2155-304 are strongly correlated with a $\sim 4.5\sigma$ indication by the simulations. More, the two local maxima at $\tau \simeq 700$ days are a signature of the periodicity studied in the next section, showing that the periodicity of both energy bands are correlated too.

Numerical computation of the DCF

The principle of the DCF is simple: one computes the correlation factor ρ (see equation below) for each time lag τ between light curves. However, in practical, it is not as simple. Light curves are defined on different time scales: the binning is different with sometimes holes in the light curve when the source is not under constant monitoring (which is the case only for *Fermi*-LAT). The correlation factor is defined as:

$$\begin{aligned}\rho(\tau) &= \frac{\mathrm{cov}(\Phi_1(t), \Phi_2(t+\tau))}{\sigma_1\sigma_2} \\ &= \frac{1}{N\sigma_1\sigma_2}\sum_{i=0}^{N}(\Phi_1(t_i) - \overline{\Phi_1}) \times (\Phi_2(t_i+\tau) - \overline{\Phi_2})\end{aligned}$$

where Φ_1 and Φ_2 are the fluxes of the 2 light curves for the DCF computation, $\overline{\Phi}$ is the mean of the flux and σ its variance. Assuming that the error on the variance is negligible, the error on the correlation factor can be written:

$$\begin{aligned}\mathrm{d}\rho(\tau) &= \frac{1}{N\sigma_1\sigma_2}\sum_{i=0}^{N}[(\mathrm{d}\Phi_1(t_i) - \mathrm{d}\overline{\Phi_1}) \times (\Phi_2(t_i+\tau) - \overline{\Phi_2}) \\ &- (\Phi_1(t_i) - \overline{\Phi_1}) \times (\mathrm{d}\Phi_2(t_i+\tau) - \mathrm{d}\overline{\Phi_2})]\end{aligned}$$

$\rho(\tau)$ can be computed for each τ where $\Phi_1(t)$ and $\Phi_2(t+\tau)$ exist. The light curves have to be in the good format to have both the same binning and same size. I chose to bin them on a 10-days binning to keep the *Fermi*-LAT light curve untouched.

Let's define a bin at the position $t_i \pm \Delta t_i$ ($\Delta t_i = 5$ days). If $\Phi_{1\mathrm{or}2}$ exists in this interval, the flux is averaged in it, otherwise, the bin will contain the value 0. This is what is represented below.

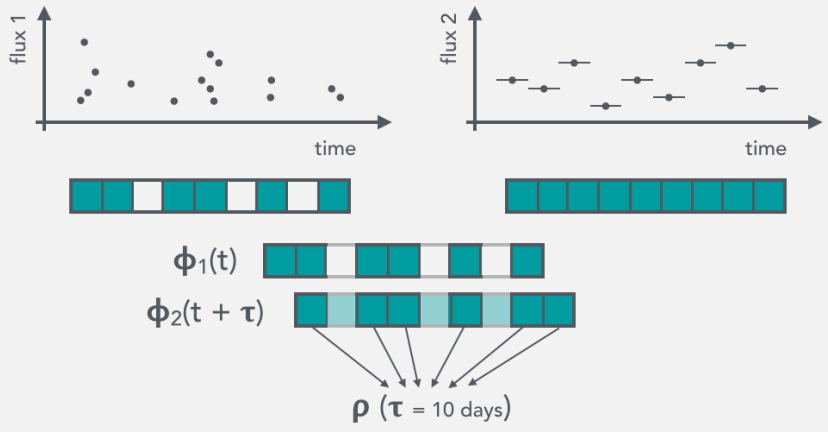

At the end of the re-binning step, the two light curves must contain the same number of points, with some of them being zero. Choosing a time lag τ, one takes only the common bin where there is no zero to compute ρ. A safety has been applied to compute ρ only if there are at least 10 points in common in both light curves (otherwise the value is subject to strong non meaningful fluctuations).

9.3.4 Periodicity

It has been reported in the litterature (Paper H.E.S.S. PKS 2155-304; Sandrinelli, Covino, and Treves, 2014, and references therein) that PKS 2155-304 was showing a possible periodic behavior of period $T \sim 300$ or ~ 700 days. The cross correlation results presented in the previous section indicate a periodic behavior with $T \sim 700$ days also in the SMARTS and *Fermi*-LAT light curves.

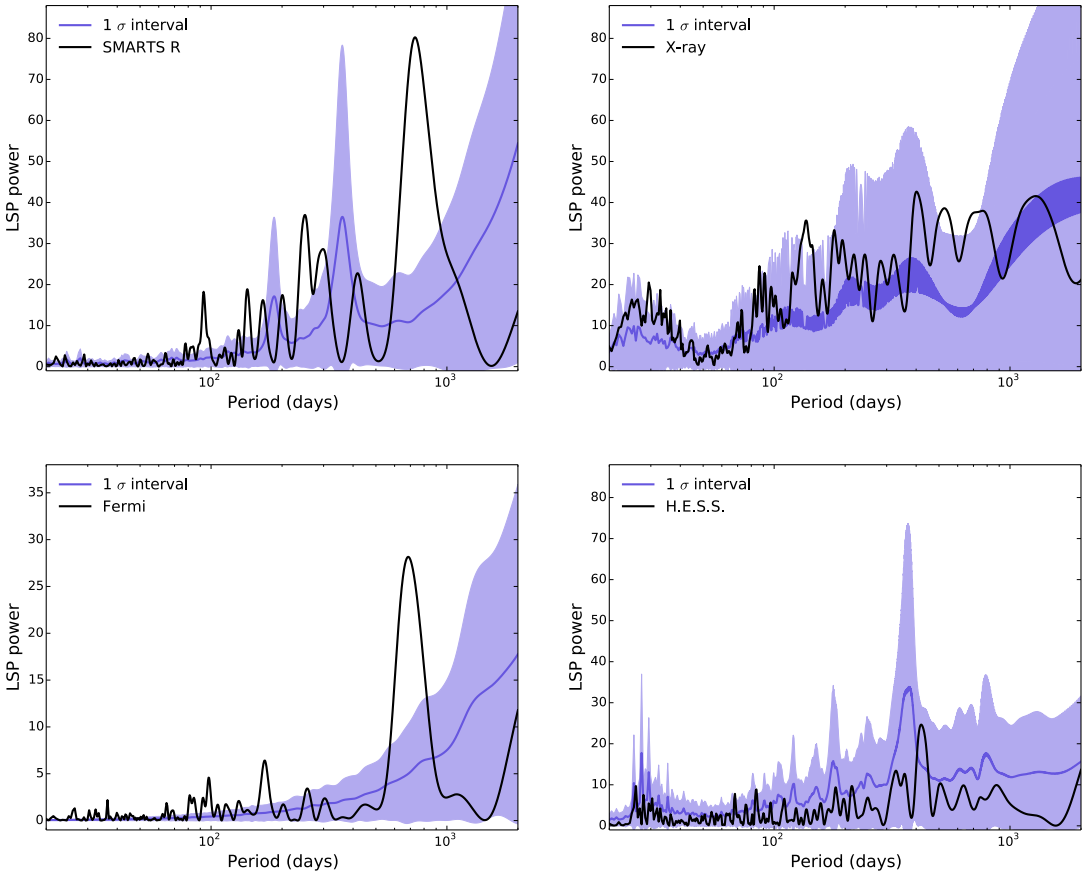

FIGURE 9.17: Lomb Scargle periodogram for the R band of SMARTS (top left), the full range Xray light curve (top right), the full range *Fermi*-LAT data (bottom left) and the H.E.S.S. full range (bottom right). The black line represents LSP applied to the data, while the blue area is the 1 σ confidence interval coming from the simulations, with the mean value represented by the blue line.

To study further this periodic feature, the multi-wavelength light curves are analyzed with a Lomb Scargle periodogram (LSP; Lomb, 1976; Scargle, 1982). The LSP is a method to estimate the PSD of a time series based on a least squares fit of sinusoids to the data sample. The advantage of the LSP compared to a classical Fourier analysis is that it takes into account the non-even spacing of the data. This is why the LSP computation is often used in astrophysics where the data, for pratical reasons, can not be evenly spaced.

The LSPs of the SMARTS, X-ray, *Fermi*-LAT and H.E.S.S. light curves are shown on Figure 9.17 along with the 1 σ confidence interval. The X-ray and H.E.S.S. light curves do not show any periodic feature, as it could be expected due to the sparsing of the data. As expected from the DCF results, the SMARTS and *Fermi*-LAT light curves show a period

TABLE 9.7: Values of the reconstructed period (taking the peak with the highest significance) with the Lomb-Scargle Periodogram for *Fermi*-LAT (all ranges) and the different optic bands of SMARTS.

	Period (days)
Fermi-LAT (full range)	685 ± 8.5
Fermi-LAT (< 1 GeV)	677.7 ± 12.6
Fermi-LAT (> 1 GeV)	687.4 ± 9.1
SMARTS (B)	731.8
SMARTS (V)	728.8
SMARTS (R)	732.8
SMARTS (J)	715.3

around 700 days. The periods found for each energy range of the SMARTS and *Fermi*-LAT light curves are summarized on Table 9.7.

In order to know if the peaks of the LSP are the products of noise/fluctuations or a feature due to the temporal binning and windowing of the light curve and to know if the periodicity seen is significant, we used the same procedure as the one describe previously: light curves are simulated following the data behavior (generation of power law noise + re-binning of the simulated light following the real data binning).

The errors on the period are calculated using a simple Monte-Carlo by propagating the flux errors on the LSP. In *Fermi*-LAT, errors are dominated by the statistical errors on the flux, and the 10-days binning does not have a strong effect on the period reconstructed since it is of the order of several hundreds of days. Contrariwise, the error on SMARTS data are really small, so the uncertainty is close to zero.

The LSP applied on *Fermi*-LAT data shows one highly significant peak at $T \simeq 680$ days with 5 σ significance compared to simulations, even when splitting the light curve below and above 1 GeV.

The LSP of SMARTS show more features because of the binning of the data (see discussion next page). The data are showing one highly significant peak at $T \simeq 730$ days with a 5σ significance compared to simulations. Other peaks at smaller time scales are believed to be traces of the windowing of the data along with some possible quasi-periodicities in the long term light curves.

A simple power law fit was made on the LSP of Figure 9.17 and gave similar results as the one of the Paper H.E.S.S. PKS 2155-304 with $\beta \sim 1$ for the X-ray and SMARTS light curves.

LSP and temporal binning

The LSP is a method sensitive to the temporal binning of the data, especially to holes in the sample. Figures below show the LSP applied only to simulations following the SMARTS, X-ray, *Fermi*-LAT and HE.S.S. binnings.

Since *Fermi*-LAT is monitoring with evenly spaced data, the LSP shows no features. However SMARTS and H.E.S.S. LSPs' show clear peaks corresponding to the periodicity of the data taking. H.E.S.S. takes data on sources every year for a period of few weeks. The peak highlighed at ~ 360 days on the LSP of H.E.S.S. is the result of such windowing. Concerning SMARTS, the light curve shows holes $\sim 100 - 150$ days, because telescopes were not taking data. This results in two peaks at ~ 172 and ~ 378 days highlighted. Concerning the X-ray light curves, its LSP only displays temporal binning and windowing features. But these features are more difficult to analyse since the X-ray light curve is the result of the merging of 3 different datasets.

The LSP of the X-ray and H.E.S.S. data do not show any periodic feature. What if the strong windowing of the light curves along with the stochastic variability was hiding or killing the periodic signal?

I did a quick test, generating a sinusoid of period $T = 700$ days following the binning of the X-ray and H.E.S.S. data. In one case, the sinusoid is free of noise, in the other case, I added 30 % and 70 % of noise (generated using a normal law). A single sinusoid with a even binning would give a single peak at $T = 700$ days. The results for these tests are shown below, with the X-ray binning on the left and the H.E.S.S. binning on the right.

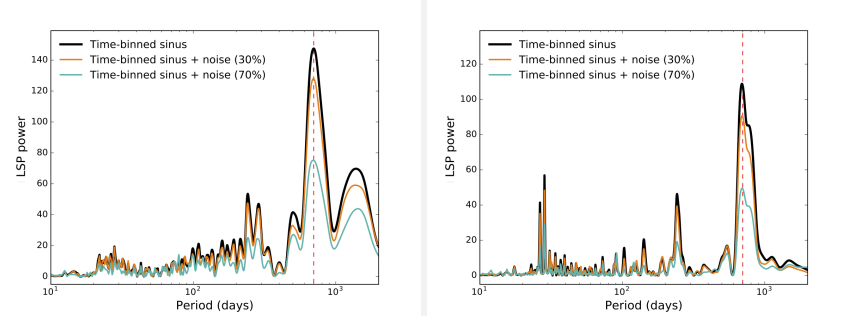

The 700 days is marked with the dashed red line. The black line represents the LSP of the noise-free sinusoids while the orange and blue lines are the LSPs of the noisy sinusoids (respectively 30 and 70 % of the amplitude). The different look and peaks of the LSP between the X-ray and H.E.S.S. is explained only by the different temporal binning of the time series. However in both cases, the addition of the noise decreases the power of the peaks, but the peak at $T = 700$ days stays visible in all cases.

Without applying any binning, the power of the peak is around 1500 instead of $120 - 140$, meaning that the re-binning of the light curves results in a great loss of power for the peak.

Why the periodicity seen in *Fermi*-LAT is not an artifact

At first puzzled by the periodic behavior of the *Fermi*-LAT light curve, I made a quick test on an other source: the Vela pulsar. The flux is known to be steady on long time scales as represented on the light curve below. The analysis has been done following the same procedure as for PKS 2155-304 except that the binning is 12 days instead of 10.

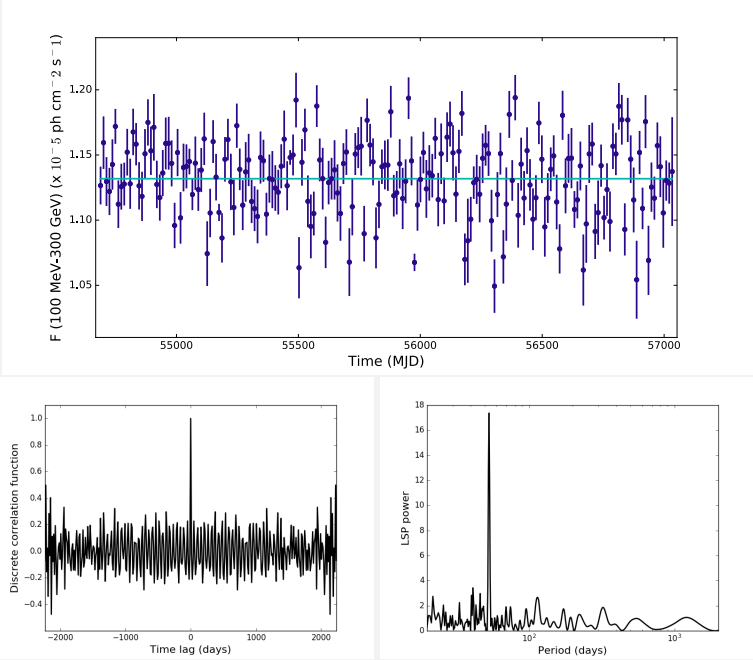

The naked eye does not see any long term periodicity on the light curve and this is confirmed by the discrete auto-correlation function showing only a peak at $\tau = 0$ days. However, the LSP is showing a strong peak at $T = 53 \pm 12$ days. The Vela pulsar is not known for any pulsation at this time scale. It corresponds to the 55 days precession of the orbit of the *Fermi* telescope. Vela is a particularly bright source, this is why this analysis effect is observable here. On the light curves of PKS 2155-304 or other objects, this effect is not observed.

9.3.5 Lognormal behavior

A lognormal behavior, in opposition to normal behavior, is when the logarithm of the variable, here the flux, follows a normal behavior, not the variable itself. Looking at the Central Limit Thereom it means that the process is multiplicative instead of additive when following a normal behavior:

$$\begin{aligned} \Phi \mapsto \mathcal{N}(\mu,\sigma) &\Rightarrow \Phi_1 + \Phi_2 + ... + \Phi_n \\ \log(\Phi) \mapsto \mathcal{N}(\mu,\sigma) &\Rightarrow \log(\Phi_1) + \log(\Phi_2) + ... + \log(\Phi_n) \\ &\Leftrightarrow \log(\Phi_1 \times \Phi_2 \times ... \times \Phi_n) \end{aligned}$$

where μ and σ represent the mean and variance of the normal distribution.

TABLE 9.8: Values of the reduced χ^2 and associated probability for the Gaussian fits to be worse for the flux and log flux distributions for each light curve. σ is the significance level on which a log-normal distribution is preferred to a normal one.

	Φ		$\log \Phi$		
	χ^2/d.o.f.	Prob	χ^2/d.o.f.	Prob	σ
H.E.S.S.	$50.8/17$	10^{-5}	$11.9/13$	0.54	5.39
Fermi-LAT	$21.6/12$	0.04	$15.0/11$	0.18	2.57
X-ray	$80.0/12$	10^{-10}	$12.5/9$	0.20	7.69
SMARTS (B)	$56.6/13$	10^{-7}	$5.1/12$	0.95	7.18
SMARTS (V)	$29.9/13$	4.9×10^{-3}	$8.7/11$	0.65	4.22
SMARTS (R)	$65.1/12$	10^{-9}	$9.1/11$	0.62	7.48
SMARTS (J)	$30.2/13$	4.4×10^{-3}	$15.4/12$	0.22	3.85

This multiplicative process implies a relation between the flux and the variability: the more the flux the more the variability.

The 2006 flare of PKS 2155-304 showed a lognormal behavior at TeV (Abramowski et al., 2010). To confirm this result for the quiescent state, the H.E.S.S. long term light curve has been tested in Paper H.E.S.S. PKS 2155-304 where lognormality is found as well.

First, the behavior of the light curves of PKS 2155-304 is investigated looking at their flux distributions. For each energy range, the flux Φ and its logarithm $\log(\Phi)$ distributions are fitted by a Gaussian using a χ^2 fit, the results of this fit are summarized in Table 9.8 Almost all light curves have a $\geq 5\sigma$ preference for a lognormal distribution, except the *Fermi*-LAT one, which might need more statistics and the J band of SMARTS.

To investigate further this lognormal behavior, the evolution of the variability, characterized by the excess variance $\sigma_{\rm XS}$ (Vaughan et al., 2003), with the average flux $\overline{\Phi}$ is studied.

Each light curve is separated in several bins with at least 20 points in them to ensure correct statistics. Then $\sigma_{\rm XS}$, which is the variance of the flux corrected from the errors on it, and $\overline{\Phi}$ are calculated for each bin. The scatter plots of $\sigma_{\rm XS}$ versus $\overline{\Phi}$ are in Figure 9.18. They have been fitted by a constant and a linear adjustments to test the rms-flux relation, the results of these fits can be found in Table 9.9. Almost all light curves have a $> 5\sigma$ preference for a linear correlation with respect to a constant fit, again except the *Fermi*-LAT data because of a possible lack of statistics. But all of them, even *Fermi*-LAT, show a strong correlation regarding the correlation factor ρ and the Kendall rank τ[11].

[11]The Kendall rank measures the similarity in the ordering of the data.

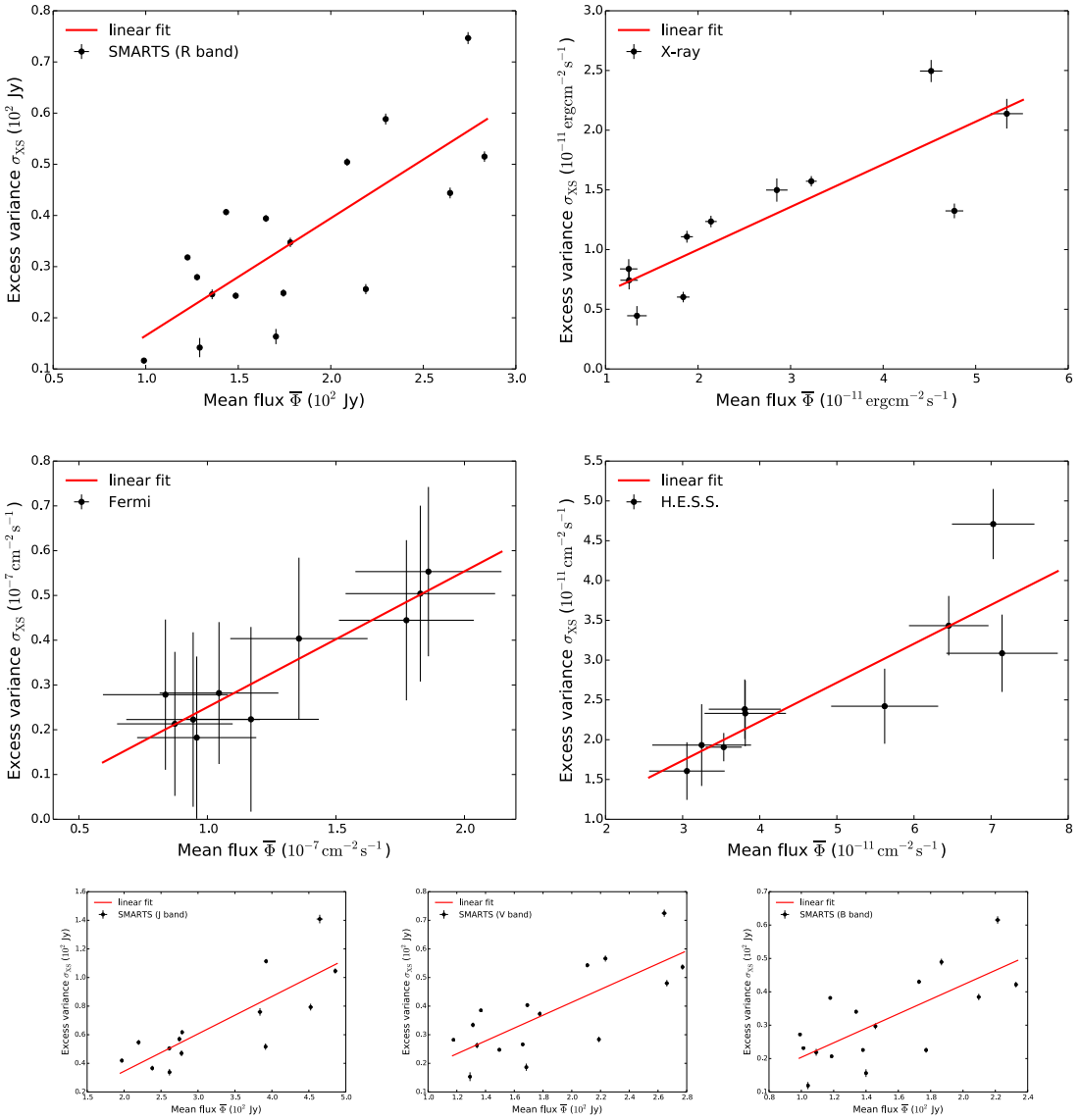

FIGURE 9.18: Scatter plots of the excess rms versus the mean flux for the multi-wavelength data set of PKS 2155-304. The linear fit is shown in red.

TABLE 9.9: Values of the reduced χ^2 of the constant and linear fits of the scatter plots shown in figure 9.18 for each light curve, with values for the significance σ, the correlation factor ρ and the Kendall rank τ.

	constant	linear increase			
	χ^2/d.o.f.	χ^2/d.o.f.	σ	ρ	τ
H.E.S.S.	46.28/8	6.21/7	6.33	0.86 ± 0.11	0.78 ± 0.26
Fermi-LAT	8.43/9	0.86/8	2.75	0.93 ± 0.19	0.69 ± 0.25
X-ray	782/10	260/9	22.8	0.85 ± 0.02	0.67 ± 0.24
SMARTS (J)	3077/13	865/12	∞	0.81 ± 0.01	0.63 ± 0.20
SMARTS (R)	22462/16	7858/15	∞	0.93 ± 0.02	0.74 ± 0.18
SMARTS (V)	3800/15	1746/14	∞	0.76 ± 0.01	0.52 ± 0.18
SMARTS (B)	3676/15	2234/14	∞	0.72 ± 0.01	0.42 ± 0.18

9.4 Discussion & conclusions

9.4.1 Evolution of the variability with the energy $F_{\rm var}(E)$

The variability energy distribution of the quiescent state of PKS 2155-304 has been studied from optical to TeV for the first time. The $F_{\rm var}(E)$ shows an interesting pattern with variability increasing the same way in the optical-X-ray and GeV-TeV ranges (Figure 9.15). The fact that we see the same behavior for the low and high energy parts of this blazar SED reminds the SSC model with the same behavior in the Synchrotron and Inverse Compton parts.

At first sight, the evolution of variability with energy of PKS 2155-304 is slightly different from the results of Mkn 421 and Mkn 501 which show a monotone rising tendancy from radio to TeV. However, there is no information concerning the behavior in the GeV range for Mkn 421, with *Fermi*-LAT data for example.

So I decided to have a look at the public *Fermi*-LAT data[12]. The data set of Ahnen et al., 2016a goes from March 2007 to June 2009, so *Fermi*-LAT data will start only from August 2008, spanning only half of the period. The GeV light curve on the common time range is composed of 45 points of 7-days binning. The variability reaches $F_{\rm var} = 0.189 \pm 0.056$ in the 100 MeV-300 GeV range. Figure 9.19 shows the evolution of the $F_{\rm var}$ of Mkn 421 (from the plot of Ahnen et al., 2016a) where I added the *Fermi*-LAT $F_{\rm var}$ point.

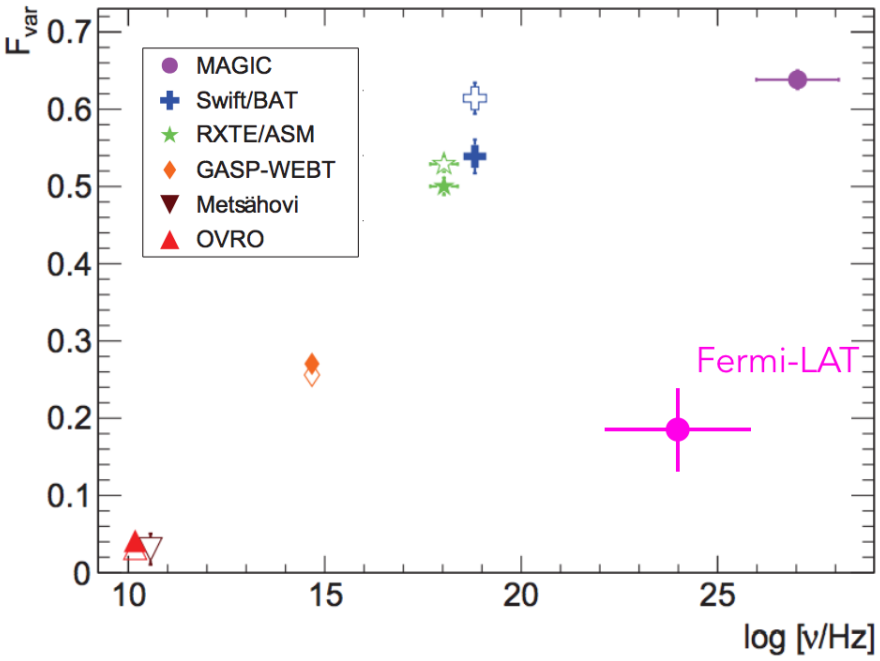

FIGURE 9.19: Evolution of the $F_{\rm var}$ with the energy for Mkn 421 (Same as the left panel of Figure 9.3) with the information at GeV with *Fermi*-LAT data.

Like PKS 2155-304, Mkn 421 shows a bimodal behavior with the variability rising in the low and high energy parts of its SED. Concerning Mkn 501 (see right panel of Figure 9.3, it looks like the variability at low energy is not as high as the other two HBLs.

[12] available at https://fermi.gsfc.nasa.gov/ssc/data/access/lat/msl_lc/

9.4.2 Correlations between energy bands

The DCF results, showing a significant correlation between the SMARTS and *Fermi*-LAT light curves go, into the direction of the SSC model in which a direct correlation between eV-GeV (as well as other energy ranges) is expected. The correlation between the X-ray, VHE and the other bands can not be resolved due to the strong windowing of the data. However, it would have been of great interest to see if the X-ray and VHE light curves were correlated since they display a comparable variability.

A similar result was found for Mkn 421, where the DCF shows a direction relation between the X-ray and VHE ranges. But no correlation is found between the optical and the HE ranges, same for PKS 0735+178.

Direct correlations are difficult to find especially when the multi-wavelength data are not taken during a dedicated campain. Two multi-wavelength campains were done on Mkn 501 (Aleksić et al., 2015; Ahnen et al., 2016b), however, no significant correlations were found between the different energy bands.

9.4.3 Periodic behavior

The DCF method showed (surprisingly) a hint of correlated periodic behavior in the SMARTS and *Fermi*-LAT light curves. This periodic feature has been explored in more details with an LSP. For the SMARTS and *Fermi*-LAT light curves, a period of respectively ~ 730 and ~ 680 days have been found. The X-ray and H.E.S.S. light curves have been tested as well but no periodic feature has been found. Either the light curves are not periodic at these energies because the stochastic variability is too high, either the strong windowing of the data does not allow us to see the periodicity.

It is not the first time periodicity is found in blazar. One of the first is OJ 287 with a ~ 12 years periodicity found on a 100 years light curve (Lehto and Valtonen, 1996; Sillanpaa et al., 1988). But depending on the dataset taken (time span and sampling of the light curve, energy range...) and the analysis done on it, different periods can be found (for illustration Bhatta et al., 2016 found a significative period of ~ 400 days in a 9-year optical light curve).

Mkn 421 too showed evidence of a periodic signal with $T \sim 310$ days in optical, X-ray and γ rays (Benitez et al., 2015) along with the other HBL PG 1553+113 with $T \sim 800$ days in optical and *Fermi*-LAT light curves (Ackermann et al., 2015a). The periodicity results on PKS 2155-304 and PG 1553+113 are similar: a period of roughly 2 years is found in the monitoring data of optical and GeV experiments.

The periodicity in blazars can not be related to the emission process as none is known to produce periodicity in the emitted photon flux. It is more likely to be related to the physical/mechanical processes in the AGN: the precessing of the jet or the accretion process feeding the jet.

The current main theory is that a binary black hole system could be at the center of some AGN instead of just one supermassive black hole as stated in the general AGN picture (Begelman, Blandford, and Rees, 1980). This binary system could cause a periodical change in the accretion rate of the matter coming from the disk and even misalign the accretion disk (Doğan et al., 2015, , and references therein).

Such a system could also create a precession of the jet were the observed periodicity would be caused by a periodicity of the Doppler effect. The AGN BL Lacertae and M 81 have shown a precession motion of their jets looking at radio knots with VLBI observations (Stirling et al., 2003; Caproni, Abraham, and Monteiro, 2013; Marti-Vidal et al., 2013). However, King, Pringle, and Hofmann, 2008 and Nixon and King, 2013 concluded

that the jet precession is unlikely to be detected as it would move on too long time scales ($\sim 10^6$ years).

Other theories can explain short term and long term periodic behavior with geometrical models (if the jet has an helical structure for example, for more details, see Rieger, 2004).

Power law noise of HE and VHE light curves

For the first time the temporal variability of the VHE and HE emission of PKS 2155-304 in the quiescent state has been analyzed on timescales from days up to more than nine years. The PSDs on these timescales are consistent with a power law ($\propto f^{-\beta}$) with an index of $\beta_{\rm VHE} \simeq 1.1$ for the H.E.S.S. light curves and $\beta_{\rm HE} \simeq 1.2$ for the *Fermi*-LAT one (corresponding to flicker noise). The slope of the HE and VHE results are both compatible, suggesting that the PSDs on these time scales are shaped by similar processes.

In the context of accretion-powered sources, X-ray variability with similar characteristics (power-law noise with $\beta \sim 1-2$, and lognormal behavior) has often been related to random fluctuations of the disk parameter α on local viscous timescales (e.g., Lyubarskii, 1997; King et al., 2004).

Aharonian et al., 2007a showed that the PSD of PKS 2155-304 during the flare of July 2006 catched by HE.S.S. is consistent with a power law of slope $\beta = 2.06 \pm 0.21$ (red noise) on timescales < 3 h showing a possible indication of a break between 3 and 20 hours at TeV. On days time scales, Kataoka et al., 2001 have characterized X-ray light curves of PKS 2155-304 (along Mkn 421 and Mkn 501) by a power law PSD of index $\beta = 2-3$. A steep PSD index around the characteristic timescale of flares imply that the X-ray emitting site in the jet is of limited spatial extent.

The PSD of Seyfert AGN exhibit a power-law behavior $\beta \simeq 1$ at low frequency, steepening to $\beta \sim 2$ on timescales shorter than some break time $T_{br} \sim 1$ day (e.g., McHardy et al., 2006). Two radio galaxies, 3C 111 and 3C 120 show a similar behavior in X-ray with a power-law slope of ~ 2 for 3C 111 (Chatterjee et al., 2011) and a steepening of the PSD at high frequency for 3C 120 (Chatterjee et al., 2009).

Longterm optical data on PKS 0735+178 showed a red noise behavior with a power law slope of around 2 (Goyal et al., 2017). Similarly, another optical dataset on PKS 2155-304 showed a red noise behavior indicating that maybe the power law slope change with energy.

9.4.4 Lognormal behavior

Concerning the lognormal behavior of PKS 2155-304, it was already discovered in VHE during the 2006 flare of the object with an indication of lognormality for the quiescent state. Here the optical, X-ray and γ-ray fluxes of PKS 2155-304 seems to behave lognormal at all wavelengths, with highly significant results for the SMARTS, X-ray and H.E.S.S. light curves. This suggest that multiplicative, i.e., self-boosting processes dominate the variability through the whole spectrum. It is interesting to note that in the context of galactic X-ray binaries, where lognormal flux variability has first been established, such a behavior is thought to be linked to the underlying accretion process (Uttley and McHardy, 2001). In the AGN context, evidence for lognormality on different time scales has in the meantime also been found in several sources, for example, in the X-ray band for the BL Lac oject BL Lacertae (Giebels and Degrange, 2009), in the TeV band for the BL Lac Mkn 501 (Tluczykont et al., 2010; Chakraborty et al., 2015), and in the X-ray band for the Seyfert 1 galaxy IRAS 13 244-3809 (Gaskell, 2004). It is important to remember here that Seyfert 1 galaxy are radio quiet AGN, they do not have a relativistic jet and display

more emission lines with more gas surrounding the central engine. The evidence of log-normality in radio quiet AGN strengthen the link between accretion disk and lognormal behavior.

9.4.5 Conclusion

This huge multi-wavelength data set of PKS 2155-304 was a great opportunity to conduct detailed variability studies on long term light curves.

All of these variability properties are signature of the underlying acceleration and emission processes and links between the supermassive black hole, accretion disk and relativistic jet. Hence, they can help to rule out some models or strenghen others. Most of the results discussed in this chapter ($F_{\rm var}(E)$, correlation between the optical-GeV bands) point towards a SSC model.

In the next chapter, a time-dependent, one zone, SSC model will be used to see if it can reproduce all the variability signatures seen in PKS 2155-304.

Chapter 10

Modeling the variability using a time dependent SSC model

Contents

This chapter is devoted to the modelling of the long term variability observed in PKS 2155-304, analyzed in Chapter 9, using a one-zone time-dependent Synchrotron Self-Compton (SSC) model. The multi-wavelength long term light curves presented in the previous chapter will be simulated and their variability tested. The aim being to see if the simpliest leptonic model can reproduce most of the variability observables.

Section 10.1 is dedicated to the presentation of the SSC model and its parameters. Before trying to reproduce the variability profile of PKS 2155-304, the SSC model has to reproduce the time-averaged SED. This will be presented in the Section 10.2. The third part shows how I choose to vary one of the parameter of the model in order to produce the light curves which will be analyzed in the fourth section. The last section is a short study to see if a periodic behavior can be integrated in the SSC model in order to reproduce the periodic behavior of PKS 2155-304.

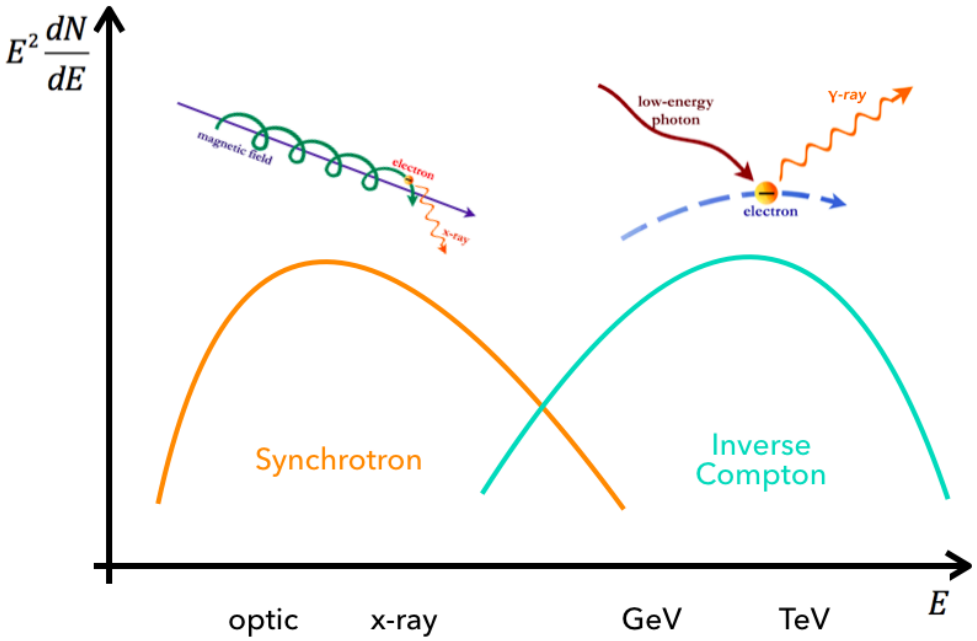

FIGURE 10.1: Simple picture of the SSC model for blazars. The emission from radio to hard X-ray is produced by Synchrotron radiation while the γ photons are produced by IC scattering.

10.1 The Synchrotron Self-Compton model

10.1.1 Basis of the model

The one-zone SSC model is the simplest leptonic model, regarding the number of parameters, one could think to explain the blazars' emission. The first bump of the SED is produced by the Synchrotron radiation of electrons spinning into the magnetic field B of the jet. The second bump of the SED is explained by Inverse Compton scaterring of the same electrons population on the previous Synchrotron photon field (Figure 10.1).

In the framework of the SSC model, the emission is assumed to be produced by a homogeneous blob propagating in the jet with a doppler factor δ. The blob is of radius R in the jet's frame and the magnetic field B in it is assumed to be constant, both in direction and intensity.

The density of electron will evolve with time because of several phenomena:

- electrons are injected in the emission region after being accelerated by an unknown process with a rate $Q(E,t)$;
- electrons cool down because of Synchrotron and Inverse Compton radiative losses (see Section 1.2.1 of Chapter 1) with rates $\dot{\gamma}_{\rm S}$ and $\dot{\gamma}_{\rm IC}$;
- electrons can escape the blob with a characteristic time $t_{\rm esc}$ independent of their energy.

The electron density population evolves following a Fokker-Planck equation:

$$\frac{{\rm d}N_e(E,t)}{{\rm d}t} = \frac{\partial}{\partial E}\left[(\dot{\gamma}_{\rm S} + \dot{\gamma}_{\rm IC})\, N_e(E,t)\right] + Q(E,t) - \frac{N_e(E,t)}{t_{\rm esc}} \tag{10.1}$$

The method to resolve this equation can be found in Sanchez, 2010. In pratical, the escape term can be ignored as t_{esc} is much greater than all the other time scales of the modelling and $N_e(E,t)/t_{\rm esc} \to 0$.

The injection of the electrons can be described by different shapes, the main ones being the power law, log-parabola, broken power law and power law with exponential cut off. Here the injection is chosen to be described by a power law exponential cut off:

$$Q(E,t) = N_0 E^{-\alpha} \exp\left(\frac{-E}{\gamma_{\rm cut}}\right) \tag{10.2}$$

where N_0 is the injection's normalisation, α the power law index and $\gamma_{\rm cut}$ the energy of the exponential cut off.

10.1.2 The impact of each parameter on the steady state shape

Even if the SSC is the simplest model to describe the blazar's emission, it still has, at least, 6 parameters, considering a power law exponential cut off shape for the electron density (Equation 10.2): the normalisation of the electron density N_0 (equivalent to the total number of electrons), the power law index α, the cut off energy $\gamma_{\rm cut}$, the magnetic field value B, the blob radius R, the Doppler factor δ.

Each of them will have an impact on the Synchroton and Inverse Compton peaks positions, on the slope of the spectrum and the brightness in each energy range. The goal at the end is to find a good combination of these parameters to have a good enough description of the SED of PKS 2155-304.

Figure 10.2 and 10.3 present different steady state's SED based on a fixed set of parameters: $N_0 = 2.7\times10^{47}$ electrons, $\alpha = 2.3$, $\log(\gamma_{\rm cut}/11{\rm eV}) = 5.3$, $B = 0.1$ G, $R = 3\times10^{16}$ cm, $\delta = 30$. In each plot, only one parameter is varying.

The first plot (starting at the upper left) presents the evolution of the steady state with the normalisation value N_0. The more we inject electrons in the blob, the more the emission is bright. Since $P_{\rm Sync}(E) \propto N_0$ and $P_{\rm IC}(E) \propto N_0^2$, the two components of the SED do not rise the same way.

The second plot shows the effet of the doppler factor δ on the steady state. Both the Synchrotron and Inverse Compton components have the same dependency on the Doppler factor δ. The higher is δ, the more emission we get since the Doppler effect enhances the brightness.

Concerning the effect of the value of the cut off energy $\gamma_{\rm cut}$ (third plot), it changes the peaks positions as well as their brightness. If the cut off happens at high energy, more energetic electrons are available to produce more energetic photons.

The effect of the power law index is shown on the fourth plot. When the power law index of the electron density population is low, it means that there are more electron at high energy compared to a high power law index, so more photons emitted by both processes. Since there are more electrons and more photons, changing the index value α has more impact on the Inverse Compton process than on the Synchrotron one.

The evolution of the steady state with the magnetic field B is shown on the fifth plot. At first, the Synchrotron and Inverse Compton components rise with the magnetic field, because the electron are cooling faster and producing more photons. But at some point the magnetic field is too strong and there are no more electrons at high energies, inducing a diminution of the IC flux.

On the sixth and last plot, the effect of the blob radius R is shown. The bigger the blob, the more the steady state is bright. The peaks positions stay the same because only the total number of electron changes.

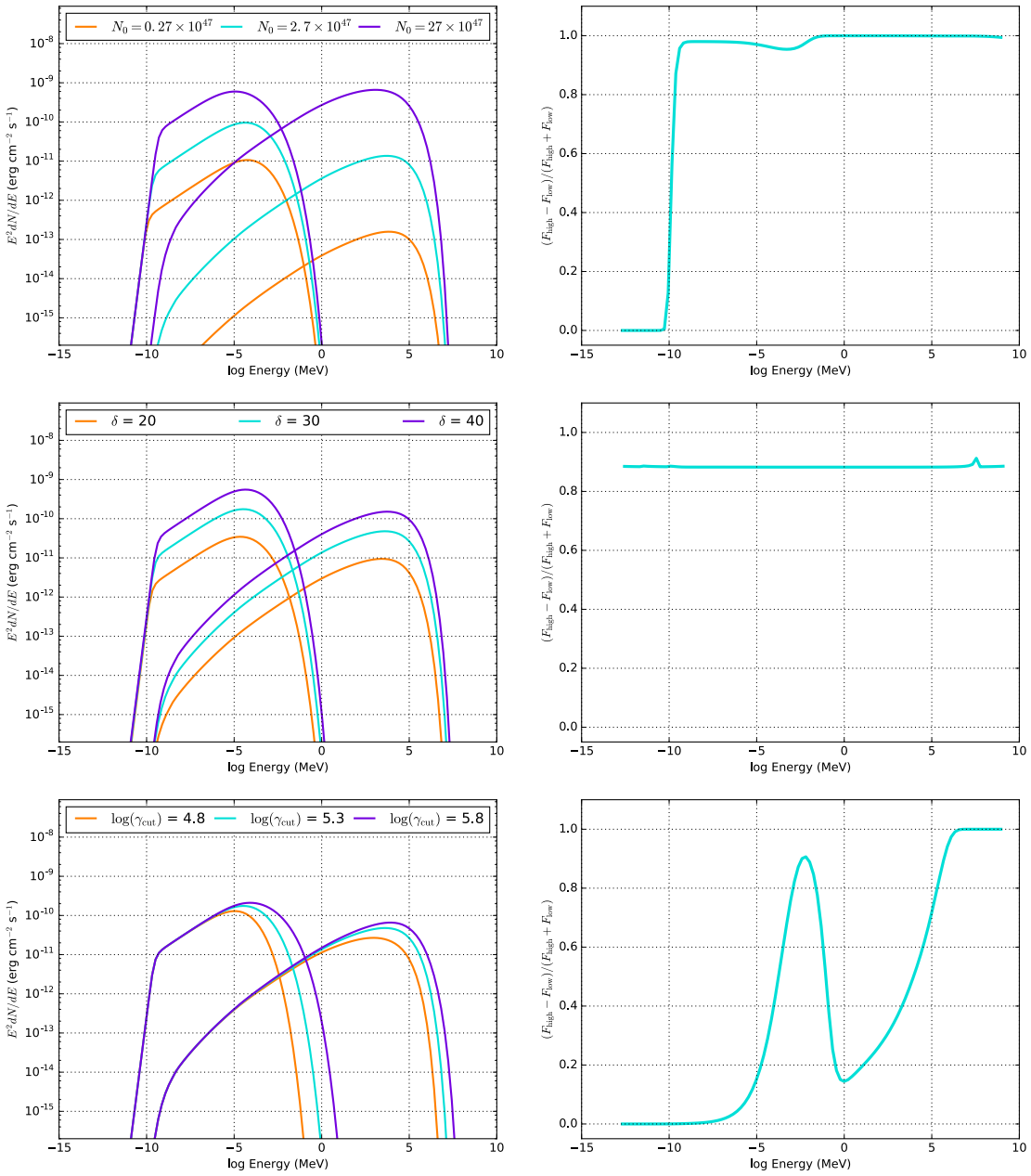

FIGURE 10.2: The impact of each SSC parameter on the SED shape and normalisation (left) and fractional flux variation between the lowest and highest states. Top: Impact of the density normalisation value $N_0 = [0.27, 2.7, 27] \times 10^{47}$ electrons. Middle: Impact of the Doppler effect value $\delta = [20, 30, 40]$. Bottom: Impact of the cut off energy $\log(\gamma_{\rm cut}) = [4.5, 5.0, 5.5]$. Next plots on Figure 10.3.

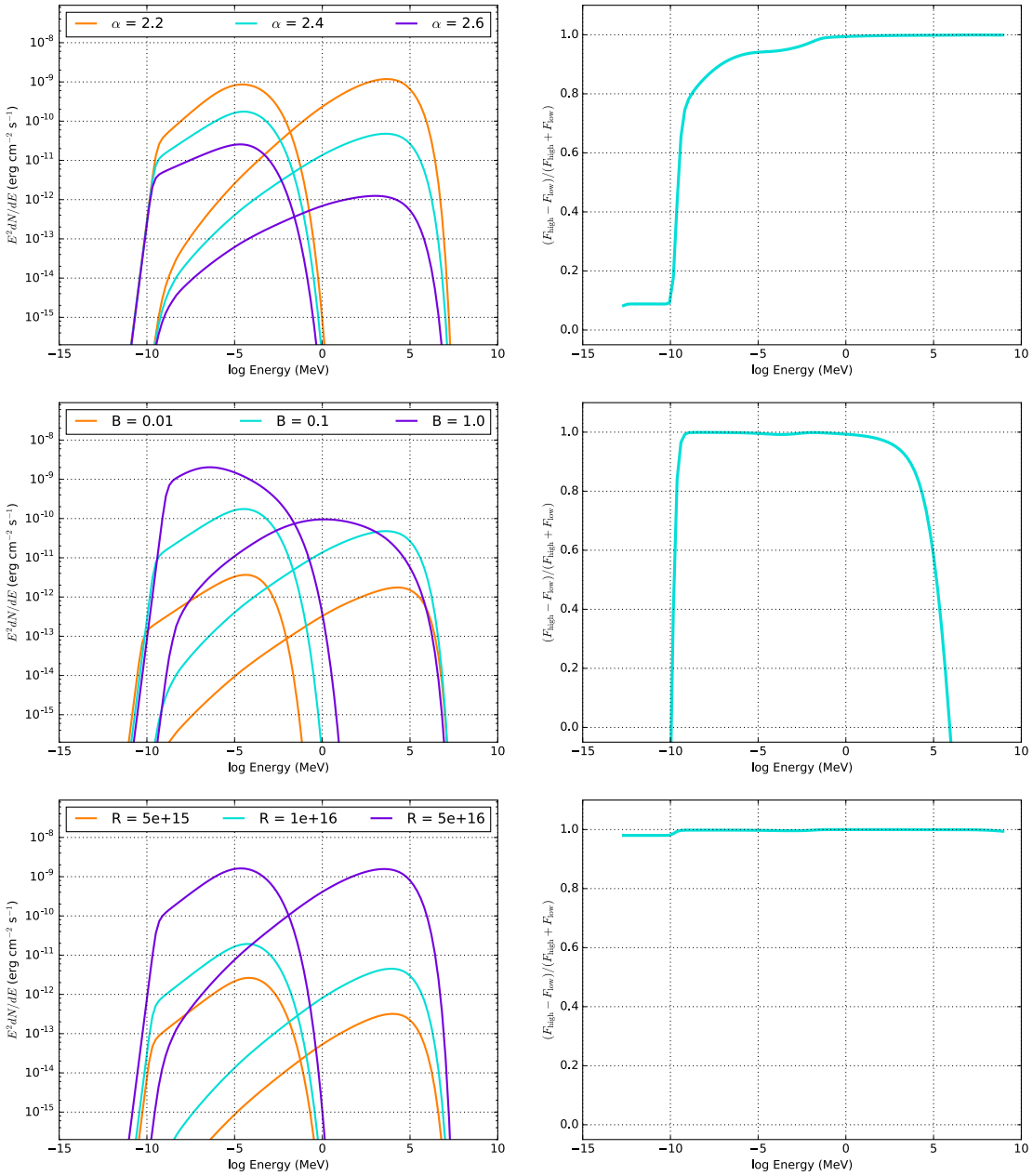

FIGURE 10.3: The impact of each SSC parameter on the SED shape and normalisation (left) and fractional flux variation between the lowest and highest states. Top: Impact of the power law index value $\alpha = [2.2, 2.4, 2.6]$. Middle: Impact of the magnetic field strengh $B = [0.01, 0.1, 1.0]$. Bottom: Impact of the blob's radius $R = [5 \times 10^{15}, 10^{16}, 5 \times 10^{16}]$.

10.1.3 Which parameter to vary in time?

In this work, $\gamma_{\rm cut}$ (more precisely its logarithm $\log(\gamma_{\rm cut})$) is the parameter chosen to vary in time. Why this one in particular and why only this one?

For a first SSC long term variability study, we did not want too much parameters to vary at the same time, it is better to keep the model as simple as possible to try to reproduce the main trend. Of course the magnetic field is not expected to be constant and in the same direction. Same for the injection's normalisation for example, it is not expected to be constant. However, since the variability depends on the energy (Figure 9.15 from Chapter 9), the parameter varying in time needs to be chromatic.

Defining the fractional flux variation[1] $(F_{\rm high} - F_{\rm low})/(F_{\rm high} + F_{\rm low})$ between the low and high fluxes of each steady state from Section 10.1.2, one can see how changing one parameter in the simulation can affect the variability of the flux per energy range. This fractional flux variation is represented on the right panels of Figure 10.2 and 10.3. Most of the parameters have an achromatic behavior: the flux variations are not energy dependent (or only at the low and high energy limits of the simulation). The only parameter showing an interesting behavior is $\log \gamma_{\rm cut}$, with a higher variability in the X-ray and TeV ranges, like the variability of PKS 2155-304.

In a study on Mkn 421, Giebels, Dubus, and Khélifi, 2007 showed similar results: varying the cut off energy of the electrons distribution was reproducing the low and high state of the blazar and was producing more variability in the X-ray and TeV regimes and less in optical and GeV.

10.2 Reproducing the final steady state of PKS 2155-304

In order to know how the steady state (normalisation and peaks position) evolves with each parameter, I just have to tune each parameter to a good value to reasonably fit the data. Multiwavelength data are taken from the ASCD SED Builder[2] and range from radio to γ rays (including flaring periods). The *Fermi*-LAT and H.E.S.S. spectrum from the data set presented in the last chapter are also used. Figure 10.4 present the steady state compute with the parameters shown in Table 10.1.

TABLE 10.1: Values of the steady state of PKS 2155-304 shown on Figure 10.4.

Normalisation	N_0	2.7×10^{47} electrons
Index	α	2.3
Cut off energy	$\log(\gamma_{\rm cut}/1\ {\rm eV})$	5.3
Magnetic field	B	0.1 G
Radius	R	2×10^{16} cm
Doppler factor	δ	35

Giebels, Dubus, and Khélifi, 2007 modeled the emission of Mkn 421 using the SSC model with similar parameters: $\delta = 40$, $R = 2 \times 10^{15}$ cm and $B = 0.2$ G. The electrons density is described with a maxwellian, so values of the index and normalisation can not be compared.

[1] This is a simple estimation of the $F_{\rm var}$ (Equation 9.1)

[2] http://tools.asdc.asi.it/SED/

Time management in the dynamical SSC modelling

The Equation 10.1 can be written slightly differently:

$$\frac{\mathrm{d}N_e(E,t)}{\mathrm{d}t} = \frac{\partial}{\partial E}\left[\left(\frac{\gamma_S}{t^{\mathrm{S}}_{\mathrm{cool}}} + \frac{\gamma_{IC}}{t^{\mathrm{IC}}_{\mathrm{cool}}}\right) N_e(E,t)\right] + Q(E,t) - \frac{N_e(E,t)}{t_{\mathrm{esc}}} \quad (10.3)$$

where the different characteristic times of the simulation can be seen:

- $t^{\mathrm{S}}_{\mathrm{cool}}$ is the cooling time of the Synchrotron process;
- $t^{\mathrm{IC}}_{\mathrm{cool}}$ is the cooling time of the Inverse Compton process;
- t_{esc} the escape time of the particle from the emission region.

There is a *hidden* time in the simulation, noted $\mathrm{d}t$: the interval between each computation step defining the binning of the raw simulated light curves. This time has to be the smallest time of the simulation in order to resolve the other physical times.

In the code (developped during the PhD work of Sanchez, 2010), each time are defined in units of R/c. The cooling times are defined by physics (see Equations 10.4) while $\mathrm{d}t$ and t_{esc} are direct parameters of the simulations and fixed.

$$t^{\mathrm{S}}_{\mathrm{cool}} = \frac{3}{4}\frac{m_e c^2}{\sigma_T c \gamma U_b} \text{ and } t^{\mathrm{IC}}_{\mathrm{cool}} = \frac{3}{4}\frac{m_e c^2}{\sigma_T c \gamma U_{\mathrm{ph}}} \quad (10.4)$$

	Code Time (R/c units)	Time (jet)	Time (observer)
$\mathrm{d}t$	0.03	5.6 h	9.5 min
t_{esc}	0.9	167 h	4.8 h
$t^{\mathrm{S}}_{\mathrm{cool}}$	0.58	107 h	3.1 h

Simulation time during the thesis work

Several tests were made in order to have a working code and a good set of parameters. At first, the step time $\mathrm{d}t$ was smaller with a value of $0.01R/c$. The value has been change in order to decrease the number of steps and the total time of simulation.

The initial simulation time was of $48-54$ hours to simulate ~ 6 months of data, depending on which computing cluster the job was going in. After a small amount of code optimisation and after changing the $\mathrm{d}t$ value to $0.03R/c$, the simulation runs in $48-54$ hours but simulates ~ 1.7 years of data.

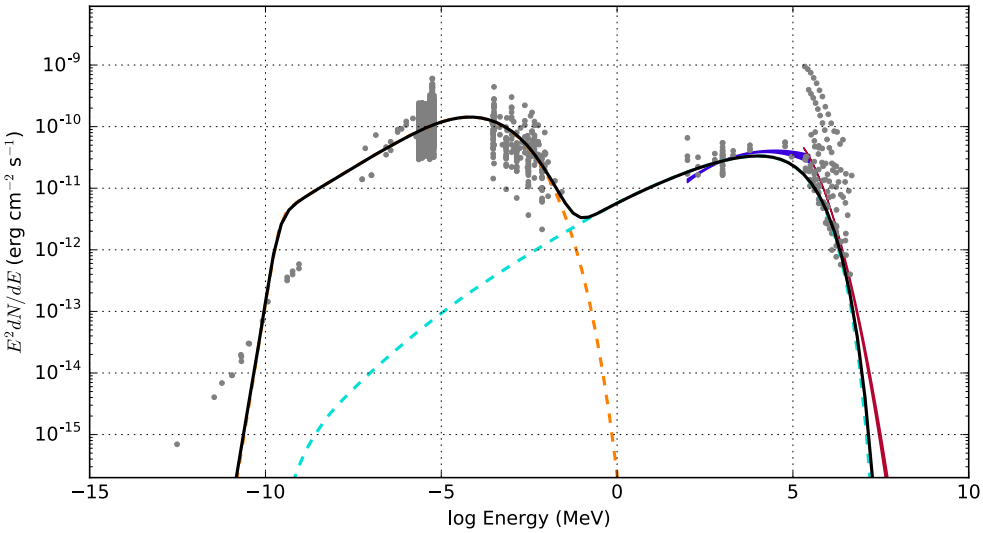

FIGURE 10.4: Simulated SSC steady state for PKS 2155-304 with the parameters presented in Table 10.1. The grey points are the archival data from SED Builder, the blue and red lines are the *Fermi*-LAT and H.E.S.S. spectra presented in the previous chapter.

10.3 Time series generation

10.3.1 Power law noise

So now, we know how to produce the photons from few eV to several TeV, we know how the electron density evolves with time (Fokker Planck equation, Equation 10.1) and which parameter we will vary in time: $\log(\gamma_{\rm cut})$, the cut off energy of the electron density. The question is now how will $\log(\gamma_{\rm cut})$ will vary? Randomly following a Gaussian probability law? Periodically? Since AGN light curves have been many times characterized by power law noise, it might be a good idea to assume that $\log(\gamma_{\rm cut}(t))$ follows a power law noise:

$$f(\omega) \propto \omega^{-\beta} \tag{10.5}$$

The type of power law noise depends on the value of the index β (see Chapter 3 for more details). When $\beta = 0$, it is called white noise, no frequency has more power than another one. The time serie is simply produced by random values with no other behavior. When $\beta = 2$, it called red noise. The in-between is called pink or flicker noise, when $\beta = 1$ (see Appendix B for more details on power law noise).

So the type of noise, and hence, the type of variability we expect at the end will vary depending on the power law index β.

The method of Timmer and Koenig, 1995 to generate power law noise is a great reference and will be used in the following. The method can be described in few steps:

1. Define a power law spectrum $S(\omega) = K\omega^{-\beta}$, where $K = 1$ is just the normalisation of the spectrum;

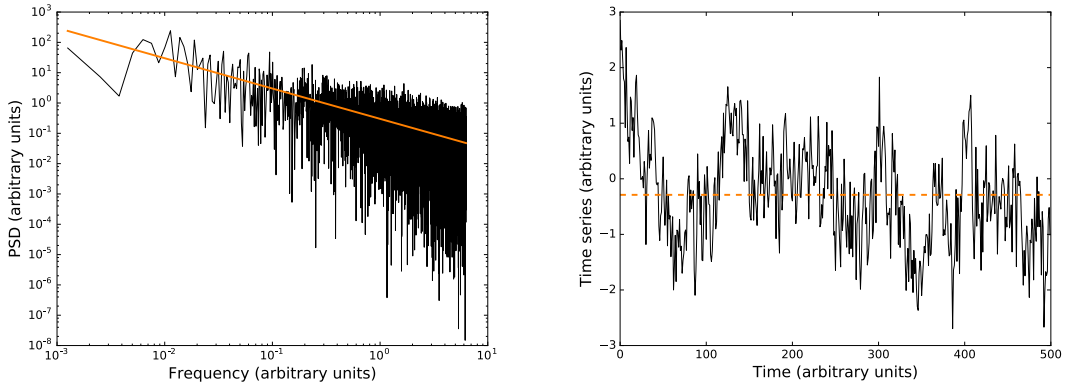

FIGURE 10.5: Example of PSD (left) and corresponding time series (right) generated following the method of Timmer and Koenig, 1995. The power law slope is $\beta = 1$ (red line) corresponding to flicker noise.

2. Draw two Gaussian variables x and y following $\mathcal{N}(0, 1)$. They are used to define the real and imaginary parts of the Fourier transform $f(w) = f_{\rm real} + i f_{\rm im}$:

$$f_{\rm real} = x \times \sqrt{\frac{1}{2} S(w)}$$

$$f_{\rm im} = y \times \sqrt{\frac{1}{2} S(w)}$$

3. In this case the imaginary part is useless since the light curves will be a real time series, so $y = 0 \Rightarrow f(w) = f_{\rm real}$;

4. The PSD is $|f(w)|^2$ (left panel of Figure 10.5).

Once the PSD is generated, a simple inverse Fourier Transform gives us a time series $\log(\gamma_{cut}(t))$ as represented on the right panel of Figure 10.5. This time series reproduces the noise behavior injected depending on β but is more or less randomly normalized. So the time serie is simply re-normalized to a mean value $< \log \gamma_{cut} >= 5.3$ with a variance $\sigma[\log(\gamma_{cut})] = \sigma_{\rm cut}$. The value of the two parameters β and $\sigma_{\rm cut}$ are of importance for the type of noise and the quantity of variability.

10.3.2 Defining the β and $\sigma_{\rm cut}$ parameters

The evolution and behavior of $\log(\gamma_{cut}(t))$ depends on two different parameters: the power lax index β and the variance $\sigma_{\rm cut}$. Only one set of parameters will be studied in details in the following, but it has to be chosen first. The mean value will be fixed to the steady state value of 5.3, but the effect of β and $\sigma_{\rm cut}$ on the light curves and their variability has to be studied to choose a configuration.

The goal here is not to have precised and detailed values of β and σ but just to choose a good enough profile by comparing the variability profile $F_{\rm var}(E)$ of the simulated light curves to the real variability profile of PKS 2155-304.

To do so, several values are tested to make a grid in this 2D parameter space:

- $\beta \in$ [1.0, 1.5, 2.0]
- $\sigma_{\rm cut} \in$ [10, 15, 20, 25] in percent of the mean value of 5.3.

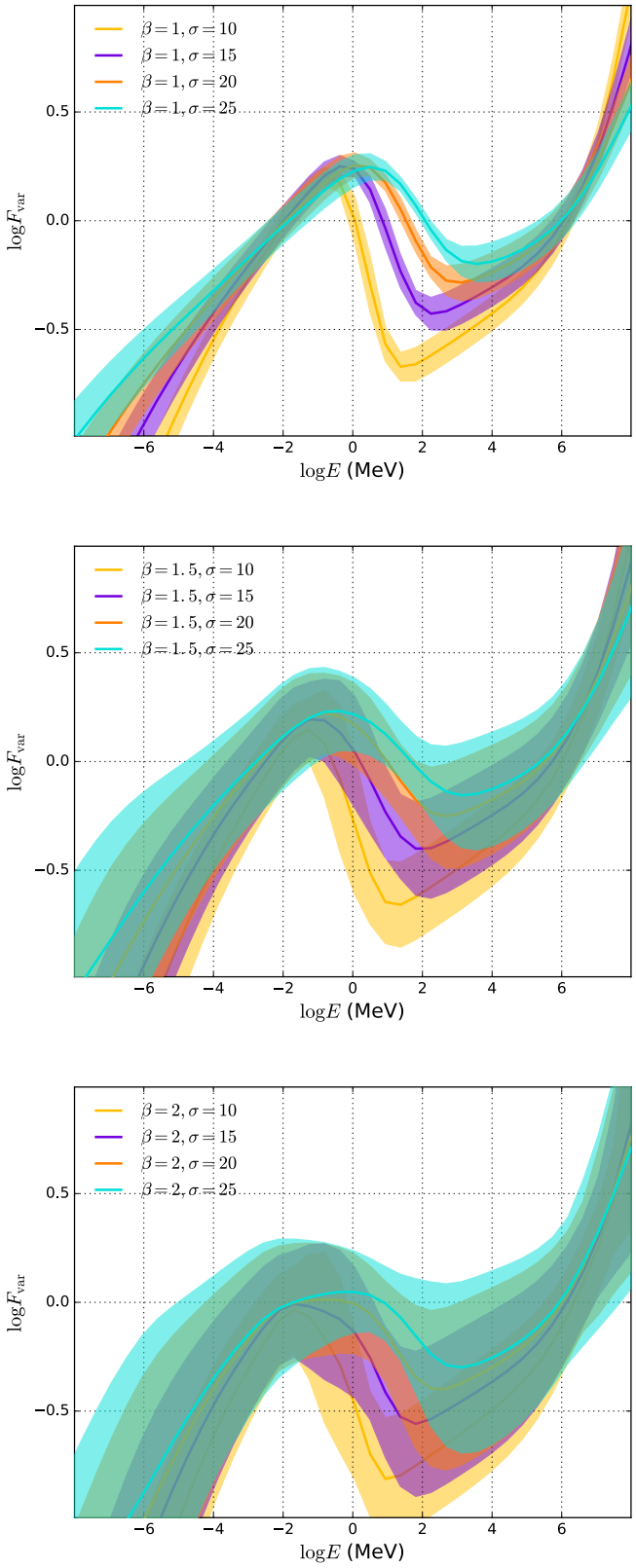

FIGURE 10.6: $F_{\rm var}(E)$ profiles for the 2.2 test years SSC modelisation. Top: $F_{\rm var}(E)$ for $\beta = 1$ and all the $\sigma_{\rm cut}$ values. Middle: $\beta = 1.5$. Bottom= $\beta = 2$.

I ran a simulation with a sample of 200 light curves per energy range of 2.2 years for each of the 12 configurations, and look at the variability profiles $F_{\rm var}(E)$ produced. In order to reproduce the binning effect of the real light curves, light curves in the energy ranges of the experiments have been re-binned following the real temporal binning and windowing of the data. However, to not run simulation on a too long time, simulations have been made only on the *Fermi*-LAT time span, as between 2008 and 2012 is the period with the most data.

Figure 10.6 shows as an example the resulting variability profiles for some of the configurations. Both parameters have an effect on the profile, either for the quantity of variability at a fixed energy or the steepness of the profile in a specific range. When β is fixed, the variability increases with $\sigma_{\rm cut}$ as expected, but stay more or less the same in the X-ray and TeV ranges. When $\sigma_{\rm cut}$ is fixed, the power law index β seems to have a significant effect when going from 1 to 1.5, then there is almost no difference between the profiles with $\beta = 1.5$ or 2.

After these tests (and the application of the temporal binning), the best profile is $[\beta = 1, \sigma_{\rm cut} = 20\%]$, shown on Figure 10.7. Hence the whole 10 years simulation is launched with these values.

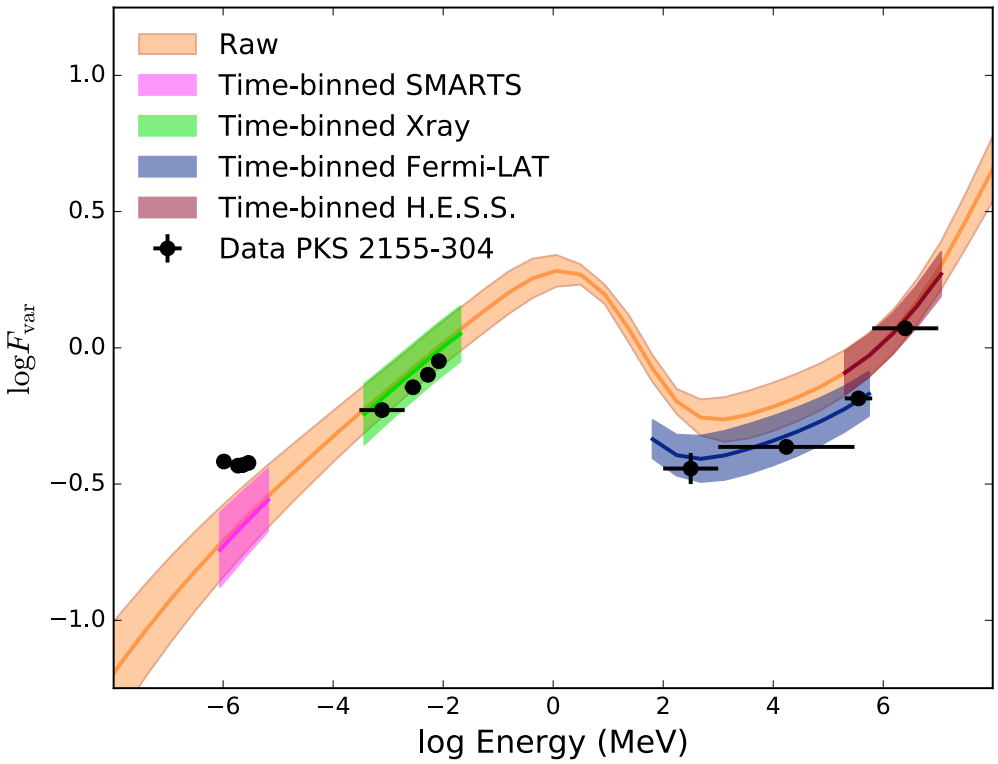

FIGURE 10.7: Best $F_{\rm var}(E)$ profile (1-year simulation) with $\beta = 1$ and $\sigma_{\rm cut} = 20\%$, the orange line is the variability of the raw simulated light curve while the pink, green, dark blue and orange lines represent the variability of the simulated light curve after applying temporal binning.

10.4 Time series analyses of the simulated light curves

The 10-years sample of 200 light curves per energy range with the $\gamma_{cut}(t)$ configuration [$\beta = 1.0$; $\sigma_{\rm cut} = 20\%$] are tested for some variability studies like the PKS 2155-304 data presented in Chapter 9.

The simulation gives the evolution of the differential flux with time (every 9.5 minutes in the observer rest frame) in 50 energy bins from 2.5×10^{-7} eV to 630 TeV. I will call later these light curves "raw light curves".

To be compared with the data, these raw light curves have first to be "re-binned" in energy. For each time step, the differential flux will be integrated between $E_{\rm min}$ and $E_{\rm max}$, with the minimum and maximum energy corresponding to the ones of the data. These light curves will be called "energy-binned light curves" in the following.

With one point every 9.5 minutes, the coverage in time is quasi-continuous and this is not the case of the data, where the temporal binning depends on the instrument. The simulated light curves (either the raw or energy-binned ones) will be rebinned in time following the exact temporal binning of the data in the corresponding energy range. These light curves will be referred as "time-binned light curves" for the time-binned raw light curves or "data-like light curves" for the time-binned energy binned light curves.

As an example, Figure 10.8 shows how the simulated energy-binned light curves look in the SMARTS (R band), X-ray, *Fermi*-LAT and H.E.S.S. energy ranges for one random trial. The raw light curves, with one point every ~ 9.5 minutes are shown in grey while the data-like light curves with the temporal binning of the data are shown in color.

10.4.1 Variability energy distribution $F_{\rm var}(E)$

The $F_{\rm var}(E)$ can be computed on each light curve type. Figure 10.7 already showed the $F_{\rm var}$ profile for the raw and time-binned light curves as a test to choose the power law noise configuration (see Section 10.3.2). The orange line represents the mean $F_{\rm var}$ over the whole sample and the orange band being the 1σ variation as the error.

The variability profile of the raw light curve reproduces already the same pattern as the data with variability increasing in the low and high energy domains, with discrepancies in the optical and GeV ranges.

However, the variability is sensitive to the binning of the data which is of importance especially for the *Fermi*-LAT data. The $F_{\rm var}(E)$ profile for the time-binned light curves is shown with pink, green, dark blue and dark red bands (respectively for the SMARTS, X-ray, *Fermi*-LAT and H.E.S.S. energy ranges). As expected, applying the temporal binning on the raw light curves does not have a strong effect in the optical, X-ray and TeV ranges. However it does for the GeV range, with the 10-days binning decreasing the variability to values corresponding of the variability observed in the *Fermi*-LAT light curve.

To compare the simulated SSC variability and the data, the best way is to apply the temporal and energy binning to the simulated light curves. Figure 10.9 shows the variability energy distribution of the data-like like curves with the blue points (along with the raw profile still represented). The global agreement within the data is good.

In the optical range, the variability of the SMARTS data is still above the SSC variability with a different slope: variability increases with increasing energy in the model while the variability of the optical data looks flat. The electron density is described by a power law exponential cut off shape, with the cut off energy $\gamma_{\rm cut}$ varying with time. In Figure 10.8, the look of the light curve shows that the optical flux is generally to its maximum value because $\gamma_{\rm cut}$ is most of the time above the optical energy range.

The variability of the X-ray data is almost perfectly reproduced by the time-dependent SSC model.

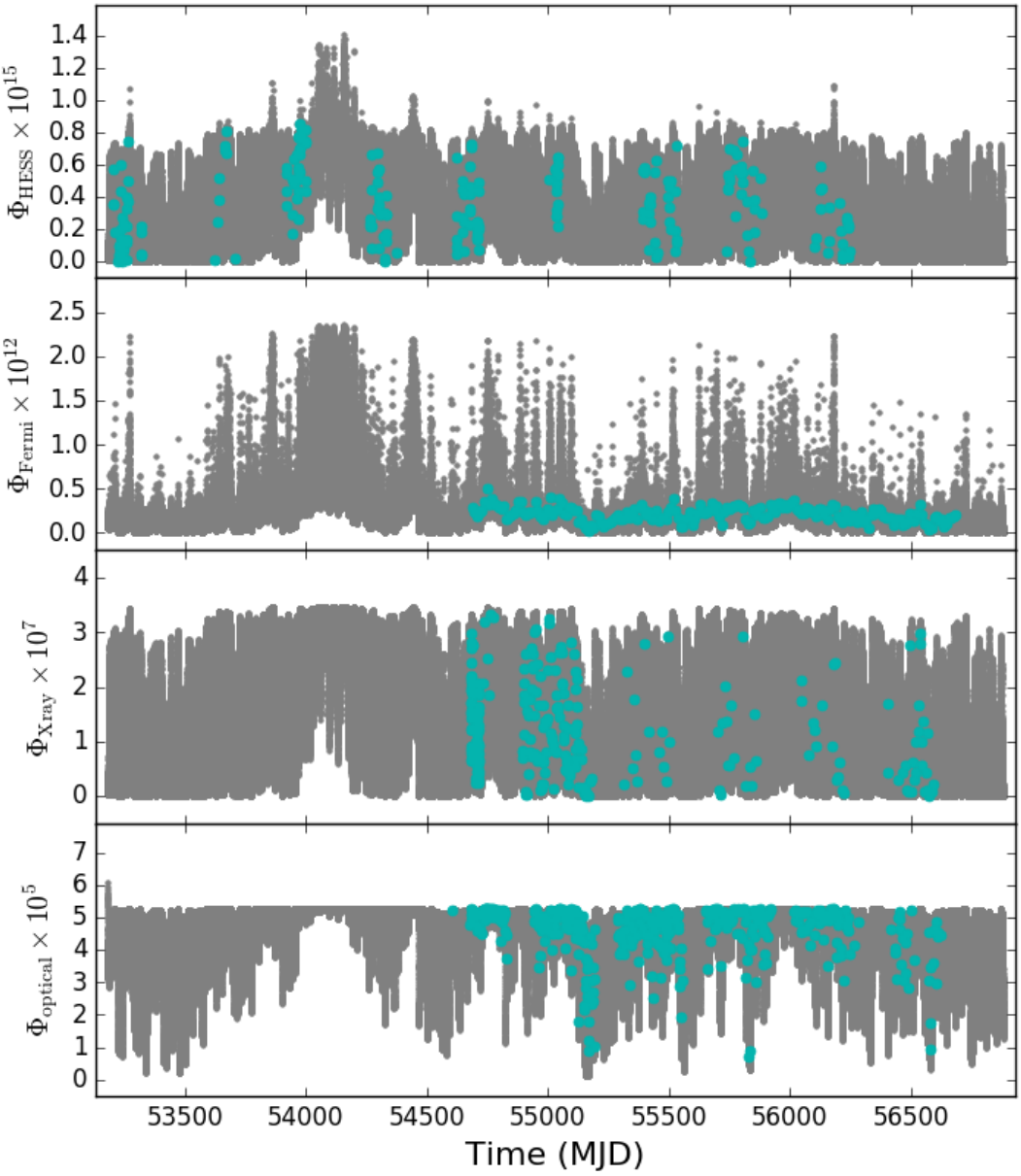

FIGURE 10.8: From bottom to top, simulated light curves in the SMARTS (R band), X-ray, *Fermi*-LAT and H.E.S.S. energy ranges. The raw light curves, with one point every $\sim$ 9 minutes are shown in grey while the light curves with the temporal binning of the data are shown in blue.

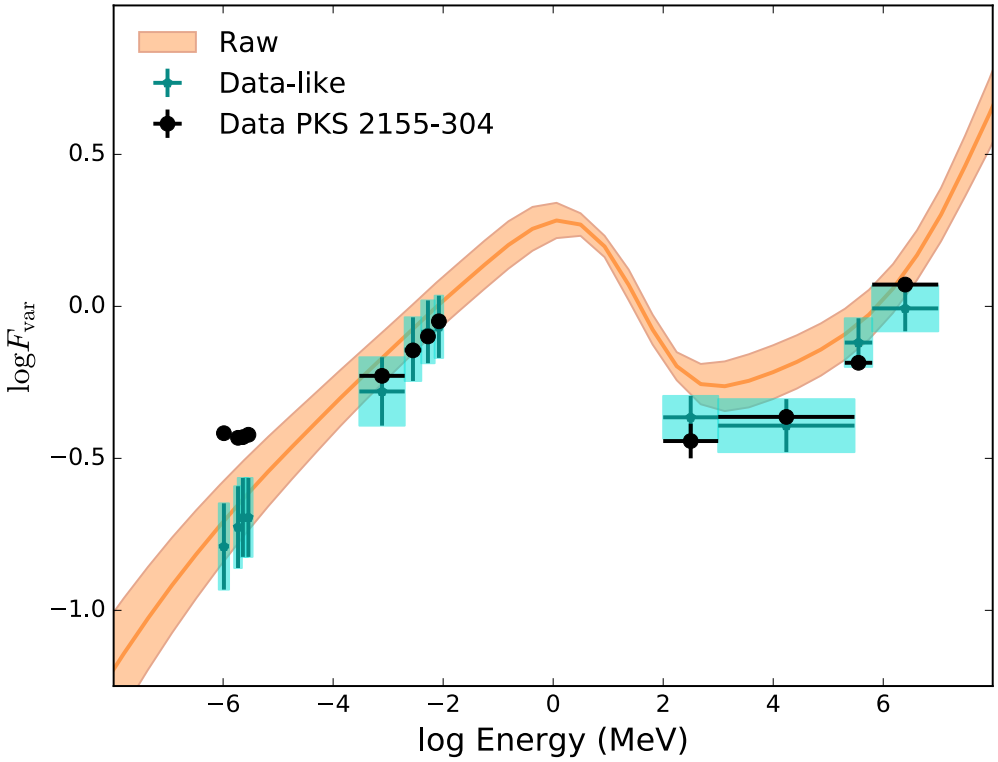

FIGURE 10.9: $F_{\rm var}(E)$ profile for the SSC modelisation. The orange line represents the $F_{\rm var}$ computed for the raw simulated light curves. The blue points correspond to the $F_{\rm var}$ of the binned (in energy and time) simulated light curves. The black points are the data points (presented in the previous chapter) for comparison.

The agreement is quite good for the *Fermi*-LAT and H.E.S.S. data as well, though there are some tensions. In the data, the variability below 1 GeV is slightly below the one above 1 GeV. In the simulated data-like light curve, it is the other way around. This is because of the change of slope around $\log E = 2$, the higher variability at low energy in the 100 MeV - 1 GeV range dominated the whole bin. Concerning H.E.S.S., the tension resides in the fact that the variability increases faster for the data than for the simulation. Still, the points stay in the 1σ interval.

10.4.2 Cross-correlations

It's expected in the SSC model that all bands are correlated with each other since the emission is created by the same electron population. The interesting part is to know if a correlation could be seen despite the different temporal binning of the real data. Hence, the correlations between the simulated light curves in the SMARTS, X-ray, *Fermi*-LAT and H.E.S.S. energy ranges, with the corresponding temporal binnings, are all tested.

The correlation between the different data-like light curves has been tested using the same technique as described in Section 9.3.3: the data-like light curves are re-binned on a 10-day binning before applying the DCF algorithm.

Results are presented on Figure 10.10 where the blue line is the mean DCF of the data-like simulated light curves, the blue area the 1σ interval and the black points are the data

from the light curves of PKS 2155-304 (only the DCFs of the SMARTS×*Fermi*-LAT data were presented on Section 9.3.3).

The data-like light curves coming from the SSC simulation are all correlated with the maximum of the DCF at $\tau = 0$ days, despite the application of the temporal binning. However the DCF of the X-ray×H.E.S.S. simulated data is looking "messier" because the windowing of the data is strong in both light curves, giving some holes in the DCF because there was no point in the sample, or not enough, to compute the value of the correlation.

Even if the DCF between most of the light curves of PKS 2155-304 (except for the correlation between SMARTS and *Fermi*-LAT light curves) were not successful to find a direct correlation, the DCF between SMARTS×X-ray, SMARTS×H.E.S.S. and *Fermi*-LAT×H.E.S.S. show a maximum around $\tau = 0 \pm 10$ days. This maximum is easier to see when the data-DCF is compared to the simulation. Because of the shape of the DCF at big time lag, a direct correlation can, of course, not be claimed. The X-ray and GeV ranges do not seem correlated in the data while the SSC shows they should be correlated, even when taking into account the binning effects.

Interestingly, the periodical shape of the light curves of PKS 2155-304 in the optical and GeV range can be seen also in their correlation with other band, although it is noisier.

10.4.3 Power spectral density

Figure 10.11 displays the periodograms of the simulated light curves and of the data using the same LSP computation as Section 9.3.4. The PSD of the energy binned light curves is showed in orange, the one of the data-like light curves in blue. The LSP of the data is represented by the dark points and is at first sight in good agreement with the simulation: without any fit, the simulations reproduce the behavior of the data, either the power law slope and the LSP level.

The PSD from the energy-binned light curves are well described by a power law noise $PSD \propto t^{\beta}$ of index $\beta \simeq 1$, for all energy ranges (see Table 10.2 for the specific values).

The PSD of the data-like simulated light curves can be directly compared to the data. Because of the temporal binning the power and the slope change: the power decreases and/or the slope softens. Table 10.2 shows the different values of the power law slope for the PSD of the data-like and data light curves. In the *Fermi*-LAT range, the binning does not change the slope of the simulated LSP, however there is a tension between the slope of the simulation $\beta = 1.05$ and the slope of the data $\beta = 0.55$ which are not compatible. Same for the TeV range where the data exhibit a slope $\beta = 0.28$ flatter than the data-like simulated PSD with its slope of 0.39. The agreement is better for the X-ray and optical range. The SMARTS data show a slope of $\beta = 0.83$ while the simulations have $\beta = 0.73$. Because of the strong temporal windowing in X-ray, the PSD slope goes from 1.06 to 0.38 and is in agreement with the data with $\beta = 0.30$.

The level of LSP power between the data and data-like simulation is quite in agreement as well. The simulations do not seem to show any break, for all energy ranges, at small or large time scales but no break was put in the temporal evolution of $\log \gamma_{\rm cut}(t)$.

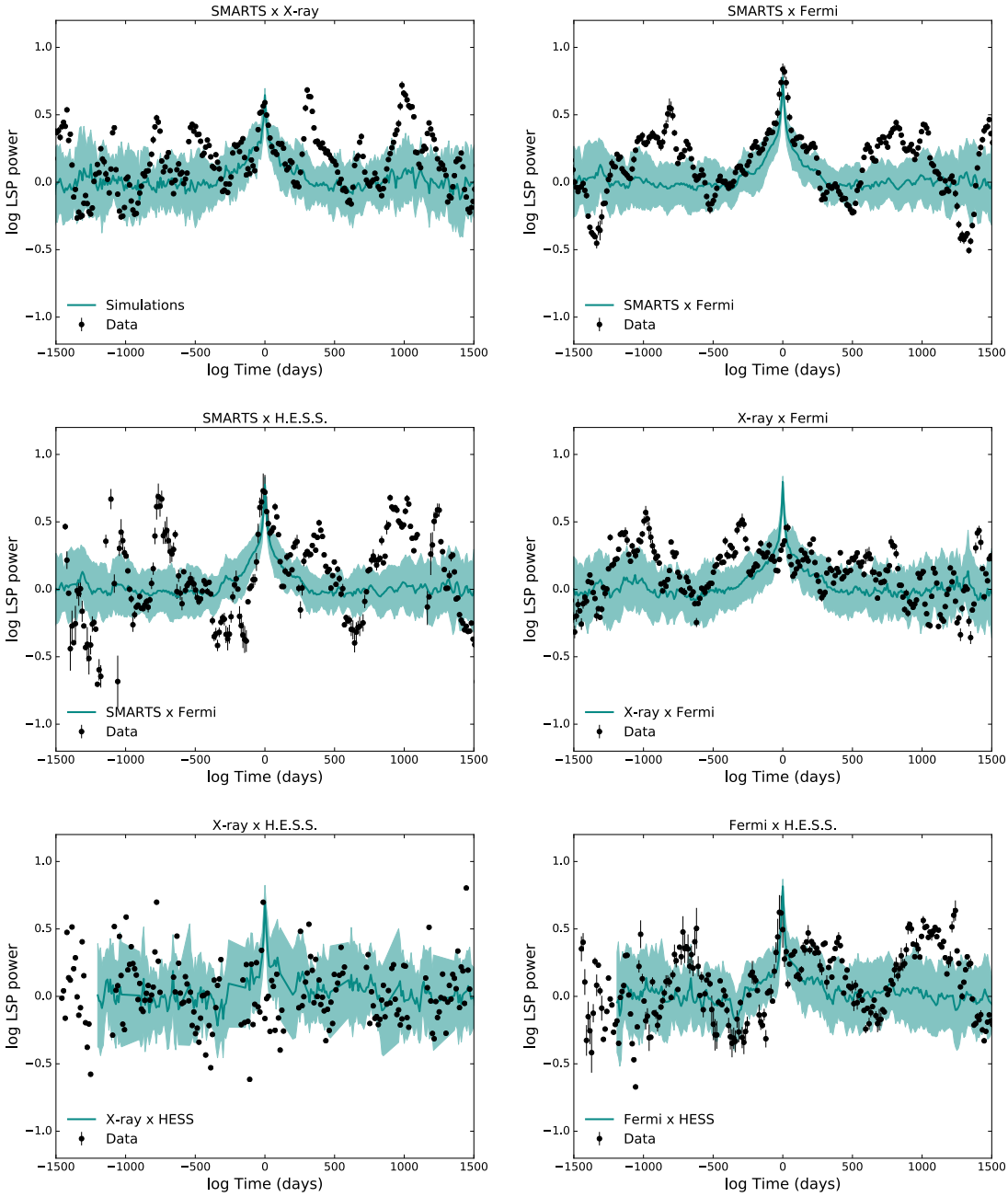

FIGURE 10.10: DCF of the simulated data-like light curves in blue and of the PKS 2155-304 data in black. From top to bottom and left to right: SMARTS×X-ray, SMARTS×*Fermi*-LAT, SMARTS×H.E.S.S., X-ray×*Fermi*-LAT, X-ray×H.E.S.S. and *Fermi*-LAT×H.E.S.S..

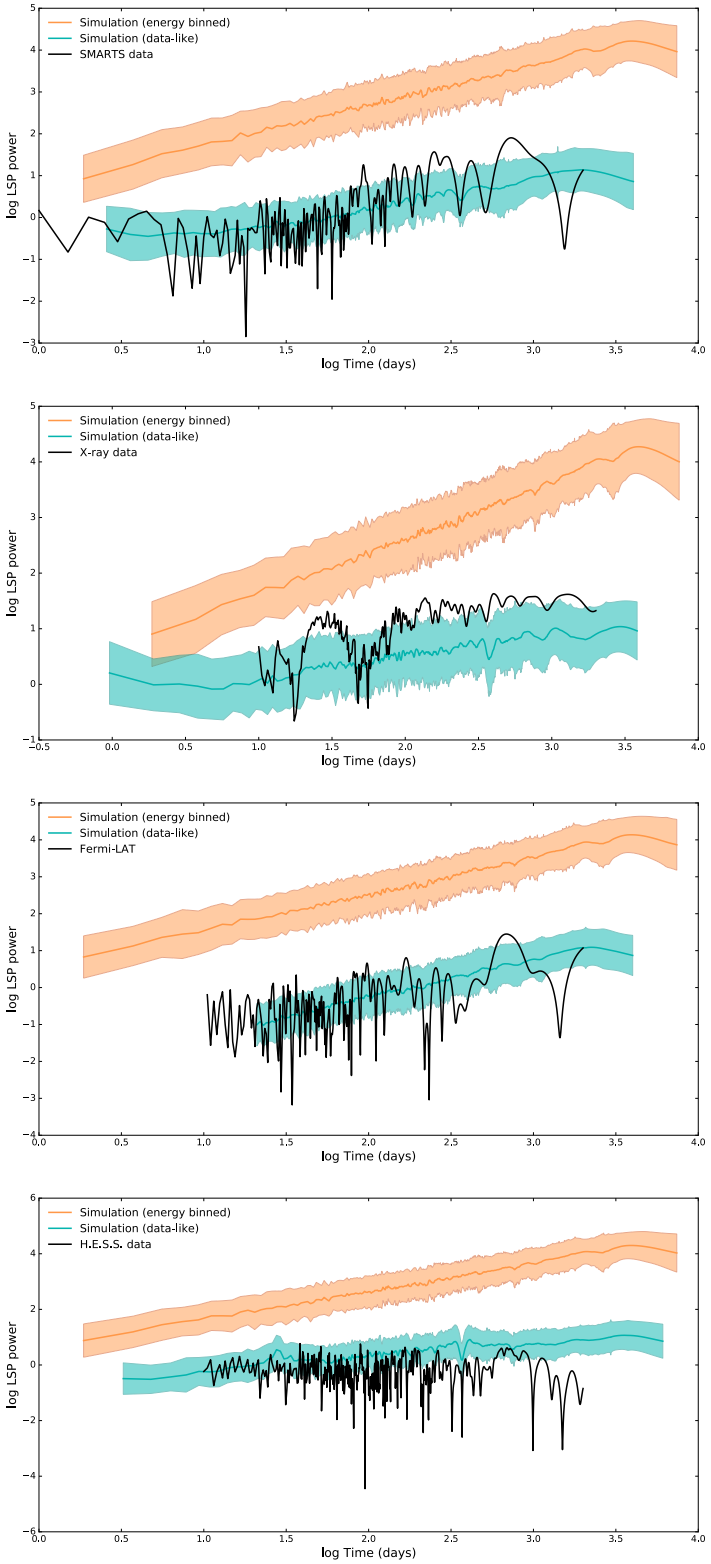

FIGURE 10.11: LSP of simulated light curves for the optical R, X-ray, *Fermi*-LAT and H.E.S.S. bands (from top to bottom). The orange curve is when the only the energy binning has been applied, whereas the blue curve is for the data-like light curves. Black points correspond to the data for PKS 2155-304.

TABLE 10.2: Values of the power law slope of the PSD presented in Figure 10.11.

Energy range	β (energy-binned only)	β (data-like)	β (data)
SMARTS	0.98	0.73	0.83 ± 0.04
X-ray	1.06	0.38	0.30 ± 0.01
Fermi-LAT	1.03	1.05	0.55 ± 0.03
H.E.S.S.	1.03	0.39	0.28 ± 0.03

Summary of the simulation results

I simulated a set of light curves over 10 years using a one-zone time-dependent SSC model. The parameter varying in time is the cut off energy $\gamma_{\rm cut}$ of the electron density, following a power law noise of index $\beta = 1$. At the end of the simulation the raw light curves are binned in energy and in time to create simulated SMARTS, X-ray, *Fermi*-LAT and H.E.S.S. light to be compared to the data.

1. **Variability energy distribution $F_{\rm var}(E)$ (Figure 10.9)**
   The shape of the variability profile, with variability increasing in the low and high energy domains, is well reproduced by the simulations. The variability levels of the simulations in X-ray, GeV and TeV match the ones of the data. We reach a limitation of the model when looking at the variability in optical which is smaller than expected.

2. **Cross-correlations (Figure 10.10)**
   Despite the application of the temporal binning to the simulated light curves, correlations are still found between all energy ranges. The comparison to the simulation results to the data show that most of the experimental light curve exhibits a strong correlation at $\tau = 0$ except for the X-ray versus GeV ranges.

3. **Power spectral density (Figure 10.11)**
   The PSD of all the energy-binned light curves are described by a power law of index 1. After application of the temporal binning, the PSD exhibit less power with a softening of the slope (except for the GeV where there is a full monitoring). The power levels between the data and simulations agree well, however there are some tension for the slope: the PSD of the data is flatter in the X-ray, GeV and TeV range.

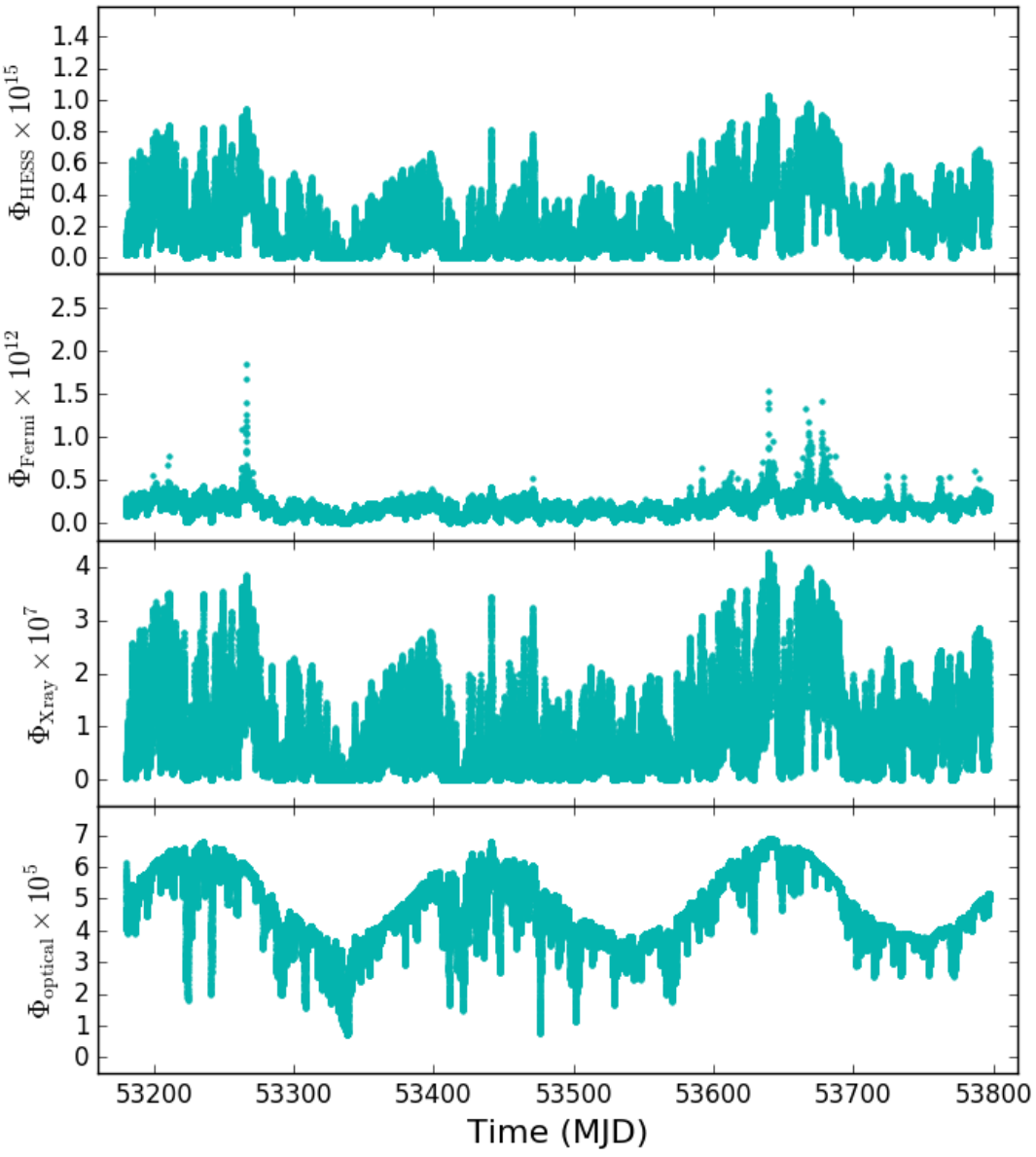

FIGURE 10.12: Short term light curves (21 months) with periodic variations of the doppler factor δ.

10.5 But what about the periodicity?

As discussed in Chapter 9, PKS 2155-304 is showing a periodic behavior in its optical and GeV light curves. This periodicity could originate in a periodic accretion rate (created for example by the orbital motion of a binary system of supermassive black holes at the center of the AGN) or in a periodic variation of the doppler factor of the emission (because of a precessing jet).

I had a look at the doppler factor hypothesis. A sinusoidal time series $\delta(t)$ will be injected in the time-dependent SSC modelisation described and used previously. The mean of the sinus corresponds to the steady state value $\delta = 35$ and the amplitude is chosen to be 5:

$$\delta(t) = 35 + 5 \times \sin(t + T)$$

Time-wise, it was not possible to do a long-term simulation like the work presented in the previous part of this chapter. I decided to run a shorter one of 21 months (taking $\sim$ 50 hours to produce). Since 3 periods are seen in the SMARTS and *Fermi*-LAT light curves, the injected period is fixed at 7 months (205.7 days to be precise) to have the same number of periods in the simulation.

Knowing (because of previous tests) that the injection of a periodic signal will increase the quantity of variability in the light curves, the power law noise configuration for the $\gamma_{\rm cut}(t)$ is chosen to be $[\beta = 1; \sigma_{\rm cut} = 15\%]$ instead of $[\beta = 1; \sigma_{\rm cut} = 20\%]$. The resulting light curves in the 4 energy ranges are shown on Figure 10.12.

The windowing of the data having more effect than its sampling, no temporal binning will be applied to the simulated light curves as the windowing of the data can't be reproduced on this time scale.

Variability energy distribution $F_{\rm var}(E)$

The variability energy profile of the periodic short-term simulation is show on Figure 10.13. The shape of the variability energy profile stays roughly the same with however a flatter part in the optical range around $F_{\rm var} = 0.20 - 0.25$, rising the variability levels of the simulation in this range compared to the non periodic one (Figure 10.9).

The periodicity could explain why the SMARTS data are more variable than the model: this energy range would be dominated by the variability of the periodicity and not by the one of the stochastic process since the changing the value of the cut off energy as a small impact on the electrons producing the optical photons.

Output of the periodicity per energy range

As seen in Chapter 9, the X-ray and H.E.S.S. data do not display even a hint of periodic behavior, either because of the strong windowing of the data or because of the strong stochastic variability. Is it the same in the simulations ?

Figure 10.14 displays the periodograms of the simulated light curves in the SMARTS, X-ray, *Fermi*-LAT and H.E.S.S. range, without applying any temporal binning on the short term simulated light curves. The optical and GeV simulated light curves have a clear and strong bump around 200 days while the X-ray and TeV light curves show a less significant one.

The reconstructed values of the period for each energy range are in Table 10.3. The period is the mean of all the periods from the 100 simulations with the error represented by the standard deviation. The period is well reconstructed in all ranges, around 207 days for the optical and GeV ranges and 211 days for the X-ray and TeV ones. However the standard deviation is of 50 days for the X-ray and H.E.S.S. ranges.

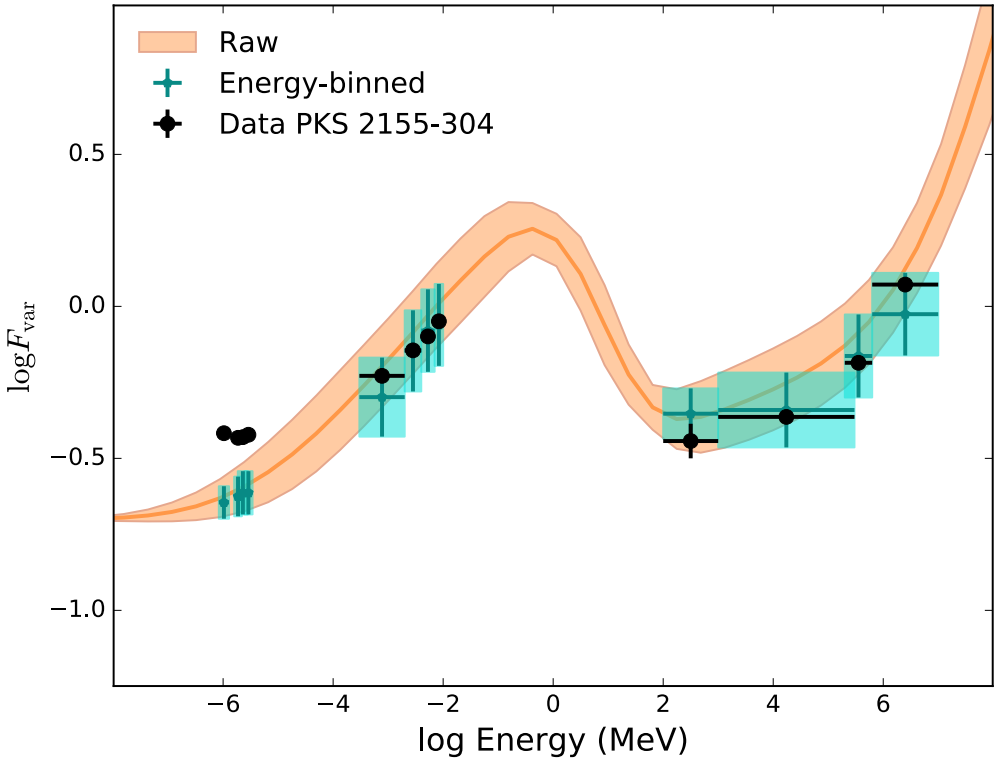

FIGURE 10.13: $F_{\rm var}(E)$ profile for the SSC modelisation with a periodic input in the Doppler factor. The orange line represents the $F_{\rm var}$ computed for the raw simulated light curves of 21 months. The blue points correspond to the $F_{\rm var}$ of the energy binned (but not time-binned) simulated light curves. The black points are the data points (presented in the previous chapter) for comparison.

TABLE 10.3: Values of the reconstructed periods from the LSP of Figure 10.14 when injecting a period of 205.7 days.

Energy range	Period (days)
SMARTS	206.9 ± 12.8
X-ray	210.9 ± 50.1
Fermi-LAT	206.4 ± 32.4
H.E.S.S.	210.7 ± 49.7

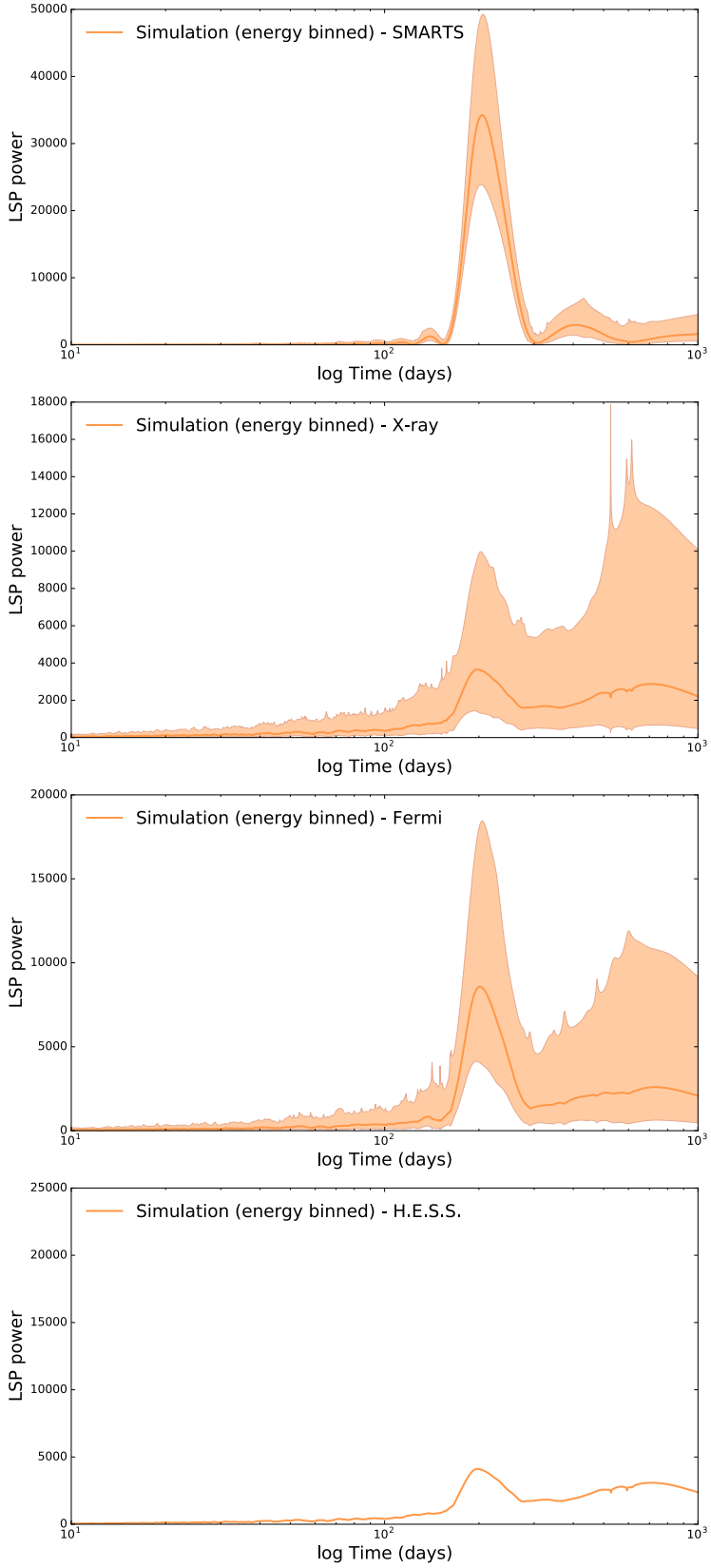

FIGURE 10.14: LSP of the short term simulated light curves with a periodicity of 205.7 days injected in the doppler factor for the optical R, X-ray, *Fermi*-LAT and H.E.S.S. bands (from top to bottom).

10.6 Conclusions

At the beginning, the aim of this work was to see if a "simple" one-zone time-dependent SSC model could reproduce the variability energy profile observed for PKS 2155-304. The first tests were made on small time scales (2 to 6 months) and the results were already conclusive: we could reproduce a similar variability behavior by varying the cut off energy parameter $\gamma_{\rm cut}$ in time. However, with these preliminary tests, it was not possible to take into account the binning, different in all energy ranges, nor to have a look at the other variability tests as well.

I decided to run a long term simulation of 10 years to see if I could reproduce the long term multi-wavelength variability behavior of PKS 2155-304 seen in Chapter 9: variability energy profile, cross-correlations, log-normal behavior and periodicity. These long term simulations would also be a good opportunity to see how the SSC behave on long time scales and how the temporal binning affects the variability behavior.

10.6.1 Variability profile

The model reproduces well the variabiltiy energy profile $F_{\rm var}(E)$ with however a discrepancy in the optical range where the model is less variable than the data. But when taking into acount a periodic input in the simulations, the variability in optical is higher and flat instead of falling when going to smaller energies. In the case of PKS 2155-304, where we now know there is a $\sim$ 700 days periodicity, the SSC modelisation has to be upgraded to take this effect into account (either by varying periodically the doppler factor or the number of electrons).

However, when looking at the variability energy profile of Mkn 421 (Figure 9.19 from the conclusion of Chapter 9), we see that the shape variability profile from the non-periodic SSC model could roughly fit the data. One would need to derive a steady state corresponding to the average state of Mkn 421 and run the dynamical evolution of the SSC again. This is something I would have liked to do but establishing this working framework, testing it and running it took already a lot of time but it could be done in a future work. The $F_{\rm var}(E)$ profile of Mkn 501 could be reproduced as well, however one would have to be careful with the flares present in the dataset.

So, if I sum up:

1. The time-independent and stationnary SSC model is known to reproduce well the SED of HBL objects like PKS 2155-304, Mkn 412 and Mkn 501.

2. The time-dependent SSC model reproduces well the variability energy profile of PKS 2155-304 and would be apparently capable of the same for the other HBL objects Mkn 421 and Mkn 501.

I would be curious to have an equivalent dataset for a LBL or FSRQ object to see how the variability evolves with time: is the shape the same as HBL? Is it different? If so, how? Could we define a blazar sequence in variability?

10.6.2 Cross-correlation

Since the Synchrotron and Inverse Compton photons are produced by the same electron population, SSC light curves in the different energy ranges are correlated. The interesting part is to see if this correlation holds when the temporal binning of the data is applied. The answer is yes. Then, if blazars' emission was to be ruled by the SSC model, or a SSC-like model, we should see a direct correlation between the light curves of the different ranges.

Nevertheless, seing correlations in the data is not as easy because the DCF is varying a lot with the time lag. All of the DCFs (except the X-ray $\times$ *Fermi*-LAT one) have a local maximum at $\tau = 0$ days indicating a direct correlation of the light curves. But the rest of the correlation function, going to larger time lags, show strong variations and other local maxima, making it difficult to conclude about the correlation.

10.6.3 Power spectral density

The input variations of the dynamical evolution of the SSC is a time series generated following a power law noise PSD ($f(\omega) \propto \omega^{-\beta}$) of index $\beta = 1$. It is then naturally that we find the same behavior with the same power law index for the simulated light curves in each energy range.

If the temporal binning of the data did not have any effect on the variability value of the optical, X-ray and TeV simulated light curves, it has one on the PSD. When binning the simulated light curves, the PSD looses power and this loss is frequency dependent, resulting in a change of index (except for the GeV light curve were there is no windowing). The behavior in frequency of the data and the simulated data-like light curves look alike althouth there are some tensions on the values of the power law index.

The power law index ~ 1 of the PSD of the simulated light curves is in agreement with the results from H. E. S. S. Collaboration et al., 2017 where we found index of $\beta_{\rm VHE} = 1.1$ and $\beta_{HE} = 1.2$.

10.6.4 Periodicity in the SSC

Shorter simulations of 21 months were done injecting a periodicity of 7 months to see if the periodicy was present in each energy range or not. These simulations showed that the periodicity is strong (and the period well reconstructed) in the SMARTS and *Fermi*-LAT light curves but not as well as in the X-ray and H.E.S.S. ones. If a data-like temporal binning would have been applied it could have killed the faint periodic signature we see. Hence, in order to see if a blazar is periodic in the X-ray and TeV ranges, experiment would have to be careful on their period of observation to reduce as much the strong windowing of the data.

Due to the long time requested (at least 3 weeks) to run long term simulations, it was not possible to produce 10-years data-like light curves to see the real effect of the temporal binning on a 700 days period.

10.6.5 Going further

According to me, variability is the key to improve our understanding of blazars and AGN in general. It will be important to have more long term multi-wavelength light curves on other objects as well to reproduce the same kind of study as the one done on PKS 2155-304: characterization of the variability and SSC modelisation. It may take some time but experiments are doing more and more monitoring programs and joint campains of observations.

Studying in details the time-dependant version of current emission models would be another direction to go to. This SSC model could be upgraded to a version taking into account external Compton as well. One could try to look at a time-dependant adaptation of hadronic models (it seems more complicated as there are two populations of emitting particles) to see how is its variability signature and if it can do as well or not than the SSC.

Chapter 11

Conclusion: Towards a systematic study of long term light curves

Contents

11.1 Exploring the variability of *Fermi*-LAT's bright sources

I selected the brightest sources ($TS > 100$) of the 3FGL catalog (Ackermann et al., 2015b). This cut gives 24 blazars, the full list provided in Table 11.1. This sample contains 15 FSRQs and 8 BL Lacs.

The light curves, between 100 MeV and 300 GeV, for each objects are derived using the same analysis procedure as the one described in Section 9.2.2. Each light curve contains 100 bins of 30 days from August 2008 to November 2016. They are shown on Figures 11.4, 11.5, 11.6, 11.7, 11.8 and 11.9 along with their LSP to be discussed in the next section. Sources are variable, with sometimes flaring events with high flux compared to the average.

The fractional root mean square variability $F_{\rm var}$ of the light curve is computed to see if the sources have a similar behavior in GeV or if the FSRQs and BL Lacs behave differently. Figure 11.1 shows that FSRQs and BL Lacs seem to behave differently, with on average a higher variability for FSRQs. Looking at the mean and standard deviation of both histograms, FSRQs display a variability $F_{\rm var} = 1.00 \pm 0.38$ while BL Lacs have $F_{\rm var} = 0.52 \pm 0.17$.

13 FSRQ objects over 15 exhibits flaring events in their light curves while only half of the BL Lacs seems to flare. Even though, the maximum value of the variability for BL Lacs and FSRQs is different: $\max(F_{\rm var}^{\rm bll}) = 0.82$ and $\max(F_{\rm var}^{\rm fsrq}) = 1.49$.

In the 3LAC catalog (Ackermann et al., 2015b), the *Fermi*-LAT collaboration already showed that FSRQs and BL Lacs behave differently spectrally and temporally (Figure 11.2). As described in the blazar sequence (seen Chapter 2), LSP (FSRQs in red and LSP BL Lacs in green) have a higher spectral index than HSP BL Lacs (equivalent to HBL) equivalent to a different peak position. The top panel of Figure 11.2 displays the value of the variability index versus the Synchrotron peak frequency. FSRQs/LSPs are seen on average more variable than BL Lacs with however the two distributions of the variability index are impossible to separate if projected on the y-axis only.

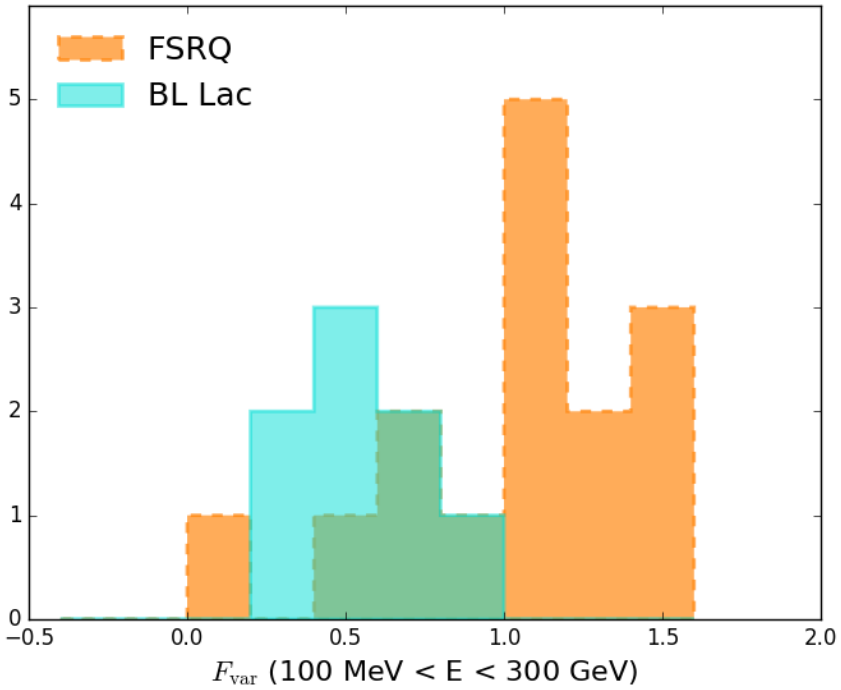

FIGURE 11.1: Histograms of the fractional root mean square variability values of the bright *Fermi*-LAT sources. The FSRQ and BL Lac sources are separated between the orange and blue histograms.

11.2 Lomb-Scargle periodograms of the GeV light curves

The Lomb-Scargle algorithm has been applied to all the GeV light curves to find if some of them were displaying a periodic behavior like PKS 2155-304.

The LSP for each source is shown on the right panels of Figures 11.4, 11.5, 11.6, 11.7, 11.8 and 11.9 along with simulation following a time series of power law noise with $\beta = 1$. In each of them, the maximum of the LSP has been searched for, and the corresponding time scale $T_{\rm max}$ (the probable period) retrieved.

Table 11.1 presents the $T_{\rm max}$ value and corresponding maximum LSP value, along with the value of the simulated LSP at $t = T_{\rm max}$. When the value of the maximum of the LSP is included in the simulation interval, it means that it does not correspond to a periodic signal. If the maximum of the LSP is above the simulation value, the corresponding source is written in bold as it could have a periodic behavior.

PKS 2155-304 is found to be periodic with $T_{\rm max} = 636$ days while a period of 680 days was found in Chapter 9. The *Fermi*-LAT light curves spans a longer time than the one presented in Chapter 9 and is binned on 30 days instead of 10. This explains the compatible ~ 50 days of difference between the two analyses.

Along with PKS 2155-304, 9 other objects are found to be variable with periods ranging from 317 days for the FSRQ PKS 1830-211 and 1585 days for the BL Lac BL Lacertae. However, a too long period $\gtrsim 1000$ days on light curves spanning ~ 3000 days is not significant. This is the case for 4C +21.53, BL Lacertae, PKS 0426-380, PKS 1502+106, PKS 2326-502 and S5 0716+71 where the peak of the maximum is just above the simulation.

For PKS 1510-08 and PKS 1830-211, the periods seem to correspond to the time interval between consecutive flares. Is it just a coincidence or do flares (at least in some

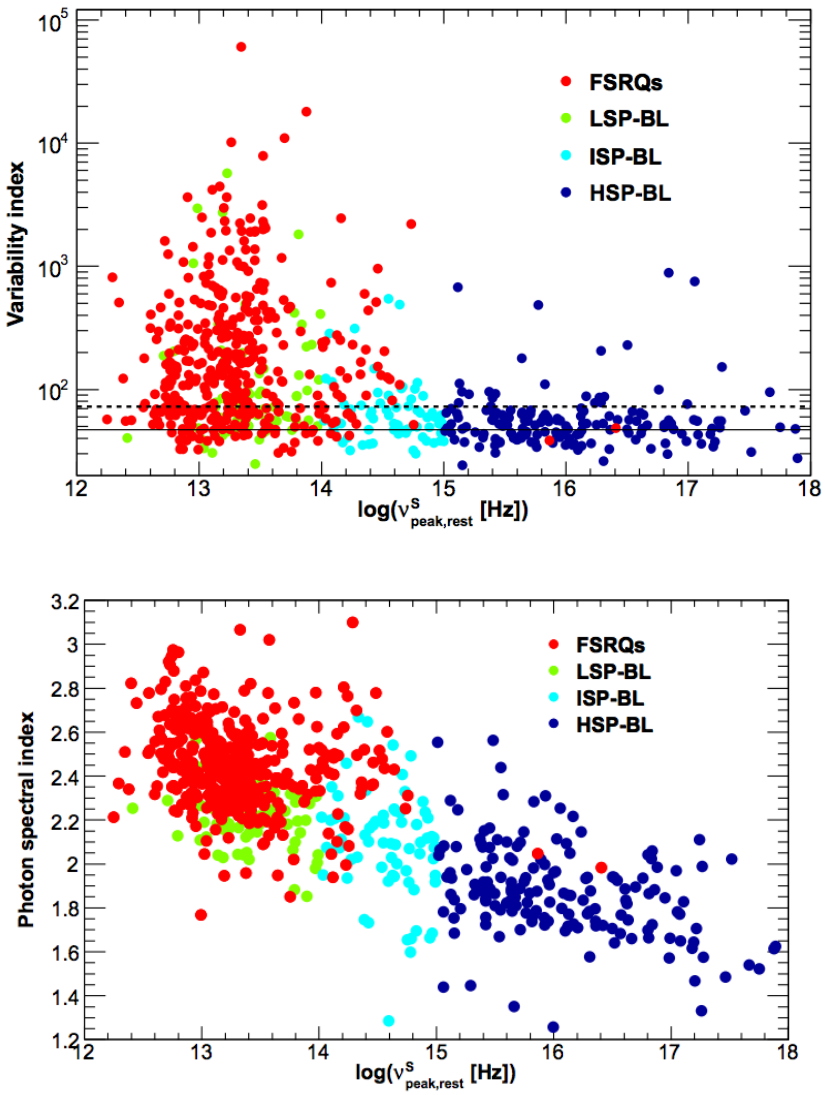

FIGURE 11.2: Left: Photon index versus the Synchrotron peak frequency for FSRQs (red) and BL Lacs (with the different LSP, ISP and HSP subclasses). Right: Variability index versus the Synchrotron peak frequency for FSRQs (red) and BL Lacs (with the different LSP, ISP and HSP subclasses).

objects) follow a periodic process?

Only PKS 1424-240 seems to have a similar behavior as PKS 2155-304: a significant period of 551 days and a light curve showing no flare. I looked over the optical monitoring program of SMARTS and the Astronomy & Steward Observatory[1], to see if a period could be seen in the optical light curves as well. But unfortunatly none of them observed this object.

TABLE 11.1: List of the selected bright *Fermi*-LAT sources with their type, time of maximum $T_{\max}$, value of maximum and value of the simulation at $T_{\max}$.

Source	Type	$T_{\max}$ (days)	LSP max	Simulation value
3C 273	FSRQ	1420.83	6.14	8.29 ± 7.04
3C 279	FSRQ	2000.0	6.30	12.11 ± 8.88
3C 454.3	FSRQ	1653.63	9.93	9.43 ± 7.80
3C 66A	BL Lac	1694.50	8.65	9.65 ± 7.89
4C +21.35	**FSRQ**	**1344.81**	**20.10**	**7.52 ± 6.48**
4C +28.07	FSRQ	1130.53	9.29	4.92 ± 4.88
4C +55.17	FSRQ	1042.16	2.22	4.39 ± 4.26
B 21520+31	FSRQ	1020.31	8.33	4.31 ± 4.15
BL Lacertae	**BL Lac**	**1585.70**	**20.40**	**9.13 ± 7.67**
Mkn 421	BL Lac	2000.0	8.59	12.11 ± 8.88
PKS 0402-362	FSRQ	1582.85	15.88	9.11 ± 7.66
PKS 0426-380	**BL Lac**	**1273.07**	**15.26**	**6.54 ± 5.92**
PKS 0454-234	FSRQ	1522.98	12.62	8.87 ± 7.51
PKS 0537-441	BL Lac	2000.0	5.854	12.11 ± 8.88
PKS 0727-11	FSRQ	2000.0	13.83	12.11 ± 8.88
PKS 1424+240	**BL Lac**	**550.89**	**8.51**	**1.45 ± 1.73**
PKS 1502+106	**FSRQ**	**1226.03**	**15.17**	**5.89 ± 5.59**
PKS 1510-08	**FSRQ**	**566.57**	**6.70**	**1.58 ± 1.78**
PKS 1830-211	**FSRQ**	**317.13**	**6.51**	**0.53 ± 0.61**
PKS 2155-304	**BL Lac**	**636.41**	**14.98**	**1.80 ± 2.07**
PKS 2326-502	**FSRQ**	**1212.73**	**18.74**	**5.72 ± 5.50**
PKS B1424-418	FSRQ	2000.0	13.21	12.11 ± 8.88
S5 0716+71	**BL Lac**	**944.76**	**12.42**	**4.00 ± 3.78**

11.3 Perspectives

With the arrival of the CTA observatory (Figure 11.3) in the next couple of years, monitoring programs at TeV should florish. With its ~ 20 telescopes in La Palma and ~ 100 in Chile, divided in 3 types to cover the GeV and TeV ranges, the sensitivity of CTA compared to the current IACT experiments will be improved by a factor 10 (see the expected sentivity of CTA in different energy ranges on the bottom panel of Figure 11.3), allowing to increase the number of TeV sources for monitoring.

This future array should improve the current number of known TeV emitters by a factor 10, allowing AGN population studies and studies of the unification and classification

[1]Ground-based Observational Support of the Fermi Gamma-ray Space Telescope at the University of Arizona: http://james.as.arizona.edu/~psmith/Fermi/#~mark6

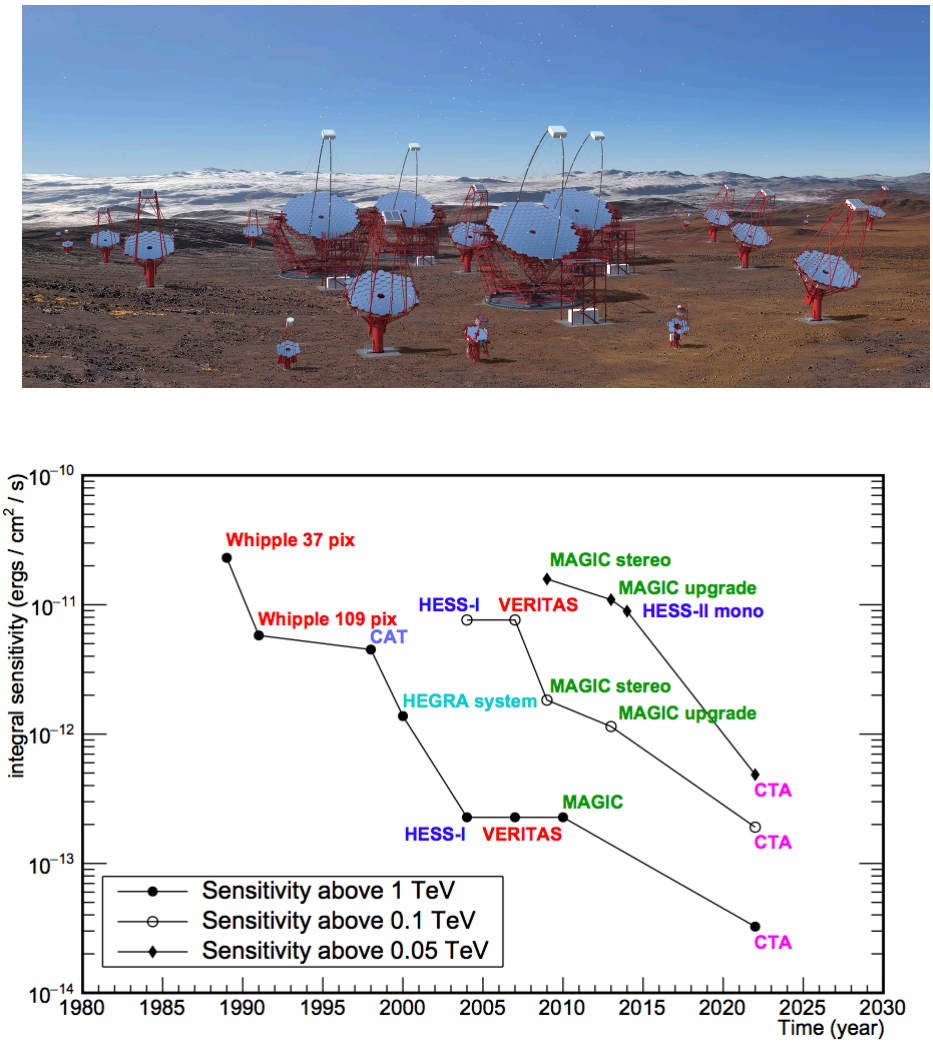

FIGURE 11.3: Top: Sketch of the Southern CTA array ©CTA. Bottom: Evolution of the integral sensitiviy ofthe IACTs over time above 50 GeV (filled diamonds), 100 GeV (open circles) and 1 TeV (filled circles).

schemes at VHE. Sol et al., 2013 stated that "*long term correlated multi-wavelength monitoring programs of a well defined sample of AGN will be a necessity*". Monitoring programs with CTA will take advantage of the number of telescopes to observe with different sub-arrays.

The future long term VHE light curves, along with light curves from other bands, will help to clarify if the variability is dominated by processes in the jet or by the accretion disk and processes in the vicinity of the black hole.

Future monitoring programs could included joint observation campaigns with the recent X-ray experiment ASTRO-H[2] (Takahashi, Uchiyama, and Stawarz, 2013), which would be of importance to probe the correlation between the X-ray and VHE energy ranges, expected in the SSC model but not always clear in the data.

Concerning an all-sky survey, CTA has the ability to survey 1/4th of the sky in 270 hours with a sensitivity of 2 % of the Crab (Dubus et al., 2013). An all-sky blind survey has never been done by IACTs, because of the sentivity of the experiments, their duty cycle and small field of view. But it would help to unbias the current VHE sample of AGN

[2] https://heasarc.gsfc.nasa.gov/docs/hitomi/

and study the blazar sequence at VHE to understand better and constraint emission processes.

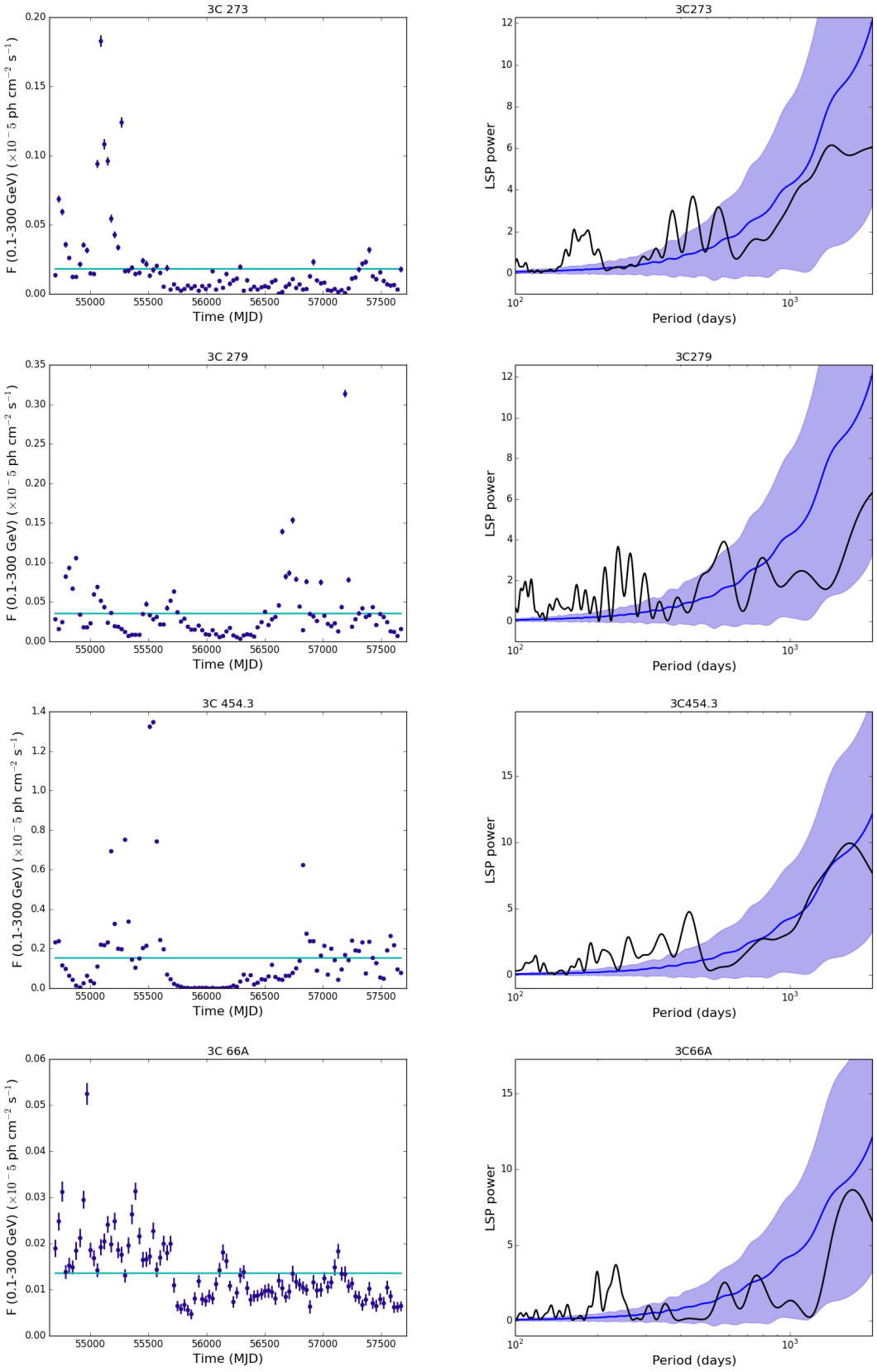

FIGURE 11.4: Light curves and corresponding LSP of *Fermi*-LAT bright sources (1).

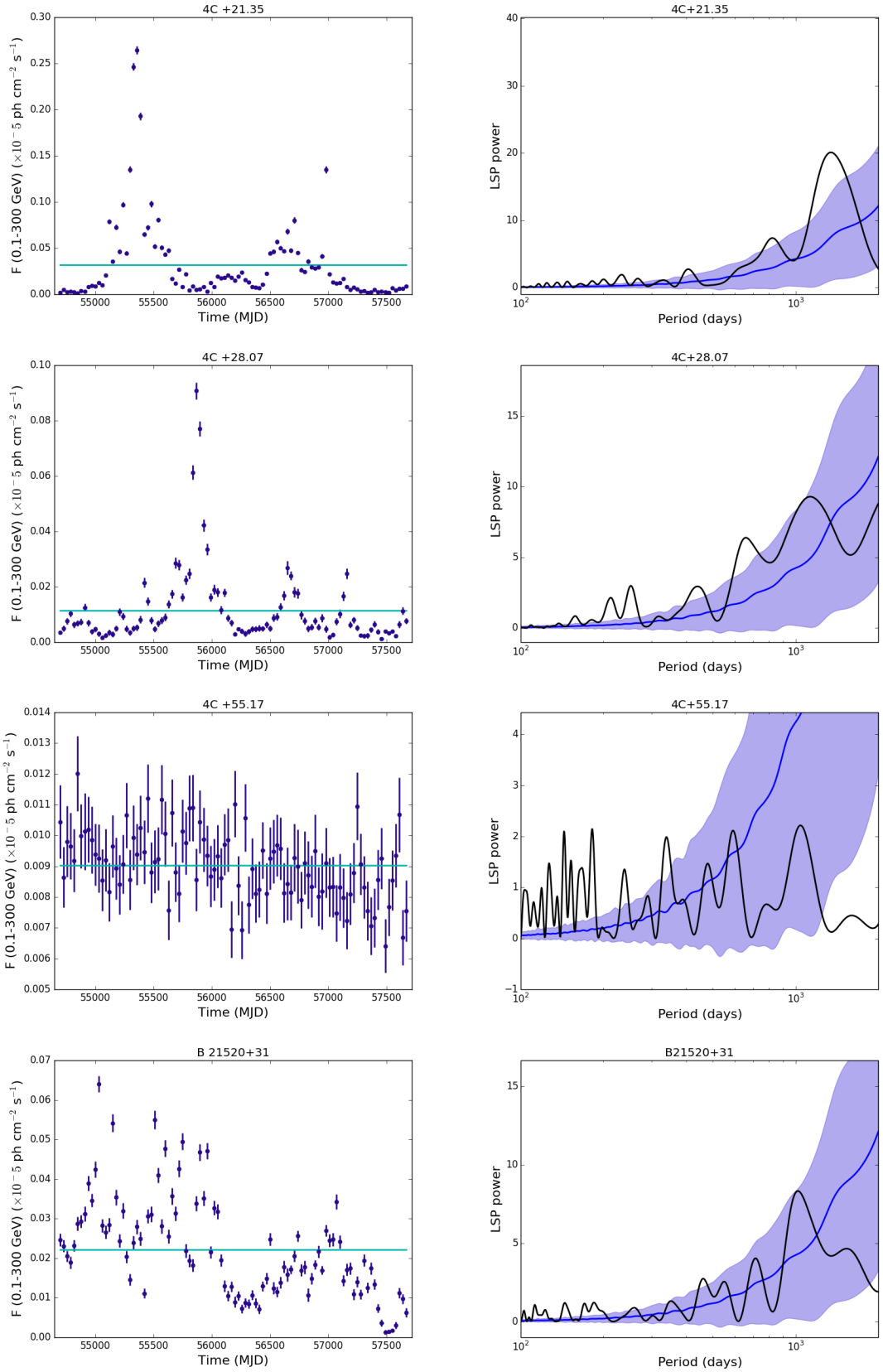

FIGURE 11.5: Light curves and corresponding LSP of *Fermi*-LAT bright sources (2).

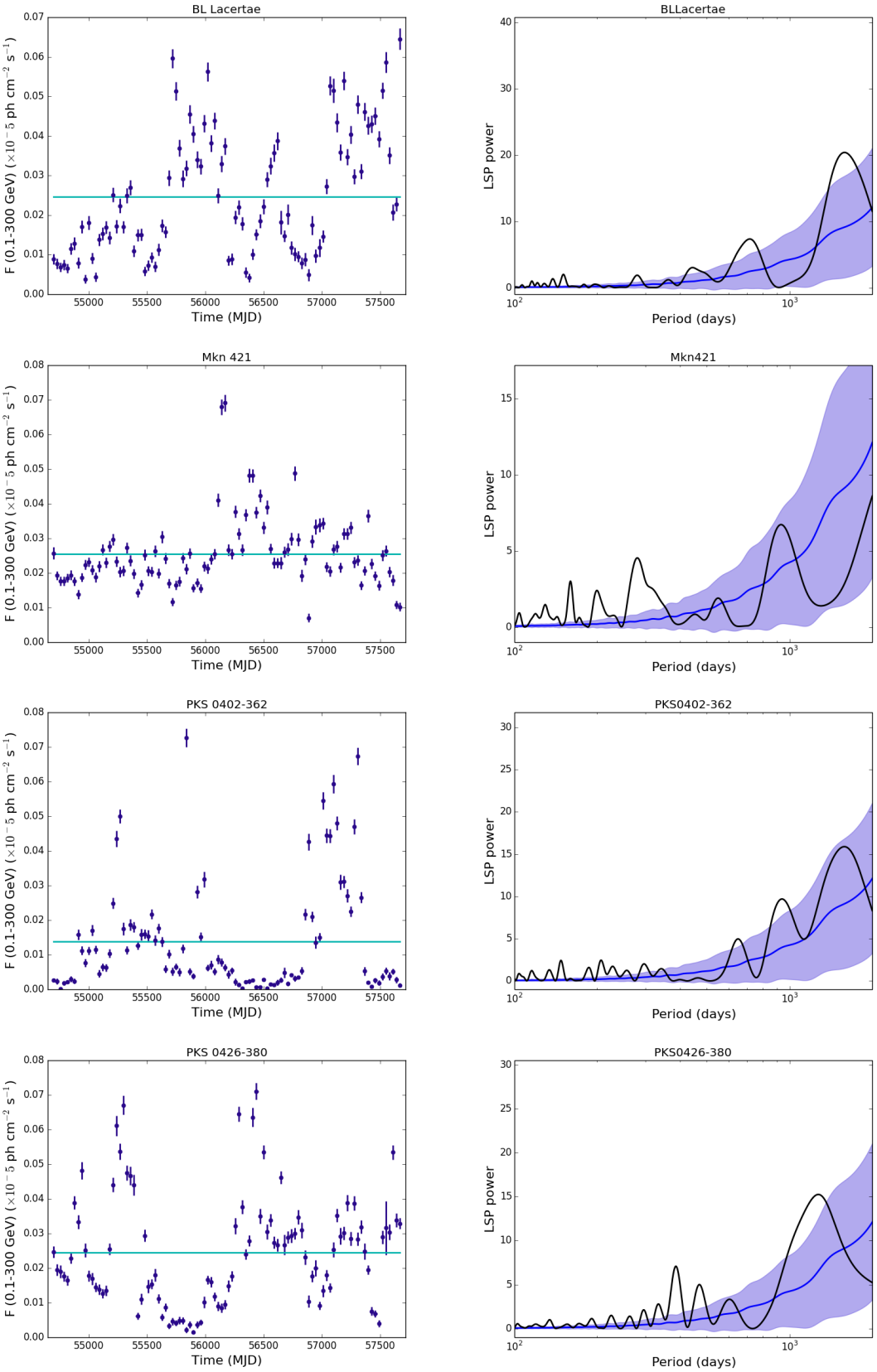

FIGURE 11.6: Light curves and corresponding LSP of *Fermi*-LAT bright sources (3).

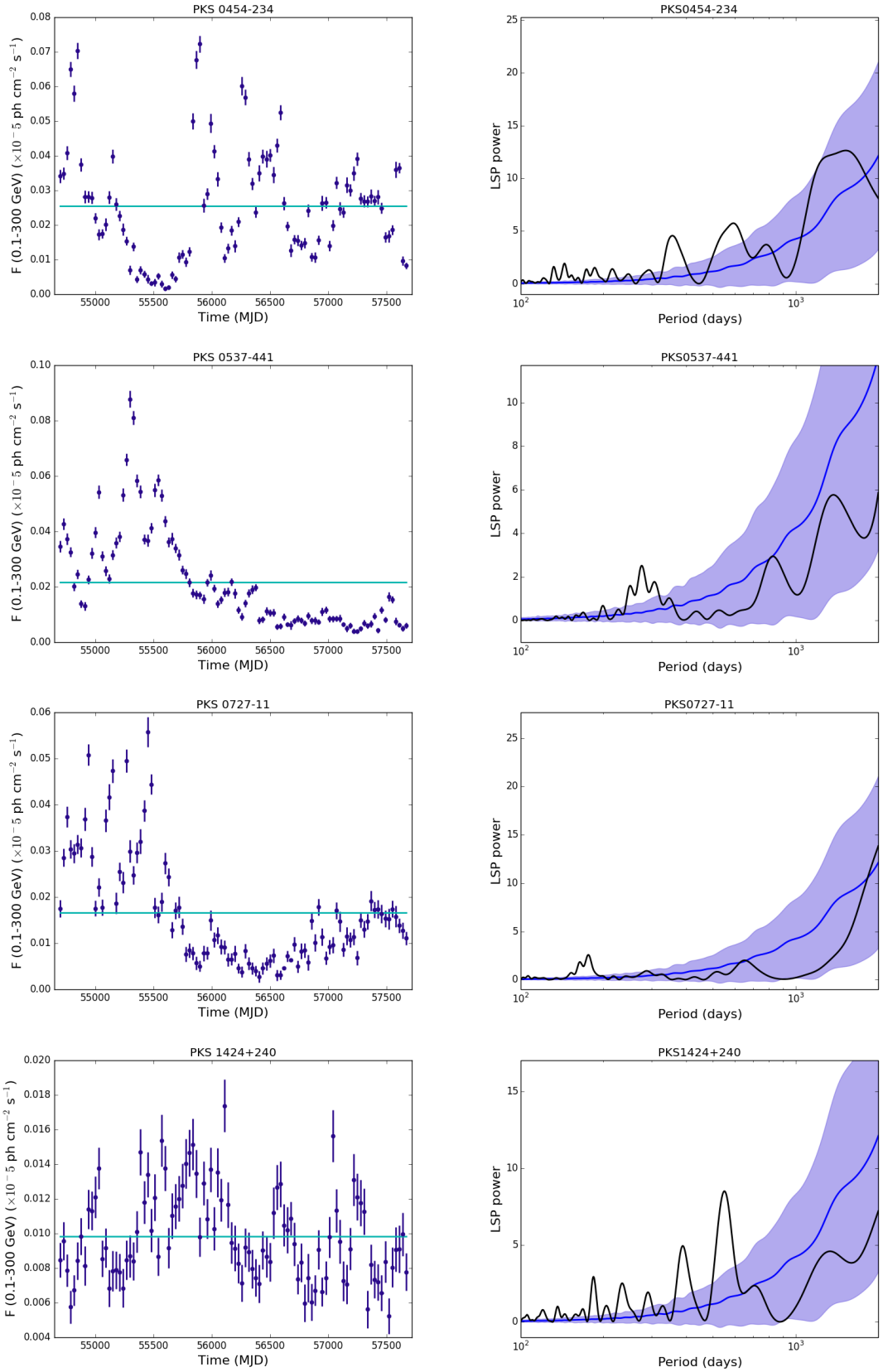

FIGURE 11.7: Light curves and corresponding LSP of *Fermi*-LAT bright sources (4).

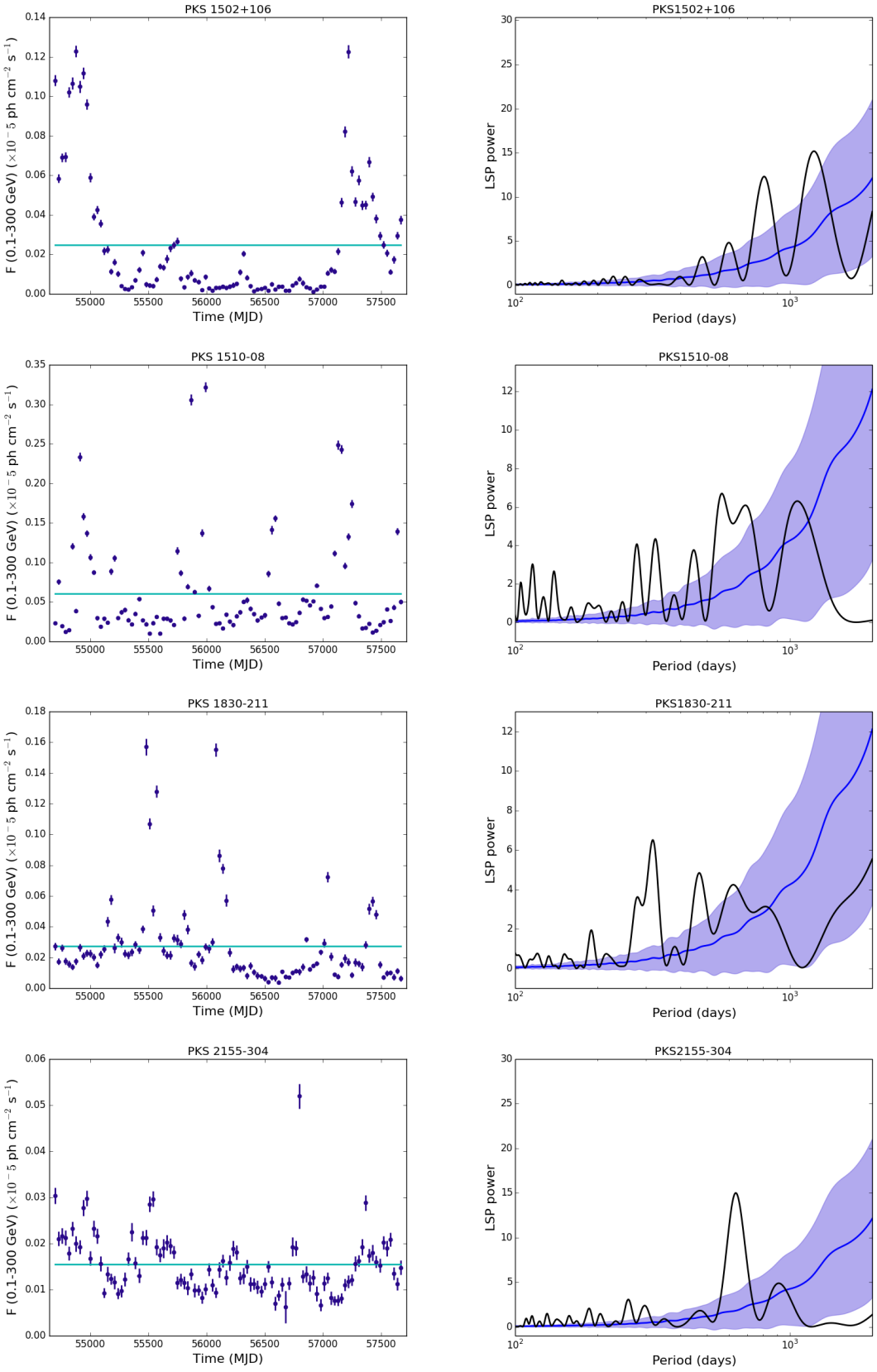

FIGURE 11.8: Light curves and corresponding LSP of *Fermi*-LAT bright sources (5).

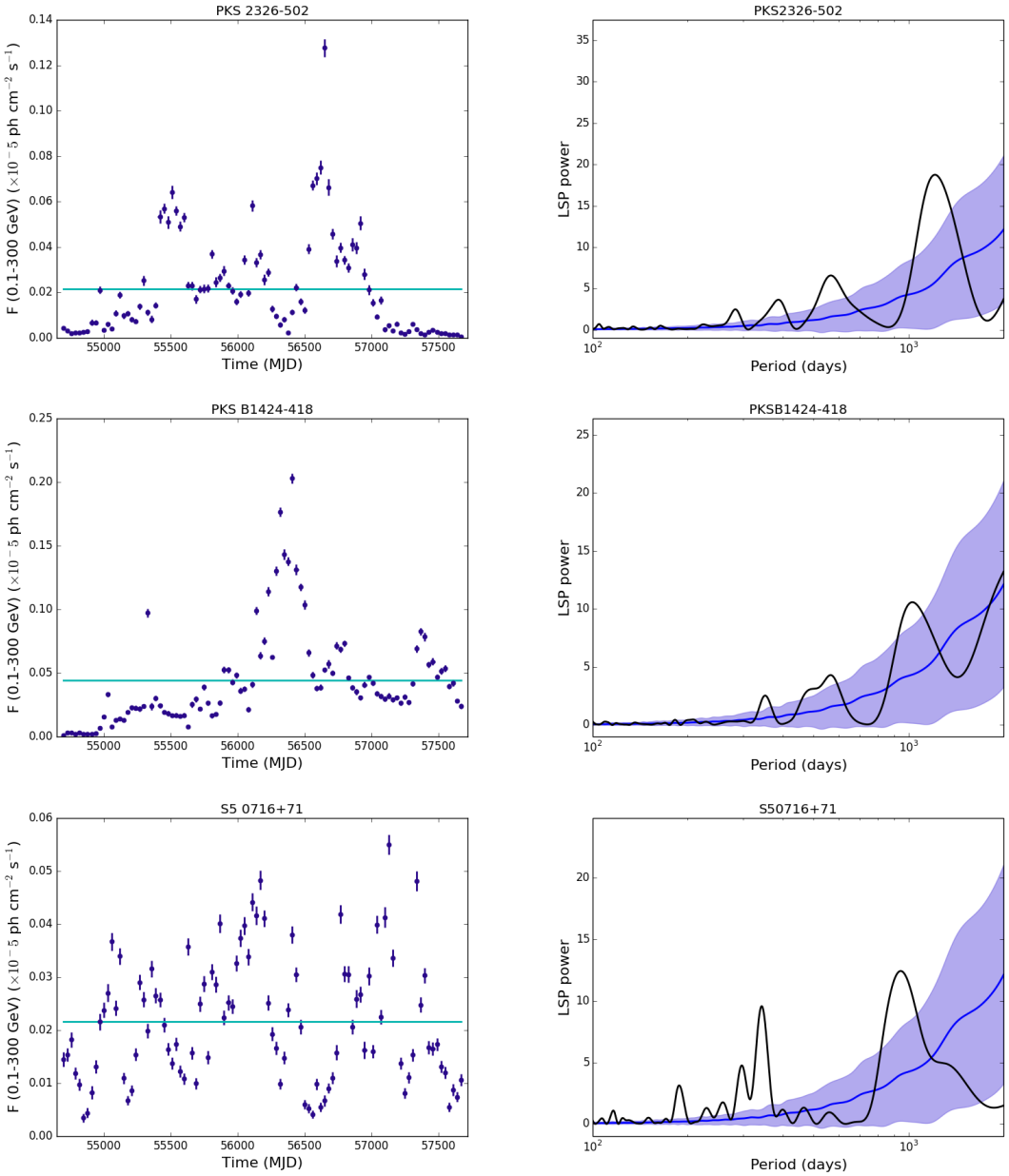

FIGURE 11.9: Light curves and corresponding LSP of *Fermi*-LAT bright sources (6).

Chapter 12

Résumé de la Partie 3 (French)

Charactérisation de la variabilité long terme de PKS 2155-304

L'étude de la variabilité est l'une des clés pour comprendre l'émission des blazars, ainsi que les liens entre le trou noir, le disque et le jet. Les modèles leptoniques et hadroniques, malgrè leurs différences, arrivent à expliquer la SED des blazars de type HBL. Mais ces deux types de modèles, en raison de leurs différences, auront des signatures en variabilité différentes, ce qui permettra de lever cette dégénérescence.

Les premières études de variabilité se sont surtout faites sur du court terme, sur des observations de quelques heures pendant des éruptions où le flux de photons augmente et varie fortement. Seulement, le mécanisme qui produit ces flares n'est pas forcément le même que celui qui produit ce qu'on appelle l'état calme du blazar.

Les études de variabilité sur le long terme (plusieurs mois à plusieurs années) à haute énergie sont plutôt récentes et se sont développées grâce à des expériences ayant un programme de monitoring comme par exemple le *Fermi*-LAT. Il est difficile pour les IACTs d'observer régulièrement la même source : le temps d'observation est séparé entre de nombreux objets et le cycle de service diminue le temps d'observation. De plus, peu de sources sont assez brillantes dans la gamme du TeV pour pouvoir construire des courbes de lumières avec assez de statistique dans chaque bin temporel. PKS 2155-304, Mkn 421 et Mkn 501 font parti de ces sources assez brillantes.

PKS 2155-304 est un blazar très connu détecté au TeV pour la première fois en 1999 (Chadwick et al., 1999). Étant l'un des blazars les plus lumineux de l'hémisphère Sud, il est régulièrement observé par H.E.S.S. depuis le début de l'expérience et nous disposons donc d'une grande quantité d'observation γ sur ce blazar ce qui m'a permis, après analyse des données, de construire une courbe de lumière de 9 ans (échantilloné nuit par nuit), entre 2004 et 2012 présentée en Figure 12.1. L'analyse a été faite avec une énergie de seuil de 200 GeV, et aussi dans deux sous-bandes en énergie : 200 - 630 GeV et au-dessus de 630 GeV.

Pour compléter le comportement en γ de PKS 2155-304, j'ai aussi analysé les données *Fermi*-LAT, entre 2008 et 2013, donnant la courbe de lumière entre 0.1 et 300 GeV montrée en Figure 12.2. La même analyse a été faite entre 0.1 et 1 GeV et 1 et 300 GeV. Du à la sensibilité et au fonctionnement du LAT, l'échantillonage temporel (on parle aussi de *binning* en utilisant le terme anglais) ne peut être aussi petit que pour d'autres expériences et cette courbe de lumière est échantillonée sur 10 jours.

En plus des données en γ, j'ai rassemblé aussi des données en X avec les expériences *RXTE*, *Swift*-XRT et XMM-Newton et en optique avec SMARTS. La courbe de lumière en X entre 2 et 10 keV est présentée en Figure 12.3, et on voit que l'intérêt de combiner plusieurs instrument était d'avoir une courbe de lumière plus complète. L'analyse en X a aussi été faite dans différentes sous-bandes en énergie : 0.3-2 keV, 2-4 keV, 4-7 keV et 7-10 keV.

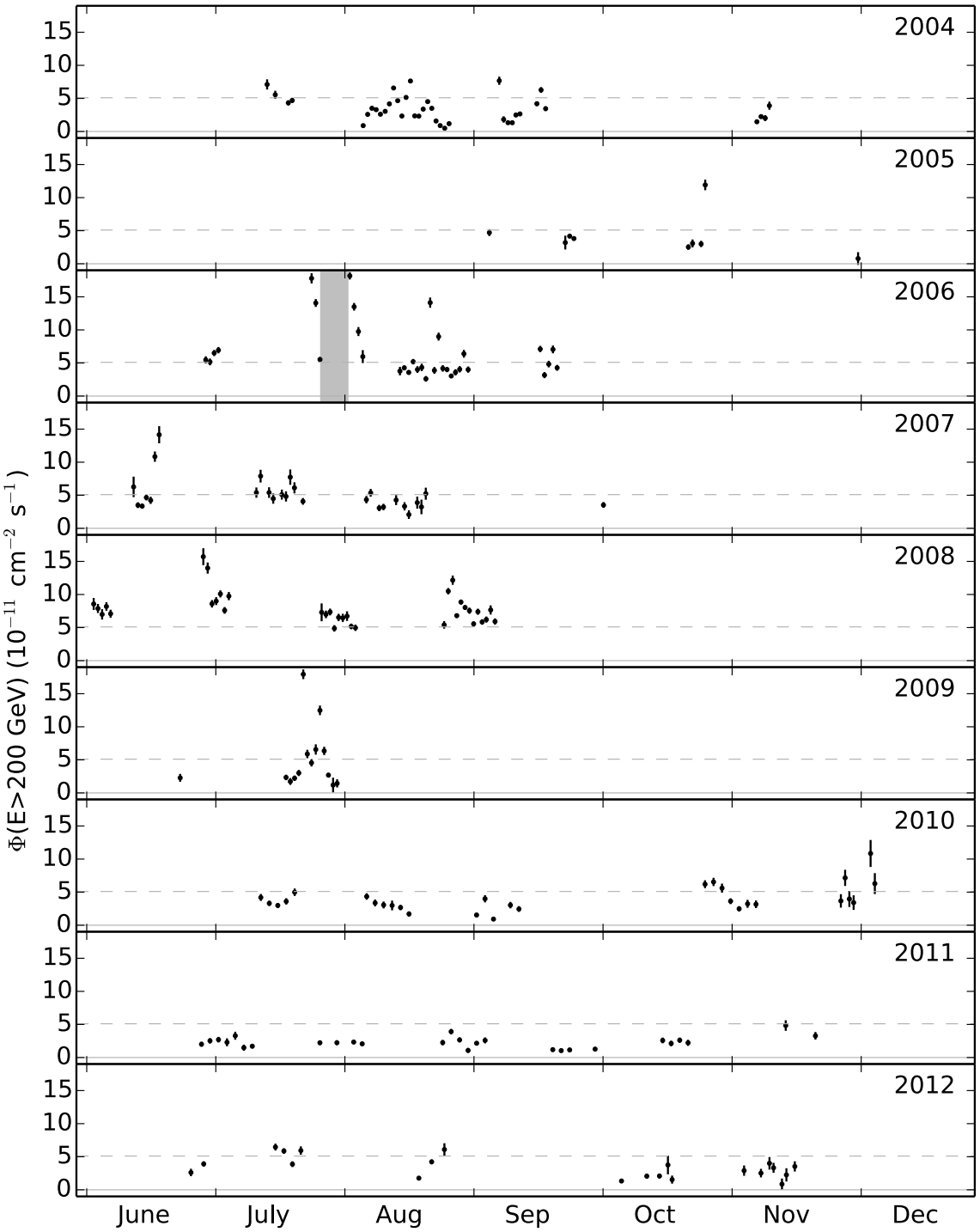

FIGURE 12.1: Courbe de lumière H.E.S.S. avec les flux nuit par nuit calculés au-dessus de 200 GeV.

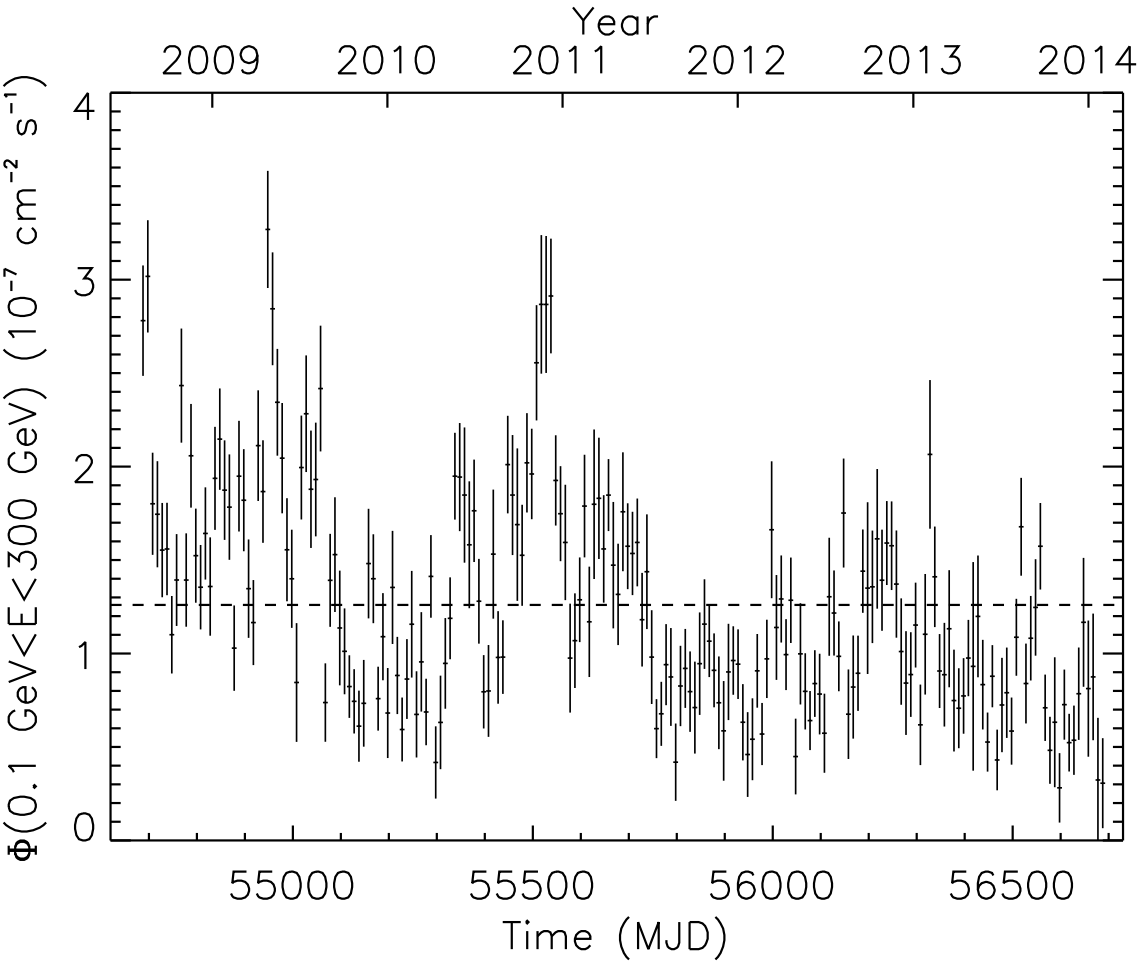

FIGURE 12.2: Courbe de lumière *Fermi*-LAT entre 0.1 et 300 GeV dans des bins de 10 jours.

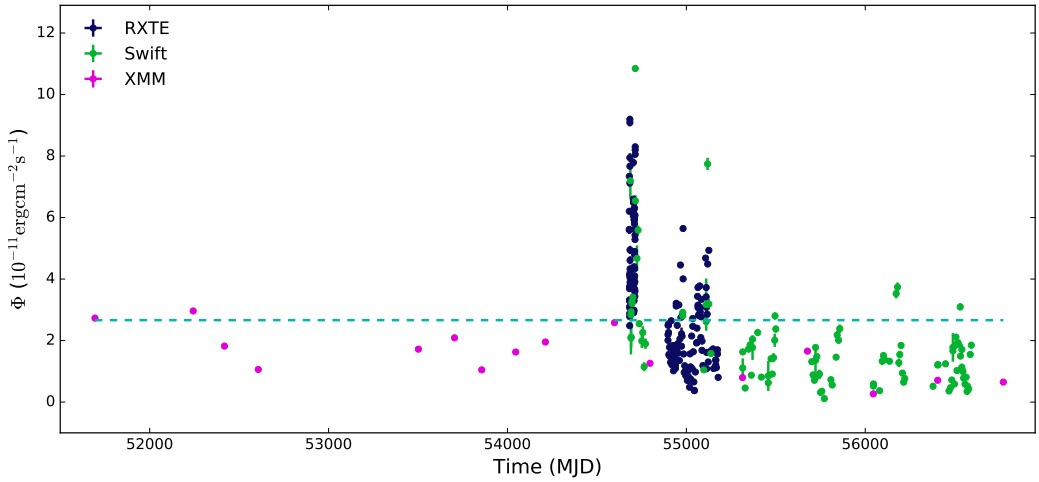

FIGURE 12.3: Courbe de lumière des flux en X entre 2 et 10 keV. Les données *Swift*-XRT sont en noir, *RXTE* en blue et XMM-Newton en rose.

Les données SMARTS sont dans 4 bandes optiques différentes : J, R, V et B, les courbes de lumières correspondantes sont visibles dans la Figure 12.4.

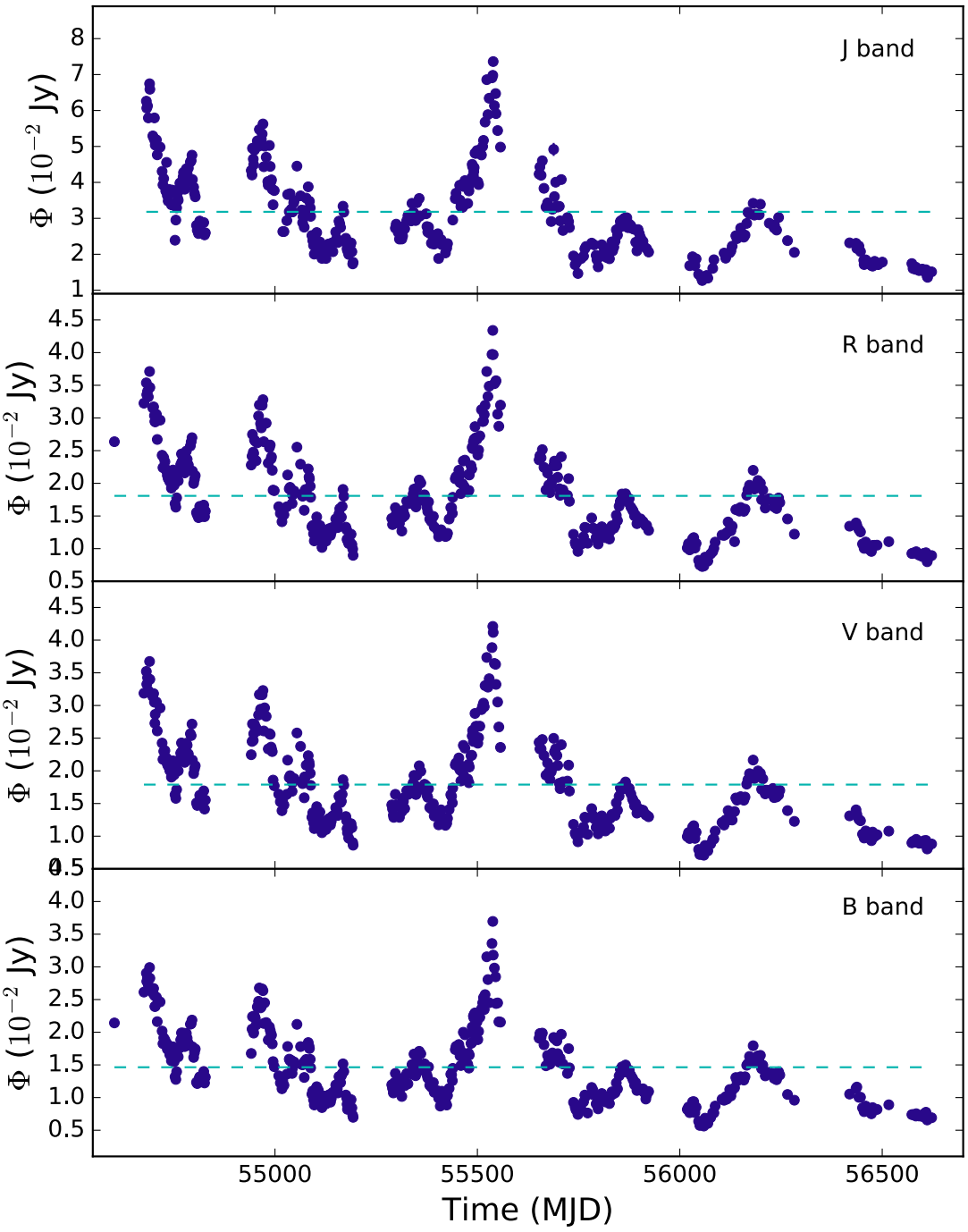

FIGURE 12.4: Courbes de lumières des flux optiques de SMARTS.

On peut caractériser les courbes de lumières et leur variabilité en utilisant différentes méthodes (liste non exhaustive) :

1. La variabilité fractionnelle $F_{\rm var}$ définie comme la variance du flux S^2 corrigée des erreurs $\overline{\sigma^2_{\rm err}}$ et normalisée par le flux moyen $\overline{\Phi}$:

$$F_{\rm var} = \frac{\sqrt{S^2 - \overline{\sigma^2_{\rm err}}}}{\overline{\Phi}}$$

   Cet outil permet de comparer la quantité de variabilité (en pourcentage) présente dans les différentes gammes en énergie.

2. Les corrélations en bandes en énergie : si on observe les mêmes variations entre le flux en optique, X, GeV ou TeV cela montrerai que les photons à ces énergies sont produits par la même population de particules, ce qui irait plutôt dans le sens des modèles leptoniques tels que le SSC.

3. Densité spectrale en énergie (ou PSD pour *Power Spectral Density* en anglais) : la PSD montre comment la puissance est divisée entre les différentes fréquences (ou les différentes échelles de temps) ce qui permet de voir les échelles de temps de la variabilité.

4. Le comportement lognormal ou non du flux permet d'avoir une vue sur l'origine de la variabilité. On pense que le comportement lognormal est lié au disque d'accrétion et aux processus d'accrétion.

Profil de variabilité $F_{\rm var}(E)$

La Figure 12.5 montre l'évolution de la variabilité avec l'énergie pour les données multi-longueur d'onde de PKS 2155-304 analysées auparavant. On voit clairement que la variabilité augmente de l'optique jusqu'aux X, puis du GeV vers le TeV. La quantité de variabilité est similaire pour les données SMARTS et *Fermi*-LAT avec $F_{\rm var} \sim 40\,\%$ et augmente fortement à la fois en X et au TeV, montrant que les parties basse et haute énergie se comportent de manière similaire.

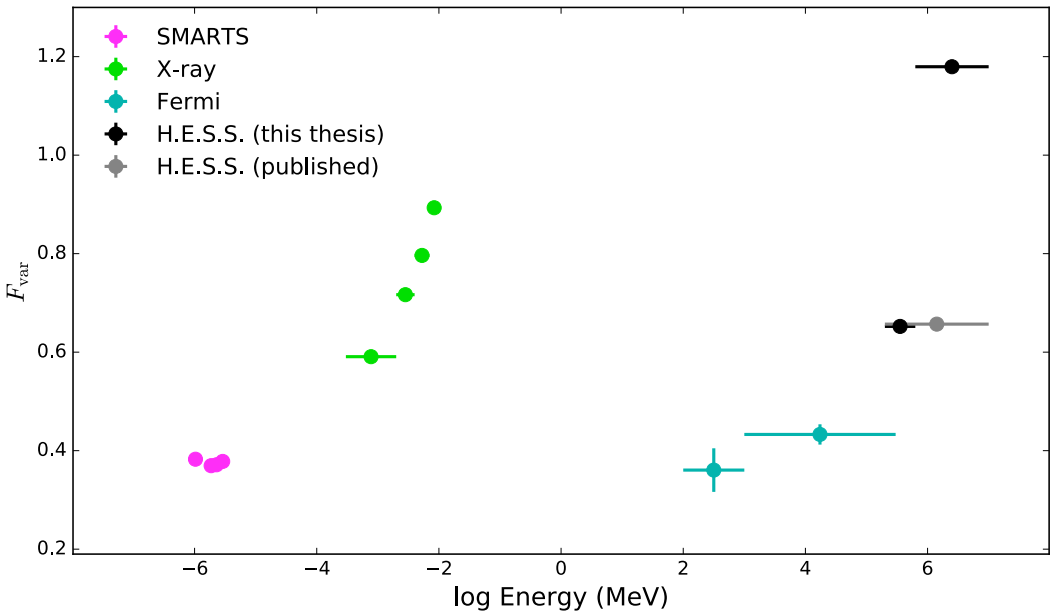

FIGURE 12.5: Profil de variabilité $F_{\rm var}(E)$ des données de PKS 2155-304.

Corrélations croisés

Le comportement similaire des données SMARTS-*Fermi*-LAT d'un côté et des données X-H.E.S.S. de l'autre laisse penser que l'on a un comportement similaire et donc possiblement des corrélations entre ces bandes. Malheureusement, les données de monitoring en X et au TeV sont trop éparses, avec trop de trous dans la prise de données, et ne permettent pas de résoudre la présence d'une corrélation ou non. Par contre, avec les données

Fermi-LAT et SMARTS qui sont des données de monitoring quasi-continu on peut calculer la corrélation entre les deux.

La corrélation est calculée grâce à une DCF (*Discrete Correlation Function* en anglais) avec la courbe de lumière SMARTS re-binnée sur 10 jours pour suivre l'échantillonage temporel des données *Fermi*-LAT. La Figure 12.6 montre le résultat de ce calcul. On voit clairement que les deux bandes énergies sont corrélées à $\tau = 0$ jour.

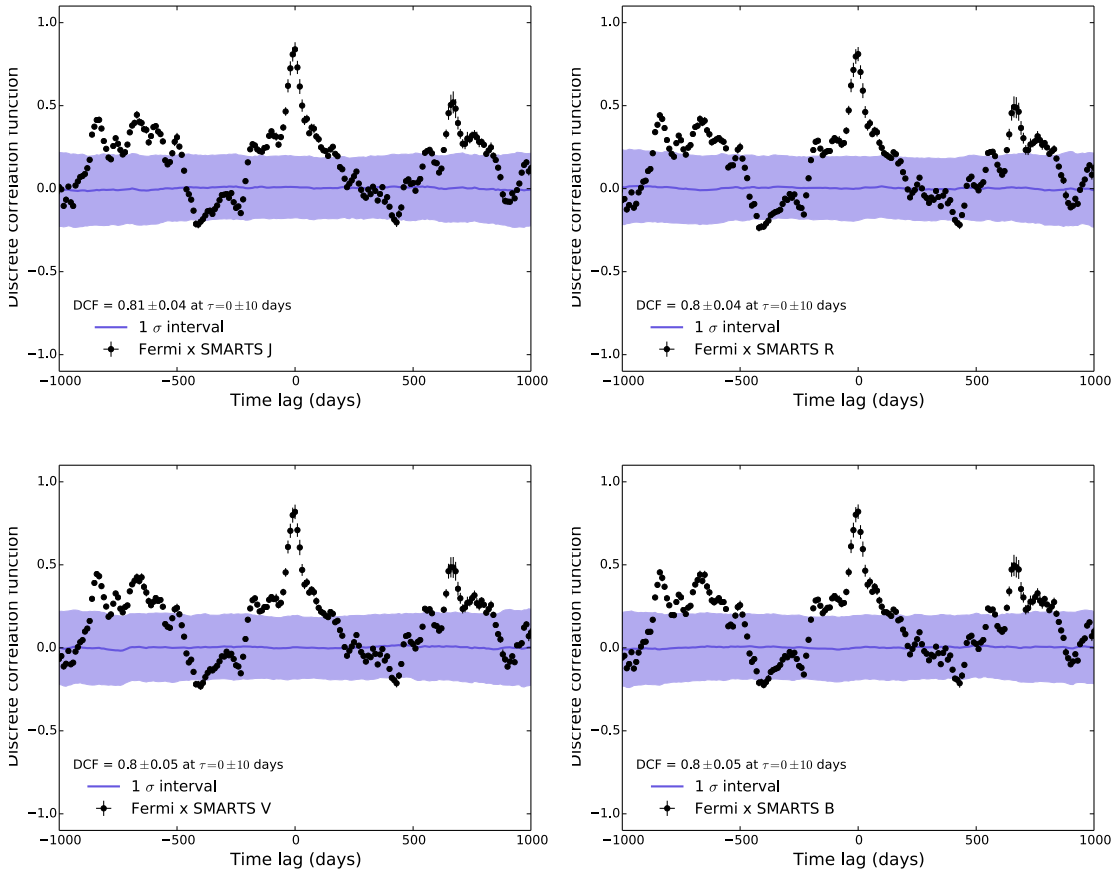

FIGURE 12.6: DCF entre les données *Fermi*-LAT et SMARTS en noir. La courbe bleue montre l'intervalle de confiance à 1 σ. De gauche à droite et de haut en bas : *Fermi*-LAT $\times$ J-band, *Fermi*-LAT $\times$ R-band, *Fermi*-LAT $\times$ V-band, *Fermi*-LAT $\times$ B-band.

Recherche de périodicité

Des pics secondaires apparaîssent dans chaque DCF à $\tau \sim \pm 700$ jours et pourraient être dû à la présence de périodicité dans les courbes de lumière. Afin d'étudier plus en détails cette périodicité, j'ai testé toutes les courbes de lumières avec un périodogramme de Lomb-Scargle (LSP; Lomb, 1976; Scargle, 1982).

Les résultats sont montrés en Figure 12.7 (courbe noire) avec l'intervalle à 1 σ (courbe bleue) pour estimer la probabilité qu'un possible signal soit du bruit. Les LSP des données X et TeV ne montrent aucun signal périodique, seulement le bruit du à l'échantillonage des données. En revanche, pour les données optique et au GeV, on voit un clair signal périodique à $T \sim 700$ jours. La période est de 685 jours pour les données *Fermi*-LAT entre 0.1 et 300 GeV et de 733 jours pour les données SMARTS (dans la bande R).

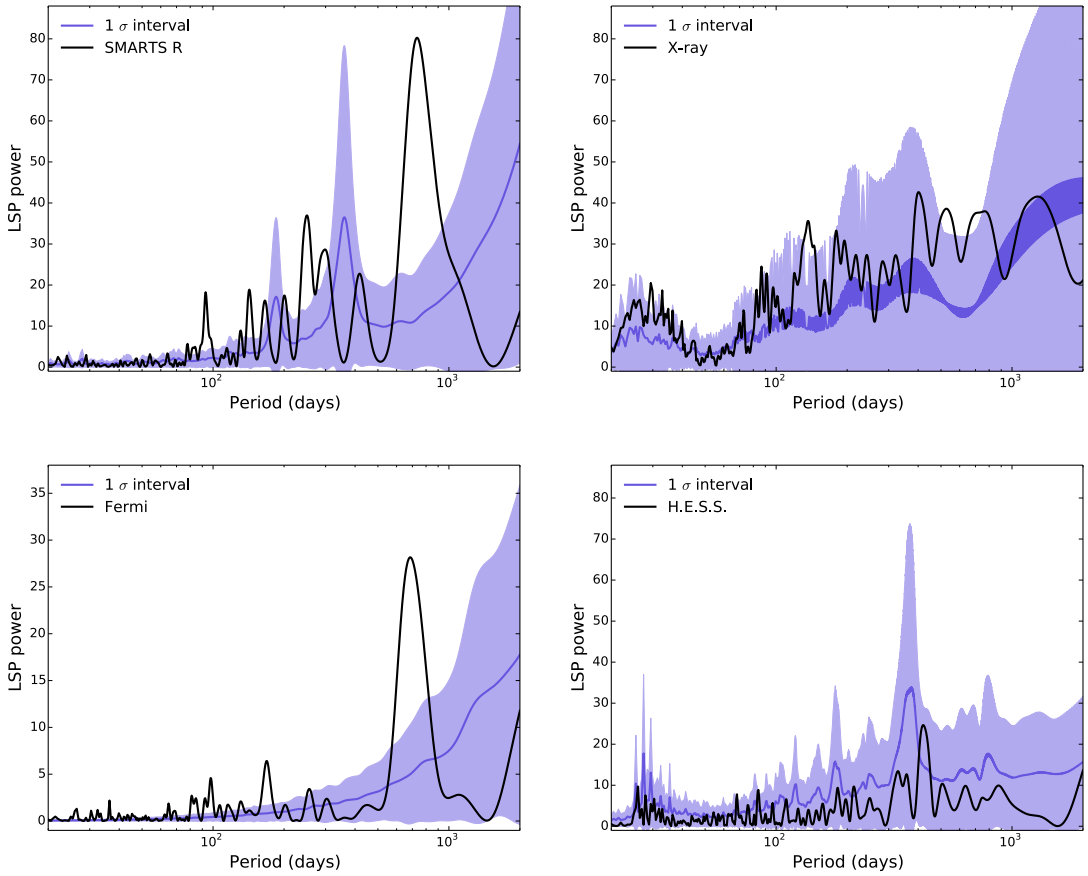

FIGURE 12.7: De gauche à droite et de haut en bas : LSP pour les courbes de lumière SMARTS (bande R), X, *Fermi-LAT* et H.E.S.S.

Comportement log-normal

On dit qu'un flux a un comportement log-normal quand le logarithme du flux suit une loi normale (et non le flux lui même). En prenant le Théorème Central Limite, cela veut dire que le processus est multiplicatif au lieu d'additif :

$$\begin{aligned} \Phi \mapsto \mathcal{N}(\mu,\sigma) &\Rightarrow \Phi_1 + \Phi_2 + ... + \Phi_n \\ \log(\Phi) \mapsto \mathcal{N}(\mu,\sigma) &\Rightarrow \log(\Phi_1) + \log(\Phi_2) + ... + \log(\Phi_n) \\ &\Leftrightarrow \log(\Phi_1 \times \Phi_2 \times ... \times \Phi_n) \end{aligned}$$

où μ et σ représentent la moyennen et la variance de la distribution normale. Ces processus multiplicatifs ont pour conséquence que la variabilité et la valeur du flux sont corrélées : plus le flux est haut, plus il est variable.

Les distribution de chaque courbes de lumière montre une préférence pour l'ajustement Gaussien du logarithme des flux plutôt que pour l'ajustement Gaussien des flux. De même la variabilité et le flux montrent une claire corrélation (Figure 12.8) prouvant que les flux multi-longueur d'onde de PKS 2155-304 ont un comportement lognormal.

Conclusion

Cette étude a permis d'étudier en détail la variabilité de PKS 2155-304 sur le long terme, le but premier étant de mieux comprendre les processus d'émission et les liens entre le

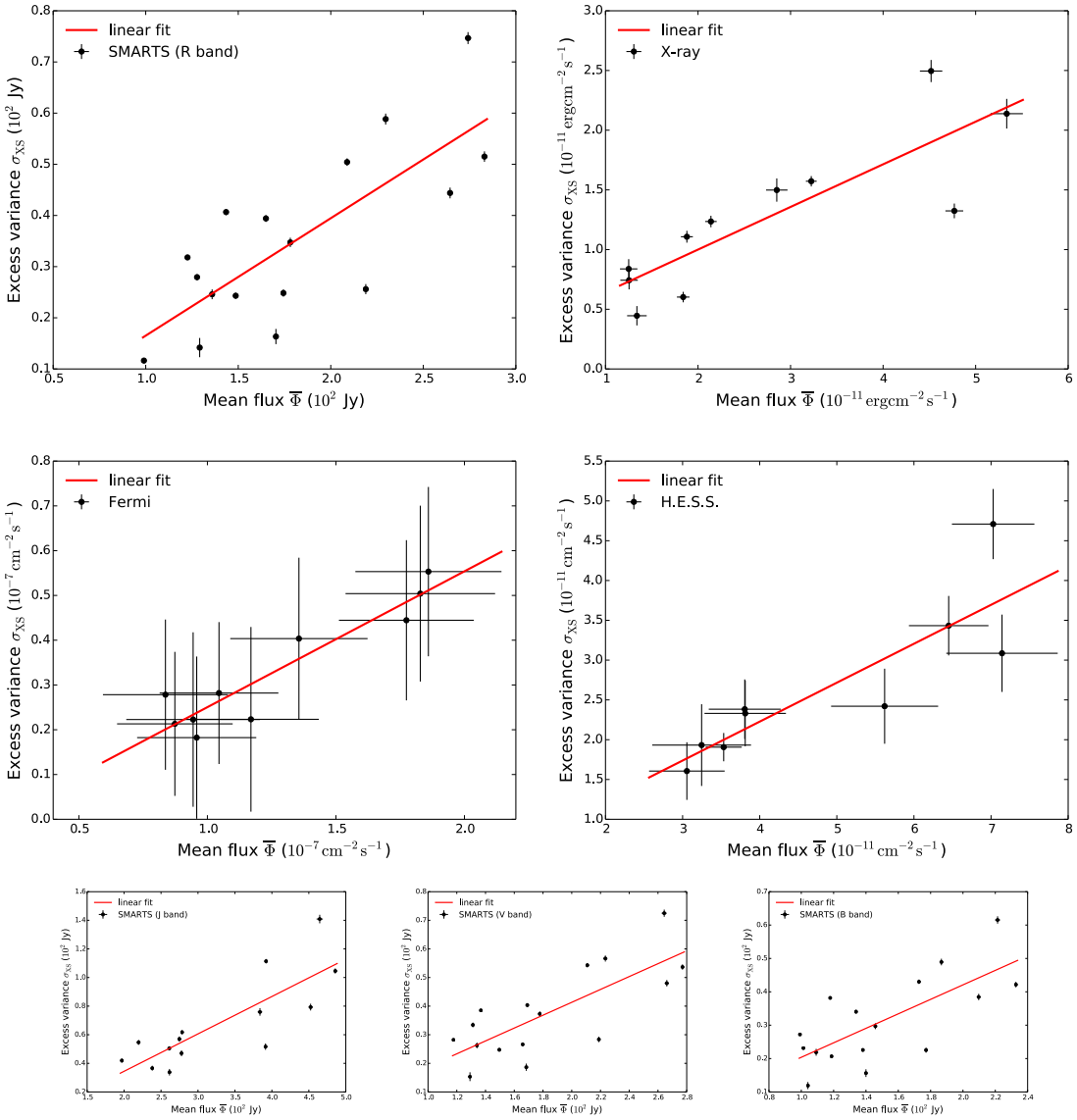

FIGURE 12.8: Scatter plots of the excess rms versus the mean flux for the multi-wavelength data set of PKS 2155-304. The linear fit is shown in red.

trou noir, le disque d'accrétion et le jet de matière.

Avec la distribution de variabilité en fonction de l'énergie et les corrélations entre les différentes bandes en énergie, on voit que les parties basse et haute énergie des données semblent se comporter de manière similaire ce qui pointe vers un modèle avec une même population de particules qui produirait l'émission, tel le modèle SSC.

La présence de périodicité peut s'expliquer avec plusieurs hypothèses. Par exemple, la présente d'une binaire de trous noirs supermassifs au centre de l'AGN pourrait produire cette périodicité dans le taux d'accrétion, ou alors le jet pourrait avoir un mouvement de précession du jet qui introduirait une périodicité dans le facteur Doppler.

Le comportement log-normal indique que le processus d'accrétion pourrait produire la variabilité observée. Ce serait plutôt la densité d'électrons (dans le cadre du modèle SSC) qui varierait dans le temps lors de l'accrétion et poserait son empreinte sur le jet.

Modélisation de la variabilité de PKS 2155-304 en utilisant un modèle SSC dynamique

Les résultats du chapitre précédent pointent vers un modèle SSC où l'émission optique et X s'explique avec le Synchrotron des électrons dans le jet et où l'émission au GeV et TeV s'explique par l'Inverse Compton de ces mêmes électrons sur les photons Synchrotron (Figure 12.9). Ce modèle leptonique est le plus simpliste car il contient peu de paramètres libres : la densité d'électrons (forme, indice spectral, énergie minimale...), le champ magnétique, la taille de la zone d'émission et le facteur Doppler.

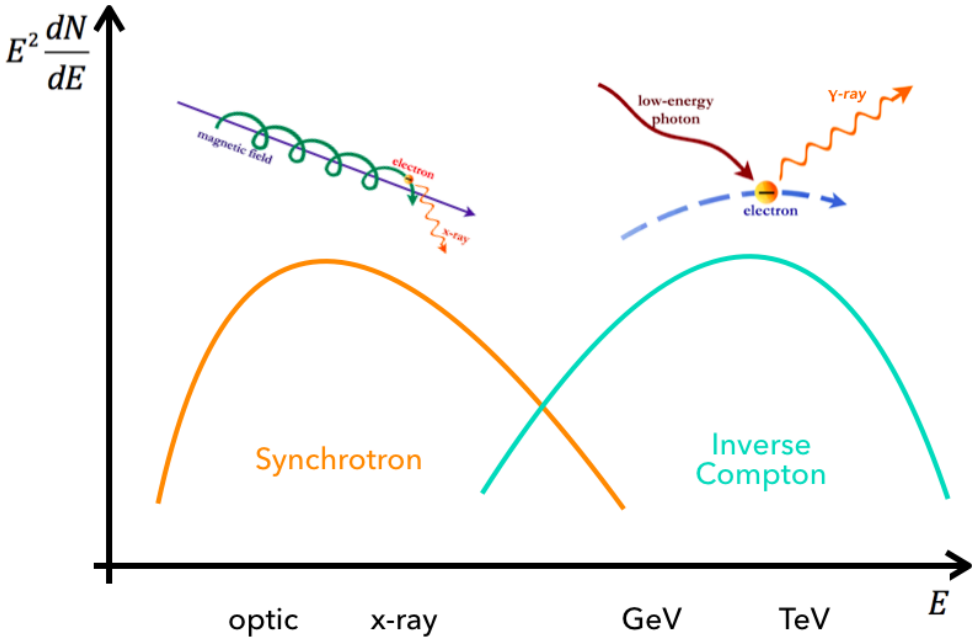

FIGURE 12.9: Schéma simple du modèle SSC pour les blazars.

La densité d'électrons $N_e(E,t)$ évolue en suivant une équation de Fokker-Planck :

$$\frac{\mathrm{d}N_e(E,t)}{\mathrm{d}t} = \frac{\partial}{\partial E}\left[(\dot{\gamma}_\mathrm{S} + \dot{\gamma}_\mathrm{IC})\, N_e(E,t)\right] + Q(E,t) - \frac{N_e(E,t)}{t_\mathrm{esc}} \tag{12.1}$$

où on considère que les électrons sont injectés avec un taux $Q(E,t)$, et qu'ils perdent de l'énergie par émission Synchrotron et Inverse Compton avec les taux $\dot{\gamma}_\mathrm{S}$ et $\dot{\gamma}_\mathrm{IC}$. Le dernier terme représente l'échappement des particules de la zone d'émission, mais ce terme étant indépendant de l'énergie, et le temps d'échappement long par rapport aux autres temps caractéristiques, il sera négligeable par la suite.

Afin de reproduire la SED de PKS 2155-304, la densité d'électrons est décrite avec une loi de puissance avec coupure exponentielle :

$$Q(E,t) = N_0 E^{-\alpha} \exp\left(-\frac{E}{\gamma_\mathrm{cut}}\right) \tag{12.2}$$

On sait déjà que le modèle SSC indépendant du temps peut reproduire la SED des HBL tel que PKS 2155-304. Ici on veut voir si en prenant le modèle SSC dépendant du temps on peut aussi reproduire la variabilité observée. Mais quel paramètre faire évoluer

dans le temps ? Afin de garder ce modèle le plus simpliste possible, un seul paramètre sera dépendant du temps.

Tout d'abord, il faut ajuster le modèle à la SED de nos données afin de connaître les valeurs moyennes de chaque paramètre. La Figure 12.10 présente cet ajustement avec les valeurs correspondantes dans le Tableau 12.1.

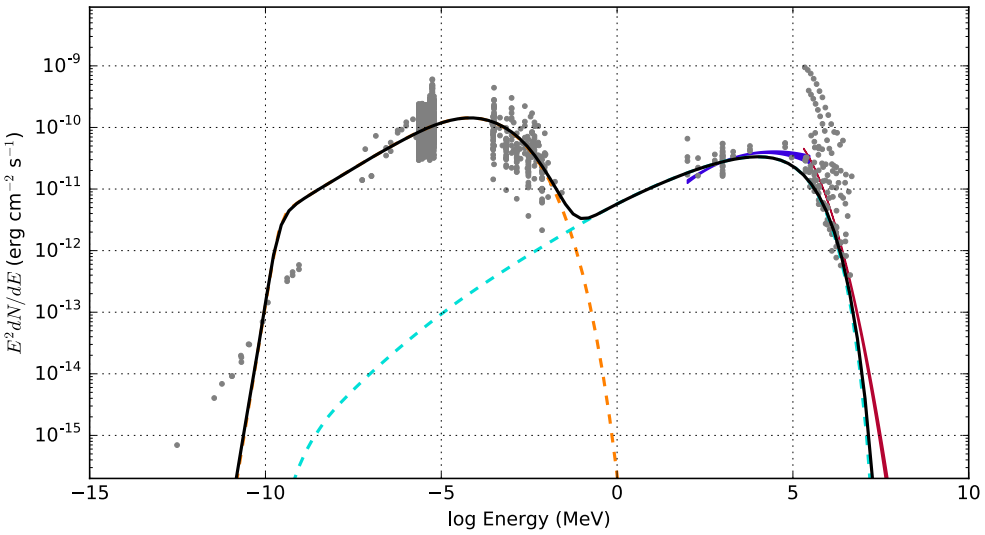

FIGURE 12.10: SED simulée avec les paramètres présentés dans le Tabelau 12.1 (orange = Synchrotron, bleu = Inverse Compton). Les points gris sont les données publiques de l'ASDC et les lignes bleue et rouge sont les spectres dérivées des analyses *Fermi*-LAT et H.E.S.S.

TABLE 12.1: Valeurs de la modélisation SSC de l'état moyenné de PKS 2155-304 montré en Figure 10.4.

Normalisation	N_0	2.7×10^{47} électrons
Indice	α	2.3
Énergie de coupure	$\log(\gamma_{\rm cut}/1\ {\rm eV})$	5.3
Champ magnétique	B	0.1 G
Rayon	R	2×10^{16} cm
Facteur Doppler	δ	35

Après tests, le paramètre choisi pour varier dans le temps est $\log(\gamma_{\rm cut})$. En effet, faire varier l'énergie de coupure exponentielle de la densité d'électrons va surtout faire varier le nombre d'électrons de haute énergie et aura plus d'incidence sur le flux en X et au TeV.

La prochaine question est : comment faire varier $\log(\gamma_{\rm cut})$? Les courbes de lumières des AGN ont souvent été caractérisées par du bruit rouge ou du bruit rose ($f(\omega) \propto \omega^{-\beta}$ avec $\beta = 2$ ou 1). $\log(\gamma_{\rm cut})$ variera donc suivant une loi de puissance. Des tests ont été fait afin de déterminer les paramètres de variations de $\log(\gamma_{\rm cut})$: β l'indice de la loi de puissance et σ, la variance de la série temporelle correspondante, après transformée inverse de Fourier, en pourcentage de la valeur moyenne. La configuration utilisée pour les simulations futures est [$\beta = 1$; $\sigma = 20\%$].

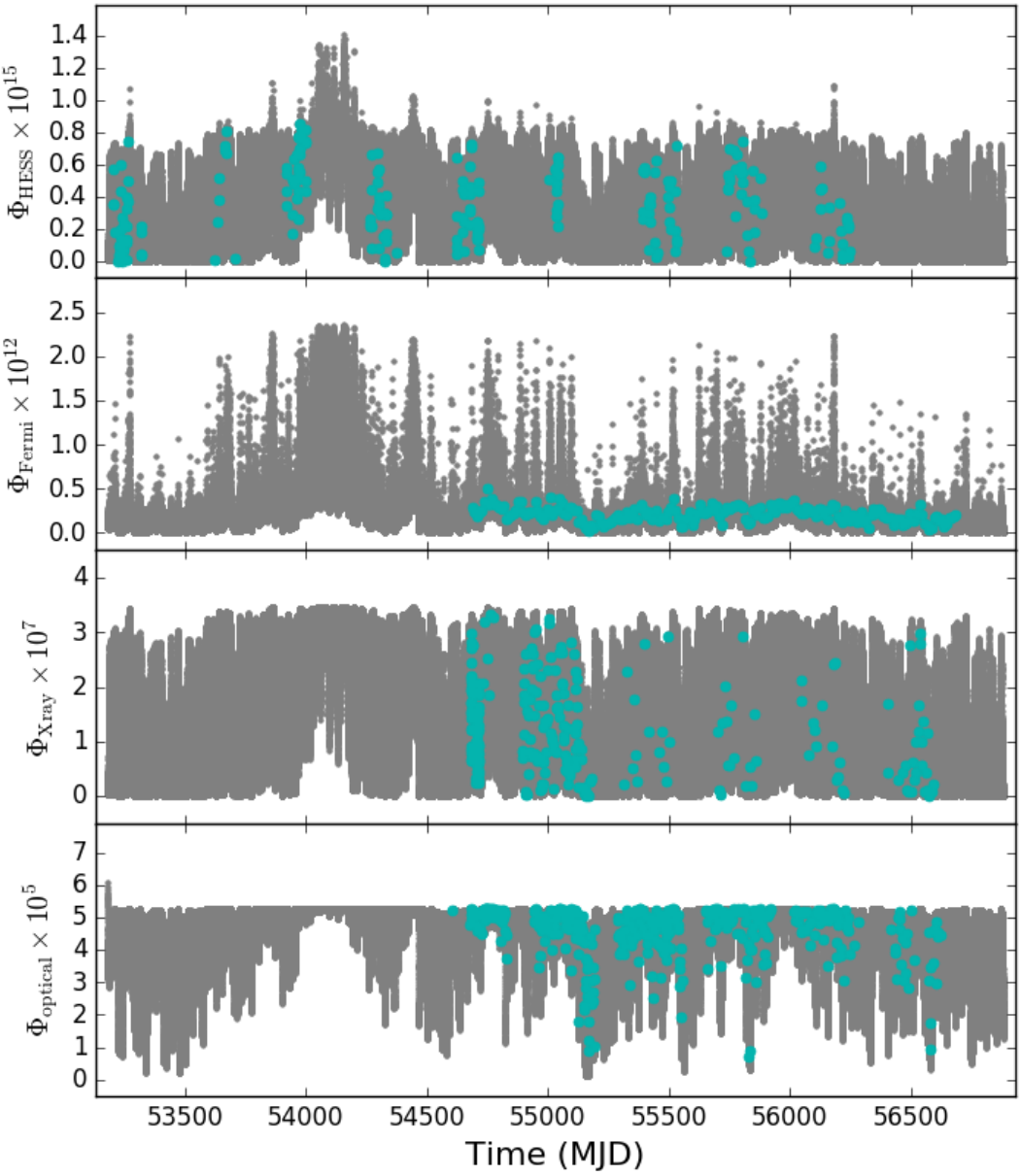

FIGURE 12.11: De bas en haut : courbes de lumière simulées pour les bandes en énergie correspondants à SMARTS (bande R), X, *Fermi*-LAT et H.E.S.S. Les courbes de lumières brutes sont en gris et les courbes de lumière re-binnées en temps en suivant les données sont en bleu.

Maintenant que le modèle est en place (on sait comment il fonctionne et il est réglé), on peut commencer les simulations pour voir si on peut reproduire le comportement des données. Pour se faire, j'ai simulé des courbes de lumières sur 10 ans. Celles-ci sont finement échantillonées, un point toutes les 9 minutes, afin de pouvoir appliquer le binning temporel des données par la suite.

La Figure 12.11 montre un exemple de courbes de lumière générées lors des simulations. Il y a en tout 50 intervalles en énergie mais ici les courbes de lumières ont déjà été re-binnées en énergie sur la même gamme que les données, ce sont les points gris. Pour les points bleus, ce sont les mêmes simulations mais qui ont été re-binnées en temps pour suivre le comportement des données.

Profil de variabilité $F_{\rm var}(E)$

Ce modèle et les réglages appliqués ont été choisis en premier lieu pour reproduire le profil de variabilité de PKS 2155-304. C'est un succès comme le montre la Figure 12.12. La courbe orange est le profil de variabilité des courbes de lumière brutes (sans aucun ré-échantillonage) et on voit qu'elle reproduit déjà le comportement général des données, excepté pour la variabilité en optique qui est plus basse que pour les données.

Dans la figure de gauche, on voit l'effet de l'échantillonage temporel des données sur les simulations : la variabilité dans la gamme de *Fermi*-LAT diminue et la valeur de $F_{\rm var}$ correspond à celle des données. Dans la figure de droite, les points bleus sont les valeurs du $F_{\rm var}$ pour les simulations re-binnées exactement sur les données (temps et énergie) et correspondent bien aux données pour les X, le GeV et le TeV.

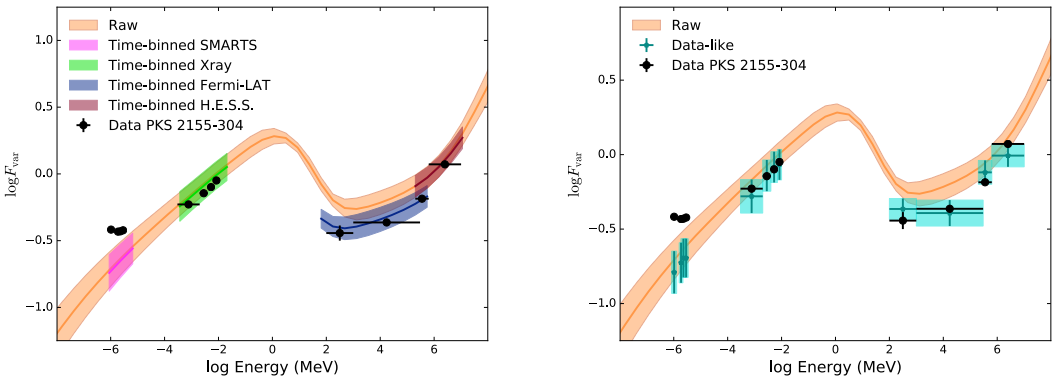

FIGURE 12.12: Profils de variabilité $F_{\rm var}(E)$ pour la modélisation SSC. La courbe orange représente $F_{\rm var}(E)$ pour les données brutes. À gauche, on voit l'effet du re-binning en temps et à droite celui du re-binning en temps et en énergie. Les points noirs sont les données.

Corrélations croisées

Des corrélations entre toutes les bandes en énergie sont attendues dans le modèle SSC. L'intérêt ici est de voir si la corrélation est encore visible après application du re-binning des données (qui est très fort pour les courbes de lumière X et TeV). La Figure 12.13 montre toutes les possibilités de corrélations entre les courbes de lumière en optique, X, GeV et TeV. La courbe bleue est la DCF des courbes de lumière simulées et les points noirs sont la DCF des données correspondantes.

Les simulations montrent toutes des corrélations à $\tau = 0$ jours malgré l'échantillonage temporel fort pour la gamme des X et celle du TeV.

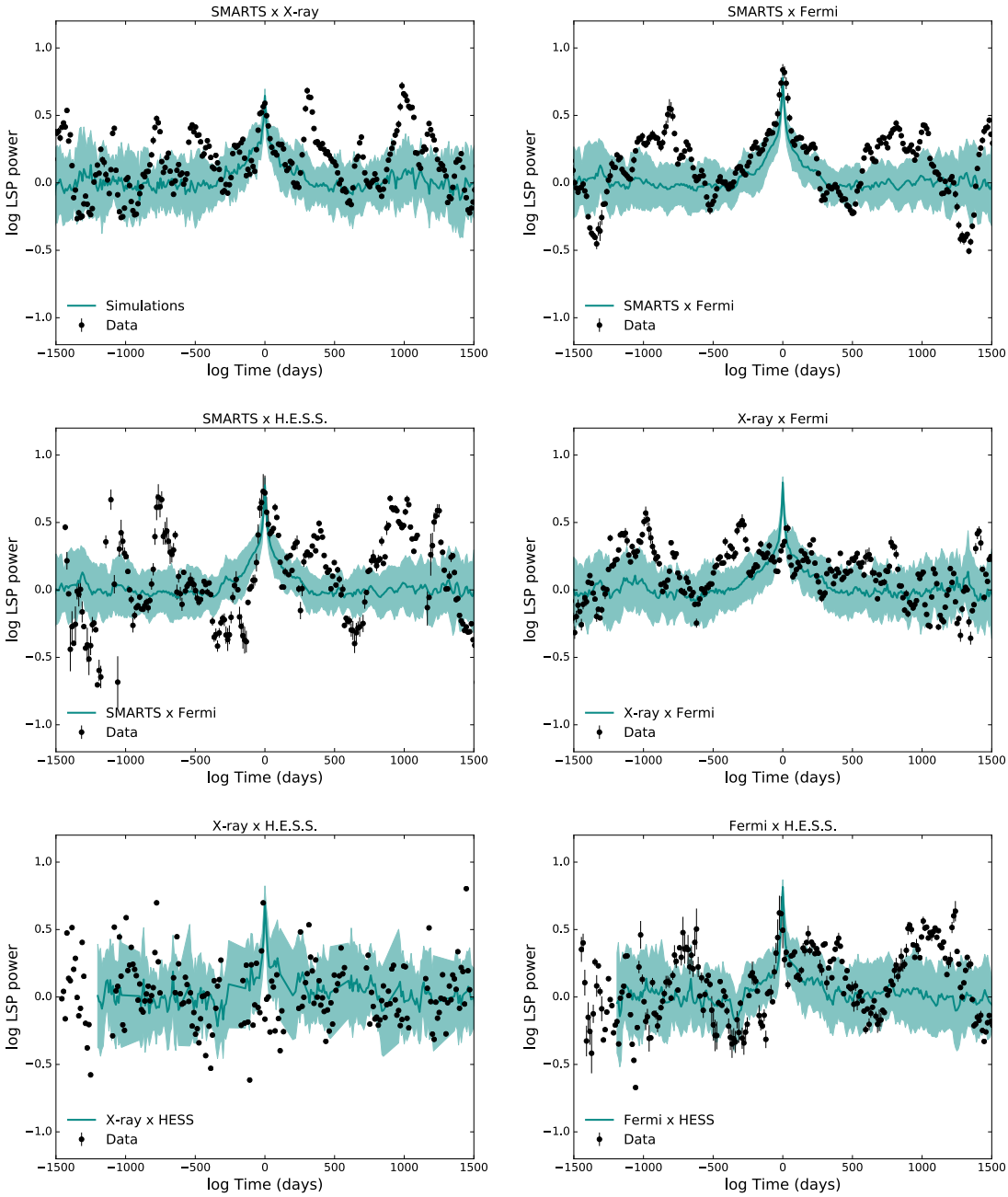

FIGURE 12.13: DCF des courbes de lumières simulées (en bleu) et des données (en noir). De gauche à droit eet de haut en bas : SMARTS×X-ray, SMARTS×*Fermi*-LAT, SMARTS×H.E.S.S., X-ray×*Fermi*-LAT, X-ray×H.E.S.S. and *Fermi*-LAT×H.E.S.S..

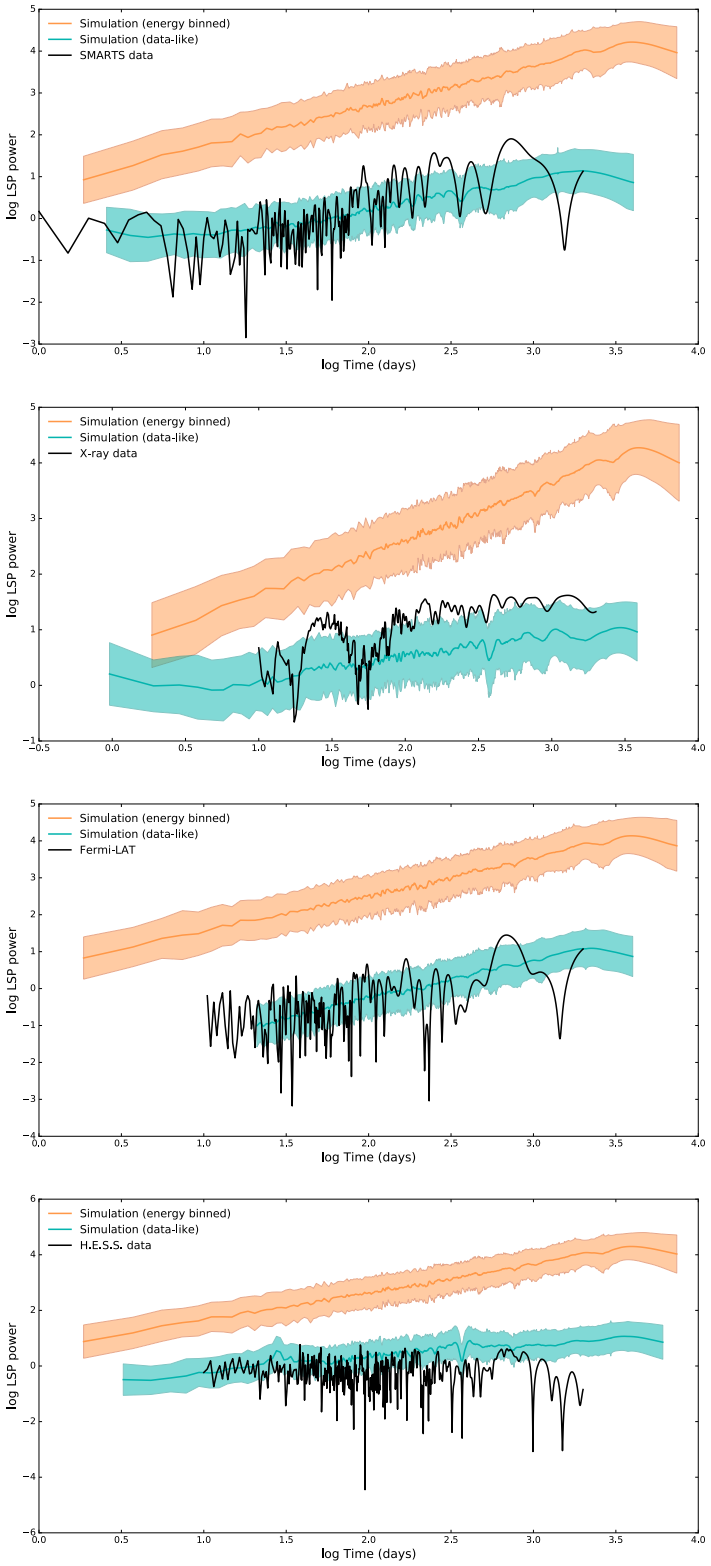

FIGURE 12.14: LSP des courbes de lumière simulées en optique, X, GeV et TeV (en orange) et dans les mêmes gammes mais avec l'échantillonage correspondant aux données (en bleu). Les LSP des données sont en noirs.

Densité spectrale en énergie

Le modèle a été paramétré pour reproduire le profil en variabilité $F_{\rm var}(E)$. Mais est-ce qu'on peut aussi reproduire le comportement spectral des données ?

Un LSP a été appliqué aux données et aux courbes de lumière simulées pour comparaison. La Figure 12.14 montre les résultats avec en orange le LSP appliqué aux courbes de lumière brutes, en bleu aux courbes de lumière re-binnées dans le temps et en noir aux données.

On voit que le binning temporel fait perdre en puissance et que la puissance finale du LSP des simulations correspond à celui des données. De plus, chaque LSP a été ajusté avec une loi de puissance pour voir si l'indice était le même. Les résultats sont résumés dans le Tableau 12.2. Les courbes de lumière brutes montrent toutes un indice de 1, qui correspond au bruit en loi de puissance injecté dans $\log(\gamma_{\rm cut}(t))$. L'indice change après binning temporel et correspond plus ou moins aux données (écart assez fort pour la gamme de *Fermi*-LAT, mais il faut noter que le pic de périodicité à 700 jours peut avoir une incidence).

TABLE 12.2: Valeur des indices des ajustements en loi de puissance des PSD présentées en Figure 12.14.

Gamme d'énergie	β (binning en énergie)	β (data-like)	β (données)
SMARTS	0.98	0.73	0.83 ± 0.04
X-ray	1.06	0.38	0.30 ± 0.01
Fermi-LAT	1.03	1.05	0.55 ± 0.03
H.E.S.S.	1.03	0.39	0.28 ± 0.03

Peut-on reproduire la périodicité avec le SSC ?

Les courbes de lumière de PKS 2155-304 sont périodiques (du moins dans les données SMARTS et *Fermi*-LAT) mais rien dans le SSC actuellement ne peut reproduire cette périodicité, à moins qu'on introduise volontairement une variation périodique. Cette périodicité pouvant s'expliquer par une binaire de trous noirs ou par la précession du jet, on pourrait indroduire la périodicité dans l'injection des électrons N_0 ou bien dans le facteur Doppler δ.

J'ai choisi de regarder l'hypothèse de précession du jet. J'ai donc fais des simulations plus courtes (21 mois) en injectant en plus une périodicité de $T = 7$ mois (pour avoir 3 périodes dans les simulations car on voit 3 périodes dans les données) dans le facteur Doppler :

$$\delta(t) = 35 + 5 \times \sin(t + T)$$

en gardant la valeur moyenne de 35 et en choisissant une amplitude de 5.

La Figure 12.15 montre le profil de variabilité résultant de ces simulations : il est similaire à ce qu'on avait avant (Figure 12.12) mais la variabilité en optique est plus forte. L'ajout de variation périodique, en plus du bruit en loi de puissance pour $\log(\gamma_{\rm cut}(t))$ rajoute de la variabilité en optique.

On voit la périodicité dans les données en optique et au GeV, mais pas dans les données en X et au TeV. Est-ce un effet du binning temporel ou bien la périodicité n'est-elle pas présente dans ces bandes en énergie ? La Figure 12.16 montre les LSP appliquées aux courbes de lumières simulées dans chaque bande en énergie afin de voir si la période est reconstruite. On voit très clairement le pic à 205 jours en optique et au GeV, mais ce pic

est beaucoup moins puissant en X et au TeV : la variabilité stochastique est trop forte et détruit le signal périodique.

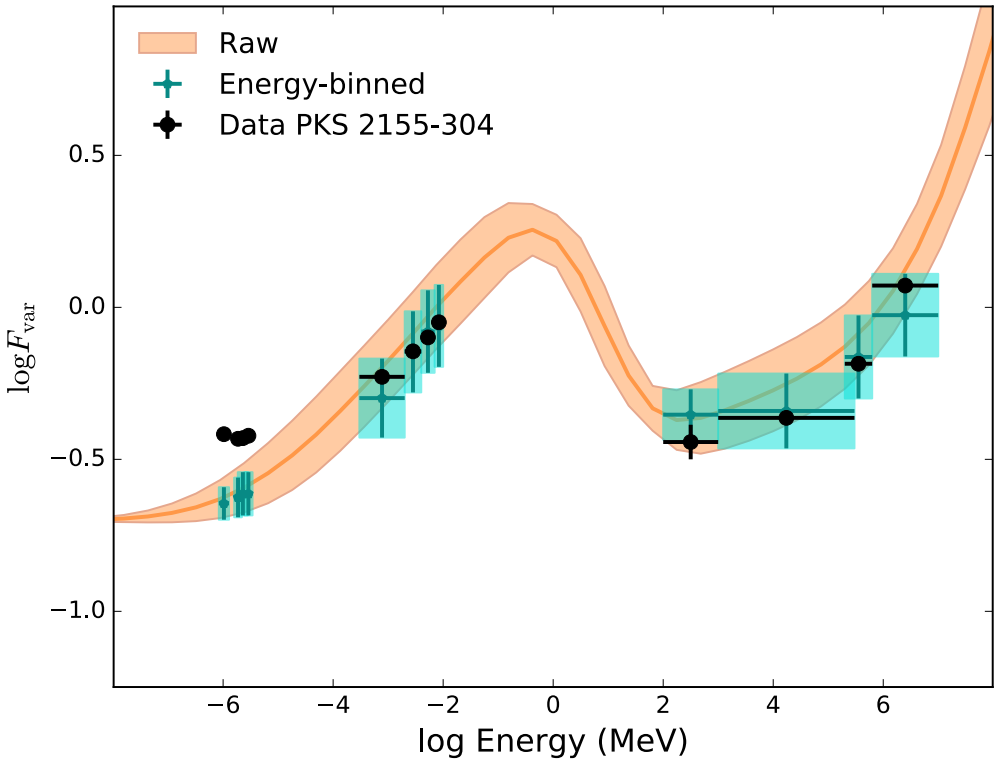

FIGURE 12.15: Profil de variabilité $F_{\rm var}(E)$ pour la modélisation SSC avec périodicité introduite dans $\delta(t)$. La courbe orange est le profil des courbes de lumière brutes et les points bleues sont les valeurs de la variabilité pour les courbes de lumières re-binnées en énergies (mais pas en temps) sur les données. Les points noirs sont les données.

Conclusion

Le but de cette modélisation était de voir si, en modélisant des courbes de lumière en suivant les conditions d'observations des données (échantillonage en énergie et en temps), on pouvait reproduire la signature en variabilité vue dans le chapitre précédent. En faisant varier l'énergie de coupure exponentielle de la densité d'électrons en suivant un bruit en loi de puissance, le modèle reproduit plutôt bien le profil de variabilité avec la variabilité augmentant de l'optique vers les X, puis du GeV vers le TeV (Figure 12.12), notamment lorsqu'on prend en compte le binning en énergie et en temps.

Ce premier résultat important est suivi de plusieurs autres :

- Malgré le binning temporel des données, on peut encore résoudre des corrélations entre les courbes de lumière simulées avec le SSC, mais ce n'est pas le cas dans toutes les DCF des données.
- Les courbes de lumière simulées ont le même comportement spectral que celui mis dans l'évolution de $\log(\gamma_{\rm cut}(t))$. La perte de puissance ainsi que le changement d'indice une fois l'application du binning temporel semble s'ajuster à la PSD des données.

- En rajoutant une variation périodique, ici dans le facteur Doppler, on peut réussir à reproduire le comportement périodique des données. Un travail plus détaillé sur ce point là devrait être fait afin de déterminer les paramètres plus fins d'une telle simulation.

D'après moi, la variabilité est l'une des clés pour améliorer notre compréhension des blazars et des AGN en général. Il est important d'avoir de plus en plus de données multi-longueur d'onde sur long terme sur plus de blazars afin de faire ce genre d'étude. De plus, étudier le comportement en variabilité d'autres modèles leptoniques et hadroniques serait un plus afin de mieux comprendre leur version dynamique.

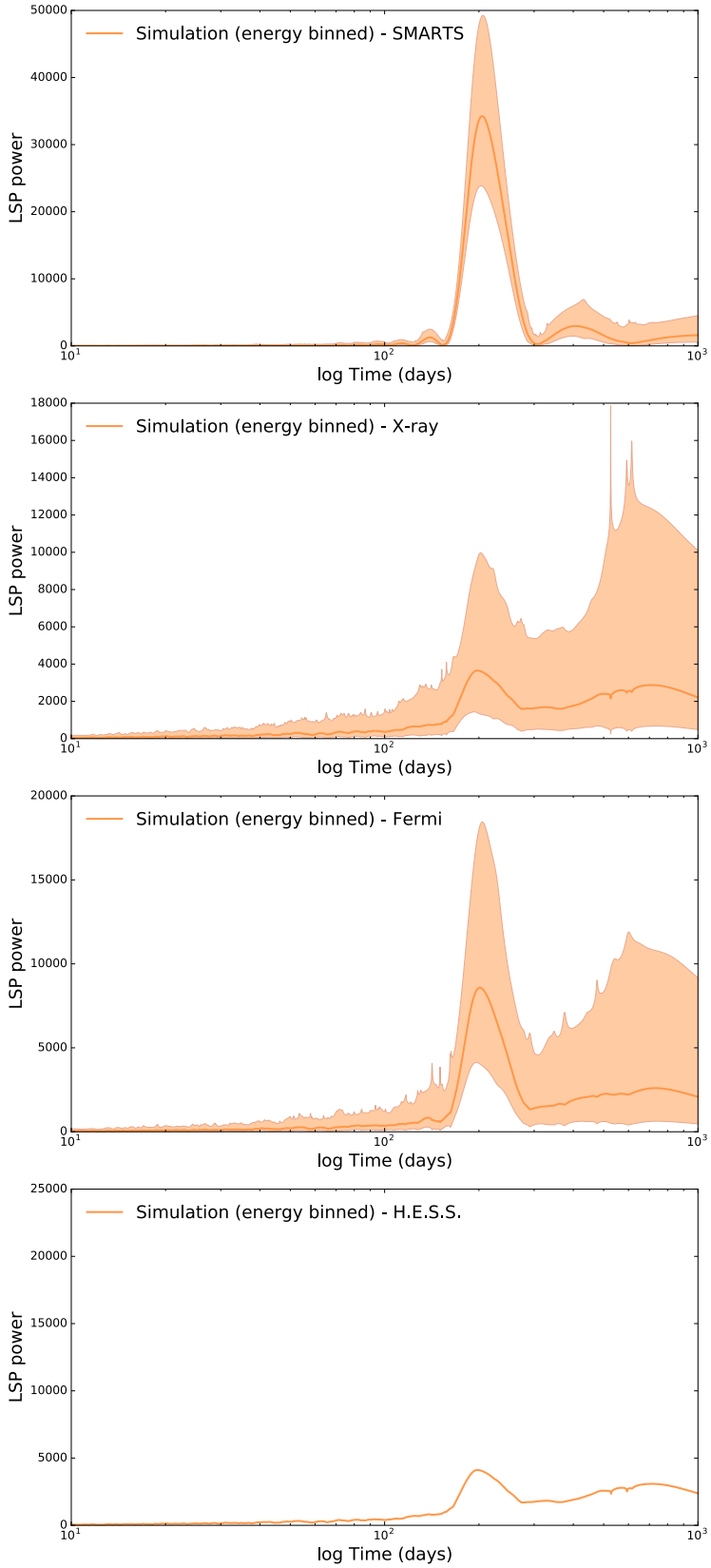

FIGURE 12.16: LSP pour les courbes de lumière simulées avec une périodicité de 205.7 jours dans le facteur Doppler pour l'optique (bande R), les X, le GeV et le TeV (de bas en haut).

Appendix A

The AGN Round-Up

After every month of observation (= a period), we do, in the extragalactic working group of the H.E.S.S. Collaboration, a review of the sources observed using the preliminary results of the on-site analysis. The goal is to have a quick look at the behavior of the targets, especially for the non-detected ones: how did the significance evolved with time? Are we close to a detection? This is the AGN "online" Round-Up. However this online Round-Up, unlike the analysis described in Chapter 4, does not use a precise calibration nor a run selection. Hence the preliminary results from this are often not reliable.

Using the tools developped for the HEGS projects (see Chapter 6), François Brun, David Sanchez and myself created the AGN "offline" Round Up. The goal is the same: to look at the data for each period, but using the collaboration analysis framework. Because of the time to bring the data back from Namibia to France, to calibrate them and to produce the DSTs, the offline Round-Up is generally delayed by 3 months compared to the online one for the same period. Depending on the availability of the data, sometimes the round-ups will gather 2 or 3 periods at a time.

During the spring of 2016, I became responsible of the Round-Up duty, taking care of both Round-Ups each month and presenting them during collaboration meetings.

Section A.1 describes the procedure for the online AGN Round-Up, showing how the results are presented to co-workers. Section A.2 presents the method to produce the offline Round-Up and how it was useful.

A.1 The online AGN Round-Up

For each period, there is a summary containing the informations on all the sources under observations: the number of runs taken, the livetime, the significance during these observations, the excess and the mean observation conditions (mean zenith and azimuth angles). Periods are named using the year and the number of the period during the year (such as P2014-07). There are 12 to 13 periods per year.

Let's consider two past periods P01 and P02. When doing the round-up of P03, I will look if the sources observed during P03 were observed as well during P01 and P02, if so, I will gather past and present informations together. This allows to know the total significance of the source looking at the total number of observations on it.

Figure A.1 shows how the round up is presented. The example is made with the round-up from P2016-05 to P2016-08. Sources are separated between those published or in preparation (top panel) and under study (mainly undetected sources at TeV but not only, bottom panel). Each panel displays histograms showing the number of runs, the livetime, the online analysis significance and the online analysis excess. The informations from the new periods is colored in light blue while the information from previous periods (starting in P2004-01) is shown in dark blue.

In this round-up, looking at the sources under study, we can see than most of them are new: 1RXS J215305.2-004227, CTA 102, PKS 0139-09, PKS 1749+096, RBS 1792. Only

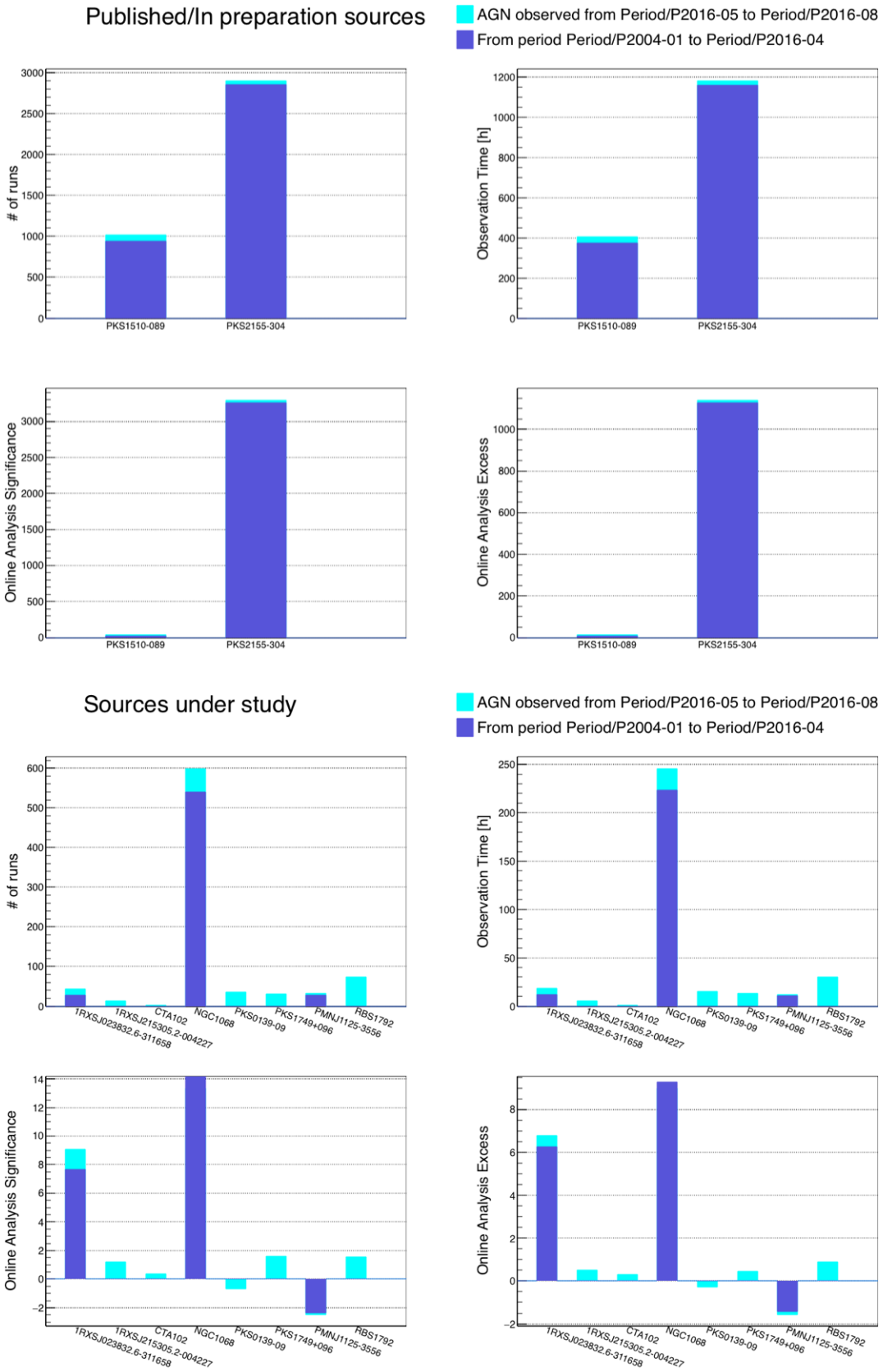

FIGURE A.1: AGN "online" Round-Up were sources are separated between those already detected (top) and the ones not detected at TeV (bottom). Each panel shows the accumulation of number of runs, the observation time, the online analysis significance and the online analysis excess.

few hours were taken on them (up to 30 for RBS 1792) with none of them reaching the 3σ level. PMN J1125-3556 (a source from the blazar sequence proposal of Chapter 6, along with few others) showed a negative excess in the previous period and is still going on this direction.

The starburst galaxy NGC 1068 has never been detected at TeV. During this round-up the significance and excess did not increase (they migh have decrease a little since no light blue can be seen) despite the additional ~ 40 hours of observations.

During the round-up I also look at how the observation were made: which telescope (or array configuration) took the most data? How many hours of dark time did we use?

Since the duty cycle of IACTs like H.E.S.S. is low because we observe only during dark time with no Moon light (and when the weather is good), it is useful to look at the observation efficiency for each period to know and, in case the number is low, to know why. Also, we want most of the observations to be done in Stereo or Mono (depending on the requirements in the proposal), so, in an ideal world the data taking should be separated in:

- XX % of observations with CT1, CT2, CT3, CT4, CT5
- YY % of observations with CT1, CT2, CT3, CT4
- ZZ % of observations with CT5

with the sum of XX, YY and ZZ making 100 %.

If there are more array configurations with a significant amount of time, it means that there was a persistent problem which should be taken into account.

A.2 The offline AGN Round-Up using the HEGS software

Runs have to be calibrated and analyzed for the offline Round Up. We organized them per period creating a library of runs represented in Figure A.2. When a new period arrives, a new folder with the period name is added. Let's consider P2016-04 as the new period to be analyzed. The past observation periods go from P2015-07 to P2016-03. These periods are already analyzed with results stored in the library.

During the analysis of P2016-04, the code will be able to retrieve the previous results on the sources from this period to merge them together.

A.2.1 Step 1: choosing the runlist

First, I take the raw runslist of all observations done during the period P2016-08. This runslist contains some Galactic observations and some ToOs which are removed. ToOs are removed not to add another trial to a future dedicated analysis.

Then, after checking the availabity of the DST, I proceed with the run quality selection. I produce two runslists using the standard Stereo and Mono selection profiles: p2016_04_stereo.list and p2016_04_mono.list. The raw runslist of this period contains 83 runs on PKS 2155-304, PKS 1510-089 and PMN J1125-3556. The Mono and Stereo runslist contain each 61 and 37 runs.

A.2.2 Step 2: Analysis

A Graphical User Interface (GUI) has been developped by David Sanchez to launch the analysis easily. A screenshot of the analysis interface is shown on Figure A.3. One just has to give the runslist, the analysis profile (standard Stereo or Mono) and the period name

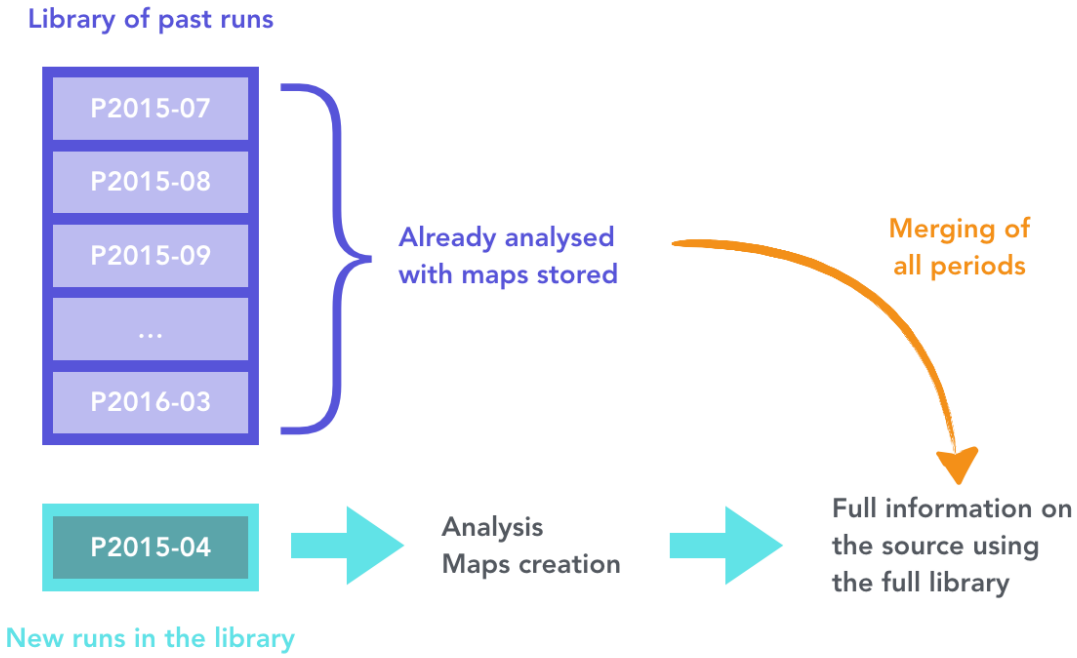

FIGURE A.2: Illustration on the process of the offline Round-Up were runs are organized using a library. Each source of the new period will be analyzed on its own and the results merged with previous observation on it if there are.

in the library. The code will read the information in the database (like the coordinates) and launch the analysis of each run of the selected period.

Once the analysis of the run is done, I merge the data for each source. The merging can be done only for the period, to see the behavior of the sources only during this period, or for all periods on the sources of P2016-04 to look at the total significance of the source for example (an option exists to merge every data on every source in the library if needed).

A.2.3 Step 3: Maps creation and results extraction

The maps are created using the HEGS framework described in Section 6.2 of Chapter 6. The code takes the merged results file for each sources and will create the ON-OFF Test and Ring Background maps. From them we can extract several informations using the tool table of the GUI: the ON-OFF Test at a specific position, the informations at one position (livetime, flux, upper limit...) and look for hotspots in the field of view.

A.3 Results of the offline AGN Round-Up

As an example I present here the offline Round-Up of the P2016-09 to P2016-11 periods. Observations during this time is specific because the four small telescopes were not observing as there were experiencing an upgrade of the cameras. This upgrade took several months the time to mount the PM in the camera, the camera onto the telescopes and to test the whole system. In the mean time, CT5 was observing in Mono mode.

During these 3 periods, the sources under observations were: PKS 2155-304, NGC 1068, 1RXS J012338.2-231100, 5BZG J0022+0006, RBS 1792, PKS 0139-09, 1RXS J023832.6-311658. PKS 2155-304 had 2 dedicated chapters and does not need more introduction. The blazars

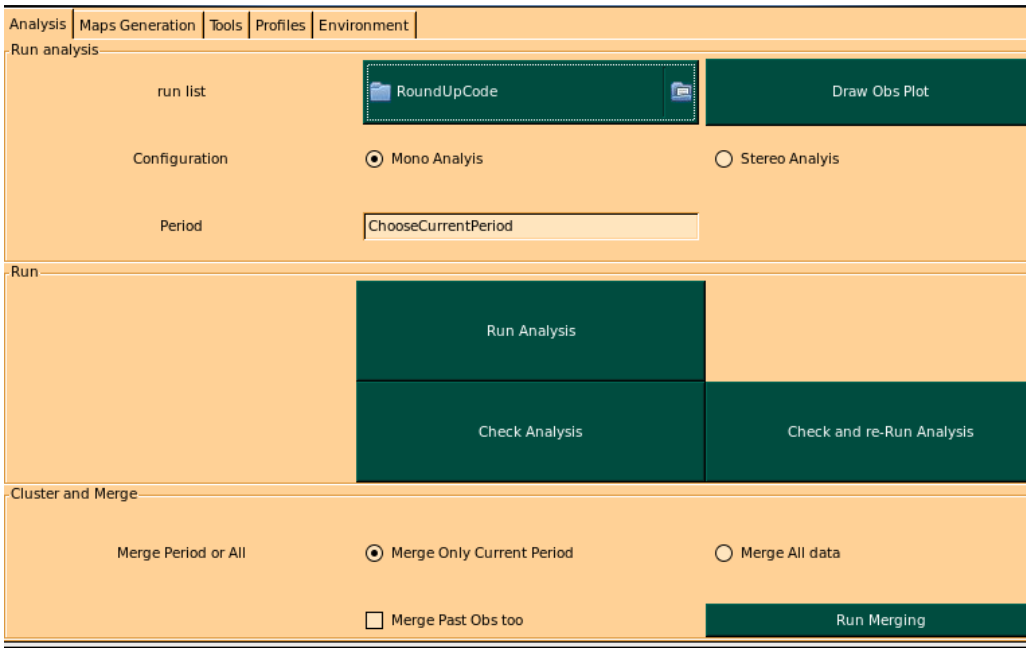

FIGURE A.3: Interface of the analysis part of the offline Round-Up GUI.

1RXS J012338.2-231100, 5BZG J0022+0006, RBS 1792 and PKS 0139-09 are part of the blazar sequence proposal presented in Chapter 7. The results on these sources won't be presented in the following (PKS 2155-304 is obviously detected and the results on the other sources were already presented). I will focus on the starburst galaxy NGC 1068 and the HBL 1RXS J023832.6-311658 ($z = 0.232$).

Figure A.4 shows the excess and significance maps and the significance distribution for the observations on NGC 1068 and 1RXS J023832.6-311658. None of them is detected in Mono:

- NGC 1068 shows only 1.3σ in 62.2 hours of observations (the time has been acceptance corrected)
- 1RXS J023832.6-311658 shows 3.1σ in 10.9 hours of observations.

These 1RXS J023832.6-311658 is know to be detected in Stereo, but not in Mono.

A.4 Systematic checks of the calibration

Even if no new source or special behavior of the sources were found during the offline Round-Up, it allowed to analyze all observations in order to be aware about what we had at that time.

Moreover, doing systematic analyses of each period is useful to detect calibration problems. And this is what happened. For example, during the period P2016-04, the maps were showing a weird behavior with artefacts on them (see Figure A.5).

It appears that this was caused by a calibration issue: some broken pixels and drawers were not identified as broken during the calibration and were creating these artefacts.

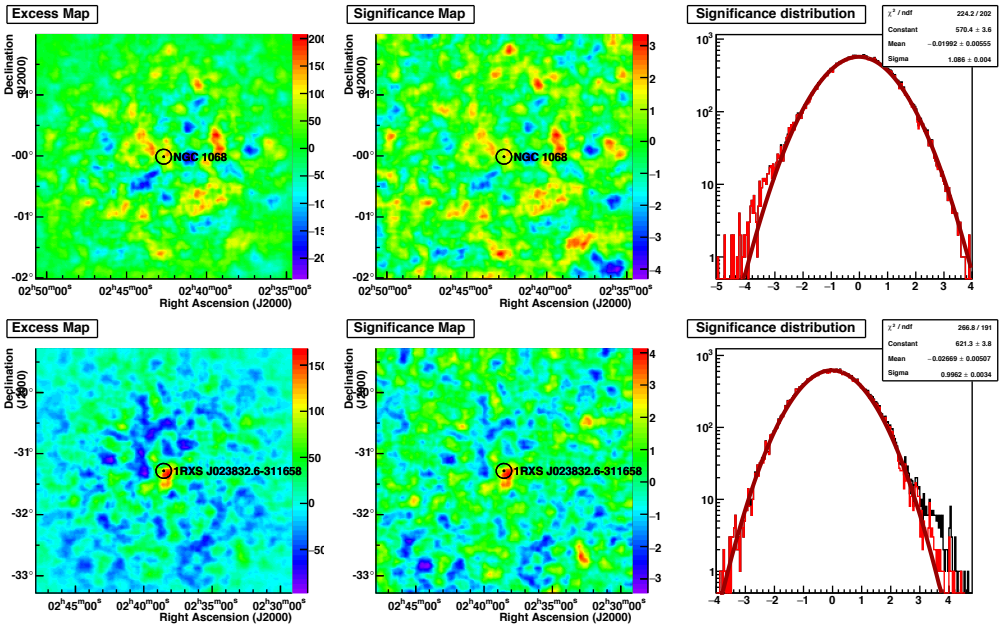

FIGURE A.4: Excess and significance maps along with the significance distribution for NGC 1068 (top) and 1RXS J023832.6-311658 (bottom).

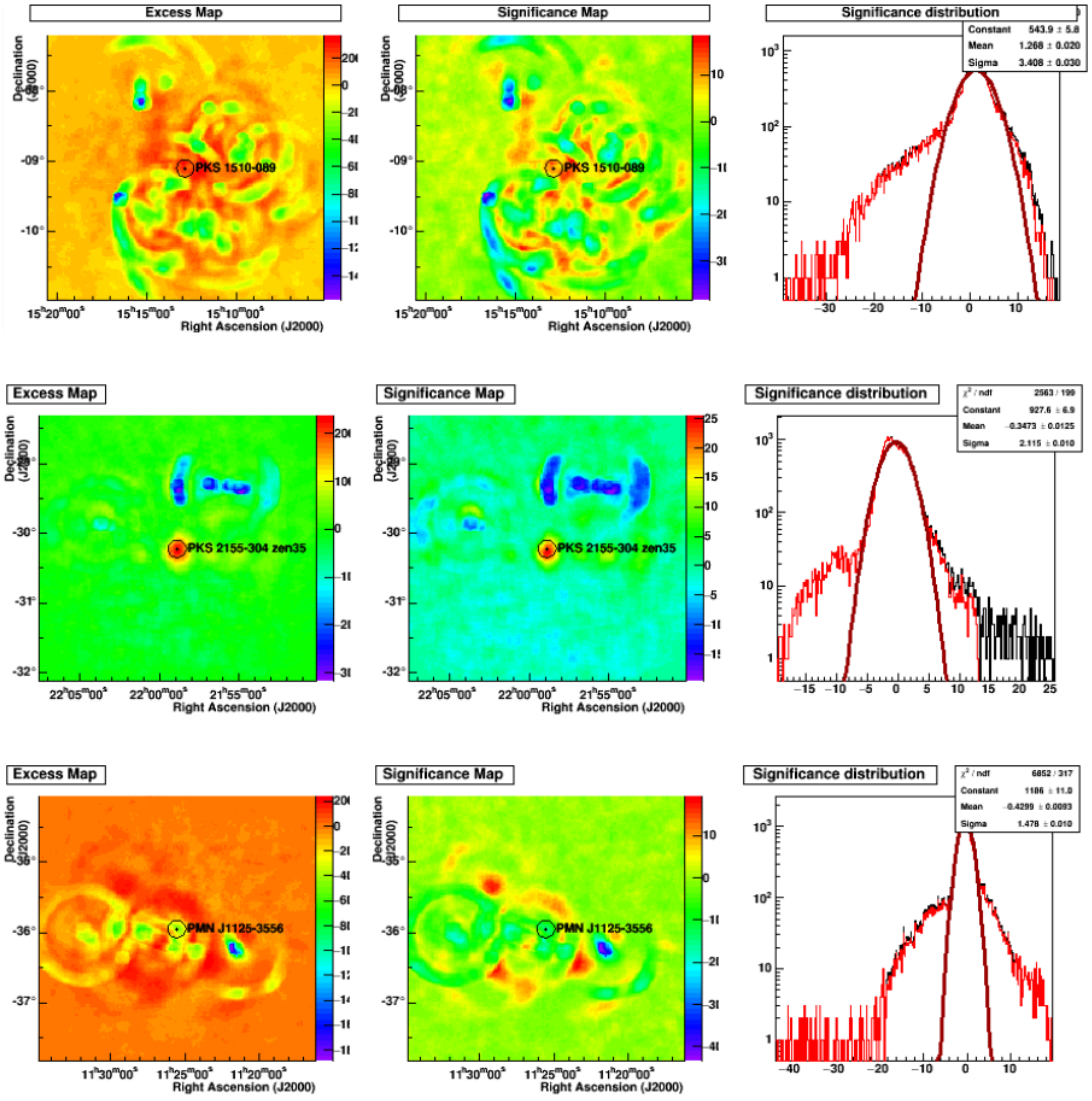

FIGURE A.5: Excess and significance maps and distribution of the sources observed during P2016-04: PKS 1510-089, PKS 2155-304 and PMN J1125-3556 (from top to bottom).

Appendix B

Time series of power law noise

In Chapter 10, the $\log(\gamma_{\rm cut})$ evolves in time following a power law noise $f(\omega) \propto \omega^{-\beta}$ using the generation method of Timmer and Koenig, 1995. Several configurations have been tested with $\beta = 1, 1.5, 2$ in order to find the one fitting the best the variability energy profile of the data of PKS 2155-304.

The behavior of the time series changes depending on the power law index β. Power law noise behavior is very common in nature (in electricity, sismicity or in the undersea ocean currents to name only three). It is called "noise" because in many physics fields, it is a background hiding the signal. In astrophysics, this noise is the signal.

B.1 The different colors of noise

B.1.1 White noise $\beta = 0$

The white noise is defined when $\beta = 0$: there is the same power in each frequency. The power spectrum converges in the long time scales, but if it is integrated towards the small time scales it diverges, as there is an infinite amount of power at high frequencies. This means that a mean value (averaging over some time) can be defined but not an instantaneous value. A typical white noise time series is shown on the first panel of Figure B.1. The variations are fast and very choppy.

B.1.2 Red noise $\beta = 2$

The red noise is defined when $\beta = 2$. Such a noise is also called random walk function because it can be generated by integrating the values of the white noise time series.

Unlike the white noise, the red noise spectrum converges at small time scales (there is a finite amount of power at high frequency) but diverges when one integrates toward long time scales: the more one waits, the more the value of the time series seems to go far from it's initial value. A typical red noise time series is shown on the third panel of Figure B.1.

B.1.3 Pink noise $\beta = 1$

The pink noise, also called flicker noise because of its shaking behavior, is characterized by a power law index $\beta = 1$. The resulting time series of pink noise is a mixture of the white and red noises, where one is too spotty ($\beta = 0$) and the other one too smooth ($\beta = 2$), as shown on the second panel of Figure B.1.

Pink noise diverges when integrated toward long and small time scales, but in a logarithmic way. One of its particularity is also to be a fractal (self-similar structure). If I would have generated a time series on an infinite small binning, by zooming into smaller and smaller time scales (or un-zooming to longer and longer time scales), we could have seen the same pattern repeting over and over.

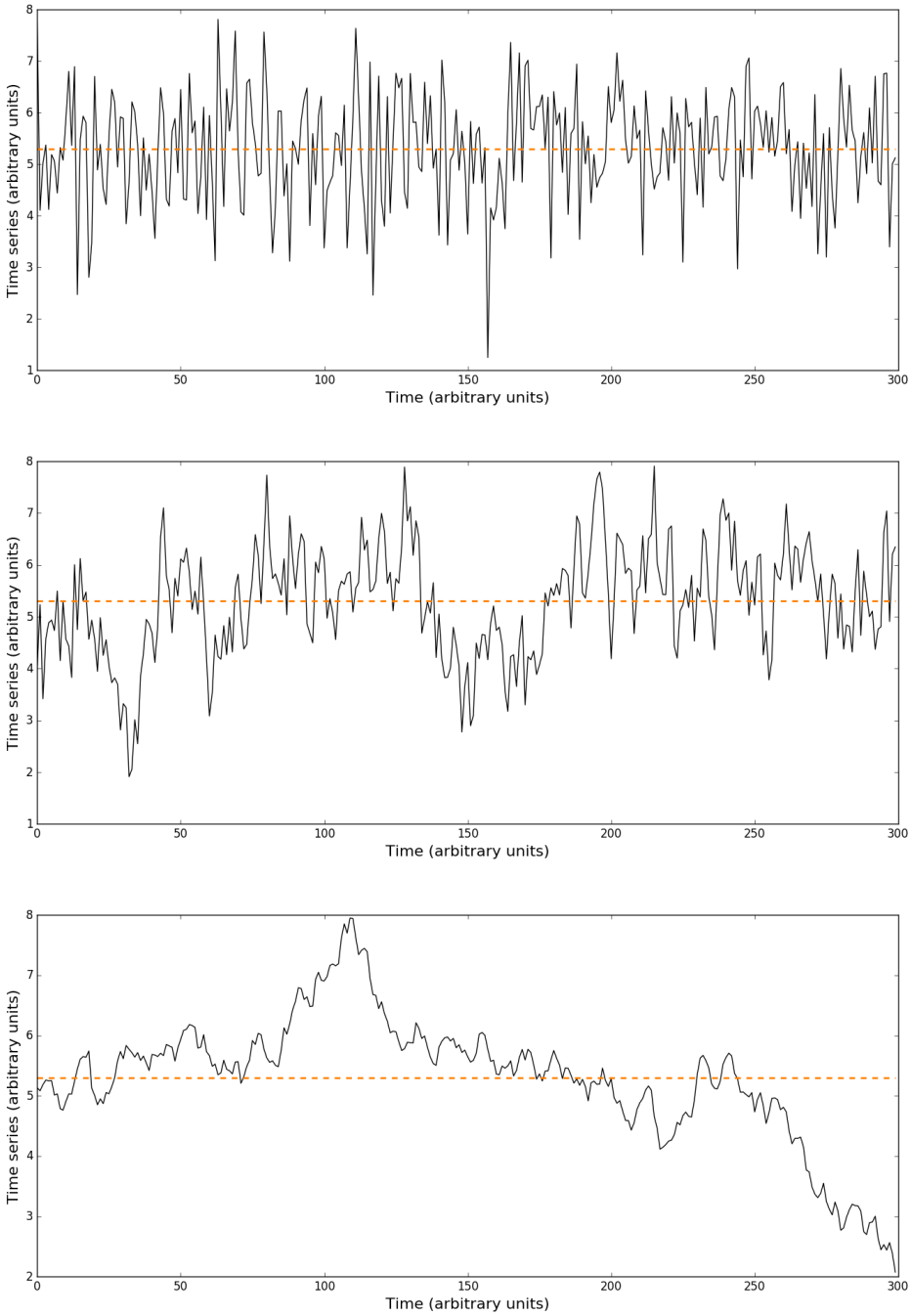

FIGURE B.1: Time series of power law noise generated with $\beta = 0$ (top), $\beta = 1$ (middle) and $\beta = 2$ (bottom).

B.2 Flicker noise in astrophysics and music

The time series generated with the pink noise looks like the light curves from blazars (or sometimes red noise depending on the state of the blazar or the energy range).

Interestingly, it was recently shown that music embodies such self-similar structure, with different composers found to prefer a particular β value[1]. In this respect, PKS 2155-304 can be said to be the Beethoven of blazars since this composer also preferred $\beta \sim 1$.

Apparently, music with a $\beta \sim 1$ displays the perfect balance of predictability and surprise for the human ear. Blazars seems to behave the same.

[1] https://www.ncbi.nlm.nih.gov/pmc/articles/PMC3309746/

Bibliography

Abramowski, A. et al. (2010). "VHE γ-ray emission of PKS 2155-304: spectral and temporal variability". In: 520, A83, A83. DOI: 10.1051/0004-6361/201014484. arXiv: 1005.3702 [astro-ph.HE].

Acero, F. et al. (2015). "Fermi Large Area Telescope Third Source Catalog". In: 218, 23, p. 23. DOI: 10.1088/0067-0049/218/2/23. arXiv: 1501.02003 [astro-ph.HE].

Ackermann, M. et al. (2015a). "Multiwavelength Evidence for Quasi-periodic Modulation in the Gamma-Ray Blazar PG 1553+113". In: 813, L41, p. L41. DOI: 10.1088/2041-8205/813/2/L41. arXiv: 1509.02063 [astro-ph.HE].

Ackermann, M. et al. (2015b). "The Third Catalog of Active Galactic Nuclei Detected by the Fermi Large Area Telescope". In: 810, 14, p. 14. DOI: 10.1088/0004-637X/810/1/14. arXiv: 1501.06054 [astro-ph.HE].

Aharonian, F. et al. (2006). "Observations of the Crab nebula with HESS". In: 457, pp. 899–915. DOI: 10.1051/0004-6361:20065351. eprint: astro-ph/0607333.

Aharonian, F. et al. (2007a). "An Exceptional Very High Energy Gamma-Ray Flare of PKS 2155-304". In: 664, pp. L71–L74. DOI: 10.1086/520635. arXiv: 0706.0797.

Aharonian, F. et al. (2007b). "New constraints on the mid-IR EBL from the HESS discovery of VHE γ-rays from 1ES 0229+200". In: 475, pp. L9–L13. DOI: 10.1051/0004-6361:20078462. arXiv: 0709.4584.

Aharonian, F. et al. (2009a). "Simultaneous multiwavelength observations of the second exceptional γ-ray flare of PKS 2155-304 in July 2006". In: 502, pp. 749–770. DOI: 10.1051/0004-6361/200912128. arXiv: 0906.2002.

Aharonian, F. et al. (2009b). "Simultaneous Observations of PKS 2155-304 with HESS, Fermi, RXTE, and Atom: Spectral Energy Distributions and Variability in a Low State". In: 696, pp. L150–L155. DOI: 10.1088/0004-637X/696/2/L150. arXiv: 0903.2924 [astro-ph.HE].

Ahnen, M. L. et al. (2016a). "Long-term multi-wavelength variability and correlation study of Markarian 421 from 2007 to 2009". In: 593, A91, A91. DOI: 10.1051/0004-6361/201628447. arXiv: 1605.09017.

Ahnen, M. L. et al. (2016b). "Multiband variability studies and novel broadband SED modeling of Mrk 501 in 2009". In: *ArXiv e-prints*. arXiv: 1612.09472 [astro-ph.HE].

Ajello, M. et al. (2015). "2FHL: The second Catalog of hard {\it Fermi}-LAT sources". In: *ArXiv e-prints*. arXiv: 1503.02664 [astro-ph.HE].

Aleksić, J. et al. (2014). "MAGIC gamma-ray and multi-frequency observations of flat spectrum radio quasar PKS 1510-089 in early 2012". In: 569, A46, A46. DOI: 10.1051/0004-6361/201423484. arXiv: 1401.5646 [astro-ph.HE].

— (2015). "Multiwavelength observations of Mrk 501 in 2008". In: 573, A50, A50. DOI: 10.1051/0004-6361/201322906. arXiv: 1410.6391 [astro-ph.HE].

Aliu, E. et al. (2014). "A Three-year Multi-wavelength Study of the Very-high-energy γ-Ray Blazar 1ES 0229+200". In: 782, 13, p. 13. DOI: 10.1088/0004-637X/782/1/13. arXiv: 1312.6592 [astro-ph.HE].

Antonucci, R. (2011). "Thermal and Nonthermal Radio Galaxies". In: *ArXiv e-prints*. arXiv: 1101.0837.

Armstrong, P. et al. (1999). "The University of Durham Mark 6 Gamma Ray Telescope". In: *Experimental Astronomy* 9, pp. 51–80. eprint: astro-ph/9804212.

Arons, J., R. M. Kulsrud, and J. P. Ostriker (1975). "A multiple pulsar model for quasi-stellar objects and active galactic nuclei". In: 198, pp. 687–705. DOI: 10.1086/153647.

Atwood, W. B. et al. (2009). "The Large Area Telescope on the Fermi Gamma-Ray Space Telescope Mission". In: 697, pp. 1071–1102. DOI: 10.1088/0004-637X/697/2/1071. arXiv: 0902.1089 [astro-ph.IM].

Baade, W. and R. Minkowski (1954). "Identification of the Radio Sources in Cassiopeia, Cygnus A, and Puppis A." In: 119, p. 206. DOI: 10.1086/145812.

Baillon, P. et al. (1993). "Energy Spectrum of the Crab Nebula in the Multi-TeV Region". In: *International Cosmic Ray Conference* 1, p. 271.

Barrau, A. et al. (1998). "The CAT imaging telescope for very-high-energy gamma-ray astronomy." In: *Nuclear Instruments and Methods in Physics Research A* 416, pp. 278–292. DOI: 10.1016/S0168-9002(98)00749-9. eprint: astro-ph/9804046.

Begelman, M. C., R. D. Blandford, and M. J. Rees (1980). "Massive black hole binaries in active galactic nuclei". In: 287, pp. 307–309. DOI: 10.1038/287307a0.

— (1984). "Theory of extragalactic radio sources". In: *Reviews of Modern Physics* 56, pp. 255–351. DOI: 10.1103/RevModPhys.56.255.

Benitez, E. et al. (2015). "An eclipsing binary black hole candidate system in the blazar Mrk 421". In: *ArXiv e-prints*. arXiv: 1512.01219.

Bentz, M. C. et al. (2013). "The Low-luminosity End of the Radius-Luminosity Relationship for Active Galactic Nuclei". In: 767, 149, p. 149. DOI: 10.1088/0004-637X/767/2/149. arXiv: 1303.1742.

Bhatta, G. et al. (2016). "Detection of Possible Quasi-periodic Oscillations in the Long-term Optical Light Curve of the BL Lac Object OJ 287". In: 832, 47, p. 47. DOI: 10.3847/0004-637X/832/1/47. arXiv: 1609.02388 [astro-ph.HE].

Biretta, J. A., W. B. Sparks, and F. Macchetto (1999). "Hubble Space Telescope Observations of Superluminal Motion in the M87 Jet". In: 520, pp. 621–626. DOI: 10.1086/307499.

Biteau, Jonathan (2013). "A window on stochastic processes and gamma-ray cosmology through spectral and temporal studies of AGN observed with H.E.S.S." PhD thesis. Ecole Polytechnique.

Bjornsson, C.-I. and G. R. Blumenthal (1982). "Spectral polarization properties of optically thin synchrotron radiation". In: 259, pp. 805–819. DOI: 10.1086/160216.

Blackett, P. M. S. (1948). "A possible contribution to the night sky from the Cerenkov radiation emitted by cosmic rays". In: *The Emission Spectra of the Night Sky and Aurorae*, p. 34.

Blandford, R. D. and A. Königl (1979a). "A model for the knots in the M87 jet". In: 20, pp. 15–21.

— (1979b). "Relativistic jets as compact radio sources". In: 232, pp. 34–48. DOI: 10.1086/157262.

Blandford, R. D. and C. F. McKee (1982). "Reverberation mapping of the emission line regions of Seyfert galaxies and quasars". In: 255, pp. 419–439. DOI: 10.1086/159843.

Blandford, R. D. and D. G. Payne (1982). "Hydromagnetic flows from accretion discs and the production of radio jets". In: 199, pp. 883–903. DOI: 10.1093/mnras/199.4.883.

Blandford, R. D. and R. L. Znajek (1977). "Electromagnetic extraction of energy from Kerr black holes". In: 179, pp. 433–456. DOI: 10.1093/mnras/179.3.433.

Bogovalov, S. and K. Tsinganos (2001). "Magnetically collimated jets with high mass flux". In: 325, pp. 249–256. DOI: 10.1046/j.1365-8711.2001.04412.x. eprint: astro-ph/0102250.

Bogovalov, S. V. (2001). "Acceleration and collimation of relativistic plasmas ejected by fast rotators". In: 371, pp. 1155–1168. DOI: 10.1051/0004-6361:20010201. eprint: astro-ph/0102415.

Bolton, J. G. and G. J. Stanley (1948). "Variable Source of Radio Frequency Radiation in the Constellation of Cygnus". In: 161, pp. 312–313. DOI: 10.1038/161312b0.

Bonning, E. et al. (2012). "SMARTS Optical and Infrared Monitoring of 12 Gamma-Ray Bright Blazars". In: 756, 13, p. 13. DOI: 10.1088/0004-637X/756/1/13. arXiv: 1201.4380 [astro-ph.HE].

Bonnoli, G. et al. (2015). "An emerging population of BL Lacs with extreme properties: towards a class of EBL and cosmic magnetic field probes?" In: 451, pp. 611–621. DOI: 10.1093/mnras/stv953. arXiv: 1501.01974 [astro-ph.HE].

Böttcher, M. (2005). "A Hadronic Synchrotron Mirror Model for the "Orphan" TeV Flare in 1ES 1959+650". In: 621, pp. 176–180. DOI: 10.1086/427430. eprint: astro-ph/0411248.

Böttcher, M., C. D. Dermer, and J. D. Finke (2008). "The Hard VHE γ-Ray Emission in High-Redshift TeV Blazars: Comptonization of Cosmic Microwave Background Radiation in an Extended Jet?" In: 679, L9, p. L9. DOI: 10.1086/588780. arXiv: 0804.3515.

Böttcher, M. et al. (2013). "Leptonic and Hadronic Modeling of Fermi-detected Blazars". In: 768, 54, p. 54. DOI: 10.1088/0004-637X/768/1/54. arXiv: 1304.0605 [astro-ph.HE].

Burbidge, G. R. (1961). "Galactic Explosions as Sources of Radio Emission". In: 190, pp. 1053–1056. DOI: 10.1038/1901053a0.

Cameron, A. G. W. (1962). "Star Formation in Elliptical Galaxies and Intense Radio Sources". In: 194, pp. 963–964. DOI: 10.1038/194963a0.

Caproni, A., Z. Abraham, and H. Monteiro (2013). "Parsec-scale jet precession in BL Lacertae (2200+420)". In: 428, pp. 280–290. DOI: 10.1093/mnras/sts014. arXiv: 1210.2286 [astro-ph.HE].

Carrigan, S. et al. (2013). "The H.E.S.S. Galactic Plane Survey - maps, source catalog and source population". In: *ArXiv e-prints*. arXiv: 1307.4690 [astro-ph.HE].

Cerruti, M. et al. (2012). "A mixed lepto-hadronic scenario for PKS 2155-304". In: *American Institute of Physics Conference Series*. Ed. by F. A. Aharonian, W. Hofmann, and F. M. Rieger. Vol. 1505. American Institute of Physics Conference Series, pp. 635–638. DOI: 10.1063/1.4772340. arXiv: 1210.5024 [astro-ph.HE].

Cerruti, M. et al. (2016). "Target of Opportunity observations of blazars with H.E.S.S. ". In: *ArXiv e-prints*. arXiv: 1610.05523 [astro-ph.HE].

Chadwick, P. M. et al. (1999). "Very High Energy Gamma Rays from PKS 2155-304". In: 513, pp. 161–167. DOI: 10.1086/306862.

Chakraborty, N. et al. (2015). "Rapid variability at very high energies in Mrk 501". In: *Proceedings of the 34th International Cosmic Ray Conference (ICRC2015), ArXiv e-prints (arXiv:1509.04893)*. arXiv: 1509.04893 [astro-ph.HE].

Chalme-Calvet, Raphaël (2015). "Etalonnage du cinquieme telescope de l'experience H.E.S.S. et observation du Centre Galactique au-dela de 30 GeV". PhD thesis. Universite Paris 6 - Pierre et Marie Curie.

Chatterjee, R. et al. (2009). "Disk-Jet Connection in the Radio Galaxy 3C 120". In: 704, pp. 1689–1703. DOI: 10.1088/0004-637X/704/2/1689. arXiv: 0909.2051 [astro-ph.HE].

Chatterjee, R. et al. (2011). "Connection Between the Accretion Disk and Jet in the Radio Galaxy 3C 111". In: 734, 43, p. 43. DOI: 10.1088/0004-637X/734/1/43. arXiv: 1104.0663 [astro-ph.HE].

Chevalier, J. et al. (2015). "Long term variability of the blazar PKS 2155-304". In: *ArXiv e-prints*. arXiv: 1509.03104 [astro-ph.HE].

Clavel, J. et al. (1991). "Steps toward determination of the size and structure of the broad-line region in active galactic nuclei. I - an 8 month campaign of monitoring NGC 5548 with IUE". In: 366, pp. 64–81. DOI: 10.1086/169540.

Cohen, M., R. G. Walker, and F. C. Witteborn (1992). "Spectral irradiance calibration in the infrared. II - Alpha Tau and the recalibration of the IRAS low resolution spectrometer". In: 104, pp. 2030–2044. DOI: 10.1086/116379.

Cohen, M. H. et al. (1971). "The Small-Scale Structure of Radio Galaxies and Quasi-Stellar Sources at 3.8 Centimeters". In: 170, p. 207. DOI: 10.1086/151204.

Costamante, L. and G. Ghisellini (2002). "TeV candidate BL Lac objects". In: 384, pp. 56–71. DOI: 10.1051/0004-6361:20011749. eprint: astro-ph/0112201.

Daum, A., G. Hermann, and HEGRA Collaboration (1997). "The Stereoscopic System of Imaging Atmospheric Cherenkov Telescopes of the HEGRA-Collaboration". In: *International Cosmic Ray Conference* 5, p. 117.

de Naurois, M. and L. Rolland (2009). "A high performance likelihood reconstruction of γ-rays for imaging atmospheric Cherenkov telescopes". In: *Astroparticle Physics* 32, pp. 231–252. DOI: 10.1016/j.astropartphys.2009.09.001. arXiv: 0907.2610 [astro-ph.IM].

Dermer, C. D. (1986). "Secondary production of neutral pi-mesons and the diffuse galactic gamma radiation". In: 157, pp. 223–229.

Dietrich, M. et al. (1993). "Steps toward determination of the size and structure of the broad-line region in active galactic nuclei. IV - Intensity variations of the optical emission lines of NGC 5548". In: 408, pp. 416–427. DOI: 10.1086/172599.

Domínguez, A. et al. (2011). "Extragalactic background light inferred from AEGIS galaxy-SED-type fractions". In: 410, pp. 2556–2578. DOI: 10.1111/j.1365-2966.2010.17631.x. arXiv: 1007.1459.

Doğan, S. et al. (2015). "Tearing up a misaligned accretion disc with a binary companion". In: 449, pp. 1251–1258. DOI: 10.1093/mnras/stv347. arXiv: 1502.05410 [astro-ph.HE].

Dubus, G. et al. (2013). "Surveys with the Cherenkov Telescope Array". In: *Astroparticle Physics* 43, pp. 317–330. DOI: 10.1016/j.astropartphys.2012.05.020. arXiv: 1208.5686 [astro-ph.HE].

Edelson, R. A. and J. H. Krolik (1988). "The discrete correlation function - A new method for analyzing unevenly sampled variability data". In: 333, pp. 646–659. DOI: 10.1086/166773.

Edge, D. O. et al. (1959). "A survey of radio sources at a frequency of 159 Mc/s." In: 68, pp. 37–60.

Elvis, M. et al. (1992). "The Einstein Slew Survey". In: 80, pp. 257–303. DOI: 10.1086/191665.

Errando, M. et al. (2008). "Discovery of very high energy gamma-rays from the flat spectrum radio quasar 3C 279 with the MAGIC telescope". In: *American Institute of Physics Conference Series*. Ed. by F. A. Aharonian, W. Hofmann, and F. Rieger. Vol. 1085. American Institute of Physics Conference Series, pp. 423–426. DOI: 10.1063/1.3076698. arXiv: 0901.3275 [astro-ph.HE].

Falomo, R., J. E. Pesce, and A. Treves (1993). "The environment of the BL Lacertae object PKS 2155-304". In: 411, pp. L63–L66. DOI: 10.1086/186913.

Fanaroff, B. L. and J. M. Riley (1974). "The morphology of extragalactic radio sources of high and low luminosity". In: 167, 31P–36P. DOI: 10.1093/mnras/167.1.31P.

Ferrara, E. C. et al. (2015). "The Fermi Large Area Telescope Third Gamma-ray Source Catalog". In: *IAU General Assembly* 22, 2255765, p. 2255765.

Fichtel, C. E. et al. (1975). "High-energy gamma-ray results from the second small astronomy satellite". In: 198, pp. 163–182. DOI: 10.1086/153590.

Finke, J. D. and P. A. Becker (2014). "Fourier Analysis of Blazar Variability". In: 791, 21, p. 21. DOI: 10.1088/0004-637X/791/1/21. arXiv: 1406.2333.

Fossati, G. et al. (1998). "A unifying view of the spectral energy distributions of blazars". In: 299, pp. 433–448. DOI: 10.1046/j.1365-8711.1998.01828.x. eprint: astro-ph/9804103.

Fraija, N. et al. (2015). "Flaring activity of Mrk 421 in 2012 and 2013: orphan flare and multiwavelength analysis". In: *ArXiv e-prints*. arXiv: 1508.01438 [astro-ph.HE].

Franceschini, A., G. Rodighiero, and M. Vaccari (2008). "Extragalactic optical-infrared background radiation, its time evolution and the cosmic photon-photon opacity". In: 487, pp. 837–852. DOI: 10.1051/0004-6361:200809691. arXiv: 0805.1841.

Gaskell, C. M. (2004). "Lognormal X-Ray Flux Variations in an Extreme Narrow-Line Seyfert 1 Galaxy". In: 612, pp. L21–L24. DOI: 10.1086/424565.

Ghisellini, G. (2016). "The Blazar Sequence 2.0". In: *Galaxies* 4, p. 36. DOI: 10.3390/galaxies4040036. arXiv: 1609.08606 [astro-ph.HE].

Ghisellini, G. and F. Tavecchio (2008). "The blazar sequence: a new perspective". In: 387, pp. 1669–1680. DOI: 10.1111/j.1365-2966.2008.13360.x. arXiv: 0802.1918.

Ghisellini, G. et al. (1998). "A theoretical unifying scheme for gamma-ray bright blazars". In: 301, pp. 451–468. DOI: 10.1046/j.1365-8711.1998.02032.x. eprint: astro-ph/9807317.

Ghisellini, G. et al. (2014). "The power of relativistic jets is larger than the luminosity of their accretion disks". In: 515, pp. 376–378. DOI: 10.1038/nature13856. arXiv: 1411.5368 [astro-ph.HE].

Ghisellini, G. et al. (2017). "The Fermi blazar sequence". In: *ArXiv e-prints*. arXiv: 1702.02571 [astro-ph.HE].

Giebels, B. and B. Degrange (2009). "Lognormal variability in BL Lacertae". In: 503, pp. 797–799. DOI: 10.1051/0004-6361/200912303. arXiv: 0907.2425 [astro-ph.CO].

Giebels, B., G. Dubus, and B. Khélifi (2007). "Unveiling the X-ray/TeV engine in Mkn 421". In: 462, pp. 29–41. DOI: 10.1051/0004-6361:20066134. eprint: astro-ph/0610270.

Gilmore, R. C. et al. (2009). "GeV gamma-ray attenuation and the high-redshift UV background". In: 399, pp. 1694–1708. DOI: 10.1111/j.1365-2966.2009.15392.x. arXiv: 0905.1144.

Giommi, P., S. G. Ansari, and A. Micol (1995). "Radio to X-ray energy distribution of BL Lacertae objects." In: 109.

González, M. M. (2011). "The High Altitude Gamma Ray Observatory, HAWC". In: *Revista Mexicana de Astronomia y Astrofisica Conference Series*. Vol. 40. Revista Mexicana de Astronomia y Astrofisica Conference Series, pp. 141–144.

Goret, P. et al. (1993). "Observations of TeV gamma rays from the Crab nebula". In: 270, pp. 401–406.

Goyal, A. et al. (2017). "Multi-wavelength variability study of the classical BL Lac object PKS 0735+178 on timescales ranging from decades to minutes". In: *ArXiv e-prints*. arXiv: 1702.02504 [astro-ph.HE].

Greenstein, J. L. and T. A. Matthews (1963). "Redshift of the Radio Source 3C 48." In: 68, p. 279. DOI: 10.1086/109140.

Grenier, I. A. and A. K. Harding (2015). "Gamma-ray pulsars: A gold mine". In: *Comptes Rendus Physique* 16, pp. 641–660. DOI: 10.1016/j.crhy.2015.08.013. arXiv: 1509.08823 [astro-ph.HE].

H. E. S. S. Collaboration et al. (2014). "Flux upper limits for 47 AGN observed with H.E.S.S. in 2004-2011". In: 564, A9, A9. DOI: 10.1051/0004-6361/201322897. arXiv: 1402.2332.

H. E. S. S. Collaboration et al. (2016a). "Characterizing the gamma-ray long-term variability of PKS 2155-304 with H.E.S.S. and Fermi-LAT". In: *ArXiv e-prints*. arXiv: 1610.03311 [astro-ph.HE].

H. E. S. S. Collaboration et al. (2016b). "Gamma-ray blazar spectra with H.E.S.S. II mono analysis: the case of PKS 2155-304 and PG 1553+113". In: *ArXiv e-prints*. arXiv: 1612.01843 [astro-ph.HE].

H. E. S. S. Collaboration et al. (2017). "Characterizing the γ-ray long-term variability of PKS 2155-304 with H.E.S.S. and Fermi-LAT". In: 598, A39, A39. DOI: 10.1051/0004-6361/201629419. arXiv: 1610.03311 [astro-ph.HE].

Hanbury Brown, R., R. C. Jennison, and M. K. D. Gupta (1952). "Apparent Angular Sizes of Discrete Radio Sources: Observations at Jodrell Bank, Manchester". In: 170, pp. 1061–1063. DOI: 10.1038/1701061a0.

Hara, T. et al. (1993). "A 3.8 m imaging Cherenkov telescope for the TeV gamma-ray astronomy collaboration between Japan and Australia". In: *Nuclear Instruments and Methods in Physics Research A* 332, pp. 300–309. DOI: 10.1016/0168-9002(93)90774-C.

Hartman, R. C. et al. (1999). "The Third EGRET Catalog of High-Energy Gamma-Ray Sources". In: 123, pp. 79–202. DOI: 10.1086/313231.

Hazard, C., M. B. Mackey, and A. J. Shimmins (1963). "Investigation of the Radio Source 3C 273 By The Method of Lunar Occultations". In: 197, pp. 1037–1039. DOI: 10.1038/1971037a0.

Heck, D. et al. (1998). *CORSIKA: a Monte Carlo code to simulate extensive air showers.*

Hervet, O., C. Boisson, and H. Sol (2015). "Linking radio and gamma-ray emission in Ap Librae". In: 578, A69, A69. DOI: 10.1051/0004-6361/201425330. arXiv: 1503.01377 [astro-ph.HE].

H.E.S.S. Collaboration et al. (2013). "H.E.S.S. discovery of VHE γ-rays from the quasar PKS 1510-089". In: 554, A107, A107. DOI: 10.1051/0004-6361/201321135. arXiv: 1304.8071 [astro-ph.HE].

H.E.S.S. Collaboration et al. (2015). "The high-energy γ-ray emission of AP Librae". In: 573, A31, A31. DOI: 10.1051/0004-6361/201321436. arXiv: 1410.5897 [astro-ph.HE].

HESS Collaboration et al. (2016). "Acceleration of petaelectronvolt protons in the Galactic Centre". In: 531, pp. 476–479. DOI: 10.1038/nature17147. arXiv: 1603.07730 [astro-ph.HE].

Hewitt, J. W. and M. Lemoine-Goumard (2015). "Observations of supernova remnants and pulsar wind nebulae at gamma-ray energies". In: *Comptes Rendus Physique* 16, pp. 674–685. DOI: 10.1016/j.crhy.2015.08.015. arXiv: 1510.01213 [astro-ph.HE].

Hey, J. S., S. J. Parsons, and J. W. Phillips (1946). "Fluctuations in Cosmic Radiation at Radio-Frequencies". In: 158, p. 234. DOI: 10.1038/158234a0.

Hillas, A. M. (1985). "Cerenkov light images of EAS produced by primary gamma". In: *International Cosmic Ray Conference* 3.

Hoyle, F. and W. A. Fowler (1963a). "Nature of Strong Radio Sources". In: 197, pp. 533–535. DOI: 10.1038/197533a0.

— (1963b). "On the nature of strong radio sources". In: 125, p. 169. DOI: 10.1093/mnras/125.2.169.

Jennison, R. C. and M. K. Das Gupta (1953). "Fine Structure of the Extra-terrestrial Radio Source Cygnus I". In: 172, pp. 996–997. DOI: 10.1038/172996a0.

Kalberla, P. M. W. et al. (2005). "The Leiden/Argentine/Bonn (LAB) Survey of Galactic HI. Final data release of the combined LDS and IAR surveys with improved stray-radiation corrections". In: 440, pp. 775–782. DOI: 10.1051/0004-6361:20041864. eprint: astro-ph/0504140.

Kastendieck, M. A., M. C. B. Ashley, and D. Horns (2011). "Long-term optical variability of PKS 2155-304". In: 531, A123, A123. DOI: 10.1051/0004-6361/201015918. arXiv: 1108.1346 [astro-ph.HE].

Kataoka, J. et al. (2001). "Characteristic X-Ray Variability of TeV Blazars: Probing the Link between the Jet and the Central Engine". In: 560, pp. 659–674. DOI: 10.1086/322442. eprint: astro-ph/0105022.

Kaufmann, S., S. J. Wagner, and O. Tibolla (2013). "Discovery of an Extended X-Ray Jet in AP Librae". In: 776, 68, p. 68. DOI: 10.1088/0004-637X/776/2/68. arXiv: 1309.6893 [astro-ph.HE].

Kelner, S. R., F. A. Aharonian, and V. V. Bugayov (2006). "Energy spectra of gamma rays, electrons, and neutrinos produced at proton-proton interactions in the very high energy regime". In: 74.3, 034018, p. 034018. DOI: 10.1103/PhysRevD.74.034018. eprint: astro-ph/0606058.

Kertzman, M. P. and G. H. Sembroski (1994). "Computer simulation methods for investigating the detection characteristics of TeV air Cherenkov telescopes". In: *Nuclear Instruments and Methods in Physics Research A* 343, pp. 629–643. DOI: 10.1016/0168-9002(94)90247-X.

Kieffer, Matthieu (2015). "Recherche indirecte de matiere noir avec l'experience H.E.S.S." PhD thesis. Universite Paris 6 - Pierre et Marie Curie.

King, A. R., J. E. Pringle, and J. A. Hofmann (2008). "The evolution of black hole mass and spin in active galactic nuclei". In: 385, pp. 1621–1627. DOI: 10.1111/j.1365-2966.2008.12943.x. arXiv: 0801.1564.

King, A. R. et al. (2004). "Variability in black hole accretion discs". In: 348, pp. 111–122. DOI: 10.1111/j.1365-2966.2004.07322.x. eprint: arXiv:astro-ph/0311035.

Knight, C. A. et al. (1971). "Detection of double-source structure in the nucleus of the quasi-stellar radio sources 3C 279." In: *Bulletin of the American Astronomical Society*. Vol. 3. P. 416.

Kollatschny, W. et al. (2001). "Short-term emission line and continuum variations in Mrk 110". In: 379, pp. 125–135. DOI: 10.1051/0004-6361:20011323. eprint: astro-ph/0109470.

Kraushaar, W. L. et al. (1972). "High-Energy Cosmic Gamma-Ray Observations from the OSO-3 Satellite". In: 177, p. 341. DOI: 10.1086/151713.

Lawrence, A. and M. Elvis (1982). "Obscuration and the various kinds of Seyfert galaxies". In: 256, pp. 410–426. DOI: 10.1086/159918.

Le Bohec, S. et al. (1998). "A new analysis method for very high definition imaging atmospheric Cherenkov telescopes as applied to the CAT telescope." In: *Nuclear Instruments and Methods in Physics Research A* 416, pp. 425–437. DOI: 10.1016/S0168-9002(98)00750-5. eprint: astro-ph/9804133.

Ledlow, M. J. and F. N. Owen (1996). "Optical Properties of FRI Radio Galaxies". In: *Extragalactic Radio Sources*. Ed. by R. D. Ekers, C. Fanti, and L. Padrielli. Vol. 175. IAU Symposium, p. 238.

Lehto, H. J. and M. J. Valtonen (1996). "OJ 287 Outburst Structure and a Binary Black Hole Model". In: 460, p. 207. DOI: 10.1086/176962.

Li, T.-P. and Y.-Q. Ma (1983). "Analysis methods for results in gamma-ray astronomy". In: 272, pp. 317–324. DOI: 10.1086/161295.

Lomb, N. R. (1976). "Least-squares frequency analysis of unequally spaced data". In: 39, pp. 447–462. DOI: 10.1007/BF00648343.

Longair, M. S. (2011). *High Energy Astrophysics*.

Lynden-Bell, D. (1969). "Galactic Nuclei as Collapsed Old Quasars". In: 223, pp. 690–694. DOI: 10.1038/223690a0.

Lyubarskii, Y. E. (1997). "Flicker noise in accretion discs". In: 292, p. 679.

Maoz, D. et al. (1993). "Variations of the ultraviolet Fe II and Balmer continuum emission in the Seyfert galaxy NGC 5548". In: 404, pp. 576–583. DOI: 10.1086/172310.

Marti-Vidal, I. et al. (2013). "Jet precession in the active nucleus of M81. Ongoing VLBI monitoring". In: *ArXiv e-prints*. arXiv: 1301.4782 [astro-ph.HE].

Massaro, E. et al. (2009). "Roma-BZCAT: a multifrequency catalogue of blazars". In: 495, pp. 691–696. DOI: 10.1051/0004-6361:200810161. arXiv: 0810.2206.

Matthews, TA et al. (1961). "American Astronomical Society Meeting, New York". In: *Sky and Telescope* 21, p. 148.

McHardy, I. M. et al. (2006). "Active galactic nuclei as scaled-up Galactic black holes". In: 444, pp. 730–732. DOI: 10.1038/nature05389. eprint: arXiv:astro-ph/0612273.

Meyer, E. T. and M. Georganopoulos (2014). "Fermi Rules Out the Inverse Compton/CMB Model for the Large-scale Jet X-Ray Emission of 3C 273". In: 780, L27, p. L27. DOI: 10.1088/2041-8205/780/2/L27. arXiv: 1307.8421 [astro-ph.HE].

Mücke, A. and R. J. Protheroe (2001). "Neutrino Emission from HBLs and LBLs". In: *International Cosmic Ray Conference* 3, p. 1153. eprint: astro-ph/0105543.

Naurois, Mathieu De (2012). "Very High Energy astronomy from H.E.S.S. to CTA. Opening of a new astronomical window on the non-thermal Universe". PhD thesis. Laboratoire Leprince-Ringuet.

Neronov, A. and D. V. Semikoz (2009). "Sensitivity of γ-ray telescopes for detection of magnetic fields in the intergalactic medium". In: 80.12, 123012, p. 123012. DOI: 10.1103/PhysRevD.80.123012. arXiv: 0910.1920 [astro-ph.CO].

Nixon, C. and A. King (2013). "Do Jets Precess... or Even Move at All?" In: 765, L7, p. L7. DOI: 10.1088/2041-8205/765/1/L7. arXiv: 1301.5321 [astro-ph.HE].

Oda, M. et al. (1971). "X-Ray Pulsations from Cygnus X-1 Observed from UHURU". In: 166, p. L1. DOI: 10.1086/180726.

Oke, J. B. (1963). "Absolute Energy Distribution in the Optical Spectrum of 3C 273". In: 197, pp. 1040–1041. DOI: 10.1038/1971040b0.

Padovani, P. (2007). "The blazar sequence: validity and predictions". In: 309, pp. 63–71. DOI: 10.1007/s10509-007-9455-2. eprint: astro-ph/0610545.

Padovani, P. et al. (2002). "BeppoSAX Observations of Synchrotron X-Ray Emission from Radio Quasars". In: 581, pp. 895–911. DOI: 10.1086/344406. eprint: astro-ph/0208501.

Pelletier, G. (2004). "Black Hole Induced Ejections". In: *ArXiv Astrophysics e-prints*. eprint: astro-ph/0405113.

Peterson, B. M. and A. Wandel (2000). "Evidence for Supermassive Black Holes in Active Galactic Nuclei from Emission-Line Reverberation". In: 540, pp. L13–L16. DOI: 10.1086/312862. eprint: astro-ph/0007147.

Peterson, B. M. et al. (1991). "Steps toward determination of the size and structure of the broad-line region in active galactic nuclei. II - an intensive study of NGC 5548 at optical wavelengths". In: 368, pp. 119–137. DOI: 10.1086/169675.

Piron, F. et al. (2001). "Temporal and spectral gamma-ray properties of <ASTROBJ>Mkn 421</ASTROBJ> above 250 GeV from CAT observations between 1996 and 2000". In: 374, pp. 895–906. DOI: 10.1051/0004-6361:20010798. eprint: astro-ph/0106196.

Pudritz, R. E., M. J. Hardcastle, and D. C. Gabuzda (2012). "Magnetic Fields in Astrophysical Jets: From Launch to Termination". In: 169, pp. 27–72. DOI: 10.1007/s11214-012-9895-z. arXiv: 1205.2073 [astro-ph.HE].

Punch, M. et al. (1992). "Detection of TeV photons from the active galaxy Markarian 421". In: 358, p. 477. DOI: 10.1038/358477a0.

Quinn, J. et al. (1996). "Detection of Gamma Rays with E 300 GeV from Markarian 501". In: 456, p. L83. DOI: 10.1086/309878.

Raue, M. and et al. (2012). "THE 2010 M 87 VHE FLARE AND ITS ORIGIN: THE MULTI-WAVELENGTH PICTURE". In: *International Journal of Modern Physics: Conference Series* 08, pp. 184–189. DOI: 10.1142/S2010194512004588. eprint: http://www.worldscientific.com/doi/pdf/10.1142/S2010194512004588. URL: http://www.worldscientific.com/doi/abs/10.1142/S2010194512004588.

Rees, M. J. (1966). "Appearance of Relativistically Expanding Radio Sources". In: 211, pp. 468–470. DOI: 10.1038/211468a0.

Rieger, F. M. (2004). "On the Geometrical Origin of Periodicity in Blazar-type Sources". In: 615, pp. L5–L8. DOI: 10.1086/426018. eprint: astro-ph/0410188.

Rolland, Loïc (2005). "Etalonnage des cameras de l'experience d'astronomie gamma H.E.S.S. et observations du Centre Galactique au-dela de 100 GeV". PhD thesis. Universite Paris 6 - Pierre et Marie Curie.

Rowan-Robinson, M. (1977). "On the unity of activity in galaxies". In: 213, pp. 635–647. DOI: 10.1086/155195.

Rybicki, G. B. and A. P. Lightman (1979). *Radiative processes in astrophysics*.

Sahu, S., A. F. O. Oliveros, and J. C. Sanabria (2013). "Hadronic-origin orphan TeV flare from 1ES 1959+650". In: 87.10, 103015, p. 103015. DOI: 10.1103/PhysRevD.87.103015. arXiv: 1305.4985 [hep-ph].

Salpeter, E. E. (1964). "Accretion of Interstellar Matter by Massive Objects." In: 140, pp. 796–800. DOI: 10.1086/147973.

Sanchez, D. A. and C. Deil (2013). "Enrico : a Python package to simplify Fermi-LAT analysis". In: *ArXiv e-prints (arXiv: 1307.4534)*. arXiv: 1307.4534 [astro-ph.IM].

Sanchez, D. A. et al. (2015). "From radio to TeV: the surprising spectral energy distribution of AP Librae". In: 454, pp. 3229–3239. DOI: 10.1093/mnras/stv2151. arXiv: 1506.00965 [astro-ph.HE].

Sanchez, David (2010). "Etude et modelisation des noyaux actifs de galaxie les plus energetiques avec le satellite Fermi". PhD thesis. Ecole Polytechnique.

Sandrinelli, A., S. Covino, and A. Treves (2014). "Quasi-periodicities of the BL Lacertae Object PKS 2155-304". In: 793, L1, p. L1. DOI: 10.1088/2041-8205/793/1/L1.

Scargle, J. D. (1982). "Studies in astronomical time series analysis. II - Statistical aspects of spectral analysis of unevenly spaced data". In: 263, pp. 835–853. DOI: 10.1086/160554.

— (2002). "Bayesian estimation of time series lags and structure". In: *Bayesian Inference and Maximum Entropy Methods in Science and Engineering*. Ed. by R. L. Fry. Vol. 617. American Institute of Physics Conference Series, pp. 23–35. DOI: 10.1063/1.1477036. eprint: math/0111127.

Schlafly, E. F. and D. P. Finkbeiner (2011). "Measuring Reddening with Sloan Digital Sky Survey Stellar Spectra and Recalibrating SFD". In: 737, 103, p. 103. DOI: 10.1088/0004-637X/737/2/103. arXiv: 1012.4804 [astro-ph.GA].

Schmidt, M. (1963). "3C 273 : A Star-Like Object with Large Red-Shift". In: 197, p. 1040. DOI: 10.1038/1971040a0.

Schwartz, D. A. et al. (1979). "X-ray emitting BL Lacertae objects located by the scanning modulation collimator experiment on HEAO 1". In: 229, pp. L53–L57. DOI: 10.1086/182929.

Seyfert, C. K. (1943). "Nuclear Emission in Spiral Nebulae." In: 97, p. 28. DOI: 10.1086/144488.

Shields, G. A. (1999). "A Brief History of Active Galactic Nuclei". In: 111, pp. 661–678. DOI: 10.1086/316378. eprint: astro-ph/9903401.

Sillanpaa, A. et al. (1988). "OJ 287 - Binary pair of supermassive black holes". In: 325, pp. 628–634. DOI: 10.1086/166033.

Sol, H. et al. (2013). "Active Galactic Nuclei under the scrutiny of CTA". In: *Astroparticle Physics* 43, pp. 215–240. DOI: 10.1016/j.astropartphys.2012.12.005. arXiv: 1304.3024 [astro-ph.HE].

Spitzer Jr., L. and W. C. Saslaw (1966). "On the Evolution of Galactic Nuclei". In: 143, p. 400. DOI: 10.1086/148523.

Stirling, A. M. et al. (2003). "Discovery of a precessing jet nozzle in BL Lacertae". In: 341, pp. 405–422. DOI: 10.1046/j.1365-8711.2003.06448.x.

Swanenburg, B. N. (1981). "Gamma ray astronomy with COS-B". In: *Annals of the New York Academy of Sciences* 375, pp. 381–390. DOI: 10.1111/j.1749-6632.1981.tb33708.x.

Swanenburg, B. N. et al. (1981). "Second COS B catalog of high-energy gamma-ray sources". In: 243, pp. L69–L73. DOI: 10.1086/183445.

Takahashi, T., Y. Uchiyama, and Ł. Stawarz (2013). "Multiwavelength Astronomy and CTA: X-rays". In: *Astroparticle Physics* 43, pp. 142–154. DOI: 10.1016/j.astropartphys.2012.05.010. arXiv: 1205.2423 [astro-ph.HE].

Tatischeff, V., A. Decourchelle, and G. Maurin (2012). "Nonthermal X-rays from low-energy cosmic rays: application to the 6.4 keV line emission from the Arches cluster region". In: 546, A88, A88. DOI: 10.1051/0004-6361/201219016. arXiv: 1210.2108 [astro-ph.HE].

Terlevich, R. and J. Melnick (1985). "Warmers - The missing link between Starburst and Seyfert galaxies". In: 213, pp. 841–856. DOI: 10.1093/mnras/213.4.841.

Timmer, J. and M. Koenig (1995). "On generating power law noise." In: 300, p. 707.

Tluczykont, M. et al. (2010). "Long-term lightcurves from combined unified very high energy γ-ray data". In: 524, A48, A48. DOI: 10.1051/0004-6361/201015193. arXiv: 1010.5659 [astro-ph.HE].

Trichard, Cyril (2015). "Etude du rayonnement gamma de vestiges de supernova en interaction avec des nuages moleculaires et optimisation de l'analyse des donnees H.E.S.S." PhD thesis. Universite Grenoble Alpes.

Urry, C. M. and P. Padovani (1995). "Unified Schemes for Radio-Loud Active Galactic Nuclei". In: 107, 803 ff. DOI: 10.1086/133630. eprint: arXiv:astro-ph/9506063.

Uttley, P. and I. M. McHardy (2001). "The flux-dependent amplitude of broadband noise variability in X-ray binaries and active galaxies". In: 323, pp. L26–L30. DOI: 10.1046/j.1365-8711.2001.04496.x. eprint: astro-ph/0103367.

Vaughan, S. et al. (2003). "On characterizing the variability properties of X-ray light curves from active galaxies". In: 345, pp. 1271–1284. DOI: 10.1046/j.1365-2966.2003.07042.x. eprint: astro-ph/0307420.

Vestrand, W. T., J. G. Stacy, and P. Sreekumar (1995). "High-Energy Gamma Rays from the BL Lacertae Object PKS 2155-304". In: 454, p. L93. DOI: 10.1086/309790.

Wagner, S. J. and H.E.S.S. Collaboration (2010). "Detection of VHE Gamma-ray Emission from a Type 1 Quasar". In: *AAS/High Energy Astrophysics Division #11*. Vol. 11. AAS/High Energy Astrophysics Division, p. 27.06.

Weekes, T. C. et al. (1989). "Observation of TeV gamma rays from the Crab nebula using the atmospheric Cerenkov imaging technique". In: 342, pp. 379–395. DOI: 10.1086/167599.

Whitney, A. R. et al. (1971). "Quasars Revisited: Rapid Time Variations Observed Via Very-Long-Baseline Interferometry". In: *Science* 173, pp. 225–230. DOI: 10.1126/science.173.3993.225.

Wright, A. and R. Otrupcek (1990). "Parkes Catalog, 1990, Australia telescope national facility." In: *PKS Catalog (1990)*.

Zdziarski, A. A. and M. Böttcher (2015). "Hadronic models of blazars require a change of the accretion paradigm". In: 450, pp. L21–L25. DOI: 10.1093/mnrasl/slv039. arXiv: 1501.06124 [astro-ph.HE].

Zheng, Y. G. and C. Y. Yang (2016). "Modelling the multi-wavelength emission of flat-spectrum radio quasar 3C 279". In: 457, pp. 3535–3540. DOI: 10.1093/mnras/stw078. arXiv: 1607.05768 [astro-ph.HE].